

BOSTON UNIVERSITY
GRADUATE SCHOOL OF ARTS AND SCIENCES

Dissertation

FLOQUET ENGINEERING
IN PERIODICALLY DRIVEN CLOSED QUANTUM SYSTEMS
FROM DYNAMICAL LOCALISATION
TO ULTRACOLD TOPOLOGICAL MATTER

by

MARIN GEORGIEV BUKOV

M.Sc., Ludwig-Maximilians-Universität and Technische Universität, München 2013

Submitted in partial fulfillment of the
requirements for the degree of
Doctor of Philosophy

2017

© Copyright by
MARIN GEORGIEV BUKOV
2017

Approved by

First Reader

Anatoli Polkovnikov, Ph.D.
Professor of Physics

Second Reader

Emanuel Katz, Ph.D.
Professor of Physics

Acknowledgements

First and foremost, I want to thank Toli Polkovnikov for being such a great advisor, providing continuous support for me during my studies at BU, with his door open all the time! The enthusiasm and excitement he brings in while doing science is unrivalled. I got indispensable knowledge and advise from him not only on how to do great research, but also on what it takes to be a good scientist.

Throughout my PhD I also learned a lot from Mike Kolodrubetz and Luca D'Alessio, who were extremely helpful with studying periodically-driven systems – and without the help of which this thesis would not contain the information it does today. Most of the understanding about shaken systems I have, appeared as a result of the many interesting discussions we had during their stay at BU.

Special thanks go to Phil Weinberg for the numerous chats on physics but, more importantly, for teaching me how to code. The *QuSpin* project which lays the foundations for more than half the numerical work presented in this thesis was so much fun – it revealed a whole new world of coding and programming to me, and has a serious impact on my interests from now on.

I would further like to thank Eugene Demler for giving me the opportunity to collaborate on Floquet prethermalisation with him and his group. Many thanks to Michi Knap and Sarang Gopalakrishnan – for the hours they spent discussing with me various technical aspects and for continuously guiding me through the project.

I'm also grateful to David Huse and Markus Heyl for the time they devoted in helping me study and understand heating and thermalisation. I'd like to acknowledge Dima Abanin and Wen-Wei Ho, with whom I've had various interesting discussions during a great time

spent in Geneva.

In the year after this thesis was defended, I've had an unforgettable experience with Pankaj Mehta, Alex Day, Ching-hao Wang, and Dries Sels teaching ourselves Reinforcement Learning and various other Machine Learning techniques/algorithms in an extremely friendly and relaxed atmosphere. This helped me realise how much I enjoy doing research but also shape my future research interests. Frankly, this made for the most enjoyable period of my stay at BU as a PhD student!

Last but not least, I would also like to thank Alex, Ashish, Harshal, Manuel, Nabeel, Rajita, and Rashi for being there for me during all my stay at BU! Many, many thanks go to my friends Milena, Krum, Dani and especially to Stefan who took time to explain to me various concepts discussed in this thesis :) Thanks a lot, guys, for making sure I got to do things other than physics during the last four years!

FLOQUET ENGINEERING
IN PERIODICALLY DRIVEN CLOSED QUANTUM SYSTEMS
FROM DYNAMICAL LOCALISATION
TO ULTRACOLD TOPOLOGICAL MATTER

MARIN GEORGIEV BUKOV

Boston University, Graduate School of Arts and Sciences, 2017

Major Professor: Anatoli Polkovnikov, Ph.D., Professor of Physics

ABSTRACT

This dissertation presents a self-contained study of periodically-driven quantum systems. Following a brief introduction to Floquet theory, we introduce the inverse-frequency expansion, variants of which include the Floquet-Magnus, van Vleck, and Brillouin-Wigner expansions. We reveal that the convergence properties of these expansions depend strongly on the reference frame chosen, and relate the former to the existence of Floquet resonances in the quasienergy spectrum. The theoretical design and experimental realisation ('engineering') of novel Floquet Hamiltonians is discussed introducing three universal high-frequency limits for systems comprising single-particle and many-body linear and nonlinear models. The celebrated Schrieffer-Wolff transformation for strongly-correlated quantum systems is generalised to periodically-driven systems, and a systematic approach to calculate higher-order corrections to the Rotating Wave Approximation is presented. Next, we develop Floquet adiabatic perturbation theory from first principles, and discuss extensively the adiabatic state preparation and the corresponding leading-order non-adiabatic corrections. Special emphasis is thereby put on geometrical and topological objects, such as the Floquet Berry curvature and the Floquet Chern number obtained within linear response in the presence of the drive. Last, pre-thermalisation and thermalisation in closed, clean periodically-driven quantum systems are studied in detail, with the focus put on the crucial role of Floquet many-body resonances for energy absorption.

Contents

1	Introduction	1
2	Floquet Theory from a Modern Perspective	11
2.1	Stroboscopic and Non-Stroboscopic Time Evolution	11
2.1.1	The Stroboscopic Floquet Hamiltonian and the Stroboscopic Kick Operator	11
2.1.2	The Non-Stroboscopic Floquet Hamiltonian and the Non-Stroboscopic Kick Operator	15
2.1.3	A Case Study: Two-Level System in a Circularly Driven Magnetic Field	18
2.1.4	Stroboscopic versus Non-stroboscopic Dynamics	22
2.2	Inverse Frequency Expansions	30
2.2.1	The Floquet-Magnus Expansion for the Stroboscopic Floquet Hamiltonian	30
2.2.2	The van Vleck Expansion for the Non-Stroboscopic Floquet Hamiltonian.	33
2.2.3	The Brillouin-Wigner Inverse-Frequency Expansion	35
2.2.4	Floquet-Magnus vs. van Vleck Expansion: the Two-Level System in a Circularly Driven Magnetic Field Revisited	36
2.2.5	The Inverse Frequency Expansion in the Rotating Frame	39
2.3	Convergence of the Inverse-Frequency Expansion: a Collection of Facts and Ideas	44

2.3.1	Systems with Bounded Hamiltonians	46
2.3.2	Systems with Unbounded Hamiltonians: the Role of Resonances	50
3	Floquet Engineering	60
3.1	Universal High-Frequency Limits of Periodically Driven Systems	60
3.1.1	The Kapitza Class	60
3.1.2	The Dirac Class	76
3.1.3	The Dunlap-Kenkre Class	83
3.2	The van Vleck Inverse-Frequency Expansion as a Schrieffer-Wolff Transformation for Periodically-Driven Systems	121
3.2.1	A Two-Level System	121
3.2.2	Low Energy Heisenberg Physics in the Periodically Driven Fermi-Hubbard Model	129
3.2.3	Low Energy Kondo Physics in the Periodically Driven Anderson Model	151
3.2.4	Discussion	159
3.3	Resonant Driving: the Rotating Wave Approximation and Beyond	159
3.3.1	The Rabi Model and the Jaynes-Cummings Hamiltonian	160
3.3.2	Parametric Resonance from the Rotating Wave Approximation	163
3.3.3	The Inverse Frequency Expansion for Systems with Real Photon Absorption Processes: Taking Resonance into Account	167
4	Floquet Adiabatic Perturbation Theory and Geometry	173
4.1	Stroboscopic and Non-Stroboscopic Dynamics for an Adiabatic Ramping of the Drive	176
4.2	Floquet Adiabatic Perturbation Theory	178
4.2.1	Adiabatic Perturbation Theory (APT)	178
4.2.2	Floquet Adiabatic Perturbation Theory (FAPT)	180
4.2.3	Observables	187
4.2.4	Floquet Berry Curvature and Floquet Chern Number	189

4.3	Single-Particle Examples	190
4.3.1	Which Floquet Hamiltonian is the Adiabatically Connected One?	191
4.3.2	The Linearly Driven Harmonic Oscillator	193
4.3.3	The Quantum Kapitza Pendulum	197
4.3.4	A Nonequilibrium Topological Transition and the Thouless Energy Pump	206
4.4	Many-Body Examples	214
4.4.1	The Driven Transverse-Field Ising Model	215
4.4.2	The Driven Transverse-Field Ising Model in a Parallel Magnetic Field	219
4.5	Floquet Adiabatic Perturbation Theory and the Inverse-Frequency Expansion	223
4.6	Breakdown of FAPT for Resonantly Coupled Drives	229
4.7	Discussion	232
5	Prethermalisation and Thermalisation in Closed Floquet Systems	235
5.1	A Mechanism for Prethermalisation in Fermionic and Spin Systems	236
5.1.1	Quasi-Conserved Integrals of Motion	237
5.2	Prethermal Floquet Steady States and Parametric Instabilities in the Weakly-Interacting Bose-Hubbard Model	239
5.2.1	The Strongly-Driven Weakly-Interacting Bose-Hubbard Model	241
5.2.2	The Weak-Coupling Conserving Approximation	242
5.2.3	Stability diagram	247
5.2.4	Stroboscopic Prethermalisation	250
5.2.5	Validity of the Weak Coupling Conserving Approximation and Thermalisation Time Scales	255
5.2.6	Discussion	257
5.3	Infinite Time Behaviour: Thermalisation through Many-Body Resonances .	259
5.3.1	A Resonantly Driven Two-Band Model	261

5.3.2	Definitions for the Microscopic Observables and Entropies Pertinent to Heating.	263
5.3.3	Heating	266
5.3.4	Thermalisation – Temporal Fluctuations and Correlations	277
5.3.5	Floquet Many-Body Resonances	280
5.3.6	Discussion	293
6	Concluding Remarks	296
6.1	Outlook and Future Perspectives	296
6.2	A Collection of Open Problems in Closed Floquet Systems	301
A	Lattice vs. Continuum Models	304
B	Outline of the Derivation of the Floquet-Magnus and van Vleck Inverse-Frequency Expansions	308
B.1	The Floquet-Magnus Expansion	308
B.2	The van Vleck Expansion	309
C	Corrections to the Inverse-Frequency Floquet Hamiltonian for the Harper-Hofstadter Model	310
C.1	Corrections to the Effective Hamiltonian $H_F[t_0]$	310
C.1.1	First-order Coefficients for the 1D Driven Boson Model	310
C.1.2	First-order Coefficients for the Harper-Hofstadter Model	311
C.2	Corrections to the Effective Hamiltonian H_{eff}	312
C.2.1	First-order Coefficients for the 1D Driven Boson Model	312
C.2.2	First-order Coefficients for the Harper-Hofstadter Model	313
D	Details in the Derivation of Floquet Adiabatic Perturbation Theory	314
E	Exact Solution to the Harmonic Oscillator with Periodically Displaced Potential	316

E.0.1	Exact Floquet Solution	318
E.0.2	Exact Solution to the Ramped Problem	321
F	Floquet Theory for Periodic Step Driving Protocols	324
Bibliography		329
Curriculum Vitae		346

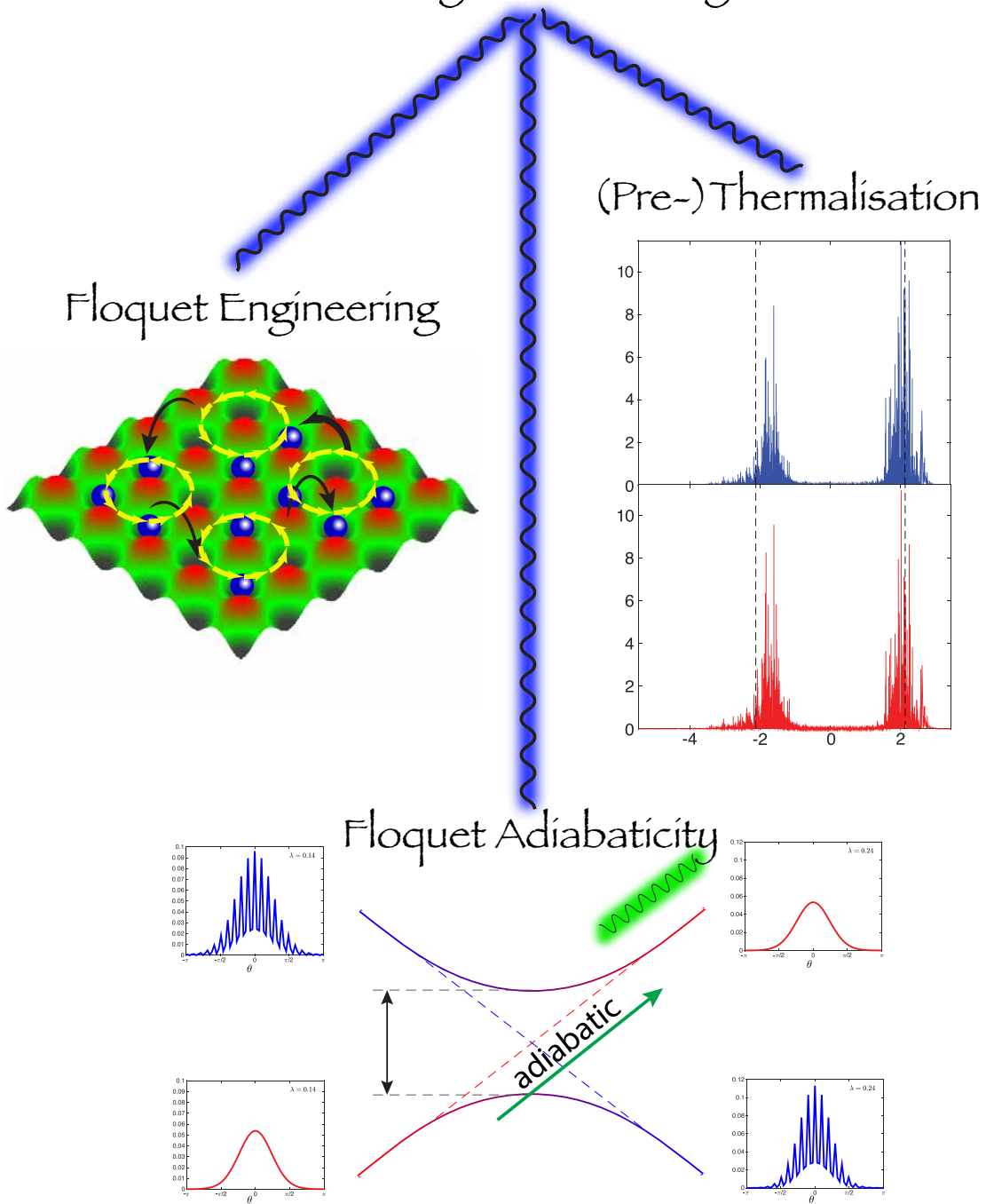
List of Abbreviations

APT	adiabatic perturbation theory
BEC	Bose-Einstein condensate
BHM	Bose-Hubbard model
BW	Brillouin-Wigner
DMRG ...	density matrix renormalisation group
ED	exact diagonalisation
EOM	equation(s) of motion
FAPT	Floquet adiabatic perturbation theory
FHM	Fermi-Hubbard model
FM	Floquet-Magnus
GS	ground state
HFE	high-frequency expansion
IPR	inverse participation ratio
nn	nearest-neighbour
nnn	next-nearest-neighbour
OBC/PBC	open/periodic boundary conditions
RHS/LHS	right- (left-)hand side
RWA	Rotating Wave approximation
SWT	Schrieffer-Wolff transformation
vV	van Vleck
WCCA ...	weak coupling conserving approximation
w.r.t.	with respect to

List of Publications Contributing to this Thesis

1. M. Bukov and A. Polkovnikov,
Stroboscopic versus non-stroboscopic dynamics in the Floquet realization of the Harper-Hofstadter model,
Physical Review A **90**, 043613 (2014).
2. M. Bukov, L. D'Alessio and A. Polkovnikov,
Universal high-frequency behaviour of periodically driven systems: from dynamical stabilization to Floquet engineering,
Advances in Physics, 2015, Vol. 64, No. 2, 139-226.
3. M. Bukov, S. Gopalakrishnan, M. Knap and E. Demler,
Prethermal Floquet Steady States and Instabilities in the Periodically Driven, Weakly Interacting Bose-Hubbard Model,
Physical Review Letters **115**, 205301 (2015).
4. M. Bukov, M. Kolodrubetz and A. Polkovnikov,
Schrieffer-Wolff Transformation for Periodically-Driven Systems: Strongly-Correlated Systems with Artificial Gauge Fields,
Physical Review Letters **116**, 125301 (2016).
5. M. Bukov, M. Heyl, D. A. Huse and A. Polkovnikov,
Heating and many-body resonances in a periodically-driven two-band system,
Physical Review B **93**, 155132 (2016).
6. P. Weinberg, M. Bukov, L. D'Alessio, A. Polkovnikov, S. Vajna and M. Kolodrubetz,
Adiabatic Perturbation Theory and Geometry of Periodically Driven Systems,
arXiv:1606.02229 (2016).

Periodically Driven Systems



Chapter 1

Introduction

The understanding of dynamics plays a central role in analysing the response of systems to periodic modulation. Such periodic systems, realized in a variety of settings from irradiation by lasers to application of periodic mechanical kicks, have been the subject of extensive experimental and theoretical study throughout the modern history of physics [1–4]. Prominent examples in mechanics include the [Kapitza pendulum](#) [5] and the closely related kicked rotor, whose dynamics feature tantalising integrability-to-chaos transitions as a function of the drive parameters. These and similar models also feature dynamical stabilization [5–7] and localization [8–17], among a variety of counter-intuitive effects induced by periodic modulations. In atomic physics, driving leads to reduced ionisation rates in systems irradiated by electromagnetic fields at high frequency and intensity [18–23], which can be traced back to decreased spreading of wave packets reported in periodically-driven systems [24, 25]. Last but not least, the effects of periodic drives on transport has recently become an active field of study, predicting non-trivial behaviour in more traditional condensed matter settings [26–31].

However, much remains to be understood in transferring these ideas to the many-body domain. The recent surge of activity in applying periodic drives to many body systems has spawned a new branch of quantum physics known as “Floquet engineering” [32, 33], i.e., the synthetic generation of novel Hamiltonians that are otherwise inaccessible in static condensed matter systems. For instance, periodic modulations have been reported to change the critical properties of systems, by either inducing critical points not present without the

drive, or by inducing a controllable dependence of the critical point on the drive parameters [34–38]. Concrete examples include the Dicke model [34], the Ising model [35], and the Haldane model [38–40]. Similarly, cold atom experiments in ‘shaken’ optical lattices have progressed to realise phenomena such as dynamical localisation and stabilisation [41–47], artificial gauge fields [48–55], topological [38, 39, 56–59] and spin-dependent [60] bands, topological pumps [61, 62], and spin-orbit coupling [63, 64]. These ideas are not restricted to cold atoms, as evidenced by Floquet topological insulators [65] and photonic topological insulators [66–68], the latter effectively obeying the Schrödinger equation with the additional spatial dimension playing the role of periodic time modulation. Future similar experiments in this vein are expected to produce synthetic Hamiltonians realizing Laughlin states, fractional topological insulators [69], and Weyl points [55, 70], realise quantum motors similar to quantum ratchets [71, 72], as well as other systems hard to create statically. Rather surprisingly, periodic driving protocols can also be important for non-driven systems, after a transformation to a rotating frame, which typically results in the emergence of fast-oscillating terms in the Hamiltonian. Floquet systems also appear naturally in digital quantum computation schemes, where one implements a continuous unitary evolution by effectively ‘trotterising’ it [73].

In the simplest case, one considers a single monochromatic driving protocol, characterised by a coupling strength (driving amplitude), and a single frequency $\Omega = 2\pi/T$. The dynamics of periodically driven systems can be highly complex even in few-body systems. Usually, it can be analysed in the two extreme regimes of slow and fast driving. In the former regime, the system almost adiabatically follows the instantaneous Hamiltonian. In the latter regime, where the driving frequency is fast compared to the natural frequencies of the non-driven model, the system typically feels an effective static potential, which can depend on the driving amplitude, c.f. Fig. 1.1. If one deviates from either of these limits, one expects that sufficiently complex systems would heat up, and eventually reach infinite temperature in the absence of a coupling to a heat bath. This has been confirmed numerically and analytically in different setups [74–80].

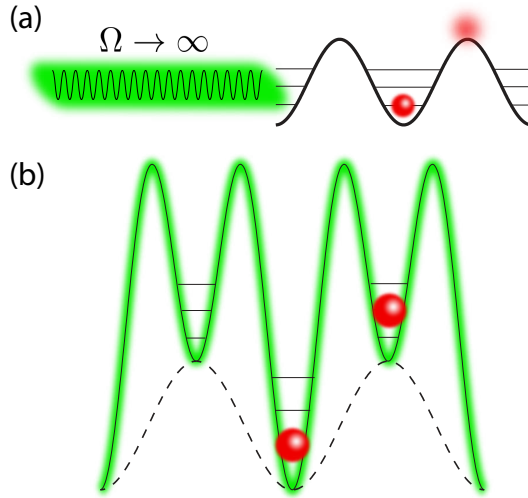


Figure 1.1: The application of a high-frequency periodic perturbation to a static Hamiltonian, (a), may lead to the emergence of an effective high-frequency Hamiltonian with renormalised parameters (b). The purpose of this thesis is to discuss under which conditions this is possible, and what types of effective Hamiltonians can be engineered in this way.

Away from the adiabatic limit, the analysis of periodically driven systems often relies on Floquet's theorem [81], which is very similar to Bloch's theorem in quantum mechanics:

Theorem (Floquet, 1883). *Let $t \mapsto H(t)$, $\mathbb{R} \rightarrow \mathbb{C}^{n \times n}$ be a continuous matrix-valued function with period T , i.e. $H(t+T) = H(t)$. Further, let $U(t)$ be the fundamental matrix of the first-order linear differential equation $i\partial_t \psi(t) = H(t)\psi(t)$. Then, $U(t+T)$ is also a fundamental matrix. Moreover, there exists a non-singular continuously differentiable matrix-valued function $t \mapsto P(t)$, $\mathbb{R} \rightarrow \mathbb{C}^{n \times n}$ with period T , and a constant (possibly complex-valued¹) matrix H_F , such that $U(t) = P(t)e^{-itH_F}$.*

Proof. Let us first check that $U(t+T)$ is indeed a fundamental matrix. We have

$$i\partial_t U(t+T) = i\dot{U}(t+T) = H(t+T)U(t+T) = H(t)U(t+T),$$

which proves the assertion. Since both $U(t)$ and $U(t+T)$ are fundamental matrices, they

¹Note that, Floquet's theorem does *not* require that the matrix $H(t)$ be hermitian. This is important in the studies of parametric resonance.

must be related by a static linear transformation $U_F \in \mathbb{C}^{n \times n}$ via $U(t+T) = U(t)U_F$. By the existence of the matrix logarithm, we can write $U_F = \exp(-iT\hat{H}_F)$. Setting $P(t) = U(t)\exp(it\hat{H}_F)$, one readily checks that

$$P(t+T) = U(t+T)\mathrm{e}^{i(t+T)\hat{H}_F} = U(t)U_F\mathrm{e}^{i(t+T)\hat{H}_F} = U(t)U_F\mathrm{e}^{it\hat{H}_F} = P(t).$$

Thus, $P(t)$ is periodic with period T . Inverting the definition of $P(t)$ above, we have $U(t) = P(t)\exp(-it\hat{H}_F)$, which concludes the short proof of the theorem. \square

In its most general form, Floquet theorem states that one can write the evolution operator $U(t_2, t_1)$ from time t_1 to time t_2 as

$$U(t_2, t_1) = \mathrm{e}^{-i\hat{K}(t_2)}\mathrm{e}^{-i(t_1-t_2)\hat{H}_F}\mathrm{e}^{i\hat{K}(t_1)}, \quad (1.1)$$

where $\hat{K}(t) = \hat{K}(t+T)$ is a periodic hermitian operator, and \hat{H}_F is the time-independent Floquet Hamiltonian. In fact, the choices of the periodic operator \hat{K} and the Floquet Hamiltonian \hat{H}_F are not unique, and there is some freedom in defining them. As we shall discuss in the next chapter, different choices correspond to different gauges. There can be several convenient gauge choices, depending on the details of the setup. Despite being equivalent, these gauge choices can lead to different approximation schemes.

The evolution operator in Floquet systems simplifies if one observes the system stroboscopically, i.e. at times $t_2 = t_1 + lT$, where lT is the stroboscopic time measured in units of the driving period. In this case the operators $\hat{K}(t_2)$ and $\hat{K}(t_1)$ are identical, and the full evolution operator is equivalent to the evolution of the system generated by the static Hamiltonian $H_F[t_1] = \exp[-i\hat{K}(t_1)]\hat{H}_F\exp[i\hat{K}(t_1)]$.

In general, it is not possible to evaluate \hat{H}_F and $\hat{K}(t)$ explicitly, and one has to rely on approximations [4, 9, 32, 82–87]. Moreover, in macroscopic systems, there is no guarantee that \hat{H}_F is a local physical Hamiltonian. In fact, in the case of generic interacting systems, a local \hat{H}_F might not exist [78]. In such situations, the dynamics of the system can be

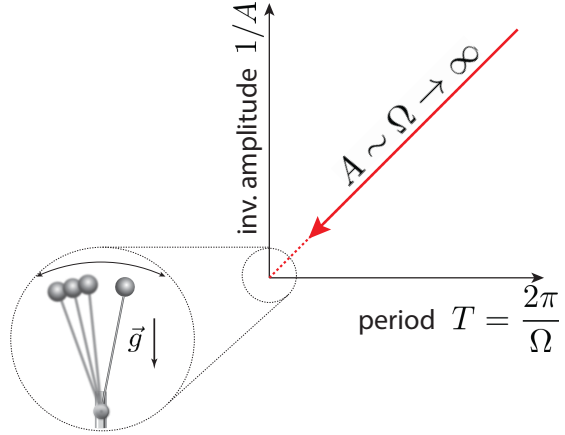


Figure 1.2: . Schematic representation of the parameter space of periodically driven systems. In this thesis we consider setups in which the amplitude of the driving scales with the frequency, i.e. $A \sim \Omega$. In the infinite-frequency limit we obtain a well-defined local Floquet Hamiltonian which is qualitatively different from the time-averaged Hamiltonian. For example, in the case of the Kapitza pendulum, the Floquet Hamiltonian allows for oscillations around the upright position, a phenomenon known as dynamical stabilisation (see Sec. 3.1.1).

completely chaotic and the Floquet theorem is not particularly useful.

An important limit, where the Floquet Hamiltonian can be defined at least perturbatively, corresponds to the fast driving regime, in which the driving frequency is larger than any natural energy scale in the problem. Then the driving does not couple resonantly to the slow degrees of freedom, but rather results in renormalisation and dressing of the low-energy Hamiltonian. In many instances the Floquet Hamiltonian in the high-frequency limit is simply the time-averaged Hamiltonian, $\frac{1}{T} \int_0^T H(t) dt$. But there are important exceptions, in which the Floquet Hamiltonian is *not* given by $\frac{1}{T} \int_0^T H(t) dt$, even in the infinite-frequency limit. These situations are of particular interest since the system can display interesting and counterintuitive behaviour, such as dynamical stabilisation, as it happens in the Kapitza pendulum [7]. Such situations naturally occur, for instance, when the amplitude of the driving is proportional to a power of the driving frequency, c.f. Fig. 1.2. This was the case in the recent experimental realisation of the Harper-Hofstadter Hamil-

tonian [52, 53, 57, 88], and the Haldane Chern insulator [38]² using cold atoms. A general understanding of such nontrivial limits is the main purpose of the present work.

Of course, in real systems the infinite-frequency limit is a mathematical abstraction. Typically, as one increases the driving frequency, new degrees of freedom can enter the game. Examples include internal molecular or atomic resonances in solid state systems or intra-band transitions in cold atom systems confined in optical lattices. Thus, one always deals with finite driving frequencies, which could still be larger than any natural frequency of the non-driven system. In such situations, the infinite-frequency limit of the Floquet Hamiltonian can be a good reference point, but finite-frequency corrections can still be significant. For this reason, here we discuss both the infinite-frequency limit of various model Hamiltonians, and the leading Ω^{-1} -corrections [89].

The main purpose of this thesis is three-fold: first and foremost – to discuss different generic scenarios, where one can engineer non-trivial Floquet Hamiltonians in the high-frequency limit. Second, once a protocol has been found to realise a desired Floquet Hamiltonian, we address the problem of preparing the desired Floquet state out of the initial state of the original non-driven Hamiltonian by deriving Floquet adiabatic perturbation theory. Last, we discuss thermalisation in closed driven systems focussing on the stability of the states w.r.t. to indefinite energy absorption.

While these high-frequency scenarios are not exhaustive, they cover a large class of driving protocols, and identify possible routes for finding new interesting Floquet systems. We shall refer to the different classes of driving protocols corresponding to these scenarios as (i) *Kapitza class*: the Hamiltonian is quadratic in momentum, and the driving potential couples only to the coordinates of the particles (either as an external potential or through the interaction term). (ii) *Dirac class*: same as the Kapitza class but for the system with relativistic linear dispersion such as graphene. (iii) *Dunlap-Kenkre class*: the periodic drive couples to a single particle potential such as a periodically driven external electric or

²We note that the key equilibrium property of topological states, namely robustness against various small perturbations, is not guaranteed to always hold true due to generic heating in ergodic driven systems [77–79].

magnetic field. In the Dunlap-Kenkre class the dispersion relation between particles is not restricted. These classes are not mutually exclusive, e.g. there is a clear overlap between the *Kapitza* class and the *Dunlap-Kenkre* class if one drives a system of non-relativistic particles by an external field, and a similar overlap exists between the *Dirac* class and the *Dunlap-Kenkre* class for particles with a relativistic dispersion.

We shall argue that, in models belonging to these three classes, the Floquet Hamiltonian has a nontrivial high-frequency limit, which is different from the time-averaged Hamiltonian allowing the systems to display new, qualitatively different features. These non-trivial limits can be used as a tool to realise synthetic matter, i.e. matter with specific engineered properties. On the theoretical side, we justify the existence of stable high-frequency fixed points in Ω -space, whose physics is governed by a well-defined effective (local) Hamiltonian. Although such fixed-point Hamiltonians may never be accessible experimentally, they provide a good reference point in many realistic situations: later on, we study the adiabatic preparation of a desired target Floquet state in the presence of strong periodic drives. Moreover, the corrections to this effective (Floquet) Hamiltonian, which we also discuss in detail, allow one to estimate the finite-frequency effects for particular setups, and find the regimes where these corrections are negligible. We stress that these non-trivial limits exist even for driven ergodic interacting many-particle systems, though interactions often lead to additional finite-frequency corrections to the effective Hamiltonian, which may ultimately result in faster heating rates. This will lead us to the discussion of prethermalisation and thermalisation in Floquet systems.

This thesis is organised as follows:

- In Chapter 2 we review some general properties of Floquet theory. Section 2.1 introduces the stroboscopic Floquet Hamiltonian and Kick operator, and the associated concept of the Floquet gauge, followed by the more general notion of the non-stroboscopic Floquet Hamiltonian and non-stroboscopic Kick operator. We illustrate

these concepts using an exactly solvable model of a two-level system in a circularly polarised periodic drive. After that, we introduce the concept of the Floquet non-stroboscopic (FNS) and Floquet stroboscopic (FS) dynamics, and compare them. In particular, we explain how Floquet theory extends to systems where the initial phase of the drive and/or the measurement time fluctuate within the driving period. In Section 2.2 we briefly review the Floquet-Magnus inverse-frequency expansion for the stroboscopic Floquet Hamiltonian and the related but not equivalent van Vleck expansion for the effective Floquet Hamiltonian. We present the discussion both in the laboratory (lab) and in the rotating (rot) frames. At the end of this chapter, we briefly comment on the convergence properties of the inverse-frequency expansion.

- Chapter 3 is devoted to Floquet engineering. We begin by defining three universal high-frequency limits of periodically-driven systems: (i) in Section 3.1.1 we define the Kapitza driving class. We thoroughly analyse the prototypical example of dynamical stabilisation - the Kapitza pendulum. We derive the leading corrections to the infinite-frequency Hamiltonian as well as the dressed observables and the dressed density matrix appearing in FNS dynamics. At the end of this section we discuss higher-dimensional and many-body generalisations of the Kapitza model. (ii) in Section 3.1.2 we define and study the Dirac class, which describes relativistic systems with a linear dispersion. We derive the infinite-frequency Hamiltonian and describe some interesting effects, such as a dynamically generated spin-orbit coupling. (iii) in Section 3.1.3, we define the Dunlap-Kenkre driving class, which includes periodically driven tight-binding models. We begin by studying the shaken bosonic chain, and demonstrate the consequences of FS and FNS dynamics for different observables. Afterwards, we derive the leading corrections to the Harper-Hofstadter Hamiltonian, and the driven Fermi-Hubbard model relevant for Floquet topological insulators. Finally, we briefly discuss some spin Hamiltonians which can be implemented in existing nuclear magnetic resonance setups. Still as part of Floquet engineering, we show the

equivalence of the van Vleck expansion and the Schrieffer-Wolff transformation in Section 3.2, which allows us to generalise the latter to the non-equilibrium setup of Floquet systems. This includes a detailed study on the application of Floquet theory to static and driven Hamiltonians with large separation between energy levels. After discussing the toy model of a static two-level system, we show that one can apply this expansion to derive the Heisenberg model out of the Fermi-Hubbard model, as well as the Kondo model from the Anderson impurity model. In Sec. 3.3 we show how one can derive the Rotating Wave Approximation (RWA) as the leading term in the inverse-frequency expansion and explain how one can derive systematic corrections to the RWA. We conclude this chapter with the discussion of the RWA and leading finite-frequency corrections applied to the Rabi model, going beyond the Jaynes-Cummings Hamiltonian, and show how ideas from the RWA can be used to extend the inverse-frequency expansion to capture resonances.

- In Chapter 4, we give a systematic review of the adiabatic theorem and the leading non-adiabatic corrections in periodically-driven (Floquet) systems. These corrections have a two-fold origin: (i) conventional ones originating from the gradually changing Floquet Hamiltonian and (ii) corrections originating from changing the micro-motion operator. These corrections conspire to give a Hall-type linear response for non-stroboscopic (time-averaged) observables allowing one to measure the Berry curvature and the Chern number related to the Floquet Hamiltonian, thus extending these concepts to periodically-driven many-body systems. The non-zero Floquet Chern number allows one to realize a Thouless energy pump, where one can adiabatically add energy to the system in discrete units of the driving frequency. We discuss the validity of Floquet Adiabatic Perturbation Theory (FAPT) using five different models covering linear and non-linear few and many-particle systems. We argue that in interacting systems, even in the stable high-frequency regimes, FAPT breaks down at ultra slow ramp rates due to avoided crossings of photon resonances, not captured

by the inverse-frequency expansion, leading to a counter-intuitive stronger heating at slower ramp rates. Nevertheless, large windows in the ramp rate are shown to exist for which the physics of interacting driven systems is well captured by FAPT.

- In Chapter 5 we study heating in periodically-driven systems. We begin by defining the concept of prethermal Floquet states and quasi-conserved integrals of motion. We then move on to study the main source of heating – resonances between states whose energy difference is close to an integer multiple of the driving frequency. In particular, by studying an experiment-related ergodic spin chain, we show that the number and strength of these resonances determines the heating rates to an infinite-temperature state. We then study the instabilities and Floquet steady states in the weakly-interacting Bose-Hubbard model at arbitrary drive strengths. A stability diagram is derived which features a stable prethermal phase at large driving frequencies, and a parametrically unstable phase at frequencies close to the single-particle bandwidth where the system starts heating up strongly immediately after the drive is turned on.
- In Chapter 6 we give the summary of the current standing of this fascinating field with an outlook to some important open problems in closed Floquet systems.

Chapter 2

Floquet Theory from a Modern Perspective

In this chapter we review Floquet's Theorem [81] and study its implications. We shall use the language of quantum mechanics but, as it becomes apparent later on in the Sec. 2.2, all results have a well-defined classical limit. Therefore, unless otherwise stated, we shall work in units of $\hbar = 1$.

2.1 Stroboscopic and Non-Stroboscopic Time Evolution

2.1.1 The Stroboscopic Floquet Hamiltonian and the Stroboscopic Kick Operator

Let us consider a dynamical process in which the Hamiltonian depends periodically on time, e.g. through a periodically modulated coupling constant. This means that the evolution operator defined as

$$U(t_2, t_1) = \mathcal{T}_t \exp \left[-i \int_{t_1}^{t_2} H(\tilde{t}) d\tilde{t} \right] \approx \prod_{j: t_1 \leq \tilde{t}_j \leq t_2} e^{-iH(\tilde{t}_j)(\tilde{t}_{j+1} - \tilde{t}_j)} \quad (2.1)$$

is invariant under discrete translations in time $(t_1, t_2) \rightarrow (t_1 + lT, t_2 + lT)$, where l is an integer. The factorisation (group) property of the evolution operator, $U(t_2, t_1) = U(t_2, t')U(t', t_1)$ for arbitrary t' , implies that $U(t_0 + 2T, t_0) = U(t_0 + 2T, t_0 + T)U(t_0 + T, t_0) = [U(t_0 + T, t_0)]^2$, which generalises to

$$U(t_0 + lT, t_0) = [U(t_0 + T, t_0)]^l. \quad (2.2)$$

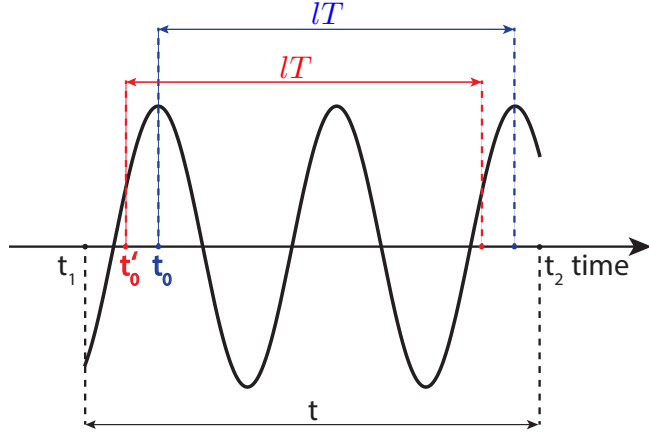


Figure 2.1: Floquet gauge: the system evolves from time t_1 to time t_2 . The stroboscopic frame begins at time t_0 which can be chosen to be anywhere within the first period $[t_1, t_1 + T]$. The choice of the Floquet gauge, i.e. the choice of t_0 , in general affects the form of the stroboscopic Floquet Hamiltonian $H_F[t_0]$ (see text).

It is convenient to formally define the evolution within one period as an evolution with the time-independent stroboscopic Floquet Hamiltonian¹ $H_F[t_0]$:

$$U(t_0 + T, t_0) = \exp [-iH_F[t_0]T]. \quad (2.3)$$

This representation is always possible because $U(t_0 + T, t_0)$ is a unitary operator. The stroboscopic Floquet Hamiltonian $H_F[t_0]$ defined in this way depends on the choice of the time t_0 which defines the beginning of the stroboscopic driving frame. This is a gauge choice, and it is completely arbitrary. To avoid confusion with general gauge transformations, related to the arbitrary choice of basis, we shall term the gauge associated with the choice of t_0 the *Floquet gauge*. Very often, one chooses a particular Floquet gauge, in which the Floquet Hamiltonian assumes its simplest form. This often happens when t_0 is a symmetric point of the driving protocol. For example, if the driving field is $\cos \Omega t$, it is often convenient to choose $t_0 = 0$.

Figure 2.1 suggests that for arbitrary times t_1 and t_2 the evolution operator can always

¹We use the word ‘Hamiltonian’ in a broad sense here; in general H_F can be a non-local hermitian operator.

be written as

$$U(t_2, t_1) = U(t_2, t_0 + lT) \exp[-iH_F[t_0]lT] U(t_0, t_1). \quad (2.4)$$

The initial and final evolution operators $U(t_0, t_1)$ and $U(t_2, t_0 + lT)$ effectively occur during small intervals of time $\delta t_1 = (t_1 - t_0)$ and $\delta t_2 = (t_2 - lT - t_0)$ which can always be chosen such that $\delta t_1 \in [-T, 0]$ and $\delta t_2 \in [0, T]$. The operators $U(t_0, t_1)$ and $U(t_2, t_0 + lT)$ are necessary to bring the time from the initial point of the evolution t_1 to t_0 , and from the last full period $t_0 + lT$ to the final point of evolution t_2 . By construction $U(t_0, t_0) = \mathbf{1}$ and $U(t_0 + T, t_0) = \exp[-iH_F[t_0]T]$. Now we can easily rewrite Eq. (2.4) in the form of Floquet's theorem [81] by doing a simple trick

$$\begin{aligned} U(t_2, t_1) &= U(t_2, t_0 + lT) e^{iH_F[t_0](t_2 - t_0 - lT)} e^{-iH_F[t_0](t_2 - t_0 - lT)} e^{-iH_F[t_0]lT} \times \\ &\quad \times e^{-iH_F[t_0](t_0 - t_1)} e^{iH_F[t_0](t_0 - t_1)} U(t_0, t_1) = \\ &= P(t_2, t_0) e^{-iH_F[t_0](t_2 - t_1)} P^\dagger(t_1, t_0) = e^{-iK_F[t_0](t_2)} e^{-iH_F[t_0](t_2 - t_1)} e^{iK_F[t_0](t_1)} \end{aligned} \quad (2.5)$$

where we have defined the fast motion unitary operator P :

$$P(t_2, t_0) \equiv U(t_2, t_0) e^{iH_F[t_0](t_2 - t_0)} \equiv e^{-iK_F[t_0](t_2)}, \quad (2.6)$$

and the last equality defines the *stroboscopic kick operator* $K_F[t_0](t)$ which depends explicitly on the Floquet gauge t_0 . Note that, with the above definition, the operator P is periodic $P(t_2 + lT, t_0) = P(t_2, t_0 + lT) = P(t_2, t_0)$ and, by construction, it also satisfies the property $P(t_0 + lT, t_0) = \mathbf{1}$, for an arbitrary integer l . This means that the stroboscopic kick operator reduces to zero at stroboscopic times, i.e. $K_F[t_0](t_0 + lT) = \mathbf{0}$. From Eq. (2.6) it immediately follows that $K_F[t_0](t) = i \log[P(t, t_0)]$.

Floquet's theorem can be simplified by choosing t_0 to coincide with either t_1 or t_2 , thus eliminating one of the two P -operators. However, this simplification can be somewhat deceptive, because in these cases, the Floquet Hamiltonian is tied to the initial (final) times of the evolution, and its definition continuously changes with one of those times.

Since in experiments, especially in the high-frequency limit, both the initial time and the final (measurement) time often fluctuate within a period, it is more convenient to tie the Floquet Hamiltonian to some fixed Floquet gauge t_0 , independent of both t_1 and t_2 .

From Eqs. (2.3) and (2.4) together with the factorisation property of the evolution operator it becomes evident that the choice of t_0 , defining the Floquet Hamiltonian, is indeed a gauge choice. To see this explicitly, we write the evolution operator $U(t_0 + lT, t_0)$ in two different (but equivalent) ways:

$$U(t_0 + lT, t_0) = e^{-iH_F[t_0]lT} = U^\dagger(t_0 + \delta t_0, t_0) e^{-iH_F[t_0 + \delta t_0]lT} U(t_0 + \delta t_0, t_0). \quad (2.7)$$

This is equivalent to the gauge transformation of the Floquet Hamiltonian

$$\begin{aligned} H_F[t_0 + \delta t_0] &= U(t_0 + \delta t_0, t_0) H_F[t_0] U^\dagger(t_0 + \delta t_0, t_0), \\ &= P(t_0 + \delta t_0, t_0) H_F[t_0] P^\dagger(t_0 + \delta t_0, t_0). \end{aligned} \quad (2.8)$$

As expected, this Floquet gauge is periodic and continuous, such that $H_F[t_0 + T] = H_F[t_0]$.

Let us also point out that one can rewrite Floquet's theorem in a differential form [10, 85, 90]. Indeed, on the one hand, for any Hamiltonian evolution one can write

$$i\partial_{t_2} U(t_2, t_1) = H(t_2) U(t_2, t_1). \quad (2.9)$$

On the other hand, using Eq. (2.5) we arrive at

$$\begin{aligned} i\partial_{t_2} U(t_2, t_1) &= [i\partial_{t_2} P(t_2, t_0)] e^{-iH_F[t_0](t_2-t_1)} P^\dagger(t_1, t_0) \\ &\quad + P(t_2, t_0) H_F[t_0] e^{-iH_F[t_0](t_2-t_1)} P^\dagger(t_1, t_0). \end{aligned} \quad (2.10)$$

Equating these two expressions, we find

$$H_F[t_0] = P^\dagger(t_2, t_0) H(t_2) P(t_2, t_0) - i P^\dagger(t_2, t_0) \partial_{t_2} P(t_2, t_0) \quad (2.11)$$

or, equivalently,

$$H(t_2) = P(t_2, t_0)H_F[t_0]P^\dagger(t_2, t_0) + i[\partial_{t_2}P(t_2, t_0)]P^\dagger(t_2, t_0). \quad (2.12)$$

Equation (2.11) can be viewed as a statement of the existence of a periodic operator $P(t, t_0)$ such that the RHS of this equation is time-independent. Very often, in the literature this equation is used as a starting point to find the Floquet Hamiltonian iteratively [10, 82, 85, 90]. Due to the gauge freedom associated with the choice of t_0 , the solution of this equation is not unique, but all solutions are gauge-equivalent. Another possible application of Eq. (2.12) is that it allows one to do ‘reverse-engineering’. Once the Floquet Hamiltonian $H_F[t_0]$ and the periodic operator $P(t, t_0)$ with interesting properties are chosen, one can use Eq. (2.12) to determine which time-dependent driving protocol $H(t)$ needs to be experimentally implemented to realise those properties².

2.1.2 The Non-Stroboscopic Floquet Hamiltonian and the Non-Stroboscopic Kick Operator

In the previous section, we showed that one can choose a family of stroboscopic Floquet Hamiltonians $H_F[t_0]$, each one of which exactly describes the evolution operator at stroboscopic times $U(t_0 + lT, t_0) = \exp[-iH_F[t_0]lT]$. As we discussed in Sec. 2.1.1, the choice of t_0 is the Floquet gauge choice, and different stroboscopic Floquet Hamiltonians are gauge equivalent. In other words, by choosing one member of this family and applying to it the gauge transformation using the P -operator, one can obtain all other Floquet Hamiltonians from this family, c.f. Eq. (2.8).

On the other hand, since t_0 is a gauge choice, all these Hamiltonians are gauge-equivalent to each other; we thus denote a general Floquet Hamiltonian by \hat{H}_F . Therefore, there exists a family of Hermitian operators $\hat{K}(t_0)$ which, following Ref. [32], we call *kick*

²The resulting drive protocols often appear too fine-tuned to be of any practical and fundamental advantage, though.

operators, such that

$$\hat{H}_F = e^{i\hat{K}(t_0)} H_F[t_0] e^{-i\hat{K}(t_0)}, \quad (2.13)$$

or equivalently

$$H_F[t_0] = e^{-i\hat{K}(t_0)} \hat{H}_F e^{i\hat{K}(t_0)}. \quad (2.14)$$

From now on we shall always reserve the hat to indicate some fixed Floquet Hamiltonian \hat{H}_F and the notation $H_F[t_0]$ to indicate the stroboscopic Floquet Hamiltonian introduced in the previous section.

It becomes evident from Eqs. (2.13) and (2.14) that the fixed kick operator and Floquet Hamiltonian are not completely independent: if S is any static, unitary transformation, then

$$e^{i\hat{K}(t_0)} \rightarrow e^{i\hat{K}'(t_0)} := S e^{i\hat{K}(t_0)}, \quad \hat{H}_F \rightarrow \hat{H}'_F := S \hat{H}_F S^\dagger$$

leaves Eq. (2.14) invariant. Usually, one uses the freedom in the definition of the kick operator to obtain \hat{H}_F in its simplest form. Developing separate inverse-frequency expansions for \hat{H}_F and the kick operator $\hat{K}(t)$ allows one to separate the Floquet-gauge independent terms, which fix the Floquet Hamiltonian, from the Floquet-gauge dependent terms, which are all part of the kick operator. The latter are also responsible for the effect of the Floquet gauge on the initial state and the observables under consideration, as we emphasise later on throughout this thesis.

It is straightforward to find the relation between the kick operator \hat{K} and the fast-motion operator P . Namely, substituting Eq. (2.14) into Eq. (2.8) we find

$$\begin{aligned} H_F[t_0 + \delta t_0] &= P(t_0 + \delta t_0, t_0) H_F[t_0] P^\dagger(t_0 + \delta t_0, t_0) \\ &= P(t_0 + \delta t_0, t_0) e^{-i\hat{K}(t_0)} \hat{H}_F e^{i\hat{K}(t_0)} P^\dagger(t_0 + \delta t_0, t_0). \end{aligned}$$

On the other hand, by construction

$$H_F[t_0 + \delta t_0] = e^{-i\hat{K}(t_0 + \delta t_0)} \hat{H}_F e^{i\hat{K}(t_0 + \delta t_0)}.$$

Since δt_0 is arbitrary, we see from these two equations that the kick operator and the fast-motion operator are not independent:

$$P(t, t_0) = e^{-i\hat{K}(t)} e^{i\hat{K}(t_0)} = e^{-i\hat{K}_F[t_0](t)}. \quad (2.15)$$

Hence, similar to the fast-motion operator P , the kick operator \hat{K} describes the dynamics of the system within the driving period [32]. We thus stress that the stroboscopic kick operator $K_F[t_0](t)$ is, in general, a different object from the fixed kick operator $\hat{K}(t)$. Using Eq. (2.15) and Eq. (2.13) we can rewrite the evolution operator in Eq. (2.5) as

$$\begin{aligned} U(t_2, t_1) &= e^{-i\hat{K}(t_2)} e^{i\hat{K}(t_0)} e^{-iH_F[t_0](t_2-t_1)} e^{-i\hat{K}(t_0)} e^{i\hat{K}(t_1)} \\ &= e^{-i\hat{K}(t_2)} e^{-i\hat{H}_F(t_2-t_1)} e^{i\hat{K}(t_1)}, \end{aligned} \quad (2.16)$$

which is precisely the form of Floquet's theorem introduced in Eq. (1.1).

By construction, the kick operator always carries a Floquet-gauge (i.e. t_0) dependence, and it is periodic in time: $\hat{K}(t_0 + lT) = \hat{K}(t_0)$. If $\hat{K}(t_0)$ satisfies the

$$\text{stroboscopic (Floquet-Magnus) boundary condition : } \hat{K}(t_0) = \mathbf{0}, \quad t_0 \in [0, T], \quad (2.17)$$

i.e. reduces to the zero operator $\mathbf{0}$ at some time t_0 then, following Eq. (2.13), \hat{H}_F coincides with the stroboscopic (Floquet-Magnus) Hamiltonian $H_F[t_0]$, and t_0 fixes the Floquet gauge. Thus, in the stroboscopic gauge, $\hat{H}_F = H_F[t_0]$ is indeed Floquet-gauge dependent. We note in passing that it is this gauge to obtain \hat{H}_F in numerical simulations. From Eq. (2.15) it also follows that if the kick operator $\hat{K}(t_0)$ vanishes for some particular value of t_0 (and as a consequence \hat{H}_F describes stroboscopic dynamics) then the kick operator

becomes identical to the stroboscopic kick operator, i.e. $\hat{K}(t) = K_F[t_0](t)$, defined in the previous section.

However, if Eq. (2.17) is not satisfied, then \hat{H}_F does not describe the stroboscopic evolution for any choice of t_0 . This happens, for instance, for circularly-polarised drives. We should mention here that there exists yet another particularly convenient choice of boundary condition for the kick operator:

$$\text{effective (van Vleck) boundary condition : } \int_0^T dt \hat{K}(t) = \mathbf{0}. \quad (2.18)$$

Adopting this gauge choice results in the *non-stroboscopic* Floquet Hamiltonian $\hat{H}_F = H_{\text{eff}}$, which is typically termed the *effective* (or van Vleck) Hamiltonian [9, 10, 32, 86, 87], and the corresponding Kick operator is commonly denoted as $\hat{K}(t) = K_{\text{eff}}(t)$. For this gauge choice, one can show that H_{eff} is manifestly t_0 -independent and, consequently, $K_{\text{eff}}(t)$ carries all the dependence on the Floquet gauge t_0 .

Notice that the stroboscopic and non-stroboscopic boundary conditions are not necessarily mutually exclusive; it can happen that both are satisfied simultaneously, e.g. when $\hat{K}(t) \sim \cos \Omega t$ and $t_0 = t_1 = T/4$. In fact, they shall lead us to find two different variants of the inverse-frequency expansion: the stroboscopic Floquet-Magnus expansion and the non-stroboscopic van Vleck expansion, see Sec. 2.2. In the next section, we discuss an example and calculate explicitly both the stroboscopic Floquet Hamiltonian $H_F[t_0]$ and the effective Floquet Hamiltonian H_{eff} .

2.1.3 A Case Study: Two-Level System in a Circularly Driven Magnetic Field

Let us illustrate the construction above using the simple example of a two-level system in a rotating magnetic field:

$$H(t) = B_z \sigma^z + B_{\parallel} (\sigma^x \cos \Omega t + \sigma^y \sin \Omega t). \quad (2.19)$$

Not surprisingly this problem becomes time-independent after a transformation to a rotating frame (such problems are part of the class of Floquet-integrable models). The evolution operator in the original (lab) frame can be evaluated by first going to the rotating reference frame, where the Hamiltonian is time-independent (and therefore the evolution is simple), and then transforming back to the lab reference frame:

$$U(t_2, t_1) = V(t_2, t_0) e^{-iH^{\text{rot}}[t_0](t_2-t_1)} V^\dagger(t_1, t_0). \quad (2.20)$$

where $V(t, t_0) = \exp \left[-i \frac{\sigma^z}{2} \Omega(t - t_0) \right]$ is the operator which transforms from the rotating frame into the lab frame and the Hamiltonian in the rotating frame is:

$$\begin{aligned} H^{\text{rot}}[t_0] &= V^\dagger(t, t_0) H(t) V(t, t_0) - i V^\dagger(t, t_0) \dot{V}(t, t_0) \\ &= B_z \sigma^z + B_{\parallel} (\sigma^x \cos \Omega t_0 + \sigma^y \sin \Omega t_0) - \frac{\Omega}{2} \sigma^z. \end{aligned} \quad (2.21)$$

Equation (2.20) for the evolution operator resembles the Floquet ansatz (2.5) with the only caveat that the function $V(t, t_0)$ is periodic with twice the period of the driving. This is however not a problem since the correct periodicity can be easily restored by redefining the operator [91] V : $V(t, t_0) \rightarrow \tilde{V}(t, t_0) = V(t, t_0) \exp[-i\Omega t/2]$. More importantly, the eigenvalues of $H^{\text{rot}}[t_0]$, $\pm \epsilon_{\text{rot}}$, where

$$\epsilon_{\text{rot}} = \sqrt{(B_z - \Omega/2)^2 + B_{\parallel}^2}, \quad (2.22)$$

diverge in the high frequency limit, while naively one would expect that for $\Omega \rightarrow \infty$ the Floquet Hamiltonian reduces to the time-averaged Hamiltonian $\frac{1}{T} \int_0^T H(t) dt = B_z \sigma^z$ whose energies do not diverge as $\Omega \rightarrow \infty$.

Before showing how to resolve this issue, we mention that the discussion here is not limited to two-level systems and the transformation to the rotating frame can be performed for any spin using the operator $V(t) = \exp[-i \mathbf{L} \cdot \boldsymbol{\Omega} t]$, where \mathbf{L} is the total angular momentum. Obviously, doing a transformation to the rotating frame helps only, if the

stationary part of the Hamiltonian is rotationally invariant. Otherwise, Floquet's theory tells us that Eq. (2.5) still applies but the stroboscopic Floquet Hamiltonian $H_F[t_0]$ is not directly related to the Hamiltonian in the rotating reference frame.

In certain situations one can completely eliminate the time dependence of the lab-frame Hamiltonian, and find $H_F[t_0]$ by performing two consecutive transformations in two rotating frames [92]. In general, however, $H_F[t_0]$ can only be written through an infinite series of transformations. In Refs. [10, 82, 90] it was realised that the operator P can be interpreted as a quantum analogue of the generating function of a canonical transformation, and $H_F[t_0]$ – as the Hamiltonian in the new reference frame (see Eq. (2.11)). Therefore, Floquet's theorem could be stated as follows. For *any* time-periodic Hamiltonian, there exists a unique³ reference frame⁴ in which the time evolution is generated by a time-independent Hamiltonian. Unfortunately, in general, it is not possible to find the transformation from the lab to this new reference frame explicitly.

We now show how to obtain the exact Floquet Hamiltonian and fast-motion operator P for this problem. We start by noting the identity

$$\exp(-iH_F[t_0]2T) = U(t_0 + 2T, t_0) = \exp(-iH^{\text{rot}}[t_0]2T), \quad (2.23)$$

from which it is clear that $H_F[t_0]$ and $H^{\text{rot}}[t_0]$ share the same eigenstates while their eigenvalues can only differ by a shift $\pm\Omega/2$. We fix the Floquet energies $\pm\epsilon_F$ by requiring that they do not diverge when $\Omega \rightarrow \infty$, i.e.:

$$\epsilon_F = \left(\epsilon_{\text{rot}} - \frac{\Omega}{2} \right) = \epsilon_{\text{rot}} \left(1 - \frac{\Omega}{2\epsilon_{\text{rot}}} \right).$$

If S is a unitary matrix diagonalising $H^{\text{rot}}[t_0]$, such that $SH^{\text{rot}}[t_0]S^\dagger = \epsilon_{\text{rot}}\sigma^z$ then it is clear that the stroboscopic Floquet Hamiltonian, which does not suffer from the infinite-

³The uniqueness is guaranteed by the theorem of Picard-Lindelöf.

⁴Note that, while static gauge transformations result in a change of basis and all quantities, such as the energy, remain unchanged, time-dependent gauge transformations result in a change of the reference frame and induce additional Galilean terms which can alter the value of observables (e.g. the energy).

frequency divergence, is

$$H_F[t_0] = S^\dagger \epsilon_F \sigma^z S = \left(1 - \frac{\Omega}{2\epsilon_{\text{rot}}}\right) H^{\text{rot}}[t_0]. \quad (2.24)$$

From Eq. (2.20), the Floquet ansatz in Eq. (2.5), and the relation between $H_F[t_0]$ and $H^{\text{rot}}[t_0]$ in Eq. (2.23) it immediately follows that the fast-motion operator P is a composition of two rotations in spin space:

$$P(t, t_0) = \exp \left[-i \frac{\sigma^z}{2} \Omega(t - t_0) \right] \exp \left[-i \frac{H^{\text{rot}}[t_0]}{2\epsilon_{\text{rot}}} \Omega(t - t_0) \right]. \quad (2.25)$$

Equations (2.24) and (2.25), together with Eqs. (2.21) and (2.22) provide the explicit solution for the Floquet Hamiltonian and the fast-motion operator. Note that, as required, P is periodic with period $T = 2\pi/\Omega$, and reduces to the identity at stroboscopic times, i.e. $P(t_0 + nT, t_0) = \mathbf{1}$. The stroboscopic kick operator is $K_F[t_0](t) = i \log(P(t, t_0))$.

Finally, as we explain in Sec. 2.1.2, there exists yet another natural choice for \hat{H}_F . It is equivalent to choosing the effective Hamiltonian: H_{eff} , where

$$\begin{aligned} H_{\text{eff}} &= \left(\frac{\Omega}{2} - \epsilon_{\text{rot}} \right) \sigma^z, \\ K_{\text{eff}}(t) &= \frac{\alpha - \pi}{2} (-\sigma^x \sin \Omega t + \sigma^y \cos \Omega t), \quad \cos \alpha = \frac{B_z - \Omega/2}{\epsilon_{\text{rot}}}, \quad \sin \alpha = \frac{B_{\parallel}}{\epsilon_{\text{rot}}}. \end{aligned} \quad (2.26)$$

This form of $K_{\text{eff}}(t)$ is valid for $\Omega > 2B_z$ ⁵. Note that in the high frequency limit, $\Omega > 2B_z$, with our convention $\alpha \rightarrow \pi$ as $B_{\parallel} \rightarrow 0$. One can check that the operator $K_{\text{eff}}(t_0)$ is the generator of the gauge transformation between $H_F[t_0]$ and H_{eff} , (c.f. Eq. (2.14)), i.e. $H_{\text{eff}} = e^{iK_{\text{eff}}(t_0)} H_F[t_0] e^{-iK_{\text{eff}}(t_0)}$. According to Eq. (1.1), in this representation (which we call the van Vleck picture) the evolution operator reads

$$U(t_2, t_1) = e^{-iK_{\text{eff}}(t_2)} e^{-iH_{\text{eff}}(t_2 - t_1)} e^{iK_{\text{eff}}(t_1)}. \quad (2.27)$$

⁵In fact, one can show that $K_{\text{eff}}(t)$ is not continuous at $\Omega = 2B_z$, which is related to a topological phase transition, see Sec. 4.3.4.1.

The effective Hamiltonian H_{eff} is clearly non-stroboscopic because $K(t)$ does not vanish at any point in time. This is a general feature of the effective kick operator for circularly-polarised drives.

The analysis above can be extended to more complex rotating setups. However, finding the properly folded Floquet Hamiltonian can, in general, be a formidable task, since it requires the knowledge of the spectrum of $H^{\text{rot}}[t_0]$, which may be quite complicated if the system is interacting. In Sec. 2.2, we shall discuss how one can perturbatively construct Floquet Hamiltonians, which have well-behaved infinite-frequency limits.

2.1.4 Stroboscopic versus Non-stroboscopic Dynamics

Following the discussion in Secs. 2.1.1 and 2.1.2, the evolution operator can be written as the exponential of the Floquet Hamiltonian, sandwiched between two periodic unitary operators in two equivalent ways, c.f. Eq. (2.16):

$$U(t_2, t_1) = e^{-i\hat{K}(t_2)} e^{-i\hat{H}_F(t_2-t_1)} e^{i\hat{K}(t_1)}.$$

We now use this observation to find the expectation values of observables. To simplify the discussion, we shall focus only on equal-time expectation values. The generalisation to nonequal-time correlation functions is straightforward⁶.

Consider an observable $\mathcal{O}(t_2)$ in the Heisenberg picture, where it explicitly depends on time. Also, let us assume that initially (at time t_1) the system is prepared in some state described by the density matrix ρ , which in the Heisenberg picture remains time-independent. Then

$$\langle \mathcal{O}(t_2) \rangle = \text{Tr} \left(\rho U^\dagger(t_2, t_1) \mathcal{O} U(t_2, t_1) \right) \quad (2.28)$$

⁶We focus on the representation of the evolution operator through the fixed kick operators $\hat{K}(t)$ and the Floquet Hamiltonian \hat{H}_F . The equivalent expressions in terms of $K_F[t_0](t)$ and $H_F[t_0]$ ($K_{\text{eff}}(t)$ and H_{eff}) can be obtained by the simple replacement $\hat{K}(t) \rightarrow K_F[t_0](t)$ and $\hat{H}_F \rightarrow H_F[t_0]$ ($\hat{K}(t) \rightarrow K_{\text{eff}}(t)$ and $\hat{H}_F \rightarrow H_{\text{eff}}$). Moreover, using Eq. (2.15), it is immediate to transform all the expressions in the language of the fast motion operator $P(t, t_0)$.

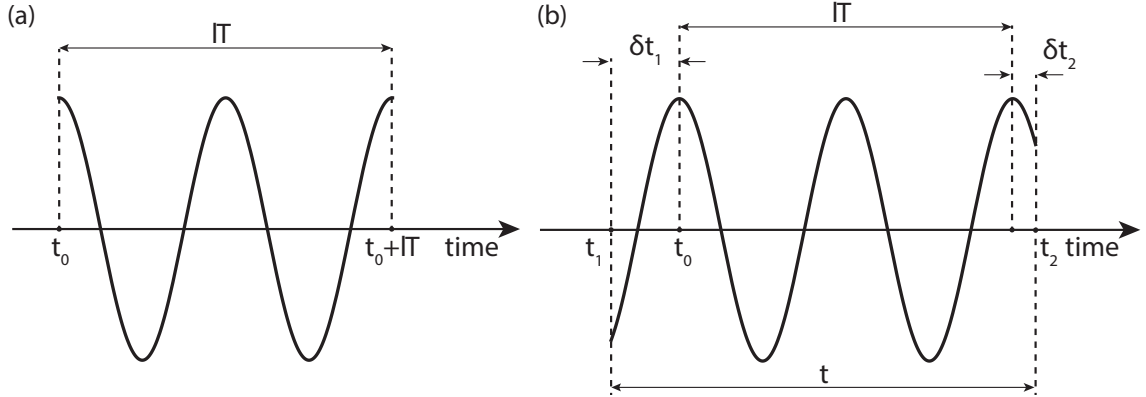


Figure 2.2: Floquet stroboscopic (FS) vs. Floquet non-stroboscopic (FNS) evolution. (a) In the FS scheme the driving is initialised at time $t_0 = 0$ when the stroboscopic frame starts and the measurement is performed after exactly l periods at time lT . (b) In the FNS scheme the driving is initiated at time t_1 , the stroboscopic evolution begins at t_0 and the measurement is carried out at time t_2 within the $(l + 1)$ -st driving period. In the FNS scheme, the initial density matrix and the expectation values of the observables are obtained by averaging over δt_1 and δt_2 .

$$\begin{aligned}
 &= \text{Tr} \left(\rho e^{-i\hat{K}(t_1)} e^{i\hat{H}_F(t_2-t_1)} e^{i\hat{K}(t_2)} \mathcal{O} e^{-i\hat{K}(t_2-t_1)} e^{-i\hat{H}_F(t_2-t_1)} e^{i\hat{K}(t_1)} \right) \\
 &= \text{Tr} \left(e^{i\hat{K}(t_1)} \rho e^{-i\hat{K}(t_1)} e^{i\hat{H}_F(t_2-t_1)} e^{i\hat{K}(t_2)} \mathcal{O} e^{-i\hat{K}(t_2)} e^{-i\hat{H}_F(t_2-t_1)} \right).
 \end{aligned}$$

We see that the dynamics of the system is solely generated by the Floquet Hamiltonian if we properly identify a new density matrix and a new observable as

$$\rho \rightarrow e^{i\hat{K}(t_1)} \rho e^{-i\hat{K}(t_1)}, \quad \mathcal{O} \rightarrow e^{i\hat{K}(t_2)} \mathcal{O} e^{-i\hat{K}(t_2)}. \quad (2.29)$$

The operators $\hat{K}(t_1)$ and $\hat{K}(t_2)$ can be viewed as time-dependent gauge transformations applied to the initial density matrix (wave function) and the observable. The main difference with the conventional gauge transformation is that the density matrix and the observable are transformed differently unless $t_2 - t_1 = lT$. In Ref. [32] the generators of these transformations were termed the initial and the final ‘kicks’. As we discussed, these operators are also periodic.

The simplest case, which is often discussed in the literature, is when the initial time t_1

coincides with t_0 , and the final time is $t_2 = t_0 + lT$ (see Fig. 2.2a). This condition defines the so-called *Floquet stroboscopic (FS)* dynamics. In this setup, it is convenient to use the stroboscopic kick operators $K_F[t_0](t_1)$ and $K_F[t_0](t_2)$ which vanish identically at times t_1 and t_2 , as defined above. As a consequence, the operators ρ and \mathcal{O} are not modified and the evolution is generated by the stroboscopic Hamiltonian $H_F[t_0]$. Sometimes, analyzing such FS dynamics is sufficient for describing the whole time evolution. This happens, for example, when the observable and the initial density matrix do not change significantly within a period. The FS dynamics can also be described in terms of the non-stroboscopic kick operator $\hat{K}(t)$ and non-stroboscopic Floquet Hamiltonian \hat{H}_F . Then one has to include the effect of the kick operator $\hat{K}(t_0)$ on the observables and the density matrix [see Eq. (2.29)]. In this case, the gauge transformations for the density matrix and the observable are identically given by the same operator $\hat{K}(t_0)$, which is equivalent to the standard static global gauge transformation.

Another common setup, which naturally occurs in experiments, emerges if the initial time of the driving t_1 (which is equivalent to the driving phase) and the measurement time t_2 are random variables which fluctuate independently. We call this scenario *Floquet non-stroboscopic (FNS)* dynamics. In this case, one has to average the expectation value of $\mathcal{O}(t)$ over the intervals δt_1 and δt_2 (c.f. Fig. 2.2b). From Eq. (2.29) it becomes clear that this averaging procedure affects both the density matrix and the observable. One can also consider other schemes, where e.g. the initial phase is deterministic but the measurement time is random, or conversely the initial phase is random but the measurement is locked to the phase of the drive. We shall not consider such situations but from our discussion it will become clear how one can find the appropriate density matrix and the observable.

In order to obtain an accurate description of the FNS evolution, one needs to average the density matrix and the operator in Eq. (2.29) with respect to the uncertainty in t_1 and t_2 :

$$\bar{\rho} = \overline{e^{i\hat{K}(t_1)} \rho e^{-i\hat{K}(t_1)}}, \quad \overline{\mathcal{O}} = \overline{e^{i\hat{K}(t_2)} \mathcal{O} e^{-i\hat{K}(t_2)}}, \quad (2.30)$$

where the bar implies averaging over some, say Gaussian, distribution for $t_{1,2}$. Further, because $\hat{K}(t)$ is a periodic operator, the averaging over t_1 and t_2 becomes equivalent to averaging over one period if the width of the distribution becomes larger than the driving period. In the following, we shall focus on this situation. Then the whole time evolution is effectively described by the quench to the Floquet Hamiltonian starting from the dressed density matrix $\bar{\rho}$ instead of ρ and measuring the dressed operator $\bar{\mathcal{O}}$ instead of \mathcal{O} . There is a certain care needed in precisely understanding this statement. We assumed that t_1 , t_2 and $t = t_2 - t_1$ are statistically independent variables, which is clearly not the case. However, they become effectively independent when the total time t is much longer than the uncertainty in both t_1 and t_2 . Intuitively, one can understand this averaging procedure using a time-scale separation argument. In the high-frequency limit, the periodic kick operator $\hat{K}(t)$ is responsible for the fast dynamics, while the Floquet Hamiltonian \hat{H}_F governs the slow dynamics. Therefore when averaging over $t_{1,2}$, provided that $t = t_2 - t_1$ is much larger than the uncertainty in both t_1 and t_2 , one can assume that the operator $\exp[-i\hat{H}_F(t_2 - t_1)]$ in (2.29) is practically unchanged and the averaging procedure only affects the observables and the density matrix (see Eq. (2.30)). Finally, notice that, by construction, $\bar{\rho}$ does not depend on the initial phase of the drive since it is averaged over a full cycle. Similarly $\bar{\mathcal{O}}$ does not depend on the final measurement time.

Note that, even if one starts from a pure state described by a wave function, in the FNS scheme, averaging over t_1 typically generates a mixed state. In this sense, the original uncertainty in the initial time t_1 plays a similar role to temperature since both broaden the initial density matrix. Intuitively, the difference between ρ and $\bar{\rho}$ is determined by how much the density matrix changes within one period. Similarly, the difference between \mathcal{O} and $\bar{\mathcal{O}}$ can be large or small, depending on how much the observable changes within one period.

The dressed operators have some unusual properties. In particular, from the definition it becomes clear that $\bar{\mathcal{O}}^2 \neq (\bar{\mathcal{O}})^2$, e.g. in the rotating spin example $\overline{(\sigma^x)^2} = \mathbf{1} \neq (\overline{\sigma^x})^2$, c.f. Sec. 2.1.4.1. Another example illustrating this property of dressed operators is discussed

in detail in Sec. 3.1.1.4, Eq. (3.24). We also observe that, in the high-frequency limit, the dressed operators satisfy the Heisenberg equations of motion with the Floquet Hamiltonian. Indeed, let us consider the Heisenberg equation of motion for some operator $\mathcal{O}(t)$. Using the Floquet ansatz (2.16) and ignoring the kick operator at t_1 because it only dresses the density matrix, we obtain:

$$\begin{aligned} i\partial_t \mathcal{O}(t) &= i\partial_t \left(e^{i\hat{H}_F(t-t_1)} e^{i\hat{K}(t)} \mathcal{O} e^{-i\hat{K}(t)} e^{-i\hat{H}_F(t-t_1)} \right) \\ &= e^{i\hat{H}_F(t-t_1)} [e^{i\hat{K}(t)} \mathcal{O} e^{-i\hat{K}(t)}, \hat{H}_F] e^{-i\hat{H}_F(t-t_1)} + i e^{i\hat{H}_F(t-t_1)} \partial_t \left(e^{i\hat{K}(t)} \mathcal{O} e^{-i\hat{K}(t)} \right) e^{-i\hat{H}_F(t-t_1)}. \end{aligned} \quad (2.31)$$

We can average both sides of this equation over a period w.r.t. the time t assuming, as before, that it is independent of the total time interval $t - t_1$. The last term in Eq. (2.32) vanishes, since the average of a derivative of a periodic function is zero. As a result we find

$$i\partial_t \overline{\mathcal{O}} = i\overline{\partial_t \mathcal{O}(t)} = [\overline{\mathcal{O}(t)}, \hat{H}_F]. \quad (2.32)$$

where we have defined the Heisenberg picture of the dressed operator

$$\overline{\mathcal{O}}(t) = e^{i\hat{H}_F(t-t_1)} \overline{\mathcal{O}} e^{-i\hat{H}_F(t-t_1)}$$

This equation is the Heisenberg equation of motion for the dressed operator. The first equality in Eq. (2.32) is similar to the Hellmann-Feynman theorem, in which the average over the quantum state plays a role analogous to the average over the period.

If \mathcal{O} represents a conserved quantity, then we can define an associated current $\mathbf{J}_{\mathcal{O}}$ through

$$\partial_t \mathcal{O}(t) + \nabla \cdot \mathbf{J}_{\mathcal{O}}(t) = 0. \quad (2.33)$$

Averaging both sides of this equation over time and using Eq. (2.32), we see that the time average of the current operator must represent the dressed current $\overline{\mathbf{J}}_{\mathcal{O}}$ governing the slow

evolution of $\overline{\mathcal{O}}$:

$$\partial_t \overline{\mathcal{O}} + \nabla \cdot \overline{\mathbf{J}}_{\mathcal{O}}(t) = 0, \quad (2.34)$$

where

$$\overline{\mathbf{J}}_{\mathcal{O}} = \overline{e^{i\hat{K}(t)} \mathbf{J}_{\mathcal{O}} e^{-i\hat{K}(t)}}, \quad (2.35)$$

Thus, both in numerical simulations and in experiments, in order to measure the current associated with the Floquet Hamiltonian one has to appropriately dress the current operator using the FNS averaging. In contrast, the current evaluated at some fixed stroboscopic time $t = lT$ will be a different object, involving both information about the Floquet evolution governed by \hat{H}_F , and an additional contribution related to the derivatives of the kick operator (the last term in Eq. (2.32)). A similar average over a period to FNS evolution arises naturally when one studies linear response in the presence of the drive, see Chapter 4. We shall return to this issue as well as to general differences between FS and FNS dynamics later on, when we discuss specific examples. In particular, we shall show that, using stroboscopic measurements, one *cannot* obtain the current corresponding to the Floquet Hamiltonian at any driving frequency whenever the latter contains a Floquet-engineered gauge field. On the other hand, implementing the FNS scheme and averaging the expectation values over the driving period, the Floquet current can be obtained in the high-frequency limit, c.f. Sec. 3.1.3.2. Recently, it was proposed to detect the topological character of the ground state in fermionic systems by measuring the magnetisation of a finite-size sample due to the chiral currents flowing at the edges [93]. This proposal explicitly made use of the FNS measurement protocol.

2.1.4.1 Non-Stroboscopic Evolution in the Two-Level-System.

Let us briefly illustrate the implications of FNS evolution for the driven spin example of Sec. 2.1.3. Consider first the stroboscopic Floquet Hamiltonian

$$H_F[0] = \left(1 - \frac{\Omega}{2\epsilon_{\text{rot}}}\right) H_{\text{rot}}, \quad H_{\text{rot}} = [(B_z - \Omega/2)\sigma^z + B_{\parallel}\sigma^x],$$

$$e^{-iK_F[0](t)} = \exp\left(-i\frac{\sigma^z}{2}\Omega t\right) \exp\left(-i\frac{H^{\text{rot}}}{2\epsilon_{\text{rot}}}\Omega t\right). \quad (2.36)$$

We discuss two representative initial states $|\psi_1\rangle$ and $|\psi_2\rangle$ defined by

$$|\psi_1\rangle = |\downarrow\rangle \rightarrow \rho_1 = \frac{1}{2}(\mathbf{1} - \sigma^z), \quad |\psi_2\rangle = \frac{1}{\sqrt{2}}(|\uparrow\rangle + |\downarrow\rangle) \rightarrow \rho_2 = \frac{1}{2}(\mathbf{1} + \sigma^x).$$

Then the corresponding dressed density matrices and dressed operators (the dressed Pauli matrices) are found according to Eq. (2.30) to be:

$$\begin{aligned} \bar{\sigma}_F^x[0] &= \overline{e^{iK_F[0](t)}\sigma^x e^{-iK_F[0](t)}} = -\cos\alpha \sin^2\frac{\alpha}{2} \sigma^x + \sin\alpha \sin^2\frac{\alpha}{2} \sigma^z, \\ \bar{\sigma}_F^y[0] &= \overline{e^{iK_F[0](t)}\sigma^y e^{-iK_F[0](t)}} = \sin^2\frac{\alpha}{2} \sigma^y, \\ \bar{\sigma}_F^z[0] &= \overline{e^{iK_F[0](t)}\sigma^z e^{-iK_F[0](t)}} = \cos^2\alpha \sigma^z + \sin\alpha \cos\alpha \sigma^x, \end{aligned} \quad (2.37)$$

where

$$\cos\alpha = \frac{B_z - \Omega/2}{\epsilon_{\text{rot}}}, \quad \sin\alpha = \frac{B_{\parallel}}{\epsilon_{\text{rot}}}, \quad \epsilon_{\text{rot}} = \sqrt{(B_z - \Omega/2)^2 + B_{\parallel}^2}$$

and

$$\bar{\rho}_1 = \frac{1}{2}(\mathbf{1} - \bar{\sigma}_F^z[0]), \quad \bar{\rho}_2 = \frac{1}{2}(\mathbf{1} + \bar{\sigma}_F^x[0]).$$

In the high frequency limit, $\Omega \gg B_z, B_{\parallel}$, we have $\alpha \approx \pi$ and the dressed operators are approximately equal to the original operators $\bar{\sigma}_F^j[0] \approx \sigma^j$. This is expected since the rapidly rotating magnetic field averages to zero without having any significant effect on the spin operators. One can obtain non-trivial dressed operators if B_{\parallel}/Ω is kept constant as Ω gets large and hence $\tan\alpha \approx -2B_{\parallel}/\Omega$ is fixed. As we discuss in subsequent sections, this is precisely the key idea behind obtaining non-trivial Floquet Hamiltonians, namely to scale the amplitude of the drive with the driving frequency. Let us also point out that, in the low-frequency regime $\Omega < 2B_z$, in the limit $B_{\parallel} \rightarrow 0$ we have $\bar{\sigma}_F^z[0] \rightarrow \sigma^z$ and $\bar{\sigma}_F^x[0], \bar{\sigma}_F^y[0] \rightarrow 0$. This result might look a bit counter-intuitive (a zero dressed operator $\bar{\sigma}_F^x[0]$ means that the outcome of any FNS measurement with any initial conditions of σ^x will be zero), but

one has to keep in mind that in the low-frequency regime there is no time scale separation. For example if $\Omega \ll 2B_z$, then averaging over one period necessarily implies averaging over many precession periods in a static magnetic field. Usually, the dressed operators are useful in the high-frequency regime, if there is a clear time scale separation between the fast dynamics governed by the kick operators and slow effective dynamic governed by the Floquet Hamiltonian.

Similarly, one can find the dressed spin operators and the density matrices in the effective Hamiltonian picture (see Eq. (2.26)). In this case we have

$$H_{\text{eff}} = - \left(1 - \frac{\Omega}{2\epsilon_{\text{rot}}}\right) \epsilon_{\text{rot}} \sigma^z, \quad K_{\text{eff}}(t) = \frac{\alpha - \pi}{2} (-\sigma^x \sin \Omega t + \sigma^y \cos \Omega t), \quad (2.38)$$

and the averaging over the period gives

$$\bar{\sigma}_{\text{eff}}^x = \sin^2 \frac{\alpha}{2} \sigma^x, \quad \bar{\sigma}_{\text{eff}}^y = \sin^2 \frac{\alpha}{2} \sigma^y, \quad \bar{\sigma}_{\text{eff}}^z = -\cos \alpha \sigma^z. \quad (2.39)$$

As expected, the effective Hamiltonian picture gives qualitatively similar asymptotic expressions for the dressed operators as the stroboscopic Floquet picture in the high frequency limit ($\alpha \rightarrow \pi$), where the dressed operators approach the bare operators. The main difference is that the effective Hamiltonian picture, unlike the stroboscopic picture, preserves the rotational symmetry around z -axes, while the stroboscopic Floquet picture breaks this symmetry. Thus the difference between stroboscopic and effective Floquet descriptions is similar to the difference between Landau and symmetric gauges for a particle in a magnetic field. Both gauges are completely equivalent. One breaks the rotational symmetry, while the other preserves it. It might seem that the symmetric (effective) gauge is more convenient, but the Floquet gauge also has its own advantages giving a more intuitive picture of the spin dynamics in the lab frame. One can check that the kick operator $K_{\text{eff}}(0)$ defines the gauge transformation between the two representations as (c.f. Eq. (2.13)):

$$H_F[0] = e^{-iK_{\text{eff}}(0)} H_{\text{eff}} e^{iK_{\text{eff}}(0)}, \quad \bar{\sigma}_F^i[0] = e^{-iK_{\text{eff}}(0)} \bar{\sigma}_{\text{eff}}^i e^{iK_{\text{eff}}(0)}$$

It is interesting to note that the dressed Pauli matrices no longer obey the commutation relations $[\bar{\sigma}^i, \bar{\sigma}^j] \neq 2i\epsilon_{ijk}\bar{\sigma}^k$. Also it is straightforward to check that the dressed density matrices represent mixed states: $\bar{\rho}^2 \neq \bar{\rho}$, unless $\alpha = \pi$.

2.2 Inverse Frequency Expansions

With very few exceptions, like uniform rotations or driven harmonic systems where the evolution operator can be found exactly, it is impossible to obtain the Floquet Hamiltonian in a closed form. Moreover, in situations where the periodic driving leads to chaotic dynamics at a single-particle level [94, 95] or to heating to infinite temperatures for many-particle systems [77–80] local Floquet Hamiltonians do not exist. An important limit, where one can define the Floquet Hamiltonian at least perturbatively, corresponds to the situations of fast driving, where the driving frequency is much faster than all natural energy scales of the system. For example, for a pendulum the driving should be fast compared to the oscillation period, for particles in a periodic potential the driving should be faster than the band width or a typical interaction scale. In such situations, the system has a hard time absorbing energy from the drive, which results in virtual processes dressing the low-energy Hamiltonian. With the high-frequency driving limit at the back of our mind, in this section, we discuss three different, but equivalent inverse-frequency expansions developed to find the effective low-energy Floquet Hamiltonian.

2.2.1 The Floquet-Magnus Expansion for the Stroboscopic Floquet Hamiltonian

A very efficient tool to compute the Floquet Hamiltonian in the high-frequency limit is the Floquet-Magnus high-frequency expansion (FM HFE), which is a perturbative scheme in the driving period T to compute $H_F[t_0]$. We refer to Ref. [96] for a summary of other stroboscopic perturbative methods to find Floquet Hamiltonians in the high-frequency limit. In general, given a model it is not known how to predict whether the Floquet-Magnus

expansion has a finite radius of convergence, especially in the thermodynamic limit. It has recently been shown that the FM HFE is at least an asymptotic series [97, 98], see Sec. 2.3. The issue of the convergence of the FM HFE is important for understanding the behaviour of the system in the limit $t \rightarrow \infty$. However, if one is interested in describing a finite-time evolution, then the short period expansion is well-behaved and the FM expansion can be safely used.

The evolution operator over a full driving cycle is, in general, given by the time-ordered exponential of $H(t)$:

$$U(T + t_0, t_0) = \mathcal{T}_t \exp \left(-\frac{i}{\hbar} \int_{t_0}^{T+t_0} dt H(t) \right) = \exp \left(-\frac{i}{\hbar} H_F[t_0] T \right),$$

where we have used Floquet's theorem (2.3). In this section we explicitly insert the factors of \hbar to highlight that the limit $\hbar \rightarrow 0$ is well-defined, and the expansion applies both to quantum and classical systems⁷. Taking the logarithm of both sides of the equation above and expanding the exponents in a Taylor series (c.f. App. B), which is justified if the period is sufficiently short, one can represent $H_F[t_0]$ as [89]:

$$\begin{aligned} H_F[t_0] &= H_F^{(0)} + H_F^{(1)}[t_0] + H_F^{(2)}[t_0] + \dots, \\ K_F[t_0](t) &= K_F^{(0)}[t_0](t) + K_F^{(1)}[t_0](t) + K_F^{(2)}[t_0](t) + \dots. \end{aligned} \quad (2.40)$$

The Floquet-Magnus expansion can be uniquely obtained from the general expression in Eq. (2.16) by imposing the boundary condition on the kick operator $K_Ft_0 = 0$. The superindex (n) means that $H_F^{(n)}[t_0]$ is of order Ω^{-n} , and similarly for the stroboscopic kick

⁷There is an important caveat here: classical systems are often governed by non-linear equations of motion, while Floquet's theorem, strictly speaking, applies to linear problems only. It is an open question what is the correct regime of validity, when one first quantises the system, then applies Floquet's theory, and finally takes the classical limit $\hbar \rightarrow 0$.

operator $K_F^{(n)}[t_0](t)$ ⁸. The first few terms are given by

$$\begin{aligned}
 H_F^{(0)} &= \frac{1}{T} \int_{t_0}^{T+t_0} dt H(t) = H_0, \\
 H_F^{(1)}[t_0] &= \frac{1}{2!T\hbar} \int_{t_0}^{T+t_0} dt_1 \int_{t_0}^{t_1} dt_2 [H(t_1), H(t_2)], \\
 &= \frac{1}{\hbar\Omega} \sum_{\ell=1}^{\infty} \frac{1}{\ell} \left([H_\ell, H_{-\ell}] - e^{i\ell\Omega t_0} [H_\ell, H_0] + e^{-i\ell\Omega t_0} [H_{-\ell}, H_0] \right) \\
 H_F^{(2)}[t_0] &= \frac{1}{3!T(i\hbar)^2} \int_{t_0}^{T+t_0} dt_1 \int_{t_0}^{t_1} dt_2 \int_{t_0}^{t_2} dt_3 \left([H(t_1), [H(t_2), H(t_3)]] + (1 \leftrightarrow 3) \right),
 \end{aligned} \tag{2.41}$$

where we have expanded the time-periodic Hamiltonian in its Fourier harmonics as:

$$H(t) = \sum_{\ell \in \mathbb{Z}} H_\ell e^{i\ell\Omega t}. \tag{2.42}$$

Similarly, the leading terms in the series for the stroboscopic kick operator are given by

$$\begin{aligned}
 K_F^{(0)}[t_0](t) &= \mathbf{0}, \\
 K_F^{(1)}[t_0](t) &= \frac{1}{\hbar} \int_{t_0}^t dt' \left(H(t') - H_F^{(1)}[t_0] \right) = \frac{1}{i\hbar\Omega} \sum_{\ell \neq 0} H_\ell \frac{e^{i\ell\Omega t} - e^{i\ell\Omega t_0}}{\ell}.
 \end{aligned} \tag{2.43}$$

Higher-order terms can be obtained directly, e.g. following Appendix B.1. The zeroth-order term in the Floquet Hamiltonian is simply the time-averaged Hamiltonian while the zeroth-order stroboscopic kick operator is identically zero. Obviously both zeroth-order terms are Floquet-gauge invariant, i.e. independent of t_0 . On the contrary, the corrections to the stroboscopic Hamiltonian $H_F[t_0]$ and kick operator $K_F[t_0](t)$ depend on the Floquet gauge t_0 . This gauge dependence is not always convenient especially for FNS dynamics. As we discussed in the previous section using the circularly driven two-level system, fixing t_0 in the stroboscopic Floquet Hamiltonian is similar to using the Landau gauge for a particle in

⁸We cautiously use the notation $+$... to emphasise that the approximate Hamiltonian on the RHS of Eq. (2.40) need not necessarily converge to the exact Floquet Hamiltonian. In fact, as we shall show later, all approximate Floquet Hamiltonians (and thus kick operators) obtained using the inverse-frequency expansion in general miss Floquet resonances, depending on the reference frame the expansion is applied in, see Chapters 4 and 5.

a constant magnetic field, which explicitly breaks the $U(1)$ symmetry of the Hamiltonian (rotations around the magnetic field). In the Floquet Hamiltonian this $U(1)$ symmetry corresponds to the symmetry with respect to the phase shift of the drive and is equivalent to the translations of t_0 . In many situations, it might be preferable to work with a Floquet Hamiltonian which does not break this $U(1)$ symmetry. This can be achieved by doing a different expansion for the effective Hamiltonian [9, 10, 32, 86, 87] which we discuss in Sec 2.2.2.

For classical systems, the equivalent FM HFE expansion can be obtained by substituting the commutators between the operators with the Poisson brackets of the corresponding classical functions: $[\cdot, \cdot]/i\hbar \rightarrow \{\cdot, \cdot\}$. It is interesting to note that there is no formal Floquet theorem for classical non-linear systems. Nevertheless, there is a well-defined classical limit for the high frequency expansion of the Floquet Hamiltonian. So if this expansion has a finite radius of convergence, effectively the result of Floquet theory applies to classical systems as well. For a numerical algorithm to implement the Floquet-Magnus series, see Ref. [99].

2.2.2 The van Vleck Expansion for the Non-Stroboscopic Floquet Hamiltonian.

As mentioned in Sec. 2.1.2, it is possible to change basis and work with the manifestly Floquet-gauge invariant effective Hamiltonian H_{eff} and the kick operator $K_{\text{eff}}(t_0)$. The latter carries all the dependence on the Floquet gauge t_0 , and describes the micromotion. This approach offers the advantage that the dependence on the Floquet gauge will not enter the inverse-frequency expansion of H_{eff} , and is enabled by the fact that the unitary change-of-basis transformation generated by $K_{\text{eff}}(t_0)$ effectively re-organises the terms in the perturbative series expansions. Such an expansion is provided by the van Vleck High-Frequency Expansion (vV HFE) for the effective Hamiltonian [9, 10, 32, 86, 87].

The vV HFE is obtained uniquely if we impose another boundary condition on the general kick operator from Eq. (2.16): $\int_0^T dt K_{\text{eff}}(t) = 0$. This condition is non-stroboscopic

in the sense that, in general, there does not exist a time t_0 for which $K_{\text{eff}}(t_0)$ vanishes, see the circularly driven two-level system in Sec. 2.1.3. In a similar fashion to the Magnus expansion, we can decompose the effective Hamiltonian and the kick operator as

$$\begin{aligned} H_{\text{eff}} &= H_{\text{eff}}^{(0)} + H_{\text{eff}}^{(1)} + H_{\text{eff}}^{(2)} + \dots, \\ K_{\text{eff}}(t) &= K_{\text{eff}}^{(0)}(t) + K_{\text{eff}}^{(1)}(t) + K_{\text{eff}}^{(2)}(t) + \dots, \end{aligned} \quad (2.44)$$

where $H_{\text{eff}}^{(n)} \sim \Omega^{-n}$ and $K_{\text{eff}}^{(n)}(t) \sim \Omega^{-n}$. Then, using the Fourier decomposition of the time-dependent Hamiltonian $H(t)$ in Eq. (2.42), one has [9, 32, 87] (see also Appendix B):

$$\begin{aligned} H_{\text{eff}}^{(0)} &= H_0 = \frac{1}{T} \int_0^T dt H(t), \\ H_{\text{eff}}^{(1)} &= \frac{1}{\hbar\Omega} \sum_{\ell=1}^{\infty} \frac{1}{\ell} [H_{\ell}, H_{-\ell}] \\ &= \frac{1}{2!T\hbar} \int_0^T dt_1 \int_0^{t_1} dt_2 \left[\left(1 - 2\frac{t_1 - t_2}{T} \right) \bmod T \right] [H(t_1), H(t_2)], \\ H_{\text{eff}}^{(2)} &= \frac{1}{\hbar^2\Omega^2} \sum_{\ell \neq 0} \left(\frac{[H_{-\ell}, [H_0, H_{\ell}]]}{2\ell^2} + \sum_{\ell' \neq 0, \ell} \frac{[H_{-\ell'}, [H_{\ell'-\ell}, H_{\ell}]]}{3\ell\ell'} \right). \end{aligned} \quad (2.45)$$

The mod-function in the integral above should be understood in the sense that the expression given by the function with dimensionless argument $\tau = \Omega t$: $f(\tau) = 1 - \tau/\pi$, $\tau \in [0, 2\pi]$ is 2π -periodic [87]. The expansion for the kick operator is given by [9, 32, 87]

$$\begin{aligned} K_{\text{eff}}^{(0)}(t) &= \mathbf{0}, \\ K_{\text{eff}}^{(1)}(t) &= \frac{1}{i\hbar\Omega} \sum_{\ell \neq 0} \frac{e^{i\ell\Omega t}}{\ell} H_{\ell} = \frac{1}{2\hbar} \int_t^{T+t} dt' H(t') \left[\left(1 - 2\frac{t - t'}{T} \right) \bmod T \right]. \end{aligned} \quad (2.46)$$

The relation between the stroboscopic and the effective (non-stroboscopic) Floquet Hamiltonian and kick operator reads

$$H_F[t_0] = H_{\text{eff}}^{(0)} + H_{\text{eff}}^{(1)} - i \left(\left[K_{\text{eff}}^{(1)}(t_0), H_{\text{eff}}^{(0)} \right] + \left[K_{\text{eff}}^{(0)}(t_0), H_{\text{eff}}^{(1)} \right] \right) + \mathcal{O}(\Omega^{-2})$$

$$\begin{aligned}
H_F^{(1)}[t_0] &= H_{\text{eff}}^{(1)} - i \left[K_{\text{eff}}^{(1)}(t_0), H_{\text{eff}}^{(0)} \right], \\
K_F^{(1)}[t_0](t) &= K_{\text{eff}}^{(1)}(t) - K_{\text{eff}}^{(1)}(t_0).
\end{aligned} \tag{2.47}$$

Unlike the FM expansion, no closed form expression for the n -th order term is known to date. Some higher-order terms in the vV HFE, including the third order, are calculated and tabulated in Ref. [59].

2.2.3 The Brillouin-Wigner Inverse-Frequency Expansion

A third alternative expansion was introduced in Ref. [59], based on Brillouin-Wigner perturbation theory in the one-photon sector. Similar to the vV HFE, the Brillouin-Wigner high-frequency expansion (BW HFE) also produces a manifestly Floquet-gauge (i.e. t_0) independent Floquet Hamiltonian H_{BW} . Like the FM HFE, it has the advantage that it allows one to write down a closed-form expression for the n -th order term, which can facilitate numerical studies. It is interesting to note that *beyond the order of the approximation* the BW expansion contains fictitious non-hermitian terms. Nonetheless, due to the difference in the perturbation theory, the BW HFE might actually have different convergence properties than the FM and the vV HFEs and can thus prove very useful. Since we shall not make use of it throughout this thesis, we do not discuss it explicitly here; instead, the interested reader is invited to consult Ref. [59], where the BW expansion is applied to topological band models.

Whenever the parameters in the Hamiltonian do not scale with the driving frequency, the n -th order term in all expansions is proportional to T^n . Thus, the higher-order terms get more and more suppressed as the period $T \rightarrow 0$. It then follows that in the infinite-frequency limit all of $H_F[t_0]$, H_{eff} and H_{BW} reduce to the time-averaged Hamiltonian, as one would intuitively expect. As we shall discuss in the next Chapter in greater detail, very interesting non-trivial limits can occur when some couplings in the Hamiltonian scale with frequency. In this case, terms in different orders in the above expansions can scale with the same power of the period T . Then in the infinite-frequency limit, one can obtain nontrivial

Floquet Hamiltonians, quite different from the time-averaged Hamiltonian, as it is the case for the Kapitza pendulum. The FM, vV and BW expansions help one identify both the leading and subleading terms in the driving period T for different models. They also allow one to understand the required scaling behaviour of the driving amplitude with frequency to obtain novel and interesting infinite-frequency limits. And finally, they can be used to design protocols suitable for engineering synthetic Floquet Hamiltonians with prescribed properties. In the next section, we discuss the differences and similarities between the FM and vV expansions using an exactly-solvable model.

2.2.4 Floquet-Magnus vs. van Vleck Expansion: the Two-Level System in a Circularly Driven Magnetic Field Revisited

Although the Floquet-Magnus expansion (FM HFE) and the van Vleck expansion (vV HFE) share many common properties, they also possess some very distinctive features. In order to illustrate them intuitively, we shall briefly revisit the exactly solvable model of a two-level system in a circularly-polarised magnetic field, see Sec. 2.1.3.

We want to compare the exact expression for $H_F[t_0]$ and H_{eff} to the approximate Hamiltonians $H_F^{(0+1+2)}[t_0]$ and $H_{\text{eff}}^{(0+1+2)}$ obtained from the FM HFE and vV HFE, respectively, up to and including order Ω^{-2} . Using Eq. (2.41) we find:

$$\begin{aligned} H_F^{(0)} &= B_z \sigma^z \\ H_F^{(1)}[t_0] &= -\frac{1}{\Omega} \left[B_{\parallel}^2 \sigma^z + 2B_{\parallel} B_z (\sigma^x \cos(\Omega t_0) + \sigma^y \sin(\Omega t_0)) \right] \\ H_F^{(2)}[t_0] &= \frac{1}{\Omega^2} \left[(2B_{\parallel}^3 - 4B_{\parallel} B_z^2) (\sigma^x \cos(\Omega t_0) + \sigma^y \sin(\Omega t_0)) - 4B_{\parallel}^2 B_z \sigma^z \right]. \end{aligned}$$

Similarly, from Eq. (2.45) we derive:

$$H_{\text{eff}}^{(0)} = B_z \sigma^z, \quad H_{\text{eff}}^{(1)} = -\frac{B_{\parallel}^2}{\Omega} \sigma^z, \quad H_{\text{eff}}^{(2)} = -\frac{2B_{\parallel}^2 B_z}{\Omega^2} \sigma^z. \quad (2.48)$$

One can check that these expansions are consistent with the corresponding ones obtained

from Eqs. (2.24) and (2.26), respectively.

Let us compute the approximate spectra $\epsilon_F^{(0+1+2)}$ and $\epsilon_{\text{eff}}^{(0+1+2)}$ obtained by summing the FM and vV HFE up to order Ω^{-2} . The inverse-frequency expansions of $\epsilon_F^{(0+1+2)}$, $\epsilon_{\text{eff}}^{(0+1+2)}$ as well as the exact Floquet spectrum ϵ_F read:

$$\begin{aligned}\epsilon_F^{(0+1+2)} &= \pm \left(-B_z + \frac{B_{\parallel}^2}{\Omega} + 2\frac{B_{\parallel}^2 B_z}{\Omega^2} + \frac{2(B_{\parallel}^4 - 4B_{\parallel}^2 B_z^2)}{\Omega^3} \right) + \mathcal{O}(\Omega^{-4}), \\ \epsilon_{\text{eff}}^{(0+1+2)} &= \pm \left(-B_z + \frac{B_{\parallel}^2}{\Omega} + 2\frac{B_{\parallel}^2 B_z}{\Omega^2} + 0 \times \frac{1}{\Omega^3} \right), \\ \epsilon_F &= \pm \left(-B_z + \frac{B_{\parallel}^2}{\Omega} + 2\frac{B_{\parallel}^2 B_z}{\Omega^2} + \frac{4B_{\parallel}^2 B_z^2 - B_{\parallel}^4}{\Omega^3} \right) + \mathcal{O}(\Omega^{-4}).\end{aligned}\quad (2.49)$$

Clearly, the spectra of the approximated Hamiltonians agree to each other, and to the exact spectrum up to order Ω^{-2} , i.e. within the validity of the approximation. They differ, however, starting from order Ω^{-3} . This is not surprising since we have computed $H_F^{(0+1+2)}[t_0]$ and $H_{\text{eff}}^{(0+1+2)}$ to order Ω^{-2} and, therefore, all terms in the spectrum to higher order should be considered spurious. If we include the Ω^{-3} -correction in both expansions, the spectra will agree to order Ω^{-3} and disagree starting from order Ω^{-4} . Other quantities, which are invariant under a change of basis, are expected to display similar behaviour.

For generic models (but not this one), it is possible that the spectrum of the approximated Floquet Hamiltonian contains t_0 (or driving phase-dependent) corrections. However these corrections always appear beyond the order of the validity of the approximation and should not be taken into consideration [87].

Equivalence of the two descriptions. Within this example it is easy to understand the difference between the stroboscopic $H_F[t_0]$ and the effective H_{eff} Hamiltonian. For simplicity, let us approximate both Hamiltonians to order Ω^{-1} . In the stroboscopic Hamiltonian the Floquet-gauge dependent term represents a small magnetic field of magnitude $-2B_{\parallel}B_z/\Omega$, confined to the xy -plane. Its direction with respect to the x -axis is determined by the angle $\phi = \Omega t_0$, i.e. it explicitly depends on the Floquet gauge. In particular, for

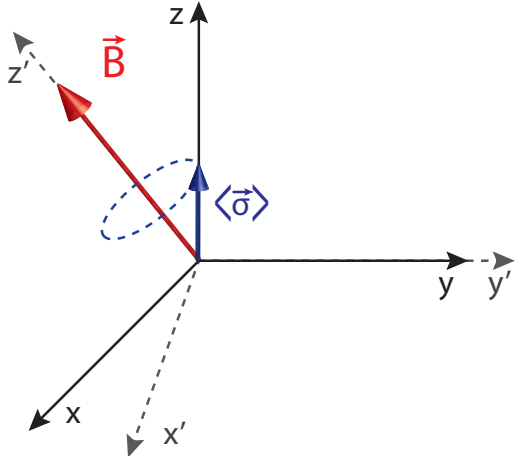


Figure 2.3: Precession of the initial state (blue) around the effective magnetic field (red) \mathbf{B} described by the Hamiltonian $H_F^{(0+1)}[0] = (B_z - B_{\parallel}^2/\Omega)\sigma^z - (2B_{\parallel}B_z/\Omega)\sigma^x$. The non-primed coordinate frame is the lab-frame, where the dynamics is described by $K_F[0](t)$ and $H_F[0]$. The primed coordinates correspond to the frame where the dynamics is governed by $K_{\text{eff}}(t)$ and H_{eff} . The transformation between the two is given by the initial kick $K_{\text{eff}}(0)$. This image assumes that the Floquet gauge is $t_0 = 0$, so that $K_{\text{eff}}(0)$ is the generator of rotations along the y -axis, c.f. Eq. (2.26).

$t_0 = 0$, it points along the x -axis (see Fig. 2.3). On the contrary, such a term is not present in H_{eff} , which is explicitly t_0 -independent. Instead, the gauge dependence is encoded in the kick operator $K_{\text{eff}}(t)$, which defines the direction of the instantaneous magnetic field, c.f. Fig. 2.3.

For instance, if we are interested in stroboscopic dynamics with $t_1 = t_0 = 0$ and $t_2 = t_1 + nT$ (i.e. we initialise the system at $t_1 = 0$ and measure observables at the final time $t_2 = nT$), we can either use the stroboscopic Floquet Hamiltonian, which contains a small x -magnetic field, or the effective Hamiltonian, whose magnetic field is purely along the z -direction. However, in the latter case one has to apply the kick operator $K_{\text{eff}}(t_0)$ to both the initial state and the measured observables. This kick operator transforms the initial state and the observables into the new coordinate system (see Fig. 2.3). Similar considerations apply to FNS evolution where the stroboscopic and effective descriptions are completely equivalent.

Whenever one is interested in stroboscopic dynamics only, the FM HFE can be preferable to the vV HFE, as one needs to calculate only the stroboscopic Floquet Hamiltonian $H_F[t_0]$. Conversely, in the vV picture, one has to compute both the effective Hamiltonian H_{eff} and the effective kick operator $K_{\text{eff}}(t)$. If one is interested in FNS dynamics, or in the spectral properties of the Floquet Hamiltonian, then the effective description offers an advantage, since it gives a Hamiltonian which does not contain terms that depend on the Floquet gauge, i.e. the phase of the drive. One has to keep in mind, though, that it is crucial to use the properly dressed operators and the dressed initial density matrix in both the stroboscopic and effective description for FNS evolution.

2.2.5 The Inverse Frequency Expansion in the Rotating Frame

In some cases, for example when the driving amplitude scales with frequency, one is confronted with the problem of re-summing an infinite sub-series in the FM (vV) HFE to obtain the proper infinite-frequency stroboscopic (effective) Hamiltonian. For example, let us imagine the simplest protocol

$$H(t) = H_0 + \Omega\lambda(t)H_1, \quad (2.50)$$

where $\lambda(t)$ is a periodic function with zero mean, whose period is T . To emphasise that the amplitude of the driving protocol is proportional to the driving frequency Ω we made this explicit in Eq. (2.50). Using Eq. (2.41) we infer that the n -th order term in the inverse-frequency expansion involves a nested commutator containing $n+1$ terms (e.g. $H_F^{(1)}[t_0]$ has a commutator containing the Hamiltonian $H(t)$ twice, $H_F^{(2)}[t_0]$ has a nested commutator containing $H(t)$ three times, etc.). It then becomes clear that the terms in the n -th order of the expansion containing once H_0 and n -times H_1 are all independent of the driving frequency, since the power-law divergence with Ω is precisely cancelled by the Ω -dependent factor coming from the measure when the time-ordered integral is made dimensionless. On the other hand, the other terms, which contain H_0 more than once are subleading and

vanish in the limit $T \rightarrow 0$ ($\Omega \rightarrow \infty$). This may look like a special case, but it is precisely the setup necessary to obtain interesting and counter-intuitive behaviour in the high-frequency limit.

One can significantly simplify the analysis if the Hamiltonian can be written in the form (2.50) or more generally as

$$H(t) = H_0 + \Omega \sum_{j=1}^n \lambda_j(t) H_j,$$

where $\lambda_j(t)$ are periodic functions with the same common period and H_j , $j = 1, \dots, n$, are mutually commuting terms (but not commuting with H_0). Notice that since the driving amplitude scales with the driving frequency, it is not immediately clear what the infinite-frequency limit is. In such situations, it is convenient to first make a transformation into a rotating frame (rot frame). Focusing on the Hamiltonian (2.50) we define the rotation operator as

$$V(t) = \exp \left[-i\Omega \int_{t_0}^t \lambda(t') dt' H_1 \right] = \exp [-i F(t) H_1], \quad (2.51)$$

where $F(t) = \int_{t_0}^t \Omega \lambda(t') dt'$ only depends on the driving frequency via its the time-periodic argument. As before, the choice of t_0 is the Floquet gauge choice for the rotating frame. The transformation to the rot frame $V(t)$ explicitly depends on the choice t_0 and hence the t_0 -dependent part of it represents a Floquet gauge transformation. We adopt the convention that $V(t)$ transforms from the rotating frame into the lab frame. Then the wave function, the density matrix and the operators transform as

$$\begin{aligned} |\psi^{\text{rot}}(t_1)\rangle &= V^\dagger(t_1) |\psi(t_1)\rangle, \\ \rho^{\text{rot}}(t_1) &= V^\dagger(t_1) \rho(t_1) V(t_1), \\ \mathcal{O}^{\text{rot}}(t_2) &= V^\dagger(t_2) \mathcal{O}(t_2) V(t_2). \end{aligned} \quad (2.52)$$

The Hamiltonian in the rotating frame acquires an extra Galilean term due to the fact that

the transformation is time-dependent:

$$\begin{aligned} H^{\text{rot}}(t) &= V^\dagger(t) [H_0 + \Omega\lambda(t)H_1] V(t) - iV^\dagger(t)\partial_t V(t) \\ &= V^\dagger(t)H_0V(t). \end{aligned} \tag{2.53}$$

Thus, the transformation to the rotating frame removes the oscillating term with a divergent amplitude H_1 , effectively replacing it by a Hamiltonian with a fast oscillating phase. Note that $H^{\text{rot}}(t)$ is a periodic function of time if $\lambda(t)$ has a zero mean (if the mean is nonzero the rot frame Hamiltonian can be still periodic in special cases, e.g. when the spectrum of H_1 is quantised in integers, as will be the case for the realisation of the Harper-Hofstadter Hamiltonian discussed in Sec. 3.1.3.3, or when we discuss the static and the dynamic Schrieffer-Wolff transformation in Sec. 3.2; alternatively, one can always separate out the mean by re-defining H_0). If $V^\dagger(t)H_0V(t)$ is a local operator, one can find the evolution in the rotating frame by applying the inverse frequency expansion. But unlike in the original lab frame, there are no more divergent terms in the transformed Hamiltonian. Hence, the infinite-frequency limit is simply determined by the time average of $H^{\text{rot}}(t)$, and the n -th order corrections in the inverse frequency are precisely given by the n -th order inverse-frequency expansion in the rotating frame. Evaluating $H^{\text{rot}}(t)$ explicitly is only possible when $V(t)$ is simple. This is the case, for example, when H_1 is a single-particle operator. These are precisely the situations, in which one can do a partial resummation of the FM (vV) HFE in the lab frame. We note in passing that for $F(-t) = F(t)$ the driving protocol in the rot frame is an even function of time, and hence all odd-order corrections in the FM expansion in this symmetric gauge vanish identically [89].

It is straightforward to find the relation between the Floquet Hamiltonians as well as the kick operators in the original lab frame and the rot frame. Recall from general Floquet theory (c.f. Eq. (2.5)) that in the lab and the rot frames the evolution operator reads as:

$$U(t_2, t_1) = e^{-i\hat{K}(t_2)} e^{-i\hat{H}_F(t_2-t_1)} e^{i\hat{K}(t_1)}$$

$$U^{\text{rot}}(t_2, t_1) = e^{-i\hat{K}^{\text{rot}}(t_2)} e^{-i\hat{H}_F^{\text{rot}}(t_2-t_1)} e^{i\hat{K}^{\text{rot}}(t_1)}. \quad (2.54)$$

On the other hand, the evolution operators in the two frames are related by

$$U(t_2, t_1) = V(t_2) U^{\text{rot}}(t_2, t_1) V^\dagger(t_1). \quad (2.55)$$

Comparing the three expressions above and noting that $V(t)$ is periodic with period T by construction, we see that:

$$e^{-i\hat{K}(t)} = V(t) e^{-i\hat{K}^{\text{rot}}(t)} = e^{-iF(t)H_1} e^{-i\hat{K}^{\text{rot}}(t)}, \quad \hat{H}_F = \hat{H}_F^{\text{rot}}, \quad (2.56)$$

where we used Eq. (2.51). The expression above allows one to transform the kick operator from the lab to the rotating frame using the operator $V(t)$. We can calculate the expansions for the kick operator and the Floquet Hamiltonian directly in the rotating frame by replacing $H(t) \rightarrow H^{\text{rot}}(t) = V^\dagger(t)H_0V(t)$ in Eqs. (2.41), (2.43), (2.45) and (2.46). Using specific examples, we shall illustrate that a successful strategy for finding the Floquet Hamiltonian and the dressed operators is: i) to first perform the transformation to the rotating frame w.r.t. the driving Hamiltonian in order to remove the terms which diverge with the driving frequency, and ii) then use the inverse-frequency expansion to find the stroboscopic (effective) Floquet Hamiltonian as well as the dressed operators. Finally, iii), (if needed) we return back to the lab frame. Going to the rotating frame can offer the same benefits for calculating dressed operators (including the density matrix) as for calculating Floquet Hamiltonians. Namely, if the amplitude of the driving diverges with the frequency, going to the rot frame and evaluating a simple time-average of the corresponding operator (or the density matrix) is equivalent to a re-summation of an infinite sub-series for \bar{O} in the lab frame. So both for the Hamiltonian and for the dressed observables the FM and vV HFE are the proper Ω^{-1} -expansions even if the driving amplitude scales with the driving frequency.

Let us also emphasise that the exact dressed operators and the exact dressed density

matrix are the same in the lab and in the rotating frames both in the stroboscopic (Floquet-Magnus) and the non-stroboscopic (van Vleck) pictures:

$$\overline{\rho^{\text{rot}}} = \overline{\rho}, \quad \overline{\mathcal{O}^{\text{rot}}} = \overline{\mathcal{O}}. \quad (2.57)$$

Obviously, this is not true in general for the bare operators and the bare density matrix

$$\rho^{\text{rot}}(t) \neq \rho, \quad \mathcal{O}^{\text{rot}}(t) \neq \mathcal{O}.$$

Equation (2.57) follows from an observation that $V(t)$ entering the new kick operator, Eq. (2.56), exactly cancels the corresponding transformation of the operator \mathcal{O} into the rotating frame (Eq. (2.52)).

As anticipated above, it is often convenient to compute the the dressed operators and dressed density matrix in the rotating frame where the driving amplitude does not scale with the driving frequency. The leading terms in Ω^{-1} are given by

$$\begin{aligned} \overline{\mathcal{O}^{\text{rot}}} &= \frac{1}{T} \int_0^T dt \left(\mathcal{O}^{\text{rot}}(t) - i \left[\hat{K}^{\text{rot},(1)}(t), \mathcal{O}^{\text{rot}}(t) \right] \right) + \mathcal{O}(\Omega^{-2}) \\ \overline{\rho^{\text{rot}}} &= \frac{1}{T} \int_0^T dt \left(\rho^{\text{rot}}(t) - i \left[\hat{K}^{\text{rot},(1)}(t), \rho^{\text{rot}}(t) \right] \right) + \mathcal{O}(\Omega^{-2}) \end{aligned} \quad (2.58)$$

where we recall that, by construction, $\hat{K}^{\text{rot},(1)} \sim \Omega^{-1}$. If an observable commutes with the operator H_1 to which the driving couples, then it is left unchanged by the transformation to the rotating frame $V(t)$, i.e. the observable $\mathcal{O}^{\text{rot}}(t)$ is time-*independent* and equal to the observable in the lab frame $\mathcal{O}^{\text{rot}}(t) = \mathcal{O}^{\text{lab}}$. As a consequence, all time dependence in the integral comes from the kick operator $\hat{K}^{(1)}(t)$. If the kick operator has a zero average (as it is the case in the van Vleck picture, $\hat{K}^{(1)}(t) = K_{\text{eff}}^{(1)}(t)$, c.f. Eq. (2.46)), then the dressed observable does not have a Ω^{-1} -correction. A similar reasoning applies to the density matrix, $\overline{\rho^{\text{rot}}}(t)$. Notice, however, that the Ω^{-1} -corrections are in general present if: i) the observables and/or the density matrix do not commute with H_1 , or ii) if one chooses the

stroboscopic picture since, in this case, $\hat{K}^{(1)}(t) = K_F^{(1)}[t_0](t)$ does not have a zero average, c.f. Eq (2.43). We demonstrate this explicitly in Sec. 3.1.1.4 using the example of the Kapitza pendulum.

Finally, the dressed observables in the FM and vV pictures are related by the transformation

$$\bar{\mathcal{O}}_F[0] = e^{-iK_{\text{eff}}(0)} \bar{\mathcal{O}}_{\text{eff}} e^{iK_{\text{eff}}(0)}, \quad \bar{\rho}_F[0] = e^{-iK_{\text{eff}}(0)} \bar{\rho}_{\text{eff}} e^{iK_{\text{eff}}(0)}. \quad (2.59)$$

Expanding these equations to leading order in Ω^{-1} and using $K_{\text{eff}}^{(0)} = \mathbf{0}$, we find

$$\bar{\mathcal{O}}_F^{(1)}[t_0] = -i \left[K_{\text{eff}}^{(1)}(t_0), \bar{\mathcal{O}}_{\text{eff}}^{(0)} \right], \quad \bar{\rho}_F^{(1)}[t_0] = -i \left[K_{\text{eff}}^{(1)}(t_0), \bar{\rho}_{\text{eff}}^{(0)} \right]. \quad (2.60)$$

2.3 Convergence of the Inverse-Frequency Expansion: a Collection of Facts and Ideas

The motivation and physical intuition behind the statements made below can be best understood after the reader has become familiar with the models from the remainder of this thesis. Nevertheless, we do not consider this topic to deserve a special Chapter due to the heuristic character of the majority of the arguments presented. Wherever references are made to specific concepts that were not yet introduced, the reader is invited to consult the corresponding discussion later on in the thesis⁹.

Below, we summarise a collection of results about the convergence of the Floquet-Magnus expansion (FM HFE). To present date, little is known about the convergence of the van Vleck expansion (vV HFE) and the Brillouin-Wigner (BW HFE), which are related to the FM HFE by a static, Ω -dependent unitary transformation, see Sec. 2.2. Therefore, here we focus predominantly on the convergence of the FM HFE. We would like to emphasise, though, that the statements we make for the inverse-frequency expansion below likely hold true for any of the three variants. There are arguments in the literature

⁹Doing a detour to a section or equation by clicking on the reference in colour, one can conveniently come back to the original page and line by using the shortcut key for *back* in the corresponding pdf viewer. For instance in Preview (Mac OS X), use “cmd + [”.

that in general the vV HFE and the BW HFE may have better convergence properties than FM HFE for some problems since they are manifestly t_0 -invariant [59, 87], but, to the best of our knowledge, there are no rigorous statements available to this date.

As we discussed throughout this thesis, the FM HFE is a very powerful tool to compute the Floquet Hamiltonian in the high-frequency limit. However, as it often happens in physics, perturbative expansions can be asymptotic, i.e. can have a zero radius of convergence. This does not mean that these expansions are useless because they still can give very accurate predictions for the behaviour of the system, e.g. for finite evolution times, but eventually such asymptotic expansions inevitably break down.

It was long believed, in the context of the Floquet-Magnus expansion, that the question of true vs. asymptotic convergence is ultimately related to the question of heating in the driven system [33]. As we shall see below, in fact, the convergence of the expansion depends strongly on the reference frame used to calculate the Floquet Hamiltonian, see Sec. 3.3.3.1 for an explicit example. In particular, if the FM HFE converges in the original lab frame, then this implies that the Floquet Hamiltonian is a local operator and, thus, the evolution of the system (up to the kick operators) is stroboscopically governed by a local static Hamiltonian, whence the total energy of the system is conserved. This is the situation for Floquet integrable systems, i.e. systems where quasienergy conservation and energy conservation are equivalent for finite (though likely large enough) frequencies. Namely, it can happen that the inverse-frequency expansion is convergent above some critical frequency, and divergent otherwise. If this scenario is realised in a generic many-body system, this leads to a dynamical localisation transition [77] where the system does not absorb energy from the external drive even in the infinite-time limit. Such an energy-space many-body localised Floquet system is given by the Hamiltonian in Eq. (3.115) for $\zeta = 0$ ¹⁰, where the Floquet Hamiltonian at any frequency Ω is given by the (ergodic) Fermi-Hubbard model with interaction strength Ω . On the other hand, a divergent HFE indicates that there exists no local

¹⁰It is currently an open problem whether this system heats up to an infinite temperature state at infinite times for large finite $\Omega \gg J_0$ and small $\zeta \ll 1$.

Floquet Hamiltonian, and the system heats up indefinitely ¹¹. In Floquet non-integrable systems, heating is believed (yet not proved!) to be generally present at infinite times and comes about through Floquet many-body resonances, cf. Sec. 5.3. Interestingly, however, energy absorption at high frequencies is at least exponentially suppressed [98, 100–102] in the thermodynamic limit, which can be explained using the concept of quasi-conserved local integrals of motion, see Sec. 5.1.1.

Even in the situations, where the HFE formally diverges, heating remains slow at fast driving frequencies [82, 98, 100–102]. Then the inverse-frequency expansion truncated to the first few orders can accurately describe the transient dynamics of the system for many periods of oscillations. In particular, in Ref. [82] it was shown that, for a dipolar-coupled periodically driven spin systems, the magnetisation quickly approaches a quasi-stationary value predicted by the Magnus expansion truncated at second order. Afterwards, at much longer times, the magnetisation decays to zero due to slow heating processes which are not captured by the HFE. Therefore, in this context, an important question is not whether the HFE expansion has a finite radius of convergence or only asymptotic, but whether there is a time-scale separation between interesting transient dynamics described by the local Floquet Hamiltonian truncated to some low order, and heating phenomena at longer times. While this issue is also not very well understood in general, there is sufficient evidence to indicate that such a time scale separation always exists at high driving frequencies [97, 98, 100–102]. For this reason, in Secs. 3.1.3.3, 3.1.3.4 and 3.1.3.5, the approximate Floquet Hamiltonians obtained by truncating the Floquet-Magnus and van Vleck expansions to order Ω^{-1} are, at the very least, expected to describe the transient dynamics and the relaxation to a quasi-steady state.

2.3.1 Systems with Bounded Hamiltonians

When the FM HFE is applied to systems, described by a bounded Hamiltonian at each point of time, it has well-behaved convergence properties. This is intimately related to the

¹¹More precisely, there are initial states, from which the system heats up indefinitely.

fact that for these systems *quasienergy* conservation, which holds at any driving frequency, suddenly turns into *energy* conservation above a fixed *finite* frequency. Such a critical frequency could, for instance, be on the order of the single particle bandwidth in non-interacting many-body systems.

From a mathematical point of view, the convergence issue has been extensively investigated in the literature, and a few different theorems are known (see Ref. [89] and references therein). In particular, the Magnus expansion is guaranteed to converge to the Floquet Hamiltonian if:

$$\int_0^T dt |\epsilon_{\max}(t) - \epsilon_{\min}(t)| < \xi \quad (2.61)$$

where $\epsilon_{\max}(t)$, $\epsilon_{\min}(t)$ are the largest and smallest eigenvalues of the Hamiltonian $H(t)$, and ξ is a number of order one (i.e. independent of the system size L for many-body systems).

The Magnus expansion can be rigorously shown to have a finite radius of convergence for integrable systems, which can be factorised into uncoupled sectors, e.g. in momentum space. Then the extensivity of the system is not important and the criterion (2.61) can be applied to each sector independently. Such systems do not heat up indefinitely and, in the long-time limit, effectively reach a steady state with respect to the Floquet Hamiltonian [103, 104].

2.3.1.1 Breakdown of the Inverse Frequency Expansion for Small Frequencies

Some conditions for the breakdown of the inverse-frequency expansion can easily be seen already in two simple exactly solvable examples studied in this thesis. Here, we explicitly draw the reader's attention to this interesting fact, which should help building up their intuition.

Shaken Lattice—The first example is the shaken lattice from Sec. 3.1.3.1. Recall the special role of the boundary condition in this problem: for PBC the model is mapped to a set of independent periodically-driven harmonic oscillators. In this case, it is easy to calculate the exact Floquet Hamiltonian and kick operators at any Ω . Furthermore, there is a perfect match with the ones obtained from the vV HFE. Interestingly, however, the

expansion is insensitive to the boundary conditions, meaning that the vV HFE Floquet Hamiltonian (and Kick operator) are the same irrespective of this choice. On the other hand, it is easy to verify numerically, that the exact Floquet Hamiltonian in the case of OBC and for frequencies smaller than the bandwidth of the non-driven model is a more complicated object. The reason for this is that, in the absence of momentum conservation, what used to be states of well-defined ‘momentum’ (in the presence of PBC) are now modes with finite transition matrix elements between each other. These matrix elements can then be resonantly enhanced by the drive whenever the energy difference of to modes becomes close enough to the drive frequency. As a result, the exact Floquet Hamiltonian becomes a non-local hermitian operator, unlike the one obtained with the help of the vV HFE for any finite system size¹². We conclude that, since the expansion misses these matrix elements, it cannot be convergent. This is the simplest example to exhibit the decisive role of resonances for the convergence of the inverse-frequency expansion.

Two-Level System in a Circular Drive—The second example is the exactly solvable two-level system from Sec. 2.1.3. In Sec. 4.3.4.1 we show that this model features a non-equilibrium topological phase transition whenever the frequency is lowered below a critical value $\Omega_c = 2$. Although this is only a two-level system, this critical value is analogous to the bandwidth threshold discussed above for the shaken lattice. Due to the topological character of the transition, it immediately follows that the two phases are not continuously connected as a function of the drive frequency which, in turn, indicates that the inverse-frequency expansion likely does not converge for $\Omega < \Omega_c$. In fact, this same discontinuity is manifestly present in the exact expression for the exact effective Kick operator¹³. In the following, we explain more closely the special role of resonances for the convergence of the expansion.

¹²The norm difference between the approximate and the exact Floquet Hamiltonians falls off as L^{-1} as $L \rightarrow \infty$.

¹³This is intimately related to the mysterious prefactor $\alpha - \pi$ in Eq. (2.26)

2.3.1.2 Changing the Reference Frame Changes the Convergence Properties

While we are revisiting models studied throughout the thesis, let us also go back to briefly discuss the convergence properties of the expansion in the two-band non-interacting model from Sec. 3.3.3.1, which is driven below the single-particle bandwidth, such that resonant processes are allowed. In particular, recall Fig. 3.23 which shows a direct comparison of the lab-frame vV HFE and the rot-frame one. Notice that, while resonances are missed in the lab frame, it is possible to capture their effect if the reference frame is chosen appropriately. Therefore, while in the original lab frame the expansion is divergent (it misses the resonances), the latter does converge in the special rotating frame discussed in Sec. 3.3.3.1, because the criterion (2.61) is satisfied there.

The fact that the lab-frame HFE does not capture the resonances has profound implications about the convergence of the expansion as a whole. From the example above it immediately becomes clear that there is no chance for an expansion, which does not capture an important feature like these Floquet resonances, to converge in general. What is more intriguing, though, is that the convergence properties of the expansion apparently do depend on the reference frame used, while the underlying stroboscopic physics described by the Floquet Hamiltonian obviously does not.

The situations described so far are, however, more delicate because in a non-interacting lattice system the spectrum is bounded also from above and, in order to observe direct resonant transitions, it is necessary for the driving frequency to be smaller than the single-particle energy scale J_0 . One might, therefore, suspect that convergence will be granted in the general non-interacting case, if only the frequency $\Omega \gg J_0$ is greater than the single-particle energy scale. However, as we demonstrate below using the example of the Kapitza pendulum, capturing the Floquet resonances is a crucial prerequisite for the converge of all types of systems.

2.3.2 Systems with Unbounded Hamiltonians: the Role of Resonances

Whenever the instantaneous Hamiltonian $H(t)$ of the system has an unbounded spectrum for some time t during the cycle, we shall refer to this driven system as *unbounded*. Unbounded Floquet systems can generally be divided into two categories: continuum models (including single-particle) with unbounded kinetic energy, such as the Kapitza pendulum, and many-body lattice systems in the thermodynamic limit. In the following, we discuss some ideas about the convergence properties of the inverse-frequency expansion in these setups.

2.3.2.1 Single-Particle Systems: the Kapitza Pendulum Revisited

Let us now ask the more general question whether the vV HFE for the Kapitza pendulum converges to the Floquet Hamiltonian in the regions away from the detrimental resonances. Recall that the Kapitza pendulum was studied extensively in Sec. 3.1.1 with the help of the FM and the vV HFE, as well as from the point of view of Floquet adiabatic perturbation theory, see Secs. 4.3.3 and 4.5. Below, we follow the setup and notation introduced in these two sections.

The quantum Kapitza pendulum is conveniently studied in the angular momentum basis, where it maps to a non-interacting lattice model in a harmonic potential with time-varying hopping matrix element, see discussion in Sec 4.3.3. If we want to compare the behaviour of the exact Floquet eigenstates and quasienergies to those of the vV HFE, as the drive strength λ is gradually being changed in the presence of the drive, we first need to make sure our results are independent of the cut-off M in the number of states kept (recall that the number of positive angular momentum modes kept to study the system numerically is given by $2M + 1$, see Sec. 4.3.3 for a precise definition), which is expected to affect the states at the top end of the spectrum. Usually, when one discusses a cut-off dependence in static systems, one makes sure the results remain unchanged with increasing the value of the cut-off itself. However, in Floquet systems a larger cut-off

amounts to a larger number of states, all folded within the same Floquet zone. Therefore, this procedure easily aggravates any quasienergy plot, making it impenetrable for the naked eye. Unfortunately, there is no straightforward algorithm to cut off the high-energy states of an exact Floquet spectrum obtained numerically, since the latter always comes out folded. Thus, we follow a slightly different route: we do the numerical calculation of the exact quasienergy spectrum both in the lab frame and in the rotating frame. In the limit of sending the cut-off $M \rightarrow \infty$, both calculations trivially result in the same Floquet spectrum. However, since the transformation to the rotating frame in Eq. (4.60) couples differently to the cut-off dependent states, this allows us to immediately identify all cut-off dependencies upon comparing the two spectra. Figure 2.4 (a) shows the exact quasienergy spectrum of the Kapitza pendulum for $\Omega/\omega_0 = 20$ obtained in the lab (blue dots) and the rotating frame (green dots), while the Floquet ground state is shown in red. Let us fix a value of λ , and focus on a particular quasienergy level, which corresponds to a single dot in the plot. Then, if the rot-frame and lab-frame data coincide, the quasienergy is identified as cut-off independent. It is interesting to note that (i) for the Kapitza pendulum, all cut-off dependent states necessarily have large physical energies, and are thus close to the top of the spectrum, and (ii), where present, the cut-off dependence becomes more pronounced at larger driving amplitude λ .

Once we have identified the cut-off dependence in the exact Floquet spectrum, we have to do so for the approximate spectrum obtained within the vV HFE. However, since the latter produces an unfolded spectrum, this is easily done with standard methods: we first calculate the approximate spectrum for a larger value of the cut-off M_{up} , and *after diagonalisation* we artificially keep only a desired small number M of the energy states satisfying $M < M_{\text{up}}$ from the bottom of the approximate spectrum. Finally, we make sure the chosen M states do not depend on the choice of M_{up} . Figure 2.4b shows the quasienergy spectra of the exact Floquet Hamiltonian H_{eff} in the rot frame, and the approximate one, $H_{\text{eff}}^{(0+1+\dots+6)}$.

Note first that all states which are relatively flat as a function of λ display a nice agree-

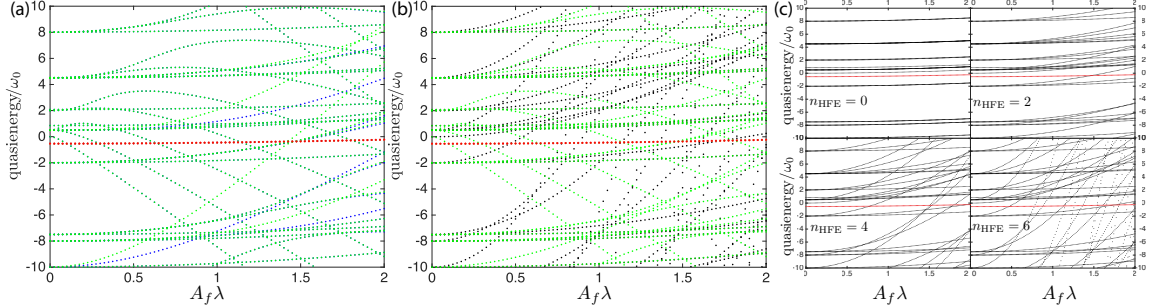


Figure 2.4: (a) Comparison between the exact quasienergy spectrum of the Floquet Hamiltonians obtained numerically using the lab frame Hamiltonian $H(t)$ (blue dots) and the rot frame Hamiltonian $H^{\text{rot}}(t)$ (green dots) for a finite cutoff $M = 30$ for the quantum Kapitza pendulum. These spectra coincide in the infinite cutoff limit but in general differ at a finite cutoff. Finding nearly but not completely identical states allows us to numerically identify cutoff independent Floquet eigenstates (see text for details). (b) Comparison between the exact Floquet quasienergy spectrum in the rot frame (green dots) and the approximate spectrum of the vV HFE to order six (black dots). (c) Spectrum of the vV HFE at different orders n_{HFE} of the vV HFE. The approximate spectra (black dots) are calculated for $M = 100$, but only the lowest 31 states are kept; hence all approximate spectra are cut-off independent. In all panels the Floquet ground state is denoted in red. The Kapitza pendulum parameters are $m\omega_0 = 1$, $A_f = 2$, and $\Omega = 20\omega_0$.

ment. Not surprisingly, these are the low-energy states, which are not resonantly coupled to the drive. Second, the entire fan of states which bend down and cross the Floquet GS (red dots) in the exact quasienergy spectrum is absent in the vV HFE spectrum. Moreover, this entire fan of exact Floquet eigenstates is cut-off independent, as can be seen from Fig. 2.4a. These are precisely the states that lead to the breakdown of Floquet adiabatic perturbation theory (FAPT), as discussed in Sec. 4.3.3. This already hints towards a serious problem with the convergence of the vV HFE for this model, although the mechanism behind it is expected to be fairly general. Figure 2.4c shows the cut-off independent folded spectra of the vV HFE depending on the order of approximation n_{HFE} . Observe how, while for the flat quasienergy levels with $E \lesssim \Omega$ the convergence seems quite reasonable, the high-energy levels with $E \gtrsim \Omega$ obviously diverge as we increase the order of the expansion. Note that the frequency used, $\Omega/\omega_0 = 20$, is already an order of magnitude larger than the single-particle parameters, and the vV HFE was naively expected to converge for such

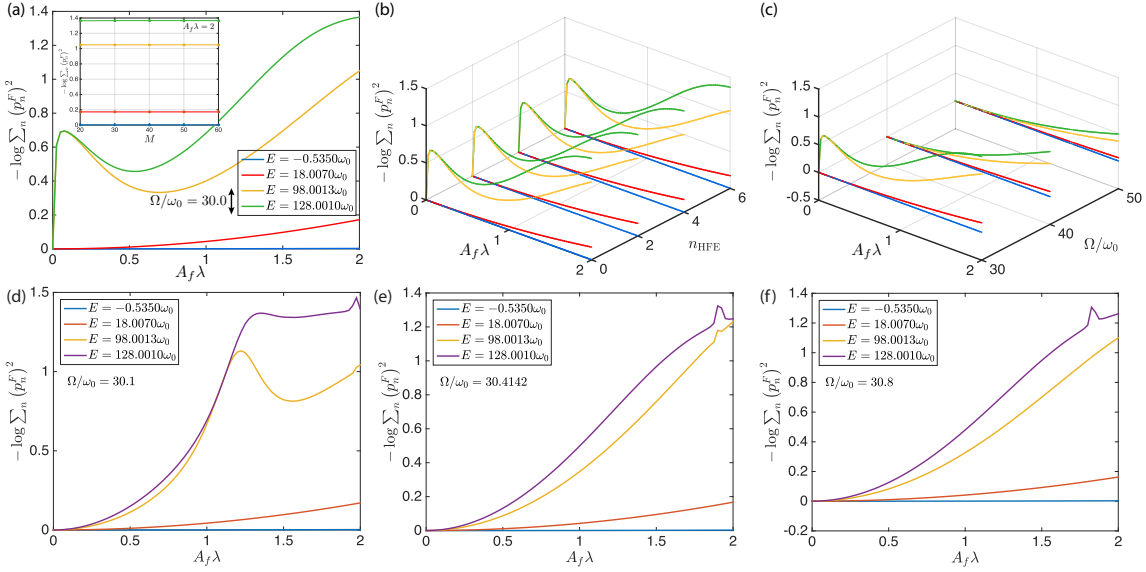


Figure 2.5: [Kapitza pendulum] Inverse participation ratio (log-IPR) of four distinguished approximate states in the exact Floquet spectrum as a function of the amplitude $A_f \lambda$. Inset: system size-dependence of the log-IPR for $A_f \lambda = 2$. $\Omega/\omega_0 = 30$. (b) The dependence of the log-IPR on the order of the vV HFE is negligible compared to the curvature of the curves for $\Omega/\omega_0 = 30$. (c) Frequency-dependence of the log-IPR as a function of λ for $n_{\text{HFE}} = 6$. (d-f) same as (a) but for the off-resonant frequencies $\Omega/\omega_0 = 30.1$, $\Omega/\omega_0 = 30.41$ and $\Omega/\omega_0 = 30.8$, respectively. The model parameters are $m\omega_0 = 1$, $A_f = 2$.

frequencies.

In the following, we focus only on states which do not exhibit any cut-off dependence. To better quantify the convergence of the vV HFE for such states to their exact Floquet counterparts, we define the log inverse participation ratio (log-IPR or collision entropy) of the approximate eigenstates $|\nu\rangle$ of the vV HFE in the exact Floquet eigenbasis $|n\rangle$ as

$$R = -\log \sum_n (p_n)^2, \quad p_n = |\langle n|\nu\rangle|^2 \quad (2.62)$$

If an approximate state matches an exact Floquet state, then $R = 0$, while whenever $R > 0$ the log-IPR measures the deviation between the two. We now focus on four representative approximate states and calculate their participation ratios in the exact Floquet spectrum; these are the Floquet ground state, a state with $E \gtrsim \Omega$, and two high-energy states whose

energy differ by approximately Ω . We label these four states by their physical energy E . Figure 2.5a shows the inverse participation ratios of these states within the sixth order vV HFE with the inset confirming that the data used is cut-off independent. As expected from examining the quasienergy spectra discussed earlier, the log-IPR increases with the physical energy. Interestingly, the participation ratios of the low-energy states grow as $R \sim \lambda^2$ for $\lambda \rightarrow 0$. Remarkably, R can exhibit a non-analytic behaviour at small λ for high-energy states. This can be explained as follows: whenever two states of the non-driven model at $\lambda = 0$ have energies close to resonance with the driving frequency, any weak coupling strongly hybridises them, leading to the opening of a photon avoided crossing at infinitesimally small λ . This means that one would not be able to do a successful adiabatic ramp-up of the drive initialising the system in one of these states, because if the ramp starts smoothly with a vanishing velocity and acceleration in the region of $\lambda \rightarrow 0$, the system will immediately absorb energy due to the avoided crossing at $\lambda \rightarrow 0$. In such cases, it is possible that quench-starting the drive will produce less excess energy than slowly turning it up. However, this non-analytic behaviour is only present when the drive frequency matches precisely the energy difference of two bare levels, as confirmed by Fig. 2.5(d-f) for frequencies close but not equal to the resonant one. This suggests that the width of such resonances can indeed be very small for non-interacting systems with non-dense spectrum. Figure 2.5b shows the inverse participation ratios as a function of the order in the vV HFE. The results clearly suggest that the vV HFE does not converge to the exact Floquet Hamiltonian. Interestingly, however, at fixed λ the log-IPR curves of these states indeed seem to converge, but it is not clear what the limit is and whether it carries a physical meaning. Last, Fig. 2.5c displays the frequency-dependence of the log-IPR R . Unlike increasing the order in the vV HFE, increasing Ω reduces the participation ratio, as expected, since the vV HFE becomes exact as $\Omega \rightarrow \infty$.

The results shown in this section put in doubt the convergence of the inverse-frequency expansion to the exact Floquet Hamiltonian for single-particle systems with unbounded spectra. It has become clear that the origin of divergence of the vV HFE can be traced

back to the unbounded spectrum due to the (angular) momentum operator p_θ^2 , which enables the appearance of photon absorption crossings. Hence, if one further eliminates this unboundedness by going to yet another rotating frame, which amounts to applying the generalised Schrieffer-Wolff transformation (SWT) [105], see Sec. 3.2, the convergence properties of the expansion are expected to improve significantly. The intuition behind is that this way of ‘folding’ the unbounded part of the spectrum is equivalent to a re-summation of an infinite vV HFE subseries [33]. Hence, if the vV HFE is divergent due to the presence of a non-analytic in $1/\Omega$ term in the exact Floquet Hamiltonian, this re-summation circumvents the expansion of the non-analytic piece. There exists evidence that the generalised SW transformation, unlike the bare vV HFE, captures these photon absorption avoided crossings, as we discuss in detail in Sec. 3.3.3.1.

2.3.2.2 Many-Body Systems

While the result of Eq. (2.61) represents a sufficient criterion, it is not particularly useful for many-particle systems. It only guarantees the convergence if the driving frequency scales with the system size, while the relevant time scales, separating the fast and slow driving regimes, are in experiments never extensive. This condition for the convergence of the Floquet-Magnus expansion is only sufficient. It does not give much insight into what happens at longer periods. Recently, a rigorous theorem was proven, according to which the inverse-frequency expansion for generic interacting spin and fermionic models is at least an asymptotic series [98, 101]. In Refs. [101, 102] it is explicitly demonstrated that there exists an optimal order of the expansion, beyond which adding more terms leads to larger and larger deviation of the stroboscopic evolution from the one produced by the exact Floquet Hamiltonian.

In generic situations, where a local transformation to a constant Hamiltonian, as is the case for the two-level system (see Sec. 2.1.3), does *not* exist, the situation with the convergence of the expansion is not completely settled. In Refs. [74, 75, 77, 106], a numerical evidence indicated that for particular driving protocols in one-dimensional fermionic or spin

chains, the radius of convergence of the Floquet-Magnus expansion is finite even in the thermodynamic limit. In other words, there exists a critical frequency Ω^* separating regimes of finite and infinite heating. At the critical frequency a dynamical transition between these two regimes is conjectured, which can be interpreted as a many-body localisation transition [107–112] in energy space. This finding is also consistent with previous numerical results obtained for periodically kicked spinless fermions in one dimension [74, 75, 113] equivalent to a periodically kicked XXZ spin chain. In these works two qualitatively different regimes were found. In the first one the evolution is well described by random matrices from the circular ensemble (see also Ref. [78]) strongly suggesting that the FM HFE is divergent, while in the other regime the system displays features consistent with the expansion being convergent to a local Hamiltonian.

At the same time a numerical study of a different driving protocol in a spin chain indicated a zero radius of convergence [78], i.e. $\Omega^* = \infty$ in the thermodynamic limit. In Ref. [79], using the Eigenstate Thermalisation Hypothesis, it was argued that an ergodic system with a local driving term always heats up to infinite temperature in the thermodynamic limit, while the energy can stay localised (and thus the FM HFE converges) if the system is in the many-body localised phase, i.e. non-ergodic. In Ref. [114] it was shown that the FM HFE has zero radius of convergence for a Kondo model if the driving frequency is smaller than the bandwidth of the conduction electrons, though for faster driving the numerical results seem to indicate convergence of the expansion. There is no contradiction with Ref. [79] because in the Kondo model the conduction band electrons were considered non-interacting (i.e. non-ergodic).

The periodic modulation in many-body systems generally falls into two categories: local and global, which we discuss separately below.

2.3.2.2.1 Local Drive

As we have seen above, the convergence of the inverse-frequency expansion for locally-driven many-body systems depends severely on the choice of reference frame. Such models

are believed to generally heat up to infinite temperature [79] which can intuitively be understood as follows: the local drive injects energy only locally in real space. The absorbed energy then ‘diffuses’ into the rest of the system increasing the total energy density to the maximum possible value which, for a closed system in the absence of a heat bath, corresponds to an infinite-temperature state.

The fact that generic locally-driven many-body systems heat up suggests that the underlying Floquet Hamiltonian is a non-local operator. Therefore, the inverse-frequency expansion in the lab frame does not converge. Nevertheless, there exists a frame in which the FM HFE satisfies the convergence criterion of Eq. 2.61.

We begin by defining the Hamiltonian for the system as

$$H(t) = H_0 + A \cos \Omega t W \quad (2.63)$$

where A is the drive amplitude, H_0 models an ergodic Hamiltonian and W is a local operator, i.e. $\|W\|_\infty \sim \mathcal{O}(L^0) = \mathcal{O}(1)$ and $\|\cdot\|_\infty$ is the supremum (maximum) norm. Note that $\|H_0\|_\infty \sim \mathcal{O}(L)$ is extensive in the system size, as expected.

To explicitly construct a reference frame where the expansion converges, we first change basis to diagonalise the non-driven Hamiltonian $S^\dagger H_0 S = \text{diag}(\{\varepsilon_0^\alpha\})$:

$$\tilde{H}(t) = \sum_{\alpha} \varepsilon_0^\alpha |\alpha\rangle\langle\alpha| + A \cos \Omega t \sum_{\alpha \neq \beta} W_{\alpha\beta} |\alpha\rangle\langle\beta| + \text{h.c.} \quad (2.64)$$

where $|\alpha\rangle$ is a many-body state corresponding to the many-body energy ε_0^α , and $W_{\alpha\beta} = \langle\alpha|S^\dagger W S|\beta\rangle$. Notice that, in those cases where W does not break the symmetries of H_0 , we have absorbed the diagonal elements $W_{\alpha\alpha}$ in the definition of the energies ε_0^α .

Since we are dealing with a periodically-driven problem at a finite frequency, quasienergy conservation suggests that we should be looking for a folded Floquet Hamiltonian. Therefore, it is convenient to artificially separate the spectrum of H_0 into Floquet zones and write $\varepsilon_0^{\alpha,l} = \varepsilon_0^\alpha + l\Omega$. The integer l enumerates the l -th Floquet zone. At this stage we

remark that, although the choice of the position of the zones might affect the convergence speed of the Floquet states corresponding to the outermost (w.r.t. the zone boundaries) levels, convergence in general will be guaranteed by Eq. (2.61). To see this, let us go to the rotating frame w.r.t. the commensurate parts $l\Omega$:

$$H^{\text{rot}}(t) = \sum_{\alpha,l} \varepsilon_0^{\alpha,l} |\alpha, l\rangle \langle \alpha, l| + A \cos \Omega t \sum_{\alpha \neq \beta} \sum_{l,l'} W_{\alpha,l;\beta,l'} e^{-i(l-l')\Omega t} |\alpha, l\rangle \langle \beta, l'| + \text{h.c.} \quad (2.65)$$

This transformation might seem trivial, but we have gained a lot from the point of view of convergence. Notice that in the rot frame, we can write the Hamiltonian as $H^{\text{rot}}(t) = H_0^{\text{rot}} + \tilde{W}^{\text{rot}}(t)$. More importantly, $\|H_0^{\text{rot}}\|_\infty \leq \Omega \sim \mathcal{O}(L^0)$ is now bounded by construction even though the spectrum of H_0 was not, and $\|W^{\text{rot}}(t)\|_\infty \leq A \|W\|_\infty \sim A \times \mathcal{O}(L^0)$ is also bounded as the drive was assumed to be local. Therefore, for a sufficiently small driving amplitude the above rot-frame Hamiltonian satisfies the convergence criterion (2.61). Note that we also tacitly assumed that A/Ω is small: however, this condition is not restrictive, since otherwise we can in the very beginning change frames to take into account the large hybridisation effects due to the strong amplitude (see Sec. 2.2 and the models discussed in Chapter 3), and then continue along the same lines.

Although the FM HFE converges in this reference frame, it is quite interesting to notice that the corresponding approximate Floquet Hamiltonian is a highly non-local operator. To understand how this comes about, note that even at the lowest level of the time-average, the drive $\cos(\Omega t)$ will constructively interfere with the oscillatory terms $e^{-i(l-l')\Omega t}$: this results in finite off-diagonal matrix elements that open up photon-absorption gaps in the folded spectrum of H_0 . In the lab-frame basis, however, the same off-diagonal matrix elements appear highly non-local. Last but not least, notice also by counting the number of Fourier harmonics, that the structure of the van Vleck (and thus also the Floquet-Magnus and Brillouin-Wigner) expansion changes drastically due to these new oscillatory terms, $e^{-i(l-l')\Omega t}$, as anticipated for a frame with improved convergence properties.

2.3.2.2.2 Global Drive

The situation for a generic global drive is much more complicated. The change-of-frame procedure from the previous section does not help much here because the drive operator $\|W\|_\infty \sim L$ is extensive in the system size L . The arguments above are suggestive enough that the Floquet Hamiltonian for a generic system is a non-local operator and, by the same token, the lab-frame expansion is expected to diverge. Whether one can find a frame, though, where convergence can be proven as in the locally-driven example above, is an open question at the moment.

All that said, it bears mentioning that the inverse-frequency expansion can definitely be convergent even in the thermodynamic limit, provided the time-dependent Hamiltonian can be mapped to a static one, by going to some rotating frame. In Sec. 3.2 we discuss such situations in the context of the Schrieffer-Wolff transformation (SWT) and show that in some cases the inverse-frequency expansion reproduces the conventional static perturbation theory, which is known to converge.

Chapter 3

Floquet Engineering

3.1 Universal High-Frequency Limits of Periodically Driven Systems

We shall now move on to apply the formalism developed in Secs. 2.1 and 2.2 to specific examples. In this section, we review various models, in which the Floquet Hamiltonian exhibits a non-trivial high-frequency limit. By ‘non-trivial’ we mean not equal to the time-averaged lab-frame Hamiltonian. We shall also discuss leading corrections in the inverse driving frequency to the infinite-frequency limit, which are important for experimental realisations. As we show below, the different setups leading to non-trivial infinite-frequency Hamiltonians can be classified according to three generic classes of driving protocols. While this classification might not be exhaustive, it covers most of the examples known in the literature, and suggests possible routes for engineering new Floquet Hamiltonians in various types of systems.

3.1.1 The Kapitza Class

Let us open the discussion analyzing the Kapitza class which comprises non-relativistic systems with a quadratic in momentum kinetic energy, and arbitrary (but momentum-independent) interactions. The driving protocol couples only to operators which depend on the coordinates. In other words, the Hamiltonian should be of the form:

$$H(p_j, x_j) = H_{\text{kin}}(\{p_j\}) + H_{\text{int}}(\{x_j\}) + \Omega f(t) H_1(\{x_j\}), \quad (3.1)$$

where

$$H_{\text{kin}}(\{p_j\}) = \sum_{j=1}^N \frac{p_j^2}{2m_j},$$

and $f(t)$ is some periodic function of time with period T and zero mean. Note that the driving term H_1 can include both single particle external potentials and interactions. Hence, the Kapitza class comprises the periodically driven nonlinear Schrödinger equation. It has been shown that when the interaction strength in the Gross-Pitaevskii equation is shaken strongly and at a high frequency, it is possible to stabilise the solitonic solution against critical collapse [115–119].

When we say that the Hamiltonian should be of the form (3.1), we imply that it should be gauge-equivalent to this form. For instance, any time-dependent scalar potential can be absorbed into a vector potential by choosing a different electromagnetic gauge, as it is well-known from classical electromagnetism. While we do not explicitly consider here systems in the presence of an orbital magnetic field, the Kapitza class can be extended to such situations as well. Such an extension will simply result in a few additional terms in the infinite-frequency Hamiltonian and the leading inverse frequency corrections. We made the prefactor $\Omega = 2\pi/T$ explicit in Eq. (3.1) to emphasise that, in order to get a non-trivial high-frequency limit, one needs to scale the driving amplitude linearly with the frequency. This scaling guarantees that, when the driving becomes infinitely fast, the system is still strongly perturbed, and its evolution cannot be described by the time-averaged Hamiltonian at any frequency.

To derive the infinite-frequency Floquet Hamiltonian, we employ the inverse frequency expansion in the lab frame up to second order. We give explicit expressions only for the stroboscopic Hamiltonian $H_F[t_0]$ obtained using the Floquet-Magnus expansion (FM HFE), Eq. (2.41). Similar arguments apply for the effective Hamiltonian using the van Vleck expansion (vV HFE), Eq. (2.45). Since, it is easier to work in the rotating frame, as we show in the next section, we shall discuss in detail the comparison between the effective

and stroboscopic pictures later on in the section.

$$H^{(0)} = \frac{1}{2\pi} \int_0^{2\pi} d\tau H(\tau) = H_{\text{kin}} + H_{\text{int}}, \quad (3.2)$$

$$H^{(1)}[0] = \frac{[H_{\text{kin}}, H_1]}{4\pi i} \int_0^{2\pi} d\tau_1 \int_0^{\tau_1} d\tau_2 f(\tau_1) - f(\tau_2) = \frac{[H_{\text{kin}}, H_1]}{2\pi i} \int_0^{2\pi} d\tau_1 (\tau_1 - \pi) f(\tau_1), \quad (3.3)$$

$$\begin{aligned} H^{(2)}[0] = & -\frac{[[H_{\text{kin}}, H_1], H_{\text{kin}}]}{12\pi\Omega} \int_0^{2\pi} d\tau_1 \int_0^{\tau_1} d\tau_2 \int_0^{\tau_2} d\tau_3 2f(\tau_2) - f(\tau_1) - f(\tau_3) \\ & - \frac{[[H_{\text{kin}}, H_1], H_1]}{12\pi} \int_0^{2\pi} d\tau_1 \int_0^{\tau_1} d\tau_2 \int_0^{\tau_2} d\tau_3 f(\tau_2)f(\tau_3) + f(\tau_2)f(\tau_1) - 2f(\tau_1)f(\tau_3), \end{aligned} \quad (3.4)$$

where $\tau_i = \Omega t_i$. In order to keep the notation consistent, we drop the subindex F in the FM HFE of the Floquet Hamiltonian in the lab frame: $H_F[t_0] = H^{(0)}[t_0] + H^{(1)}[t_0] + \dots$, to contrast with the proper inverse-frequency Magnus expansion $H_F[t_0] = H_F^{(0)}[t_0] + H_F^{(1)}[t_0] + \dots$, defined in Sec. 2.2. The difference between the two expansions is due to the non-trivial scaling of the driving amplitude with frequency. For instance, $H^{(2)}[0]$ contains both the term scaling as the first power of the inverse frequency, and the term which survives the infinite-frequency limit. We reserve, the subindex F in $H_F^{(n)}[t_0]$ for terms which scale strictly as Ω^{-n} . The term $H_F^{(n)}[t_0]$ can be viewed as a result of either finite or infinite resummation of a lab-frame subseries.

It becomes clear that, for $\Omega \rightarrow \infty$, the first term in $H^{(2)}[0]$ vanishes (it represents one of the subleading Ω^{-1} corrections) while the other term in $H^{(2)}[0]$ together with $H^{(0)}$ and $H^{(1)}[0]$ give the correct Floquet Hamiltonian in the infinite-frequency limit. The term $H^{(1)}[0]$ in the lab-frame FM expansion can always be set to zero by choosing an appropriate Floquet gauge t_0 , such that the time-integral appearing in Eq. (3.3) vanishes. For example, if the protocol is symmetric around the middle of the period: $f(t) = f(T-t)$, say $f(t) = \cos \Omega t$, then this integral is identically zero. One has to be cautious, though, that this may not be the case in other gauges. For instance, if $f(t) = \sin \Omega t$, then the integral

in Eq. (3.3) is non-zero, and one either has to shift the stroboscopic point t_0 to $T/2$, or deal with this term. Choosing the symmetric Floquet gauge, the time-ordered integral in the last term in Eq. (3.4) is finite, and has a well-defined non-zero infinite-frequency limit. Note that because the kinetic energy is quadratic in momentum this term depends only on the coordinates $\{x_j\}$, and hence represents an additional external potential or an interaction. Indeed,

$$[[H_{\text{kin}}, H_1], H_1] = - \sum_{j=1}^N \frac{1}{m_j} \left(\frac{\partial H_1}{\partial x_j} \right)^2,$$

and thus, for symmetric driving protocols, the infinite-frequency limit of the Floquet Hamiltonian reads as:

$$H_F^{(0)} = H_{\text{kin}} + H_{\text{int}} + A \sum_j \frac{1}{m_j} \left(\frac{\partial H_1}{\partial x_j} \right)^2, \quad (3.5)$$

where

$$A = \frac{1}{12\pi} \iiint_{0 < \tau_3 < \tau_2 < \tau_1 < 2\pi} d\tau_1 d\tau_2 d\tau_3 (f(\tau_2)f(\tau_3) + f(\tau_2)f(\tau_1) - 2f(\tau_1)f(\tau_3)). \quad (3.6)$$

The time integral here depends on the details of the periodic function $f(\tau)$. For instance, if $f(\tau) = \lambda \cos(\tau)$ then $A = \lambda^2/4$. If the time average of $f(\tau)$ is zero then one can show that

$$A = \frac{1}{4\pi} \int_0^{2\pi} \Delta^2(\tau) d\tau, \text{ where } \Delta(\tau) = \int_0^\tau f(\tau') d\tau'. \quad (3.7)$$

Let us argue that the asymptotic form of the Floquet Hamiltonian in the infinite-frequency limit given by Eq. (3.5) for the Kapitza class is exact. In other words, there are no other terms in the Floquet-Magnus expansion which survive as $\Omega \rightarrow \infty$. From the structure of the expansion, it is clear that the only non-vanishing terms in the n -th order contribution are those which contain n -times the driving term H_1 , and once the kinetic energy. Since the driving amplitude scales with frequency, each extra time integral (giving an extra factor Ω^{-1}) will be precisely compensated for by the corresponding factor coming from the driving amplitude. So the only terms which survive have the structure

of $[[\dots [H_{\text{kin}}, H_1], H_1], \dots H_1]$ multiplied by some dimensionless number. However, because the kinetic energy is quadratic in momentum, all such terms containing more than two commutators vanish identically. Hence, the only surviving terms beyond the second order must contain the kinetic energy at least twice, so they are at least of order Ω^{-1} . Note that, in principle, one can evaluate the Ω^{-1} -corrections to $H_F^{(0)}$ in a similar way. But the general expressions become very involved so we shall rather show these corrections for a specific case of the Kapitza pendulum. As we show below, it is much easier to derive these corrections going first to the rotating frame, where there is a systematic and convenient way to count the powers of frequency.

3.1.1.1 The Kapitza Pendulum

We now illustrate how the infinite-frequency limit, the leading corrections, the Floquet-gauge freedom, and the dressing of the observables and the density matrix emerge for a specific setup of a single Kapitza pendulum [5, 77]. At the end of the section, we shall briefly discuss many-particle generalisations of the Kapitza pendulum.

The Kapitza pendulum is a rigid pendulum of length l in which the point of suspension is being displaced periodically along the vertical direction according to the time-dependent protocol $y_0 = a \cos \Omega t$. We parametrize the problem in polar coordinates:

$$x = l \sin \theta, \quad y = (y - y_0) + y_0 = l \cos \theta + a \cos \Omega t$$

where θ is the angle measured from the downward direction, c.f. Fig. 3.1. The Lagrangian is

$$\mathcal{L} = \frac{m}{2} (\dot{x}^2 + \dot{y}^2) + mgy = \frac{ml^2}{2} \left(\dot{\theta}^2 + \frac{2a\Omega}{l} \sin \Omega t \dot{\theta} \sin \theta \right) + ml^2 \omega_0^2 \cos \theta \quad (3.8)$$

with $\omega_0 = \sqrt{g/l}$. In the last equality we have dropped all terms which are independent of θ and $\dot{\theta}$, since they have no physical meaning. Using the standard definitions for the

canonical momentum $p_\theta = \partial\mathcal{L}/\partial\dot{\theta}$ and the Hamiltonian $H = p_\theta\dot{\theta} - \mathcal{L}$ we arrive at [5, 77]

$$H = \frac{1}{2ml^2} (p_\theta - mla\Omega \sin \theta \sin \Omega t)^2 - ml^2\omega_0^2 \cos \theta. \quad (3.9)$$

The shift in momentum can be removed by a standard gauge transformation in the Hamiltonian, resulting in the scalar potential, which effectively modulates the internal frequency ω_0 , so that the Hamiltonian becomes equivalent to

$$H = \frac{p_\theta^2}{2ml^2} - ml^2 \cos \theta \left(\omega_0^2 + \frac{a\Omega}{l} \Omega \cos \Omega t \right). \quad (3.10)$$

To simplify the notations we redefine $ml^2 \rightarrow m$, $a\Omega/l \rightarrow \lambda$ which produces the celebrated Kapitza Hamiltonian

$$H = \frac{p_\theta^2}{2m} - m \cos \theta (\omega_0^2 + \lambda \Omega \cos \Omega t). \quad (3.11)$$

In this form the Kapitza Hamiltonian obviously belongs to the Kapitza class (hence its name). As we discussed above, it has a well-defined infinite-frequency limit if we keep λ fixed, i.e. scale the driving amplitude linearly with frequency¹. Formally one can obtain the Kapitza Hamiltonian by directly modulating the coupling constant in the cosine potential (gravitational constant g in this case). However, notice that the large frequency limit effectively corresponds to changing the sign of this coupling, which is not always easy to achieve experimentally.

The Floquet Hamiltonian in the infinite-frequency limit, Eq. (3.5), is

$$H_F^{(0)} = H_{\text{eff}}^{(0)} = \frac{p_\theta^2}{2m} - m\omega_0^2 \cos \theta + m\frac{\lambda^2}{4} \sin^2 \theta. \quad (3.12)$$

When $\lambda > \sqrt{2}\omega_0$ the effective potential in Eq. (3.12) supports a stable local minimum at the inverted position $\theta = \pi$. In the absence of the driving, the equilibrium position $\theta = \pi$ is clearly unstable. Therefore, by driving the pendulum, it is possible to change the stability

¹It should be noted that it is the driving amplitude in the Hamiltonian (3.11) which scales linearly in frequency. The shaking amplitude a scales inversely proportional to the frequency.

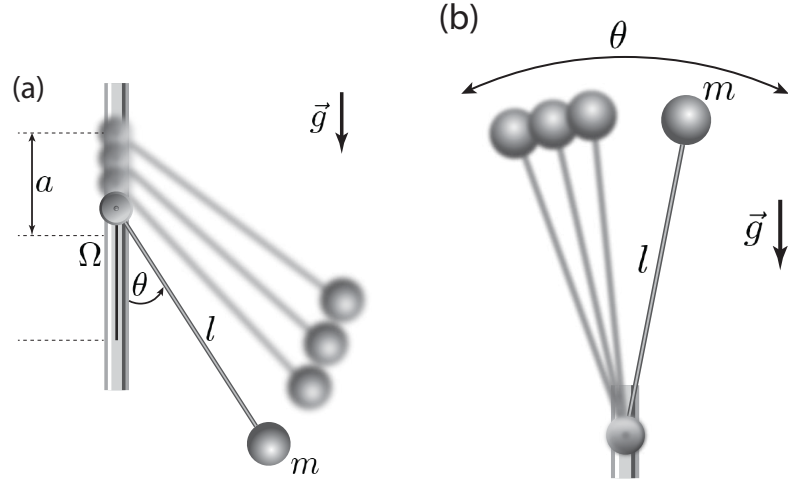


Figure 3.1: The Kapitza pendulum. (a) The point of suspension of a rigid pendulum of mass m and natural frequency $\omega_0 = \sqrt{g/l}$ is periodically modulated in the vertical direction with an amplitude a and frequency Ω . (b) In the high-frequency limit, the upper equilibrium at $\theta = \pi$ becomes dynamically stable and the system can oscillate around the inverted position.

of the upper equilibrium. This phenomenon is known as dynamical stabilisation and it is widely used in many areas of physics [120–123].

3.1.1.2 The Kapitza Hamiltonian in the Rotating Frame

In this section we demonstrate a simpler derivation of the infinite-frequency Floquet Hamiltonian by going to a rotating frame. First we transform the Kapitza Hamiltonian (3.11) to the rotating frame defined by the rotator

$$\begin{aligned} V(t) &= \exp(-i\Delta(t)\cos\theta) \\ \Delta(t) &= -m\lambda\Omega \int_0^t dt \cos(\Omega t) = -m\lambda\sin(\Omega t). \end{aligned} \quad (3.13)$$

As everywhere else in this thesis, $V(t)$ is the transformation which goes from the rotating to the lab frame. It is often (but not always) convenient to define the rotating frame such that $V(0) = \mathbf{1}$, so that the initial states in the lab and the rotating frame are the same at $t = 0$.

By construction, this transformation eliminates the divergence of the driving protocol with Ω in the infinite-frequency limit. Hence, as $\Omega \rightarrow \infty$, the Floquet Hamiltonian becomes effectively equivalent to the time-averaged Hamiltonian in the rotating frame, as discussed in Sec. 2.2.5. In this rotating frame, the transformed Hamiltonian is given by

$$\begin{aligned} H^{\text{rot}}(t) &= V^\dagger(t) \left[\frac{p_\theta^2}{2m} - m\omega_0^2 \cos \theta \right] V(t) \\ &= \frac{p_\theta^2}{2m} - m\omega_0^2 \cos \theta + \frac{\Delta^2(t)}{2m} \sin^2 \theta + \frac{\Delta(t)}{2m} \{\sin \theta, p_\theta\}_+, \end{aligned} \quad (3.14)$$

where $\{\cdot, \cdot\}_+$ denotes the anti-commutator. Noticing that $\frac{1}{T} \int_0^T dt \Delta(t) = 0$ and $\frac{1}{T} \int_0^T dt \Delta^2(t) = m^2 \lambda^2 / 2$, we find for the infinite-frequency Floquet-Hamiltonian:

$$H_F^{(0)} = H_{\text{eff}}^{(0)} = \frac{p_\theta^2}{2m} - m\omega_0^2 \cos \theta + m \frac{\lambda^2}{4} \sin^2 \theta. \quad (3.15)$$

This is exactly the Hamiltonian from Eq. (3.12), showing explicitly the equivalence of the Floquet Hamiltonians in the lab and rotating frames.

The Floquet Hamiltonian (3.15) is consistent with the predictions based on classical mechanics (see for example Landau and Lifshitz [7]). Usually the effective potential (i.e. the θ -dependent terms in Eq. (3.15)) is obtained by splitting the degrees of freedom into fast and slow modes. One eliminates the fast modes, and derives the effective potential for the slow modes. It then follows that the effective potential is proportional to the time integral of the squared driving protocol [7], i.e. $\propto \int_0^T dt [f(t)]^2$. However, according to Eq. (3.7), the effective potential is proportional to the average of its time integral squared, i.e. $\propto \int_0^T dt [\Delta(t)]^2$, where $\Delta(t) = \int_0^t dt' f(t')$. This makes no difference for a simple $\cos \Omega t$ driving protocol, but will be important for more complex periodic protocols, e.g. $f(t) = \cos \Omega t + \cos 2\Omega t$.

We showed in Sec. 2.2 that, in the infinite-frequency limit, the stroboscopic and effective Hamiltonians coincide, i.e. $H_F^{(0)} = H_{\text{eff}}^{(0)}$, and the kick operators are equal to zero. One has to keep in mind, though, that the bare observables in the rotating frame are in general

different from the bare observables in the lab frame, except for times at which $V(t)$ reduces to the identity operator. For this reason, the dressed observables in the lab frame are generally modified even in the infinite-frequency limit (see Sec. 3.1.1.4).

3.1.1.3 Finite-Frequency Corrections

The inverse-frequency expansion allows one to identify leading finite-frequency corrections to the stroboscopic (effective) Hamiltonian $H_F^{(0)}$ ($H_{\text{eff}}^{(0)}$). This can be done both in the lab frame and in the rotating frame. However, going to the rotating frame makes the calculations much simpler because, as we discussed, there the FM (vV) expansion coincides with the proper Ω^{-1} -expansion. In contrast, in the lab frame, terms from different order in the FM (vV) expansion can have the same scaling with Ω .

To see this explicitly, let us first identify all terms of order Ω^{-1} appearing in the lab frame. To avoid lengthy expressions, we only state the relevant commutators, which have to be multiplied by the corresponding time integrals. Clearly, two-fold nested commutators appear in the second-order Magnus expansion $H^{(2)}[t_0]$, three-fold nested commutators appear in the third order, and so on. However, each additional commutator comes with an extra Ω^{-1} suppression factor coming from the time integral. It is straightforward to see that all the terms which scale as Ω^{-1} are those containing twice the static Hamiltonian H_0

$$H_0 = \frac{p_\theta^2}{2m} - m\omega_0^2 \cos \theta,$$

and arbitrary many times the driving term

$$H_1(t) = -m\lambda\Omega \cos(\Omega t) \cos \theta.$$

The relevant corrections are given by

$$\begin{aligned} & [H_1, [H_0, H_1]], \\ & [H_0, [H_1, [H_0, H_1]]], \quad [H_1, [H_0, [H_0, H_1]]], \end{aligned}$$

$$[H_1, [H_0, [H_1, [H_0, H_1]]]], [H_1, [H_1, [H_0, [H_0, H_1]]]]]. \quad (3.16)$$

These commutators are non-zero because H_0 depends on the momentum p while H_1 depends on the coordinate θ . Every time the commutator with H_1 is applied, the power of the momentum operator is lowered by one. For example, for $H_0 \sim p^2$, we have $[H_0, H_1] \sim p$, and $[[H_0, H_1], H_1]$ does not depend on p , i.e. it is a function of the coordinates alone and therefore commutes with H_1 . It then immediately follows that all higher-order nested commutators, containing two H_0 and four or more times H_1 , vanish identically. If we work in the symmetric Floquet-gauge $t_0 = 0$, the driving protocol becomes symmetric w.r.t. the origin of the time axis, i.e. $\cos(\Omega t) = \cos(-\Omega t)$. One can then show that all odd-order terms in the FM expansion vanish identically [89] and, thus, only the second-order (first line in Eq. (3.16)) and the fourth-order (third line in Eq. (3.16)) terms contribute.

While the evaluation of all these terms and the corresponding time integrals is in principle possible, it is quite cumbersome and computationally heavy. Instead, it is much easier to get the same Ω^{-1} -correction in the rotating frame by simply evaluating the first order term

$$H_F^{(1)}[0] = \frac{1}{4\pi i\Omega} \int_0^{2\pi} d\tau_1 \int_0^{\tau_1} d\tau_2 [H^{\text{rot}}(\tau_1), H^{\text{rot}}(\tau_2)],$$

where $H^{\text{rot}}(t)$ is the Hamiltonian of Eq. (3.14) and, as before, $\tau = \Omega t$. Likewise, one can use Eq. (2.43) to find the stroboscopic kick operator. Then the calculation of $H_F^{(1)}[0]$ and $K_F^{\text{rot},(1)}[0](t)$ becomes very simple and yields

$$\begin{aligned} H_F^{(1)}[0] &= \frac{1}{\Omega} \left[\frac{\lambda}{4m} (p_\theta^2 \cos \theta + 2p_\theta \cos \theta p_\theta + \cos \theta p_\theta^2) - m\omega_0^2 \lambda \sin^2 \theta - m \frac{\lambda^3}{2} \cos \theta \sin^2 \theta \right], \\ K_F^{\text{rot},(1)}[0](t) &= \int_0^t dt' H^{\text{rot}}(t') - H_F^{(0)}[0] \\ &= \frac{1}{\Omega} \left(\frac{\lambda}{2} (\cos \Omega t - 1) \{\sin \theta, p_\theta\}_+ - \frac{m\lambda^2}{8} \sin 2\Omega t \sin^2 \theta \right). \end{aligned} \quad (3.17)$$

In parallel, we also give the first correction to the van Vleck effective Hamiltonian in the rotating frame. According to the Eq. (2.45) this correction is given by $\sum_\ell [H_\ell, H_{-\ell}] / \ell \Omega$

where H_ℓ are the Fourier harmonics of $H^{\text{rot}}(t)$ (see Eq. (3.14)). One can convince oneself that $H_\ell = H_{-\ell}$ and, therefore, the first order correction to the effective Hamiltonian vanishes:

$$H_{\text{eff}}^{(1)} = \mathbf{0}. \quad (3.18)$$

The difference between the Ω^{-1} -correction terms $H_F^{(1)}[0]$ and $H_{\text{eff}}^{(1)}$ means that the Ω^{-1} terms in the Floquet Hamiltonian only contribute to the Floquet spectrum starting from order Ω^{-2} . Using Eq. (2.46) we find that the effective kick operator is given by:

$$K_{\text{eff}}^{\text{rot},(1)}(t) = \frac{1}{\Omega} \left(\frac{\lambda}{2} \cos(\Omega t) \{\sin \theta, p_\theta\}_+ - \frac{m\lambda^2}{8} \sin(2\Omega t) \sin^2 \theta \right). \quad (3.19)$$

Using Eq. (2.45) and (2.46) it is also straightforward to calculate higher-order corrections in the rotating frame.

3.1.1.4 Dressed Observables and Dressed Density Matrix

Let us now derive the dressed operators and the dressed density matrix which are important to analyse correctly the FNS dynamics of the system, c.f. Sec. 2.1.4. Again, all calculations can be carried out both in the lab and the rotating frames, but we choose the latter for simplicity.

As before, we show the dressed density matrix and observables both in the stroboscopic (FM) and the non-stroboscopic (vV) pictures, using the FM and the vV expansions, respectively. We consider the following natural observables: $\sin \theta$, $\sin^2 \theta$, p_θ , and p_θ^2 , and explicitly consider the initial state characterised by the Gaussian wave-function

$$\langle \theta | \psi_0 \rangle = \frac{1}{(2\pi)^{1/4} \sqrt{\sigma}} e^{-\frac{\sin^2 \theta}{4\sigma^2}} \quad (3.20)$$

with the corresponding density matrix

$$\rho_0(\theta_1, \theta_2) = \frac{1}{\sqrt{2\pi}\sigma} \exp \left(-\frac{\sin^2 \theta_1 + \sin^2 \theta_2}{4\sigma^2} \right). \quad (3.21)$$

We assume that the Gaussian state is well-localised around $\theta = n\pi$, i.e. the width $\sigma \ll 1$. In the rotating frame, the operators $\sin \theta$ and $\sin^2 \theta$ remain the same as in the lab frame, while the operators p_θ and p_θ^2 , as well as the off-diagonal elements of the density matrix acquire a time dependence:

$$\begin{aligned}\sin \theta^{\text{rot}}(t) &= \sin \theta, \\ \sin^2 \theta^{\text{rot}}(t) &= \sin^2 \theta, \\ p_\theta^{\text{rot}}(t) &= V^\dagger(t)p_\theta V(t) = p_\theta + \Delta(t)\sin \theta, \\ p_\theta^{2,\text{rot}}(t) &= p_\theta^2 + \Delta(t)^2 \sin^2 \theta + \Delta(t)\{\sin \theta, p_\theta\}_+, \\ \rho^{\text{rot}}(\theta_1, \theta_2; t) &= e^{i\Delta(t)(\cos \theta_1 - \cos \theta_2)}\rho_0(\theta_1, \theta_2).\end{aligned}\tag{3.22}$$

The rotator $V(t)$ and the function $\Delta(t)$ are defined in Eq. (3.13).

The definition of the dressed operators and density matrix are given by Eqs. (2.30). To compute the leading and the first subleading terms in Ω^{-1} we use Eq. (2.58). In the infinite-frequency limit, the dressed operators and density matrix are obtained from the corresponding time-averaged quantities in the rotating frame (this is true both in the stroboscopic and the effective (vV) picture). This implies that all operators, which are functions of θ are unaffected, while those operators, which depend on momentum beyond linear order, get dressed:

$$\begin{aligned}\overline{\sin \theta}_F^{(0)} &= \overline{\sin \theta}_{\text{eff}}^{(0)} = \sin \theta, & \overline{\sin^2 \theta}_F^{(0)} &= \overline{\sin^2 \theta}_{\text{eff}}^{(0)} = \sin^2 \theta \\ \overline{p_\theta}_F^{(0)} &= \overline{p_\theta}_{\text{eff}}^{(0)} = p_\theta, & \overline{p_\theta^2}_F^{(0)} &= \overline{p_\theta^2}_{\text{eff}}^{(0)} = p_\theta^2 + m^2 \frac{\lambda^2}{2} \sin^2 \theta.\end{aligned}\tag{3.23}$$

The density matrix, being a function of both coordinates and momenta, also gets dressed. In particular,

$$\begin{aligned}\overline{\rho}_F^{(0)}(\theta_1, \theta_2) = \overline{\rho}_{\text{eff}}^{(0)}(\theta_1, \theta_2) &= \frac{1}{T} \int_0^T e^{i\Delta(t)(\cos \theta_1 - \cos \theta_2)} \rho_0(\theta_1, \theta_2) \\ &= \mathcal{J}_0(m\lambda(\cos \theta_1 - \cos \theta_2)) \rho_0(\theta_1, \theta_2),\end{aligned}\tag{3.24}$$

where, \mathcal{J}_0 is the zero-th Bessel function of the first kind. Note that the diagonal elements of ρ_0 , defining the probabilities of a particular value of θ , are not dressed in the infinite-frequency limit (recall that $\mathcal{J}_0(0) = 1$), while the off-diagonal elements, which determine the momentum distribution, get renormalised by the drive. To gain more intuition about this density matrix one can take a partial Fourier transform which defines the Wigner function (dropping the subindices F and $_{\text{eff}}$ for simplicity):

$$\overline{W}^{(0)}(\theta, p_\theta) = \frac{1}{2\pi} \int_{-\infty}^{\infty} d\xi \bar{\rho}^{(0)}(\theta + \xi/2, \theta - \xi/2) e^{ip_\theta \xi}. \quad (3.25)$$

If the width of the Wigner function, σ , in Eq. (3.21) is small, the weight of the density matrix is largest for $\theta_1, \theta_2 \ll 1$ and we can approximate $\cos \theta \approx 1 - \theta^2/2$ in the expression above. This immediately leads to:

$$\begin{aligned} \overline{W}(\theta, p_\theta) &\approx \frac{e^{-\theta^2/(2\sigma^2)}}{(2\pi)^{3/2}\sigma} \int_{-\infty}^{\infty} d\xi e^{-\xi^2/(8\sigma^2)} \mathcal{J}_0(m\lambda\theta\xi) e^{ip_\theta \xi} \\ &\approx \frac{e^{-\theta^2/(2\sigma^2)}}{(2\pi)^{3/2}\sigma} \int_{-\infty}^{\infty} d\xi e^{-\xi^2/(8\sigma^2)} e^{-m^2\lambda^2\theta^2\xi^2/4} e^{ip_\theta \xi} \\ &\approx \frac{1}{\pi\sqrt{1+2m^2\lambda^2\sigma^2\theta^2}} \exp\left[-\frac{\theta^2}{2\sigma^2} - \frac{2p_\theta^2\sigma^2}{1+2m^2\lambda^2\sigma^2\theta^2}\right] \\ &\approx \frac{1}{\pi\sqrt{1+2m^2\lambda^2\sigma^2\sin^2\theta}} \exp\left[-\frac{\sin^2\theta}{2\sigma^2} - \frac{2p_\theta^2\sigma^2}{1+2m^2\lambda^2\sigma^2\sin^2\theta}\right], \end{aligned} \quad (3.26)$$

where we used $\sigma \ll 1$, $\theta \ll 1$, and we have approximated the Bessel function for small arguments by a Gaussian (recall the symmetry of the Bessel function, $\mathcal{J}_0(x) = \mathcal{J}_0(-x)$). In the last line, we made use of the identity $\theta \approx \sin \theta$ for $\theta \ll 1$ to restore the periodicity in θ . As expected, the dressed density matrix features a broadening of the momentum distribution. The new uncertainty in momentum is

$$\langle p_\theta^2 \rangle \approx \frac{1}{2\sigma^2} + m^2 \frac{\lambda^2}{2} \langle \sin^2 \theta \rangle, \quad (3.27)$$

which is consistent with Eq. (3.23) given that we relied on $|\theta| \ll 1$. Not surprisingly, the

momentum uncertainty given by the dressed density matrix is precisely the uncertainty of the dressed $\overline{p_\theta^2}$ operator calculated with the original density matrix (see Eq. (3.23)).

Using Eq. (2.58) together with Eqs. (3.19) and (3.22) it is immediate to compute the Ω^{-1} -corrections to the dressed operators and the density matrix. We find that, in the non-stroboscopic vV picture, all these corrections are zero:

$$\overline{\sin \theta}_{\text{eff}}^{(1)} = 0, \quad \overline{\sin^2 \theta}_{\text{eff}}^{(1)} = 0, \quad \overline{p_\theta}_{\text{eff}}^{(1)} = 0, \quad \overline{p_\theta^2}_{\text{eff}}^{(1)} = 0, \quad \overline{\rho}_{\text{eff}}^{(1)} = 0 \quad (3.28)$$

This follows from the fact that the time integrals and/or the commutators in Eq. (2.58) vanish. The corresponding corrections in the stroboscopic picture can either be computed ab initio using Eq. (2.58) together with Eqs. (3.17) and (3.22), or by transforming the zeroth-order (in Ω^{-1}) dressed observables/density matrix calculated above, from the effective to the stroboscopic picture using Eq. (2.60). The two approaches are equivalent and lead to:

$$\begin{aligned} \bar{\theta}_F^{(1)}[0] &= -\frac{\lambda}{2\Omega} \sin 2\theta, \\ \bar{\theta}^2_F[0] &= -\frac{2\lambda}{\Omega} \sin^2 \theta \cos \theta, \\ \bar{p}_\theta F^{(1)}[0] &= \frac{\lambda}{2\Omega} \{p_\theta, \cos \theta\}_+, \\ \bar{p}_\theta^2 F^{(1)}[0] &= \frac{\lambda}{\Omega} \left(\frac{\{\cos \theta, p_\theta^2\}_+}{2} + p_\theta \cos \theta p_\theta - m\lambda^2 \cos \theta \sin^2 \theta \right) \\ \bar{\rho}_F^{(1)}[0](\theta_1, \theta_2) &= -\frac{1}{\Omega} \left\{ \lambda \mathcal{J}_0(m\lambda(\cos \theta_1 - \cos \theta_2)) \left(\frac{1}{2}(\cos \theta_1 + \cos \theta_2) \right. \right. \\ &\quad \left. \left. + \left(\frac{\cos \theta_1}{2\sigma^2} \sin^2 \theta_1 + \frac{\cos \theta_2}{2\sigma^2} \sin^2 \theta_2 \right) \right) \right. \\ &\quad \left. + m\lambda^2 (\sin^2 \theta_1 + \sin^2 \theta_2) \mathcal{J}_1(m\lambda(\cos \theta_1 - \cos \theta_2)) \right\} \rho_0(\theta_1, \theta_2), \\ &= -\frac{\lambda}{\Omega} \left\{ \left(\sin \theta_1 \partial_{\theta_1} + \frac{1}{2} \cos \theta_1 \right) \bar{\rho}_F^{(0)}(\theta_1, \theta_2) + (1 \leftrightarrow 2) \right\}. \end{aligned} \quad (3.29)$$

3.1.1.5 Multi-Dimensional Generalisation of the Kapitza Pendulum

Last, let us discuss two generalisations of the Kapitza pendulum. First, we consider a single-particle multi-dimensional generalisation. Namely, we analyse a particle of unit mass whose motion is constrained to a d -dimensional hyper-surface embedded in a D -dimensional coordinate space. For example, this can be a particle confined to a 2-dimensional sphere or other, more complicated surface. Let this surface be parameterised by the coordinates $\mathbf{r} = (r_1(\theta_1, \dots, \theta_d), \dots, r_D(\theta_1, \dots, \theta_d))$ with $\theta_1, \dots, \theta_d$ being local coordinates. Now, suppose we choose a preferred direction \mathbf{e}_i in \mathbb{R}^D , to shake the entire hyper-surface periodically:

$$\mathbf{r}(\theta_1, \dots, \theta_d) \rightarrow \mathbf{r}(\theta_1, \dots, \theta_d) + a \cos(\Omega t) \mathbf{e}_i = \mathbf{r}'(t). \quad (3.30)$$

We follow steps similar to those in Eqs. (3.8) – (3.11) and compute the Lagrangian:

$$\mathcal{L} = \frac{m}{2} |\dot{\mathbf{r}}'|^2 - U_{\text{pot}} = \frac{m}{2} (|\dot{\mathbf{r}}|^2 + 2\Omega a \sin(\Omega t) \mathbf{e}_i \cdot \dot{\mathbf{r}}) - U_{\text{pot}},$$

where U_{pot} is an unspecified external potential which only depends on the coordinate \mathbf{r} and, similar to Eq. (3.8), we have dropped the terms independent of \mathbf{r} and $\dot{\mathbf{r}}$. Using the standard definitions for the canonical momentum $\mathbf{p} = \partial \mathcal{L} / \partial \dot{\mathbf{r}}$ and the Hamiltonian $H = \mathbf{p} \cdot \dot{\mathbf{r}} - \mathcal{L}$ we arrive at

$$\begin{aligned} H &= \frac{1}{2m} (\mathbf{p} - ma\Omega \sin(\Omega t) \mathbf{e}_i)^2 + U_{\text{pot}} \longrightarrow \frac{1}{2m} |\mathbf{p}|^2 + U_{\text{pot}} - ma\Omega^2 \cos(\Omega t) \mathbf{e}_i \cdot \mathbf{r} \\ &= \frac{1}{2m} |\mathbf{p}|^2 + U_{\text{pot}} - m\lambda\Omega \cos(\Omega t) \mathbf{e}_i \cdot \mathbf{r} \end{aligned}$$

where in the second step we cast the vector potential as a scalar potential and made the identification $\lambda = a\Omega = \text{const}$. Thus, we arrive at the conclusion that by shaking the surface at high frequency and small amplitude (i.e. $\Omega \rightarrow \infty$ and $\lambda = \text{const.}$) we effectively create a large time-dependent “gravitational-like” potential along the shaking direction. This large effect has been achieved by shaking the entire hypersurface, on which the particle

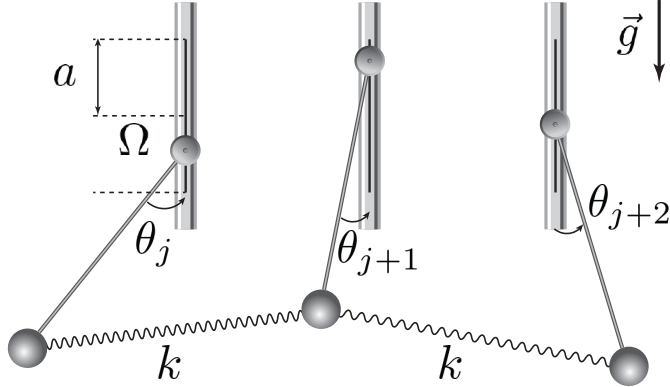


Figure 3.2: A system of coupled Kapitza pendula: a many-body representative of the Kapitza class.

is constrained to move, and could not have been achieved by periodically driving any intrinsic model parameter (such as the gravity g), unless one finds a way to scale the driving amplitude with Ω . The Floquet Hamiltonian can be found from Eqs. (3.5) – (3.7). All finite-frequency corrections as well as the dressed operators can be found by a simple extension of the corresponding results for the Kapitza pendulum.

3.1.1.6 Multi-Particle Generalisation of the Kapitza Pendulum

As a last example we generalise the Kapitza pendulum to a chain of coupled pendula (see Fig. 3.2). Consider N coupled pendula, shaken along the y -direction using some specific driving protocol. In a way, this example can be thought of as a single particle confined to an N -dimensional hyper-surface embedded in a $2N$ -dimensional space, where N is the number of pendula. One can repeat the derivation of Sec. 3.1.1.1 to find that the Hamiltonian of this system reads

$$H = \sum_{j=1}^N \frac{p_j^2}{2m} - J \cos(\theta_j - \theta_{j+1}) - m\omega_0^2 \cos \theta_j - m\lambda\Omega \cos \Omega t \cos \theta_j, \quad (3.31)$$

where $J = kl^2$ is the coupling proportional to the spring constant k and, as usual, λ is proportional to the product of the driving frequency and the driving amplitude. In the limit

of large frequency and $\lambda = \text{const.}$, this Hamiltonian leads to a discretised version of the Sine-Gordon model, which is also very close to the famous Frenkel-Kontorova model [124]:

$$H_F^{(0)} = H_{\text{eff}}^{(0)} = \sum_{j=1}^N \frac{p_j^2}{2m} - J \cos(\theta_j - \theta_{j+1}) - m\omega_0^2 \cos \theta_j + m \frac{\lambda^2}{4} \sin^2 \theta_j. \quad (3.32)$$

This model can undergo a quantum phase transition, between the gapless and gapped phases, depending on the value of λ , and the magnitude of the other couplings. It supports various interesting excitations, such as solitons and breathers, and their nature can change with varying the effective drive strength λ [124]. This model is integrable in the limits $\lambda \ll \omega_0$ and $\lambda \gg \omega_0$ but non-integrable when these couplings are comparable to one another. This opens up the possibility of studying interesting thermalisation-type dynamics [106]. Additionally, it becomes possible to create interesting infinite-frequency limits by driving different pendula with different amplitudes and phases. This can be used to generate artificial position-dependent gravitational fields, making the emergent physics even more interesting.

3.1.2 The Dirac Class

In this section, we consider periodically driven systems with a kinetic energy linear in momentum. According to relativistic quantum mechanics, this requires an additional spin structure in the Hamiltonian [125]. Such systems describe the low-energy physics of graphene [126], Weyl semi-metals [127], and other related materials [56, 128, 129].

3.1.2.1 Periodically Driven Magnetic Fields

The *Dirac* class is defined by the following Hamiltonian

$$\begin{aligned} H(t) &= H_0 - \lambda \Omega \sin(\Omega t) H_1, & H_1 &= \mathbf{B}(\mathbf{r}) \cdot \boldsymbol{\sigma}, \\ H_0 &= H_{\text{kin}} + H_{\text{int}} = v_F \mathbf{p} \cdot \boldsymbol{\sigma} + H_{\text{int}}, \end{aligned} \quad (3.33)$$

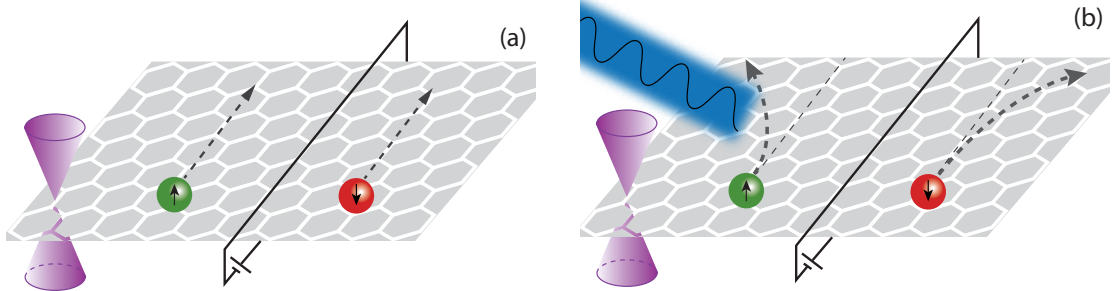


Figure 3.3: Light induced spin-orbit coupling. Shining light on fermions with a relativistic dispersion, such as graphene close to the neutrality point, leads to spin-orbit coupling whose strength is controlled by the driving amplitude. (a) In absence of the driving, a potential bias generates a longitudinal current. (b) In presence of the driving, a potential bias generates a longitudinal and a *transverse* current whose direction depends on the value of the spin.

where v_F is the Fermi velocity, $\mathbf{B}(\mathbf{r})$ is an external magnetic field and $\boldsymbol{\sigma}$ is the vector of 2×2 Pauli matrices (we could similarly analyse a coupling to the 4×4 Dirac γ -matrices without any need to define a new class). Here H_{int} contains arbitrary spin-independent external potentials and (for many-particle systems) arbitrary spin-independent many-body interactions. Taking additional spin-dependent static external potentials into account is straightforward but will unnecessarily aggravate the discussion. Furthermore, to avoid technical complications, our analysis is restricted to situations where the magnetic field does not change its direction in time. To simplify the notation we shall keep the discussion at the single-particle level.

Similarly to the Kapitza class, the analysis of the FM and vV HFE for the Dirac class can be significantly simplified by performing a transformation to a rotating frame given by

$$\begin{aligned} V(t) &= \exp(-i\Delta(t)\mathbf{B}(\mathbf{r}) \cdot \boldsymbol{\sigma}), \\ \Delta(t) &= \lambda \cos \Omega t. \end{aligned} \quad (3.34)$$

Clearly, $V(t)$ is a periodic function of time, but with our choice of $\Delta(t)$, it does not satisfy the condition $V(0) = \mathbf{1}$. Hence, the initial state in the rotating frame is related to the initial

state in the lab frame via a unitary rotation by $V(0)$, i.e. $|\psi^{\text{lab}}\rangle = V(0)|\psi^{\text{rot}}\rangle$, c.f. Sec. 2.2.5.

One can of course change $V(t)$ by redefining $\Delta(t) \rightarrow \Delta(t) - \Delta(0)$, but this leads to additional gauge-dependent terms in the Floquet Hamiltonian. This is a manifestation of the Floquet-gauge, discussed in Sec. 2.1.

After the transformation to the rotating frame the kinetic energy becomes

$$\begin{aligned} \frac{H_{\text{kin}}^{\text{rot}}(t)}{v_F} &= V^\dagger(t) (\mathbf{p} \cdot \boldsymbol{\sigma}) V(t) \\ &= \frac{1}{2} \{ \cos(2\Delta(t)B(\mathbf{r})), \mathbf{p} \cdot \boldsymbol{\sigma} - (\mathbf{n} \cdot \mathbf{p})(\mathbf{n} \cdot \boldsymbol{\sigma}) \}_+ \\ &\quad - \frac{1}{2} \{ \sin(2\Delta(t)B(\mathbf{r})), (\mathbf{n} \times \mathbf{p}) \cdot \boldsymbol{\sigma} \}_+ - \Delta(t)\mathbf{n} \cdot \nabla B(\mathbf{r}) + (\mathbf{n} \cdot \mathbf{p})(\mathbf{n} \cdot \boldsymbol{\sigma}), \\ H_{\text{int}}^{\text{rot}}(t) &= V^\dagger(t) H_{\text{int}} V(t) = H_{\text{int}}, \end{aligned} \quad (3.35)$$

where $B(\mathbf{r})$ and \mathbf{n} are the magnitude and the direction of the magnetic field $\mathbf{B}(\mathbf{r})$, i.e. $\mathbf{B}(\mathbf{r}) = B(\mathbf{r})\mathbf{n}$ with $|\mathbf{n}| = 1$. H_{int} is not affected by the transformation to the rotating frame since it is, by assumption, spin independent². We can now readily obtain the effective high-frequency Floquet Hamiltonian by taking the time-average of Eq. (3.35):

$$H_F^{(0)} = H_{\text{eff}}^{(0)} = v_F (\mathbf{n} \cdot \mathbf{p})(\mathbf{n} \cdot \boldsymbol{\sigma}) + \frac{v_F}{2} \{ \mathcal{J}_0(2\lambda B(\mathbf{r})), \mathbf{p} \cdot \boldsymbol{\sigma} - (\mathbf{n} \cdot \mathbf{p})(\mathbf{n} \cdot \boldsymbol{\sigma}) \}_+ + H_{\text{int}}, \quad (3.36)$$

where \mathcal{J}_0 is the 0-th order Bessel function of the first kind. One can show that there are no Ω^{-1} -corrections to the Floquet Hamiltonian for the chosen Floquet gauge. This follows from the fact that, for a symmetric driving protocol $\Delta(t) = \Delta(-t)$, all odd-order terms in the FM expansion vanish identically [89], see Eq. (2.41). Moreover, there are no Ω^{-1} -corrections to the effective vV Hamiltonian either. This follows from the fact that, for this model, H_ℓ and $H_{-\ell}$ commute with each other and, therefore, the first-order correction vanishes, c.f. Eq. (2.45). Hence, the leading non-vanishing correction to this Floquet Hamiltonian is of order Ω^{-2} suggesting that the infinite-frequency limit in the

²If the original Hamiltonian contains additional spin-dependent external fields or interactions, then the transformation to the rotating frame will dress H_{int} , too.

Dirac class is robust to finite-frequency effects.

3.1.2.1.1 Dresselhaus Spin-Orbit Coupling

We now consider an example in which we drive a linearly polarised constant magnetic field along a fixed direction in the xy -plane. We find an effective Dresselhaus spin-orbit coupling (SOC) in the high-frequency limit. Proposals for Floquet realisations of SOC (see Fig. 3.3 for a schematic representation) have already been made for bosons using constant pulse sequences [130–133]. For fermions, the periodically driven spin-orbit coupling has been studied in graphene [134].

We consider the Hamiltonian (3.33) with:

$$B(\mathbf{r}) = 1, \quad \mathbf{n} = \frac{1}{\sqrt{2}} (1, 1, 0). \quad (3.37)$$

Specialising Eq. (3.36) to $B(\mathbf{r}) = 1$ we arrive at:

$$\begin{aligned} H_F^{(0)} &= H_{\text{eff}}^{(0)} = v_F (1 - \mathcal{J}_0(2\lambda)) (\mathbf{n} \cdot \mathbf{p}) (\mathbf{n} \cdot \boldsymbol{\sigma}) + v_F \mathcal{J}_0(2\lambda) (\mathbf{p} \cdot \boldsymbol{\sigma}) + H_{\text{int}} \\ &= v'_F (\mathbf{p} \cdot \boldsymbol{\sigma}) + \frac{v_F}{2} (1 - \mathcal{J}_0(2\lambda)) (p_x \sigma^y + p_y \sigma^x) + H_{\text{int}}, \end{aligned} \quad (3.38)$$

where, to obtain the last equality, we have used the explicit form of \mathbf{n} and we have defined the modified Fermi velocity $v'_F = (v_F/2)(1 + \mathcal{J}_0(2\lambda)) \leq v_F$. Hence, besides the expected renormalisation of the Fermi velocity, one finds an effective Dresselhaus spin-orbit coupling term without affecting the interactions.

3.1.2.2 Periodically Driven External Potentials

When one takes into consideration driving systems with a linear dispersion, there exists yet a second possibility in which the driving protocol couples to a scalar external potential.

The general form of the lab-frame Hamiltonian is

$$H(t) = H_0 + \frac{\lambda}{v_F} \Omega^2 \cos(\Omega t) H_1, \quad (3.39)$$

where H_0 is defined in Eq. (3.33) and H_1 is an arbitrary spin-independent scalar potential. As we show below, the Hamiltonian above is intimately related to the Hamiltonian (3.33) defining the Dirac class, and thus there is no need to define a new “class” to accommodate it. Notice that in the above Hamiltonian the driving amplitude scales with Ω^2 while in Eq. (3.33) the driving scales with Ω . The scaling of the drive with Ω^2 is intimately related to the existence of the additional spin structure in the Hamiltonian and it will be explained from two different perspectives: the lab-frame FM expansion, and a transformation to a rotating frame.

First, we apply the Floquet-Magnus expansion *in the lab frame*. The zeroth order term gives the time-averaged Hamiltonian $H_{\text{kin}} + H_{\text{int}}$. The Ω^{-1} -corrections vanish identically due to the symmetry of the drive, i.e. $\cos(\Omega t) = \cos(-\Omega t)$. Therefore, the leading contributions to the Floquet Hamiltonian are given by the commutators:

$$[H_{\text{kin}}, [H_{\text{kin}}, H_1]], [H_1, [H_{\text{kin}}, H_1]].$$

where each H_1 term brings an extra factor of Ω^2 due to the scaling of the driving amplitude and both terms are multiplied by a factor T^2 which comes from the double time integral (c.f. definition of the Floquet-Magnus expansion in Sec. 2.2). For systems with a Dirac dispersion it is easy to verify that the second term vanishes identically. In fact $[H_{\text{kin}}, H_1] \propto \nabla H_1 \cdot \boldsymbol{\sigma}$ and, therefore, it commutes with H_1 which is diagonal in spin space and depends on the position \mathbf{r} exclusively. As a result, only the term $[H_{\text{kin}}, [H_{\text{kin}}, H_1]]$ contributes to the Floquet Hamiltonian. Therefore, to keep this term finite in the infinite-frequency limit, we need to scale the driving amplitude as Ω^2 . Recall that in the non-relativistic Kapitza class the term $[H_1, [H_{\text{kin}}, H_1]]$ was non-zero and dominant. Therefore, to keep the

dominant contribution to the Floquet Hamiltonian finite in the infinite-frequency limit, in the Kapitza class the driving amplitude scales only linearly with Ω .

There are other important differences in the inverse-frequency expansion between the Dirac and Kapitza classes. While in the Kapitza class the FM HFE in the limit $\Omega \rightarrow \infty$ truncates in the lab frame after the second order, this is not the case in the Dirac class due to the additional spin structure in the kinetic energy term. For instance, consider the fourth-order commutator $[H_{\text{kin}}, [H_1, [H_{\text{kin}}, [H_1, H_{\text{kin}}]]]]$, which scales as Ω^4 . Taking into account the factor T^4 from the time-ordered integrals, we find that this term remains finite as $\Omega \rightarrow \infty$. Although the kinetic energy is linear in \mathbf{p} , this four-nested commutator does not vanish due to the spin commutation relations $[\sigma_\alpha, \sigma_\beta] = 2i\varepsilon_{\alpha\beta\gamma}\sigma_\gamma$. Similar expressions appear in any even higher-order terms in the Floquet-Magnus expansion (all odd terms being zero due to the symmetry of the drive).

Next, we explain the scaling Ω^2 in Eq. (3.39) from the point of view of a transformation $\tilde{V}(t)$ to a preliminary rotating frame:

$$\tilde{V}(t) = \exp\left(-i\frac{\lambda}{v_F}\Omega \sin(\Omega t) H_1(\mathbf{r})\right). \quad (3.40)$$

In this preliminary rotating frame the Hamiltonian is:

$$\begin{aligned} \tilde{H}(t) &= \tilde{H}_{\text{kin}}(\mathbf{r}, t) + H_{\text{int}}, \\ \tilde{H}_{\text{kin}}(\mathbf{r}, t) &= \tilde{V}^\dagger(t) (v_F \mathbf{p} \cdot \boldsymbol{\sigma}) \tilde{V}(t) = v_F \mathbf{p} \cdot \boldsymbol{\sigma} - \lambda \Omega \sin(\Omega t) \mathbf{B}(\mathbf{r}) \cdot \boldsymbol{\sigma}, \end{aligned} \quad (3.41)$$

where $\mathbf{B}(\mathbf{r}) = \nabla H_1(\mathbf{r})$ is the “magnetic field”, generated by the spatial gradient of the time-dependent scalar potential. This is only an analogy with real magnetic fields, which are always divergence-free, while a synthetic magnetic field need not be. For example choosing a parabolic driving potential $H_1(\mathbf{r}) = r^2$ induces an effective radial “magnetic field” $\mathbf{B}(\mathbf{r}) = 2\mathbf{r}$ in the first rotating frame. The amplitude of this oscillatory “magnetic field” scales only linearly with the driving frequency, reflecting the re-summation of an infi-

nite lab-frame inverse-frequency subseries. The interaction term H_{int} is not affected by this transformation. Notice that in this first rotating frame, the Hamiltonian in Eq. (3.41) becomes of the form of Eq. (3.33). Therefore, we can adopt the entire discussion of Sec. 3.1.2.1 to further analyse this type of models.

This procedure highlights the fact that the Hamiltonians (3.33) and (3.41) are intimately related as we anticipated above. We conclude that, within the Dirac class of systems with a linear dispersion, one can either drive the system via a spatially-dependent scalar potential with an amplitude scaling as Ω^2 , or with a spatially-dependent “magnetic field” with an amplitude scaling linearly with Ω . Using the scalar potential allows one to generate synthetic “magnetic fields”, which need not satisfy the ordinary Maxwell equations (in particular, this might allow one to introduce effective magnetic monopoles into the system). We stress that the Hamiltonian (3.41) can be used as a starting point instead of the Hamiltonian (3.33).

3.1.2.2.1 Periodically Driven Linear Potential

As an illustration let us consider a graphene-type setup in which the momentum of the particle is confined to the (x, y) -plane. The external potential depends linearly on the out-of-the-plane coordinate z via $H_1(z) = z$. The Hamiltonian is

$$H(t) = H_{\text{kin}} + H_{\text{int}} + \frac{\lambda}{v_F} \Omega^2 \cos(\Omega t) z. \quad (3.42)$$

Going to the preliminary rotating frame we find a constant in space, time-dependent “magnetic field” along the z -axis: $\mathbf{B} = \hat{z}$ so that

$$\tilde{H}(t) = v_F (\mathbf{p} \cdot \boldsymbol{\sigma}) + \lambda \Omega \sin(\Omega t) \mathbf{B} \cdot \boldsymbol{\sigma} + H_{\text{int}}.$$

We now do a transformation to a second rotating frame, as discussed in Sec. 3.1.2.1. For $B(\mathbf{r}) = 1$ and $\mathbf{n} = (0, 0, 1)$ the general Floquet Hamiltonian in Eq. (3.36) reduces to

$$H_F^{(0)} = H_{\text{eff}}^{(0)} = v_F \mathcal{J}_0(2\lambda) (\mathbf{p} \cdot \boldsymbol{\sigma}) + H_{\text{int}} = v_F \mathcal{J}_0(2\lambda) (p_x \sigma^x + p_y \sigma^y) + H_{\text{int}}. \quad (3.43)$$

Note that there are no terms proportional to p_z , since the motion of the particles is confined to the two-dimensional (x, y) -plane. This driving protocol essentially leads to a renormalised Fermi velocity, which can be tuned to zero by choosing 2λ to coincide with the zero of the Bessel function \mathcal{J}_0 . This dynamical localisation effect can be used for enhancing interaction effects in weakly-interacting many-body systems, such as graphene.

If, in the same setup, the effective potential depends linearly on x , then the resulting Floquet Hamiltonian becomes anisotropic:

$$H_F^{(0)} = H_{\text{eff}}^{(0)} = v_F p_x \sigma^x + v_F \mathcal{J}_0(2\lambda) p_y \sigma^y + H_{\text{int}}, \quad (3.44)$$

and tuning $\mathcal{J}_0(2\lambda) = 0$ makes the kinetic term one-dimensional.

3.1.3 The Dunlap-Kenkre Class

As a third class of Hamiltonians, where one can engineer interesting infinite-frequency limits, we consider a setup where the driving couples to a non-interacting term in an arbitrary interacting system. Examples include interacting particles with arbitrary dispersion relation in an external time-dependent electric field, or interacting spin systems in a time-periodic magnetic field, just to name a few. As we shall see in this section, this class of Hamiltonians is paradigmatic for ‘Floquet engineering’. In this way one can generate Wannier-Stark ladders [86, 135–137], non-trivial tight-binding models with engineered dispersion relations [86, 138–140], including the Harper-Hofstadter Hamiltonian [52–54, 88] and other models exhibiting artificial gauge fields [49, 86, 141–143], effective spin Hamiltonians [51, 144, 145], quantum Hall states [146], topologically non-trivial Floquet Hamil-

tonians [38, 39, 56, 57, 66, 147–150], spin-dependent bands [60], and many others.

To the best of our knowledge, the first theoretical proposal for the realisation of a non-trivial high-frequency limit in a tight-binding model with an external periodic electric field was proposed by Dunlap and Kenkre in Refs. [41, 42]. They discussed the phenomenon of dynamical localisation, where the hopping between neighbouring lattice sites can be completely suppressed in the high frequency limit by choosing an appropriate fixed ratio between the driving amplitude and the driving frequency. Motivated by their idea, we consider the following general class of Hamiltonians

$$H(t) = H_0 + \Omega H_1(t), \quad (3.45)$$

where H_0 represents some (interacting) lattice Hamiltonian, and

$$H_1 = \sum_m f_m(t) n_m \quad (3.46)$$

with n_m being the density operator on the m -th lattice site, and $f_m(t)$ is an arbitrary site-dependent periodic function of time with period T . Notice that in Eq. (3.45), we have explicitly put the Ω -dependence of the driving term H_1 to highlight the non-trivial scaling of the driving amplitude with frequency.

Instead of the lattice system, we could consider a continuum model using $\sum_m f_m(t) n_m \rightarrow \int d^d x f(t, \mathbf{x}) n(\mathbf{x})$ with $f(t+T, \mathbf{x}) = f(t, \mathbf{x})$. Obviously, in the continuum limit there is an overlap between the DK class and the Kapitza class, if the kinetic energy in H_0 is quadratic in momentum, and with the Dirac class if it is linear. The relation between continuum and lattice models is discussed in Appendix A. In the DK class, we allow for arbitrary dispersion relations at the expense of restricting the driving to couple to single-particle terms. Later on, in Sec. 3.1.3.5, we shall show that the DK class extends to driven spin systems, where H_0 describes some arbitrary interacting spin Hamiltonian, while the driving term couples to a spatially dependent, periodic in time magnetic field.

After giving an overview of the general theory of the DK class, we shall discuss the recent dynamical realisation of the Harper Hamiltonian [52, 53], as a special case of the periodically driven Bose-Hubbard model. We shall derive both the infinite-frequency limit, and the leading Ω^{-1} -corrections to the Floquet Hamiltonian. We shall also give examples for the dressed operators and density matrix. After that, we continue with the fermionic case illustrated on the driven Fermi-Hubbard model, and discuss the infinite-frequency limit and the Ω^{-1} -corrections, which are expected to be important for interacting Floquet topological insulators, as realised in Ref. [56]. Finally, we discuss interacting driven spin chains.

To be specific, we assume that H_0 is the sum of the kinetic energy term, represented by the nearest-neighbour (nn) hopping, and the density-density interactions – which can also include a static external potential linearly coupled to the density:

$$H_0 = H_{\text{kin}} + H_{\text{int}}, \quad (3.47)$$

where $[n_m, H_{\text{int}}] = 0$, and

$$H_{\text{kin}} = -J_0 \sum_{\langle m,n \rangle} a_m^\dagger a_n + \text{h.c.}$$

The angular brackets in the sum stand for nearest neighbours.

The terms in the inverse-frequency expansion, which do not vanish in the infinite-frequency limit are of the type

$$H_0, [H_1, H_0], [H_1, [H_1, H_0]], [H_1, [H_1, [H_1, H_0]]], \dots \quad (3.48)$$

Since each commutator brings an extra factor of Ω^{-1} from the time integral (see the discussion in Sec. 2.2), and each H_1 term brings an extra factor of Ω due to the scaling of the driving amplitude, it is easy to see that all these terms are of the same order in Ω . Furthermore, these are the only terms that survive in the infinite-frequency limit. However, unlike in the Kapitza class, this series does not terminate at any finite order and, thus,

one has to re-sum an infinite lab-frame subseries to obtain the correct infinite-frequency Floquet Hamiltonian. This is intimately related to the fact that the dispersion relation in H_0 is arbitrary and not quadratic in momentum as in the Kapitza class.

From this structure of the inverse-frequency expansion, it is also clear why the Hamiltonian H_1 should couple linearly to the density. Only then do these nested commutators not grow both in space (meaning that the resulting effective operators remain local) and in the number of creation and annihilation operators (i.e. we avoid the generation of three and higher-body interactions). One can also consider other situations where the commutators do not grow, for example, when the driving couples to the local in space density-density interaction between fermions [151] or even bosons [152–154] (though the bosonic case is more subtle), or when the protocol couples to local in space spin interactions for spin models with spin larger than one half.

While re-summation of an infinite (sub)series is possible and it yields the proper infinite-frequency limit, calculating the subleading corrections directly becomes very involved. These complications can be overcome, as before, by going to the rotating frame, which is defined via the transformation

$$V(t) = \exp \left[-i \sum_m \Delta_m(t) n_m \right], \quad \Delta_m(t) = \Omega \int_{t_0}^t dt' f_m(t'). \quad (3.49)$$

The lower limit of the integral defining $\Delta_m(t)$ is a gauge choice, related to the Floquet-gauge, e.g. one can choose $t_0 = 0$. Applying this transformation eliminates the term linear in the density operator, which in the lab frame diverges linearly with the frequency. At the same time, in the rotating frame, a periodic drive is imprinted to the kinetic energy:

$$\begin{aligned} H^{\text{rot}}(t) &= W(t) + W^\dagger(t) + H_{\text{int}} \\ W(t) &= -J_0 \sum_{\langle mn \rangle} e^{i[\Delta_m(t) - \Delta_n(t)]} a_m^\dagger a_n. \end{aligned} \quad (3.50)$$

Notice that this transformation leaves the interaction term H_{int} invariant. As in the previ-

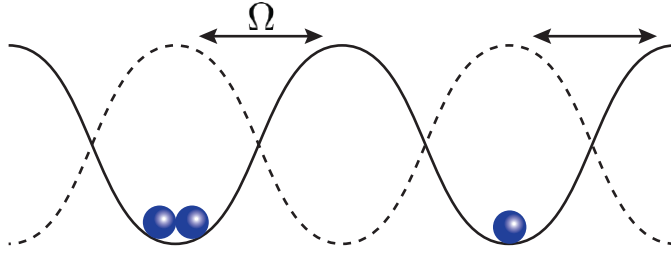


Figure 3.4: A periodically driven (shaken) optical lattice in which the lattice is shifted periodically at frequency Ω : the prototypical example of the DK class.

ous classes we discussed, going to the rotating frame generates an effective complex driving protocol, which is well-behaved in the infinite-frequency limit. The infinite-frequency limit of the Floquet Hamiltonian is then simply given by the time average of $H^{\text{rot}}(t)$. Due to the large value of the drive amplitude in the lab frame, in the rotating frame, owing to the strong hybridisation of Floquet states via virtual photon absorption processes, averaging over time is equivalent to a re-summation of an infinite lab-frame inverse-frequency sub-series, in agreement with the general discussion in Sec. 2.2. Similarly to the Kapitza class, the inverse-frequency expansion in the rotating frame can be used to compute the subleading correction in Ω^{-1} to the Floquet Hamiltonian. Rather than discussing these corrections in the most general form, we will show and analyse them for specific examples.

3.1.3.1 The Periodically Shaken Lattice: An Exactly Solvable Model

As a first representative of the DK class, we consider a chain of noninteracting, periodically driven spinless particles, which can be either bosons or fermions (see Fig. 3.4) with the following Hamiltonian

$$H(t) = -J_0 \sum_m a_{m+1}^\dagger a_m + \text{h.c.} + \Omega \zeta \cos \Omega t \sum_m m n_m, \quad (3.51)$$

where J_0 is the hopping, and a_m^\dagger is the operator which creates a particle at site m , and $n_m = a_m^\dagger a_m$ is the number operator. This system was first analysed by Dunlap and Kenkre in Refs. [41, 42] and features the phenomenon dynamical localisation, which we explain in

detail now.

Due to the large driving amplitude in the lab frame, the Floquet states are strongly hybridised by virtual photon absorption processes. To capture this virtual hybridisation mathematically, we go to a rotating frame as follows:

$$\begin{aligned} V(t) &= \exp\left(-i\zeta \sin \Omega t \sum_m m n_m\right), \\ H^{\text{rot}}(t) &= -J_0 \sum_m e^{-i\zeta \sin \Omega t} a_{m+1}^\dagger a_m + \text{h.c.} \end{aligned} \quad (3.52)$$

Notice the highly oscillatory time-dependence of the hopping matrix elements. In the high-frequency limit, where the dynamics of the system is effectively described by the time-averaged Hamiltonian, we find

$$H_F^{(0)}[0] = H_{\text{eff}}^{(0)} = -J_0 \mathcal{J}_0(\zeta) \sum_m a_{m+1}^\dagger a_m + \text{h.c.}, \quad (3.53)$$

where we used the defining relation of the Bessel function of the first kind $\mathcal{J}_0(\zeta) = 1/(2\pi) \int_0^{2\pi} d\tau e^{-i\zeta \sin \tau}$. When the parameter ζ is tuned to a zero of the Bessel function \mathcal{J}_0 , the hopping is completely suppressed due to interference showing the phenomenon of dynamical localisation as first discussed in Ref. [41], and experimentally verified in Ref. [43]. The thermodynamics of such driven chains has been studied in Ref. [155].

Let us now solve the problem exactly in the case of periodic boundary conditions. Note that, while in the lab frame translational invariance is broken by the position-dependent drive, this breaking is not explicitly present in the rot frame. Thus, we ‘close our eyes’ and adopt periodic boundaries, which allows us to define momentum as a good quantum number and go to the reciprocal lattice space:

$$H^{\text{rot}}(t) = -2J_0 \sum_{k \in \text{BZ}} \cos(k - \zeta \sin \Omega t) a_k^\dagger a_k, \quad (3.54)$$

where we put the lattice spacing to unity, and k is the momentum quantum number. In

momentum space, it is easy to integrate the Heisenberg equation of motion

$$\begin{aligned} i\dot{a}_k(t) &= -2J_0 \cos(k - \zeta \sin \Omega t) a_k(t), \\ a_k(t) &= a_k e^{2iJ_0 \int_0^t \cos(k - \zeta \sin \Omega t') dt'} = a_k e^{2iJ_0 \int_0^t [\cos(k - \zeta \sin \Omega t') - \mathcal{J}_0(\zeta) \cos(k)] dt'} e^{2iJ_0 \mathcal{J}_0(\zeta) \cos(k) t} \end{aligned} \quad (3.55)$$

From here, we can read off the rot-frame kick operator and the exact Floquet Hamiltonian in momentum space

$$\begin{aligned} K_{\text{eff}}^{\text{rot}}(t) &= -2J_0 \sum_{k \in \text{BZ}} \left(\int_0^t [\cos(k - \zeta \sin \Omega t') - \mathcal{J}_0(\zeta) \cos(k)] dt' \right) a_k^\dagger a_k, \\ H_{\text{eff}} &= -2J_0 \mathcal{J}_0(\zeta) \sum_{k \in \text{BZ}} \cos(k) a_k^\dagger a_k. \end{aligned} \quad (3.56)$$

The kick operator in the lab frame, on the other hand, is a more complicated object: $K_{\text{eff}}(t) = i \log [V(t) e^{-iK_{\text{eff}}^{\text{rot}}(t)}]$.

Let us now make a few remarks: first, we emphasise that this solution holds at any frequency and, in particular, those below the single-particle bandwidth. Therefore, all variants of the inverse-frequency expansion converge and, in fact, truncate after the leading-order term. Physically, this is the case because states of different momenta are not coupled due to the selection rule imposed by momentum conservation.

Second, an interesting observation can be made, if we impose open boundary conditions instead. While the expansions are completely insensitive to the boundary conditions, a quick numerical check shows that, whenever $\Omega < 4J_0 \mathcal{J}_0(\zeta)$ is below the effective single-particle bandwidth, the Floquet Hamiltonian and Kick operator in Eq. (3.56) do not agree with the numerically calculated ones. This interesting phenomenon arises because, once momentum is no longer conserved, there are finite matrix elements between (what used to be the momentum) states which are resonantly enabled for frequencies below the single-particle bandwidth. As expected, these matrix elements vanish in the thermodynamic limit where an emergent momentum conservation is found, see also Sec. 5.1.1. Since we already established the insensitivity of the inverse-frequency expansion to the boundary conditions,

this gives a hint that the HFE can fail to converge, even for non-interacting systems, as anticipated in Sec. 2.3.2. It is expected, though, that these resonances can be captured using rotating-wave approximation methods, see Sec. 2.3.2.2.1 and Sec. 3.3.

Nevertheless, if we put aside the aforementioned problem of capturing the Floquet resonances, the inverse-frequency expansion provides a very powerful tool to study the hybridisation due to virtual photon absorption which underlies the concept of Floquet engineering.

3.1.3.2 Non-interacting Particles in a Periodically Driven Potential: Floquet Theory and Experimental Realisation

Let us now consider a more general driving protocol. While the model below is not exactly solvable, it teaches us an important lesson in imprinting complex matrix elements that prove useful for Floquet-engineering artificial gauge fields. The Hamiltonian is

$$H(t) = -J_0 \sum_m \left(a_{m+1}^\dagger a_m + \text{h.c.} \right) + \Omega \sum_m \frac{\zeta}{2} \sin(\Omega t - \Phi m + \Phi/2) n_m. \quad (3.57)$$

Once again, the driving protocol couples to the density and breaks translational invariance through the site-dependent phase (which may have a more-complicated spatial dependence). The driving amplitude $V_0 = \Omega\zeta$ is constant in space and, in agreement with the general discussion, is proportional to the frequency. The above choice of the Floquet gauge (or the phase lag) ensures a familiar form (i.e. gauge choice) of the infinite-frequency Floquet Hamiltonian. In the next sections we shall generalise our analysis by adding interactions, a second spatial dimension, and finally by adding a spin degree of freedom.

The transformation to the rotating frame is done using Eq. (3.49) with $\Delta_m(t) = -\zeta \cos(\Omega t - \Phi m + \Phi/2)$ and $t_0 = 0$. We pause to note that, for this particular Floquet gauge choice, $V(0) \neq \mathbf{1}$. As a consequence, one needs to transform the initial state to

the rotating frame as well. Combining this with Eq. (3.50) we find:

$$H^{\text{rot}}(t) = -J_0 \sum_m g^{m,m+1}(t) a_{m+1}^\dagger a_m + \text{h.c.} = \sum_{\ell \in \mathbb{Z}} H_\ell e^{i\ell\Omega t}, \quad (3.58)$$

where

$$\begin{aligned} g^{m,m+1}(t) &= e^{-i\zeta \sin(\Omega t - \Phi m)}, \quad \zeta = \lambda \sin(\Phi/2), \\ H_\ell &= \sum_m \left(e^{-i\ell\Phi m} \left[\mathcal{J}_{-\ell}(\zeta) a_{m+1}^\dagger a_m + \mathcal{J}_\ell(\zeta) a_m^\dagger a_{m+1} \right] \right). \end{aligned} \quad (3.59)$$

We label the function $g^{m,m+1}(t)$ by two site indices to highlight that it is a link variable, i.e. defined on the bonds of the lattice. The infinite-frequency Floquet Hamiltonian and the leading correction are then found from the FM (vV) expansion:

$$\begin{aligned} H_F^{(0)} &= H_{\text{eff}}^{(0)} = -J_{\text{eff}}(\zeta) \sum_m \left(a_{m+1}^\dagger a_m + \text{h.c.} \right), \\ H_F^{(1)}[0] &= -\frac{J_0^2}{\Omega} \sum_m \left(\mathcal{C}_{m,m+2}(\zeta) a_{m+2}^\dagger a_m + \text{h.c.} \right) + \frac{J_0^2}{\Omega} \sum_m \mathcal{G}_{m,m+1}(\zeta) (n_m - n_{m+1}), \\ H_{\text{eff}}^{(1)} &= -\frac{J_0^2}{\Omega} \sum_m \left(\tilde{\mathcal{C}}_{m,m+2}(\zeta) a_{m+2}^\dagger a_m + \text{h.c.} \right) + \frac{J_0^2}{\Omega} \sum_m \tilde{\mathcal{G}}_{m,m+1}(\zeta) (n_m - n_{m+1}), \end{aligned} \quad (3.60)$$

where $J_{\text{eff}}(\zeta) = J_0 \mathcal{J}_0(\zeta)$ is the renormalised hopping parameter and \mathcal{J}_0 is the 0-th order Bessel function of the first kind.

The leading Ω^{-1} -corrections represent an additional second-nearest-neighbour hopping term, and an extra static potential, which is periodic for any rational Φ/π . To order Ω^{-1} the stroboscopic and effective Hamiltonians are qualitatively the same but the values of the renormalised parameters are different. The coupling constants for the Floquet-Magnus correction $\mathcal{C}_{m,m+2}(\zeta)$ and $\mathcal{G}_{m,m+1}(\zeta)$ are given in Appendix C.1.1, while the ones for the van Vleck correction are denoted by tilde and are given in Appendix C.2.1. Higher-order corrections in the inverse frequency appear as longer-range hopping terms, and modifica-

tions to the static potential. The leading correction to the kick operator $K_{\text{eff}}^{\text{rot}}(t)$ can be obtained using Eq. (2.46).

Next we discuss the dressed operators emerging in FNS evolution, i.e. the operators describing observables averaged over fast oscillations, c.f. Sec. 2.1.4. Two natural observables are the local density operator on site m and the local current operator flowing from site m to site $m+1$:

$$\begin{aligned} n_m &= a_m^\dagger a_m, \\ j_{m,m+1} &= -iJ_0(a_{m+1}^\dagger a_m - a_m^\dagger a_{m+1}). \end{aligned} \quad (3.61)$$

The transformation to the rotating frame leaves the density operator (commuting with the driving term) invariant, while the current operator (which does not commute with the driving H_1) changes in the same way as the hopping term in the Hamiltonian. As we mentioned in Sec. 2.2.5, it is convenient to study the finite-frequency corrections to the dressed observables in the rotating frame. One then finds

$$\begin{aligned} n_m^{\text{rot}}(t) &= a_m^\dagger a_m = n_m^{\text{lab}}, \\ j_{m,m+1}^{\text{rot}}(t) &= J_0 \left(-ig^{m,m+1}(t)a_{m+1}^\dagger a_m + \text{h.c.} \right), \end{aligned} \quad (3.62)$$

Applying Eq. (2.58) leads to the following infinite-frequency behaviour of the dressed operators in the FM (stroboscopic) and the vV picture:

$$\begin{aligned} \bar{n}_{\text{eff},m}^{(0)} &= \bar{n}_{F,m}^{(0)} = n_m, \\ \bar{j}_{\text{eff},m,m+1}^{(0)} &= \bar{j}_{F,m,m+1}^{(0)} = J_{\text{eff}}(\zeta)(-ia_{m+1}^\dagger a_m + \text{h.c.}) \end{aligned} \quad (3.63)$$

As in the Kapitza case the difference between the stroboscopic and non-stroboscopic pictures appears in the structure of the subleading Ω^{-1} corrections to these observables. On one hand, the observables \mathcal{O} which remain invariant under the transformation to the

rotating frame $V(t)$ do not get dressed in the infinite-frequency limit, i.e. $\overline{\mathcal{O}}^{(0)} = \mathcal{O}$. Furthermore, these observables do not possess Ω^{-1} -corrections in the vV (non-stroboscopic) picture (though they do have Ω^{-1} -corrections in the stroboscopic picture). On the other hand, all observables which are not invariant with respect to the transformation to the rotating frame get dressed even in the infinite-frequency limit. In agreement with our general results (see Eq. (2.35)) the dressed current operator is precisely the current operator associated with the Floquet Hamiltonian. In other words, the dressed current describes the slow charge dynamics with respect to H_F . Such a dressed chiral current was successfully measured in a recent cold-atom experiment realising the Harper-Hofstadter model in a ladder geometry [54]. The Ω^{-1} -corrections to the dressed operators can be calculated with the help of the general expression, Eq. (2.58). Since they are quite lengthy, we shall not show them explicitly. Physically the corrections are responsible for delocalisation of the corresponding dressed operators, meaning that the operator support on the lattice grows as Ω deviates from infinity. For example, the corrections to the dressed density involve terms which involve hopping between neighbouring sites, etc.

Next we compute the dressed density matrices. We consider two natural initial states in which the particle is either localised in position space or in momentum space, corresponding to the bare density matrices:

$$\rho_m = |m\rangle\langle m|, \quad \rho_k = |k\rangle\langle k|. \quad (3.64)$$

We shall distinguish between the two density operators by the subindex m or k . In the rotating frame, the two operators transform to

$$\begin{aligned} \rho_m^{\text{rot}}(t) &= |m\rangle\langle m|, \\ \rho_k^{\text{rot}}(t) &= \frac{1}{N_s} \sum_{mn} e^{ik(m-n)} e^{-i\zeta \sin \frac{\Phi(m-n)}{2} \sin(\Omega t - \Phi \frac{m+n-1}{2})} |m\rangle\langle n|. \end{aligned} \quad (3.65)$$

Here N_s is the number of lattice sites. In the infinite-frequency limit, averaging over the

time t leads to

$$\begin{aligned}\bar{\rho}_{\text{eff},m}^{(0)} &= |m\rangle\langle m|, \\ \bar{\rho}_{\text{eff},k}^{(0)} &= \frac{1}{N_s} \sum_{mn} e^{ik(m-n)} \mathcal{J}_0\left(\zeta \sin \frac{\Phi(m-n)}{2}\right) |m\rangle\langle n|.\end{aligned}\quad (3.66)$$

As expected, the Fock-state density matrix, which commutes with the driving protocol, is not modified in the infinite-frequency limit and hence it still represents a pure state. On the contrary, the momentum-state density matrix gets dressed. In momentum space, this density matrix remains diagonal:

$$\bar{\rho}_{\text{eff},k}^{(0)} = \sum_q \sum_{l=-\infty}^{\infty} e^{i(k-q)l} \mathcal{J}_0\left(\zeta \sin \frac{l\Phi}{2}\right) |q\rangle\langle q|.\quad (3.67)$$

and it represents a mixed state. We mention in passing that finite-frequency corrections to the density matrices result in a mixed state even for a pure Fock-state.

3.1.3.2.1 Experimental Observation of Dynamical Localisation in Cold Atom Systems

Let us briefly describe some recent experimental setups where the renormalisation of the hopping amplitude, $J_0 \rightarrow J_0 \mathcal{J}_0(\zeta)$, has been measured. For example, in Refs. [43, 156] the dynamical localisation of a strongly driven chain of ^{87}Rb atoms was observed. First, the atoms are cooled down to form a Bose-Einstein condensate (BEC). With the help of acousto-optical modulators, the 1D optical lattice is moved back and forth, c.f. Fig. 3.4, creating a periodic net force of the form $V_0 \sum_m m \cos \Omega t n_m$ on the atoms in the wells (recall that V_0 has to scale with the frequency, i.e. $V_0 = \zeta \Omega$). According to the predictions of Floquet theory, the system is expected to exhibit dynamical localisation [46, 157] when the effective hopping approaches zero. This can be achieved by tuning to one of the zeros of the Bessel function [the first zero occurring at $\zeta \approx 2.4$, c.f. Eqs. (3.59) and (3.60)]. The tunneling can be measured experimentally by turning down the confining potential

along the lattice direction and allowing the atom cloud to expand in the lattice [47] as it is shown in the left panel of Fig. 3.5 taken from Ref. [140]. The right panel in this figure shows an image of the cloud taken with a CCD camera from a similar experiment [158]. From this image one can extract the in situ width of the atom cloud after the expansion. It is evident that the expansion is very slow near the zero of the Bessel function (plot c) indicating dynamical localisation. The resulting data showed an excellent agreement with the theoretical predictions.

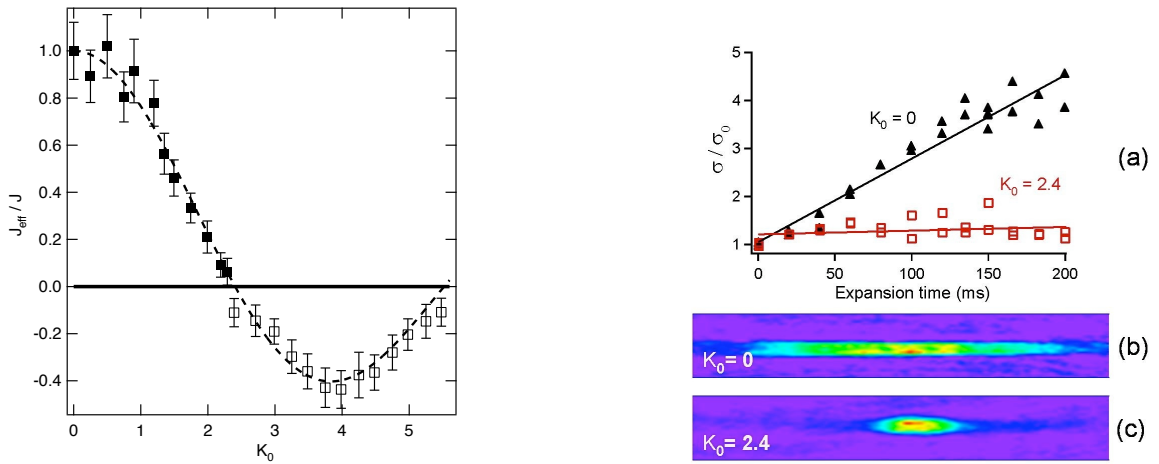


Figure 3.5: Left panel (taken from Ref. [140]). Reproduced by permission of World Scientific. Observation of dynamical localisation with cold atoms. The magnitude of the effective tunnelling coupling J_{eff} is extracted from an in situ image, while the relative sign is determined through the interference pattern using a TOF image. Right panel (taken from Ref. [158]). Reproduced by permission of Springer. In situ images reveal the change in the condensate width σ during free expansion of a BEC in an optical lattice. (a) Normalised expansion width σ/σ_0 of the atomic cloud versus expansion time for $K_0 = 0$ (black triangles) and $K_0 = 2.4$ (red squares). (b) CCD in situ images of the condensate cloud for $K_0 = 0$ and $K_0 = 2.4$. The parameters on the figure are related to those in the main text by $J = J_0$, $K_0 = \zeta$ and $J_{\text{eff}} = J_0 \mathcal{J}_0(\zeta)$. For more details, see Refs. [43, 46, 47, 139, 140, 155, 158].

To investigate the coherence of the BEC in the driven system, both the confining potential and the lattice beams are switched off. The atom cloud undergoes a free fall, and the degree of phase coherence is determined from the visibility of the interference pattern after time-of-flight imaging. It was shown that the system starts losing its coherent

behaviour when the effective hopping approaches zero. Phase coherence is restored soon after passing through the zero of the Bessel function when the effective hopping changes sign.

In the same experiments, the authors also investigated closely the regions of parameter space of the shaken Bose-Hubbard model which correspond to dynamical localisation [46, 139, 158]. There they found loss of coherence and attributed this to the Mott-insulator-to-superfluid transition. By performing time-of-flight measurements, the momentum distribution of the atom cloud was mapped out for different values of the driving amplitude. Far away from the zeros of the Bessel function, where the hopping is expected to be large compared to the atom-atom interactions, the experiments found a momentum distribution with well-defined peaks at quasimomentum $q = 0$, indicating that the system is in the phase-coherent superfluid state. However, when the value of the driving amplitude is tuned to the zero of the Bessel function the visibility in the corresponding interference pattern is reduced drastically. The atoms lose phase coherence and the system is believed to enter the Mott insulating phase. Past the zero of the Bessel function, the hopping amplitude changes sign, since the Bessel function becomes negative, and the lowest Bloch band gets inverted. In agreement with theory, the position of the momentum peaks in the experiment reappears at quasimomentum $q = \pi$ at the edge of the Brillouin zone and the phase coherence in the system is being restored.

3.1.3.3 Cold Atoms Realisation of the Harper-Hofstadter Hamiltonian

We now extend the model from the previous section adding a second spatial dimension and a magnetic field gradient along this new direction. This setup was first proposed in Refs. [88, 159] for the simulation of the Harper-Hofstadter Hamiltonian with cold atoms and was recently realised experimentally [52, 53, 55, 57]. After giving an overview of the infinite-frequency limit, we discuss the leading Ω^{-1} -corrections using both the Floquet-Magnus and the van Vleck inverse frequency expansions. These corrections, as well as the dressing of the operators, may be important for the existing experimental setups. The

discussion of their effect on the dynamics goes beyond the scope of this thesis but they are discussed in a different work [160].

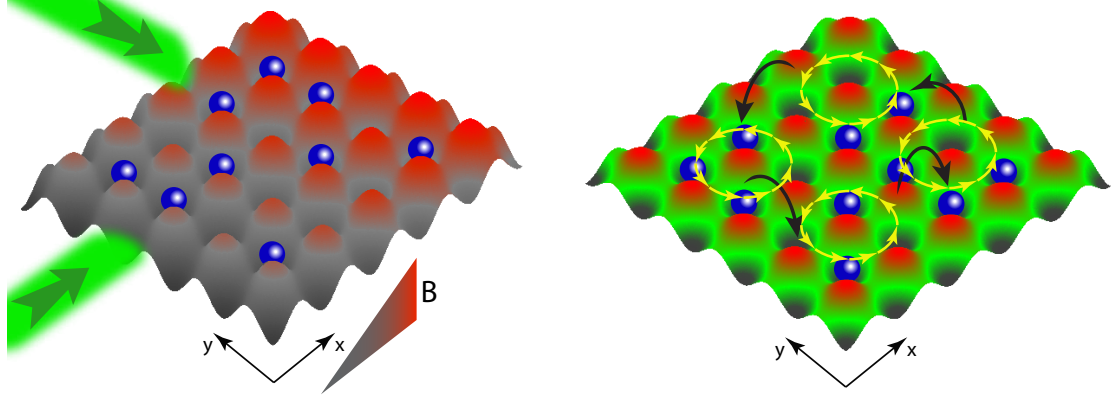


Figure 3.6: The Floquet realisation of the Harper-Hofstadter model. Electrically neutral bosons are loaded in an optical lattice and subject to a Zeeman magnetic field gradient of value Ω , which plays the role of the external potential along the x -direction. In addition, two Raman lasers of resonant frequency Ω , with site-dependent phase lags, create a second running lattice. In the high-frequency limit, when the amplitude of the Raman lasers scales with the frequency, one generates an effective orbital magnetic field, realising the bosonic Harper-Hofstadter Hamiltonian [161, 162]. Figure taken from Ref. [160].

Consider a bosonic system on a square lattice subject to a linear potential along the x -direction and a periodic driving. In two recent experiments, the linear potential was achieved using either a static Zeeman magnetic field gradient [52] or gravity [53]. In both cases this creates a constant force on the system. The periodic driving was realised by using a running (dynamical) optical lattice (c.f. Fig. 3.6). The system is described by the following Hamiltonian:

$$H(t) = H_0 + H_1(t), \quad (3.68)$$

where

$$\begin{aligned} H_0 = & - \sum_{m,n} \left[J_x \left(a_{m+1,n}^\dagger a_{mn} + \text{h.c.} \right) + J_y \left(a_{m,n+1}^\dagger a_{mn} + \text{h.c.} \right) \right] \\ & + \frac{U}{2} \sum_{m,n} n_{mn} (n_{mn} - 1), \end{aligned}$$

$$H_1(t) = \Omega \sum_{m,n} \left[\frac{\zeta}{2} \sin \left(\Omega t - \phi_{mn} + \frac{\Phi_{\square}}{2} \right) + \Omega m \right] n_{mn}. \quad (3.69)$$

Here J_x and J_y denote the hopping amplitude, and $V_0 = \Omega\zeta$ is the strength of the dynamical (running) lattice which, as in the previous example, should scale linearly with the driving frequency. The field gradient along the x -direction is resonant with Ω (see the term $\Omega m n_{mn}$ in H_1). The phase ϕ_{mn} is spatially inhomogeneous $\phi_{mn} = \Phi_{\square}(n + m)$ and makes it impossible to find a global Floquet gauge (i.e. a choice of the initial time of the stroboscopic period) for which the driving is symmetric. Breaking time-reversal symmetry ultimately allows for a synthetic static magnetic field to appear in the infinite-frequency Floquet Hamiltonian.

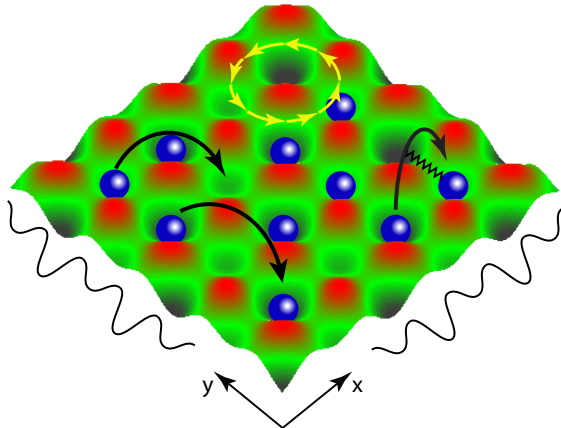


Figure 3.7: The leading corrections in Ω^{-1} to the Harper-Hofstadter Hamiltonian: second-neighbour hopping including along the diagonal (solid black lines), interaction-dependent hopping (solid black lines connected to zig-zag lines) and a site-dependent chemical potential (indicated by the thin black lines on the side and the green colour gradient). The interaction dependent hopping does not influence the Floquet spectrum to order Ω^{-1} but is important for the correct description of the stroboscopic evolution. In the effective Floquet picture these terms show up the in kick operator instead (see main text).

Upon applying a transformation to the rotating frame [53], the Hamiltonian takes the form

$$H^{\text{rot}}(t) = W(t) + W^{\dagger}(t) + H_{\text{int}}, \quad (3.70)$$

where

$$W(t) = - \sum_{m,n} \left[J_x e^{-i\zeta_\Phi \sin(\Omega t - \phi_{nm}) + i\Omega t} a_{m+1,n}^\dagger a_{mn} + J_y e^{-i\zeta_\Phi \sin(\Omega t - \phi_{nm})} a_{m,n+1}^\dagger a_{mn} \right], \quad (3.71)$$

and $\zeta_\Phi = \zeta \sin(\Phi_\square/2)$. To zeroth order, the Floquet Hamiltonian coincides with the effective Hamiltonian and it is obtained by averaging Eq. (3.70) over a period:

$$\begin{aligned} H_F^{(0)} = H_{\text{eff}}^{(0)} &= -K \sum_{m,n} \left(e^{i\phi_{mn}} a_{m+1,n}^\dagger a_{mn} + \text{h.c.} \right) - J \sum_{m,n} \left(a_{m,n+1}^\dagger a_{mn} + \text{h.c.} \right) \\ &\quad + \frac{U}{2} \sum_{m,n} n_{mn} (n_{mn} - 1). \end{aligned} \quad (3.72)$$

The effective hoppings are given by $K = J_x \mathcal{J}_1(\zeta_\Phi)$, $J = J_y \mathcal{J}_0(\zeta_\Phi)$, and \mathcal{J}_ν is the ν -th Bessel function. The next order in the FM expansion delivers the leading finite-frequency corrections to the stroboscopic Floquet Hamiltonian:

$$\begin{aligned} H_F^{(1)}[0] = & - \sum_{m,n} \left(\frac{J_x^2}{\Omega} \rightarrow C_{m,m+2}^n(\zeta_\Phi) a_{m+2,n}^\dagger a_{mn} + \frac{J_y^2}{\Omega} \uparrow C_m^{n,n+2}(\zeta_\Phi) a_{m,n+2}^\dagger a_{mn} + \text{h.c.} \right) \\ & - \sum_{m,n} \left(\frac{J_x J_y}{\Omega} \nearrow D_{m,m+1}^{n,n+1}(\zeta_\Phi) a_{m+1,n+1}^\dagger a_{mn} + \frac{J_x J_y}{\Omega} \nwarrow D_{m,m-1}^{n,n+1}(\zeta_\Phi) a_{m-1,n+1}^\dagger a_{mn} + \text{h.c.} \right) \\ & + \sum_{m,n} \left(\frac{J_x^2}{\Omega} \rightarrow E_{m,m+1}^n(\zeta_\Phi) (n_{mn} - n_{m+1,n}) + \frac{J_y^2}{\Omega} \uparrow E_m^{n,n+1}(\zeta_\Phi) (n_{mn} - n_{m,n+1}) \right) \\ & - \sum_{m,n} \left(\frac{J_x U}{\Omega} \rightarrow B_{m,m+1}^n(\zeta_\Phi) a_{m+1,n}^\dagger a_{mn} (n_{mn} - n_{m+1,n} + 1) \right. \\ & \quad \left. + \frac{J_y U}{\Omega} \uparrow B_m^{n,n+1}(\zeta_\Phi) a_{m,n+1}^\dagger a_{mn} (n_{mn} - n_{m,n+1} + 1) + \text{h.c.} \right). \end{aligned} \quad (3.73)$$

The arrows on the corresponding hopping coefficient indicate the direction of the hopping. The complex-valued functions $B(\zeta_\Phi)$, $C(\zeta_\Phi)$, $D(\zeta_\Phi)$ and $E(\zeta_\Phi)$ are defined on the bonds of the lattice. They are obtained from the time-ordered integrals in the FM expansion, and are given in Appendix C.1.2. We see that, when we include the Ω^{-1} -corrections,

the Floquet Hamiltonian becomes quite complicated. These corrections introduce effective static potentials (periodic for rational Φ_{\square}/π) along both directions of the lattice, second-nearest-neighbour hopping both across the diagonals and along the lattice directions, and interaction-dependent hopping (see Fig. 3.7). The consequences of these corrections for the single-particle dynamics, as well as the dressing of the density matrix and observables, were discussed in Ref. [160].

Similarly, the Ω^{-1} -corrections to the effective Hamiltonian are obtained from the first order van Vleck expansion:

$$\begin{aligned}
H_{\text{eff}}^{(1)} = & - \sum_{m,n} \left(\frac{J_x^2}{\Omega} \rightarrow \tilde{C}_{m,m+2}^n(\zeta_{\Phi}) a_{m+2,n}^\dagger a_{mn} + \frac{J_y^2}{\Omega} \uparrow \tilde{C}_m^{n,n+2}(\zeta_{\Phi}) a_{m,n+2}^\dagger a_{mn} + \text{h.c.} \right) \\
& - \sum_{m,n} \left(\frac{J_x J_y}{\Omega} \nearrow \tilde{D}_{m,m+1}^{n,n+1}(\zeta_{\Phi}) a_{m+1,n+1}^\dagger a_{mn} + \frac{J_x J_y}{\Omega} \nwarrow \tilde{D}_{m,m-1}^{n,n+1}(\zeta_{\Phi}) a_{m-1,n+1}^\dagger a_{mn} + \text{h.c.} \right) \\
& + \sum_{m,n} \left(\frac{J_x^2}{\Omega} \rightarrow \tilde{E}_{m,m+1}^n(\zeta_{\Phi}) (n_{m,n} - n_{m+1,n}) + \frac{J_y^2}{\Omega} \uparrow \tilde{E}_m^{n,n+1}(\zeta_{\Phi}) (n_{mn} - n_{m,n+1}) \right). \quad (3.74)
\end{aligned}$$

The effective Hamiltonian is similar to the stroboscopic Hamiltonian. However, the coefficients defining the renormalised parameters in the effective Hamiltonian are, in general, different from those for the stroboscopic Hamiltonian, and are denoted by a tilde. They are defined in Appendix C.2.2 and are Floquet-gauge invariant, i.e. do not depend on the phase of the drive.

The main qualitative difference between the stroboscopic and effective expansions is the absence of interaction-dependent hopping terms in $H_{\text{eff}}^{(1)}$ which are instead present in $H_F^{(1)}[0]$. This means that those terms modify the Floquet spectrum (and all other invariants under a change of basis) at the order Ω^{-2} , i.e. beyond the validity of the current approximation. In the van Vleck picture these terms appear in the kick operator affecting the initial density matrix and observables to the order Ω^{-1} . In particular,

$$K_{\text{eff}}^{\text{rot},(1)}(t) = \sum_{m,n} \left[J_x \kappa_x(t) a_{m+1,n}^\dagger a_{mn} + J_y \kappa_y(t) a_{m,n+1}^\dagger a_{mn} + \text{h.c.} \right],$$

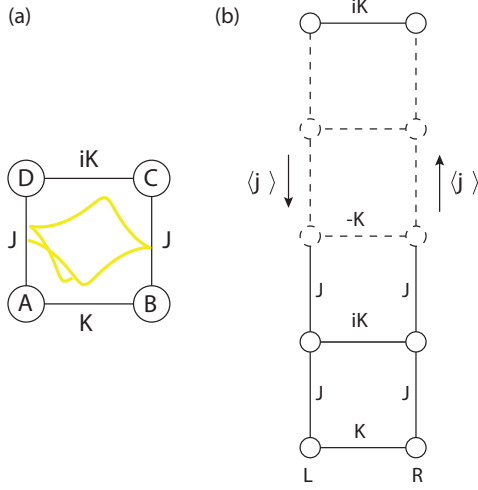


Figure 3.8: (a) The plaquette geometry used to study the quantum cyclotron orbits (yellow) in the Harper-Hofstadter Hamiltonian. (b) The ladder geometry with the chiral currents used to study the transition between the vortex and the Meissner phases. Figure taken from Ref. [160].

$$K_F^{\text{rot},(1)}[0](t) = \sum_{m,n} \left[J_x [\kappa_x(t) - \kappa_x(0)] a_{m+1,n}^\dagger a_{mn} + J_y [\kappa_y(t) - \kappa_y(0)] a_{m,n+1}^\dagger a_{mn} + \text{h.c.} \right], \quad (3.75)$$

where

$$\begin{aligned} \kappa_x(t) &= -\frac{1}{2} \int_t^{T+t} dt' \left[\left(1 - 2 \frac{t-t'}{T} \right) \bmod T \right] e^{-i\zeta_\Phi \sin(\Omega t' - \phi_{nm}) + i\Omega t'}, \\ \kappa_y(t) &= -\frac{1}{2} \int_t^{T+t} dt' \left[\left(1 - 2 \frac{t-t'}{T} \right) \bmod T \right] e^{-i\zeta_\Phi \sin(\Omega t' - \phi_{nm})}. \end{aligned}$$

Applying Eq. (2.47) in the rotating frame, we have

$$H_F^{(1)}[0] = H_{\text{eff}}^{(1)} - i \left[K_{\text{eff}}^{\text{rot},(1)}(0), H_{\text{eff}}^{(0)} \right].$$

Therefore, whenever one chooses to work in the van Vleck picture, the interaction-dependent hopping terms are implicitly contained in the kick operator $K_{\text{eff}}(0)$.

Before we close the discussion on the theoretical Floquet realisation of the Harper-

Hofstadter model, we mention that a different method of engineering artificial gauge fields using a high-frequency periodic perturbation was proposed in Ref. [163] (but see also Ref. [164]), based on an oscillating field gradient, where $H_1(t) = \sum_{mn} m(\Omega + V_0 \cos \Omega t) n_{mn}$. Moreover, in Ref. [85] the flow-equation method, which is an alternative to the Floquet-Magnus expansion, has been used to compute the finite-frequency corrections to the Floquet Hamiltonian. As expected, this method reproduces the same results as the FM expansion. Recently, the stability [165–167] of a related Bose-Hubbard model under a periodic driving, and scattering properties of periodically-driven lattice systems [168, 169] have been studied too.

3.1.3.3.1 Experimental Realisation of the Harper-Hofstadter Model

As we alluded to above, the Harper-Hofstadter Model has been realised experimentally using cold atoms in optical lattices [52–55, 57]. First, Rb atoms are cooled down to form a BEC and loaded in a 2D optical lattice. Then a field gradient is applied along the x -direction, such that tunnelling along the x -direction is suppressed. The latter is then restored by a running lattice, which consists of two additional laser beams which interfere at an angle with respect to one another, c.f. Fig. 3.6. The resulting running lattice leads to a periodic on-site modulation with a site-dependent phase. The frequency of the running lattice is chosen to match the magnetic field gradient, realising the Hamiltonian (3.69) with $\Phi_{\square} = \pi/2$. This flux can be controlled by the angle between the running lattice beams. In the infinite-frequency limit, the flux is equivalent to a very strong static magnetic field (see Eq. (3.72)).

In the experiment of Ref. [52] the authors additionally introduced a static superlattice potential, which effectively divided the 2D lattice in 2×2 plaquettes (see Fig. 3.8a), and completely suppressed the tunnelling among different plaquettes. Then they studied the analogue of the classical cyclotron orbit and found a good agreement with the predictions of the effective Hamiltonian (3.72). In another experiment [54], the superlattice was switched only along the x -direction, such that the 2D lattice was divided into many

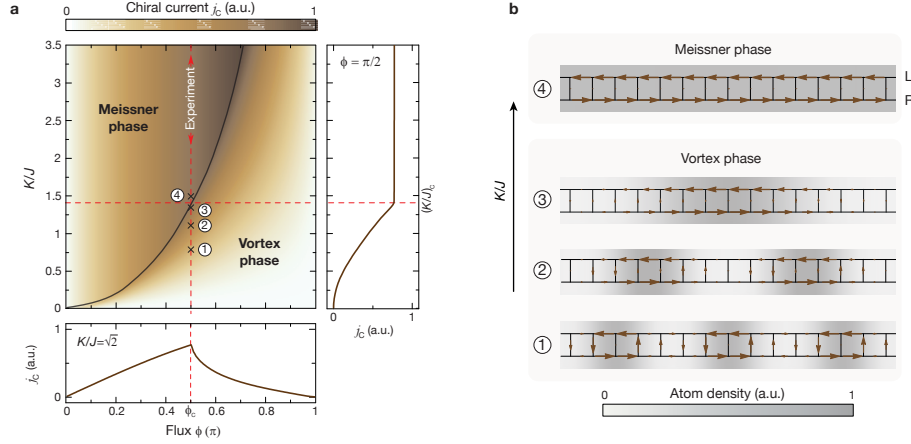


Figure 3.9: (a) Phase diagram of the Harper-Hofstadter model on a ladder in $(K/J, \phi)$ -space. The insets show the chiral current j_c as a function of the ratio of the effective hoppings K/J and the flux per plaquette ϕ . (b) Pictorial representation of the Meissner and vortex phases for several values of the ratio K/J . The parameters are related to those in the main text by $\phi = \Phi_D$. Reprinted by permission from Macmillan Publishers Ltd: [Nature Physics] ([54]), copyright (2014).

ladders along the y -axis, c.f. Fig. 3.8b, and the tunneling between different ladders was completely suppressed. The atoms in the ground state of the system move along the edges of the ladders in the form of chiral currents. Depending on the ratio between the effective hopping parameters in the x - and y -directions, a phase transition between a vortex phase and a Meissner phase was found at which the chiral current undergoes a cusp singularity. For the flux $\Phi_D = \pi/2$ this transition occurs at the critical ratio $(K/J)_c = \sqrt{2}$ (recall that K and J are the effective hopping along the x and y directions, c.f. Eq. (3.72)). For $K/J < (K/J)_c$ (vortex phase) the current increases and the vortex density decreases with K until it hits zero (in the thermodynamic limit) at the critical ratio. For $K/J > (K/J)_c$ (Meissner phase) the current at a fixed value of J is independent of K , see Fig. 3.9. Effectively the authors performed an FNS measurement of the current by projecting the system into an array of decoupled double wells along the horizontal direction. Then they fit the Josephson density oscillations in a double well to a simple formula with the chiral current entering through the initial (i.e. pre-quench) conditions (see Ref. [54] for details).

In a follow-up experiment, the realisation of the Harper-Hofstadter model has been

optimised. The field gradient has been replaced by a superlattice, and the running lattice has been modified accordingly [57]. This phase rectification scheme allowed to measure the Chern number of the lowest band by detecting the differential drift of the atom cloud in momentum space, which arises due to the Berry curvature of the band [170]. The Chern number was measured to be close to unity with excellent precision. This most recent experiment also took into account the relevant first order corrections to the time-averaged Hamiltonian.

3.1.3.4 The Periodically Driven Fermi-Hubbard Model: Floquet Topological Insulators

In this section, we analyse a spinful fermionic system on a bipartite lattice driven by a periodic external field which couples to the atomic density. First, we shall describe the setup in general, and later on we restrict our attention to the case of graphene subject to a circularly polarised electric field.

Let z be the lattice coordination number, and let A denote the set of all points in the sublattice A , which we label by the vector \mathbf{r} . Let us also define the vectors \mathbf{s}_j ($j = 1, \dots, z$) to connect a fixed point on the sublattice A to all its adjacent neighbours on the sublattice B . The vectors \mathbf{s}_j point from A to B (c.f. Fig. 3.10a). To simplify the notation we skip the bold notation for vectors in the subscripts of operators.

The system is thus described by the Hamiltonian

$$\begin{aligned}
H(t) &= H_0 + H_1(t) \\
H_1(t) &= \Omega \frac{\zeta}{z} \sum_{r \in A} \sum_{j=1}^z \sum_{\sigma} \left(f_r(t) n_{r,\sigma}^a + f_{r+s_j}(t) n_{r+s_j,\sigma}^b \right) \\
H_0 &= H_{\text{kin}} + H_{\text{int}}, \\
H_{\text{kin}} &= -J_0 \sum_{r \in A} \sum_{j=1}^z \sum_{\sigma} \left(a_{r,\sigma}^{\dagger} b_{r+s_j,\sigma} + \text{h.c.} \right) \\
H_{\text{int}} &= \frac{U}{2z} \sum_{r \in A} \sum_{j=1}^z \sum_{\sigma} \left(n_{r,\sigma}^a n_{r,\bar{\sigma}}^a + n_{r+s_j,\sigma}^b n_{r+s_j,\bar{\sigma}}^b \right)
\end{aligned}$$

$$+U' \sum_{r \in A} \sum_{j=1}^z \sum_{\sigma, \sigma'} n_{r, \sigma}^a n_{r+s_j, \sigma'}^b. \quad (3.76)$$

where $\sigma = \uparrow, \downarrow$ indicates the spin with the convention $\bar{\uparrow} = \downarrow$ and $\bar{\downarrow} = \uparrow$. The factors $1/z$ are introduced to avoid over-counting. The operators $a_{r, \sigma}^\dagger$ and $b_{r+s_j, \sigma}^\dagger$ create a fermion of spin σ on sublattices A and B , respectively. In the Hamiltonian, $n_{r, \sigma}^a = a_{r, \sigma}^\dagger a_{r, \sigma}$ and $n_{r+s_j, \sigma}^b = b_{r+s_j, \sigma}^\dagger b_{r+s_j, \sigma}$ denote the number operators on sublattices A and B . The bare tight-binding hopping is J_0 , the on-site interaction strength which couples fermions of opposite spin is U , while the next-nearest neighbour interaction is U' . The driving protocol $f_j(t) = f_j(t + T)$ is periodic and site-dependent. The driving potential has the amplitude $V_0 = \Omega \zeta$.

In the rotating frame the Hamiltonian reads:

$$\begin{aligned} H^{\text{rot}}(t) &= W(t) + W^\dagger(t) + H_{\text{int}}, \\ W(t) &= -J_0 \sum_{r \in A, \sigma} \sum_{j=1}^z \lambda_j(t) a_{r, \sigma}^\dagger b_{r+s_j, \sigma} \\ \lambda_j(t) &= \exp \left(i\zeta \Omega \int_{t_0}^t dt' (f_{r+s_j}(t') - f_r(t')) \right). \end{aligned} \quad (3.77)$$

To zeroth order in the inverse-frequency expansion, the Floquet Hamiltonian is given by the time-average of the above Hamiltonian (similarly to the bosonic case described in Sec. 3.1.3.3):

$$H_F^{(0)} = H_{\text{eff}}^{(0)} = \overline{W(t)} + \overline{W^\dagger(t)} + H_{\text{int}}. \quad (3.78)$$

It has the same form of Eq. (3.77) but with renormalised hopping parameters. The leading Ω^{-1} -corrections to the Floquet-Magnus Hamiltonian in the Floquet gauge $t_0 = 0$ are given by

$$H_F^{(1)}[0] = \frac{J_0^2}{\Omega} \sum_{r \in A} \sum_{j=1}^z \sum_{\sigma} \left[F_{jj}(\zeta) \left(n_{r\sigma}^a - n_{r+s_j, \sigma}^b \right) \right] \quad (3.79)$$

$$\begin{aligned}
& + \frac{J_0^2}{\Omega} \sum_{r \in A} \sum_{\sigma} \sum_{j>k=1}^z \left[F_{jk}(\zeta) \left(a_{r\sigma}^\dagger a_{r+s_j-s_k,\sigma} - b_{r+s_k}^\dagger b_{r+s_j} \right) + \text{h.c.} \right] \\
& + \frac{J_0 U}{2\Omega} \sum_{r \in A} \sum_{j=1}^z \sum_{\sigma} \left[G_j(\zeta) \left(n_{r\sigma}^a - n_{r+s_j,\sigma}^b \right) a_{r\bar{\sigma}}^\dagger b_{r+s_j,\bar{\sigma}} + \text{h.c.} \right] \\
& - \frac{J_0 U'}{\Omega} \sum_{r \in A} \sum_{j,k=1}^z \sum_{\sigma,\sigma'} \left[G_j(\zeta) \left(n_{r+s_j-s_k,\sigma}^a a_{r\sigma'}^\dagger b_{r+s_j,\sigma'} - a_{r\sigma'}^\dagger b_{r+s_j,\sigma'} n_{r+s_k,\sigma}^b \right) + \text{h.c.} \right],
\end{aligned}$$

where $\zeta = V_0/\Omega$ is the ratio of the driving amplitude and the driving frequency. The stroboscopic kick operator is given by

$$\begin{aligned}
K_F^{\text{rot},(1)}[0](t) &= J_0 \sum_{r \in A, \sigma} \sum_{j=1}^z [\kappa_j(t) - \kappa_j(0)] a_{r,\sigma}^\dagger b_{r+s_j,\sigma} + \text{h.c.}, \\
\kappa_j(t) &= -\frac{1}{2} \int_t^{T+t} dt' \left[\left(1 - 2\frac{t-t'}{T} \right) \bmod T \right] \lambda_j(t').
\end{aligned} \tag{3.80}$$

For comparison, we also show the leading Ω^{-1} -corrections to the effective van Vleck Hamiltonian:

$$\begin{aligned}
H_{\text{eff}}^{(1)} &= \frac{J_0^2}{\Omega} \sum_{r \in A} \sum_{j=1}^z \sum_{\sigma} \left[\tilde{F}_{jj}(\zeta) \left(n_{r\sigma}^a - n_{r+s_j,\sigma}^b \right) \right] \\
&+ \frac{J_0^2}{\Omega} \sum_{r \in A} \sum_{\sigma} \sum_{j>k=1}^z \left[\tilde{F}_{jk}(\zeta) \left(a_{r\sigma}^\dagger a_{r+s_j-s_k,\sigma} - b_{r+s_k}^\dagger b_{r+s_j} \right) + \text{h.c.} \right], \\
K_{\text{eff}}^{\text{rot},(1)}(t) &= J_0 \sum_{r \in A, \sigma} \sum_{j=1}^z \kappa_j(t) a_{r,\sigma}^\dagger b_{r+s_j,\sigma} + \text{h.c.}
\end{aligned} \tag{3.81}$$

One readily sees that the first-order correction to both the stroboscopic and effective Hamiltonian contains a static potential and next-nearest-neighbour (nnn) hopping. These nnn hopping terms in $H_F^{(1)}[0]$, in general, have a Floquet-gauge dependent magnitude and direction while the hopping elements of $H_{\text{eff}}^{(1)}$ are Floquet-gauge invariant. Furthermore to order Ω^{-1} , interaction-dependent hopping terms enter the stroboscopic Floquet Hamiltonian, but not the effective Hamiltonian. Similarly to the Harper-Hofstadter model discussed in the previous section, the interaction-dependent hopping in the van Vleck picture is encoded

in the operator $K_{\text{eff}}^{\text{rot}}$, via the relation $H_F^{(1)}[0] = H_{\text{eff}}^{(1)} - i \left[K_{\text{eff}}^{\text{rot},(1)}(0), H_{\text{eff}}^{(0)} \right]$. We note in passing that interaction-dependent hopping terms also appear in the Floquet spectrum of the Fermi-Hubbard model, when one drives the interaction term [151]. In Sec. 3.2.2 we shall show how to re-sum an infinite interaction-dependent hopping subseries.

The effective parameters of the two expansions can be obtained from the following integrals

$$\begin{aligned} F_{jk}[0](\zeta) &= \frac{1}{4\pi i} \int_0^{2\pi} d\tau_1 \int_0^{\tau_1} d\tau_2 [\lambda_j(\tau_1)\lambda_k^*(\tau_2) - (1 \leftrightarrow 2)], \\ G_j[0](\zeta) &= \frac{1}{4\pi i} \int_0^{2\pi} d\tau_1 \int_0^{\tau_1} d\tau_2 [\lambda_j(\tau_1) - \lambda_j(\tau_2)], \\ \tilde{F}_{jk}(\zeta) &= \frac{1}{4\pi i} \int_0^{2\pi} d\tau_1 \int_0^{\tau_1} d\tau_2 \left(1 - \frac{\tau_1 - \tau_2}{\pi}\right) [\lambda_j(\tau_1)\lambda_k^*(\tau_2) - (1 \leftrightarrow 2)], \end{aligned} \quad (3.82)$$

where $\tau_i = \Omega t_i$.

We would like to make a few remarks about a possible overlap of this model, as part of the DK class, with the Dirac class defined in Sec. 3.1.2. The overlap is possible because the lattice models considered here can have relativistic low energy dispersion, e.g. if we consider a graphene-type honeycomb lattice (see below). However, we work in the limit where the amplitude of the driving protocol scales with the driving frequency Ω which is considered to be higher than the single-particle bandwidth. In this limit, the low-energy relativistic description of the spectrum is inadequate. In order to realise the Dirac class in graphene, one has to make sure that all involved energy scales, including the lattice potential, are small compared to the band width, so that only the linear part of the dispersion relation is important. The relation between lattice and continuum models is discussed in detail in App. A.

In Sec. 3.1.2, we also used a symmetry argument to argue that there are no Ω^{-1} -corrections to the infinite-frequency Floquet Hamiltonian in the Dirac class. That argument relied on the linear polarisation of the driving protocol and does not apply to a circularly polarised protocol, where the phase of the driving depends on the direction. Such a protocol

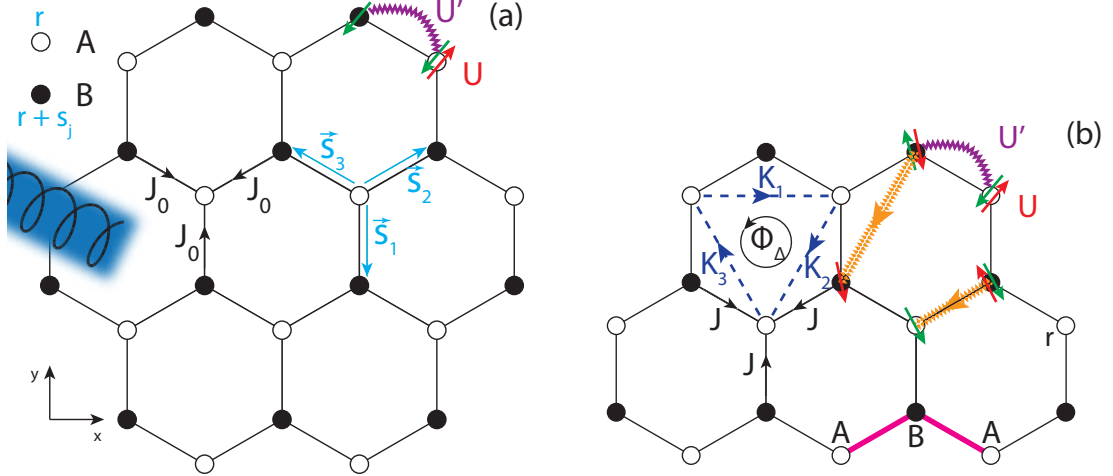


Figure 3.10: Floquet realisation of the Haldane-Fermi-Hubbard Model (see also Refs. [38, 56]). (a) A circularly polarised electric field is shone on a sheet of graphene. The non-driven model includes spinful fermions with hopping matrix elements J_0 , on-site interactions U between spin-up (dark green arrows) and spin-down (dark red arrows) fermions, as well as nn interactions U' (purple full zigzag line) between either spin species. (b) To zeroth order the Floquet Hamiltonian has the same form as the non-driven Hamiltonian but with renormalised parameters. The leading Ω^{-1} -corrections include complex next-nearest-neighbour hopping elements K_j (dashed blue lines), such that the flux through a sublattice is $\Phi_\Delta = -\pi/2$. If the system is interacting, to the same order in perturbation theory, an interaction-dependent hopping is induced (orange lines) in the stroboscopic Floquet Hamiltonian $H_F^{(1)}[0]$. These interaction-dependent hopping terms enter the Floquet spectrum starting from order Ω^{-2} and are, therefore, absent in the effective Floquet Hamiltonian, $H_{\text{eff}}^{(1)}$ (see text). However, in the van Vleck picture the interaction-dependent hopping shows up in the kick operator $K_{\text{eff}}^{\text{rot},(1)}$ (see Eq. (3.81)), and should be included in dressing the observables and the initial density matrix for a correct description of both stroboscopic and non-stroboscopic dynamics.

was suggested to realise a Floquet Chern Insulator [38] and we will briefly discuss it next.

3.1.3.4.1 Circularly Polarised Drive and the Floquet Realisation of Haldane's Model

We now focus on graphene, where two triangular lattices build up the hexagonal structure, and consider the situation in which the driving frequency is higher than the band width. This scheme has been suggested theoretically to induce topological properties in

graphene [38, 66, 171–178], and turn it into a Chern insulator. The topological properties of the quasi-energy spectrum of Floquet systems, in general, depend on the lattice geometry [150]. Moreover, in Refs. [69, 179] it was shown that Floquet Chern insulators with sufficiently strong nearest-neighbour interactions exhibit the phenomenon fractionalisation at fractional fillings. Cold atom experiments managed to realise a fermionic system with topological bands in the laboratory [56]. As in Ref. [38] we consider a circularly polarised electric field. The driving protocol in this case reads as

$$f_r(t) = \mathbf{E}(t) \cdot \mathbf{r}, \quad \mathbf{E}(t) = V_0(\cos \Omega t, \sin \Omega t), \quad (3.83)$$

where, in agreement with the general discussion, the amplitude of the electric fields needs to scale with the driving frequency Ω , that is $V_0 = \zeta \Omega$. For a honeycomb lattice, the unit vectors \mathbf{s}_j point from the sublattice A to B (see Fig. 3.10a):

$$\mathbf{s}_1 = (0, -1), \quad \mathbf{s}_{2,3} = \frac{1}{2}(\pm\sqrt{3}, 1).$$

In the rotating frame, this leads to

$$\lambda_j(t) = \exp(i\mathbf{s}_j \cdot \mathbf{A}(t)), \quad \mathbf{A}(t) = \frac{V_0}{\Omega}(\sin \Omega t, -\cos \Omega t).$$

where $\mathbf{A}(t)$ is the vector potential describing the electric field. One can show that all three renormalised nn hopping amplitudes in $H_F^{(0)}$ and $H_{\text{eff}}^{(0)}$ are real and equal in magnitude. As in the bosonic case, they are given by $J_j = J_0 \mathcal{J}_0(\zeta)$, where $\zeta = V_0/\Omega$ is kept constant in the high-frequency limit and \mathcal{J}_0 is the Bessel function of the first kind. To order Ω^{-1} we find that the site-dependent chemical potential vanishes identically for the circularly polarised drive owing to $\sum_j F_{jj} = 0$, while the next-nearest-neighbour terms are finite and complex. As proposed in Ref. [38] they lead to a topological band structure in the Floquet spectrum. For the case of a circularly polarised drive, we further obtain that the next-nearest-neighbour hopping elements in the van Vleck picture are imaginary and equal in

magnitude (while in the stroboscopic picture they are complex numbers whose magnitude and direction depend on the Floquet gauge), such that they lead to opposite fluxes of $\Phi_\Delta = \mp\pi/2$ penetrating the two sublattices A and B (see Fig. 3.10b). At half-filling, the model realises Haldane's Chern insulator [180], which is the prototypical example of a quantum Hall insulator without an external magnetic field.

3.1.3.4.2 Experimental realisation of Haldane's model

Haldane's model has been realised using ultracold fermionic ^{40}K atoms in a brick-wall (almost hexagonal) optical lattice [56]. A superlattice induced an energy off-set between the two sublattices which resulted in a staggered potential Δ_{AB} . By mechanically shaking the lattice position along the x and y -direction using piezo-electric actuators, the lattice sites were moved on elliptical trajectories which mimic the application of elliptically polarised electric field in the lattice plane, and break time-reversal symmetry. As discussed in the previous paragraphs, this leads to complex-valued nnn hopping terms between sites of the same sublattice. As a result, the Dirac cones open up a topological band gap, which is reflected in the non-zero and opposite Chern numbers of the two lowest bands, see Fig. 3.11, left panel.

In a topologically non-trivial band, atoms moving in the Brillouin zone acquire a Berry phase. This, in turn, results in a force, perpendicular to the direction of movement, pretty much like the Lorentz force acts on a charged particle moving in a real-space region of nonzero *orbital* magnetic field³. By turning on a Zeeman magnetic field gradient which acts as an external potential [170], a constant force is applied on the atoms, leading to Bloch oscillations. Hence, the atoms are brought to explore the region of the Brillouin zone near the two Dirac cones, where the Berry curvature and, therefore, the Lorentz-like force the atoms experience, is the strongest. The experiment measured the motion of the centre of mass in the presence of the topological gap. Reversing the sign of the magnetic field

³Note that an orbital magnetic field leads to cyclotron orbits, while a static magnetic field gradient (a Zeeman field) acts as an external potential and is responsible for the hyperfine splitting of atoms.

gradient flips the sign of the force the atoms feel, and the displacement is experienced in the opposite direction. Subtracting the two drifts from one another defines the differential drift which is proportional to the strength of the Berry curvature near the topological gaps, see Fig. 3.11, right panel.

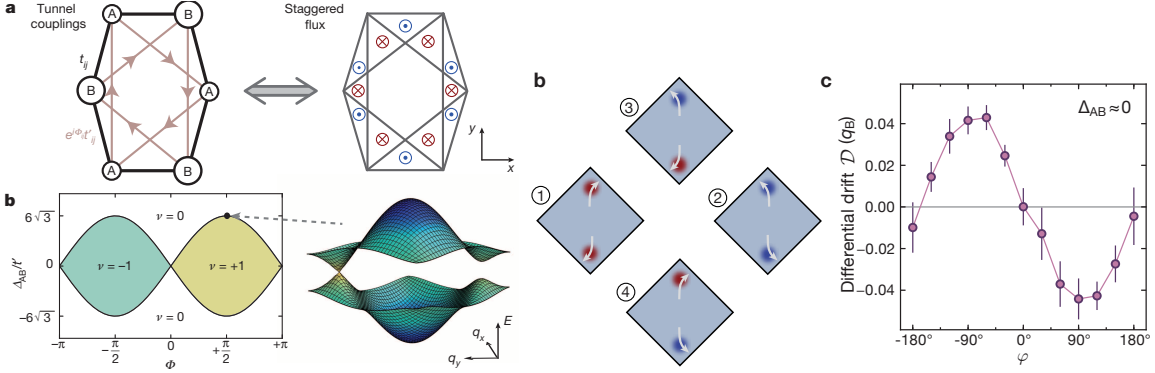


Figure 3.11: Left panel: Cold atom realisation of Haldane's model. (a) The brick-wall lattice unit cell and the dynamically generated staggered flux pattern. (b) Topological phase diagram of Haldane's model and dispersion relation for the brick-wall lattice. Right panel: Differential drift of the fermions in the first Brillouin zone. (b) Pictorial representation of the differential drift near the Dirac cones for fixed parameters. (c) Differential drift vs. sublattice flux ϕ for a near zero staggered potential $\Delta_{AB} \approx 0$ Hz. The parameters are related to those in the main text by $\varphi = \Phi_\Delta$. Reprinted by permission from Macmillan Publishers Ltd: [Nature] ([56]), copyright (2014).

A fraction of the atoms passing near the band gaps undergoes a Landau-Zener transition and transfers to the upper band. The precise band population can be extracted from the integrated column density in the absorption image following a band mapping technique. This provides a confirmation for the existence of the Floquet-engineered dispersion relation of Haldane's model.

In the same experiments, using a Feshbach resonance the authors turned on the interaction between atoms in different hyper-fine states and briefly studied the interacting model. In general, the topological phases of the interacting Fermi-Hubbard model are expected to be strongly susceptible to heating effects. In the experiment conducted in Ref. [56], the authors observed a 25% increase in entropy for the driven interacting system, when compared to the non-driven interacting case. Heating effects in ultracold fermionic systems in

the high-frequency limit [60] are a subject of current experimental and theoretical research, see Chapter 5.

3.1.3.5 Periodically Driven Spin (Hardcore Boson) Systems

As a final model in the DK class, we consider a spin-1/2 system on a lattice of arbitrary dimension, driven by a time-periodic, linearly-polarised external magnetic field. As we discussed in Sec. 2.2 the inverse-frequency expansion works both for quantum and classical systems. So with minor modifications the results of this section apply equally to driven classical spins (i.e. rotor) models. The effect of resonant driving on benchmark properties, such as the Rabi oscillations, was investigated [181]. A topological Floquet spin system was realised in Ref. [182]. Here, we assume that the magnetic field on each lattice site m points along a fixed in time, but site-dependent direction. The magnitude of the magnetic field is allowed to vary from one lattice site to another. In agreement with the discussion in the introduction to the DK class, we assume that the amplitude of the magnetic field scales linearly with the frequency of the drive Ω . The Hamiltonian in the lab frame reads as:

$$H(t) = H_0 + \Omega \sum_m f_m(t) \mathbf{n}_m \cdot \boldsymbol{\sigma}_m, \quad (3.84)$$

where H_0 is time-independent and can include arbitrary spin-spin interactions, $\boldsymbol{\sigma}_m = (\sigma_m^x, \sigma_m^y, \sigma_m^z)$ is the vector of the three Pauli matrices on the m -th site, \mathbf{n}_m is a time-independent unit vector, and $f_m(t)$ is a periodic function with period $T = 2\pi/\Omega$.

In the high-frequency limit, the Floquet Hamiltonian is equal to the time-average of the Hamiltonian in the rotating frame:

$$H^{\text{rot}}(t) = V^\dagger(t) H_0 V(t), \quad (3.85)$$

where

$$V(t) = \exp \left[-i \sum_m \Delta_m(t) \mathbf{n}_m \cdot \boldsymbol{\sigma}_m \right],$$

$$\Delta_m(t) = \Omega \int_{t_0}^t dt' f_m(t').$$

The lower limit in the integral above can be used to change the Floquet gauge when going to the rotating frame. Since spins at different sites commute, the operator $V(t)$ factorizes, and can be written as

$$V(t) = \prod_m V_m(t), \quad V_m(t) = \exp [-i \Delta_m(t) \mathbf{n}_m \cdot \boldsymbol{\sigma}_m],$$

where $V_m(t)$ is the operator rotating the spin at the site m by an angle $\theta_m(t) = 2\Delta_m(t)$ around the direction \mathbf{n}_m . Using Eq.(3.85) it is easy to see that the Hamiltonian in the rotating frame is given by the Hamiltonian H_0 with the substitution $\boldsymbol{\sigma}_m \rightarrow \boldsymbol{\sigma}_m^{\text{rot}}(t) = V_m^\dagger(t) \boldsymbol{\sigma}_m V_m(t)$ or explicitly:

$$\boldsymbol{\sigma}_m \rightarrow \cos \theta_m \boldsymbol{\sigma}_m + \sin \theta_m \mathbf{n}_m \times \boldsymbol{\sigma}_m + (1 - \cos \theta_m) (\mathbf{n}_m \otimes \mathbf{n}_m) \boldsymbol{\sigma}_m, \quad (3.86)$$

where \times and \otimes indicate the vector and tensor product. The entries of the matrix $M_m \equiv \mathbf{n}_m \otimes \mathbf{n}_m$ are defined by $(M_m)_{\alpha\beta} = n_m^\alpha n_m^\beta$.

We now consider two specific examples. First let us assume that:

$$H(t) = H_0 + \alpha \Omega \cos \Omega t \sum_m \sigma_m^z \quad (3.87)$$

$$H_0 = J_0 \sum_{\langle m,n \rangle} (\sigma_m^x \sigma_n^x - \sigma_m^y \sigma_n^y).$$

Here the driving corresponds to a uniform magnetic field along the z -direction, $\mathbf{n}_m = (0, 0, 1)$, with oscillating intensity, $f_m(t) = \alpha \cos \Omega t$, c.f. Fig. 3.12. Using Eqs. (3.85) and (3.86) we find that the Hamiltonian in the rotating frame is obtained from H_0 via the

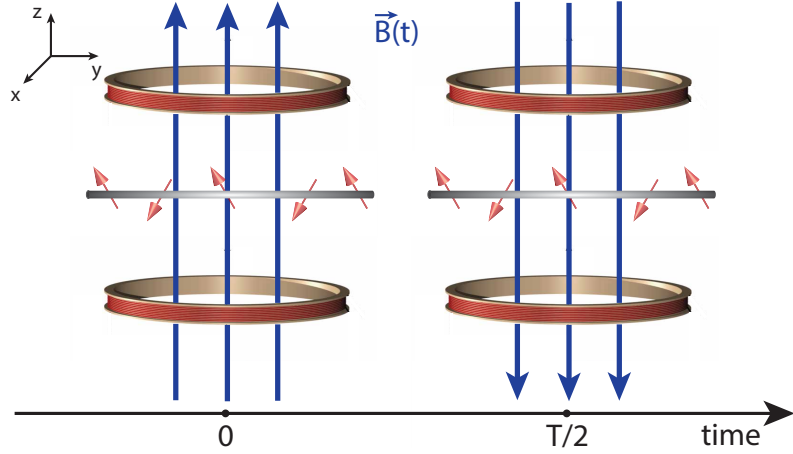


Figure 3.12: The flip-flop model: a periodically modulated, spatially uniform magnetic field $\mathbf{B}(t)$ is applied to a spin chain, c.f. Eq. (3.87).

substitutions:

$$\begin{aligned}
 \sigma_m^x &\longrightarrow \cos \theta(t) \sigma_m^x - \sin \theta(t) \sigma_m^y, \\
 \sigma_m^y &\longrightarrow \cos \theta(t) \sigma_m^y + \sin \theta(t) \sigma_m^x, \\
 \sigma_m^z &\longrightarrow \sigma_m^z,
 \end{aligned} \tag{3.88}$$

where $\theta(t) = 2\Delta(t) = 2\alpha \sin \Omega t$. After some algebra, we arrive at:

$$H^{\text{rot}}(t) = J_0 \sum_{\langle m,n \rangle} \cos(2\theta(t)) (\sigma_m^x \sigma_n^x - \sigma_m^y \sigma_n^y) - \sin(2\theta(t)) (\sigma_m^x \sigma_n^y + \sigma_m^y \sigma_n^x). \tag{3.89}$$

In the infinite-frequency limit, the Floquet Hamiltonian can be calculated as:

$$H_F^{(0)} = H_{\text{eff}}^{(0)} = \frac{1}{T} \int_0^T dt H^{\text{rot}}(t) = \mathcal{J}_0(4\alpha) H_0, \tag{3.90}$$

where \mathcal{J}_0 is the Bessel function of the first kind, and we used the mathematical identities:

$$\frac{1}{T} \int_0^T dt \cos(4\alpha \sin \Omega t) = \mathcal{J}_0(4\alpha), \quad \frac{1}{T} \int_0^T dt \sin(4\alpha \sin \Omega t) = 0.$$

By choosing 4α to coincide with the zero of the Bessel function, periodically driven spin systems can exhibit dynamical freezing [183, 184].

We also derive the leading Ω^{-1} -corrections by computing the next term in the Floquet-Magnus (van Vleck) expansion. We choose to focus on a 1D chain for simplicity:

$$\begin{aligned}
 H_F^{(1)}[0] &= G \frac{J_0^2}{\Omega} \sum_m (\sigma_m^x \sigma_m^z \sigma_{m+1}^y + \sigma_{m-1}^y \sigma_m^z \sigma_{m+1}^x), \\
 H_{\text{eff}}^{(1)} &= \mathbf{0}, \\
 K_F^{\text{rot},(1)}[0](t) &= J_0 \sum_{\langle m,n \rangle} [\kappa_c(t) - \kappa_c(0)] (\sigma_m^x \sigma_n^x - \sigma_m^y \sigma_n^y) - [\kappa_s(t) - \kappa_s(0)] (\sigma_m^x \sigma_n^y + \sigma_m^y \sigma_n^x), \\
 K_{\text{eff}}^{\text{rot},(1)}(t) &= J_0 \sum_{\langle m,n \rangle} \kappa_c(t) (\sigma_m^x \sigma_n^x - \sigma_m^y \sigma_n^y) - \kappa_s(t) (\sigma_m^x \sigma_n^y + \sigma_m^y \sigma_n^x), \tag{3.91}
 \end{aligned}$$

where G , \tilde{G} , $\kappa_c(t)$ and $\kappa_s(t)$ are of order one and given by the expressions:

$$\begin{aligned}
 G &= \frac{1}{\pi} \int_0^{2\pi} d\tau_1 \int_0^{\tau_1} d\tau_2 [\sin(4\alpha \sin(\tau_1)) \cos(4\alpha \sin(\tau_2)) - (\tau_1 \longleftrightarrow \tau_2)], \\
 \kappa_c(t) &= \frac{1}{2} \int_t^{T+t} dt' \left[\left(1 - 2 \frac{t-t'}{T} \right) \bmod T \right] \cos(2\theta(t')), \\
 \kappa_s(t) &= \frac{1}{2} \int_t^{T+t} dt' \left[\left(1 - 2 \frac{t-t'}{T} \right) \bmod T \right] \sin(2\theta(t')). \tag{3.92}
 \end{aligned}$$

We thus see that, in this example, the infinite-frequency limit results in a renormalisation of the spin-spin interactions of the bare Hamiltonian, while the first subleading correction in Ω^{-1} introduces 3-spin interaction terms in the stroboscopic Floquet-Magnus Hamiltonian. In the basis of σ^z , these terms play a role similar to the interaction-dependent hopping in Eqs. (3.73) and (3.80). They induce next-nearest-neighbour spin flip processes, whose amplitude depends on the direction of the spin at the middle-site. The effective van Vleck Floquet Hamiltonian does not contain these terms, since they are encoded in the kick operator $K_{\text{eff}}(t)$ via Eq. (2.47).

Let now us analyse another, slightly more complicated example on a two-dimensional

lattice. The system is driven by a linearly-polarised magnetic field along the z -direction

$$H(t) = H_0 + \alpha \Omega \cos \Omega t \sum_{m,n} m \sigma_{m,n}^z, \quad (3.92)$$

where H_0 is a standard XY -Hamiltonian:

$$H_0 = \sum_{m,n} J_y \left(\sigma_{m,n}^x \sigma_{m,n+1}^x + \sigma_{m,n}^y \sigma_{m,n+1}^y \right) + J_x \left(\sigma_{m,n}^x \sigma_{m+1,n}^x + \sigma_{m,n}^y \sigma_{m+1,n}^y \right) \quad (3.93)$$

and J_x and J_y are the bare coupling along the x and y directions. In analogy with the previous example, we find $\theta_{m,n}(t) = 2\Delta_{m,n}(t) = 2m\alpha \sin \Omega t$. Using the transformation in Eq. (3.88) we arrive at:

$$H^{\text{rot}}(t) = \sum_{m,n} J_y \left(\sigma_{m,n}^x \sigma_{m,n+1}^x + \sigma_{m,n}^y \sigma_{m,n+1}^y \right) + h(t) J_x \left(\sigma_{m,n}^x \sigma_{m+1,n}^x + \sigma_{m,n}^y \sigma_{m+1,n}^y \right), \quad (3.94)$$

where we defined

$$h(t) \equiv \cos(\theta_{m,n}(t) - \theta_{m+1,n}(t)) = \cos(2\alpha \sin \Omega t).$$

Observe that if the magnetic field were uniform, i.e. if there were no magnetic gradients, then $h(t) \equiv 1$ and $H^{\text{rot}}(t) = H_0$. This is not surprising since, in this case, the driving would commute with H_0 . In the infinite-frequency limit, the Floquet Hamiltonian reads:

$$H_F^{(0)} = H_{\text{eff}}^{(0)} = \sum_{m,n} J_y \left(\sigma_{m,n}^x \sigma_{m,n+1}^x + \sigma_{m,n}^y \sigma_{m,n+1}^y \right) + \mathcal{J}_0(2\alpha) J_x \left(\sigma_{m,n}^x \sigma_{m+1,n}^x + \sigma_{m,n}^y \sigma_{m+1,n}^y \right).$$

This expression shows that, for $\Omega \rightarrow \infty$, the coupling strength along the x direction is renormalised, while the one along the y direction is not. By changing the value of α the Bessel function $\mathcal{J}_0(2\alpha)$ can be tuned to zero or even take negative values, in the same

spirit as the original work by Dunlap and Kenkre [41, 42]. This opens up possibilities for studying dimensional crossovers, effectively tuning the spin system between the $1d$ and the $2d$ regimes, and dynamically switching between ferromagnetic and anti-ferromagnetic couplings.

Finally, notice that a close analogue to the Harper-Hofstadter Hamiltonian can be realised for spins by choosing the static Hamiltonian on a two-dimensional lattice as in Eq. (3.93) and the periodic driving:

$$H_1(t) = \Omega \sum_{m,m} f_{m,n}(t) \sigma_{m,n}^z, \quad f_{m,n}(t) = m + \alpha \cos(\Omega t + \phi_{n,m}), \quad (3.95)$$

where $\phi_{m,n} = \Phi_{\square}(n+m)$ (see Sec. 3.1.3.3 for details). The calculation of the dominant and subleading correction to the Floquet Hamiltonian follows closely the steps shown above and in Sec. 3.1.3.3. In the infinite-frequency limit, this leads to complex interaction amplitudes with a flux Φ_{\square} per plaquette. Hence, one can expect to observe nontrivial spin-wave dynamics.

3.1.3.5.1 Cold Atom Experiments with Spins Systems

We now briefly mention some recent experimental realisations of classical spin systems using periodically driven cold atoms [48, 49, 51, 145, 171]. In Ref. [48] the authors employed a quantum system to simulate classical magnetism. A weakly-interacting ^{87}Rb Bose gas was loaded in a two-dimensional triangular lattice. In the superfluid regime where phase fluctuations are suppressed and for high filling numbers, the system is effectively described by the classical XY-model

$$H_0 = -J \sum_{\langle ij \rangle} \cos(\varphi_i - \varphi_j) + \frac{U}{2} \sum_j (S_j^z)^2 = -J \sum_{\langle ij \rangle} \mathbf{S}_i \cdot \mathbf{S}_j + \frac{U}{2} \sum_j (S_j^z)^2,$$

where the effective spin interaction J is proportional to the boson hopping matrix element. U is the effective local interaction related to the Hubbard coupling in the Bose-Hubbard

model, and \mathbf{S}_i is a unit vector confined to the (x, y) -plane such that $S_j^x = \cos \varphi_j$, $S_j^y = \sin \varphi_j$, which represents the classical spin or rotor variable.

As we saw in Secs. 3.1.3.2, 3.1.3.3, 2.1.3, and 3.1.3.5, it is possible to modify the hopping matrix elements along the bonds by applying a periodic modulation. Mechanically moving the lattice along an elliptical orbit is equivalent to applying the force $\mathbf{F}(t) = F_c \cos \Omega t \mathbf{e}_c + F_s \sin \Omega t \mathbf{e}_s$ where $\mathbf{e}_{c/s}$ are two orthonormal vectors in the lattice plane and $F_{c/s}$ are experimentally controlled amplitudes [145]. This driving protocol can be taken into account by the following effective spin Hamiltonian

$$H(t) = -J \sum_{\langle ij \rangle} \mathbf{S}_i \cdot \mathbf{S}_j + \sum_j \mathbf{F}(t) \cdot \mathbf{r}_j S_j^z + \frac{U}{2} \sum_j (S_j^z)^2. \quad (3.96)$$

The setup is very similar to the realisation of Haldane's model with circularly polarised electric field, c.f. Eq. (3.83). Using Eq. (3.88) together with the discussion after Eq. (3.92) and the identification $\mathbf{S}_j \leftrightarrow \boldsymbol{\sigma}_j$, we can transform to the rotating frame. This results in a modification of the hopping matrix elements $J \rightarrow J \mathcal{J}_0(\zeta_{ij})$ with

$$\zeta_{ij} = \Omega^{-1} \sqrt{(F_c \mathbf{e}_c \cdot \mathbf{r}_{ij})^2 + (F_s \mathbf{e}_s \cdot \mathbf{r}_{ij})^2},$$

where the vectors $\mathbf{r}_{ij} = \mathbf{r}_i - \mathbf{r}_j$ connect nearest-neighbouring sites. Consequently, as a result of the periodic shaking, it is possible to establish control over the spin-interactions on the three bonds of the triangular plaquette. The infinite-frequency Floquet Hamiltonian is

$$H_F^{(0)} = H_{\text{eff}}^{(0)} = - \sum_{\langle ij \rangle} J_{ij} \mathbf{S}_i \cdot \mathbf{S}_j + \frac{U}{2} \sum_j (S_j^z)^2, \quad (3.97)$$

where $J_{23} = J_{31} = J'$ and $J_{12} = J$, c.f. Fig. 3.13. In the original paper [48] the last term did not appear in the Hamiltonian because the interactions were tuned to a small value and also because they do not affect the thermal phase diagram in the classical limit (large filling). By tuning the driving amplitudes F_c and F_s , it is possible to reach regimes in which the spin-interactions J, J' flip sign independently. This opens up the way towards

studying a rich phase diagram where spin order competes with frustration due to the lattice geometry.

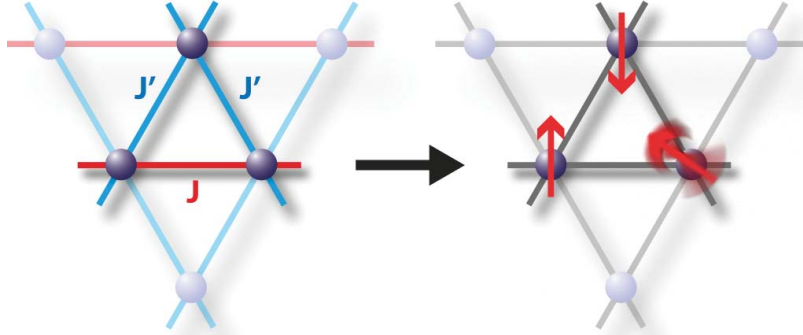


Figure 3.13: Realisation of the classical XY -model on a frustrated triangular lattice using ultracold bosons. By applying a periodic driving, it is possible to establish independent control over the two spin interactions J, J' . From Ref. [48]. Reprinted with permission from AAAS.

As a main tool to study the phase diagram, c.f. Fig. 3.14, the authors performed time-of-flight measurements which gives access to the momentum distribution of the superfluid Bose gas. By assigning a unique momentum distribution to the ground states of the candidate ordered phases, the phase diagram was mapped out with a very high precision. It was even possible to observe spontaneous symmetry breaking directly in the case where the two degenerate ground states lead to different time-of-flight images. For $J, J' > 0$ the system was found in a rhombic state (R), while for $J > 0, J' < 0$ it undergoes a first-order phase transition to a ferromagnet (F). On the transition boundary ($J' = 0, J > 0$) ferromagnetic chains build up in the ground state. Frustration effects become relevant when $J < -|J'|/2$, where the system undergoes a second-order phase transition to two different spiral states, (SP2) and (SP1), depending on whether it is approached from the ferromagnetic ($J' < 0$) or the rhombic ($J' > 0$) side, respectively. These spiral states are connected by a continuous crossover at $J' = 0$ and $J < 0$, where the ground state displays the order of staggered spin-chains (SC). For more details, see Ref. [48].

In a subsequent experiment [51], the interplay between the continuous $U(1)$ symmetry of the XY -model in the presence of a \mathbb{Z}_2 Ising-like artificial gauge field was studied. Once

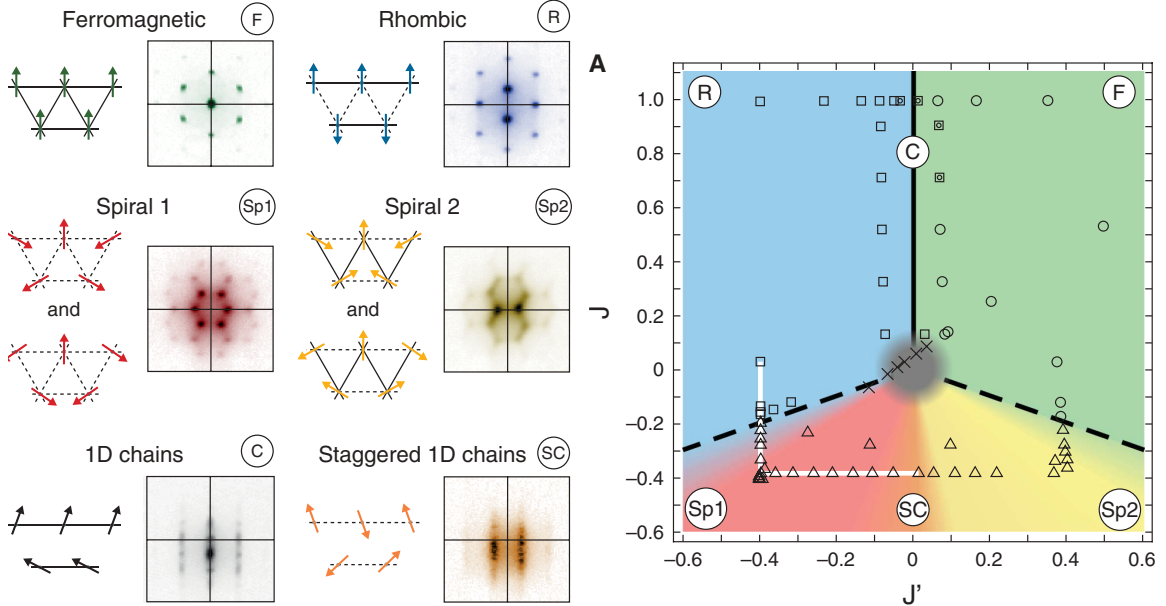


Figure 3.14: Left panel: Ground states of the frustrated XY model on a triangular lattice for different values of the hopping parameters J and J' (see right panel). Right panel: Phase diagram of the frustrated XY model on a triangular lattice in the (J, J') -plane. The symbols refer to the states in the left panel. The solid line is a first-order, while the dashed lines represent a second-order phase transition. In the grey region where tunnelling is suppressed the bosonic system is strongly interacting and the interference pattern is destroyed. From Ref. [48]. Reprinted with permission from AAAS.

again, ^{87}Rb was loaded in a 3d triangular lattice (weakly confined along the vertical direction) which realised the classical XY -model. In addition, an artificial magnetic field in the form of complex Peierls phases was imprinted in the hopping amplitudes J_{ij} , created by shaking the positions of the lattice wells according to an elliptically polarised polychromatic modulation which breaks time-reversal symmetry at the level of the time-average Hamiltonian. The model realises a nonzero net flux which penetrates the triangular plaquettes in an alternating fashion. This flux leads to mass currents along the plaquettes whose direction, clockwise or counter-clockwise, constitutes the classical Ising variable, which was indirectly measured through the occupation of the momentum modes. In addition from such measurements the authors were able to identify a thermal phase transition between an anti-ferromagnetic and a paramagnetic phase.

3.2 The van Vleck Inverse-Frequency Expansion as a Schrieffer-Wolff Transformation for Periodically-Driven Systems

In this section we demonstrate that the van Vleck (Floquet-Magnus) expansion can be used even in static, i.e. non-driven, systems by first going into the interaction picture, see for example Refs. [25, 185–188] for Floquet studies of Bloch oscillations and the Wannier-Stark ladder. In particular, it can be used to eliminate highly excited states, which are rarely/never populated but nevertheless lead to renormalisation and modification (dressing) of the low-energy Hamiltonian. These ideas are also behind the widely used Schrieffer-Wolff transformation [189] which, as we shall show, is closely related to the van Vleck expansion⁴.

The formalism introduced in Sec. 2.2 can be applied to find the leading behaviour and the first subleading correction to the Floquet Hamiltonian, the dressed operators and the dressed density matrix. As we illustrate below, this framework has an additional advantage allowing one to extend the Schrieffer-Wolff transformation to periodically driven systems. More interestingly, we demonstrate that the analysis in Chapter 3.1 is based on virtual photon absorption processes, while with the help of the generalised Schrieffer-Wolff transformation, one can extend this formalism to also study the physics of periodically-driven systems on resonance.

3.2.1 A Two-Level System

3.2.1.1 Non-Driven Regime

To appreciate the relation between the inverse-frequency expansion and time-independent perturbation theory, consider first a time-independent problem of a single particle hopping in a tilted double well potential, c.f. Fig. 3.15. This model is exactly solvable and, with the correct identification of the lab and rotating frames, it is equivalent to the two-level system in a circularly driven magnetic field described in Sec. 2.1.3. Here we revisit this model paying specific attention to the convergence properties of the Floquet-Magnus (van

⁴We are grateful to A. Rosch for pointing this out.

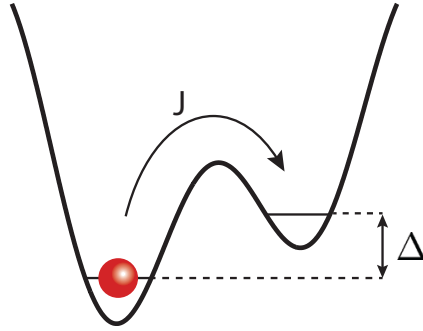


Figure 3.15: A single particle in a tilted double well: the two wells have an energy difference Δ and are connected by the tunnelling matrix element J .

Vleck) expansion. The system is described by the Hamiltonian

$$H = -J (d_2^\dagger d_1 + d_1^\dagger d_2) + \Delta n_2, \quad (3.98)$$

where the operator d_m^\dagger creates a particle on site m and $n_m = d_m^\dagger d_m$ is the particle number operator. The tilt is given by the parameter Δ , while the hopping matrix element is denoted by J . We are interested in the limit $\Delta \gg J$. The exact single-particle eigenenergies of this Hamiltonian are $E_\pm = 1/2 (\Delta \pm \sqrt{\Delta^2 + 4J^2})$.

The Hamiltonian in Eq. (3.98) does not have any explicit time dependence, let alone a periodic one. In order to make use of the inverse-frequency expansion, we apply a unitary transformation into the interaction picture w.r.t. the diagonal part $H_1 = \Delta n_2$, given by $V(t) = \text{diag}(1, \exp(-i\Delta t))$ in the Fock basis. We thus obtain a time-dependent Hamiltonian in the rotating frame (a.k.a. interaction picture):

$$H^{\text{rot}}(t) = -J \left(e^{i\Delta t} d_2^\dagger d_1 + e^{-i\Delta t} d_1^\dagger d_2 \right), \quad (3.99)$$

which is similar to Eq. (2.19) with the identification $B_z \rightarrow 0$, $B_{\parallel} \rightarrow -J$, and $\Delta \rightarrow \Omega$, whenever the system is populated by a single particle. Notice that $H^{\text{rot}}(t)$ contains only the harmonics $H_{\ell=\pm 1}$, see Eq. (2.42). Therefore, for this example the Floquet-Magnus expansion coincides with the van Vleck expansion to order Ω^{-1} , c.f. Eqs. (2.41) and (2.45).

In the following, we choose the Floquet gauge $t_0 = 0$.

Observe that by doing the transformation to the interaction picture, we eliminate the high-energy on-site potential from the problem at the expense of introducing an explicit time dependence. This transformation is identical to the gauge transformation in electromagnetism, where a static scalar potential can be traded for a linear in time vector potential. Now we can apply Floquet theory to the Hamiltonian in Eq. (3.99). Using Eqs. (2.21) and (2.24) we find that the full time-independent Floquet Hamiltonian coincides with the original Hamiltonian, i.e. $H_F[0] = H$, as expected. Moreover, from Eqs. (2.6) and (2.56) we also see that the fast-motion operator is $P(t, 0) = e^{-iK_F[0](t)} = V^\dagger(t)$. This implies that, if we are interested in the time evolution at scales slower than Δ^{-1} , we can compute the dressed density matrix for the initial state and the dressed operator for the observable of interest and evolve them in time with the Floquet Hamiltonian. If we are interested in the high-frequency (i.e. large Δ) structure of the dynamics, we can fully recover it from the operator $P(t, 0)$.

For the Hamiltonian in Eq. (3.99) the leading few orders in the Floquet-Magnus (van Vleck) expansion result in

$$\begin{aligned} H_F^{(0)} &= 0, & H_{\text{eff}}^{(0)} &= 0, \\ H_F^{(1)}[0] &= \frac{J^2}{\Delta}(n_2 - n_1), & H_{\text{eff}}^{(1)} &= \frac{J^2}{\Delta}(n_2 - n_1), \\ H_F^{(2)}[0] &= 2\frac{J^3}{\Delta^2} \left(d_2^\dagger d_1 + d_1^\dagger d_2 \right), & H_{\text{eff}}^{(2)} &= 0, \end{aligned} \quad (3.100)$$

with the following kick operators in the rotating frame:

$$\begin{aligned} K_F^{\text{rot},(1)}[0](t) &= -\frac{J}{i\Delta} \left((e^{i\Delta t} - 1)d_2^\dagger d_1 - (e^{-i\Delta t} - 1)d_1^\dagger d_2 \right), \\ K_{\text{eff}}^{\text{rot},(1)}(t) &= -\frac{J}{i\Delta} \left(e^{i\Delta t} d_2^\dagger d_1 - e^{-i\Delta t} d_1^\dagger d_2 \right). \end{aligned} \quad (3.101)$$

It is easy to see that the stroboscopic Floquet Hamiltonian up to order Ω^{-2} , i.e. $H_F^{(0)} + H_F^{(1)}[0] + H_F^{(2)}[0]$, is equivalent to the original static Hamiltonian when one rescales the

original couplings Δ and J by a factor of $2J^2/\Delta^2$. In fact, for this simple problem one can re-sum the entire series to obtain the Hamiltonian (3.98), i.e. $H = \sum_{n=0}^{\infty} H_F^{(n)}[0]$. Note that for $2J/\Delta > 1$, the square root in the exact eigenenergies $E_{\pm} = 1/2(\Delta \pm \sqrt{\Delta^2 + 4J^2})$ cannot be expanded in a convergent Taylor series in J/Δ . Thus, for $2J/\Delta > 1$, the inverse-frequency expansion is doomed to diverge. This coincides precisely with the general convergence criterion of Eq. (2.61). For more complicated Hamiltonians, however, it is hard to find the condition for the convergence of the HFE series (c.f. Sec. 2.3).

As was the case for a two-level system in the circularly-polarised field (see Sec. 2.2.4), the effective and stroboscopic Floquet Hamiltonians correctly reproduce the exact spectrum to the order of Δ^{-2} (recall that $\Delta = \Omega$). The effective and stroboscopic Floquet Hamiltonians differ at order Δ^{-2} , i.e. $H_F^{(2)}[0] \neq H_{\text{eff}}^{(2)}$ but this difference becomes manifest in the spectrum to order Δ^{-3} , i.e. beyond the validity of the approximation. The hopping (mixing) between the two levels is encoded into $H_F^{(2)}[0]$ but it is absent in $H_{\text{eff}}^{(2)}$. However, the kick operator $K_{\text{eff}}^{\text{rot},(1)}(t)$ precisely compensates for this and hybridises the two levels. Hence, in order to describe the dynamics (FS or FNS) of the system using H_{eff} , one has to take into account the transformation of orbitals encoded in the kick operator. Conversely, the stroboscopic Hamiltonian correctly describes the full evolution of the system if we are interested in the stroboscopic times lT , as the stroboscopic kicks vanish at those times, i.e. $K_F[0](lT) = 0$.

Let us briefly comment on the physical meaning of the different terms in the Hamiltonian. In the leading approximation, the Floquet Hamiltonian is zero which indicates that, in the infinite-frequency limit, i.e. when the energy offset of the two wells is larger than the hopping ($\Delta \gg J$), the system remains frozen since the two levels are effectively uncoupled. The first correction is responsible for the (opposite) energy shifts of the ground and the excited states and introduces a level repulsion. The second correction, in turn, leads to renormalisation of the eigenstates, since it represents a hopping (hybridisation) between the two levels.

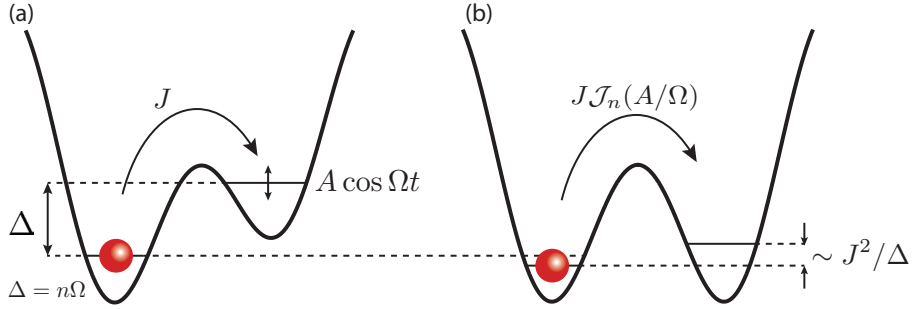


Figure 3.16: The periodically driven two-level system. (a) The higher energy level is modulated periodically w.r.t. the lower level in the lab frame. (b) As a result, the Floquet Hamiltonian governing the slow dynamics features a mixing term between the two levels to leading order (absent in the non-driven system), while the first Ω^{-1} -correction has the physical meaning of a small level repulsion.

3.2.1.2 Periodically Driven Regime

The application of the inverse-frequency expansion in the previous example might not be the easiest way to study this simple system, but it paves the way for studying the behaviour of a more complicated system containing both a high-energy level and a periodic driving. Suppose that we now shake the higher-energy level with an amplitude A and a frequency Ω , c.f. Fig. 3.16. The Hamiltonian becomes

$$H = -J \left(d_2^\dagger d_1 + d_1^\dagger d_2 \right) + (\Delta - A \cos \Omega t) n_2. \quad (3.102)$$

We are interested in the limit $\Delta, \Omega \gg J$. Our first goal is to understand how the drive changes the physics compared to the non-driven case. Extending the procedure from the static example to the driven case above, we eliminate both the higher-energy level and the driving term altogether by a transformation to a rotating frame:

$$\begin{aligned} V(t) &= \exp \left[-i \left(\Delta t - \frac{A}{\Omega} \sin \Omega t \right) n_2 \right], \\ d_2 &\rightarrow e^{i \Delta t - i \zeta \sin \Omega t} d_2, \quad d_1 \rightarrow d_1, \end{aligned} \quad (3.103)$$

where we defined $\zeta = A/\Omega$. The Hamiltonian in the rotating frame is now given by

$$H^{\text{rot}}(t) = -J \left(e^{i\Delta t - i\zeta \sin \Omega t} d_2^\dagger d_1 + e^{-i\Delta t + i\zeta \sin \Omega t} d_1^\dagger d_2 \right). \quad (3.104)$$

Note that, as before, in the rotating frame there is no energy offset between the two levels, but the hopping term has a more complex time dependence encoding both static and dynamic information.

In general, the new Hamiltonian (3.104) is not strictly periodic in time, since Δ and Ω are arbitrary real numbers. One can deal with this in several ways. One possibility is to find co-prime integers l and k and a frequency Ω_0 such that $l\Omega_0 \approx \Delta$ and $k\Omega_0 \approx \Omega$. As long as $\Omega_0 \gg J$ the Floquet analysis should hold. If the frequencies are not exactly commensurate then one can define a commensurate $\tilde{\Delta} = l\Omega_0$ and make the transformation to the rotating frame using $\tilde{\Delta}$ instead of Δ in Eq. (3.103). It is easy to see that this will result in a small extra static term $(\Delta - \tilde{\Delta})d_2^\dagger d_2$ in the rot-frame Hamiltonian (3.104). And finally, one can take the commensurate limit, e.g. $\Delta = l\Omega$ and make an analytic continuation in the final result to non-integer l . This should work if the result, e.g. the Floquet Hamiltonian, is a simple analytic function of l . We shall show below that this trick works indeed in the case of the Schrieffer-Wolff transformation. It is intuitively clear that especially in many-particle systems with continuous spectra the exact commensurability of the driving should not play a crucial role.

We now leave all these subtleties aside and assume that Δ and Ω are commensurate such that $\Delta = l\Omega_0$ and $\Omega = k\Omega_0$, where l and k are positive co-prime integers. We shall also assume that $\Omega_0 \gg J$. First, let us understand the leading time averaged Hamiltonian $H_F^{(0)}$, which was strictly zero in the non-driven case. We note the mathematical identity:

$$\frac{1}{T_0} \int_0^{T_0} dt e^{i\Delta t - i\zeta \sin \Omega t} = \sum_{\ell \in \mathbb{Z}} \mathcal{J}_\ell(\zeta) \frac{1}{T_0} \int_0^{T_0} dt e^{i(-\ell k + l)\Omega_0 t}, \quad (3.105)$$

where $\mathcal{J}_\ell(\zeta)$ is the ℓ -th Bessel function of the first kind and $T_0 = 2\pi/\Omega_0$ is the common

period. The integral above is nonzero if and only if there is a solution to the equation $\ell k = l$ or, in other words, l is an integer multiple of k . Because by assumption k and l are co-prime this equality can only be satisfied when $k = 1$ (and hence $\Omega_0 = \Omega$ and $\Delta = l\Omega$). This means that the leading Floquet Hamiltonian $H_F^{(0)}$ simply corresponds to the l -photon resonance. Let us focus on this resonant scenario. Clearly in this case

$$H_F^{(0)} = H_{\text{eff}}^{(0)} = -J\mathcal{J}_l(\zeta) \left(d_2^\dagger d_1 + d_1^\dagger d_2 \right). \quad (3.106)$$

In the infinite-frequency limit (at fixed l) $H_F^{(0)}$ determines the Floquet Hamiltonian. It splits the two levels into the symmetric and antisymmetric combinations. This is very different from the non-driven or non-resonantly driven case where $H_F^{(0)} = 0$, and the leading order contribution in the Floquet-Magnus (van Vleck) expansion, i.e. $H_F^{(1)}[0]$, gives the energy splitting between the levels (c.f. $H_F^{(1)}$ in Eq. (3.100)) and hence keeps the eigenstates essentially unmixed (up to a small correction of the order J/Δ). This observation already hints to possible heating mechanisms in Floquet systems. For example, if one prepares the two-level system in the lower-energy state then in the resonant case this state is equally projected on the symmetric and antisymmetric Floquet eigenstates, resulting in an equal population of the two levels. This is equivalent to heating to an infinite-temperature state. In the non-resonant case, conversely, the Floquet eigenstates are still predominantly the eigenstates of the non-driven Hamiltonian, and thus the initial state is only weakly perturbed, while the excited state is only weakly populated. Admittedly, this example is too simple to understand real heating mechanisms in more complex interacting systems, but it shows how resonant periodic driving can fundamentally change the nature of the Floquet eigenstates [97]. Thermalisation in periodically driven systems is discussed in Chapter 5.

If the amplitude of the driving is small, then $\zeta \ll 1$ and we find $\mathcal{J}_l(\zeta) \sim \zeta^l$ such that the effective hopping is proportional to the l -th power of the driving amplitude. This is not surprising, since it means that the l -photon absorption processes are exponentially

suppressed. This result can also be obtained using time-dependent perturbation theory. However, for $\zeta \sim 1$, i.e. in the strong-coupling regime, this term becomes non-perturbative and it is not meaningful to think of single or multi-photon absorption in the lab frame⁵.

For completeness, we give the leading correction term in the Floquet-Magnus (van Vleck) expansion for this resonant case:

$$\begin{aligned}
H_F^{(1)}[0] &= \frac{J^2}{\Delta} g_l(\zeta)(n_2 - n_1), \\
g_l(\zeta) &= -l \operatorname{Im} \left\{ \int_0^{2\pi} \frac{d\tau_1}{2\pi} \int_0^{\tau_1} d\tau_2 e^{-il(\tau_1 - \tau_2) + i\zeta(\sin \tau_1 - \sin \tau_2)} \right\}, \\
H_{\text{eff}}^{(1)} &= \frac{J^2}{\Delta} \tilde{g}_l(\zeta)(n_2 - n_1), \\
\tilde{g}_l(\zeta) &= -l \operatorname{Im} \left\{ \int_0^{2\pi} \frac{d\tau_1}{2\pi} \int_0^{\tau_1} d\tau_2 \left(1 - \frac{\tau_1 - \tau_2}{\pi} \right) e^{-il(\tau_1 - \tau_2) + i\zeta(\sin \tau_1 - \sin \tau_2)} \right\}.
\end{aligned} \tag{3.107}$$

Similarly to the non-driven case, this correction gives the level repulsion term, but with a renormalised coefficient. If the amplitude is not very strong, $\zeta \lesssim 1$, then $g_l(\zeta), \tilde{g}_l(\zeta) \approx 1$ for all $l \neq 1$, i.e. the presence of the driving results in a small modification of the non-driven Floquet Hamiltonian. For $l = 1$ the functions $g_1(\zeta), \tilde{g}_1(\zeta)$ are small, oscillate and even become zero at special values of ζ . This indicates that the driving can have a strong effect if $l = 1$. We want to emphasise again that the Ω^{-1} -term is now only a sub-dominant correction, provided that $\mathcal{J}_l(\zeta) \gg J/\Delta = J/(l\Omega)$. For completeness we also show the leading order approximation for the kick operators:

$$\begin{aligned}
H_\ell &= -J \left(\mathcal{J}_{l-\ell}(\zeta) d_2^\dagger d_1 + \mathcal{J}_{l+\ell}(\zeta) d_1^\dagger d_2 \right), \\
K_F^{\text{rot},(1)}[0](t) &= \frac{1}{i\Omega} \sum_{\ell=1}^{\infty} \frac{1}{\ell} \left((e^{i\ell\Omega t} - 1) H_\ell - (e^{-i\ell\Omega t} - 1) H_{-\ell} \right), \\
K_{\text{eff}}^{\text{rot},(1)}(t) &= \frac{1}{i\Omega} \sum_{\ell=1}^{\infty} \frac{1}{\ell} \left(e^{i\ell\Omega t} H_\ell - e^{-i\ell\Omega t} H_{-\ell} \right).
\end{aligned} \tag{3.108}$$

⁵The notion of single or multi-photon absorption in systems with classical drives is reference-frame dependent: e.g. in the rot frame all parameters remain finite in the limit $\Omega \rightarrow \infty$ and it makes sense to speak about photon absorption processes even at $\zeta \sim 1$. There is no contradiction, because of the appearance of non-perturbative Bessel functions in the resulting matrix elements.

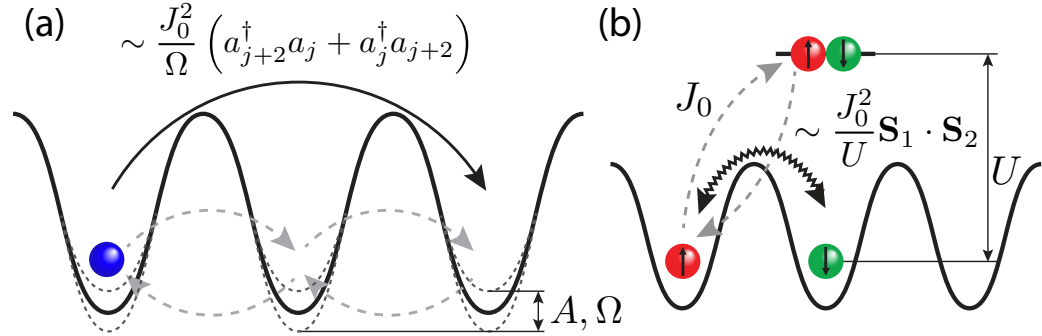


Figure 3.17: Similarity between renormalisation of tunnelling, an interference effect induced virtually by an off-resonant drive (a), and Heisenberg interactions induced by virtual off-resonant interaction processes (b).

3.2.2 Low Energy Heisenberg Physics in the Periodically Driven Fermi-Hubbard Model

The Schrieffer-Wolff transformation (SWT) [189–192] is a generic procedure to derive effective low-energy Hamiltonians for strongly-correlated many-body systems. It allows one to eliminate high-energy degrees of freedom via a canonical transform. The SWT has proven useful for studying systems with a hugely degenerate ground-state manifold, such as the strongly-interacting limit of the Fermi-Hubbard model (FHM) [190], without resorting to conventional perturbation theory.

In this section, we consider strongly-interacting periodically-driven systems and show how the SWT can be extended to derive effective static Hamiltonians of non-equilibrium setups. The parameter space of such models, to which we add the driving amplitude and frequency, opens up the door to new regimes. We use this to discuss realisations of novel Hamiltonians, including spin models in artificial gauge fields and the Fermi-Hubbard model with enhanced doublon association and dissociation processes.

3.2.2.1 Schrieffer-Wolff Transformation from the van Vleck Inverse-Frequency Expansion.

Intuitively, the van Vleck high-frequency expansion for periodically-driven systems (vV HFE) and the SWT share the same underlying concept: they allow for the elimination of virtually-populated high-energy states to provide a dressed low-energy description, as illustrated in Fig. 3.17. For a system driven off-resonantly (Fig. 3.17a), virtual absorption of a photon leads to tunnelling between next-nearest neighbours. Similarly, non-driven fermions develop Heisenberg interactions via off-resonant (virtual) tunnelling processes (Fig. 3.17b). In this Section we combine the van Vleck HFE and the SWT into a single framework allowing one to treat both resonantly and non-resonantly driven systems on equal footing.

Let us illustrate this connection by deriving the SWT using the van Vleck HFE. Consider the non-driven FHM:

$$H = -J_0 \sum_{\langle ij \rangle, \sigma} c_{i\sigma}^\dagger c_{j\sigma} + U \sum_j n_{j\uparrow} n_{j\downarrow}, \quad (3.109)$$

where J_0 is the bare hopping and U is the fermion-fermion interaction. We are interested in the strongly-correlated regime $J_0 \ll U$. Going to the rotating frame $|\psi^{\text{rot}}(t)\rangle = V^\dagger(t)|\psi(t)\rangle$ w.r.t. the operator $V(t) = \exp\left(-iUt \sum_j n_{j\uparrow} n_{j\downarrow}\right)$ eliminates the interaction energy U in favour of fast oscillations. If $i\text{d}_t|\psi^{\text{rot}}\rangle = H^{\text{rot}}(t)|\psi^{\text{rot}}\rangle$, then

$$\begin{aligned} H^{\text{rot}}(t) &= -J_0 \sum_{\langle ij \rangle, \sigma} \left[g_{ij\sigma} + \left(e^{iUt} h_{ij\sigma}^\dagger + \text{h.c.} \right) \right], \\ h_{ij\sigma}^\dagger &= n_{i\bar{\sigma}} c_{i\sigma}^\dagger c_{j\sigma} (1 - n_{j\bar{\sigma}}), \\ g_{ij\sigma} &= (1 - n_{i\bar{\sigma}}) c_{i\sigma}^\dagger c_{j\sigma} (1 - n_{j\bar{\sigma}}) + n_{i\bar{\sigma}} c_{i\sigma}^\dagger c_{j\sigma} n_{j\bar{\sigma}}, \end{aligned} \quad (3.110)$$

where $\bar{\uparrow} = \downarrow$ and vice-versa. The first term $g_{ij\sigma}$ models the hopping of doublons and holons, while the second term $h_{ij\sigma}^\dagger$ represents the creation and annihilation of doublon-holon pairs.

Since $H^{\text{rot}}(t)$ is time-periodic with frequency U , we can apply Floquet's theorem [81]. Thus, the evolution of the system at integer multiples of the driving period $T_U = 2\pi/U$ [i.e. stroboscopically] is governed by the effective Floquet Hamiltonian H_{eff} . If we write $H^{\text{rot}}(t) = \sum_{\ell} H_{\ell}^{\text{rot}} e^{i\ell U t}$, the van Vleck HFE (see Sec. 2.2.2) gives an operator expansion for $H_{\text{eff}} = H_0^{\text{rot}} + \sum_{\ell>0} [H_{\ell}^{\text{rot}}, H_{-\ell}^{\text{rot}}]/\ell U + \mathcal{O}(U^{-2})$. From Eqs. (2.45) it follows that the zeroth-order term $H_{\text{eff}}^{(0)} = H_0^{\text{rot}}$ is the period-averaged Hamiltonian [here the doublon-holon hopping term g], while the first-order correction is proportional to the commutator $H_{\text{eff}}^{(1)} \sim J_0^2 [h^{\dagger}, h]/U$, cf. Fig. 3.17b:

$$H_{\text{eff}} \approx -J_0 \sum_{\langle ij \rangle, \sigma} g_{ij\sigma} + \frac{4J_0^2}{U} \sum_{\langle ij \rangle} \left(\mathbf{S}_i \cdot \mathbf{S}_j - \frac{n_i n_j}{4} \right) + \mathcal{O}(U^{-2}). \quad (3.111)$$

The approximate sign in Eq. (3.111) is used, since we neglected part of the U^{-1} -correction terms, as is common for the conventional SWT calculation cf. Ref. [193], with which the above effective Hamiltonian is in precise agreement. At half-filling, doublons and holons are suppressed in the ground state and this reduces to the Heisenberg model. Away from half-filling this Hamiltonian reduces to the $t - J$ model [190, 193]. Similar to the conventional SWT, the exact Floquet Hamiltonian H_{eff} contains all degrees of freedom of the original Hamiltonian of interest, but they are ‘ordered’ according to the large energy scale (here U). It is only when the series is truncated to a finite order in U^{-1} , or when further subspaces of the Hilbert space are projected out based on physical reasoning, that the large energy scale is ‘integrated out’.

Using the van Vleck HFE to perform the SWT offers a few advantages: (i) the SWT generator comes naturally out of the calculation, (ii) one can systematically compute higher-order corrections, see Sec. 2.2, and (iii) the van Vleck HFE allows for obtaining not only the effective Hamiltonian but also the kick operator, which keeps track of the mixing between orbitals and describes the intra-period dynamics [32, 33]. This is important for identifying the fast timescale associated with the large frequency U in dynamical measurements [194], and expressing observables through creation and annihilation operators dressed by orbital

mixing [33].

3.2.2.2 Generalisation to Periodically-Driven Systems

The van Vleck HFE allows us to extend the SWT to time-periodic Hamiltonians. Related approaches have been used to study non-interacting Floquet topological insulators [195] and ultrafast dynamical control of the spin exchange coupling [196] in fermionic Mott insulators [197]. Let us add to the FHM an external periodic drive:

$$H(t) = -J_0 \sum_{\langle ij \rangle, \sigma} c_{i\sigma}^\dagger c_{j\sigma} + U \sum_j n_{j\uparrow} n_{j\downarrow} + \sum_{j\sigma} f_{j\sigma}(t) n_{j\sigma}. \quad (3.112)$$

The driving protocol $f_{j\sigma}(t)$ with frequency Ω encompasses experimental tools such as mechanical shaking, external electromagnetic fields, and time-periodic chemical potentials, relevant for the recent realisations of novel Floquet Hamiltonians, see Chapter 3.1. In the following, we work in the limit $J_0 \ll U, \Omega$ and assume that the amplitude of the periodic modulation also scales with Ω [33].

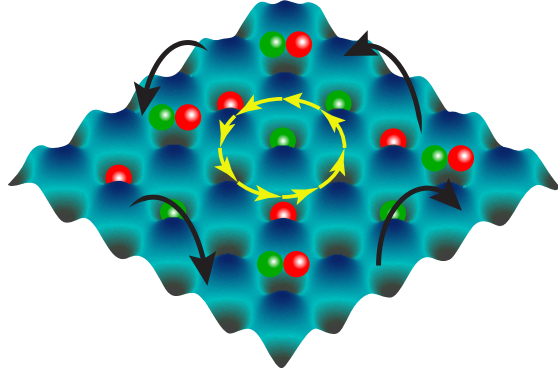


Figure 3.18: The strongly-interacting Fermi-Hubbard model with an artificial gauge field.

Since both the interaction strength U and the driving amplitude are large, we go to the rotating frame w.r.t. $V(t) = e^{-i[Ut \sum_j n_{j\uparrow} n_{j\downarrow} + \sum_{j,\sigma} F_{j\sigma}(t) n_{j\sigma}]}$, where $F_{j\sigma}(t) = \int^t f_{j\sigma}(t') dt'$. Going to the rotating frame is equivalent to a re-summation of two infinite lab-frame

inverse-frequency subseries [33]. The first subseries leads to a non-perturbative renormalisation of the hopping amplitude by resumming single-particle terms (recall the usual Bessel(-like) function to zeroth order), while the second subseries contains the many-body nn interaction-dependent hopping terms. The drive induces time-dependent phase shifts into the hopping:

$$H^{\text{rot}}(t) = -J_0 \sum_{\langle ij \rangle, \sigma} [1 - n_{i\bar{\sigma}}(1 - e^{iUt})] e^{i\delta F_{ij,\sigma}(t)} c_{i\sigma}^\dagger c_{j\sigma} [1 - n_{j\bar{\sigma}}(1 - e^{-iUt})], \quad (3.113)$$

where $\delta F_{ij,\sigma}(t) = F_{i\sigma}(t) - F_{j\sigma}(t)$. It is convenient to cast this expression in the following form

$$H^{\text{rot}}(t) = -J_0 \sum_{\langle ij \rangle, \sigma} \left[e^{i\delta F_{ij,\sigma}(t)} g_{ij\sigma} + \left(e^{i[\delta F_{ij,\sigma}(t) + Ut]} h_{ij\sigma}^\dagger + \text{h.c.} \right) \right]. \quad (3.114)$$

We draw the reader's attention to the fact that the overall sign of the function $\delta F_{ij,\sigma}$ in the Hamiltonian above depends on the direction of hopping. For instance, for a one-dimensional chain with drive $f_{j\sigma}(t) = j\Omega\zeta \cos \Omega t$ the Hamiltonian (3.114), when fully written out, reads

$$\begin{aligned} H^{\text{rot}}(t) = & -J_0 \sum_{j,\sigma} e^{i\zeta \sin \Omega t} g_{j+1,j,\sigma} + e^{-i\zeta \sin \Omega t} g_{j,j+1,\sigma} \\ & -J_0 \sum_{j,\sigma} e^{iUt} \left(e^{i\zeta \sin \Omega t} h_{j+1,j,\sigma}^\dagger + e^{-i\zeta \sin \Omega t} h_{j,j+1,\sigma}^\dagger \right) + \text{h.c.} \end{aligned} \quad (3.115)$$

Note also that while $g_{j+1,j,\sigma} = g_{j,j+1,\sigma}^\dagger$, $h_{j+1,j,\sigma} \neq h_{j,j+1,\sigma}^\dagger$; in other words destroying a doublon to the left $h_{21,\downarrow} |\cdot, \uparrow\downarrow\rangle = |\uparrow, \downarrow\rangle$ is different from creating a doublon to the left $h_{12,\downarrow}^\dagger |\uparrow, \downarrow\rangle = -|\uparrow\downarrow, \cdot\rangle$.

Let us pause for a moment and check the non-driven case, i.e. $F_{ij,\sigma} = 0$. Then the terms proportional to $h_{ij\sigma}^\dagger$ vanish in $H_{\text{eff}}^{(0)}$ after time-averaging over one period $T = 2\pi/U$, cf. Eq. (2.45). On the other hand, the $g_{ij\sigma}$ -terms do not have a time-dependent pre-factor

and hence they give rise to the leading-order Hamiltonian.

$$\begin{aligned} H_{\text{eff}}^{(0)} &= -J_0 \sum_{\langle ij \rangle, \sigma} g_{ij\sigma} = -J_0 \sum_{\langle ij \rangle, \sigma} P_{i\bar{\sigma}} c_{i\sigma}^\dagger c_{j\sigma} P_{j\bar{\sigma}}, \\ P_{i\bar{\sigma}} c_{i\sigma}^\dagger c_{j\sigma} P_{j\bar{\sigma}} &\equiv n_{i\bar{\sigma}} c_{i\sigma}^\dagger c_{j\sigma} n_{j\bar{\sigma}} + (1 - n_{i\bar{\sigma}}) c_{i\sigma}^\dagger c_{j\sigma} (1 - n_{j\bar{\sigma}}), \end{aligned} \quad (3.116)$$

where the above expression is understood as the defining relation for the projector $P_{i\sigma}$ which projects out the subspace of doubly-occupied states. The U^{-1} -correction, as given by Eq. (2.45), is proportional to the commutator $H_{\text{eff}}^{(1)} \sim J_0^2 U^{-1} \sum_{\langle ij \rangle, \sigma} \sum_{\langle kl \rangle, \sigma'} [h_{ij\sigma}^\dagger, h_{kl\sigma'}]$, and results in the familiar Heisenberg spin exchange. Notice that already at this level the calculation for the static model reduces exactly to the standard SWT calculation.

Now let us turn on the periodic drive again. Pay attention how the zeroth order Hamiltonian changes, since the terms proportional to $h_{ij\sigma}^\dagger$, which average to zero in the non-driven case, now remain finite after averaging over one period, similarly to the resonantly driven two-level system described in the previous section. These are precisely the doublon association and dissociation processes in the resonant limit $J_0 \ll U = l\Omega$ whose physics we discuss in Sec. 3.2.2.4.

3.2.2.3 Spin Models from the Fermi-Hubbard Model for Generic Off-Resonant Drive

Notice that, in general, in the rotating frame there are two frequencies in the full time-dependent problem: U and Ω . Hence, $H^{\text{rot}}(t)$ is not strictly periodic in either. To circumvent this difficulty, once again we choose a common frequency Ω_0 by writing $\Omega = k\Omega_0$ and $U = l\Omega_0$ where k and l are co-prime integers. Then $H^{\text{rot}}(t)$ becomes periodic with period $T_{\Omega_0} = 2\pi/\Omega_0$, and we can proceed using the van Vleck HFE. Alternatively, before going to the rotating frame, we could decompose the interaction strength as $U = l\Omega + \delta U$, where δU acts as a detuning, and can continue without including the term proportional to δU in the rotator $V(t)$.

3.2.2.3.1 Half-Filling

In this Section, we discuss the two off-resonant regimes $U \ll \Omega$ and $\Omega \ll U$ at half-filling. Consider a generic driving protocol, which gives the rotating frame Hamiltonian in Eq. (3.114):

$$\begin{aligned} H^{\text{rot}}(t) &= -J_0 \sum_{\langle ij \rangle, \sigma} e^{i\delta F_{ij\sigma}(t)} g_{ij\sigma} - J_0 \sum_{\langle ij \rangle, \sigma} e^{i[\delta F_{ij\sigma}(t) + Ut]} h_{ij\sigma}^\dagger + \text{h.c.}, \\ h_{ij\sigma}^\dagger &= n_{i\bar{\sigma}} c_{i\sigma}^\dagger c_{j\sigma} (1 - n_{j\bar{\sigma}}), \\ g_{ij\sigma} &= (1 - n_{i\bar{\sigma}}) c_{i\sigma}^\dagger c_{j\sigma} (1 - n_{j\bar{\sigma}}) + n_{i\bar{\sigma}} c_{i\sigma}^\dagger c_{j\sigma} n_{j\bar{\sigma}}. \end{aligned}$$

Since $\delta F_{ij\sigma}$ is Ω -periodic, we can most generally write it in terms of Fourier coefficients:

$$e^{i\delta F_{ij\sigma}(t)} = \sum_{\ell} A_{ij\sigma}^{(\ell)} e^{i\ell\Omega t}. \quad (3.117)$$

We shall consider the case $\Omega = k\Omega_0$ and $U = l\Omega_0$ with k and l relatively prime and $\Omega_0 \gg J_0$. Furthermore, assume that $k, l \gg 1$ such that resonance effects can be ignored and that the state of the system at half-filling has no doublons or holons which, as we shall shortly see, will not be dynamically generated at low orders in the high-frequency expansion. Then the leading correction is of order Ω_0^{-1} , and we shall only be interested in the singly-occupied conserving (a.k.a. spin) terms in the expansion.

Before expanding in powers of Ω_0^{-1} , let us quickly comment on properties of the Fourier coefficients $A_{ij\sigma}^{(\ell)}$. While not necessary for all driving protocols, it will be useful in driving spin Hamiltonians to demand that spin up and down are driven oppositely, i.e., $\delta F_{ij\sigma} = -\delta F_{ij\bar{\sigma}}$. In terms of the Fourier transform, Eq. (3.117), this implies that $A_{ij\bar{\sigma}}^{(\ell)} = (A_{ij\sigma}^{(-\ell)})^*$. Similarly, flipping the direction of the bond flips the sign of δF , so $A_{ji\sigma}^{(\ell)} = (A_{ij\sigma}^{(-\ell)})^*$.

The leading correction to the effective Hamiltonian is $H_{\text{eff}}^{(1)} = \sum_{\ell>0} [H_{\text{rot}}^{(\ell)}, H_{\text{rot}}^{(-\ell)}]/\ell\Omega_0$. There are two types of commutators that occur in this sum. The first comes from terms

that have no oscillation with frequency U , giving commutators of the form:

$$\left[\sum_{ij\sigma} A_{ij\sigma}^{(\ell)} g_{ij\sigma}, \sum_{i'j'\sigma'} A_{i'j'\sigma'}^{(\ell)} g_{i'j'\sigma'} \right] . \quad (3.118)$$

One can readily check that all of these commutators vanish. The second class of commutators are those that are relevant for the Schrieffer-Wolff transformation:

$$\left[\sum_{ij\sigma} A_{ij\sigma}^{(\ell)} h_{ij\sigma}^\dagger, \sum_{i'j'\sigma'} A_{i'j'\sigma'}^{(-\ell)} h_{j'i'\sigma'} \right] . \quad (3.119)$$

These involve terms rotating with $e^{i(U+\ell\Omega)t}$, and thus will be suppressed by a $(U + \ell\Omega)$ denominator. The commutators vanish if i , i' , j , and j' are all different. For $i = i'$ and $j \neq j'$, the non-vanishing commutators correspond to next-neighbour doublon/holon hopping which is suppressed at half filling. Therefore, the only relevant commutators come from $i = i'$ and $j = j'$ or $i = j'$ and $j = i'$. Note that these are the same commutators that were implicitly used in the conventional SWT calculation; we explicitly write them out here for clarity. There are four cases.

- $i' = i$, $j' = j$, $\sigma' = \sigma$: The commutator vanishes trivially.
- $i' = i$, $j' = j$, $\sigma' = \bar{\sigma}$: The commutator gives

$$\mathcal{C}_1 = A_{ij\sigma}^{(\ell)} A_{ij\bar{\sigma}}^{(-\ell)} c_{i\sigma}^\dagger c_{j\sigma} c_{i\bar{\sigma}}^\dagger c_{j\bar{\sigma}} [(1 - n_{i\bar{\sigma}}) n_{j\bar{\sigma}} (1 - n_{i\sigma}) n_{j\sigma} - n_{i\sigma} (1 - n_{j\sigma}) n_{i\bar{\sigma}} (1 - n_{j\bar{\sigma}})] .$$

Using properties of $A^{(\ell)}$ discussed above, the coefficient may be rewritten as $|A_{ij\sigma}^{(\ell)}|^2$.

- $i' = j$, $j' = i$, $\sigma' = \sigma$: The commutator gives

$$\mathcal{C}_2 = A_{ij\sigma}^{(\ell)} A_{ji\sigma}^{(-\ell)} (n_{i\sigma} - n_{j\sigma}) n_{i\bar{\sigma}} (1 - n_{j\bar{\sigma}}) .$$

The coefficient may be rewritten to $|A_{ij\sigma}^{(\ell)}|^2$.

- $i' = j, j' = i, \sigma' = \bar{\sigma}$: The commutator gives

$$\mathcal{C}_3 = A_{ij\sigma}^{(\ell)} A_{ji\bar{\sigma}}^{(-\ell)} c_{i\sigma}^\dagger c_{j\sigma} c_{j\bar{\sigma}}^\dagger c_{i\bar{\sigma}} [(1 - n_{i\bar{\sigma}}) n_{j\bar{\sigma}} (1 - n_{j\sigma}) n_{i\sigma} - n_{j\sigma} (1 - n_{i\sigma}) n_{i\bar{\sigma}} (1 - n_{j\bar{\sigma}})] .$$

The coefficient may be rewritten $A_{ij\sigma}^{(\ell)} A_{ij\sigma}^{(-\ell)}$.

For later convenience, we define the above coefficients for $\sigma = \uparrow$ as

$$\alpha_{ij}^{(\ell)} \equiv A_{ij\uparrow}^{(\ell)} A_{ij\uparrow}^{(-\ell)}, \quad \beta_{ij}^{(\ell)} \equiv |A_{ij\uparrow}^{(\ell)}|^2 . \quad (3.120)$$

The first term, \mathcal{C}_1 , yields doublon-holon exchange ($|\uparrow\downarrow, 0\rangle \leftrightarrow |0, \uparrow\downarrow\rangle$) and is therefore irrelevant at half filling. Up to a constant energy shift, \mathcal{C}_2 and \mathcal{C}_3 correspond to Ising and exchange terms respectively. Thus the effective spin Hamiltonian may be written

$$H_{\text{eff}}^{(1)} = \sum_{\langle ij \rangle, \ell} \frac{J_0^2}{U + \ell\Omega} \left[\alpha_{ij}^{(\ell)} S_i^+ S_j^- + (\alpha_{ij}^{(\ell)})^* S_i^- S_j^+ + 2\beta_{ij}^{(\ell)} S_i^z S_j^z \right] . \quad (3.121)$$

Hence, we see that the general result is an interacting spin-1/2 Hamiltonian where hopping of the spins is accompanied by a phase that depends on properties of the driving. One can now see how to simply take the limits $U \gg \Omega$ and $\Omega \gg U$.

First, if $\Omega \gg U$, then only the $\ell = 0$ term in the sum survives:

$$H_{\text{eff}}^{\Omega \gg U} = \frac{J_0^2}{U} \sum_{\langle ij \rangle} \left[\alpha_{ij}^{(0)} S_i^+ S_j^- + (\alpha_{ij}^{(0)})^* S_i^- S_j^+ + 2\beta_{ij}^{(0)} S_i^z S_j^z \right] . \quad (3.122)$$

In the opposite limit, $U \gg \Omega$, not only do all the ℓ 's contribute, but they contribute with equal weight $1/(U + \ell\Omega) \approx 1/U$:

$$H_{\text{eff}}^{U \gg \Omega} = \frac{1}{U} \sum_{\langle ij \rangle, \ell} \left[\alpha_{ij}^{(\ell)} S_i^+ S_j^- + (\alpha_{ij}^{(\ell)})^* S_i^- S_j^+ + 2\beta_{ij}^{(\ell)} S_i^z S_j^z \right] . \quad (3.123)$$

This approximation is technically only valid if the sum is dominated by $\ell \ll U/\Omega$. This condition will generally hold because higher ℓ 's corresponds to higher harmonics of the

drive, which have amplitudes $A^{(\ell)}$ that are exponentially suppressed in ℓ .

To see how the above calculation can give rise to a Hamiltonian with novel low-energy properties, one can Floquet-engineer the Heisenberg model with a uniform magnetic flux per plaquette Φ_{\square} , see Fig. 3.19. To this end, we choose the spin-dependent driving protocol (c.f. Fig. 3.19, inset)

$$f_{mn\sigma} = \sigma[A \cos(\Omega t + \Phi_{\square}(m+n)) + \Omega m] , \quad (3.124)$$

where $\phi_j = \phi_{mn} = \Phi_{\square}(m+n)$, $\sigma \in \{\uparrow, \downarrow\} \equiv \{1, -1\}$, and we denote the square-lattice position by $\mathbf{r}_j = (m, n)$. Such spin-sensitive drives are realised in experiments via the Zeeman effect using a periodically-modulated [60] and static [52, 53] magnetic-field gradients which couple to atomic hyperfine states.

From the second term in Eq. (3.124) we see that bonds in the x -direction and y -direction behave differently. In particular, hopping in the positive x -direction gives

$$e^{i\delta F_{\uparrow}^x} \equiv e^{i(F_{m,n,\uparrow} - F_{m+1,n,\uparrow})} = e^{-i\Omega t} e^{i\zeta(\sin(\Omega t + \Phi_{\square}(m+n)) - \sin(\Omega t + \Phi_{\square}(m+n+1)))} = e^{-i\Omega t} e^{i\delta F_{\uparrow}^y} . \quad (3.125)$$

Fourier-transforming this simple harmonic driving, one can readily check that

$$A_{y\uparrow}^{(\ell)} = e^{i\ell(\phi_{mn} + (\Phi_{\square} + \pi)/2)} \mathcal{J}_{\ell}(2\zeta_{\Phi}) , \quad (3.126)$$

from which it is clear that A_x is just shifted by one harmonic:

$$A_{x\uparrow}^{(\ell)} = e^{i(\ell+1)(\phi_{mn} + (\Phi_{\square} + \pi)/2)} \mathcal{J}_{\ell+1}(2\zeta_{\Phi}) . \quad (3.127)$$

This gives coefficients on the spin Hamiltonian of

$$\begin{aligned} \alpha_y^{(\ell)} &= A_y^{(\ell)} A_y^{(-\ell)} = \mathcal{J}_{\ell}(2\zeta_{\Phi}) \mathcal{J}_{-\ell}(2\zeta_{\Phi}) \\ \alpha_x^{(\ell)} &= e^{2i(\phi_{mn} + (\Phi_{\square} + \pi)/2)} \mathcal{J}_{\ell+1}(2\zeta_{\Phi}) \mathcal{J}_{-\ell+1}(2\zeta_{\Phi}) \end{aligned}$$

$$\begin{aligned}\beta_y^{(\ell)} &= [\mathcal{J}_\ell(2\zeta_\Phi)]^2 \\ \beta_x^{(\ell)} &= [\mathcal{J}_{\ell+1}(2\zeta_\Phi)]^2.\end{aligned}\quad (3.128)$$

The overall phase factor $\Phi_\square + \pi$ in α_x is irrelevant to the global physics, so we gauge it away by rotating $S_{mn}^+ \rightarrow S_{mn}^+ e^{im(\Phi_\square + \pi)}$. Then, for $\Omega \gg U$ the Hamiltonian reduces to

$$\begin{aligned}H_{\text{eff}}^{\Omega \gg U} &= \frac{2J_0^2}{U} \sum_{mn} \left[[\mathcal{J}_1(2\zeta_\Phi)]^2 (e^{2i\phi_{mn}} S_{m,n}^+ S_{m+1,n}^- + e^{-2i\phi_{mn}} S_{m,n}^- S_{m+1,n}^+ + 2S_{m,n}^z S_{m+1,n}^z) \right. \\ &\quad \left. + [\mathcal{J}_0(2\zeta_\Phi)]^2 (S_{m,n}^+ S_{m,n+1}^- + S_{m,n}^- S_{m,n+1}^+ + 2S_{m,n}^z S_{m,n+1}^z) \right].\end{aligned}\quad (3.129)$$

The $U \gg \Omega$ limit can be obtained by using sum rules for the Bessel functions: $\sum_\ell \alpha_x^{(\ell)} = \mathcal{J}_2(4\zeta_\Phi)$, $\sum_\ell \alpha_y^{(\ell)} = \mathcal{J}_0(4\zeta_\Phi)$, and $\sum_\ell \beta_{x/y}^{(\ell)} = 1$. Thus,

$$\begin{aligned}H_{\text{eff}}^{U \gg \Omega} &= \frac{2J_0^2}{U} \sum_{mn} \left[\mathcal{J}_2(4\zeta_\Phi) (e^{2i\phi_{mn}} S_{m,n}^+ S_{m+1,n}^- + e^{-2i\phi_{mn}} S_{m,n}^- S_{m+1,n}^+ + 2S_{m,n}^z S_{m+1,n}^z) \right. \\ &\quad \left. + \mathcal{J}_0(4\zeta_\Phi) (S_{m,n}^+ S_{m,n+1}^- + S_{m,n}^- S_{m,n+1}^+ + 2S_{m,n}^z S_{m,n+1}^z) \right].\end{aligned}\quad (3.130)$$

The exchange strengths depend on Ω and U , but both limits give spin Hamiltonians with phases along x . This phase physically appears on the flip-flop and not the Ising term because the drive is spin-dependent. Thus, a phase difference only occurs if the electron virtually hops as one spin and returns as the other.

Let us discuss the regime $J_0 \ll \Omega \ll U$ a bit more, from a physics point of view. This spin Hamiltonian can be identified with the Heisenberg model in the presence of an artificial gauge field with flux Φ_\square per plaquette. Whenever the $S^z S^z$ -interaction is small, the Hamiltonian reduces to the fully-frustrated XY model in 2d, in which one cannot choose a spin configuration minimising the spin-exchange energy for all XY -couplings. In the classical limit, similarly to a type-II superconductor, the minimal energy configuration is known to be the Abrikosov vortex lattice [198, 199]. The realisation of the deep XY -regime with this particular driving protocol is limited, since $|\mathcal{J}_2(4\zeta_\Phi)| < 1$ but, at finite $S^z S^z$ -interaction a semi-classical study showed that vortices persist and can be thought

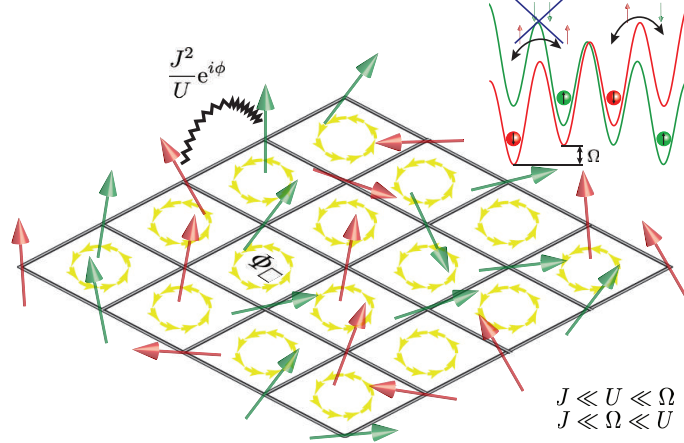


Figure 3.19: In the presence of a spin-dependent drive off-resonant with the interaction strength U (inset), the stroboscopic physics of the strongly-driven, strongly-correlated Fermi-Hubbard model is governed by an effective spin Hamiltonian in the presence of a gauge field.

of as half-skyrmion configurations of the Neél field [200–202]. Another interesting feature of the spin Hamiltonian is that it exhibits a Dzyaloshinskii-Moriya interaction term [203–206], $\mathbf{D}_{mn} \cdot (\mathbf{S}_{m+1,n} \times \mathbf{S}_{mn})$. The Dzyaloshinskii-Moriya coupling is spatially-dependent, polarised along the z -direction $\mathbf{D}_{mn} = \sin(\phi_{mn})\mathcal{J}_2(4\zeta_\Phi)\hat{\mathbf{n}}_z/2$, and present only along the x -lattice direction.

Finally, let us mention that spin-1/2 systems are equivalent to hard-core bosons. In this respect, $H_{\text{eff}}^{U \ll \Omega}$ and $H_{\text{eff}}^{\Omega \ll U}$ model hard-core bosons with strong nearest-neighbour interactions in the presence of a gauge field. For a flux of $\Phi_\square = \pi/2$ the non-interacting model has four topological Hofstadter bands. If we then consider the strongly-interacting model, and half-fill the lowest Hofstadter band ($S_{\text{tot}}^z = -3N_{\text{site}}/8$), the Heisenberg model supports a fractional quantum Hall ground state [69, 146, 207, 208]. Away from half-filling of the fermions, doublon and holon hopping terms appear in the effective Hamiltonian, and it would be interesting to study the effect of such correlated hopping terms [209] on this topological phase.

3.2.2.3.2 Away from Half-Filling: Consecutive Application of Schrieffer-Wolff Transformations

Let us now consider the case away from half-filling. We shall adopt a rather different (but equivalent) approach to derive the effective Hamiltonian in this case. In particular, we shall prove the validity of consecutive application of SWTs in models with clear time-scale separation in the regimes $U \ll \Omega$ and $\Omega \ll U$ ⁶.

Once again we choose a spin-dependent periodic driving of the type used to engineer the Harper-Hofstadter Hamiltonian [52, 53], see Eq. (3.124). From the definition of the drive, it becomes clear that opposite spin species are subject to opposite gradient potentials. Notice that spin-exchange processes along the x -direction are enabled by a resonant absorption of two photons, leading to an effective gauge field for the Heisenberg model at half-filling, see the inset of Fig. 3.19. We denote by $\zeta = A/\Omega$ the dimensionless interaction strength.

Let us first focus on the regime $J_0 \ll \Omega \ll U$ and show a different but equivalent derivation of the effective Hamiltonian comprising the Heisenberg model in an artificial gauge field. We can identify the largest frequency in the problem to be the interaction strength U , followed by the driving frequency Ω . Time-scale separation allows us to first perform an SWT on with the Hamiltonian in Eq. (3.114) w.r.t. the fast period $T_U = 2\pi/U$. In doing so we treat the time-fluctuations in the Hamiltonian due to the driving protocol at frequency Ω as slow variables, and apply the van Vleck HFE expansion with the fast period T_U only. This allows us to effectively take the T_Ω -oscillating terms out of the integrals in the van Vleck HFE, which results in the familiar $t - J$ model in a presence of a T_Ω -periodic drive. The remaining effective dynamics induced by the drive happens at time-scales T_Ω and, in the rotating frame, it is governed by the following intermediate Hamiltonian:

$$\begin{aligned} H_{\text{inter}}^{\text{rot}}(t) = & -J_0 \sum_{mn,\sigma} P_{m+1,n\bar{\sigma}} \left(e^{i\delta F_{m+1,n\sigma}(t)} c_{m+1,n\sigma}^\dagger c_{mn\sigma} + \text{h.c.} \right) P_{mn\bar{\sigma}} \\ & -J_0 \sum_{mn,\sigma} P_{m,n+1,\bar{\sigma}} \left(e^{i\delta F_{m,n+1,\sigma}(t)} c_{m,n+1,\sigma}^\dagger c_{mn\sigma} + \text{h.c.} \right) P_{mn\bar{\sigma}} \end{aligned} \quad (3.131)$$

⁶These two regimes of the off-resonant driving limit were reconciled in the previous section for half-filling.

$$\begin{aligned}
& + \frac{4J_0^2}{U} \sum_{m,n} \left[S_{m+1,n}^z S_{mn}^z + \frac{1}{2} \left(e^{i2\delta F_{m+1,n\sigma}(t)} S_{m+1,n}^+ S_{mn}^- + \text{h.c.} \right) - \frac{n_{m+1,n} n_{mn}}{4} \right] \\
& + \frac{4J_0^2}{U} \sum_{m,n} \left[S_{m,n+1}^z S_{mn}^z + \frac{1}{2} \left(e^{i2\delta F_{m,n+1,\sigma}(t)} S_{m,n+1}^+ S_{mn}^- + \text{h.c.} \right) - \frac{n_{m,n+1} n_{mn}}{4} \right],
\end{aligned}$$

where, again we drop the holon hopping term to order J_0^2/U , as it will be a minor correction to the order- J_0 hopping above [193]. If we consider the system away from half-filling, double occupancies are not suppressed and the spin part of the Hamiltonian (3.132) is merely a correction. The leading effective Hamiltonian away from half-filling after applying the van Vleck HFE once again with period T_Ω reads

$$\begin{aligned}
H_{\text{eff}}^{(0)} = & -J_0 \mathcal{J}_1(2\zeta_\Phi) \sum_{mn,\sigma} P_{m+1,n,\bar{\sigma}} \left(e^{i\phi_{mn}} c_{m+1,n,\sigma}^\dagger c_{mn\sigma} + \text{h.c.} \right) P_{mn\bar{\sigma}} \\
& -J_0 \mathcal{J}_0(2\zeta_\Phi) \sum_{mn,\sigma} P_{m,n+1,\bar{\sigma}} \left(c_{m,n+1,\sigma}^\dagger c_{mn\sigma} + \text{h.c.} \right) P_{mn\bar{\sigma}}.
\end{aligned} \quad (3.132)$$

Notice the presence of a gauge field in the hopping of doublons and holons.

Let us briefly see how we recover the half-filling result from the previous section within this method of consecutive SWT's. At half filling, one can safely neglect the terms in Eq. (3.132) containing the projectors P , as well as the terms proportional to $n_{m+1,n} n_{mn}/4$, similarly to the case for the static SWT. Now we apply the van Vleck HFE again with the slow frequency Ω . Since the leading correction term scales as $J_0^3/(\Omega U)$ we can safely neglect it to obtain

$$\begin{aligned}
H_{\text{eff}} \approx & \frac{4J_0^2}{U} \sum_{m,n} \left[S_{m+1,n}^z S_{mn}^z + \frac{\mathcal{J}_2(4\zeta_\Phi)}{2} \left(e^{2i\phi_{mn}} S_{m+1,n}^+ S_{mn}^- + \text{h.c.} \right) + S_{m,n+1}^z S_{mn}^z \right. \\
& \left. + \frac{\mathcal{J}_0(4\zeta_\Phi)}{2} \left(S_{m,n+1}^+ S_{mn}^- + \text{h.c.} \right) \right].
\end{aligned}$$

As anticipated, we once again confirm that in the regime $J_0 \ll \Omega \ll U$, applying the SWT at half filling leads to the Heisenberg model in an artificial gauge field. We stress that the effective dynamics of the system is best governed by the above effective Hamiltonian for

times $t \lesssim \Omega U / J_0^3$, set by the magnitude of the next-order correction term. Furthermore, choosing Ω and U to be incommensurate will lead to suppression of resonant effects, thus enhancing the time interval for which time-scale separation holds. This is possible because the spectra of both H_{int} and H_{drive} are discrete and commensurate.

Let us also briefly discuss the other non-resonant case $J_0 \ll U \ll \Omega$. This time the fastest frequency in the problem is the driving frequency Ω , followed by the interaction strength U . Thus, we go to the rotating frame w.r.t. the driving term first:

$$\begin{aligned} H_{\text{inter}}^{\text{rot}}(t) = & -J_0 \sum_{mn,\sigma} \left(e^{i\delta F_{m+1,n\sigma}(t)} c_{m+1,n\sigma}^\dagger c_{mn\sigma} + \text{h.c.} \right) \\ & -J_0 \sum_{mn,\sigma} \left(e^{i\delta F_{m,n+1,\sigma}(t)} c_{m,n+1,\sigma}^\dagger c_{mn\sigma} + \text{h.c.} \right) + U \sum_{mn} n_{mn,\uparrow} n_{mn,\downarrow}. \end{aligned} \quad (3.133)$$

Once again we make use of time-scale separation; applying the van Vleck HFE with period T_Ω results in the intermediate Hamiltonian to order $\mathcal{O}(\Omega^0) = \mathcal{O}(1)$:

$$\begin{aligned} H_{\text{inter}}^{(0)} = & -J_0 \mathcal{J}_1 (2\zeta_\Phi) \sum_{mn,\sigma} \left(e^{i\phi_{mn}} c_{m+1,n\sigma}^\dagger c_{mn\sigma} + \text{h.c.} \right) \\ & -J_0 \mathcal{J}_0 (2\zeta_\Phi) \sum_{mn,\sigma} \left(c_{m,n+1,\sigma}^\dagger c_{mn\sigma} + \text{h.c.} \right) \\ & + U \sum_{mn} n_{mn,\uparrow} n_{mn,\downarrow}. \end{aligned} \quad (3.134)$$

To complete the derivation, all one has to do is to apply the static SWT with frequency U . This mimics the conventional static SWT and directly leads to the following Heisenberg model at any filling

$$\begin{aligned} H_{\text{eff}} \approx & -J_0 \mathcal{J}_1 (2\zeta_\Phi) \sum_{mn,\sigma} P_{m+1,n,\bar{\sigma}} \left(e^{i\phi_{mn}} c_{m+1,n\sigma}^\dagger c_{mn\sigma} + \text{h.c.} \right) P_{mn\bar{\sigma}} \\ & -J_0 \mathcal{J}_0 (2\zeta_\Phi) \sum_{mn,\sigma} P_{m,n+1,\bar{\sigma}} \left(c_{m,n+1,\sigma}^\dagger c_{mn\sigma} + \text{h.c.} \right) P_{mn\bar{\sigma}} \\ & + J_{\text{eff}}^{\text{ex},x} \sum_{mn} \left[S_{m+1,n}^z S_{mn}^z + \frac{1}{2} \left(e^{2i\phi_{mn}} S_{m+1,n}^+ S_{mn}^- + \text{h.c.} \right) - \frac{n_{m+1,n} n_{mn}}{4} \right] \end{aligned}$$

$$+J_{\text{eff}}^{\text{ex},y} \sum_{mn} [S_{m,n+1}^z S_{mn}^z + \frac{1}{2} (S_{m,n+1}^+ S_{mn}^- + \text{h.c.}) - \frac{n_{m,n+1} n_{mn}}{4}], \quad (3.135)$$

with the effective exchange interactions $J_{\text{eff}}^{\text{ex},y} = 4 [J_0 \mathcal{J}_0(2\zeta_\Phi)]^2 / U$ and $J_{\text{eff}}^{\text{ex},x} = 4 [J_0 \mathcal{J}_1(2\zeta_\Phi)]^2 / U$. Notice that since $U \ll \Omega$ the leading Ω^{-1} -correction succumbs to the leading U^{-1} -Heisenberg model, so our assumption to drop the former is justified.

3.2.2.4 Resonant Driving and Doublon-Holon Physics

Novel physics arises in the resonant-driving regime $J_0 \ll U = l\Omega$. To illustrate this, we choose a one-dimensional system with the driving protocol

$$f_{j\sigma}(t) = jA \cos \Omega t,$$

which was realised experimentally by mechanical shaking [43, 43, 46, 47]. Unlike off-resonant driving, resonance drastically alters the effective Hamiltonian by enabling the lowest-order term $H_{\text{eff}}^{(0)}$: on resonance, the doublon-holon (dh) creation/annihilation terms h^\dagger survive the time-averaging, and the leading-order effective Hamiltonian reads

$$H_{\text{eff}}^{(0)} = \sum_{\langle ij \rangle, \sigma} \left[-J_{\text{eff}} g_{ij\sigma} - K_{\text{eff}} \left((-1)^{l\eta_{ij}} h_{ij\sigma}^\dagger + \text{h.c.} \right) \right], \quad (3.136)$$

where $\eta_{ij} = 1$ for $i > j$, $\eta_{ij} = 0$ for $i < j$, $J_{\text{eff}} = J_0 \mathcal{J}_0(\zeta)$, and $K_{\text{eff}} = J_0 \mathcal{J}_\ell(\zeta)$. The first term, $g_{ij\sigma}$, is familiar from the static SWT, with a renormalised coefficient J_{eff} . The term proportional to $h_{ij\sigma}^\dagger$ appears only in the presence of the resonant periodic drive and is the source of new physics in this regime. The sign factor η_{ij} arises from the distribution of negative signs in the time-periodic exponents, cf. Eq. (3.115). By adjusting the drive strength, one can tune J_{eff} and K_{eff} to a range of values, including zeroing out either one. Starting from a state with unpaired spins, dh pairs are created via resonant absorption of drive photons. Hence, holons and doublons become dynamical degrees of freedom governed by $H_{\text{eff}}^{(0)}$, with the Heisenberg model as a subleading correction. The dh production

rates and further properties of the system have been investigated both experimentally and theoretically [196, 210–220]. A DMFT study found that the AC field can flip the band structure, switching the interaction from attractive to repulsive [221].

The presence of double occupancies in strongly-interacting fermions in periodically-modulated optical lattices is intimately related to energy absorption [210, 211]. It has been shown that the doublon production rate is the same as the energy absorption rate [212, 213]. The former has been measured in a recent experiment [214] and a linear increase in time was found for weak driving amplitudes. In general, lattice modulation spectroscopy can be employed to determine the value of the interaction strength in the strongly-interacting limit. Furthermore, the weight of the double occupancy peak contains information about the spin ordering in the system. For example, an anti-ferromagnetic state is more amenable to formation of doublons, compared to a ferromagnetic or a paramagnetic state. Near half-filling, doublon formation has been proposed as a tool to detect an AFM state, expected to appear in the phase diagram of the FHM with repulsive interactions at low temperatures [215]. Previous work studying similar models focused on the weak-driving limit and employed time-dependent perturbation theory to second order [the linear-response term vanishes averaged over one cycle of the drive] [210, 211, 215, 216], and Fermi’s Golden rule [217]. The effective Floquet Hamiltonian in Eq. (3.137) is clearly non-perturbative and, therefore, allows for an accurate description of the dynamics over multiple cycles of the drive and in the regime of strong amplitudes, $\zeta \gtrsim 1$. For a better precision, one can compute the first leading correction. Micromotion effects can be understood by studying the kick operator.

Such correlated hopping models have been proposed to study high- T_c superconductivity [222–224]. To get an intuition about the effect of the new terms, we use the ALPS DMRG and MPS tools [225, 226] to calculate the ground state of $H_{\text{eff}}^{(0)}$ at half-filling. The many-body gap in the thermodynamic limit Δ is extracted from simulations of even-length chains with open boundary conditions by extrapolation in the system size: $\Delta(L) = \text{const}/L + \Delta$. We numerically confirm that the model features a transition be-

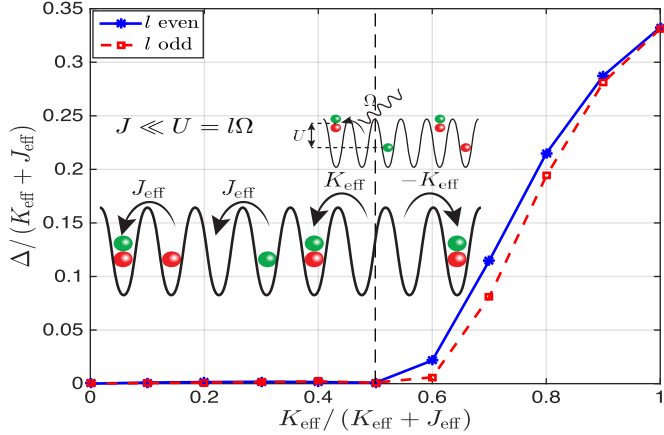


Figure 3.20: Resonant driving of the Fermi-Hubbard model enables doublon creation and dissociation processes (inset). The many-body gap Δ shows a phase transition from a gapless Luttinger liquid to gapped translation-invariance-broken phase. The doublon/holon hopping and creation coefficients J_{eff} and K_{eff} are controlled by varying the driving amplitude.

tween a symmetry-broken ordered phase and a gapless Luttinger liquid phase [222–224] as follows. For $K_{\text{eff}} > J_{\text{eff}}$, the physics is dominated by the dh creation/annihilation processes. In this regime, fermions can hop along the lattice by forming and destroying dh pairs. Thus, for l even the ground state exhibits bond-wave order with order parameter $B_j = \sum_{\sigma} c_{j+1,\sigma}^{\dagger} c_{j\sigma} + \text{h.c.}$, while the corresponding order parameter for l odd is not yet known. This order breaks translation invariance with a 2-site unit cell, and thus yields a many-body gap for even-length chains with open boundary conditions (cf. Fig. 3.20). For $K_{\text{eff}} < J_{\text{eff}}$, renormalisation group arguments show that bond ordering terms become irrelevant, leading to a gapless Luttinger liquid [227]. At $K_{\text{eff}} = J_{\text{eff}}$ and for l even, one surprisingly finds that the system is equivalent to free fermions. The existence of such a non-interacting point is rather striking, since it means that a strongly-driven, strongly-interacting system can effectively behave as if the fermions were free. This phenomenon can be understood by noticing that double occupancies, effectively forbidden in the absence of the drive by strong interactions, are re-enabled by the resonant driving term. As a result, whenever the amplitude of the driving field matches a special value to give $K_{\text{eff}} = J_{\text{eff}}$, the

matrix element for creation of doublons and holes becomes equal to their hopping rate and the effect of the strong interaction is completely compensated by the strong driving field. We emphasise that this is a highly non-perturbative effect since it requires a large drive amplitude $A \sim U = l\Omega$.

3.2.2.4.1 Doublon-Holon Physics with Artificial Gauge Fields

Let us now promote the dimensionality of the system to $d = 2$. Unlike above, here we choose the spin-dependent driving protocol of Eq. (3.124) which allows us to engineer doublon-holon physics in the presence of a gauge field. In this regime, the Hamiltonian $H^{\text{rot}}(t)$ in Eq. (3.114) is indeed periodic with the single frequency $\Omega = U$. Locking the driving frequency to the interaction strength leads to resonances which drastically change the behaviour of the system. Here, we show that they are captured by the van Vleck HFE, beyond linear response theory, since the effective Hamiltonian governs the slow dynamics over a multitude of periods, depending on how well the time-scale separation is pronounced. Moreover, this procedure does not suffer from vanishing denominators as is the case in conventional perturbation theory.

To this end, we average Eq. (3.114) over one period which is equivalent to keeping only the leading order term in the effective Hamiltonian:

$$\begin{aligned}
H_{\text{eff}}^{(0)} = & -J_{\text{eff}}^x \sum_{mn,\sigma} P_{m+1,n\sigma} \left(e^{i\phi_{mn}} c_{m+1,n\sigma}^\dagger c_{mn\sigma} + \text{h.c.} \right) P_{mn\bar{\sigma}} \\
& - J_{\text{eff}}^y \sum_{mn,\sigma} P_{m,n+1,\sigma} \left(c_{m,n+1,\sigma}^\dagger c_{mn\sigma} + \text{h.c.} \right) P_{mn\bar{\sigma}}, \\
& - \sum_{mn,\sigma} (K_{\text{eff}}^{L,x} n_{m,n\bar{\sigma}} e^{i\phi_{mn}} c_{mn\sigma}^\dagger c_{m+1,n\sigma} (1 - n_{m+1,n\bar{\sigma}}) \\
& \quad + K_{\text{eff}}^{R,x} n_{m+1,n\bar{\sigma}} e^{i\phi_{mn}} c_{m+1,n\sigma}^\dagger c_{mn\sigma} (1 - n_{mn\bar{\sigma}}) + \text{h.c.}) \\
& - \sum_{mn,\sigma} (K_{\text{eff}}^y n_{mn\bar{\sigma}} c_{mn,\sigma}^\dagger c_{m,n+1\sigma} (1 - n_{m,n+1,\bar{\sigma}}) \\
& \quad - K_{\text{eff}}^y n_{m,n+1,\bar{\sigma}} c_{m,n+1,\sigma}^\dagger c_{mn\sigma} (1 - n_{mn\bar{\sigma}}) + \text{h.c.}),
\end{aligned} \tag{3.137}$$

with $K_{\text{eff}}^{R,x} = J_0 \mathcal{J}_2(2\zeta_\Phi)$, $K_{\text{eff}}^{L,x} = J_0 \mathcal{J}_0(2\zeta_\Phi)$ and $K_{\text{eff}}^y = J_0 \mathcal{J}_1(2\zeta_\Phi)$. If the resonant periodic drive couples to the interaction strength instead, one can realise homogeneous doublon-holon creation amplitudes along the x -direction $K_{\text{eff}}^{L,x} = K_{\text{eff}}^{R,x} = J_0 \mathcal{J}_2(2\zeta_\Phi)$, as well as equal-sign doublon-holon amplitudes along the y -direction $K_{\text{eff}}^y = J_0 \mathcal{J}_1(2\zeta_\Phi)$. Note how the resonance condition $U = \Omega$ brings in additional terms in the effective Hamiltonian even in the leading order, which would not be there in the absence of the drive, i.e. for $A = 0$. Hence, these terms are dominant, compared to the Heisenberg model appearing at order U^{-1} , and lead to a fundamentally different physics. In fact, as we have already seen, they are responsible for enhancing the probability amplitude for doublon association and dissociation processes, in which two particles, initially populating neighbouring sites, are put on top of each other, or vice-versa. The necessary energy U is provided by one driving quantum Ω .

3.2.2.5 Reconciling the Resonant and Off-Resonant Limits: Crossover Regime

Since the argument we used for the Floquet realisation of strongly-correlated condensed matter models relies on a clear time-scale separation, it is interesting to explore how the three limits of (i) high-frequency $J_0 \ll U \ll \Omega$, (ii) strong interactions $J_0 \ll \Omega \ll U$, and (iii) resonant driving $J_0 \ll U = l\Omega$ can be reconciled to reproduce the stroboscopic dynamics of the system in the presence of the drive. To illustrate this, it suffices to consider the driven two-site Hubbard model. Thus, we also leave aside the gauge fields which would only obscure the equations. The Hamiltonian is

$$H(t) = -J_0 \sum_{\sigma} \left(c_{1\sigma}^\dagger c_{2\sigma} + \text{h.c.} \right) + A \cos(\Omega t) n_2 + U(n_{1\uparrow} n_{1\downarrow} + n_{2\uparrow} n_{2\downarrow}). \quad (3.138)$$

Following the discussion and notation of Eq. (3.114), we find the following rotating-frame Hamiltonian

$$H^{\text{rot}}(t) = -J_0 \sum_{\sigma} (\gamma^*(t) g_{12\sigma} + \text{h.c.}) - J_0 \sum_{\sigma} \left(\chi_R^*(t) h_{21\sigma}^\dagger + \chi_L^*(t) h_{12\sigma}^\dagger + \text{h.c.} \right),$$

$$\gamma^*(t) = e^{i\zeta \sin \Omega t}, \quad \chi_R^*(t) = e^{i(\zeta \sin \Omega t + U t)}, \quad \chi_L^*(t) = e^{-i(\zeta \sin \Omega t - U t)}, \quad (3.139)$$

where the operators $h_{ij\sigma}^\dagger$ and $g_{ij\sigma}$ are defined in Eq. (3.114), and $\zeta = A/\Omega$.

As we have already mentioned, in general the Hamiltonian $H^{\text{rot}}(t)$ is neither periodic with the frequency Ω , nor with the frequency U . In order to apply the high-frequency expansion, we first find two co-prime integers l and k such that $\Omega = k\Omega_0$ and $U = l\Omega_0$, where $\Omega_0 = 2\pi/T_{\Omega_0}$ is the common frequency, such that $H(t + T_{\Omega_0}) = H(t)$. We first need to Fourier-expand the functions $\gamma^*(t)$ and $\chi^*(t)$ in this common frequency Ω_0 . Note that, in principle, in order to apply the van Vleck HFE, one needs to make sure that $J_0 \ll \Omega_0$ which may not be true. However, as we shall see shortly, this condition is somewhat artificial since Ω_0 is not a physical scale but rather a mathematical construct. From the Jacobi-Anger identity it follows that $\chi_R^*(t) = \sum_{\ell=-\infty}^{\infty} \mathcal{J}_\ell(\zeta) e^{i(\ell k + l)\Omega_0 t} \equiv \sum_{\ell=-\infty}^{\infty} a_\ell^R e^{i\ell\Omega_0 t}$, and similarly for $\chi_L^*(t)$. Clearly, $\chi_R^*(t)$ has a non-zero time average. On the other hand, one can convince oneself that the coefficient a_0 is nonzero if and only if $l = -\ell k$. However, since l and k are co-prime, this can only hold true for $k = 1$ which means $U = l\Omega$. Physically, this condition is a manifestation of the conservation of quasienergy, saying that the doublon-holon creation term $h_{ij\sigma}^\dagger$ is non-zero at the level of the time-average Hamiltonian only when the interaction strength matches a multiple of the driving frequency.

We therefore focus only on the resonant case $U = l\Omega$, for which we find $a_\ell^R = \mathcal{J}_{\ell-l}(\zeta)$ and $a_\ell^L = \mathcal{J}_{-\ell-l}(\zeta)$. Fourier-decomposing the Hamiltonian in the rotating frame immediately leads to

$$\begin{aligned} H_\ell = -J_0 \sum_{\sigma} & \left[\mathcal{J}_\ell(\zeta) g_{12\sigma} + \mathcal{J}_{-\ell}(\zeta) g_{12\sigma}^\dagger \right. \\ & \left. + \mathcal{J}_{\ell-l}(\zeta) h_{21\sigma}^\dagger + \mathcal{J}_{-\ell+l}(\zeta) h_{12\sigma}^\dagger + \mathcal{J}_{-\ell-l}(\zeta) h_{21\sigma} + \mathcal{J}_{\ell+l}(\zeta) h_{12\sigma} \right]. \end{aligned} \quad (3.140)$$

All leading correction terms can be obtained from $H_{\text{eff}}^{(1)} = \sum_{\ell \neq 0} [H_\ell, H_{-\ell}] / \ell \Omega_0$. For simplicity let us concentrate on the spin exchange term only, which is proportional to the commutator $[h_{ij\sigma}^\dagger, h_{ji\bar{\sigma}}]$ [193]. One can shift the index of the Bessel functions in the sum

over ℓ , and after some algebra we obtain the resonant drive-renormalised exchange interaction $J_{\text{eff}}^{\text{ex}}$ as

$$J_{\text{eff}}^{\text{ex}}(\zeta) = 4 \frac{J_0^2}{\Omega_0} \sum_{\substack{\ell=-\infty \\ \ell \neq -l}}^{\infty} \frac{\mathcal{J}_\ell^2(\zeta)}{l + \ell} = 4 \frac{J_0^2}{U} \sum_{\substack{\ell=-\infty \\ \ell \neq -l}}^{\infty} \frac{\mathcal{J}_\ell^2(\zeta)}{1 + \ell/l} = 4 \frac{J_0^2}{U} \sum_{\substack{\ell=-\infty \\ \ell \neq -l}}^{\infty} \frac{\mathcal{J}_\ell^2(\zeta)}{1 + \ell\Omega/U}, \quad (3.141)$$

where in the second and third equalities we used $U = l\Omega_0 = l\Omega$ on resonance. We can now analytically continue U/Ω from an integer to the entire real axis. In doing so, note that the restriction in the summation $\ell \neq -l$ is superfluous for all non-integer values of U/Ω , i.e. everywhere away from resonance. This expression was first derived in Ref. [196] using an extended Hilbert space approach, which is different but equivalent [87] to the one presented in our work. We note in passing that the renormalisation of the spin-exchange coupling is the same, no matter whether the periodic driving couples to the density (as in our case) or to the interaction strength. The general validity of this type of analytic continuation is a subject of current investigation. It is clear that it will fail for nearly-resonant drives, but these cases can be treated introducing a small detuning δ to separate out the resonant part already in the lab frame, cf. Sec. 3.3.3. Nevertheless, we have verified that this procedure produces the correct answer also in the derivation of the Kondo model from the Anderson model where the two incommensurate energy scales are given by the interaction strength U for two electrons occupying the impurity level, and the relative shift V of the impurity level w.r.t. the Fermi sea, cf. Sec. 3.2.3.

Let us now briefly discuss the three limits of interest from the point of view of the general expression, Eq. (3.141). Consider first $J_0 \ll \Omega \ll U$. In this case, we can safely drop the restriction on the summation and, using the ‘trigonometric’ identity $\sum_\ell \mathcal{J}_\ell^2(\zeta) = 1$, we find the same exchange interaction as in the non-driven model, $J_{\text{eff}}^{\text{ex}} = 4J_0^2/U$. This is consistent with first doing the SWT w.r.t U and then applying the FHE w.r.t Ω , as we explained in Sec. 3.2.2.3.2. The Bessel functions which appear in front of the S^+S^- terms in Eqs. (3.129) and (3.130) are due to the spin-dependent drive and are not present for spin-independent protocols as the one considered in this section. In the high-frequency

regime $J_0 \ll U \ll \Omega$, only the $\ell = 0$ term contributes, and we find $J_{\text{eff}}^{\text{ex}} = 4J_{\text{eff}}^2/U$, with $J_{\text{eff}} = J_0 \mathcal{J}_0(\zeta)$. Again, this is exactly what one would expect from first applying the van Vleck HFE to obtain the FHM with renormalised hopping amplitude, and subsequently doing the SWT. Last, the resonant case $J_0 \ll U = l\Omega$ is clear from the derivation above. Note, however, that the exchange physics is of order Ω^{-1} , and hence it succumbs entirely to the doublon-holon physics in this regime.

3.2.2.6 Outlook

It bears mention that all regimes of the model are accessible using present-day cold atoms experiments [214]. For the resonant case, we discuss a loading sequence into the ground state of $H_{\text{eff}}^{(0)}$ in Sec. 4.6. Moreover, by tuning the frequency away from resonance, one can write $U = \delta U + l\Omega$ and go to the rotating frame w.r.t. the $l\Omega$ -term, keeping a finite on-site interaction δU in the effective Hamiltonian. This is required if one wants to capture important photon-absorption avoided crossings in the exact Floquet spectrum. Including artificial gauge fields is also straightforward in higher dimensions and expected to produce novel topological phases. By utilising resonance phenomena, this scheme only requires shaking the on-site potentials, which is easier in practice than other schemes which have suggested modulating the interaction strength to realise similar Hamiltonians [151, 228]. Both the resonant and non-resonant regimes that we analyse for the FHM yield systems directly relevant to the study of high-temperature superconductivity. More generally, we show that by using the generalised SWT, one can Floquet-engineer additional knobs controlling the model parameters of strongly-correlated systems, such as the spin-exchange coupling. Our methods are readily extensible to strongly-interacting bosonic systems, as well as many other systems under active research.

3.2.3 Low Energy Kondo Physics in the Periodically Driven Anderson Model

Another famous example of the SWT, actually its original application, is the reduction of the Anderson impurity model to the Kondo model [189]. In this section we continue our

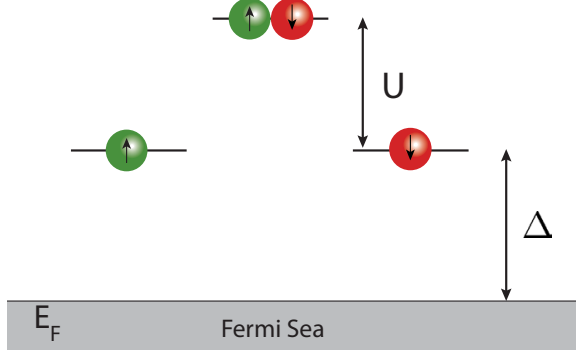


Figure 3.21: The Anderson model: spinful fermions can occupy an impurity level, separated from the Fermi sea by an energy Δ . The coupling between the impurity atom and the conducting electrons is V_d (not shown). Moreover, in the presence of interactions, an additional energy cost U has to be paid for the double occupancy of the impurity atom.

discussion of the equivalence of the SWT and the van Vleck HFE. Following the simple case of a two-level system, and the more sophisticated case of periodically-driven strongly interacting fermions, we now apply the generalised SWT to a periodically-driven impurity model. To make the discussion more transparent we shall analyse three specific examples of increasing complexity. First, we describe the non-driven non-interacting system, then a driven non-interacting one, and finally an interacting, non-driven one. The driven interacting system is very similar to the driven non-interacting one, and we only comment on the result.

3.2.3.1 A Non-Interacting Impurity Coupled to a Conducting Band

Consider the non-interacting Anderson model (also called the Resonant Level model or the Friedrichs model [229]) describing a single impurity coupled to free electrons (cf. Fig 3.21):

$$\begin{aligned}
 H &= H_0 + H_1, \\
 H_0 &= \sum_{k,s} \epsilon_k n_{ks} + \Delta \sum_s n_{ds}, \\
 H_1 &= \frac{1}{\sqrt{L^D}} \sum_{ks} \left(V_d c_{ks}^\dagger d_s + \text{h.c.} \right).
 \end{aligned} \tag{3.142}$$

Here d refers to the impurity atom with an energy Δ , $s = \uparrow, \downarrow$ is the spin index, $\epsilon_k \geq 0$ is the dispersion of the band electrons, V_d is the hybridisation strength, L is the linear system size, and D is the dimensionality of the system. The prefactor $1/\sqrt{L^D}$ ensures that in real space the coupling to the impurity V_d is independent of the system size. The fermionic creation and annihilation operators obey the canonical commutation relations $\{c_{ks}, c_{k's'}^\dagger\}_+ = \delta_{kk'}\delta_{ss'}$, and $\{d_s, d_{s'}^\dagger\}_+ = \delta_{ss'}$. As usual, $n_{ks} = c_{ks}^\dagger c_{ks}$ and $n_{ds} = d_s^\dagger d_s$ are the number operators. This is a generalisation of the simple two-level setup discussed in Sec. 3.2.1. We are interested in the situation where Δ is the largest energy scale in the system: $\Delta \gg V_d, \epsilon_k$, and the coupling V_d between the conducting band and the impurity is small (compared to the Fermi energy). In this limit, the impurity can only be occupied by virtual processes, which effectively dress the low-energy conduction-band electrons.

As Schrieffer and Wolff pointed out [189], standard perturbation theory fails to provide an accurate description of the weak-coupling limit, $V_d \rightarrow 0$, since higher order terms in V_d appear together with energy denominators $\epsilon_k - \epsilon_{k'}$. Near the Fermi surface, the latter can be arbitrarily small, and hence render perturbation theory divergent. To solve this problem, they suggested to perform a unitary transformation, which later became known as the Schrieffer-Wolff transformation (SWT) [189]. This transformation eliminates the dependence of the Hamiltonian on V_d to linear order. As a result, the limiting procedure $V_d \rightarrow 0$ becomes well-defined.

Here, we show that we can achieve a similar goal by first doing a transformation into a rotating frame with respect to the operator $\Delta \sum_s n_{ds}$, and subsequently applying the van Vleck high-frequency expansion (HFE) to this new periodic Hamiltonian. This is a direct extension of the procedure we used for the two-site single-particle problem discussed in Sec. 3.2.1, and follows the same guidelines as the discussion of the periodically-driven strongly-interacting Fermi-Hubbard model in Sec. 3.2.2. By doing this transformation, we are eliminating the energy scale Δ from the effective description at the expense of

introducing a fast periodic time dependence in the hybridisation term:

$$H^{\text{rot}}(t) = H_{\text{band}} + e^{-i\Delta t} H^- + e^{i\Delta t} H^+,$$

$$H_{\text{band}} = \sum_{k,s} \epsilon_k n_{ks}, \quad H^- = \frac{1}{\sqrt{L^D}} \sum_{ks} V_d c_{ks}^\dagger d_s, \quad H^+ = (H^-)^\dagger. \quad (3.143)$$

We can now apply the van Vleck HFE, since we have a periodic Hamiltonian. Evidently, the time-averaged Hamiltonian, $H_{\text{eff}}^{(0)} = H_{\text{band}}$, so the linear terms in V_d average to zero. Notice how the absence of linear terms, which can be considered as the main requirement for the choice of the generator of SWTs, arises naturally in this setup. The Δ^{-1} -correction includes the following commutator⁷ $[H^+, H^-]$. This commutator leads to scattering between band electrons to order Δ^{-1} , and thus has to be taken into account for finite Δ . If we restrict the discussion to order Δ^{-1} , we find

$$H_{\text{eff}} = H_{\text{band}} - \frac{|V_d|^2}{\Delta L^D} \sum_{kk'} \Psi_k^\dagger \Psi_{k'} + \frac{|V_d|^2}{\Delta} \Psi_d^\dagger \Psi_d + \mathcal{O}(\Delta^{-2}), \quad (3.144)$$

where we introduced the compact spinor notation:

$$\Psi_k = \begin{pmatrix} c_{k\uparrow} \\ c_{k\downarrow} \end{pmatrix}, \quad \Psi_d = \begin{pmatrix} c_{d\uparrow} \\ c_{d\downarrow} \end{pmatrix}, \quad (3.145)$$

and the sum over spin indices is assumed. For example $\Psi_d^\dagger \Psi_d = c_{d\uparrow}^\dagger c_{d\uparrow} + c_{d\downarrow}^\dagger c_{d\downarrow} = n_{d\uparrow} + n_{d\downarrow}$. The second term in this effective Hamiltonian represents the static scattering from the impurity atom, while the third term is the new impurity potential. As in the two-level system from Sec. 3.2.1, the kick operator $K_{\text{eff}}(t)$ governing the micromotion can be calculated explicitly using Eqs. (2.45):

$$K_{\text{eff}}(t) = \frac{1}{i\Omega} (e^{i\Delta t} H^+ - e^{-i\Delta t} H^-) \quad (3.146)$$

⁷Here we do not consider the commutators $[H^\pm, H_0]$ since we are discussing the van Vleck series, c.f. Eq. (2.45), not the Floquet-Magnus series, c.f. Eq.(2.41).

In particular, if we evaluate it at stroboscopic times lT we find

$$K_{\text{eff}}(lT) = \frac{1}{i\Omega} \frac{V_d}{\sqrt{L^D}} \sum_{ks} [d_s^\dagger c_{ks} - c_{ks}^\dagger d_s]. \quad (3.147)$$

In the language of the SWT, the effective Hamiltonian H_{eff} keeps track of the spectrum of the system and the kick operator $K_{\text{eff}}(t)$ realises the rotation of the basis. As we discussed many times already, the dynamics of the system can be studied using either the effective Hamiltonian and the effective kick, or the stroboscopic Hamiltonian and the stroboscopic kick. As usual, the stroboscopic Hamiltonian $H_F[t_0]$ is less symmetric than the effective Hamiltonian H_{eff} and the stroboscopic kick operator is identically zero at times $t = t_0 + lT$, i.e. $K_F[t_0](t_0 + lT) = 0$ signifying that in the stroboscopic picture there is no need to rotate the basis states.

Usually, in the context of the conventional SWT, the subtleties associated with the kick operators are not discussed. Moreover, the SWT can become quite cumbersome if one needs to go to higher order. On the other hand, the van Vleck HFE naturally allows us to deal with the kick operators and go to higher order in Δ^{-1} if necessary [59].

3.2.3.2 A Periodically-Driven Impurity Model

Once again we demonstrate how to extend the SWT to periodically driven systems. Let us add the additional time-periodic term

$$H_1(t) = -A \cos \Omega t \sum_s n_{d,s}$$

to the Hamiltonian (3.142). This system was studied from the point of view of Floquet theory in Refs. [97, 230, 231]. As in the example of the two-level system, we assume a commensurate driving frequency and impurity energy: $\Delta = l\Omega$, where $l \in \mathbb{N}$ (see the discussion in Sec. 3.2.1.2 about the motivation for this assumption and how to relax it). Furthermore, as before we assume that Ω and hence Δ are the largest energy scales in the

problem.

We eliminate the impurity level and the driving altogether, by going to the rotating frame defined by $V(t) = \exp [i(\zeta \sin \Omega t - l\Omega) \sum_s n_{d,s}]$, $\zeta = A/\Omega$. This leads to

$$H^{\text{rot}}(t) = \sum_k \epsilon_k \Psi_k^\dagger \Psi_k + \frac{1}{\sqrt{L^D}} \sum_k V_d e^{i\zeta \sin \Omega t - il\Omega t} \Psi_k^\dagger \Psi_d + \text{h.c.} \quad (3.148)$$

We can now apply the van Vleck expansion. The derivation of the effective Hamiltonian follows the same guidelines as that of the driven two-level system. The resulting time-averaged Hamiltonian and the leading correction are given by

$$\begin{aligned} H_{\text{eff}}^{(0)} &= \sum_k \epsilon_k \Psi_k^\dagger \Psi_k + \frac{1}{\sqrt{L^D}} \sum_k V_d \mathcal{J}_l(\zeta) \Psi_k^\dagger \Psi_d + \text{h.c.}, \\ H_{\text{eff}}^{(1)} &= -\frac{|V_d|^2}{\Delta L^D} \tilde{g}_l(\zeta) \sum_{k,k'} \Psi_k^\dagger \Psi_{k'} + \frac{|V_d|^2}{\Delta} \tilde{g}_l(\zeta) \Psi_d^\dagger \Psi_d, \end{aligned} \quad (3.149)$$

where \mathcal{J}_l is the l -th Bessel Function of first kind, and the function $\tilde{g}_l(\zeta)$ is defined in Eq. (3.108).

Contrary to the situation in the non-driven case, here in the infinite-frequency limit, the hybridisation terms which mix the band and the impurity levels do not vanish. This is very similar to the effect we already observed for the driven two-level system and the resonant driving regime of the FHM. So unlike the static case this linear coupling has direct physical implications, because the impurity level in the rotating frame is resonant with the bottom of the band. It then follows that the population of the impurity will be significant at any finite driving frequency as long as $\mathcal{J}_l(\zeta)$ is not too small. Physically, this corresponds to multi-photon absorption processes.

Let us point out that one can similarly analyse the limits where $\Delta = l\Omega + \delta\Delta$, with the off-set $|\delta\Delta| < \Omega/2$. As we discussed earlier, in the rotating frame, this off-set leads to an extra (small) static impurity potential $\delta\Delta n_d$. It is intuitively clear that the occupation of the impurity in the steady state will be sensitive to the position of this potential with respect to the Fermi level. A large impurity occupation is possible for $0 \leq \delta\Delta \leq E_F$ (where

E_F is the Fermi energy). This mechanism of populating the higher level is expected to open up the way towards studying heating in the high-frequency regime if one replaces the impurity atom by an entire excited band. The issue of heating requires a separate careful analysis, and is discussed in Chapter 5. We also refer the reader to recent works, where this issue was partially addressed for the Kondo model [114].

3.2.3.3 The Anderson Model

Let us now go back to the static model and add an interaction term to the lab-frame Hamiltonian. The Hamiltonian describing repulsion between the electrons on the impurity is given by:

$$H_{\text{int}} = U n_{d\uparrow} n_{d\downarrow}. \quad (3.150)$$

For large interactions this term effectively penalises the double occupancy of the impurity site. It is well known that this leads to the effective low-energy Kondo Hamiltonian [189].

To emphasise once again the relation between the van Vleck expansion and the SWT, we assume that Δ and U are the largest energy scales and once again we eliminate both of them together by going to the rotating frame:

$$V(t) = \exp \left(-i\Delta t \sum_s n_{ds} \right) \exp (-iUt n_{d\uparrow} n_{d\downarrow}). \quad (3.151)$$

Note that this transformation consists of the product of two commuting operators and it is a direct generalisation of the transformation used in the non-interacting non-driven model above. The Hamiltonian in the rotating frame gets modified according to:

$$\begin{aligned} H^{\text{rot}}(t) &\longrightarrow H^{\text{rot}}(t) + e^{-i\Delta t} (e^{-iUt} - 1) W^- + e^{i\Delta t} (e^{iUt} - 1) W^+, \\ W^- &= \frac{1}{\sqrt{L^D}} \sum_{ks} V_d c_{ks}^\dagger d_s n_{d,\bar{s}}, \end{aligned} \quad (3.152)$$

where $H^{\text{rot}}(t)$ on the RHS above is the Hamiltonian (3.143), and \bar{s} denotes the opposite spin species to s . The new terms W^\pm represent an interaction-dependent hopping from the

conducting band to the impurity. In general, the interaction U and the impurity energy Δ need not be commensurate, and thus the transformation to the rotating frame is not periodic. In the spirit of our previous discussion we assume commensurability, $U = m\Delta$, and moreover choose $m = 1$. One can check that the resulting Kondo Hamiltonian is correctly reproduced for any m and by taking analytic continuation to non-integer m one obtains the correct result for any values of U and Δ . In addition, one can easily convince oneself that by choosing a common frequency Ω from the two energies U and Δ : $U = l\Omega$, $\Delta = m\Omega$, one also reproduces exactly the result of the conventional SWT.

The interaction-dependent hopping W^\pm does not contribute to the time-averaged Hamiltonian $H_{\text{eff}}^{(0)}$. However, it gives an important contribution to the first-order correction to the effective Hamiltonian coming from the commutators $[W^+, W^-]$, $[W^+, H^-]$, and $[W^-, H^+]$. Evaluating these explicitly, we find

$$\begin{aligned} H_{\text{eff}} = & H_{\text{band}} - \frac{|V_d|^2}{4\Delta L^D} \sum_{kk'} \left(\Psi_k^\dagger \boldsymbol{\sigma} \Psi_{k'} \right) \cdot \left(\Psi_d^\dagger \boldsymbol{\sigma} \Psi_d \right) \\ & + \frac{|V_d|^2}{\Delta L^D} \sum_{kk'} \left[-1 + \frac{1}{4} \Psi_d^\dagger \Psi_d \right] \Psi_k^\dagger \Psi_{k'} + \frac{|V_d|^2}{\Delta} \Psi_d^\dagger \Psi_d + \mathcal{O}(\Omega^{-2}). \end{aligned} \quad (3.153)$$

For our choice of parameters we have $U = \Delta$. Here $\boldsymbol{\sigma}$ is the vector of Pauli matrices and the summation over the spin indices is taken care of using the spinor notation. It is immediate to recognize that we have reproduced precisely the Kondo coupling, which one otherwise derives with the conventional SWT [189].

As before, we note that the inverse-frequency (van Vleck) expansion, allows one to explicitly take into account both the slow dynamics of the system through the Floquet Hamiltonian, and the fast dynamics through the kick operator $K_{\text{eff}}(t)$. Finally, we note in passing that including the driving in the interacting model is straightforward. The new term appearing in $H_{\text{eff}}^{(0)}$ will be identical to the one in Eq. (3.149) for the non-interacting model, while the other terms will be modified by functions similar to $\tilde{g}_l(\zeta)$. Last, we also

point out that from Eq. (2.45) it becomes clear that, to leading order in Ω^{-1} , the kick operator $K_{\text{eff}}^{(1)}(t)$ is modified by the interactions, accordingly, both in the driven and the non-driven Anderson model.

3.2.4 Discussion

It becomes evident from the analysis in the preceding sections how to generalise the SWT to arbitrary strongly-interacting periodically-driven models: First, we identify the large energy scale denoted by λ (e.g., $\lambda = U$) and write the Hamiltonian as $H = H_0 + \lambda H_1 + H_{\text{drive}}(t)$. Second, we go to the rotating frame using the transformation $V(t) = \exp\left(-i\lambda t H_1 - i \int^t H_{\text{drive}}(t') dt'\right)$ to get a new time-dependent Hamiltonian with frequencies⁸ λ and Ω : $H^{\text{rot}}(t) = V^\dagger(t) H_0 V(t)$. Finally, depending on whether we want to discuss resonant or nonresonant coupling, we apply the van Vleck HFE to obtain the effective Hamiltonian H_{eff} order by order in λ^{-1} and Ω^{-1} . This procedure will generally work if a closed-form evaluation of $H^{\text{rot}}(t)$ is feasible. For instance, H_1 can be a local Hamiltonian or can be written as a sum of local commuting terms. The method also works if the interaction strength is periodically modulated [151, 154, 228].

3.3 Resonant Driving: the Rotating Wave Approximation and Beyond

The Rotating Wave Approximation (RWA) is a powerful tool in (quantum) optics and atomic physics, which allows one to study the dynamics of atoms exposed to electromagnetic radiation. Laser-driven transitions between atomic levels are fundamental to many present-day experiments with ultracold atoms [232, 233], and can be performed with astonishing precision. More generally, the RWA can be used to study resonant photon absorption processes, and quantify the dynamics of states population in noninteracting systems, featuring Rabi oscillations.

In this section, we shall revisit the Rotating Wave Approximation from the point of view

⁸Formally, the identification of a well-defined frequency λ in the rotating frame requires that the spectrum of H_1 is discrete and commensurate, which is the case whenever H_1 is a density-density interaction.

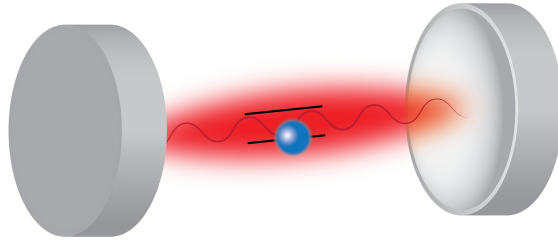


Figure 3.22: The Rabi Model: a two-level system interacts with a quantised electromagnetic field.

of Floquet theory. We focus on the Rabi model, the RWA limit of which is the famous Jaynes-Cummings Hamiltonian governing the physics of a two-level system interacting with a quantised electromagnetic mode. Below, we first discuss how the inverse-frequency expansion allows one to derive corrections to the leading-order RWA physics. After that, we briefly elaborate on the phenomenon of parametric resonance and show how one can understand it within the RWA. This will ultimately lead us to an improved description of the inverse-frequency expansion for frequencies below the single-particle bandwidth, and discuss the limitations of this approach.

3.3.1 The Rabi Model and the Jaynes-Cummings Hamiltonian

The prototypical example for the Rotating Wave Approximation (RWA) is the Rabi model, which describes a two-level atom coupled to a quantised electromagnetic field, see Fig. 3.22. In this system, once again a transformation to the rotating frame eliminates highly excited states, and leads to a renormalised description of the low-energy physics. The lab-frame Hamiltonian is static and reads

$$H = \frac{\omega_L}{2} a^\dagger a + \frac{\Omega}{4} \sigma^z + g (a^\dagger \sigma^- + a \sigma^+) + g' (a \sigma^- + a^\dagger \sigma^+), \quad (3.154)$$

where a^\dagger (a) creates (destroys) a photon in the electromagnetic (cavity) mode of frequency $\omega_L/2$, and the two atomic levels, with energy separation $\Omega/2$, are described by the Pauli matrices. Choosing the laser frequency ω_L to match resonantly the difference of the energies of the two levels of the atom, $\Omega = \omega_L$, and going to the rotating frame, $a \rightarrow a e^{-i\Omega t/2}$, $\sigma^- \rightarrow \sigma^- e^{-i\Omega t/2}$, the Rabi Hamiltonian reads

$$\begin{aligned} H^{\text{rot}}(t) &= H_0 + H^+(t) + H^-(t), \\ H_0 &= g \left(a^\dagger \sigma^- + a \sigma^+ \right), \\ H^-(t) &= g' e^{-i\Omega t} a \sigma^-, \quad H^+(t) = g' e^{+i\Omega t} a^\dagger \sigma^+. \end{aligned} \quad (3.155)$$

Notice that this rot-frame Hamiltonian is periodic with the frequency Ω . We mention in passing that the solution of the Rabi model for $g = g'$ can be expressed in terms of a functional differential equation [234]. Moreover by adding a magnetic field along the z -direction one can obtain an entire line of integrable points, where the generalised Rabi model is supersymmetric [235].

Applying the Floquet-Magnus (van Vleck) inverse-frequency expansion to order Ω^{-1} to the Rabi Hamiltonian gives:

$$\begin{aligned} H_F[0] &= g \left(a^\dagger \sigma^- + a \sigma^+ \right) + \frac{g'^2}{\Omega} \left(a^\dagger a \sigma^z - \sigma^+ \sigma^- \right) + \frac{g g'}{\Omega} \left(a^2 + (a^\dagger)^2 \right) \sigma^z + \mathcal{O}(\Omega^{-2}), \\ H_{\text{eff}} &= g \left(a^\dagger \sigma^- + a \sigma^+ \right) + \frac{g'^2}{\Omega} \left(n \sigma^z - \sigma^+ \sigma^- \right) + \mathcal{O}(\Omega^{-2}), \\ K_F^{(1)}[0](t) &= \frac{g'}{i\Omega} \left((e^{i\Omega t} - 1) a^\dagger \sigma^+ - (e^{-i\Omega t} - 1) a \sigma^- \right), \\ K_{\text{eff}}^{(1)}(t) &= \frac{g'}{i\Omega} \left(e^{i\Omega t} a^\dagger \sigma^+ - e^{-i\Omega t} a \sigma^- \right). \end{aligned} \quad (3.156)$$

It is also straightforward to obtain the second-order correction to the Floquet Hamiltonian:

$$\begin{aligned} H_F^{(2)}[0] &= -\frac{2g^2g'}{\Omega^2} (a^2 a^\dagger \sigma^- - 2a \sigma^- - a^3 \sigma^+ + \text{h.c.}) \\ &\quad - 2\frac{g'^3}{\Omega^2} (n a \sigma^- - 2a \sigma^- + \text{h.c.}) \end{aligned}$$

$$\begin{aligned}
& + 2 \frac{gg'^2}{\Omega^2} (2a^\dagger \sigma^- + a^\dagger n \sigma^- - \frac{1}{2} a^3 \sigma^- + \text{h.c.}), \\
H_{\text{eff}}^{(2)} &= \frac{gg'^2}{\Omega^2} (a^\dagger \sigma^- \sigma^z + \text{h.c.})
\end{aligned} \tag{3.157}$$

It follows that, up to order Ω^{-2} , the effective Hamiltonian conserves the sum of the total number of photons and the z -component of the spin and, therefore, it only couples pairs of states such as $|1\rangle = |n, +\rangle$ and $|2\rangle = |n + 1, -\rangle$.⁹ Here n is the number of photons and \pm indicates the values of the spin-projection along the z -axis. Thus, to obtain the spectrum to order Ω^{-2} , we simply need to diagonalise a collection of independent two-by-two Hamiltonians. The matrix elements of the effective Hamiltonian in the sector with n and $n + 1$ photons coupled read:

$$\begin{aligned}
\langle 1 | H_{\text{eff}}^{(0)} + H_{\text{eff}}^{(1)} + H_{\text{eff}}^{(2)} | 1 \rangle &= -\frac{g'^2}{\Omega} (1 - n), \\
\langle 2 | H_{\text{eff}}^{(0)} + H_{\text{eff}}^{(1)} + H_{\text{eff}}^{(2)} | 2 \rangle &= -\frac{g'^2}{\Omega} (n + 1) \\
\langle 1 | H_{\text{eff}}^{(0)} + H_{\text{eff}}^{(1)} + H_{\text{eff}}^{(2)} | 2 \rangle &= \sqrt{n + 1} \left(g + \frac{gg'^2}{\Omega^2} \right).
\end{aligned}$$

From this it is immediate to compute the spectrum:

$$E_{n+1} = -\frac{g'^2}{\Omega} \pm g\sqrt{n+1} \left(1 + \left(\frac{g'}{g} \right)^2 \frac{n^2}{2(n+1)} + \frac{g'^2}{\Omega^2} \right) + \mathcal{O}(\Omega^{-3}). \tag{3.158}$$

In the case of $g' = 0$, the spectrum reduces to the Jaynes-Cummings one, as it should, and exhibits the hallmark feature of a quantised Rabi frequency $\Omega_R = g\sqrt{n+1}$. The inverse-frequency expansion captures both the Bloch-Siegert shift g'^2/Ω , which has been known to be the leading correction to the spectrum for a long time, as well as the sub-leading correction of order Ω^{-2} . Many terms in the stroboscopic Hamiltonian break the conservation of the total number of photons and spins, and significantly complicate the

⁹One has to keep in mind though that the photons and the spins are dressed by the kick operator and this conservation law breaks down for the bare (undressed) operators. In this sense, the kick operator helps one find dressed photon-spin states, in which the physics is described by a few degrees of freedom, similarly to the Landau quasiparticles in Fermi liquid theory.

analysis of the Floquet Hamiltonian. However, these terms do not appear in the effective Hamiltonian, and hence their effect must be captured by the kick operator $K_{\text{eff}}(t)$ (see Eqs. (2.46) and (3.146)). Recently, it was argued that this type of terms can be important for the stabilisation of finite-density quantum phases [236].

The Rabi model can be realised experimentally using highly controllable optical cavities, whose size determines the mode frequency $\Omega/2$ through the quantisation/boundary conditions. In the same spirit as in the two-level system, the driven FHM or the Anderson model, one can imagine shaking the cavity boundaries out of phase periodically, which would induce a periodic modulation of the frequency Ω . To study the physics of this model, one could go to a rotating frame and apply the HFE. In this case, the counter-rotating (particle non-conserving) terms, $g'a\sigma^- + \text{h.c.}$, will not vanish in the zeroth order, in analogy with the emergent hybridisation terms at the level of the time-averaged Hamiltonian in the models discussed in Secs. 3.2.1 and 3.2.3.2, potentially leading to new qualitative phenomena.

Let us conclude this section by pointing out that, through the leading terms in the inverse-frequency expansion, one can formally understand the generation of stationary optical lattice potentials used to trap neutral atoms [232]. It is then not difficult to find subleading terms including those responsible to various heating processes [237].

3.3.2 Parametric Resonance from the Rotating Wave Approximation

One of the most fascinating phenomena in periodically-driven systems is parametric resonance. It models, among others, the dynamics of a child playing on a swing by periodically standing and squatting to keep the system driven. Parametric resonance occurs whenever the drive frequency is close to twice the natural frequency of the non-driven oscillator. A hallmark feature is the exponentially (in time) growing amplitude of oscillations of various physical quantities and their fluctuations which is observed on top of the regular oscillatory motion. In realistic physical systems, where the harmonicity of the non-driven model is rather approximate, parametric resonance is generally expected to govern the transient

dynamics before the role of the non-linearity sets in.

Let us dive into the details of the parametric stability analysis by demonstrating how to derive the stability criterion with the help of the Rotating Wave Approximation (RWA)¹⁰. Since the dynamics of quadratic models is the same in quantum and classical systems, we choose to study the quantum parametric oscillator with Hamiltonian

$$H(t) = \frac{1}{2} (p^2 + \omega_0^2 x^2 + \alpha \omega_0^2 \cos(\Omega t) x^2). \quad (3.159)$$

Writing this Hamiltonian using ladder operators $x = 1/\sqrt{2\omega_0}(\gamma^\dagger + \gamma)$ and $p = i\sqrt{\omega_0/2}(\gamma^\dagger - \gamma)$, and dropping any (time-dependent) constants leads to

$$H(t) = \omega_0 \left(1 + \frac{\alpha}{2} \cos \Omega t \right) \gamma^\dagger \gamma + \frac{\alpha \omega_0}{4} \cos \Omega t \left(\gamma^\dagger \gamma^\dagger + \text{h.c.} \right).$$

If we parametrise the operators as $\gamma(t) = u'(t)\gamma(t=0) - v'^*(t)\gamma^\dagger(t=0)$, with $u'(t=0) = 1$ and $v'(t=0) = 0$, we can write Heisenberg's EOM for the functions $u(t)$ and $v(t)$ as

$$\begin{aligned} i \frac{d}{dt} \begin{pmatrix} u' \\ v' \end{pmatrix} &= \begin{pmatrix} \omega_0 + \frac{\alpha}{2} \omega_0 \cos \Omega t & \frac{\alpha}{2} \omega_0 \cos \Omega t \\ -\frac{\alpha}{2} \omega_0 \cos \Omega t & -(\omega_0 + \frac{\alpha}{2} \omega_0 \cos \Omega t) \end{pmatrix} \begin{pmatrix} u' \\ v' \end{pmatrix} \\ &= [\omega_0 \sigma^z + W(t)] \begin{pmatrix} u' \\ v' \end{pmatrix} + \frac{\alpha}{2} \omega_0 \cos \Omega t \begin{pmatrix} 0 & 1 \\ -1 & 0 \end{pmatrix} \begin{pmatrix} u' \\ v' \end{pmatrix}, \end{aligned} \quad (3.160)$$

where the matrix $W(t) = \frac{\alpha}{2} \omega_0 \cos(\Omega t) \sigma^z$ has zero time-average and σ^z is the Pauli matrix in Bogoliubov space. We now apply the transformation $\tilde{u}'(t) = e^{i2\omega_0 t} u'(t)$, $\tilde{v}'(t) = v'(t)$ which brings the EOM into the form

$$i \frac{d}{dt} \begin{pmatrix} \tilde{u}' \\ \tilde{v}' \end{pmatrix} = \left[\omega_0 + W(t) + \frac{\alpha}{2} \omega_0 \begin{pmatrix} 0 & e^{-2i\omega_0 t} \cos \Omega t \\ -e^{+2i\omega_0 t} \cos \Omega t & 0 \end{pmatrix} \right] \begin{pmatrix} \tilde{u}' \\ \tilde{v}' \end{pmatrix}.$$

¹⁰A very similar method was used to study the parametric instability in periodically-driven Luttinger liquids [76].

So far the treatment of the parametric oscillator EOM was exact. However, the present form of the equation allows to easily identify the terms responsible for the parametric resonance. To this end, we apply the rotating wave approximation (RWA) (i) keeping in mind that the time-average of $W(t)$ vanishes identically, and (ii) dropping any counter-rotating terms. We find that the dominant contribution to the dynamics appears for $2\omega_0 = \Omega_c$, which sets the critical driving frequency on resonance. In general, however, we can allow for some detuning δ , defined by $\Omega = 2\omega_0 - \delta$. The resulting effective RWA-EOM assumes the simple form:

$$i\frac{d}{dt} \begin{pmatrix} \tilde{u}' \\ \tilde{v}' \end{pmatrix} = \begin{pmatrix} \omega_0 & \frac{\omega_0\alpha}{4}e^{i\delta t} \\ -\frac{\omega_0\alpha}{4}e^{-i\delta t} & \omega_0 \end{pmatrix} \begin{pmatrix} \tilde{u}' \\ \tilde{v}' \end{pmatrix}. \quad (3.161)$$

Solving exactly the equation above, we find the two Lyapunov exponents $\lambda_{1,2} = \omega_0 \pm i\omega_0\alpha/4\sqrt{1 - (2\delta/\alpha\omega_0)^2}$ as a function of the detuning $\delta = \Omega - 2\omega_0$. Hence, the maximum instability growth rate appears on resonance, i.e. for $\delta = 0$, and is given by $\alpha\omega_0/4$. The stability criterion and the instability growth rate derived above with the help of the RWA agree precisely with the standard results obtained using two-times perturbation theory or by other means [7].

From the point of view of Floquet theory, the situation is much more interesting. As we showed above, whenever the driving frequency hits twice the natural frequency of the oscillator, $\Omega = 2\omega_0$, various physical observables feature exponential growth in time due to the imaginary Lyapunov exponents. However, the full quantum mechanical treatment of this driven oscillator is much more intriguing, as it has to accommodate this exponential growth in the wave function of the system which is expected to be normalised.

The Floquet solution of the periodically driven quantum oscillator was derived in Ref. [238] for a system described by the Hamiltonian:

$$H(t) = \frac{p^2}{2m} + \frac{m\omega_0^2}{2}x^2 + \frac{\alpha}{2} \{p, x\}_+ \sum_{n=-\infty}^{+\infty} \delta(t - nT), \quad (3.162)$$

where α is the strength of the kick and $T = 2\pi/\Omega$ is the period of the drive. Although this Hamiltonian differs from the standard one, it has the advantage of being exactly solvable. Namely, it was shown that the Floquet Hamiltonian for this problem takes the form (see Ref. [238] for a detailed discussion)

$$H_F = \Delta \frac{\sin \omega_0 T}{\omega_0 T} \left(\frac{p^2}{2m e^\alpha} + \frac{m \omega_0^2 e^\alpha}{2} x^2 + \omega_0 \sinh \alpha \cot \omega_0 T \{p, x\}_+ \right), \quad (3.163)$$

where $T = 2\pi/\Omega$ is the driving period, $D = 2\sqrt{\cosh^2 \alpha \cos^2 \omega_0 T - 1}$, and $\Delta = \arcsin(D)/D$. Notice that $\Delta(\alpha = 0) = \omega_0 T / \sinh \omega_0 T$, and thus $H_F = H_0$ reduces to the non-driven model, as expected.

Rotating the operators $x \rightarrow X$ and $p \rightarrow P$, one can change basis, to bring the Floquet Hamiltonian into a more intuitive form:

$$\tilde{H}_F = \frac{1}{2}(P^2 + \Omega_F^2 X^2); \quad e^{i\Omega_F} = \cosh \alpha \cos \omega_0 T + \sqrt{\cosh^2 \alpha \cos^2 \omega_0 T - 1}. \quad (3.164)$$

This allows us to make some tantalising observations. It is easy to see that for $\Omega_F > 0$ the system is stable, and the Floquet Hamiltonian is equivalent to that of a harmonic oscillator with drive-renormalised driving frequency and particle mass. In particular, the quasienergies are $\epsilon_F = \Omega_F(n+1/2)$. Strikingly, on resonance, we find $\Omega_F = 0$, which means that $\tilde{H}_F \sim P^2$ describes free particles. Thus, the Floquet states are plane waves which are non-normalisable. Consequently, the quasienergy spectrum becomes continuous [238, 239] and this marks the transition between the stable and the unstable phases. Finally, in the unstable region, the effective parabolic potential becomes inverted, $\Omega_F^2 < 0$, and the drive turns the static confining problem into a scattering one. As a result, the quasienergy spectrum remains continuous in the unstable regime.

Although the physics described in this section is that of single-particles, it is easy to imagine that the Floquet Hamiltonian of weakly-interacting bosons will feature a very similar behaviour. The parametric instabilities for such a system are studied in Sec. 5.2.

3.3.3 The Inverse Frequency Expansion for Systems with Real Photon Absorption Processes: Taking Resonance into Account

Resonance phenomena play a crucial role for the proper understanding of periodically-driven systems. Having already described the phenomenon of parametric resonance, we now turn our attention to real photon absorption transitions, which we call Floquet resonances. Once again we employ the RWA to derive an effective static description of the underlying physics. Interestingly, as anticipated already in Sec. 3.1.3.1, we demonstrate that these resonances are beyond the inverse-frequency expansion at any order, but can be captured perturbatively by the generalised Schrieffer-Wolff transformation (SWT) introduced in Sec. 3.2.

3.3.3.1 Two-Level Systems

Let us make a detailed comparison between the generalised SWT from Sec. 3.2 and the van Vleck inverse frequency expansion applied ad hoc in the lab frame. In particular, in the following we point out and explain some important conceptual differences between the two: (i) as we have seen, the SWT takes into account real photon absorption resonances which open up gaps in the Floquet spectrum, while the lab frame vV HFE generally fails to do so; it only captures virtual photon absorption, see Sec. 3.1. (ii) while the HFE is applicable at high frequencies only, and generically fails for $\Omega \sim J_0$ where J_0 is a natural energy scale of the non-driven model, the SWT can be carried out successfully at much lower driving frequencies, in a suitably chosen rotating frame.

To illustrate this, we choose a non-interacting system on a bipartite lattice with periodic boundary conditions, described by the following Hamiltonian in momentum space:

$$\begin{aligned}
 H(t) &= -J_0 \begin{pmatrix} 0 & a_1(1 + e^{ik}) \\ a_1(1 + e^{-ik}) & 0 \end{pmatrix} + \left[-J_0 \begin{pmatrix} b_1 & a_0 e^{ik} \\ a_0 e^{-ik} & -b_1 \end{pmatrix} e^{i\Omega t} + \text{h.c.} \right], \\
 &= h_0 + h_1 e^{i\Omega t} + h_1^\dagger e^{-i\Omega t}.
 \end{aligned} \tag{3.165}$$

The parameter J_0 is the bare hopping, k is the lattice momentum, while a_0 , a_1 and b_1 are dimensionless parameters.

There is no closed-form solution for the Floquet Hamiltonian of this system. Therefore, we use the high-frequency expansion to calculate the effective vV Hamiltonian H_{eff} to leading order in Ω^{-1} . In this section, we are interested in the properties of the quasienergy spectrum only, and shall not discuss the kick operator explicitly. Using the Pauli matrices to span the space of 2×2 hermitian matrices, we have [9, 32, 33, 87]

$$\begin{aligned} H_{\text{eff}} &\approx H_{\text{eff}}^{(0)} + H_{\text{eff}}^{(1)} + H_{\text{eff}}^{(2)}, \\ H_{\text{eff}}^{(0)} &= -J_0 [a_1(1 + \cos k)\sigma^x + a_1 \sin k\sigma^y], \\ H_{\text{eff}}^{(1)} &= \frac{J_0^2}{\Omega} [2a_0b_1(1 - \cos k)\sigma^x + 2a_0b_1 \sin k\sigma^y], \\ H_{\text{eff}}^{(2)} &= \frac{J_0^3}{\Omega^2} [4a_1b_1^2(1 + \cos k)\sigma^x + 4a_1b_1^2 \sin k\sigma^y - 4a_0a_1b_1(1 + \cos k)\sigma^z]. \end{aligned} \quad (3.166)$$

To point out some differences with the vV HFE, we also apply the generalised SWT. In doing so, it is convenient to think of the frequency Ω as being smaller than the single-particle bandwidth. However, we stress that this assumption is not necessary and, as we show below, the results are also valid for arbitrary frequencies larger than the bandwidth. We start by explicitly separating out the zeroth harmonic of the time-dependent Hamiltonian in Eq. (3.165):

$$H(t) = h_0 + h_1 e^{i\Omega t} + h_1^\dagger e^{-i\Omega t}. \quad (3.167)$$

Next, we diagonalise the Hamiltonian $h_0 = S^\dagger E_k \sigma^z S$ applying a static, k -dependent unitary transformation S . In this basis, the full Hamiltonian reads

$$\tilde{H}(t) = E_k \sigma^z + 2J_0 a_0 \cos(\Omega t + k/2) \sigma^z + 2J_0 b_1 \cos \Omega t \sigma^x. \quad (3.168)$$

Now comes the SWT step. Pretending we drive the system below the single particle

bandwidth, there will be modes to which the drive couples resonantly. As we have seen in Sec. 3.2 above, this warrants the application of the generalised SWT. We can arbitrarily choose the Floquet zone in between $[-\Omega/2, \Omega/2]$; while we do this here only for convenience, our results are independent of this choice. Thus, we write $E_k = \delta_k/2 + \Omega/2$, with the ‘detuning’ $\delta_k = 2E_k - \Omega$, whence, the lab-frame Hamiltonian becomes

$$\tilde{H}(t) = \frac{\delta_k}{2}\sigma^z + \left[\frac{\Omega}{2} + 2J_0a_0 \cos(\Omega t + k/2) \right] \sigma^z + 2J_0b_1 \cos \Omega t \sigma^x. \quad (3.169)$$

In this form the Hamiltonian has the generic form required to apply the generalised SWT, as introduced in Sec. 3.2. Therefore, the next step is to go to the rotating frame w.r.t. the terms proportional to σ^z , leaving the ‘small’ detuning term δ_k in the lab frame, in order to preserve the periodicity in time of the Hamiltonian in the rotating frame:

$$\begin{aligned} \tilde{H}^{\text{rot}}(t) &= \frac{\delta_k}{2}\sigma^z + 2J_0b_1 \cos \Omega t \times \\ &\times \begin{pmatrix} 0 & e^{-i(\Omega t + 4\frac{J_0}{\Omega}a_0[\sin(\Omega t + k/2) - \sin(k/2)])} \\ e^{+i(\Omega t + 4\frac{J_0}{\Omega}a_0[\sin(\Omega t + k/2) - \sin(k/2)])} & 0 \end{pmatrix} \end{aligned} \quad (3.170)$$

We can now apply the full machinery of the inverse-frequency expansion in the rotating frame. Although this analysis is straightforward, notice the following conceptually important points: (i) interestingly, the small parameter in the Hamiltonian is now δ_k . Hence, the validity regime is given by $\delta_k/\Omega \ll 1$. By construction, however, this automatically incorporates the original high-frequency limit $J_0/\Omega \ll 1$, see Fig. 3.23. We note here that this analysis works as long as the amplitude of the drive is not too large, i.e. $b_1/\Omega \lesssim 1$. Whenever this condition does not hold, higher-order terms of an entire subseries in the expansion become important progressively, and one should go to a rotating frame in the very first step, i.e. before defining the harmonics h_ℓ , as we have demonstrated on multiple occasions in Sec. 3.1. (ii) although the mathematical machinery of the generalised SWT and the vV HFE is the same, *physically* something quite different just happened: instead

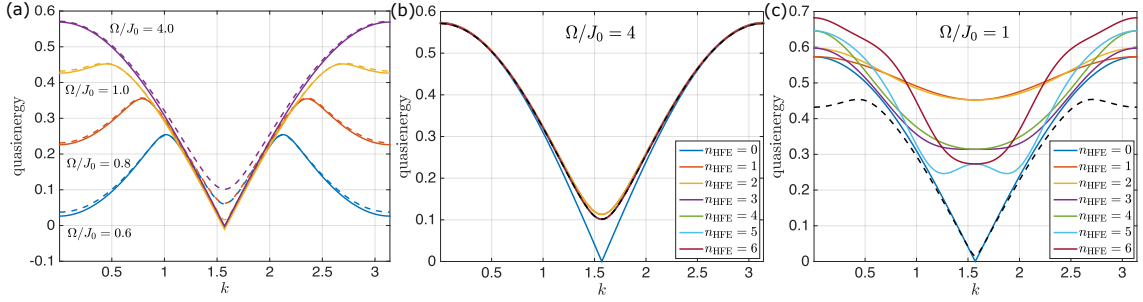


Figure 3.23: Upper band of the quasienergy spectrum of the driven system in Eq. (3.165). (a) comparison between the generalised SWT to zeroth order (solid lines) and exact numerics (dashed lines) for different driving frequencies Ω . Two photon absorption gaps symmetrically situated around $k = \pi/2$ open close to $\Omega/2$ in each case. The gap opening at $k\pi/2$ present in the exact numerical curves is captured by the higher-order terms in the generalised SW[not shown] as is the case for the HFE [see (b)]. Comparison between the spectra of H_{eff} to order n_{HFE} of the HFE for $\Omega/J_0 = 4$ (b) and $\Omega/J_0 = 1$ (c). The dashed black line is the exact numerical curve. The parameters are $a_0 = 0.912$, $a_1 = 0.2867$ and $b_1 = 0.1214$.

of dressing the low-energy physics only by *virtual* photon absorption processes, which is also achieved by the vV HFE in the limit $J_0/\Omega \ll 1$ [think of the usual renormalisation of the hopping parameter by a Bessel function at $\Omega \rightarrow \infty$], the SWT analysis goes further and captures *real* photon absorption processes coupling the resonant states. Hence, we obtain a tool to describe systems on resonance.

The leading-order term in the generalised SWT can be calculated by taking the time-average, which is equivalent to applying the Rotating Wave Approximation (RWA):

$$H_{\text{SW}}^{(0)} = \begin{pmatrix} \delta_k/2 & \alpha_k \\ \alpha_k^* & -\delta_k/2 \end{pmatrix}, \quad \alpha_k = J_0 b_1 \left[\mathcal{J}_0(w) + e^{ik} \mathcal{J}_2(w) \right] e^{iw \sin k/2} \quad (3.171)$$

where $w = 4J_0 a_0 / \Omega$. Hence, the SWT approximation to the quasienergies is given by $E_k^{\text{SW}} = \pm \sqrt{(E_k - \Omega/2)^2 + |\alpha_k|^2} \mp \Omega/2$. The extra additive piece $\mp \Omega/2$ needs to be included to properly take into account the shift in energy due to the Galilean term in the rotating frame ¹¹. Notice how a photon absorption gap of magnitude $2|\alpha_k|$ opens at the k modes

¹¹Note that the transformation to the rot frame is not stroboscopic.

for which $E_k \approx \Omega/2$. Higher-order terms can be obtained in a straightforward manner.

Figure 3.23a shows the generalised SWT quasienergies E_k^{SW} compared to the exact quasienergies obtained numerically for a few different driving frequencies. Notice how it captures the correct physics even at the frequencies larger than the bandwidth where photon absorption processes are only allowed virtually. In Fig. 3.23b we show the approximate dispersion obtained from the vV HFE numerically to sixth order in the regime of validity $J_0/\Omega \ll 1$. However, the expansion fails at low frequencies, Fig. 3.23c, where the generalised SWT does an excellent job.

3.3.3.2 The General Case

Let us make a few important remarks about the applicability of the above procedure to systems whose Hilbert space dimension is large. At a first sight, it seems like the steps above carry over to any system directly. Note, however, that identifying the position of the resonances requires the knowledge of the spectrum of the unperturbed Hamiltonian h_0 , which may involve further approximations/techniques to obtain. An interesting scenario appears when one considers systems with unbounded spectra of h_0 , such as the Kapitza pendulum. In such cases, it can very well be that the condition $\Omega/J_0 \gg 1$ for the applicability of the HFE is satisfied, and yet there exist states of h_0 with energies on the order of the driving frequency, due to the unbounded character of the spectrum. Whenever two states of h_0 differ by an integer multiple of the driving frequency [modulo a small detuning], they will be hybridised by the drive and a photon absorption gap in the exact Floquet spectrum will open, see Secs. 2.3.2.1 and 4.5. Nevertheless, the vV HFE will never be able to capture this resonance effect, leaving an unavoidable level crossing in the approximate Floquet spectrum, i.e. the spectrum of H_{eff} to any order in the inverse frequency. Thus, in such cases one needs to resort to the generalised SWT even in the limit $J_0/\Omega \ll 1$ [240].

While the procedure outlined in the previous section works flawlessly for two-level systems, it is not clear whether it generalises trivially to the many-body setup. The problem we are faced with is the definition of the Floquet zone: any physical results should not

depend on this choice. However, one can easily convince oneself that there are situations, where the above procedure can potentially fail. For instance, consider four states with finite matrix elements between each other. After folding, two of them can happen to be very close to the outer zone edge, and another two – close to the zone centre. With this folding choice, however, the states far away have a large energy gap in between them, on the order of the driving frequency, although the real quasienergy gap is actually pretty small due to the periodicity of the Floquet zone. As long as there is only one pair of levels involved in the resonance, as was the case in Sec. 3.3.3.1, it is always possible to choose the Floquet zone such that the zero energy appears right in between the two folded energies. This way we choose a folding gauge which selects the minimum gap between the folded energies¹². With the presence of a third and a fourth level, however, it becomes impossible to do a choice such that all gaps between the folded states are minimal simultaneously. Needless to say, the situation becomes even more aggravated, if there are more energies to fold, all corresponding to states with finite matrix elements, as in a non-integrable interacting system. The efficient analytical treatment of Floquet resonances in generic systems is currently an open problem, see Sec. 6.2.

¹²On the circle, where quasienergies are defined, there are two natural distances between any two arbitrary points: the small and the big arc. The minimum gap corresponds to the small arc.

Chapter 4

Floquet Adiabatic Perturbation Theory and Geometry

The concept of adiabaticity in equilibrium systems has profound importance of both a fundamental and practical nature. Fundamentally, it allows one to identify and label families of adiabatically connected microscopic states and macroscopic phases. The existence of the adiabatic limit is a cornerstone of equilibrium thermodynamics, as it allows one to calculate thermodynamic forces, formulate the notion of reversibility, define the laws of thermodynamics, and put restrictions on possible outcomes of macroscopic processes, such as efficiency bounds of heat engines and refrigerators [241, 242]. Practically, the existence of an adiabatic limit allows for the preparation of complex ground or excited states in interacting isolated systems by slowly changing the couplings of the Hamiltonian. This idea, for instance, underlies adiabatic quantum computation and quantum annealing [243–245].

Adiabatic protocols are also extensively applied in NMR and qubit experiments. Adiabatic passages are robust protocols based on the Floquet adiabatic principle to prepare excited states with a high tolerance to the inhomogeneity of the applied radio-frequency (RF) field [246, 247]. Different driving protocols have been applied successfully to reach higher speed and to increase robustness [248–251]. Adiabatic protocols are also used to enhance sensitivity of spins with low gyromagnetic ratio [252], for spin-decoupling [253], and for refocusing [254]. Adiabatic passages for population transfer between quantum states are also applied in the optical domain [255]. We shall always work in this stroboscopic Floquet gauge, unless explicitly otherwise stated.

Despite this striking similarity with their static counterparts, periodically driven systems are a priori out-of-equilibrium. In systems with an unbounded spectrum, e.g. in the thermodynamic or classical limits, the Floquet Hamiltonian, as a local operator, is not even guaranteed to exist [33, 256]. Therefore, the question as to *how to prepare the system in a desired state* is of equal importance as engineering the effective parent Hamiltonian [32, 33]. Adiabatic preparation of Floquet states in certain quantum many-body systems has been reported both numerically and experimentally. For instance, in Ref. [257], the authors studied a large but finite periodically-driven Bose-Hubbard chain using DMRG. They found an adiabatic regime for intermediate velocities, which enabled the adiabatic transfer of a superfluid from the zero-momentum to the π -momentum mode at high driving frequencies. At the same time, a study on periodically-driven Luttinger liquids reported that the momentum distribution of fermions changes immediately after the drive is turned on, due to enhanced photon-assisted scattering near the Fermi edge, and concluded that the existence of an adiabatic limit is not possible at low drive frequencies [76]. More recently, a number of exciting experiments [52, 54, 56] with cold atoms slowly turned on the amplitude of the drive to come sufficiently close to the desired ground state of a carefully engineered topological Floquet Hamiltonian. It must be noted, though, that another experiment, which managed to prepare the ground state of the π -flux Hofstadter model [55], reported lower fidelities when adiabatically ramping the drive compared to a sudden switch on of the periodic modulation.

Conventional adiabatic perturbation theory (APT) predicts that for very slow and smooth ramps, during which the system remains gapped, the excitations accumulated during the ramp are small, and thus the system follows the adiabatically connected eigenstates of the Hamiltonian without transitions [258, 259]. The leading non-adiabatic corrections to observables, such as the energy or various generalised forces, are analytic functions of the ramp rate. These corrections give rise to various velocity-dependent forces, such as the Lorentz force, the Magnus force, or the Coriolis force, as well as to various inertia-type forces proportional to the acceleration of the system [260]. In gapless or open systems, finite

ramp rates result in additional dissipative forces, such as friction [261–264]. These forces, however, also vanish in the adiabatic limit and can be captured within APT [264, 265].

The idea of an adiabatic passage between continuously connected Floquet eigenstates was introduced to study the behaviour of single particle quantum systems in the presence of intense radiation fields. It was soon afterwards argued that resonant transitions can be understood as Landau-Zener (LZ) processes between Floquet levels. For these few-level systems, APT was successfully extended to incorporate Floquet theory, and produced accurate estimates of the ionisation rates in various single-atomic systems [23, 266–269]. Besides contributing to the understanding of the physical processes involved, APT has also lead to the development of dynamic control over the population of single-particle states in strongly-driven atoms [270–273]. Beyond few-level systems, it was conjectured that generic periodically-driven many-body Hamiltonians do not possess a well-defined adiabatic limit due to the exponentially large number of interacting states in the thermodynamic limit [157, 274, 275].

As we discuss in this thesis, APT can be extended to Floquet systems essentially retaining the form of leading non-adiabatic corrections. However, there is a crucial caveat for generic Floquet systems: one must in addition avoid photon resonances, which correspond to the closing of effective gaps in the Floquet spectrum due to hybridisation of (nearly) resonant states [274, 275]. This is only possible if the ramp rate is not too slow. In this sense, one can anticipate a finite window of rates where Floquet adiabatic perturbation theory (FAPT) is applicable: the rates should be sufficiently fast that the photon resonances are passed diabatically, but also sufficiently slow that non-adiabatic processes, which do not involve photon absorption remain suppressed. Intuitively, one expects that this window can exist only for special protocol conditions, typically at fast driving frequencies – larger than the natural energy scales of the non-driven system or, more accurately, away from single-particle resonances.

In this chapter, we present an extensive overview of the problem of slowly changing the parameters in a periodically driven system. We illustrate the main ideas discussed

here using various different models which cover a range of single-particle and many-body condensed matter systems. At the same time, we complement the general theory with new, previously unpublished results, by pointing out new constraints on adiabaticity imposed by the presence of the micromotion. Intuitively, as a consequence of the ramp, the $P(t)$ operator never comes back exactly to itself after one period, which induces additional non-adiabatic corrections to the wave function. Hence, in systems where the Floquet Hamiltonian vanishes identically, such as some topological pumps [61], the dynamics is governed entirely by the micromotion operator and understanding its contribution to non-adiabatic corrections is crucial. Since Floquet engineering often requires one to scale the driving amplitude with the driving frequency [33], the effects of micromotion can remain finite even in the infinite-frequency limit. As we discuss in detail below, it is only the sum of the contributions to FAPT coming from micromotion and the Floquet Hamiltonian, which leads to a unique, Floquet gauge-invariant result which is insensitive to the choice of folding.

4.1 Stroboscopic and Non-Stroboscopic Dynamics for an Adiabatic Ramping of the Drive

While in the thermodynamic limit, adiabaticity in interacting periodically-driven systems is conjectured to be absent due to the appearance of densely distributed avoided crossings in the Floquet spectrum [274], the general understanding of adiabaticity in the experimentally-relevant finite-size systems is still a subject of an active research. However, in simple setups of finite-size systems with few degrees of freedom or noninteracting systems, it is possible to show that the adiabatic limit is well defined [240]. In this section, we show that in the case of a driven two-level system, a slow ramping-up of the driving amplitude, starting from the ground state¹ of the non-driven Hamiltonian, results in the system following the ground state of the instantaneous stroboscopic Floquet Hamiltonian

¹By Floquet ground state we mean the adiabatically-connected Floquet state.

$H_F[t]$ with a very good accuracy:

$$|\psi(t)\rangle \approx |\psi_{GS}(H_F[t])\rangle. \quad (4.1)$$

Thus, all observables evaluated stroboscopically at times $t_0 + lT$ in this case are given by the ground state expectation values of $H_F[t_0]$:

$$\langle\psi(t_0 + lT)|\mathcal{O}|\psi(t_0 + lT)\rangle = \langle\psi_{GS}(H_F[t_0])|\mathcal{O}|\psi_{GS}(H_F[t_0])\rangle. \quad (4.2)$$

This statement has immediate consequences for the FNS dynamics, where the measurement times are fluctuating within a period. We assume that, either the measurement is done after the ramp is over, or that the dynamical phase accumulated due to the Floquet quasi-energies is small. From the gauge equivalence of the Floquet Hamiltonians in Eq. (2.13) we see that, up to an unimportant phase factor, Eq. (4.1) implies that

$$|\psi(t)\rangle = e^{-i\hat{K}(t)}|\psi_{GS}(\hat{H}_F)\rangle,$$

where \hat{H}_F is an arbitrary fixed gauge Floquet Hamiltonian and $\hat{K}(t)$ is the corresponding kick operator. Using this result it is straightforward to calculate the average over one period of the expectation value of an observable \mathcal{O} :

$$\begin{aligned} \frac{1}{T} \int_{t_0}^{t_0+T} dt \langle\psi(t)|\mathcal{O}|\psi(t)\rangle &= \frac{1}{T} \int_{t_0}^{t_0+T} dt \langle\psi_{GS}(\hat{H}_F)|e^{i\hat{K}(t)}\mathcal{O}e^{-i\hat{K}(t)}|\psi_{GS}(\hat{H}_F)\rangle \\ &= \langle\psi_{GS}(\hat{H}_F)|\overline{\mathcal{O}}|\psi_{GS}(\hat{H}_F)\rangle. \end{aligned} \quad (4.3)$$

Since we average over the period, the result does not depend on t_0 . Therefore, in the following, we choose to work in the stroboscopic Floquet gauge, unless explicitly otherwise stated. Throughout this chapter, to simplify the notation we drop Floquet gauge label $[t_0]$ whenever possible.

Note that instead of the ground state in Eq. (4.3) one can use any other Floquet

eigenstate. In other words, if the system is in an eigenstate of the stroboscopic Floquet Hamiltonian, the FNS expectation value of any observable can be found by evaluating the expectation value of the dressed observable in the eigenstate of the fixed-gauge Floquet Hamiltonian.

4.2 Floquet Adiabatic Perturbation Theory

After this short discussion on stroboscopic and non-stroboscopic ramping, we open up the discussion of the adiabatic theorem in the presence of a periodic drive. We begin by briefly recapitulating the main results of conventional adiabatic perturbation theory (APT) for non-driven systems, and then proceed to generalise this formalism to periodically-driven systems, which we shall refer to as Floquet adiabatic perturbation theory (FAPT).

4.2.1 Adiabatic Perturbation Theory (APT)

Let us first outline some key results of quantum adiabatic perturbation theory; for more details see Refs. [258, 259, 276]. Consider a Hamiltonian $H(\lambda)$ which depends on some parameter λ that slowly changes in time. For simplicity, we assume that the Hamiltonian has a discrete energy spectrum with no degeneracies so that the adiabatic limit is well defined. Furthermore, we assume that the system is prepared in the ground state of the initial Hamiltonian and thus, in the adiabatic limit, it remains in the instantaneous ground state as λ is ramped².

Suppose that $V(\lambda)$ is a unitary transformation which diagonalises the Hamiltonian, i.e., $\tilde{H}(\lambda) = V^\dagger(\lambda)H(\lambda)V(\lambda)$ is a diagonal matrix whose entries are the eigenenergies of $H(\lambda)$. It is convenient to go to a moving frame with respect to the instantaneous Hamiltonian by defining $|\tilde{\psi}\rangle = V^\dagger(\lambda)|\psi\rangle$. Substituting this into the time-dependent Schrödinger equation, the time evolution $i\partial_t|\tilde{\psi}\rangle = \tilde{H}_m|\tilde{\psi}\rangle$ of $|\tilde{\psi}\rangle$ is governed by the moving-frame Hamiltonian

$$\tilde{H}_m(\lambda) = \tilde{H}(\lambda) - \dot{\lambda}\tilde{\mathcal{A}}_\lambda,$$

²Notice that this discussion applies as well to any excited state

where $\tilde{\mathcal{A}}_\lambda = iV^\dagger(\lambda)\partial_\lambda V(\lambda)$ is the adiabatic gauge potential in the moving-frame, i.e., the generator of translations of the energy eigenstates w.r.t. λ [260]. This gauge potential is a Hermitian operator whose diagonal elements are the Berry connections of the energy eigenstates. Moreover, it follows from the above definition that the unitary $V(\lambda)$ also describes the basis transformation of the instantaneous energy eigenstates $|n(\lambda)\rangle$ to a λ -independent basis $|e_n\rangle$:

$$|n(\lambda)\rangle = V(\lambda)|e_n\rangle.$$

This implies that $\mathcal{A}_\lambda \equiv V(\lambda)\tilde{\mathcal{A}}_\lambda V^\dagger(\lambda) = i[\partial_\lambda V(\lambda)]V^\dagger(\lambda)$ acts as $i\partial_\lambda$ in the energy basis:

$$\langle m(\lambda)|\mathcal{A}_\lambda|n(\lambda)\rangle = \langle e_m|\tilde{\mathcal{A}}_\lambda|e_n\rangle = \langle m(\lambda)|i\partial_\lambda|n(\lambda)\rangle.$$

Since in the moving frame the Hamiltonian $\tilde{H}(\lambda)$ is diagonal, it does not lead to transitions between the instantaneous levels. Consequently, all the transitions are due to the Galilean term $\dot{\lambda}\tilde{\mathcal{A}}_\lambda$. As this term is suppressed at slow ramp rates (a.k.a. velocities) $\dot{\lambda}$, the system approximately (i.e., up to order $\dot{\lambda}^2$) follows the instantaneous ground state of $H_m(\lambda)$. In order to obtain the transition amplitudes in the moving frame, one uses first-order static perturbation theory with respect to the Galilean term. Then, expanding in the instantaneous basis $|\psi(t)\rangle = \sum_n c_n(t)|n(\lambda)\rangle$, we find

$$\begin{aligned} c_0(t) &\approx \exp[i\Phi_0] = \exp\left[-i \int_{t_0}^t dt' \left(\epsilon_0(\lambda(t')) - \dot{\lambda}(t')A_\lambda(\lambda(t'))\right)\right] \\ c_{n \neq 0}(t) &\approx e^{i\Phi_0} \dot{\lambda} \frac{\langle n(\lambda)|\mathcal{A}_\lambda|0(\lambda)\rangle}{\epsilon_n - \epsilon_0} = ie^{i\Phi_0} \dot{\lambda} \frac{\langle n(\lambda)|\partial_\lambda|0(\lambda)\rangle}{\epsilon_n - \epsilon_0} = -ie^{i\Phi_0} \dot{\lambda} \frac{\langle n(\lambda)|(\partial_\lambda H)|0(\lambda)\rangle}{(\epsilon_n - \epsilon_0)^2}, \end{aligned} \quad (4.4)$$

where $A_\lambda(\lambda') = \langle 0(\lambda')|\mathcal{A}_\lambda(\lambda')|0(\lambda')\rangle$ is the ground state Berry connection.

Using these expressions for the transition amplitudes, one can go one step further and find the leading non-adiabatic correction to various observables. It is convenient to represent such observables \mathcal{M}_μ as conjugate to the parameters of the Hamiltonian:

$\mathcal{M}_\mu = -\partial_\mu H$, where μ can coincide with λ or be any other parameter. Then we find

$$M_\mu(t) \equiv \langle \psi(t) | \mathcal{M}_\mu | \psi(t) \rangle = M_\mu^{(0)} + F_{\mu\lambda} \dot{\lambda} + \mathcal{O}(\dot{\lambda}^2, \ddot{\lambda}), \quad (4.5)$$

where $F_{\mu\lambda} = i \langle 0 | [\mathcal{A}_\mu, \mathcal{A}_\lambda] | 0 \rangle \equiv i \langle [\mathcal{A}_\mu, \mathcal{A}_\lambda] \rangle_0$ is the Berry curvature evaluated in the instantaneous ground state and $M_\mu^{(0)} = \langle 0 | \mathcal{M}_\mu | 0 \rangle$ is the instantaneous ground state expectation of the generalised force, which reduces to the Born-Oppenheimer force for heavy nuclei interacting with fast electrons [242], or to the Casimir force for macroscopic objects interacting with fast photon modes [277]. For the special class of observables which commute with the instantaneous Hamiltonian, e.g. the Hamiltonian itself, the leading non-adiabatic contribution is quadratic in the ramp speed $\dot{\lambda}$. For example, we find for the energy and the energy variance

$$\begin{aligned} \langle H \rangle &\approx \epsilon_0 + \dot{\lambda}^2 \sum_{n \neq 0} \frac{|\langle n(\lambda) | (\partial_\lambda H) | 0(\lambda) \rangle|^2}{(\epsilon_n - \epsilon_0)^3} + \mathcal{O}(\dot{\lambda}^4, \ddot{\lambda}^2), \\ \langle H^2 \rangle - \langle H \rangle^2 &\approx \dot{\lambda}^2 \sum_{n \neq 0} \frac{|\langle n(\lambda) | (\partial_\lambda H) | 0(\lambda) \rangle|^2}{(\epsilon_n - \epsilon_0)^2} + \mathcal{O}(\dot{\lambda}^4, \ddot{\lambda}^2) = \dot{\lambda}^2 g_{\lambda\lambda} + \mathcal{O}(\dot{\lambda}^4, \ddot{\lambda}^2), \end{aligned}$$

where $g_{\lambda\lambda} = \langle \mathcal{A}_\lambda^2 \rangle_0 - (\langle \mathcal{A}_\lambda \rangle_0)^2$ is the fidelity susceptibility [278, 279] or equivalently the diagonal component of the Fubini-Study metric tensor [260, 280–282].

4.2.2 Floquet Adiabatic Perturbation Theory (FAPT)

After this brief introduction to conventional adiabatic perturbation theory, we proceed with a similar approach to Floquet systems. As before, we assume that the Floquet Hamiltonian and the adiabatic limit are well defined. In particular, we assume that the Floquet “ground state” (or more accurately the Floquet state we target) is non-degenerate. These conditions can be realised, for instance, in a driven system with a finite-dimensional Hilbert space. They are also realised in special classes of “Floquet integrable” systems [283, 284]. As we show later in Sec. 4.3.3, the situation becomes much more interesting and complex in Floquet systems whose time-averaged Hamiltonian features an unbounded spectrum,

where these assumptions may break down in a fascinating and physically important way.

We now consider a system described by the Hamiltonian $H(\lambda, t)$, which is periodic in time with period $T = 2\pi/\Omega$ at any fixed λ . The parameter λ can be the amplitude, phase, or frequency of the drive, or some other parameter which is not directly related to the drive. We mostly focus on the situations where the Floquet Hamiltonian is adiabatically connected to some static non-driven Hamiltonian, in which case it is often convenient to think of λ as the driving amplitude. However, this assumption is not essential in the general discussion presented below. Also, let us point out that any smooth time dependence of the driving frequency can be eliminated by rescaling time $t \rightarrow \tau = \Omega(t)t$ in Schrödinger's equation, effectively resulting in the smooth time dependence of the other coupling parameters [275].

Since the Hamiltonian is time-periodic, it satisfies Floquet's theorem (Eq. (1.1)) at fixed λ . It is useful to define the instantaneous Floquet Hamiltonian,

$$H_F(\lambda) = P^\dagger(\lambda, t)H(\lambda, t)P(\lambda, t) - iP^\dagger(\lambda, t)\partial_t P(\lambda, t) , \quad (4.6)$$

where ∂_t is used to emphasise that these expressions are for fixed λ ³. Let us denote by $|n_F(\lambda)\rangle$ the eigenbasis of this Floquet Hamiltonian, for which $H_F(\lambda)|n_F(\lambda)\rangle = \epsilon_n^F(\lambda)|n_F(\lambda)\rangle$. By our assumption regarding the absence of level crossings⁴, the basis states $|n_F(\lambda)\rangle$ and the Floquet Hamiltonian $H_F(\lambda)$ are smooth functions of λ . Note that this generally implies that we are dealing with a Floquet Hamiltonian whose spectrum is unfolded, for otherwise, if the Floquet energy crosses the edge of the Floquet zone, we would have to introduce a discontinuity into the Floquet spectrum and the P operator. The final expressions for observables, however, will be insensitive to the choice of folding.

Similarly to the stationary case, let us denote by $V(\lambda)$ the unitary transformation which diagonalises the Floquet Hamiltonian such that $\tilde{H}_F(\lambda) = V^\dagger(\lambda)H_F(\lambda)V(\lambda)$ is diagonal and $|n_F(\lambda)\rangle = V(\lambda)|e_n\rangle$. Now the moving frame for this Floquet Hamiltonian is defined by two

³Note that the Floquet Hamiltonian defined in this way generally depends on the choice of the initial time t_0 via the Floquet gauge t_0 which is suppressed in this notation.

⁴The importance of the level crossings is discussed in detail starting from Sec. 4.3.3.

consecutive unitary transformations,

$$|\tilde{\psi}\rangle = V^\dagger(\lambda)P^\dagger(\lambda, t)|\psi\rangle ,$$

yielding the effective moving Floquet Hamiltonian

$$i\dot{d}_t|\tilde{\psi}\rangle = (\tilde{H}_F - \dot{\lambda}\tilde{\mathcal{A}}_\lambda^F)|\tilde{\psi}\rangle , \quad (4.7)$$

where

$$\tilde{\mathcal{A}}_\lambda^F(t) = iV^\dagger(\lambda)\partial_\lambda V(\lambda) + iV^\dagger(\lambda)P^\dagger(\lambda, t)[\partial_\lambda P(\lambda, t)]V(\lambda) \quad (4.8)$$

is the Floquet generalisation of the adiabatic gauge potential. Unlike in static APT, the gauge potential naturally splits into two contributions: the first one describes the adiabatic changes of the instantaneous eigenstates of the Floquet Hamiltonian and thus only depends on V , while the second one describes transitions due to the micromotion P . Intuitively, this new contribution can be understood by noticing that during the ramp the Hamiltonian is not strictly periodic, and thus there are corrections induced when the P operator does not come back to itself after one cycle. In the Floquet stationary frame, obtained by removing the V -rotation, $\mathcal{A}_\lambda^F \equiv V\tilde{\mathcal{A}}_\lambda^F V^\dagger$ is given by

$$\begin{aligned} \mathcal{A}_\lambda^F &= \mathcal{A}_\lambda^V(\lambda) + \mathcal{A}_\lambda^P(\lambda, t) , \\ \mathcal{A}_\lambda^V(\lambda) &\equiv -iV(\lambda)\partial_\lambda V^\dagger(\lambda) , \\ \mathcal{A}_\lambda^P(\lambda, t) &\equiv iP^\dagger(\lambda, t)\partial_\lambda P(\lambda, t) , \\ \langle m_F | \mathcal{A}_\lambda^F | n_F \rangle &= i\langle m_F | \partial_\lambda | n_F \rangle + \langle m_F | \mathcal{A}_\lambda^P | n_F \rangle \end{aligned} \quad (4.9)$$

While the first term here does not explicitly depend on time, the second one depends on time both implicitly via the slowly changing λ and explicitly through the oscillating in time terms. Similarly to APT, the matrix elements of $i\partial_\lambda$ are related to the matrix elements of

the Floquet generalised forces and the Floquet energies via

$$\langle m_F(\lambda) | i\partial_\lambda | n_F(\lambda) \rangle = -i \frac{\langle m_F(\lambda) | \partial_\lambda H_F(\lambda) | n_F(\lambda) \rangle}{\epsilon_m^F(\lambda) - \epsilon_n^F(\lambda)} ; \quad m \neq n, \quad (4.10)$$

which can be obtained by differentiating $\langle m_F | H_F | n_F \rangle = 0$ with respect to λ . The \mathcal{A}_λ^P part of the gauge potential describes adiabatic changes in the micromotion operator and is unrelated to the Floquet Hamiltonian. It therefore does not have a simple equilibrium analogue.

It bears mention that the Floquet gauge potential takes on an even simpler form when written out in the basis $|n_F(\lambda, t)\rangle \equiv P(\lambda, t)|n_F(\lambda)\rangle$. One can think of these states as the natural basis in the absence of ramping because if one starts in the state $|n_F(\lambda, t)\rangle$ at time t , then at later time t' for fixed λ one will end up in $|n_F(\lambda, t')\rangle$. Then defining $\mathcal{A}_\lambda^{F'} \equiv P\mathcal{A}_\lambda^F P^\dagger = (PV)\tilde{\mathcal{A}}_\lambda^F(PV)^\dagger$, it has matrix elements $\langle m_F(\lambda, t) | \mathcal{A}_\lambda^{F'} | n_F(\lambda, t) \rangle = i\langle m_F(\lambda, t) | \partial_\lambda | n_F(\lambda, t) \rangle$. Our results can be easily re-expressed in this basis, but doing so makes it harder to distinguish between micromotion and non-micromotion effects of \mathcal{A}_λ^F . Therefore, for the remainder of this article we work in the “stroboscopic” basis $|n_F(\lambda)\rangle$.

Combining all these transformations together we see that the exact time evolution of the amplitude c_n in the instantaneous Floquet basis

$$|\psi(t)\rangle = \sum_n c_n(t) P(\lambda, t) |n_F(\lambda)\rangle$$

reads:

$$i\dot{c}_n = \left(\epsilon_n^F(\lambda) - \dot{\lambda} \langle n_F(\lambda) | \mathcal{A}_\lambda^F(\lambda, t) | n_F(\lambda) \rangle \right) c_n - \dot{\lambda} \sum_{m \neq n} \langle n_F(\lambda) | \mathcal{A}_\lambda^F(\lambda, t) | m_F(\lambda) \rangle c_m. \quad (4.11)$$

In general, we will not be able to solve these equations analytically, but we will show how FAPT allows us to solve them to a good approximation in the limit of slow ramps.

Adiabatic limit. Assuming that the system is initially prepared in the (Floquet) ground state at time $t = t_i$, i.e. $c_0(t_i) = 1$ and $c_n(t_i) = 0$ for $n \neq 0$, we see that, similarly to the

non-driven case, the system follows the instantaneous Floquet ground state and the wave function acquires a phase:

$$\Phi_0^F(t) = - \int_{t_i}^t \epsilon_0^F(\lambda(t')) dt' + \int_{t_i}^t dt' \dot{\lambda}(t') \langle 0_F(\lambda(t')) | \mathcal{A}_\lambda^F(\lambda(t'), t') | 0_F(\lambda(t')) \rangle. \quad (4.12)$$

The first term here is the usual dynamic phase. The second term gives both the Berry phase associated with the Floquet Hamiltonian (coming from \mathcal{A}_λ^V) and an additional contribution due to the P operator, which explicitly depends on time. The expression for the phase Φ_0^F greatly simplifies if we ramp over many periods, such that only its period-averaged value contributes,

$$\begin{aligned} \gamma &\equiv \int_{t_i}^t dt' \dot{\lambda}(t') \langle 0_F(\lambda(t')) | \mathcal{A}_\lambda^F(\lambda(t'), t') | 0_F(\lambda(t')) \rangle \\ &\approx \int_{t_i}^t dt' \dot{\lambda}(t') \overline{\langle 0_F(\lambda(t')) | \mathcal{A}_\lambda^F(\lambda(t'), t') | 0_F(\lambda(t')) \rangle} = \int_{\lambda(t_i)}^{\lambda(t)} d\lambda' (\langle 0_F(\lambda') | \overline{\mathcal{A}_\lambda^F}(\lambda') | 0_F(\lambda') \rangle), \end{aligned} \quad (4.13)$$

where $\overline{(\cdot)} = T^{-1} \int_0^T (\cdot) dt$ is the average over a cycle at fixed λ .

Leading non-adiabatic response. In order to approximate Eq. (4.11) beyond the adiabatic limit, it is convenient to go to the interaction picture with respect to the diagonal term:

$$c_n = c'_n \exp[-i\Phi_n^F(t)],$$

where the phase $\Phi_n^F(t)$ is defined similar to Eq. (4.12). Then Eq. (4.11) becomes

$$i\dot{c}'_n = -\dot{\lambda} \sum_{m \neq n} \langle n_F(\lambda) | \mathcal{A}_\lambda^F(\lambda, t) | m_F(\lambda) \rangle e^{i(\Phi_n^F(t) - \Phi_m^F(t))} c'_m. \quad (4.14)$$

To leading order in $\dot{\lambda}$ we thus find for $n \neq 0$

$$c'_n(t) = i \int_{t_i}^t dt' \dot{\lambda}(t') \langle n_F(\lambda) | \mathcal{A}_\lambda^F(\lambda, t) | 0_F(\lambda) \rangle e^{i(\Phi_n^F(t') - \Phi_0^F(t'))} + \mathcal{O}(\dot{\lambda}^2). \quad (4.15)$$

To evaluate this integral it is convenient to decompose the gauge potential into Fourier

harmonics:

$$\mathcal{A}_\lambda^F(\lambda, t) = \sum_{\ell=-\infty}^{\infty} e^{i\Omega\ell t} \mathcal{A}_\lambda^{F,\ell}(\lambda)$$

Assuming that the protocol starts smoothly ($\dot{\lambda}(t_i) = 0$) such that transients can be neglected, we can approximately evaluate the integrals by expanding around $t' = t$. This procedure is similar to what is done in standard APT (cf. Ref. [259]), and is detailed in Appendix D. Returning to the Floquet stationary frame, we obtain to the leading order in $\dot{\lambda}$:

$$c_n(t) = e^{-i\Phi_0^F(t)} \dot{\lambda}(t) \sum_{\ell=-\infty}^{\infty} e^{i\ell\Omega t} \frac{\langle n_F(\lambda) | \mathcal{A}_\lambda^{F,\ell} | 0_F(\lambda) \rangle}{\epsilon_n^F - \epsilon_0^F + \ell\Omega} + O(\ddot{\lambda}, \dot{\lambda}^2). \quad (4.16)$$

We note that this expression for the transition amplitudes has previously been derived by different means in Ref. [275] in the context of quantum chemistry. In the following, we discuss the implications of this result to various physical observables. Examining this expression, we see that unlike the non-driven case, the leading non-adiabatic response in Floquet systems generates additional oscillating terms which can be interpreted as non-adiabatic corrections to the P -operator. As we shall see, in a wide class of problems these oscillating terms are equally or sometimes even more important than the non-adiabatic corrections due to the slowly changing Floquet Hamiltonian.

To measure the deviations from the adiabatic limit, we consider the probability $p_n^F = |c_n(t)|^2$ of being in the Floquet state $|n_F\rangle$. Using Eq. (4.16) one finds that the probabilities p_n^F are given by:

$$p_n^F = \dot{\lambda}(t)^2 \sum_{\ell,\ell'} e^{i(\ell-\ell')\Omega t} \frac{\langle n_F(\lambda) | \mathcal{A}_\lambda^{F,\ell} | 0_F(\lambda) \rangle \langle 0_F(\lambda) | \mathcal{A}_\lambda^{F,\ell'} | n_F(\lambda) \rangle}{(\epsilon_n^F - \epsilon_0^F + \ell\Omega)(\epsilon_n^F - \epsilon_0^F + \ell'\Omega)} \quad (4.17)$$

From these probabilities, we can define the log-fidelity f_d and the associated Floquet diagonal entropy S_d^F as

$$f_d = -\log |c_0|^2 = -\log \left(1 - \sum_{n>0} |c_n|^2 \right), \quad S_d^F = -\sum_n p_n^F \log p_n^F. \quad (4.18)$$

Since $c_{n \neq 0} \sim v = \dot{\lambda}(t_f)$ for small velocities, both f_d and S_d^F scale as v^2 in the low velocity limit, up to a small log correction in S_d^F . We shall use this characteristic feature as a benchmark of adiabaticity in various models. While one can use either f_d or S_d^F to measure the magnitude of the non-adiabatic corrections, notice that the former requires the identification of the Floquet ground state, while the latter does not. Hence, in complicated models, the entropy often constitutes a simpler measure of adiabaticity. As in non-Floquet systems the diagonal entropy is simply a measure of delocalisation of the wave-function (or more generally density matrix) among the eigenstates of the instantaneous Floquet Hamiltonian.

It is useful to understand Eq. (4.16) in two important limits. First, in the limit of vanishing driving amplitude, there is no micromotion, and therefore all terms with $\ell \neq 0$ may be neglected. Furthermore in this limit $\epsilon_n^F(\lambda) \rightarrow \epsilon_n(\lambda)$ and $\mathcal{A}^F(\lambda) \rightarrow \mathcal{A}(\lambda)$. As a result, Eq. (4.16) reduces to Eq. (4.5), reproducing conventional APT as expected.

A similar situation occurs in the infinite-frequency limit, where all the Fourier modes in (4.16) disappear leaving only the $\ell = 0$ component⁵:

$$c_n(t) \approx e^{-i\Phi_0^F(t)} \dot{\lambda}(t) \frac{\langle n_F(\lambda) | \mathcal{A}_\lambda^{F,0} | 0_F(\lambda) \rangle}{\epsilon_n^F - \epsilon_0^F} + O(\ddot{\lambda}, \dot{\lambda}^2). \quad (4.19)$$

This is equivalent to assuming time-scale separation and averaging over the fast time variable (cf. Ref. [38]), in which case one loses information about the higher Fourier modes. While the probability amplitudes in the limits of vanishing drive amplitude, Eq. (4.16), and infinite frequency, Eq. (4.19), look deceptively similar, there exists a subtle difference: the physics in the two limits could be governed by two Hamiltonians with completely different properties. This is particularly relevant when Floquet engineering methods are applied, which requires that the driving amplitude is of the order of the driving frequency [33].

⁵When the amplitude of the drive scales with the frequency, which is the relevant case for Floquet engineering, $\mathcal{A}^{F,\ell}$ acquires Ω dependence, and $\ell \neq 0$ terms may also survive the infinite frequency limit of (4.16)

4.2.3 Observables

Using the transition amplitudes it is straightforward to find the leading non-adiabatic corrections to the expectation values of observables. As in the the non-driven case, it is convenient to represent observables in terms of generalised forces, $\mathcal{M}_\mu(t) = -\partial_\mu H(t)$. Using Eq. (4.16) we find

$$M_\mu(t) \equiv \langle \psi(t) | \mathcal{M}_\mu(t) | \psi(t) \rangle \approx \langle 0_F | P^\dagger(t) \mathcal{M}_\mu(t) P(t) | 0_F \rangle + \lambda \sum_{n \neq 0} \sum_{\ell=-\infty}^{\infty} \left(e^{i\ell\Omega t} \frac{\langle 0_F | P^\dagger(t) \mathcal{M}_\mu(t) P(t) | n_F \rangle \langle n_F | \mathcal{A}_\lambda^{F,\ell} | 0_F \rangle}{\epsilon_n^F - \epsilon_0^F + \ell\Omega} + \text{c.c.} \right) \quad (4.20)$$

Here we have dropped the argument λ in the P operator to simplify the notation. The result above can be simplified further by expressing it through the Floquet generalised force, $\mathcal{M}_\mu^F = -\partial_\mu H_F$. In order to do this we note that

$$\begin{aligned} P^\dagger(t) \partial_\mu H(t) P(t) &= \partial_\mu [P^\dagger(t) H(t) P(t) - i P^\dagger(t) \partial_t P(t) + i P^\dagger(t) \partial_t P(t)] \\ &\quad - [\partial_\mu P(t)^\dagger] H(t) P(t) - P^\dagger(t) H(t) \partial_\mu P(t) \\ &= \partial_\mu H_F + \partial_t \mathcal{A}_\mu^P(t) + i[H_F, \mathcal{A}_\mu^P(t)], \end{aligned} \quad (4.21)$$

where we separated out the P -component of the gauge potential $\mathcal{A}_\mu^P(t) = i P^\dagger(t) \partial_\mu P(t)$ as in Eq. (4.9). Recall that $\mathcal{A}_\mu^V = -i V \partial_\mu V^\dagger$ does not explicitly depend on time. Then, using the right-hand side of Eq. (4.21), we have

$$\begin{aligned} \langle 0_F | \partial_t \mathcal{A}_\mu^P(t) | n_F \rangle &= \langle 0_F | \partial_t \mathcal{A}_\mu^F(t) | n_F \rangle = -i \sum_{\ell'=-\infty}^{\infty} e^{-i\ell'\Omega t} \ell' \Omega \langle 0_F | \mathcal{A}_\mu^{F,-\ell'} | n_F \rangle, \\ \langle 0_F | \partial_\mu H_F + i[H_F, \mathcal{A}_\mu^P(t)] | n_F \rangle &= -i(\epsilon_n^F - \epsilon_0^F) \langle 0_F | \mathcal{A}_\mu^V | n_F \rangle \\ &\quad - i \sum_{\ell'=-\infty}^{\infty} e^{-i\ell'\Omega t} (\epsilon_n^F - \epsilon_0^F) \langle 0_F | \mathcal{A}_\mu^{P,-\ell'} | n_F \rangle \\ &= -i \sum_{\ell'=-\infty}^{\infty} e^{-i\ell'\Omega t} (\epsilon_n^F - \epsilon_0^F) \langle 0_F | \mathcal{A}_\mu^{V,-\ell'} + \mathcal{A}_\mu^{P,-\ell'} | n_F \rangle \end{aligned}$$

$$= -i \sum_{\ell'=-\infty}^{\infty} e^{-i\ell'\Omega t} (\epsilon_n^F - \epsilon_0^F) \langle 0_F | \mathcal{A}_\mu^{F,-\ell'} | n_F \rangle. \quad (4.22)$$

To see the last equality note that that by constructions all non-zero harmonics of $\mathcal{A}_\mu^{V,\ell \neq 0} = 0$ vanish identically, while $\mathcal{A}_\mu^{V,\ell=0} = \mathcal{A}_\mu^V$. We then combined the two gauge potentials into the single Floquet gauge potential using Eq. (4.9).

Adding the expression above in the right-hand side of Eqs. (4.21) and substituting the result in Eq. (4.20), we find that the generalised force reads

$$\begin{aligned} M_\mu(t) \approx & \langle 0_F | \mathcal{M}_\mu^F | 0_F \rangle - i \sum_{\ell \neq 0} \Omega \ell e^{i\ell\Omega t} \langle 0_F | \mathcal{A}_\mu^{F,\ell} | 0_F \rangle + \quad (4.23) \\ & i\dot{\lambda} \sum_{n \neq 0} \sum_{\ell, \ell'=-\infty}^{\infty} \left(e^{i(\ell-\ell')\Omega t} \frac{\epsilon_n^F - \epsilon_0^F + \ell'\Omega}{\epsilon_n^F - \epsilon_0^F + \ell\Omega} \langle 0_F | \mathcal{A}_\mu^{F,-\ell'} | n_F \rangle \langle n_F | \mathcal{A}_\lambda^{F,\ell} | 0_F \rangle - \text{c.c.} \right) \end{aligned}$$

As we explained in Sec. 4.1, there are two types of measurements one usually applies to periodically driven systems. Floquet stroboscopic (FS) measurements are performed at integer multiples of the driving period and are given by the general expression in Eq. (4.24). Floquet non-stroboscopic (FNS) measurements are averaged over many cycles, or equivalently averaged over the driving phase φ_0 [33]. We thus refer to FNS measurements as “phase-averaged” throughout the course of this chapter. The choice of driving phase is often uncontrolled in experiments and, thus, its fluctuations from shot to shot effectively lead to phase-averaged measurements. The expressions for observables in FAPT greatly simplify for the phase-averaged measurement protocol as all non-zero harmonics average to zero. Then the generalised force becomes the Floquet generalised force, as anticipated:

$$\overline{M_\mu^{(0)}} = \langle 0_F | \mathcal{M}_\mu^F | 0_F \rangle = -\partial_\mu \epsilon_0^F, \quad (4.24)$$

where in the second equality we have used the (Floquet) Feynman-Hellmann theorem [125].

Meanwhile, the leading non-adiabatic correction becomes

$$\overline{M_\mu^{(1)}} = i\dot{\lambda} \sum_\ell \left\langle 0_F \left| \left[\mathcal{A}_\mu^{F,\ell}, \mathcal{A}_\lambda^{F,-\ell} \right] \right| 0_F \right\rangle = i\dot{\lambda} \overline{\langle 0_F | [\mathcal{A}_\mu^F(t), \mathcal{A}_\lambda^F(t)] | 0_F \rangle} , \quad (4.25)$$

where as before

$$\overline{\mathcal{O}} = \frac{1}{T} \int_0^T \mathcal{O}(t) dt \quad (4.26)$$

denotes period (or equivalently phase) averaging over the cycle at fixed λ .

4.2.4 Floquet Berry Curvature and Floquet Chern Number

In APT, the leading-order correction to M_μ for a ramp of the parameter λ is related to the Berry curvature [285] $F_{\lambda\mu}$ (see Sec. 4.2.1). Thus, it is natural to ask in which sense this generalises to Floquet systems. If we consider the state $|0_F(\lambda, t)\rangle = P(\lambda, t)|0_F(\lambda)\rangle$ introduced earlier, then the natural extension of the Berry curvature to Floquet systems is

$$F_{\lambda\mu}^F(t) = i\langle \partial_\lambda 0_F(t) | \partial_\mu 0_F(t) \rangle + \text{h.c.} = i \langle 0_F | [\mathcal{A}_\lambda^F(t), \mathcal{A}_\mu^F(t)] | 0_F \rangle . \quad (4.27)$$

Obviously, the Floquet Berry curvature can be expressed through the derivatives of the instantaneous Berry connection $A_\lambda^F(t) = i\langle 0_F(t) | \partial_\lambda | 0_F(t) \rangle$ in a standard fashion: $F_{\lambda\mu}^F(t) = \partial_\lambda A_\mu^F(t) - \partial_\mu A_\lambda^F(t)$. While the instantaneous non-adiabatic response of observables in Floquet systems is not directly related to the Berry curvature (c.f. Eqs. (4.24) and (4.27)), the leading non-adiabatic correction is proportional to the period (phase) averaged Floquet Berry curvature. Indeed, comparing Eqs. (4.25) and (4.27) we see that:

$$\overline{M_\mu} \approx \overline{M_\mu^{(0)}} + \dot{\lambda} \overline{F_{\lambda\mu}^F} . \quad (4.28)$$

Whereas $\overline{F_{\lambda\mu}^F}$ is an interesting curvature form in its own right, one may ask how to use it to obtain geometric and topological properties of the time-dependent system. One nice topological invariant which is unaffected by this time averaging is the Floquet Chern

number [38, 39, 56–58], which is defined for any given time t during the cycle as $C_1(t) = \frac{1}{2\pi} \int d\lambda d\mu F_{\lambda\mu}^F(\lambda, \mu, t)$. Notice that the Floquet eigenstates corresponding to different times within the period are connected by a continuous unitary gauge transformation, which does not change the energy spectrum and cannot lead to gap closings. Therefore, the corresponding Floquet Chern number [286] is independent of the time within the period, and hence also independent of the driving phase. Thus, $C_1(t) = C_1(t') = C_1^F$ defines the Floquet Chern number, which can be found by measuring $\overline{F_{\lambda\mu}^F}$ and integrating:

$$C_1^F = \frac{1}{T} \int_0^T dt C_1(t) = \frac{1}{2\pi} \iint d\lambda d\mu \int_0^T \frac{dt}{T} F_{\lambda\mu}^F(\lambda, \mu; t) = \frac{1}{2\pi} \iint d\lambda d\mu \overline{F_{\lambda\mu}^F(\lambda, \mu)}. \quad (4.29)$$

This important result tells us that one can engineer, at least in principle, Floquet systems with quantised Hall-type response. In order to do this, one has to be in a position to prepare these systems sufficiently close to the corresponding Floquet ground state and perform phase-averaged measurements of the current [54, 160] or other related observables.

4.3 Single-Particle Examples

Having introduced the FAPT formalism to derive non-adiabatic corrections and their relation to the Berry curvature, we now move on to illustrate these ideas with a variety of examples of increasing complexity. We start with the simplest case of the two-level system in a circular drive, followed by the exactly-solvable single particle in a periodically-displaced harmonic potential, where corrections due to FAPT may be cleanly isolated and analysed. We then move on to the quantum Kapitza pendulum – a non-linear single-particle system – where we delineate the role of photon absorption resonances. Finally, we study linear response and non-adiabatic corrections to observables in a driven qubit system, where a simple measurable connection to the topological Floquet Chern number is demonstrated through the Thouless energy pump.

4.3.1 Which Floquet Hamiltonian is the Adiabatically Connected One?

We open up the discussion of examples on adiabaticity in Floquet systems by analysing the two-level system in a circularly polarised field, see Sec. 2.1.3. We also use this opportunity to briefly comment on what happens in the van Vleck and Floquet-Magnus descriptions if one turns on the driving adiabatically. Recall that a detailed comparison of the two expansions was presented in Sec. 2.2.4. In particular, here we would like to show numerical results for this simple example, and highlight how one should correctly understand the gauge transformation defined by the initial kick in the van Vleck expansion in the context of FAPT.

Let us consider the system to be initially prepared in the ground state $|\downarrow\rangle$ of the non-driven Hamiltonian H_0 (see Eq. (2.19) with $B_{\parallel} = 0$). We then slowly turn on the driving amplitude B_{\parallel} , using the ramp:

$$B_{\parallel}(t) = B_{\parallel}^{\max} \times \begin{cases} 0 & \text{for } t \leq 0 \\ \cos^2\left(\frac{\pi}{2} \frac{t-t_R}{t_R}\right) & \text{for } 0 < t < t_R \\ 1 & \text{for } t \geq t_R \end{cases}$$

This ramp protocol is chosen because it starts and ends smoothly, i.e. $\dot{B}_{\parallel}(t=0) = \dot{B}_{\parallel}(t=t_R) = 0$ and, therefore, it is expected to minimize non-adiabatic effects related to the discontinuities in the velocity during the ramp (see e.g. Ref. [287]). Here t_R is the ramp time which is taken to be an integer multiple of the driving period, i.e. $t_R = lT$. It is also convenient to define the ramp speed/rate v as the rate of change of the magnetic field in the middle point of the ramp, i.e. $v = \dot{B}_{\parallel}(t_R/2) = \pi B_{\parallel}^{\max}/(2t_R)$.

The question we are interested in is whether the system, initially prepared in the ground state of H_0 , evolves into the GS of H_F or the GS of H_{eff} . In other words, we would like to know which ground state (i.e. the one of the stroboscopic or the non-stroboscopic Floquet Hamiltonian) is adiabatically connected to the ground state of the non-driven Hamiltonian. In Fig. 4.1 we show the value, at the end of the ramp, of the logarithmic fidelity to find the

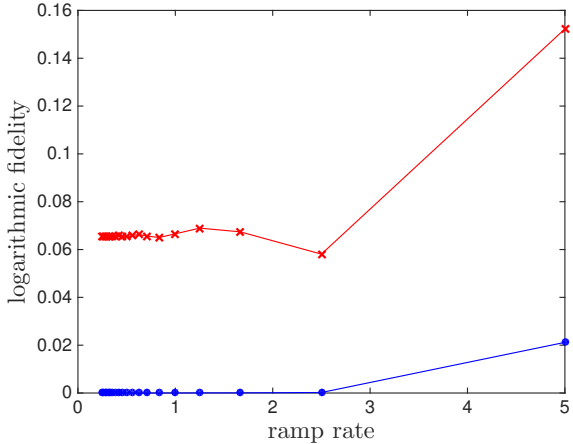


Figure 4.1: Logarithmic fidelity as a function of the ramp rate to find the system in the GS of the Floquet Hamiltonian $H_F[t_R]$, $-\log |\langle \psi(t_R) | \psi_{GS}(H_F) \rangle|^2$ (blue dots) and the GS of the effective Hamiltonian H_{eff} , $-\log |\langle \psi(t_R) | \psi_{GS}(H_{\text{eff}}) \rangle|^2$ (red crosses). The ramp rate is $v = \pi B_{\parallel}^{\max} / (2t_R)$. In order to reproduce the blue line in the non-stroboscopic (van Vleck) picture, one needs to apply the kick operator at time t_R to rotate the state: $|\psi_{GS}(H_{\text{eff}})\rangle = e^{iK_{\text{eff}}(t_R)} |\psi_{GS}(H_F[t_R])\rangle$.

system in each ground state: $-\log |\langle \psi(t_R) | \psi_{GS}(H_{\text{eff}}) \rangle|^2$. We find that, in the adiabatic limit (for large t_R or equivalently small ramp rate v), the system is in the ground state of the stroboscopic Floquet Hamiltonian $H_F[t_R]$ with unity probability, i.e. the GS of H_0 is adiabatically connected to the GS of $H_F[t_R]$. From this fact it immediately follows that the system cannot be in the GS of H_{eff} since the two ground states are different:

$$|\psi_{GS}(H_{\text{eff}})\rangle = e^{iK_{\text{eff}}(t_R)} |\psi_{GS}(H_F[t_R])\rangle$$

Therefore, in the van Vleck picture, the effect of the final kick at time t_R , which is responsible for a change of basis from the lab frame to the basis of H_{eff} , cannot be eliminated by the adiabatic ramp.

This finding also has very simple consequences for FNS dynamics, e.g. if we are interested in the average over one period of any observable \mathcal{O} after the ramp. Using the relation

between the ground states above and Eq. (4.3) we find

$$\begin{aligned}
\frac{1}{T} \int_{t_R}^{t_R+T} dt \langle \mathcal{O}(t) \rangle &= \frac{1}{T} \int_{t_R}^{t_R+T} dt \langle \psi_{GS}(H_F[t]) | \mathcal{O} | \psi_{GS}(H_F[t]) \rangle \\
&= \langle \psi_{GS}(H_F[t_R]) | \overline{\mathcal{O}}_F[t_R] | \psi_{GS}(H_F[t_R]) \rangle \\
&= \langle \psi_{GS}(H_{\text{eff}}) | \overline{\mathcal{O}}_{\text{eff}} | \psi_{GS}(H_{\text{eff}}) \rangle.
\end{aligned} \tag{4.30}$$

As discussed in Sec. 2.1.4, if the system is in an eigenstate of the Floquet Hamiltonian (here the ground state), the FNS expectation value of any observable is given by the expectation value of the corresponding dressed observable, calculated in the eigenstate of the Floquet Hamiltonian. One can freely choose whether one works in the stroboscopic (Floquet-Magnus) or the non-stroboscopic (van Vleck) pictures.

4.3.2 The Linearly Driven Harmonic Oscillator

Let us now consider the quantum harmonic oscillator with a periodically-displaced confining potential. This model is also exactly solvable and shall therefore prove useful as a first check of the FAPT expressions derived in Sec. 4.2.2. We consider the case where the drive consists of an oscillating force with frequency Ω whose amplitude is ramped according to some slow parameter $\lambda(t)$:

$$H(t) = \frac{p^2}{2m} + \frac{1}{2}m\omega_0^2 x^2 - A_f \Omega^2 \lambda(t) \cos(\Omega t + \varphi_0) x. \tag{4.31}$$

We pick units with $m\omega_0 = 1$ and explicitly introduce the driving phase φ_0 , such that one can easily distinguish between phase-averaged and non-averaged protocols. Further, we chose the amplitude of the drive to scale quadratically with the driving frequency, which leads to a non-trivial high-frequency regime.

We consider slow ramps, such that the oscillator starts in its ground state with the drive off at some $t_i < 0$ [$\lambda(t_i) = \dot{\lambda}(t_i) = 0$], and then smoothly ramp up the drive amplitude $\lambda(t)$ to the final value. It is convenient to set the final measurement time where we evaluate all

observables to $t_f = 0$ such that $|t_i|$ is equal to the ramp time. To simplify the notation, we define v as the instantaneous velocity at the final time, i.e. $v \equiv \dot{\lambda}(0)$ and we set the final value of $\lambda(0)$ to unity. The simplest protocol which satisfies these constraints is a quadratic ramp:

$$\lambda(t) = \left(\frac{t - t_i}{|t_i|} \right)^2 \quad (4.32)$$

with $v = 2/|t_i|$. As a consequence of the analysis in Sec. 4.2.2, the FAPT expansion is independent of the protocol used for the ramp. We confirmed this by comparing the exact dynamics numerically for various ramping protocols, and found an excellent agreement in the small $\dot{\lambda}$ limit.

One advantage of choosing this Hamiltonian is that it is exactly solvable. Namely for any driving protocol $f(t)$

$$H(t) = \frac{p^2}{2m} + \frac{m\omega_0^2 x^2}{2} - f(t)x$$

one can reduce the time-dependent problem to an effective static harmonic oscillator by transforming into a moving frame with respect to the classical trajectory $\eta(t)$, whose equation of motion is $\ddot{\eta}(t) + \omega_0^2 \eta(t) = f(t)/m$. The eigenstates in this frame and in the position basis are given in terms of the static harmonic oscillator states $\phi_n(x)$ and eigenenergies $E_n = \omega_0(n + 1/2)$ as:

$$\chi_n(x, t) = \phi_n(x - \eta(t)) \exp \left[i \left(m\dot{\eta}(t) (x - \eta(t)) - E_n t + \int_{t_i}^t dt' L(\eta, \dot{\eta}, t') \right) \right] \quad (4.33)$$

where $L(\eta, \dot{\eta}, t)$ is the classical Lagrangian for a driven oscillator:

$$L(\eta, \dot{\eta}, t) = \frac{1}{2} m \dot{\eta}^2(t) - \frac{1}{2} m \omega_0^2 \eta^2(t) + \eta(t) f(t).$$

Any solution to the time-dependent Schrödinger equation with Hamiltonian (4.31) is given by a linear combination of $\chi_n(x, t)$ with *time independent* coefficients. Using this method, we obtain not only the exact solution of the dynamics for arbitrary $\lambda(t)$ protocols, but also

the exact Floquet eigenstates at any fixed λ . For more details on the exact solution used to compare this model to FAPT see Appendix E.

To see why this model is interesting in the context of FAPT, let us start by solving it in the infinite-frequency limit. This is trivially done by a pair of unitary rotations, $|\psi^{\text{rot}}(t)\rangle = V_2^\dagger(t)V_1^\dagger(t)|\psi(t)\rangle$, where

$$V_1(t) = e^{iA_f\Omega\lambda\sin(\Omega t+\varphi_0)x}, \quad V_2(t) = e^{iA_f\lambda\cos(\Omega t+\varphi_0)p/m}. \quad (4.34)$$

One may readily confirm that this gives the rotating frame Hamiltonian

$$H^{\text{rot}}(t) = \frac{p^2}{2m} + \frac{1}{2}m\omega_0^2x^2 - A_f\omega_0^2\lambda(t)\cos(\Omega t + \varphi_0)x. \quad (4.35)$$

up to an irrelevant constant. This looks identical to the original Hamiltonian, except with $\Omega \rightarrow \omega_0$. But now the $\Omega \rightarrow \infty$ limit is trivial because the drive strength remains finite, and thus the infinite frequency Floquet Hamiltonian is simply the time average of H_{rot} [33]. This Floquet Hamiltonian is obviously λ -independent, and so are its eigenstates. However, as we shall see shortly, there is an important difference in the micromotion between the time-evolution due to Eq. (4.31) and Eq. (4.35). Hence, any non-adiabatic effects can occur solely due to the λ -dependence of the micromotion operator $P(\lambda, t)$. In App. E we explicitly demonstrate that the contribution due to this operator to the transition probabilities and observables has a well-defined infinite-frequency limit. Thus, this example serves as a direct proof that neglecting the effects of the micromotion operator on the non-adiabatic response can lead to erroneous conclusions.

Next, let us discuss the exact results for this setup and compare them with the predictions of the FAPT. In Fig. 4.2a and b we show the log-fidelity and the Floquet diagonal entropy versus the ramp rate v . As we discussed in the previous section, these are the observable-independent measures of the non-adiabatic corrections. We also show a comparison of the exact results with the predictions of FAPT, and find an excellent agreement

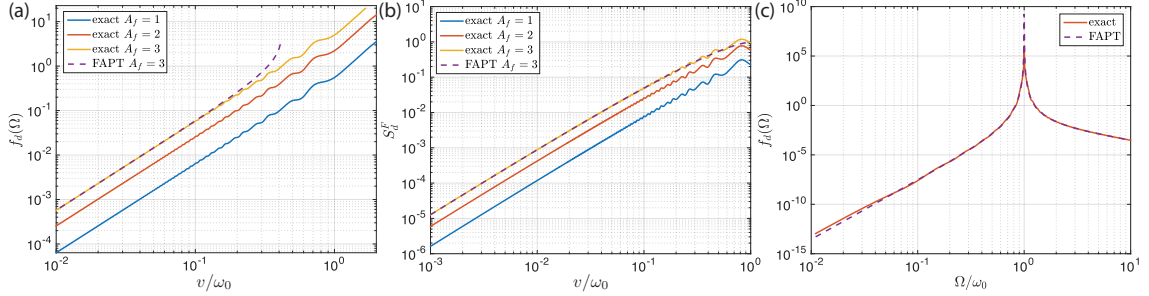


Figure 4.2: [Driven harmonic oscillator]. Non-adiabatic transitions: exact results for the log-fidelity (a) and Floquet diagonal entropy (b) at $\Omega/\omega_0 = 5$ as a function of the driving amplitude and the ramp velocity. The FAPT prediction is shown for $A_f = 3$ as a dashed line. (c) Log-fidelity as a function of Ω/ω_0 for $A_f = 3$, $m\omega_0 = 1$, and $v/\omega_0 = 0.04$. The red line shows the FAPT prediction. All excitations in the model are solely due to the micromotion (see text). The data is shown for the driving phase $\varphi_0 = 0$.

at small values of v . At this point we should briefly highlight a few important features of this model: first, it is interesting to note that the only source of excitations is the micromotion, not just at infinite frequency, but at any finite frequency as well; see App. E for details. One readily can check that in the leading order of FAPT and in the infinite frequency limit the system can only undergo the transitions to the first excited state, yielding:

$$p_1^F \xrightarrow{\Omega \rightarrow \infty} \frac{A_f^2 v^2}{2m\omega_0} \cos^2(\varphi_0). \quad (4.36)$$

In turn, this transition probability defines the log-fidelity and the Floquet diagonal entropy:

$$f_d = -\log(1 - p_1^F) \approx p_1^F, \quad S_d^F \approx p_1^F(1 - \log(p_1^F)),$$

which match well the numerical results plotted in Figs. 4.2a and b.

The above story is also supported by the behaviour of observables. For large v , the expectation values $\langle p^2 \rangle$ and $\langle x \rangle$ are misaligned from the corresponding expectations in the Floquet ground state, as seen in Fig. 4.3a and b. As the velocity approaches zero, they converge to the ground state expectation values. One caveat when scaling the amplitude of the drive quadratically with the driving frequency is that observables, which do not

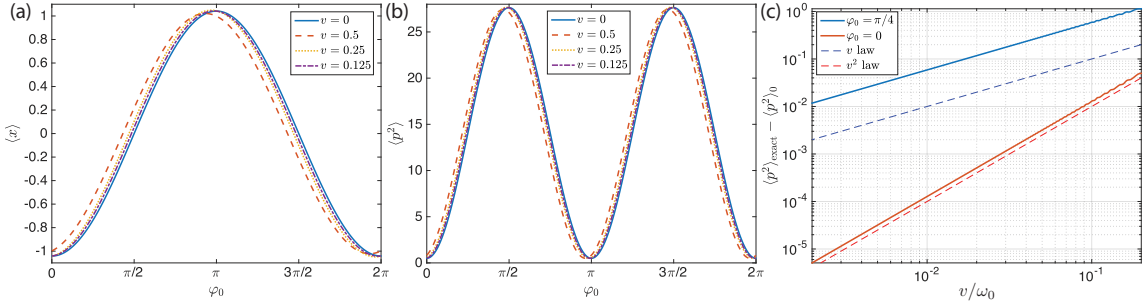


Figure 4.3: [Driven harmonic oscillator]. Observables for $A_f = 1$ and $\Omega/\omega_0 = 5$. Position operator $\langle x \rangle$ (a) and momentum-squared $\langle p^2 \rangle$ (b) as a function of the driving phase φ_0 , showing agreement in the adiabatic limit $v \rightarrow 0$. (c) Difference between the exact value of $\langle p^2 \rangle$ and the value predicted by FAPT for $\varphi_0 = 0$ (red) and $\varphi_0 = \pi/4$ (blue). The blue and red dashed lines show a v and a v^2 -power law for comparison.

commute with the driving, may not have a well-defined behaviour in the strict $\Omega \rightarrow \infty$ limit due to a divergent amplitude of the micromotion in the lab frame. In this example, the adiabatic expectation value $\langle p^2 \rangle$ diverges as Ω^2 , while the non-adiabatic correction remains finite. For the expectation value $\langle x \rangle$, on the other hand, the ground state converges to a finite value in the infinite-frequency limit, but the non-adiabatic corrections vanish as Ω^{-1} . Figure 4.3c shows the difference between the exact expectation value of p^2 at the measurement point and the corresponding FAPT prediction to order $\mathcal{O}(v)$. Whenever the measurement is taken at a time-reversal symmetric point of the original time-periodic Hamiltonian (4.31), i.e., for $\varphi_0 = 0, \pi$, where $H(t) = H(-t)$, there is no linear non-adiabatic correction to the observables [cf. Sec. 4.2.3] and the leading non-adiabatic contribution scales as v^2 . However, if the measurement breaks time-reversal symmetry, then a linear correction appears. This situation is very reminiscent to that in non-driven systems, where time-reversal symmetry (specifically real Hamiltonians) leads to the zero Berry curvature and hence vanishing linear non-adiabatic corrections to generalised forces [260, 287].

4.3.3 The Quantum Kapitza Pendulum

We now turn our attention to a more complicated single-particle model – the quantum Kapitza pendulum. In the classical limit, this model is the prototype to study dynamical

localisation [5], since strong fast shaking of the pivot point of a pendulum bob leads to stabilisation of the originally unstable inverted equilibrium ($\theta = \pi$). In the classical limit, this problem is also known to feature coexisting regions of regular and chaotic behaviour suggesting that the Floquet Hamiltonian as a local operator is ill-defined. Nevertheless, we shall see that one can make use of the quantum Floquet theory by first introducing an ultraviolet (UV) cutoff, which makes the Hilbert space finite-dimensional, and then identifying the states, which are insensitive to the cutoff. The Kapitza pendulum differs from the harmonic oscillator due to the non-linearity of the confining potential. We shall also shortly see that this non-linearity is, in fact, responsible for the existence of photon resonances, which result in new non-adiabatic effects absent in non-driven systems or integrable Floquet systems.

The Hamiltonian of the quantum Kapitza pendulum reads

$$H(t) = \frac{p_\theta^2}{2m} - m\omega_0^2 \cos \theta - mA_f \lambda(t) \Omega \cos \Omega t \cos \theta, \quad (4.37)$$

where p_θ is the angular momentum operator and m is the pendulum's momentum of inertia. As in the previous example we scale the driving amplitude to have non-trivial infinite-frequency limit. For practical purposes, we work in the angular momentum basis⁶, $p_\theta|l\rangle = l|l\rangle$, such that the operator $\exp(i\theta)|l\rangle = |l+1\rangle$ shifts the angular momentum by one quantum. Consequently, the Hamiltonian assumes the form

$$H(t) = \frac{1}{2m} \sum_{l=-\infty}^{\infty} l^2 |l\rangle \langle l| - \frac{m}{2} (\omega_0^2 + A_f \lambda(t) \Omega \cos \Omega t) \sum_{l=-\infty}^{\infty} (|l+1\rangle \langle l| + |l\rangle \langle l+1|), \quad (4.38)$$

which is equivalent to a free particle hopping on a lattice in the presence of a harmonic trap. The drive translates to periodically-modulated hopping. We note that this Hamiltonian could be readily realised, for instance, with non-interacting ultracold atoms in a harmonic trap.

⁶Since the Kapitza pendulum is a one-dimensional system, the angular momentum has only a z -component, and thus the quantum number l is understood as the eigenvalue of the operator $p_\theta = L_z$.

The angular momentum basis is particularly convenient to simulate the time-dependence of the system because it discretises the Hilbert space. To deal with the unbounded spectrum, we impose a high-frequency cut-off by keeping only a finite number of angular momentum states: $l = -M, -M + 1, \dots, 0, \dots, M - 1, M$. We made sure that the results presented here do not change with M . Further, we use parity symmetry ($l \rightarrow -l$) to divide the total Hilbert space into an even-parity subspace, containing $M + 1$ states including the ground state, and an odd subspace containing the remaining M states.

We are now interested in slowly ramping up the driving amplitude according to a smooth protocol, which we choose to be slightly different than the quadratic protocol used in the harmonic oscillator example:

$$\lambda(t) = 2 \sin^2 \left(\frac{\pi}{2} \frac{t - t_i}{2|t_i|} \right) \quad (4.39)$$

from time $t_i < 0$ to the final time at $t = 0$. This protocol slowly ramps the driving amplitude from zero to a finite value $\lambda(0) = 1$ with the final velocity $v \equiv \dot{\lambda}(0) = \pi/2|t_i|$. We start in the ground state of the non-driven Hamiltonian $H(t_i)$. Due to the unbounded character of the Kapitza spectrum, the numerical simulations necessarily produce a folded quasienergy spectrum at any fixed driving frequency. This poses the fundamental problem of identifying the adiabatic state in the first place. As we shall see shortly, this is not a mere mathematical difficulty but rather a genuine physical problem. Obviously, if we cannot identify the proper adiabatic state the whole concept of FAPT is meaningless.

However, the situation is not as bad as it seems. It is intuitively clear that at high driving frequencies the Kapitza pendulum should remain stable against small perturbations, at least near the equilibrium positions. One can readily observe this stability numerically as well. To find the adiabatically-connected state, we start from the non-driven Hamiltonian at $\lambda = 0$ and continuously follow it as we gradually increase the drive amplitude (see red dots in Fig. 4.5). We refer to this state of smallest angular momentum spread as the Floquet ground state, and this is the state we choose to target. We checked nu-

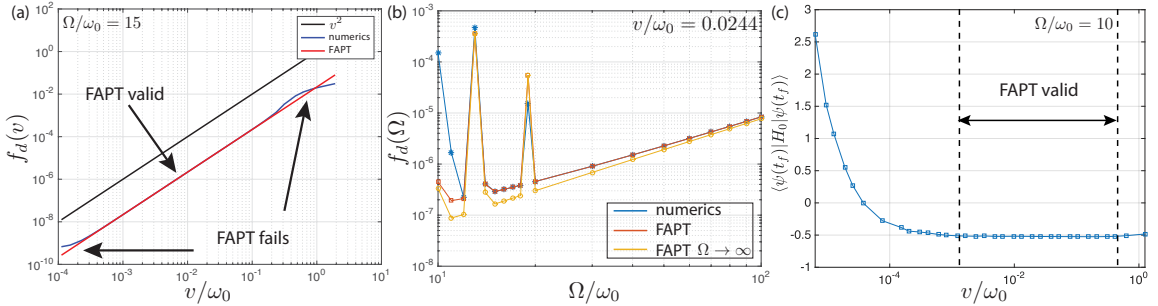


Figure 4.4: [Kapitza pendulum]. (a) Comparison between FAPT and exact numerics shows the existence of an adiabatic regime in the excitation probability (similar to log-fidelity) in for $\Omega/\omega_0 = 15$. (b) Frequency-dependence of the excitation probability (log fidelity) displaying the exact numerical data (blue stars), FAPT (red squares), and the infinite-frequency FAPT (yellow circles) for $v = 0.0244$. (c) Velocity dependence of the energy absorbed from the drive at the measurement time for $\Omega/\omega_0 = 10$. The model parameters are $m\omega_0 = 1$, $A_f = 2$. The infinite-frequency FAPT is obtained by keeping the $\ell = 0 = \ell'$ term from the sum in Eq. (4.17).

merically that this procedure is reliable for frequencies $\Omega/\omega_0 \gtrsim 7$, but it eventually fails once the Floquet operator becomes nonlocal and then there is no natural state to call the Floquet ground state. We note that, while this procedure seems somewhat ad-hoc, it may be systematically extended to arbitrary systems using the inverse-frequency expansion. In particular, one can identify the Floquet ground state as the eigenstate that has the largest overlap with the effective static ground state obtained via the first few orders of the high-frequency expansion. We shall explore this connection to the inverse-frequency expansion in more detail in Sec. 4.5. Instead of the HFE one can use some other expansion producing a local Floquet Hamiltonian or even use some variational approach giving a local Hamiltonian having the highest overlap of eigenstates with the eigenstates of the Floquet Hamiltonian. Alternatively, in Ref. [288] the Floquet ground state for an extended spin system was defined as the lowest entanglement state. Generically this identification is also only applicable to high driving frequencies. At low frequencies all Floquet eigenstates are expected to become maximally entangled infinite-temperature states [256], and therefore the very notion of adiabaticity becomes ill-defined.

Figure 4.4 gives a confirmation that there exists an adiabatic regime at large frequencies

in which the Floquet ground state can be prepared with high fidelity. Not only does the excitation probability scale quadratically with the ramp speed, but there also exists a large interval of velocities for which the FAPT formula in Eq. (4.18) quantitatively reproduces the correct results for the leading non-adiabatic correction⁷. Interestingly, lowering the ramp speed too far leads to an increase of the excitations in the system. This increase in excitations and Floquet diagonal entropy (Fig. 4.6) with decreasing velocity is also associated with a stronger heating of the system at slower ramp rates, as seen in Fig. 4.4c. This is clearly inconsistent with the expectations from equilibrium thermodynamics, representing an important fundamental consideration for Floquet thermodynamics⁸. Moreover such a non-monotonic increase in entropy and energy implies that there is no differentiable local Floquet Hamiltonian even in the high-frequency regime.

In Fig. 4.4b we show the frequency dependence at fixed ramp rate of the log-fidelity f_d , see Eq. (4.18). In the infinite-frequency limit, we find an agreement between the exact numerical curve (blue stars) with both the finite-frequency (red squares) and infinite-frequency (yellow circles) stroboscopic FAPT predictions. However, at finite frequencies the two deviate, with the difference reaching up to a factor of 2 at low frequencies. Notice that finite-frequency FAPT is significantly more accurate than its infinite-frequency counterpart, as it includes the crucial contributions due to \mathcal{A}_λ^P , i.e. due to the kick operator. The exact numerical curve features isolated peaks at specific values of Ω , which we will see correspond to strong resonances encountered during the ramp. Figure 4.4c, shows the energy at the measurement time as a function of the ramp velocity. There exists a large plateau at intermediate velocities which is described by FAPT. However, at smaller ramp speeds the excitations appear in the energy as well. We thus see that the failure of FAPT for small frequencies and velocities is related to physically-observable heating.

⁷We note that in the figures comparing the FAPT formula with the numerical solution, we evaluated (4.16) numerically, and did not use any high frequency approximants discussed in later sections.

⁸Similar non-adiabatic effects can be anticipated in disordered systems with localised excitations, both single-particle and MBL, see Ref. [289] for a discussion.

4.3.3.1 The Role of the Level Crossings

We now demonstrate that these excitations at low ramp rate are due to the existence of photon absorption avoided crossings in the Floquet spectrum[157, 274]. The basic idea is that energy in Floquet systems is only defined modulo Ω . Then as the UV cutoff M is taken to infinity, the quasienergy spectrum becomes increasingly dense. As the density goes to infinity, one will find many accidental crossings between quasienergies (cf. Fig. 4.5b), which in turn have very small gaps opened up at high order in perturbation theory by multi-photon processes. So as the UV and/or thermodynamic limit is taken, the Floquet spectrum approaches an infinitely-dense set of infinitely-weak avoided crossings. We refer to these as photon-absorption avoided crossings or resonances. It is precisely these resonances that led Hone et al. in Ref. [274] to conclude that no adiabatic limit exists for Floquet systems, but as our numerics just demonstrated, there is still a wide range of ramp velocities for which these resonances are unimportant and FAPT provides a good description of the excitations in the system. This is especially relevant for experiments which need to target the correct parameter regime. Let us examine the effect of these resonances on adiabaticity more closely, using the Kapitza pendulum as an example.

To better elucidate the role of these photon absorption avoided crossings, consider first ramping the non-driven Hamiltonian

$$H_{\text{ave}}(t) = \frac{p_\theta^2}{2m} - m\omega_0^2 \cos \theta + \frac{m\lambda^2 A_f^2}{4} \sin^2 \theta, \quad (4.40)$$

which is nothing but the Floquet Hamiltonian for the Kapitza pendulum in the infinite-frequency limit, see Sec. 3.1.1. Since this system is not periodically-driven, the conventional quantum adiabatic theorem applies. As the spectrum exhibits avoided level crossings upon tuning λ the adiabatic theorem requires that the velocity be small enough so that one remains in the same *energy* manifold while passing through the avoided crossing. An example of such crossing, which should be avoided in adiabatic limit is shown in Fig. 4.5a.

These crossings also occur in the finite frequency Floquet Hamiltonian identified by a green circle in Fig. 4.5b. One can numerically identify these crossings by comparing the spectra of the Floquet Hamiltonian and of the approximate unfolded Floquet Hamiltonian obtained e.g. within the inverse-frequency expansion. Physically these crossings occur between Floquet eigenstates with small difference in both Floquet energies (Fig. 4.5b), and the energies defined as expectation values of the infinite frequency Hamiltonian (Fig. 4.5a). In the following, we refer to this type of avoided crossings as ‘standard’.

At any fixed driving frequency one can also identify additional avoided crossings, which do not show up in the infinite frequency Hamiltonian and, in fact, in any order in inverse-frequency expansion. These “photon-absorption crossings” or “photon resonances” only show up in the *quasienergy* spectrum (Fig. 4.5b) and appear as a result of strong hybridisation between energy levels and the photon field. Such crossings correspond to a small difference between the Floquet quasienergies but large, of the order of $n\Omega$ with $n = 1, 2, \dots$, difference between the energies of the infinite-frequency Floquet Hamiltonian. Adiabatic transition through such photon resonances should be understood as in fact a diabatic crossing of these levels as shown in Fig. 4.5d. Indeed these crossings arise due to a finite matrix element with a highly excited folded state such that the wave functions of the two participating states exhibit a very different behaviour. For instance, in the case of the Kapitza pendulum, the GS is a smooth non-oscillatory function resembling a Gaussian, while a highly excited scattering state typically has many oscillations corresponding to its large kinetic energy, cf. Fig. 4.5d. When passing a photon-absorption avoided crossing, the two states hybridize strongly and probability amplitude may be transferred to the high-energy state, depending on the crossing speed. If one goes too slowly the wave function changes *drastically* after the crossing and we find the system in the highly excited state instead. Hence, we are lead to the conclusion that photon-absorption avoided crossings should be passed *diabatically*, so that the system will remain in the appropriately connected *energy* manifold. Therefore, when we speak of “adiabaticity” in the context of FAPT, we keep in mind that this truly involves adiabatic ramping across standard avoided crossings (Fig.

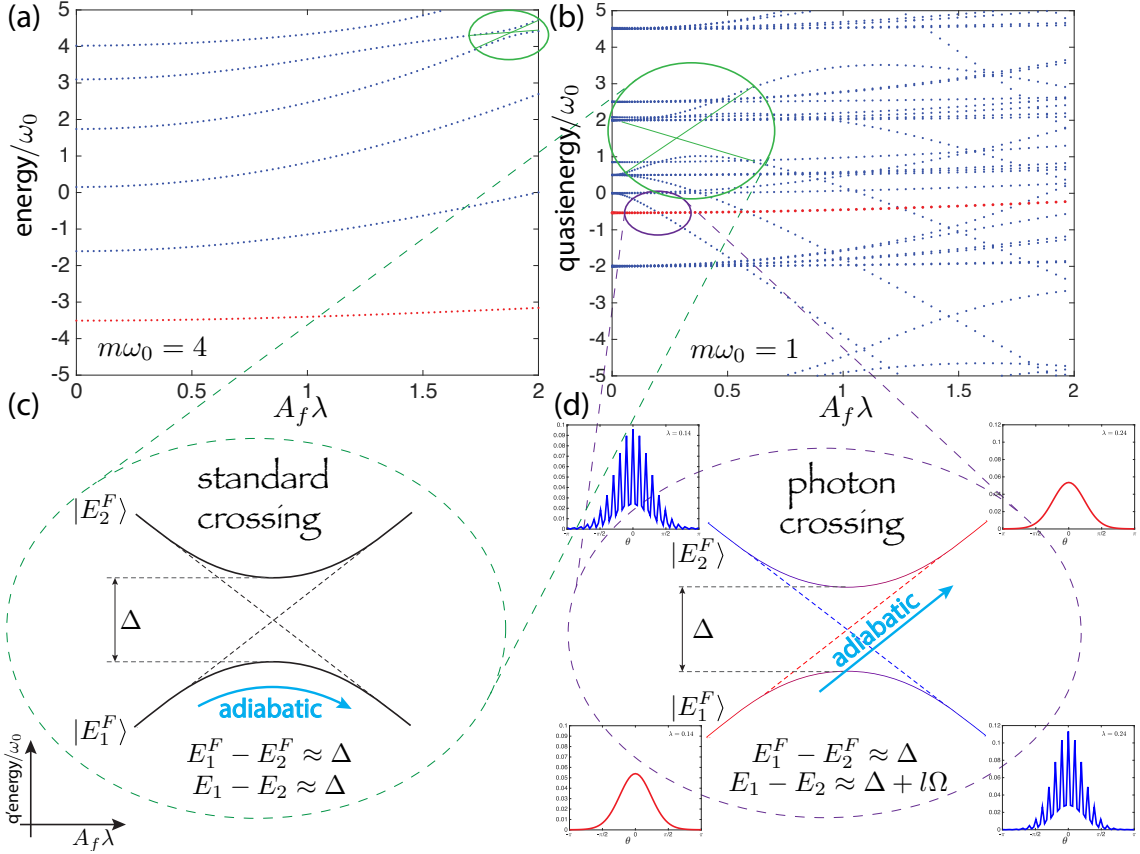


Figure 4.5: [Kapitza pendulum]. (a) The low-energy spectrum of the Hamiltonian (4.40) for $m\omega_0 = 4$ showing the standard avoided crossings (within green ellipse), which impose the limits for the validity of static adiabatic perturbation theory. (b) The Floquet spectrum of the Kapitza Hamiltonian (4.37) for $m\omega_0 = 1$. Apart from the standard avoided crossings (green ellipse), new avoided crossings appear due to photon absorption processes (purple ellipse). The Floquet ground state is shown in red dots. The insets show the wave function right before and after such a photon-absorption avoided crossing. We see that standard gaps must be crossed adiabatically (c), while photon absorption gaps need to be crossed *diabatically* for FAPT to hold (d). The parameters are $\Omega/\omega_0 = 10$, and the cut-off parameter is $M = 20$.

4.5c) and diabatic ramping across photon absorption crossings (Fig. 4.5d), meaning that adiabaticity in the conventional sense is not adiabaticity in the Floquet sense.

The physics at ultra small velocities beyond FAPT can be understood as a cascade of Landau-Zener (LZ) transitions due to resonances with higher-energy states induced by the drive [157]. To test this idea heuristically, we compare the prediction of LZ theory

and find a reasonable agreement, cf. Fig. 4.6a, b. Note that, the LZ physics is only valid in the immediate vicinity of the level crossings but, in general, the system traverses a multitude of these, and the simple LZ formula is expected to break down. Finding the sweet spot in velocity between standard and photon-absorption avoided crossings becomes increasingly difficult to achieve as the driving frequency decreases (or the driving amplitude increases) and eventually at low frequencies this window disappears and adiabaticity is completely lost, as seen in Fig. 4.6. Indeed, while this distinction between the two types of avoided crossings is quite sharp for the data shown, at lower driving frequencies it will be lost, and the choice of the target state will require more care. We also note that the scenario described above generalises to other nonintegrable models. In the generic situation one cannot always classify all crossings as being ‘standard’ or originating from photon-absorption resonances. In Sec. 4.5, we shall argue that these photon absorption level crossings are absent not only in the spectrum of the infinite frequency Floquet Hamiltonian, but are in fact beyond any order of the inverse-frequency expansion.

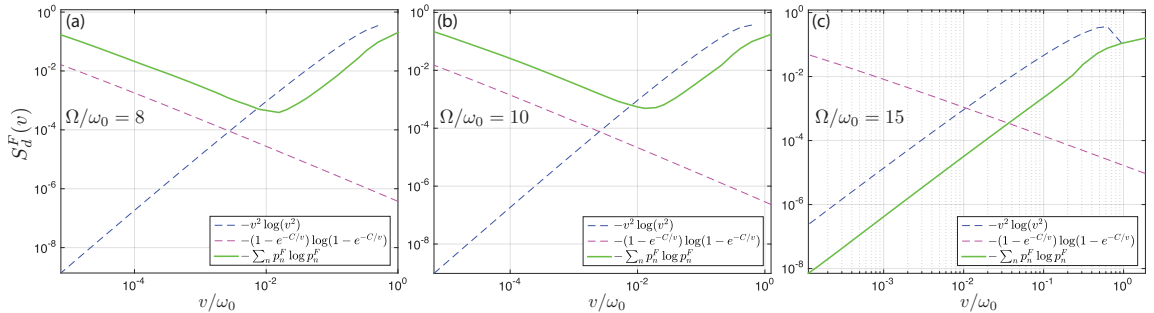


Figure 4.6: [Kapitza pendulum]. Numerical results for the Floquet diagonal entropy $S_d^F = -\sum_n p_n^F \log p_n^F$, $p_n^F = |\langle n_F | \psi(t_f) \rangle|^2$ in the basis of the final Floquet Hamiltonian as a function of the ramp speed v . The three panels correspond to $\Omega/\omega_0 = 8$ (a), $\Omega/\omega_0 = 10$ (b), and $\Omega/\omega_0 = 15$ (c). The regime of validity of FAPT is determined by the velocity range for which the entropy approximately follows the v^2 -law. The breakdown of FAPT is well-captured by Landau-Zener transitions between resonantly coupled states (cf. Fig. 4.5). The model parameters are $m\omega_0 = 1$, $A_f = 2$. The constant C in low velocity fitting was chosen arbitrary.

4.3.4 A Nonequilibrium Topological Transition and the Thouless Energy Pump

Having demonstrated that the adiabatic theorem for periodically driven systems agrees well with numerical simulations, we now elaborate on the previously-stated connection between non-adiabatic corrections and Berry curvature, cf. Sec. 4.2.4. Previous work generalised and studied the Kubo response of noninteracting systems with electron conduction using the example of driven graphene [39, 290, 291], and derived expressions for the Floquet Berry curvature and the Chern number (a.k.a. the quantised conductivity) in the limits of weak probe coupling. These papers tacitly assumed the presence of an adiabatic limit, which we have seen does not always exist for Floquet systems. Furthermore, a number of cold-atoms experiments reported successful measurements of the Berry curvature and the associated Chern number of a topological Floquet band [56–58] using linear response techniques. The experiments involved high-frequency driving, relative to the bare energy scales. Hence, it is natural to expect that for $\Omega \rightarrow \infty$, this procedure allows one to measure the Chern number of the bands associated with the Floquet Hamiltonian H_F . However, as experiments are performed at finite frequencies, where non-equilibrium effects become important, one might wonder how this simple picture acquires modification.

In Sec. 4.2.4, we generalised these results to arbitrary interacting systems and drive strengths, and demonstrated that they hold true only as long as FAPT holds. One important point that we have seen in the Kapitza pendulum is that FAPT is not generally valid for all ramp velocities, which is intricately related to the absence of a generic Floquet adiabatic limit [274]. Therefore, the discussion of Floquet geometry and topology holds exclusively in the regime of validity of FAPT, and is expected to fail when the effect of photon absorption resonances becomes sizeable and FAPT fails. This is an important result of our theory, suggesting that care must be taken in measuring Floquet geometry and topology using these linear response techniques.

4.3.4.1 The Circularly Driven Qubit

Before we discuss the more interesting case of a linearly-driven qubit, let us briefly study its exactly solvable circularly driven counterpart. Setting the energy scale to unity, let us conveniently parametrise the Hamiltonian (2.19) by $B_z = \cos \theta$ and $B_{\parallel} = \sin \theta$ as follows:

$$H(t, \theta, \phi) = \cos \theta \sigma^z + \sin \theta \left(e^{-i(\Omega t + \phi)} \sigma^+ + \text{h.c.} \right). \quad (4.41)$$

We now change the parameter θ slowly in time, such that $\theta(t_i) = 0$ and $\theta(t_f) = \pi$. In the limit $\Omega \rightarrow 0$ the system is known to be topological with the (first) Chern number $C_1^F = 1$ [125].

In Sec. 2.1.3 we applied a transformation to a rotating frame to solve the model exactly,

$$\begin{aligned} V(t) &= \exp(-i\sigma^z \Omega t/2), \\ H^{\text{rot}}(\theta, \phi) &= \left(\cos \theta - \frac{\Omega}{2} \right) \sigma^z + \sin \theta (\cos \phi \sigma^x + \sin \phi \sigma^y) \end{aligned}$$

finding the non-stroboscopic van Vleck Hamiltonian:

$$H_{\text{eff}}(\theta) = \left(\frac{\Omega}{2} - \sqrt{(\cos \theta - \Omega/2)^2 + \sin^2 \theta} \right) \sigma^z,$$

whose eigenvalues are denoted by ϵ^F , and have a well-defined infinite-frequency limit. The Floquet gauge potential in the moving frame is a function of the slowly-changing parameter θ , and is given by

$$\mathcal{A}_F^{l=+1}(\theta) = \frac{i \sin \theta \cos^2 \alpha(\theta)}{2 \cos \theta - \Omega/2} \sigma^-, \quad \mathcal{A}_F^{l=-1}(\theta) = [\mathcal{A}_F^{l=+1}]^\dagger, \quad \mathcal{A}_F^{l \neq \pm 1}(\theta) = 0, \quad (4.42)$$

where, as before, $\tan \alpha = \frac{\sin \theta}{\cos \theta - \Omega/2}$. This allows us to calculate exactly the Berry curvature associated with the Floquet Hamiltonian. Making use of azimuthal symmetry, the operator

we need to measure (a.k.a. the generalised force) is given by

$$\begin{aligned}\mathcal{M}_\phi^F(t) &= \partial_\phi|_{\phi=0} H(t, \theta, \phi) = V(t) \partial_\phi|_{\phi=0} H^{\text{rot}}(\theta, \phi) V^\dagger(t), \\ \partial_\phi|_{\phi=0} H^{\text{rot}}(\theta, \phi) &= \frac{i}{2} [\sigma^z, H^{\text{rot}}(\theta, \phi = 0)] = \sin \theta \sigma^y.\end{aligned}\quad (4.43)$$

In turn, the Floquet Berry curvature and the Floquet Chern number can be calculated as

$$\begin{aligned}F_{\theta\phi}^F(\theta, \phi, t) &= \frac{\mathcal{A}_{\uparrow\downarrow}^{(-1)} e^{i(\Omega t + \phi)}}{\epsilon_\uparrow^F - \epsilon_\downarrow^F - \Omega} \times \sin \theta \left[V \sigma^y V^\dagger \right]_{\downarrow\uparrow}(t) + \text{h.c.} \\ &= \frac{\sin \theta}{2} \frac{8 - 4\Omega \cos \theta}{(\Omega^2 + 4 - 4\Omega \cos \theta)^{3/2}}, \\ C_1^F(\Omega) &= \int_0^{2\pi} \frac{d\phi}{2\pi} \int_0^\pi d\theta \overline{F_{\theta\phi}^F(\theta, \phi)} = \frac{1}{2} [\text{sgn}(\Omega - 2) - (\Omega + 2)].\end{aligned}\quad (4.44)$$

Note how measuring σ^y in the rotating frame gets rid of the fast time-dependence of \mathcal{F} and, as a result, leads to a quantised Chern number.

Observe that a non-equilibrium topological phase transition occurs at $\Omega = 2$. Because of this, if one applies the inverse-frequency expansion, one will find $C_1^F = 0$ at any frequency (also for $\Omega < 2$), since the series assumes a smooth dependence on Ω . The presence of this phase transition necessarily means that the expansion breaks down at low frequencies. As we discussed in Sec. 3.2.1.1, this critical frequency corresponds to the maximal radius of convergence of the exact quasienergies $\epsilon_0^F(\Omega) = \epsilon^F(\Omega, \theta = \pi)$ ⁹ when expanded in Ω . Unlike in chaotic or non-integrable systems, though, due to the small dimensionality of the Hilbert space, the Floquet Hamiltonian of this model for $\Omega < 2$ is a well-defined local operator where a different expansion for it can be written down using the exact solution. A similar situation occurs in the Floquet realisation of Haldane's model where the Chern number at low frequencies jumps discontinuously when $\Omega < W_{\text{eff}}(\Omega)$ [the effective band width] and the Floquet spectrum folds [59].

⁹The subscript 0 in ϵ_0^F refers to the final ramp time which is assumed to be at $t = 0$, and corresponds to $\theta = \pi$.

4.3.4.2 The Linearly Driven Qubit

We now illustrate the same ideas from geometry and topology using an example of a linearly-driven two-level system, a.k.a. a qubit. In Sec. 4.2.4 we showed that the leading correction to the phase average of the expectation value of the generalised force $M_\mu(t) = -\langle\psi(t)|\partial_\mu H(t)|\psi(t)\rangle$ is proportional to the phase-averaged Berry curvature. This is very similar to the static APT case, where leading corrections to adiabaticity have been used to measure the Berry curvature of one and two-qubit systems and subsequently integrated over a closed manifold to give their topologically-invariant Chern number [292, 293]. However, a detailed look at these particular superconducting qubits shows that they are actually Floquet systems. In particular, at first approximation, they consist of two far-detuned bare levels $|\uparrow\rangle$ and $|\downarrow\rangle$ whose splitting ω_q is much larger than the desired qubit operation frequency. Then microwave fields are shone on this system at frequency Ω_0 that is nearly resonant with the qubit transition, which is able to couple these levels (see Fig. 4.7a).

In the lab frame, this system is described by the Hamiltonian

$$H_{\text{lab}} = \frac{\omega_q}{2} \sigma^z + g \cos(\Omega_0 t + \phi) \sigma^x , \quad (4.45)$$

where g is proportional to the strength of the driving field. In general, the drive is controllable such that Ω_0 , g , and ϕ are arbitrary functions of time. Going to the rotating frame via the unitary $V(t) = e^{i\sigma^z\Omega_0 t/2}$, $|\psi^{\text{rot}}(t)\rangle = V(t)|\psi_{\text{lab}}(t)\rangle$ we find the effective Hamiltonian

$$\begin{aligned} H^{\text{rot}}(t) &= \frac{\omega_q - \Omega_0}{2} \sigma^z + g \cos(\Omega_0 t + \phi) [\sigma^x \cos(\Omega_0 t) - \sigma^y \sin(\Omega_0 t)] \\ &= \frac{\omega_q - \Omega_0}{2} \sigma^z + \frac{g}{2} (\sigma^x \cos \phi + \sigma^y \sin \phi) + \frac{g}{2} (\sigma^x \cos(2\Omega_0 t + \phi) - \sigma^y \sin(2\Omega_0 t + \phi)) . \end{aligned} \quad (4.46)$$

To more clearly demonstrate the Hamiltonians that are generally simulated in these systems, we parameterize the detuning $\delta \equiv \omega_q - \Omega_0$ and the drive strength g as $g = -B \sin \theta$ and $\delta = -B \cos \theta$. Then keeping these values constant while taking the high frequency limit, $\Omega_0 \rightarrow \infty$, this model allows one to simulate arbitrary single-qubit Hamiltonians of

the form $H = -\mathbf{B} \cdot \boldsymbol{\sigma}/2$. It is precisely in this limit that Schroer et al. [292] measured topological transitions in a superconducting qubit using leading non-adiabatic corrections akin to Eq. (4.25).

However, at lower frequencies, the strong micromotion induced by the time-dependent third term in Eq. (4.47), will have a strong effect on the non-adiabatic corrections to the dynamics. Note that the rotating frame Hamiltonian is actually periodic with frequency $\Omega = 2\Omega_0$; therefore we rewrite the Hamiltonian as

$$H^{\text{rot}}(t) = -\frac{B}{2} \left[\cos \theta \sigma^z + \sin \theta (\sigma^x \cos \phi + \sigma^y \sin \phi) + \sin \theta (\sigma^x \cos(\Omega t + \phi) - \sigma^y \sin(\Omega t + \phi)) \right]. \quad (4.47)$$

Unlike the related model of a qubit in a circularly-polarised drive, which can be solved exactly by mapping it to a time-independent Hamiltonian, there exists no simple closed-form solution for the present model.

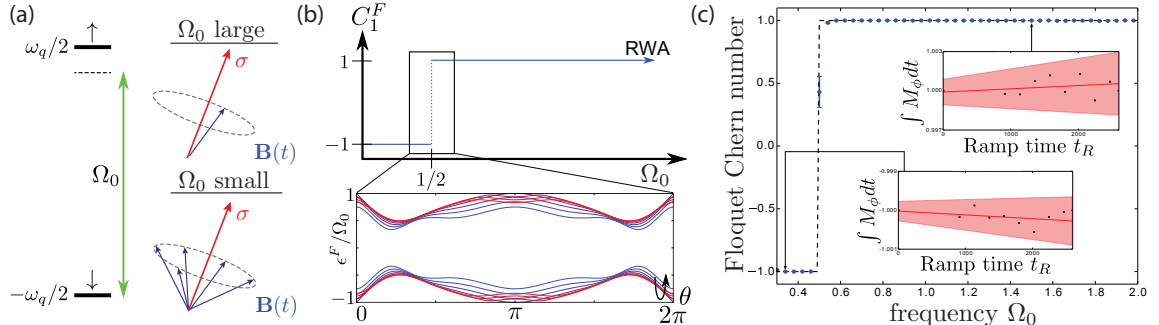


Figure 4.7: [Driven qubit]. Floquet topology of a strongly driven two-level system. (a) Setup: two levels are split by a bare frequency ω_q and driven near resonance at frequency Ω_0 . In the rot frame the system looks like a spin-1/2 in a rotating magnetic field $\mathbf{B}(t)$ with frequency $\Omega = 2\Omega_0$. At large Ω_0 , the Rotating Wave Approximation (Sec. 3.3) applies, but at low Ω_0 it does not. (b) By sweeping $\mathbf{B}(t)$ over a sphere in parameter space, one measures the Floquet Chern number C_1^F . At high frequency the Chern number is 1, like that of a spin-1/2 in a magnetic field. However, at $\Omega_0 = 1/2$ the system undergoes a topological transition where a gap closes at the edge of the Floquet zone. This gap closing is shown in the bottom panel, where the colour varies from blue at $\Omega_0 = 0.4$ to red at $\Omega_0 = 0.6$. (c) The topological transition can be measured by linear response as described in the text. Using the protocol $\theta(t) = \pi \sin^2 \left(\frac{\pi(t+t_R)}{2t_R} \right)$, a linear fit to the time-integrated generalised force M_ϕ gives the Floquet Chern number as the y -intercept (insets). The main figure shows the frequency-driven topological Chern transition obtained from these fits.

As discussed earlier, the phase-averaged Berry curvature $\overline{F}_{\theta\phi}$ is measurable from Floquet linear response and is given by

$$\overline{M}_\phi = \overline{M}_\phi^{(0)} + \dot{\theta} \overline{F}_{\phi\theta} + \mathcal{O}(\dot{\theta}^2), \quad (4.48)$$

where $M_\phi = \langle -\partial_\phi H_{\text{lab}} \rangle$ is the generalised force in the moving frame and $\overline{M}_\phi^{(0)}$ indicates its phase average in the Floquet ground state. This average is equal to zero by gauge invariance of the Floquet spectrum; according to Eq. (4.24)

$$\overline{M}_\phi^{(0)} = -\partial_\phi \epsilon_0^F = 0.$$

We also note that $-\partial_\phi H_{\text{lab}}$, which for static problems can be interpreted as a simple magnetisation, is now a more complicated time-dependent observable.

Consider now a ramp of θ in the time interval $[-t_R, t_R]$ such that $\theta(t = -t_R) = 0$ and $\theta(t = t_R) = \pi$. For larger t_R , this ramp more adiabatically interpolates between $\theta = 0$ and $\theta = \pi$. Then for fixed ϕ , integrating the expectation value \overline{M}_ϕ along the ramp gives

$$\int \overline{M}_\phi(t, \theta) dt \approx \int \dot{\theta} \overline{F}_{\phi\theta}(\theta) dt = \int \overline{F}_{\phi\theta}(\theta) d\theta = \frac{1}{2\pi} \int \overline{F}_{\phi\theta}(\theta) d\theta d\phi = C_1^F. \quad (4.49)$$

Here we use the fact that since ϕ is just the driving phase in the lab frame, phase-averaged values of the Floquet Berry curvature are ϕ -independent. Therefore one can extract the Floquet Chern number by simply averaging the experimentally-measurable generalised force over the angle θ . Note that Eq. (4.49) is completely general, relying solely on the validity of FAPT. Below we will show that this generalised force is also related to the work done on the system.

This procedure is carried out for the qubit model in Fig. 4.7. Note that the long-time integration automatically averages over many cycles, so the phase averaging is done automatically by the slow ramp. In the high-frequency limit, as expected, the Chern number is found to be one as in the $\Omega \rightarrow \infty$ case. However, this behaviour continues down

to much lower frequencies where the high-frequency limit is no longer valid. Even more interesting is the fact that, as the frequency is further lowered, the Floquet ground state “inverts,” as seen in Fig. 4.7b. This causes the Chern number to jump discontinuously to -1 , i.e., the system undergoes a topological transition, similar to those found in non-interacting Floquet topological insulators [59]. This is confirmed by numerical simulation in Fig. 4.7c. Thus we see that not only is the Floquet Chern number measurable, but we can actually get novel topological transitions in the low-frequency regime.

While these ideas have been illustrated for the case of a qubit model, they are completely general. Thus situations such as cold atoms in flux lattices or Floquet topological insulators that have quantised Floquet invariants should in principle be susceptible to having these invariants measured by procedures analogous to that above. It bears mention that these techniques require one to measure $\partial_\lambda H(t)$, which can be a highly oscillatory observable especially if the driven part of the Hamiltonian is directly coupled to λ . However, this is not an issue in the experimentally-relevant case of measuring the transverse response of a Floquet Chern insulator in cold atoms, where an effective electric field is created by introducing a static magnetic field gradient which effectively tilts the lattice [56–58]. The transverse generalised force is then the current along the direction perpendicular to the field gradient, a static observable. Note that while this transverse current operator is static, its expectation value is still oscillating in time [160], and thus appropriate averaging over the phase of the measurement must be done to obtain the topological response.

4.3.4.3 The Driven Qubit as a Topological (Discrete) Energy Pump

An interesting consequence of the fact that one of our parameters, ϕ , was simply the phase of the drive in the lab frame, is that there is a deep connection between the topology measured above and energy absorption. Consider a generic Floquet Hamiltonian for which a closed manifold is defined by some parameter $\theta \in [0, \pi]$ and the driving phase ϕ , such that $H_{\text{lab}} = H_{\text{lab}}(\theta, \Omega_0 t + \phi)$. By construction the Hamiltonian is a periodic function of ϕ .

Let us observe that the generalised force with respect to ϕ is

$$\begin{aligned} M_\phi &= -\langle \partial_\phi H_{\text{lab}} \rangle = -\frac{1}{\Omega_0} \langle \partial_t H_{\text{lab}} \rangle = -\frac{1}{\Omega_0} \left\langle \frac{dH_{\text{lab}}}{dt} \right\rangle + \frac{\dot{\theta}}{\Omega_0} \langle \partial_\theta H_{\text{lab}} \rangle \\ &= -\frac{1}{\Omega_0} \frac{d}{dt} \langle H_{\text{lab}} \rangle + \frac{\dot{\theta}}{\Omega_0} \langle \partial_\theta H_{\text{lab}} \rangle. \end{aligned} \quad (4.50)$$

At order $\dot{\theta}$, we can replace the last expression by its value in the Floquet ground state. Then performing the phase average and integrating over time from $-t_R$ to t_R (see the protocol in the caption of FIG. 4.7), we see that

$$\begin{aligned} C_1^F &= \int \overline{M}_\phi dt \approx -\frac{1}{\Omega_0} \int_{-t_R}^{t_R} dt \frac{d}{dt} \langle H_{\text{lab}} \rangle + \frac{1}{\Omega_0} \int_0^\pi d\theta \overline{\langle \partial_\theta H_{\text{lab}} \rangle}_0 \\ &\stackrel{(4.24)}{=} -\frac{W}{\Omega_0} + \frac{1}{\Omega_0} \int_0^\pi d\theta \partial_\theta \epsilon_0^F = \frac{W_{\text{ad}}^F - W}{\Omega_0}, \end{aligned} \quad (4.51)$$

where $W = \Delta E$ is the phase-averaged work done *on* the system, or equivalently the energy pumped into the system, and $W_{\text{ad}}^F = \epsilon_0^F(\pi) - \epsilon_0^F(0)$ is the adiabatic Floquet work done on the system. Note that W_{ad}^F vanishes identically for any cyclic process, and in particular vanishes for the qubit system discussed above. Thus the Chern number is simply related to work done on the system during the adiabatic cycle:

$$W = -C_1^F \Omega_0$$

This result indicates that the work done on the system during one adiabatic cycle is quantised in units of the driving frequency, opening the possibility of realising a Floquet energy pump similar to the Thouless pump in equilibrium systems [294]. Physically this energy change amounts to generating (or removing) an integer number of photons from the driving field. For the particular example of the qubit one can check that if the angle θ keeps increasing from π to 2π the total Chern number will be zero, and thus the system will not continuously absorb the energy. In order to realise the continuous energy pump in this system, during the second half of the cycle one can uncouple the qubit from the drive and

reinitialise it in the ground state corresponding to $\theta = 0$. Alternatively, one can apply the process to a sequence of qubits and do the π -rotation to each of them. We leave the detailed analysis of this interesting possibility, including the particularly intriguing situation where the system couples coherently to a photonic reservoir such that they cannot be treated as an external periodic drive, to future work.

4.4 Many-Body Examples

We now analyse the applicability of FAPT by applying it to more complex, many-body systems. We first study the transverse-field Ising chain, a quintessential integrable many-body system. We show that an integrability-preserving drive of the transverse field results in obeying FAPT for driving frequencies above the single-particle bandwidth where photon absorption is only virtual (off-shell). Below the single-particle bandwidth, real (on-shell) photon absorption processes become important and the adiabaticity becomes only limited with a non-analytic power-law dependence of observables on the ramp rate. This comes from the fact that for such low driving frequencies even infinitesimal driving amplitude opens a gap in the Floquet spectrum. Therefore the whole setup becomes very similar to the Kibble-Zurek type scenario, where one starts the ramp protocol at a critical point (see e.g. Ref. [287] for details).

We then introduce a parallel field which breaks integrability and makes the model generic. By measuring the Floquet diagonal entropy S_d^F (cf. Eq. (4.18)), we show that even for this complicated model, a regime of validity exists for FAPT at least for finite-size systems. At the same time, similarly to the Kapitza pendulum, very slow ramps result in strong heating due to crossing many-body photon resonances.

4.4.1 The Driven Transverse-Field Ising Model

The transverse-field Ising model (TFIM) is the prototypical example to study quantum phase transitions [295]. The Hamiltonian is given by

$$H = -J_0 \sum_j \sigma_j^z \sigma_{j+1}^z - h_0^x \sum_j \sigma_j^x, \quad (4.52)$$

with the nearest-neighbour Ising interaction J_0 and transverse magnetic field h_0^x . We consider periodic boundary conditions and restrict the discussion to chains with even total number of sites. It is well-known that this model exhibits a quantum phase transition at $J_0/h_0^x = 1$ from an x -paramagnet to a z -ferromagnet [295]. More importantly for our purposes, it is an exactly solvable many-body model that serves as a jumping off point to even more complicated cases.

We now add a periodic modulation of the transverse field $h_1(t) = A_f \lambda \Omega \cos \Omega t$, so the total Hamiltonian of the system reads

$$H(t) = -J_0 \sum_j \sigma_j^z \sigma_{j+1}^z - (h_0^x + A_f \lambda \Omega \cos \Omega t) \sum_j \sigma_j^x. \quad (4.53)$$

At fixed λ , this model was studied in Ref. [296], where it was shown that the ground state of the Floquet Hamiltonian still defines two different phases separated by a quantum critical point as in equilibrium. The critical magnetic field is controlled by λ and can be made arbitrarily small if we tune the system to the dynamical localisation regime where the effective spin-spin interaction becomes very small. The nonequilibrium physics in the presence of the drive near this critical point was extensively studied by Russomanno et al. [103, 288, 297–300]. In the discussion below, we carefully avoid crossing any critical points, as we want to focus on the perturbative non-adiabatic effects in Floquet systems which requires avoiding any Kibble-Zurek-type physics that would unnecessarily complicate the analysis.

The TFIM can be solved exactly using the Jordan-Wigner transformation [295], which

maps the Hamiltonian of spins to a quadratic Hamiltonian of spinless fermions $\{c_i, c_j^\dagger\} = \delta_{ij}$ that conserves particle number modulo two. The ground state is in the sector with an even number of particles, and thus we restrict ourselves to that sector. Because our Hamiltonian is translationally invariant it is also advantageous to Fourier transform to momentum space leading to:

$$H(t) = \sum_{k \in \text{BZ}} \left[2(h_0^x + A_f \lambda \Omega \cos \Omega t - J_0 \cos k) c_k^\dagger c_k + J_0 \sin k (c_{-k}^\dagger c_k^\dagger + c_k c_{-k}) \right], \quad (4.54)$$

where $\text{BZ} = [-\pi, \pi]$ is the first Brillouin zone. Since the driving amplitude scales with the driving frequency Ω , we go to the rotating frame using the following transformation [296]:

$$V(t) = \exp \left(-2iA_f \lambda \sin(\Omega t) \sum_{k \in \text{BZ}} c_k^\dagger c_k \right) \quad (4.55)$$

which leads to the following rotating-frame Hamiltonian:

$$\begin{aligned} H^{\text{rot}}(t) &= H_{\text{ave}} + \sum_{k \in \text{BZ}} J_0 \sin k \left[\sum_{\substack{\ell=-\infty \\ \ell \neq 0}}^{\infty} \mathcal{J}_\ell(4A_f \lambda) (\text{e}^{i\ell\Omega t} c_{-k}^\dagger c_k^\dagger + \text{e}^{-i\ell\Omega t} c_k c_{-k}) \right], \\ H_{\text{ave}} &= \sum_{k \in \text{BZ}} \left[2(h_0^x - J_0 \cos k) c_k^\dagger c_k + J_{\text{ave}}(\lambda) \sin k (c_{-k}^\dagger c_k^\dagger + c_k c_{-k}) \right]. \end{aligned} \quad (4.56)$$

We separated the time average explicitly, taking into account the renormalisation of the model parameters by the drive: $J_{\text{ave}}(\lambda) = J_0 \mathcal{J}_0(4A_f \lambda)$, where \mathcal{J}_ℓ is the ℓ^{th} Bessel function of the first kind. The single-particle dispersion relation of the time-averaged Hamiltonian has the two bands

$$E_k = \pm \sqrt{(h_0^x - J_0 \cos k)^2 + J_{\text{ave}}^2(\lambda) \sin^2 k}. \quad (4.57)$$

The drive in the rotating frame couples to the two-particle excitation operator, which suggests that one can excite two particles with a single drive quantum Ω . Thus, whenever the driving frequency becomes smaller than *twice* the single-particle bandwidth of the time-

averaged Hamiltonian, $\Omega \leq 2W_{\text{ave}}$, with $W_{\text{ave}} = 2\max_k|E_k| = 2|h_0^x + J_{\text{ave}}|$, a resonance occurs. The situation is similar to the parametric resonance observed in the periodically-driven weakly-interacting Bose-Hubbard model, as seen perturbatively in Ref. [167]. Based on this argument, we expect that the FAPT fails for this model if $\Omega \leq 2W_{\text{ave}}$. On the other hand, our previous results suggest that FAPT should reproduce the correct behaviour of the system at small ramp speeds for $\Omega > 2W_{\text{ave}}$.

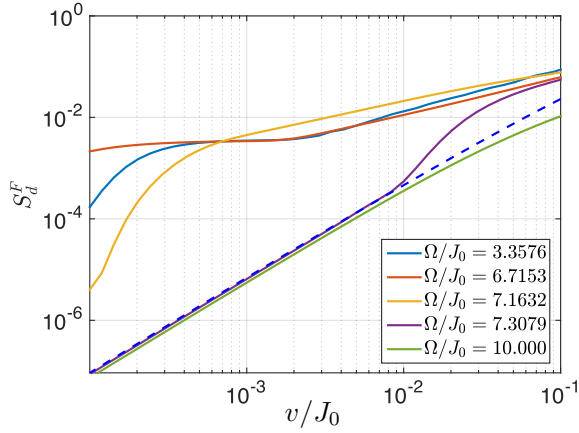


Figure 4.8: [Driven transverse-field Ising model]. Floquet diagonal entropy of the driven TFI chain, showing that FAPT applies for $\Omega > 2W_{\text{ave}}$ (the effective single-particle bandwidth, see text). The dashed lines shows a v^2 power law. Model parameters are $A_f = 0.5$, $h_0^x/J_0 = 0.809$, $2W_{\text{ave}}/J_0 = 7.235$.

To test these predictions, we prepare the system in the ferromagnetic GS of the Hamiltonian $H_0(\lambda = 0) = H_{\text{ave}}(\lambda = 0)$ and ramp up the amplitude of the drive slowly according to the protocol $\lambda(t) = [(t - t_i)/|t_i|]^2$ from zero to unity. We put the system on a ring of $L = 200$ sites, and ensure that the results do not change if we further increase the system size. As a measure of adiabaticity, we choose the Floquet diagonal entropy S_d^F , cf. Eq. (4.18), to avoid the difficulties associated with identifying the adiabatically-connected state. Figure 4.8 clearly shows that for $\Omega > 2W_{\text{ave}}$ FAPT applies and the non-adiabatic excitations are captured by the leading-order correction. On the other hand, for $\Omega < 2W_{\text{ave}}$ FAPT breaks down and the system is excited much stronger than in the high frequency regime. Nevertheless, a certain notion of limited adiabaticity still holds in

a sense that slower rates result in fewer excitations of the system. This behavior can be traced back to the equilibrium-like Kibble-Zurek physics resulting in a non-analytic scaling of various observables with the ramp rate v (see e.g. Ref. [287]), associated with the emergence of a degeneracy analogous to a quantum critical point in the Floquet system. We leave the details of this interesting story to a future work, as this setup is not sufficiently generic. Let us only point out that the existence of the singular point is intuitively clear by noting that at zero driving amplitude all Floquet levels are completely decoupled while an infinitesimal driving amplitude immediately opens a gap in the resonantly coupled states, which always exist for $\Omega < 2W_{\text{res}}$. This gap opening is similar to the ordinary second-order phase transition in the Floquet Hamiltonian and drives this Kibble-Zurek physics. Therefore, increasing the driving amplitude from zero is similar to starting at the quantum critical point leading to the Kibble-Zurek scenario. If one starts the ramp from the finite driving amplitude the FAPT is expected to be restored in this system even in this low-frequency regime if one appropriately defines the adiabatic limit.

The conclusions drawn from this model apply to arbitrary periodically-driven non-interacting band systems. In particular, our results are readily extensible to capture the dynamics of free bosons and fermions in various lattice geometries with periodic boundary conditions. Hence, it proves useful to study the applicability of FAPT to such non-interacting quantum many-body systems before we consider the fully interacting case in the next section. We note in passing that these results pertain directly to recent cold atoms experiments realising dynamical localisation, artificial gauge fields, and topological bands with non-interacting particles.

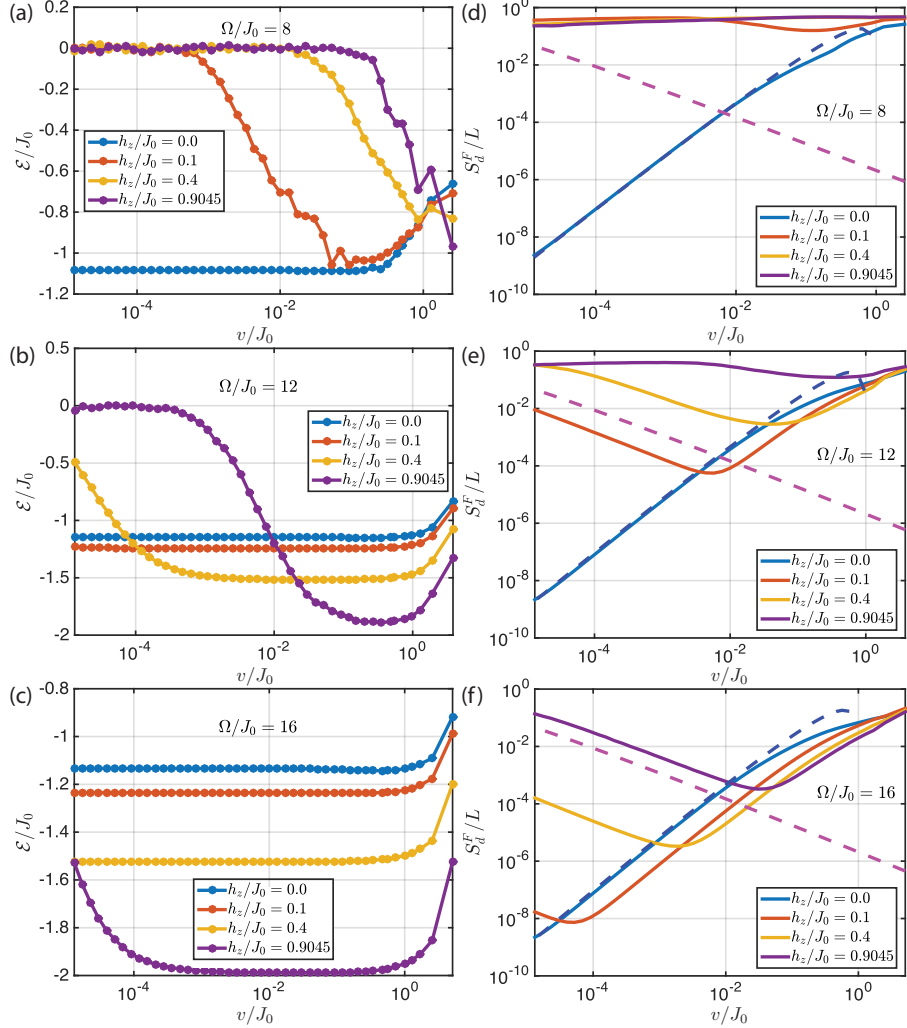


Figure 4.9: [Driven non-integrable transverse-field Ising model]. Energy density $\mathcal{E} = \langle \psi(t=0) | H(\lambda=0) | \psi(t=0) \rangle / L$ (a-c) and Floquet diagonal entropy density S_d^F / L (d-f) as a function of v , showing heating due to resonances at low velocities and for large h_z . The dashed lines are the same as in Fig. (4.6). The model parameters are $A_f = 0.5$, and $h_0^x / J_0 = 0.809$. The system size is $L = 18$ with a many-body bandwidth: $W_{\text{ave}}^{\text{MB}} / J_0 = 42.19$, 43.80, 48.90, 58.16 for $h^z / J_0 = 0, 0.1, 0.4, 0.9045$ respectively.

4.4.2 The Driven Transverse-Field Ising Model in a Parallel Magnetic Field

Let us generalise the TFIM from the previous section by switching on an additional static magnetic field h^z along the z -direction. The driven Hamiltonian now reads

$$H(t) = -J_0 \sum_j \sigma_{j+1}^z \sigma_j^z - (h_0^x + A_f \lambda \Omega \cos \Omega t) \sum_j \sigma_j^x - h^z \sum_j \sigma_j^z. \quad (4.58)$$

The non-driven version is no longer analytically solvable. Its spectrum exhibits Wigner-Dyson statistics which suggests that this model is quantum chaotic [301]. Hence, it represents a generic interacting periodically-driven quantum system.

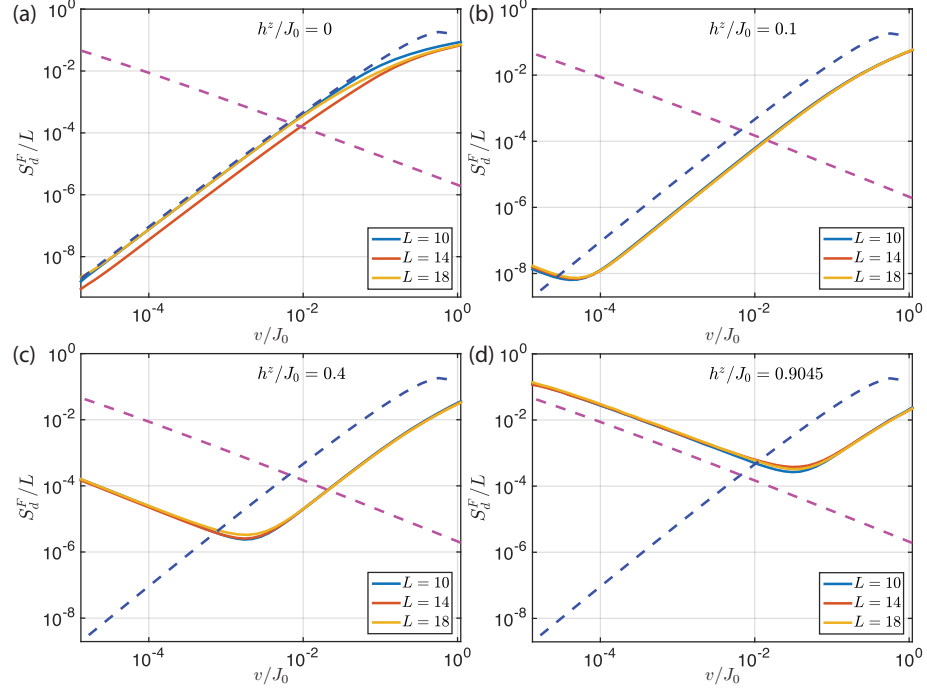


Figure 4.10: [Driven non-integrable transverse-field Ising model]. Diagonal entropy density in the Floquet eigenbasis versus the ramp speed v for different system sizes, confirming the presence of a regime of applicability for FAPT. The dashed lines are the same as in Fig. (4.6). The many-body bandwidth at $\lambda = 0$ and $h^z/J_0 = 0.9045$ as a function of the system size L reads: $W_{\text{ave}}^{\text{MB}}/J_0 = 32.34$ for $L = 10$; $W_{\text{ave}}^{\text{MB}}/J_0 = 45.24$ for $L = 14$, and $W_{\text{ave}}^{\text{MB}}/J_0 = 58.16$ for $L = 18$. The model parameters are $A_f = 0.5$, $h_0^x/J_0 = 0.809$, and $\Omega/J_0 = 16$.

Studying periodically-driven many-body systems in the thermodynamic limit requires a certain degree of caution, in order not to be misled by finite-size effects. As these systems have unbounded spectra for $L \rightarrow \infty$, it is necessary to clearly define the meaning of the thermodynamic limit $L \rightarrow \infty$ and the infinite-frequency limit $\Omega \rightarrow \infty$, none of which are strictly speaking accessible either experimentally or numerically. Here, we consider the situation where we first send $L \rightarrow \infty$ and only then are allowed to take $\Omega \rightarrow \infty$. We thus choose a driving frequency much less than the many-body bandwidth $W_{\text{ave}}^{\text{MB}}$, while still

larger than twice the single-particle bandwidth: $W_{\text{ave}}^{\text{MB}} \gg \Omega > 2W_{\text{ave}}$. This condition is crucial to allow for the appearance of Floquet many-body resonances [256, 288] which, as we already demonstrated, represent the limiting factor in the applicability of FAPT, while preventing single-particle resonances that, as we already encountered, lead to the trivial breakdown of FAPT. For a given driving frequency, we test the largest values L possible in an attempt to push towards the thermodynamic limit. All simulations in this section were performed in the zero (total) momentum sector of positive parity.

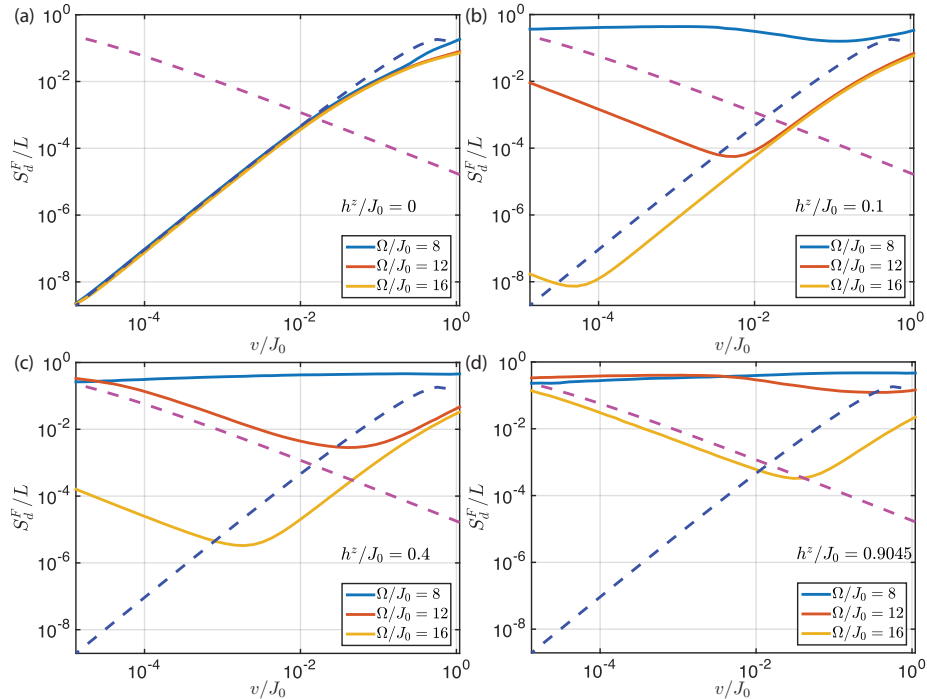


Figure 4.11: (Color online)[Driven non-integrable transverse-field Ising model]. Diagonal entropy density in the Floquet eigenbasis versus the ramp speed v for different driving frequencies, confirming the presence of a regime of applicability for FAPT. The dashed lines are the same as in Fig. (4.6). The model parameters are $A_f = 0.5$, and $h_0^z/J_0 = 0.809$. The system size is $L = 18$ and the many-body bandwidths are given in Fig. 4.9.

Similarly to the TFIM, we start from the GS of the non-driven Hamiltonian and slowly ramp-up the periodic drive. We measure the Floquet diagonal entropy as a function of the ramp speed. Figures 4.9, 4.10 and 4.11 show the existence of large velocity windows at intermediate frequencies for which FAPT holds, so long as one does not cross any phase

transitions [288]. We find that this window shrinks down as a function of the integrability breaking parameter h^z , as expected, but remains clearly visible even at moderate-to-strong parallel fields. When the ramp speed v becomes too small, however, similarly to the situation in the quantum Kapitza pendulum, photon absorption resonances become important and the system eventually heats up. This can be easily detected numerically by looking at the expectation value of the non-driven Hamiltonian H_0 at the measurement point, i.e. the physical energy of the system, in Fig. 4.9. While there is a clear plateau which holds over several decades along the v -axis, energy absorption is eventually enabled by the strong hybridisation of the Floquet many-body levels in the vicinity of the photon absorption avoided crossings.

Even though we cannot conclude from the available system sizes what the fate of this window is in the thermodynamic limit, we observe that the region of validity of FAPT does not show any severe system-size dependence, see Fig. 4.10. Let us point out that, at high frequencies in the thermodynamic limit, in the *absence* of a ramp, energy absorption in spin and fermion systems can happen at most exponentially slowly in the driving frequency due to the exponentially suppressed matrix elements responsible for the appearance of many-body resonances [98, 100–102]. Therefore, for a ramped system at high-frequencies, the photon absorption gaps leading to the appearance of many-body resonances and consequently to non-adiabatic heating, become invisible to the system at these small but finite ramp rates. Hence, we expect that the large window where FAPT is valid will be present in experimentally-relevant setups with Floquet many-body Hamiltonians.

It has been recently shown that the onset of heating in driven nonintegrable many-body systems can be traced back to the proliferation of many-body resonances [256]. Here, we have identified the same resonances as the origin of breakdown of FAPT. This explains the observation that the window of adiabaticity shrinks as we lower the driving frequency, see Fig. 4.11. To explore this phenomenon of adiabaticity breaking analytically and understand its origin in a greater detail we shall return to the simpler example of the Kapitza pendulum in the next section and apply the inverse-frequency expansion.

4.5 Floquet Adiabatic Perturbation Theory and the Inverse-Frequency Expansion

With the exception of special Floquet integrable situations such as a two-level system in the presence of circularly polarised time-periodic fields, cf. Sec. 2.1.3, the driven harmonic oscillator discussed in Sec. 4.3.2, or the shaken lattice, cf. Sec. 3.1.3.1, it is hard or even impossible to compute the Floquet Hamiltonian analytically. As we advocate throughout this thesis, an important tool for studying periodically driven systems at high frequencies is the inverse-frequency expansion [9, 10, 32, 33, 59, 87] for the Floquet Hamiltonian, which is the cornerstone of present-day Floquet engineering, see Chapter 3. Specifically, one uses strongly or resonantly-coupled periodic drives [33, 86, 105] to generate nontrivial properties in the Floquet Hamiltonian in the high-frequency limit. It is, therefore, important to analyse the regimes of applicability of FAPT within the inverse-frequency expansion.

Below we demonstrate that the photon absorption resonances in the Floquet spectrum that lead to the failure of FAPT also carry far-reaching consequences for the convergence properties of the inverse-frequency expansion, variants of which, such as the Floquet-Magnus expansion [33, 89], the van Vleck expansion [9, 10, 32, 33, 87] or the Brillouin-Wigner expansion [59], are widely used to study Floquet problems. FAPT was recently combined with the van Vleck inverse-frequency expansion in a unified description [302]. In systems with unbounded spectra, such as many-particle systems in the thermodynamic limit, or generic single-particle systems with an unbounded kinetic energy, the convergence of the inverse-frequency expansion cannot be easily justified in mathematical sense. Nevertheless, if the driving frequency is much higher than the natural frequencies in the system, one can anticipate that this expansion should give a very good approximation to the exact Floquet Hamiltonian. In Refs. [97, 101], it was indeed proven that the inverse frequency expansion is at least asymptotic, which implies that the corresponding approximate Floquet Hamiltonian is guaranteed to describe the dynamics up to exponentially long (in the driving frequency) times. For single-particle systems like the Kapitza pendulum, the very

notion of a natural frequency depends on the energy: for example, at small energies close to the stable minimum of the potential, the system is nearly a harmonic oscillator with a well-defined oscillation frequency. At high energies, the Kapitza pendulum becomes a free rotor weakly perturbed by the driving field. Because the energy gaps between consecutive levels of the free rotor are linearly spaced, even at high driving frequencies one can always find high-energy states, which are nearly resonant with the drive, and thus the validity of the inverse-frequency expansion should depend on the energy. To investigate all these and other issues, we give a detailed comparison between the exact Floquet spectrum and eigenstates, and those obtained within the inverse-frequency expansion for the Kapitza pendulum.

A peculiarity of the inverse-frequency expansion, see Sec. 2.2, is that it gives rise to an unfolded Floquet spectrum. This is intuitively clear for a many-body system, since each of the subsequent orders of the series produces static many-body Hamiltonians, the spectra of which all scale with the system size. For many-body systems this follows from the extensivity of the harmonics H_ℓ of the Hamiltonian and their commutators. For single-particle systems with unbounded spectra, one can easily convince oneself that at any order in the inverse-frequency expansion one also obtains an unbounded effective Hamiltonian. If we now recall that the Floquet spectrum is defined modulo Ω , and fold it artificially (i.e. ad hoc), we find that the approximate van Vleck Floquet Hamiltonian necessarily features a multitude of unavoided level crossings. The level crossings are unavoided because there are no matrix elements in the approximate Floquet Hamiltonian to couple the resonant states [256], since all these Hamiltonians are local operators¹⁰. However, this is in contradiction with the appearance of avoided photon absorption level crossings, which as we argued earlier, are ultimately responsible for the breakdown of FAPT. From this simple argument we can conclude that the Floquet spectrum close to such absorption resonances *cannot* be reproduced in any finite order of the inverse frequency expansion. Recalling

¹⁰In this sense, any approximate Floquet Hamiltonian obtained via the inverse-frequency expansion is “Floquet integrable”, although the exact Floquet Hamiltonian may not be.

that the approximate Floquet Hamiltonian is a well-defined static many-body Hamiltonian, which satisfies conventional adiabatic perturbation theory (APT, see Sec. 4.2.1), from the argument above we can also conclude that the violation of adiabaticity we observed in the models discussed so far is a non-perturbative effect, which cannot be captured by the inverse-frequency expansion.

To confirm these qualitative considerations we come back to the Kapitza pendulum, a single-particle Hamiltonian with an unbounded spectrum, whose photon absorption avoided crossings were studied in Sec. 4.3.3 (cf. Refs. [5, 33, 77] for more details on this model). Let us recall that the Hamiltonian for the Kapitza pendulum (cf. Eq. (4.37)) is

$$H(t) = \frac{p_\theta^2}{2m} - m\omega_0^2 \cos \theta - mA_f \lambda(t) \Omega \cos \Omega t \cos \theta. \quad (4.59)$$

Since the driving amplitude scales linearly with the driving frequency [33, 160], before we apply the inverse-frequency expansion it is advantageous to bring the Hamiltonian to the rotating frame, see Sec. 3.1.1.2:

$$\begin{aligned} H_{\text{rot}}(t) &= V^\dagger(t) H(t) V(t) - iV^\dagger(t) \partial_t V(t), \\ V(t) &= \exp [-imA_f \lambda \sin \Omega t \cos \theta], \end{aligned} \quad (4.60)$$

where $V(t)$ is a periodic unitary transformation which obeys $V(lT) = \mathbf{1}$. It is straightforward to check that the rotating frame Hamiltonian reads

$$\begin{aligned} H_{\text{rot}}(t) &= \frac{p_\theta^2}{2m} - m\omega_0^2 \cos \theta + \frac{m\lambda^2 A_f^2 \sin^2 \Omega t}{2} \sin^2 \theta - \frac{\lambda A_f \sin \Omega t}{2} \{\sin \theta, p_\theta\}_+ \\ &= \sum_{\ell=-2}^2 H_\ell e^{i\ell \Omega t}, \\ H_0 &= \frac{p_\theta^2}{2m} - m\omega_0^2 \cos \theta + \frac{m\lambda^2 A_f^2}{4} \sin^2 \theta, \\ H_1 &= i \frac{\lambda A_f}{4} \{\sin \theta, p_\theta\}_+ = -H_{-1}, \\ H_2 &= -\frac{m\lambda^2 A_f^2}{8} \sin^2 \theta = H_{-2}, \end{aligned}$$

where $\{\cdot, \cdot\}_+$ denotes the anti-commutator and all parameters remain finite as $\Omega \rightarrow \infty$. We then compare the exact Floquet spectrum obtained numerically to the spectrum produced by the vV HFE, including terms up to sixth order $H_{\text{eff}}^{[n_{\text{HFE}}=6]}$ [all odd orders $H_{\text{eff}}^{(2n+1)} = 0$ vanish for this model] for a frequency of $\Omega/\omega_0 = 20$. In doing so we make sure we eliminate all dependence on the spectral cut-off M from the discussion; see Sec. 4.3.3 for the precise definition of the cut-off parameter M . Since we have identified the Floquet ground state, it is straightforward to find a *photon absorption* avoided crossing in the quasienergy spectrum: all we need to do is locate a state which crosses the Floquet ground state (a.k.a. the adiabatically-connected state) coming from below on the quasienergy axis (see green curve in Fig. 4.12a). Moreover, for a reliable comparison with the vV HFE, the candidate Floquet states have to be well-approximated by the eigenstates of $H_F^{[n_{\text{HFE}}]}_{\text{11}}$. In Sec. 2.3.2.1 we show a detailed analysis of the logarithmic inverse participation ratio (log-IPR) of the exact Floquet eigenstates in the basis of approximate Hamiltonian $H_F^{[n_{\text{HFE}}]}$ for different orders of the vV HFE. Interestingly close to resonances increasing the order of the expansion barely affects the log-IPR (see Fig. 2.5c), while increasing the frequency makes the log-IPR visibly closer to unity.

Figure 4.12a shows a photon absorption avoided crossing of the Floquet ground state and a higher-energy state. As anticipated above, we see that the vV HFE up to sixth order does not know about the avoided crossing. We stress that to that order the matrix elements in the effective Hamiltonian that would induce a direct transition between the two states participating in the crossing are already enabled by the high number of nested commutators in the sixth order of the expansion¹². From the point of view of adiabaticity, this means that within the vV HFE, FAPT can fail only due to standard avoided crossings, whose physics is unrelated to that of the photon absorption crossings as seen in Sec. 4.3.3.

¹¹Let us remark that since we work with the van Vleck expansion, the eigenstates of the non-stroboscopic $H_{\text{eff}}^{[n_{\text{HFE}}=6]}$ need to be rotated back to the basis of stroboscopic Floquet-Magnus Hamiltonian $H_F[0]$ with the help of the kick operator. This is because numerically it is straightforward to diagonalise the unitary evolution operator over the period yielding the eigenstates of the stroboscopic Floquet-Magnus Hamiltonian $H_F[0]$.

¹²Figure 4.12a actually holds to seventh order since all odd orders of the effective Hamiltonian vanish. This is not true for the kick operator, though.

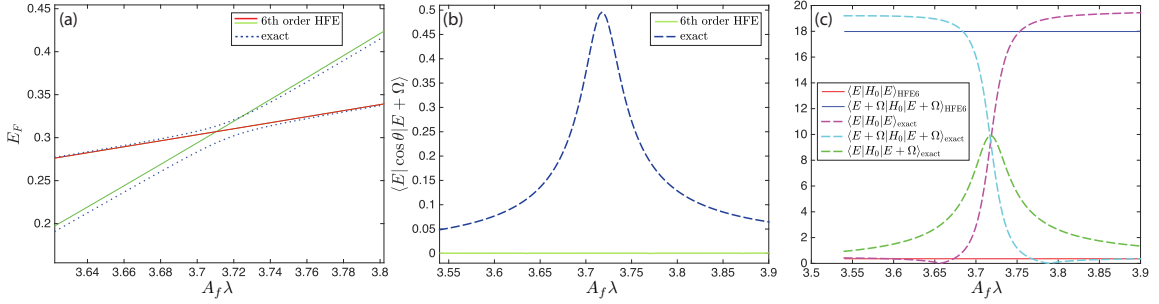


Figure 4.12: [Kapitza pendulum]. High-frequency expansions and resonance effects on a characteristic photon absorption avoided crossing between the Floquet GS and a state one drive quantum higher in energy. (a) Photon absorption level crossing in the exact quasienergy spectrum of the Kapitza pendulum (blue dots), which is not present in the approximate spectrum calculated with the sixth order vV HFE [the approximate Floquet GS (red line) and the excited state (green line)]. (b) Transition matrix element of the dipole operator $d = \cos \theta$ between the two exact Floquet states show a resonance, which is not captured by the approximate states. (c) Matrix elements of the non-driven Hamiltonian $H_0 = H(t, \lambda = 0)$ in the exact Floquet states (dashed lines) and the approximate vV HFE states (solid lines). The model parameters are $m\omega_0 = 1$, $A_f = 2$, and $\Omega/\omega_0 = 20$, and the data shown corresponds to a single-photon resonance.

Thus, a certain amount of caution needs to be exerted when one uses the vV HFE in such problems.

To bring about the nature of the avoided crossing we define the dipole operator $d = \cos \theta$, which changes the angular momentum of a basis state by one quantum, $\langle l | \cos \theta | l' \rangle = \delta_{l,l' \pm 1}$. The matrix element of the dipole operator between the two states that undergo the crossing is shown in Fig. 4.12b. Clearly, due to the large angular momentum difference of the approximate states in the vV HFE, the matrix element not surprisingly vanishes identically, while the exact Floquet states produce a nice resonance owing to the strong hybridisation present in the vicinity of the crossing. Finally, Fig. 4.12c shows the matrix elements of the non-driven Hamiltonian $H_0 = H(t, \lambda = 0)$ in the exact and approximate Floquet states. Once again, this is a measure of the hybridisation between the two Floquet states involved in the crossing, which is completely absent in their approximate counterparts. In Sec. 2.3.2.1 we analyse in detail the convergence properties of the vV HFE for the Kapitza pendulum, by looking at the negative logarithmic inverse participation ratio

(log-IPR) of the approximate Floquet states w.r.t. to the exact Floquet states. We find that, away from resonances the log-IPRs are small (though the expansion is probably still asymptotic), while on resonance the approximation is much worse.

The failure of the vV HFE to capture resonance effects can also be observed in simpler systems. For instance, consider a harmonic oscillator with periodically stretched confining potential, which models the dynamics of a child on a swing. This simple system exhibits the phenomenon of parametric resonance: whenever the driving frequency hits twice the natural frequency of the oscillator, $\Omega = 2\omega_0$, all physical observables feature exponential growth in time. The quantum version of this driven oscillator is even more intriguing, as one has to accommodate this exponential growth in the wave functions of the system which are expected to be normalised. Strikingly, it was shown that, on resonance, the Floquet states are non-normalisable and the Floquet spectrum becomes continuous [238, 239], see also Sec. 3.3.2. In a more complicated system, the spectrum of the non-driven model might not be commensurate, but the appearance of resonances is guaranteed, as we have seen in various examples throughout this work. Recently, it was also shown that in a spin chain the second derivative of the Floquet ground state quasienergy with respect to the driving frequency features divergences [288], which was used as a precursor of frequency-induced topological phase transitions [59, 288], and hints towards a non-analytic (in frequency) behaviour. The vV HFE, on the other hand is by assumption/construction analytic in the inverse frequency and, as we have seen using the example of the Kapitza pendulum, it is not sensitive to such resonances. If we decompose the interactions of the system's degrees of freedom with the drive into real (on shell) and virtual (off-shell), the vV HFE only captures the virtual excitations, similarly to the Schrieffer-Wolff transformation in equilibrium systems [105].

4.6 Breakdown of FAPT for Resonantly Coupled Drives

As we have seen, FAPT breaks down due to resonances between Floquet states. The careful reader might recall that, in Sec. 3.2, we used the generalised Schrieffer-Wolff transformation to derive effective Hamiltonians for resonant drives [105]. Such drives couple the states of the non-driven Hamiltonian at any finite riving amplitude, and thus the Floquet resonances are guaranteed to exist at the beginning of any smooth ramp where the ramp speed approaches zero. While this mechanism renders FAPT inefficient, it turns out that there exist alternative methods to prepare desired Floquet states of such resonantly-driven systems. In this section, we present in detail one such possibility, although the general theory of non-adiabatic loading is beyond the scope of this thesis.

Let us now briefly comment on a possible procedure to load the system in the ground state of the effective Floquet Hamiltonian $H_{\text{eff}}^{(0)}$, describing the doublon-holon model for resonant driving:

$$H_{\text{eff}}^{(0)} = \sum_{\langle ij \rangle, \sigma} \left[-J_{\text{eff}} g_{ij\sigma} - K_{\text{eff}} \left((-1)^{l\eta_{ij}} h_{ij\sigma}^\dagger + \text{h.c.} \right) \right], \quad (4.61)$$

where $\eta_{ij} = 1$ for $i > j$, $\eta_{ij} = 0$ for $i < j$, $J_{\text{eff}} = J_0 \mathcal{J}_0(\zeta)$, $K_{\text{eff}} = J_0 \mathcal{J}_l(\zeta)$, and $U = l\Omega$. Recall that this model was discussed in large detail in Sec. 3.2.2.4. In the following, we concentrate on the case $l = 2$ which, as we have shown in the aforementioned section, contains a free-fermion point for $J_{\text{eff}} = K_{\text{eff}}$.

While most experimental realisations of Floquet Hamiltonians use an adiabatic ramp up of the driving protocol by gradually switching on the drive amplitude [240], we follow a slightly different approach, which we find to be more efficient in this case. To minimise heating effects due to resonant absorption from the drive, we use a multi-step loading procedure similar to the one proposed in Ref. [221]. First, at time $t = 0$ we prepare the system in the ground state of free fermions. Then we suddenly quench-start the drive [including the interactions] with an amplitude corresponding to the free fermion point:

$\zeta = A/\Omega \approx 1.8412$. This procedure preserves the state to leading order in the HFE. Second, we ramp down the driving amplitude smoothly into the Luttinger liquid phase, Sec. 3.2.2.4, for a total of forty driving periods and stop whenever the amplitude reaches a value such that $K_{\text{eff}}/(K_{\text{eff}} + J_{\text{eff}}) \approx 0.2$. Last, we evolve the system at this constant final amplitude for five more driving periods. We note in passing that a similar procedure works when the amplitude is instead increased and the system enters the gapped bond density wave phase.

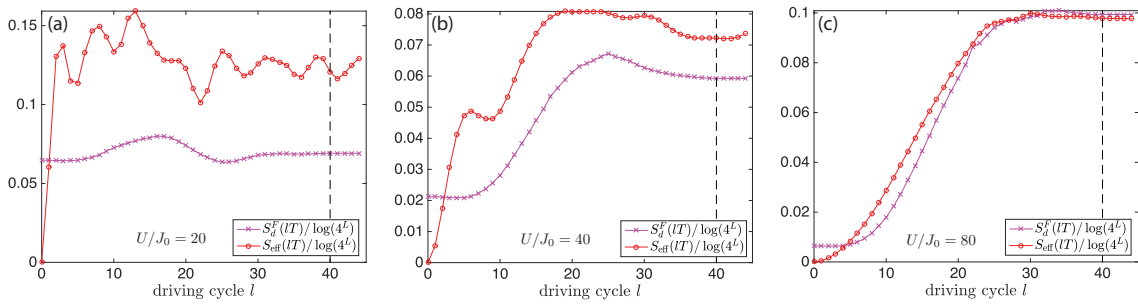


Figure 4.13: [Resonantly driven Fermi-Hubbard Model.] Stroboscopic time evolution of the Floquet diagonal entropies (S_{eff} – in the basis of the zeroth-order H_{eff} , and S_d^F – in the basis of the exact stroboscopic $H_F[0]$) for the ramp into the Luttinger Liquid phase on resonance for a chain of $L = 8$ sites. The dashed vertical line marks the end point of the ramp, after which the evolution continues at a constant driving amplitude. Unity on the y -axis corresponds to maximum entropy while zero – to minimum. The three panels correspond to different interaction strengths (drive frequencies): a) $U/J_0 = 20$, b) $U/J_0 = 40$, and c) $U/J_0 = 80$. The other parameters are $U = 2\Omega$, $A_i/\Omega = 1.8412$ [$J_{\text{eff}} = K_{\text{eff}}$] and $A_f/\Omega = 1.2$ [$K_{\text{eff}}/(J_{\text{eff}} + K_{\text{eff}}) \approx 0.2$].

To measure the amount of non-adiabaticity introduced during the ramp process, we compute numerically the Floquet diagonal entropy which, as we already explained, effectively measures occupation of higher-energy Floquet states. Let us denote by $|\psi(t)\rangle$ the state, exactly evolved with the full lab-frame time-dependent Hamiltonian $H(t)$, whose driving amplitude is ramped down smoothly. Further, we denote the set of eigenstates of the leading-order Floquet Hamiltonian $H_{\text{eff}}^{(0)}$ by $\{|\nu\rangle\}$, and the probability to be in each of these states at the stroboscopic times $t = lT$ is given by $p_{\nu\psi}^{\text{eff}}(lT) = |\langle\psi(lT)|\nu\rangle|^2$. While calculating the fidelity requires the unique identification of the Floquet ground state [more

precisely the adiabatically-connected Floquet state] at each point of time, we choose to look at the stroboscopic Floquet diagonal entropy $S_{\text{eff}}(lT) = -\sum_{\nu} p_{\nu\psi}^{\text{eff}}(lT) \log p_{\nu\psi}^{\text{eff}}(lT)$, which measures the spread of the initial state over the basis of the approximate Floquet Hamiltonian as a function of time [240]. A small value of the entropy automatically means that the system predominantly occupies a single state without the need of identifying it.

Since the Hamiltonian $H_{\text{eff}}^{(0)}$ is just the zeroth order term in the HFE, and because any realistic experimental set-up requires a finite frequency, it is also interesting to study the effect of the higher-order terms. This can be done along the same lines by defining the exact Floquet states $\{|n\rangle\}$, and the corresponding probabilities $p_{n\psi}^F(lT) = |\langle\psi(lT)|n\rangle|^2$ and diagonal entropy $S_d^F(lT) = -\sum_n p_{n\psi}(lT) \log p_{n\psi}(lT)$. The entropy S_{eff} shows how close the state is to the desired ground state of the Hamiltonian $H_{\text{eff}}^{(0)}$, while the entropy S_d^F shows how close the state is to the ground state of the exact instantaneous, i.e. stroboscopic, Floquet Hamiltonian $H_F[0]$, which knows about the higher-order correction terms.

Figure 4.13 shows the two entropies during the ramp. Notice that the nonadiabatic (and hence heating) rates are minimal. This plot also implies that the exact Floquet ground state is very close to the ground state of the approximate Floquet Hamiltonian $H_{\text{eff}}^{(0)}$. We have verified that a longer ramp duration corresponds to smaller heating rates. We also checked that the mismatch between the two entropies decreases with increasing the drive frequency, as expected. While we cannot numerically verify the feasibility of such a loading scheme for larger systems, based on the DMFT results of Ref. [221] where a similar procedure has been employed, we believe that this protocol should be robust even in thermodynamic limit, as the heating effects due to the drive are at most exponentially slow in frequency [98, 100–102] and should not play any role during the finite-time loading process. Therefore, we anticipate that such a protocol will allow one to load larger systems into a low-entropy state which is close enough to the desired Floquet ground state in order to detect the corresponding Luttinger liquid physics.

4.7 Discussion

In this chapter, we extensively discussed Floquet adiabatic perturbation theory in various single-particle and many-body models, focusing on non-adiabatic corrections due to a smooth change of parameters in a periodically driven Hamiltonian. We first analysed those “Floquet integrable” systems in which the Floquet adiabatic limit is well defined. Examples of such systems include the driven harmonic oscillator and the driven one-dimensional transverse field Ising spin chain. We identified the leading non-adiabatic corrections to various observables generalising the Quantum Adiabatic Theorem to Floquet systems. We showed that non-adiabatic response in general is determined by both the slowly changing Floquet Hamiltonian and the slowly changing kick operator. For the phase-averaged observables (i.e., observables averaged over the period or equivalently over the driving phase), these corrections take a remarkably simple form, similar to non-driven systems. In particular, we showed that the leading linear non-adiabatic response to generalised forces is proportional to the Floquet Berry curvature even in interacting systems suggesting the possibility of measuring it together with the associated Chern numbers in experiments. Based on these results, we showed how one can realise an energy Thouless pump, where by adiabatically changing some parameter in the Floquet Hamiltonian one can increase or decrease the energy of the system in discrete units of the driving frequency with the energy quantum determined by the Floquet Chern number. Physically, this corresponds to adding or removing an integer number of photons from the drive in each cycle. Our results also imply that the Floquet Chern numbers for band insulators [38, 39, 56, 57, 290, 291] are measurable through the standard Hall-type response if one averages the signal over the driving period.

For generic Floquet systems, whose non-driven part features an unbounded spectrum, the adiabatic limit strictly speaking does not exist, as infinitesimally slow ramping leads to infinite heating through a cascade of photon-absorption resonances. Nevertheless, we demonstrated that at high driving frequencies FAPT still works very well in a broad window

of ramp speeds such that the ramp rates are sufficiently fast for the resonant level crossings to be passed diabatically, while all standard avoided crossings (i.e. the level crossings of the approximate unfolded Floquet Hamiltonian) are passed adiabatically, as illustrated in Fig. 4.5. As the driving frequency is decreased, this adiabaticity window shrinks down and, at sufficiently slow frequencies, it completely disappears. We carefully analysed these photon absorption resonances using the example of the quantum Kapitza pendulum and presented a strong evidence that they are beyond any finite order of the inverse frequency expansion. This suggests that the non-adiabatic effects associated with the Floquet resonances might have a non-perturbative dependence on the inverse frequency.

In some cases, Floquet engineering makes use of resonant drives, where the driving frequency is locked to an integer multiple of some (mostly single-particle) energy scale in the non-driven problem. If possible, for such high-frequency resonant driving, one can significantly simplify the theoretical analysis by first going to a rotating frame w.r.t. both the driving protocol and the resonant term [86, 105]. Effectively, this leads to strong hybridisation between the resonant levels. One can then apply FAPT in this rotating frame ¹³. However, if one starts the resonant driving from a zero driving amplitude, then FAPT is expected to break down due to Kibble-Zurek type physics. One can understand this as follows: the drive amplitude sets the degree of the hybridisation between the resonant levels. Starting from zero amplitude and slowly ramping it up, one opens up a gap between the quasienergies and the physics of the problem is essentially that of the Kibble-Zurek problem starting from the critical point. Therefore, it could be advantageous to design a protocol which avoids this scenario by, e.g., first quenching to some finite value of the drive amplitude, and then sweeping it gradually to the desired final value (see Ref. [221] and Sec. 4.6 for specific examples). In doing so, the quench helps avoid the initial non-analyticities in the Floquet spectrum as $\lambda \rightarrow 0$ leading to complications associated with Kibble-Zurek physics. This combination of an initial quench followed up by an adiabatic sweep has not yet been studied systematically but offers an intriguing alternative to the

¹³This is analogous to our analysis of the TFIM, see Sec. 4.4.1.

conventional ramp-through approach, to be analysed in future studies.

The breakdown of FAPT in generic Floquet systems is intimately related to heating. At a fixed drive coupling, recent numerical studies suggest that energy absorption can be either completely absent for finite-size systems [74, 75, 77, 113, 256, 303] or, if present in the thermodynamic limit, it is typically exponentially suppressed with increasing the drive frequency Ω . This provides a justification for the existence of long-lived Floquet steady states in certain parameter regimes at high frequencies [98, 100–102, 167, 304]. As we have demonstrated in this chapter, the situation becomes even more complex once a model parameter is being ramped up in the presence of the drive. In particular, during ramps one necessarily crosses photon-absorption resonances and, when the ramp speeds are infinitesimal, this leads to heating of the system even in the high-frequency regime. These results are strikingly similar to those recently predicted in single-particle disordered systems [289], and they most likely also apply to many-body localised (MBL) systems.

Chapter 5

Prethermalisation and Thermalisation in Closed Floquet Systems

This chapter deals with prethermalisation and thermalisation in periodically-driven systems. To study the amount of heating, i.e. excess energy and entropy produced by the drive in a closed system, it is enough to consider stroboscopic dynamics. Mathematically, this follows from Floquet's theorem¹, cf. Eq.(1.1). Intuitively, one needs to close a full driving cycle before comparing the value of the energy (entropy) to the initial one. Only then can one make a statement about the amount of energy (entropy) pumped into the system by the drive. However, if one of the parameters in the model, e.g. the driving amplitude, is being changed in the presence of the drive [240], see Chapter 4, then one needs to take into account the heating effects due to the change of the P -operator as well.

In this chapter, we first give an intuitive explanation for the expected slow heating rates in fermionic and spin systems. In particular, we argue that heating is suppressed at least exponentially with the driving frequency, even in the thermodynamic limit. We then move on to study the prethermal Floquet steady states and instabilities in the weakly-interacting Bose-Hubbard model. For this purpose, we develop the weak-coupling conserving approximation – which features a particle-number conserving dynamics. Last, we also study numerically the microscopic mechanism behind heating – the appearance of Floquet many-body resonances between states of energy difference $l\Omega$ for an integer l . We demon-

¹We set the Floquet gauge to $t_0 = 0$ and omit this label setting $P(t, t_0 = 0) = P(t)$ and $H_F[t_0] = H_F$ throughout this section.

strate that at a fixed system size, there is a crossover frequency, below which the system trivially absorbs energy from the drive and quickly heats up to infinite temperature. At high enough frequencies, however, energy absorption is inhibited for the fixed system sizes considered. These two thermalising regimes are separated by a crossover which exhibits nonthermalising dynamics featuring strong temporal fluctuations and correlations.

5.1 A Mechanism for Prethermalisation in Fermionic and Spin Systems

Since periodically-driven systems are a priori out of equilibrium, energy transfer between the system and the drive is allowed. In order for experiments to be able to study the low-energy physics of the interesting Floquet-engineered Hamiltonians, see Chapter 3, it is necessary to ensure that the system under consideration does not absorb energy from the drive on the experimentally-relevant time scales.

Fermionic and spin (i.e. hardcore boson) models, unlike softcore bosons, feature in common a bounded on-site Hilbert space. As a consequence, it turns out that energy absorption in these periodically-driven systems with local (or sum of local) Hamiltonians is (at least) exponentially suppressed with the driving frequency. Put differently, it takes (at least) exponentially long times [98, 100–102] for these systems to start heating up, times which are way beyond realistic present-day experiments and numerical simulations. This is good news for experimentalists which, provided they can prepare the desired initial state, c.f. Chapter 4, should be able to design and perform experiments to access Floquet engineered models, such as the ones discussed in Chapter 3.

From a physical point of view, the heating of the system can be traced back to the existence of Floquet resonances [157, 256]. When the frequency of the drive Ω is close to a single particle energy scale J , i.e. $\Omega \approx J$, the system can efficiently absorb energy from the periodic drive leading to fast heating. Here J can represent, for example, the energy associated with a single spin flip in a spin system, and then the process described above corresponds to the absorption of a photon of the driving field with a simultaneous

spin flip in the system. When the driving frequency is increased, $\Omega \gg J$, the photon energy can be absorbed, only if many spins are flipped simultaneously. These *many-body* processes are described by higher-order perturbation theory and, therefore, occur with very small probabilities. Hence, they can become important only at exponentially long times. For the rigorous proof of this statement, see Refs. [98, 100–102]. The same large-energy absorption processes determine whether in the high-frequency off-resonant regime, i.e. $\Omega \gg J$, the heating is slow and finite, or completely absent. All that said, if for a given model there exists a finite heating rate, no matter how small, a closed periodically-driven system will heat up to an infinite-temperature state where all eigenstates of the Floquet Hamiltonian contribute with equal probability. In Sec. 5.3 we demonstrate that heating happens exclusively due to such Floquet many-body resonances, and show that they are a non-perturbative phenomenon in the driving frequency.

5.1.1 Quasi-Conserved Integrals of Motion

As we alluded to above, a *generic* periodically-driven system is expected to heat up indefinitely to an infinite-temperature state. Nevertheless, this heating can only happen exponentially slowly in the driving frequency. Before the onset of heating becomes sizeable, however, this suggests that the system spends an exponentially-long time in a so-called prethermal state. The small but finite temperature in this early stage of the evolution is set by the energy density of the system immediately after the periodic drive is switched on.

This leads to the interesting concept of quasi-conserved integrals of motion – local quantities which ‘almost commute’ with the Hamiltonian. To elaborate more on this concept, let us make an analogy with a static 1d lattice system with a Hamiltonian H . If the system is translational invariant, guaranteed e.g. by choosing periodic boundary conditions (PBC), then the total momentum \mathcal{P} , i.e. the generator of translations $\mathcal{T} = \exp(-ia\mathcal{P})$ at a distance a , is a local integral of motion: $[H, \mathcal{T}] = 0$. On the other hand, whenever the system has a sharp open boundary (OBC), momentum is no longer well-defined and, as a result, it is

not a conserved quantity, but one can still define a translation operator \mathcal{T} : $[H, \mathcal{T}] \neq 0$. In the thermodynamic limit, however, when the system size $L \rightarrow \infty$, the boundary condition cannot possibly matter, and thus the system acquires an emergent conservation law. This suggests that, at any finite but large system size, the Hamiltonian of a lattice system with OBC almost commutes with the translation operator: $[H, \mathcal{T}] = 0 + \mathcal{O}(L^{-1})$. Intuitively, this $\mathcal{O}(L^{-1})$ -contribution comes from the first and last lattice sites of the open chain, and is therefore intensive in the system size L .

It is possible to modify the operator $\mathcal{T} \rightarrow \tilde{\mathcal{T}} = \sum_{n=0}^{\infty} \tilde{\mathcal{T}}^{(n)}$ ² with $\tilde{\mathcal{T}}^{(0)} = \mathcal{T}$ and $\tilde{\mathcal{T}}^{(n)} \sim L^{-n}$, such that even in the case of OBC we have $[H, \tilde{\mathcal{T}}] = 0$ for any finite L : the price to pay is the locality of the generator $\tilde{\mathcal{P}}$ of the dressed translation operator $\tilde{\mathcal{T}}$. Intuitively, this makes sense, since one cannot simply turn a non-conserved quantity into a conserved one by locally dressing it. Note, however, that if one only decides to suppress the leading-order non-commuting part $\mathcal{O}(L^{-1})$ of $[H, \mathcal{T}]$, one can still define a local-ish dressed ‘momentum’ operator by truncating the series $\tilde{\mathcal{T}} \approx \mathcal{T} + \tilde{\mathcal{T}}^{(1)}$ and calculating the corresponding generator. As a result, we now have $[H, \mathcal{T} + \tilde{\mathcal{T}}^{(1)}] = 0 + \mathcal{O}(L^{-2})$. This dressed momentum operator is an example of a quasi-conserved integral of motion.

Coming back to periodically-driven systems, the role of $H \leftrightarrow H_F$ is taken by the Floquet Hamiltonian, and the parameter $L \leftrightarrow \Omega$ can be thought of the driving frequency. The emergent quasi-conserved integrals of motion [98, 100–102] are then given by the first few orders of the inverse-frequency expansion. They are quasi-conserved in the above sense, namely: $[H_F, H_F^{(0+\dots+n_{\text{HFE}})}] = 0 + \mathcal{O}(\Omega^{-(n_{\text{HFE}}+1)})$. As anticipated, the full dressed generator to all orders in Ω^{-1} is given by the exact Floquet Hamiltonian which is, in general, a non-local operator. As a result, the dressed conserved quantity at all frequencies is the quasienergy (which is however unphysical in the same way as the dressed nonlocal momentum operator $\tilde{\mathcal{P}}$ would be), while the emergent conservation law at $\Omega \rightarrow \infty$ is the extensive energy of $H_F^{(0)}$. In Sec. 5.3 below we shall demonstrate that it is the Floquet

²One should keep in mind, though, that in general $\tilde{\mathcal{T}}$ might have a non-analytic in L^{-1} part which would not be captured in a power series ansatz.

resonances that cause this non-local character of H_F which is intimately related to the anticipated indefinite heating at infinite times.

5.2 Prethermal Floquet Steady States and Parametric Instabilities in the Weakly-Interacting Bose-Hubbard Model

Before we analyse the physics of heating at infinite times, we explore the prethermal Floquet steady states and instabilities of the weakly interacting two-dimensional Bose-Hubbard model subject to periodic driving. It is interesting to note that so far there are no rigorous bounds reported on energy absorption in *bosonic* systems, whose short-time dynamics is expected to be much more complicated and intricate as it can easily be dominated by parametric resonance effects. One of the reasons for this is that interacting bosonic lattice systems have an unbounded on-site Hilbert space. This complication affects not only mathematical proofs but also numerical simulations, and is reflected in the absence of exact-diagonalisation studies on thermalisation in bosonic Floquet systems as of present time. Instead, below we develop a description of the nonequilibrium dynamics, at arbitrary drive strength and frequency, using a weak-coupling conserving approximation. Based on it, we establish the regimes in which conventional (zero-momentum) and unconventional $[(\pi, \pi)\text{-momentum}]$ condensates are stable on intermediate time scales. Interestingly, the condensate stability is found to be *enhanced* by increasing the drive strength, because this decreases the bandwidth of quasiparticle excitations and thus impedes resonant absorption and heating. The results presented below are directly relevant to a number of current experiments with ultracold bosons.

It is believed, based on the Eigenstate Thermalisation Hypothesis [305–307] (see Ref. [308] for a review) that driven interacting systems will generically heat up to infinite temperature at sufficiently late times [77, 78, 80, 98, 100, 101, 104, 309]. Nevertheless, in some parameter regimes these heating times will be parametrically slower than the system’s characteristic time scales. In that case, as we discussed in the previous section, the system

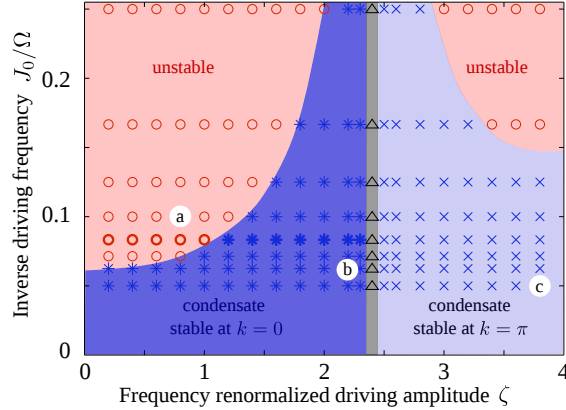


Figure 5.1: Stability diagram of the driven BHM for $U/J_0 = 0.2$. In the pink regions the condensate is unstable as the drive parametrically excites pairs of quasiparticles. In contrast, in the blue regions the condensate is stable on intermediate time scales. In the grey shaded region around $\zeta \approx 2.405$ the system is strongly correlated (see text). The symbols represent numerical WCCA results; the boundaries are given by the analytical expression Eq. (5.18). Points marked (a), (b), (c) correspond to the panels in Fig. 5.5.

will rapidly approach a “prethermalised” Floquet steady state [101, 102, 304, 310], which governs the dynamics until the much later heating time scales.

In the section, we study these prethermal states in the weakly interacting, two-dimensional, periodically-driven Bose-Hubbard model (BHM). The regime we explore is directly relevant to experiments [43, 46, 48, 51–53, 55, 57, 58], in which weak interactions are present. We employ a self-consistent weak-coupling conserving approximation (WCCA) which treats the coupled nonlinear dynamics of the condensate and the quasiparticle spectrum while neglecting collisions between quasiparticles. This approximation is justified at weak coupling since nonlinearities are important at much shorter times than the collisional time scales.

Within the WCCA, we find a phase diagram (Fig. 5.1) featuring at low drive frequency a regime in which the superfluid state is *already* unstable within Bogoliubov theory, owing to the resonant creation of quasiparticle pairs, and a regime (at high drive frequency) where the superfluid is stable. In the WCCA, there is a sharp phase transition between these; when effects beyond weak coupling are included, there will be a qualitative difference in

heating rates. Thus, in the “stable” regions of Fig. 5.1, the system initially reaches a prethermalised superfluid state – featuring a nonequilibrium quasiparticle distribution – and then eventually heats up. For strong driving, the prethermalised superfluid state is exotic, involving condensation at momentum $\boldsymbol{\pi} = (\pi, \pi)$. The existence of this exotic phase in the high-frequency limit has previously been established [41, 46, 139]; we show that it persists for intermediate frequencies as well.

Remarkably, we find that the stable phase is *enhanced* for intermediate drive strengths, since the drive both creates quasiparticle pairs when this is a resonant process, and decreases the effective hopping rate and thus the effective bandwidth of quasiparticle excitations. It then follows that, for weak interactions but general drive amplitude and frequency, the condensate becomes unstable when the drive frequency is parametrically resonant with the *drive-renormalised* time-averaged bandwidth. Therefore, parametric resonance occurs at *lower* frequencies when the drive strength is ramped up.

5.2.1 The Strongly-Driven Weakly-Interacting Bose-Hubbard Model

We consider the Bose-Hubbard model on a square lattice in the presence of a circularly-polarised time-periodic force $\mathbf{E}(t) = A(\cos \Omega t, \sin \Omega t)^t$:

$$H_{\text{lab}}(t) = -J_0 \sum_{\langle ij \rangle} b_i^\dagger b_j + \sum_j \left[\frac{U}{2} n_j(n_j - 1) + \mathbf{E}(t) \cdot \mathbf{r}_j n_j \right]. \quad (5.1)$$

The operator b_j^\dagger creates a boson on lattice site \mathbf{r}_j . The tunnelling and interaction strength are denoted by J_0 and U , respectively. To achieve non-trivial dynamics in the high-frequency regime, we scale the driving amplitude linearly with the driving frequency $A \sim \Omega$ [33], and define $\zeta \equiv A/\Omega$. We transform this Hamiltonian into a rotating frame, giving:

$$H(t) = -J_0 \sum_{\langle ij \rangle} e^{i\mathcal{A}(t) \cdot (\mathbf{r}_i - \mathbf{r}_j)} b_i^\dagger b_j + \frac{U}{2} \sum_j n_j(n_j - 1). \quad (5.2)$$

Thus, in the rotating frame, the system experiences an effective time-dependent gauge potential $\mathcal{A}(t) = \zeta (\sin \Omega t, -\cos \Omega t)^t$. The time evolution of $U(1)$ -invariant quantities (and thus the stability) remains the same in both frames [160].

5.2.2 The Weak-Coupling Conserving Approximation

To study the driven system at arbitrary frequencies, we employ a self-consistent, weak-coupling conserving approximation (WCCA). The WCCA involves deriving equations of motion from a two-particle irreducible effective action [311] within the nonequilibrium Schwinger-Keldysh formalism [312, 313], keeping only diagrams to first order in U , see Sec. 5.2.2.1. Unlike simple perturbation theory or Bogoliubov theory, the WCCA respects unitarity and conservation laws [314], and thus gives physically sensible results for all times; in particular, it allows the exponential growth of unstable modes to be cut off by the resulting depletion of the condensate. While the WCCA is *not* guaranteed to yield a gapless excitation spectrum [314, 315], the low-frequency behaviour of the spectrum is irrelevant for the phenomena discussed here. Our approach is equivalent to a fully self-consistent, time-dependent Hartree-Fock-Bogoliubov (HFB) approximation [315, 316]; our formulation, however, can more readily be extended to higher orders in U .

The WCCA equations of motion, see Sec. 5.2.2.1, are solved numerically. For the results presented here, we prepared the system on a $N_s = 100 \times 100$ lattice in the ground state of Bogoliubov theory. We allow for a macroscopic population of the $\mathbf{k} = \pi$ mode to enable a condensate at momentum π . To study the nonequilibrium dynamics, we abruptly turn on the periodic drive and propagate the initial state for a total of 801 driving cycles using Eqs. (5.15). We checked that the results are insensitive to the system size.

5.2.2.1 Derivation of the Equations of Motion within the WCCA

In this section, we derive the equations of motion (EOM) using the weak-coupling conserving approximation (WCCA). We are interested in studying the periodically driven

Bose-Hubbard model on a 2D lattice:

$$H(t) = - \sum_{ij} J_{ij}(t) b_i^\dagger b_j + \text{h.c.} + \frac{U}{2} \sum_j n_j(n_j - 1), \quad (5.3)$$

In order to treat efficiently the dynamics of the condensate after spontaneous symmetry breaking, we introduce the Bogoliubov spinor for the bosonic fields $b \rightarrow b_a$, with $a = 1, 2$, where $b_1 = b$ and $b_2 = b^\dagger$. Adopting the notation $(j, t) = x$, the time-dependent action can be cast into the compact form

$$\begin{aligned} S[b, b^*] &= S_0 + S_{\text{int}} \\ S_0[b, b^*] &= \frac{1}{2} \int_C dx b_a^*(x) \left(G_{\text{free}}^{(-1)} \right)_{ab} (x, y) b_b(y) \\ S_{\text{int}}[b, b^*] &= -\frac{U}{2} \int_C dx dy \delta_C(x - y) b^*(x) b^*(x) b(x) b(x). \end{aligned} \quad (5.4)$$

where the integral over time is taken along the Keldysh roundtrip contour C [311, 317, 318] and we introduced the delta function $\delta_C(x - x') = \delta_C(t - t') \delta_{jj'}$. In Bogoliubov space, the noninteracting Green's function thus has the form

$$\left(G_{\text{free}}^{(-1)} \right)_{ab} = \begin{pmatrix} i\partial_t + J_{ij}(t) & 0 \\ 0 & -i\partial_t + J_{ij}^*(t) \end{pmatrix}_{ab}. \quad (5.5)$$

We define the vacuum expectation value (VEV) $\varphi(x)$ and the quasiparticle (phonon) propagator $G(x, y)$ as

$$\varphi_a(x) = \langle b_a(x) \rangle, \quad iG_{ab}(x, y) = \langle b_a(x) b_b^*(y) \rangle_c = \begin{pmatrix} \langle \tilde{b}(x) \tilde{b}^*(y) \rangle_c & \langle \tilde{b}(x) \tilde{b}(y) \rangle_c \\ \langle \tilde{b}^*(x) \tilde{b}^*(y) \rangle_c & \langle \tilde{b}^*(x) \tilde{b}(y) \rangle_c \end{pmatrix}. \quad (5.6)$$

The microscopically occupied fields are denoted with a tilde $\tilde{b}(x)$. Thus, the Green's function G defined above does *not* include the condensate fraction. The effective action is given by the double Legendre transform of the original action w.r.t. the VEV $\varphi(x)$ and the

correlator $G_{ab}(x, y)$ [311, 318]:

$$\begin{aligned}\Gamma[\varphi, G] &= S[\varphi, \varphi^*] + \frac{1}{2}\text{Tr}[\log G^{-1}] + \frac{1}{2}\text{Tr}[G_0^{-1}(\varphi)G] - \Gamma_2[\varphi, G], \\ S[\varphi, \varphi^*] &= \int dxdy\varphi^*(x)G_{\text{free}}^{-1}(x, y)\varphi(y) - \frac{U}{2}\int dx|\varphi(x)|^4 \equiv \int dxdy\varphi^*(x)G_0^{-1}(x, y; \varphi)\varphi(y),\end{aligned}\quad (5.7)$$

where the sum over the Bogoliubov-Nambu index a is implicit. The Bogoliubov propagator $G_0^{-1}(x, y; \varphi)$ generates the motion of the Gross-Pitaevskii equation. Notice that it depends on the field φ itself since the GPE is nonlinear. From that we obtain the inverse Bogoliubov propagator $(G_0^{-1})_{ab}(x, y; \varphi)$ via:

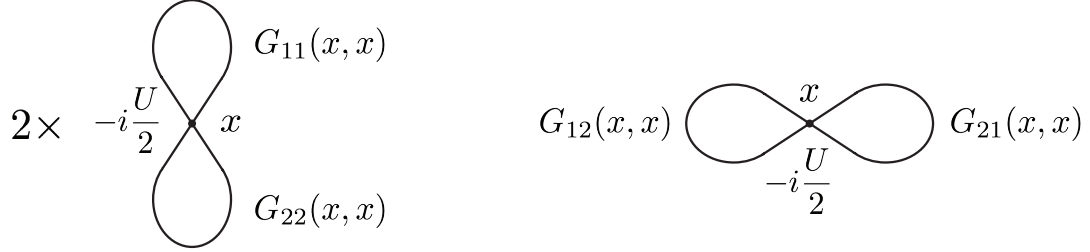
$$\begin{aligned}\frac{1}{2}(G_0^{-1})_{ab}(x, y; \varphi) &= \frac{\delta^2 S[\varphi, \varphi^*]}{\delta\varphi_a^*(x)\delta\varphi_b(y)} \\ &= \frac{1}{2}(G_{\text{free}}^{-1})_{ab}(x, y) - \frac{U}{2}\delta_C(x - y)\begin{pmatrix} 2|\varphi(x)|^2 & \varphi(x)^2 \\ (\varphi(x)^*)^2 & 2|\varphi(x)|^2 \end{pmatrix}_{ab}.\end{aligned}\quad (5.8)$$

So far the calculation is exact, although yet we have not specified the Luttinger-Ward functional $\Gamma_2[\varphi, G]$ which is the sum of all two-particle irreducible diagrams and thus has to be treated approximately. Here, we consider a weak-coupling expansion which amounts to keeping diagrams to first order in U , see Fig. 5.2.

The EOM for the VEV and the propagator are obtained by making the effective action Γ stationary with respect to the fields $\frac{\delta\Gamma[\varphi, G]}{\delta\varphi^*} = 0$, and the unknown propagator $\frac{\delta\Gamma[\varphi, G]}{\delta G_{ab}} = 0$, which leads to:

$$\begin{aligned}\int_C dy(G_{\text{free}}^{-1})_{11}(x, y)\varphi(y) - U\varphi^*(x)\varphi^2(x) - U(2\varphi(x)G_{11}(x, x) + \varphi^*(x)G_{12}(x, x)) &= 0, \\ \sum_b \left[(G_{\text{free}}^{-1})_{ab}(t) - U\delta_C(x - y) \begin{pmatrix} 2(iG_{11} + |\varphi|^2) & iG_{12} + \varphi^2 \\ iG_{21} + (\varphi^*)^2 & 2(iG_{22} + |\varphi|^2) \end{pmatrix}_{ab} \right] G_{bc}(t, t') &= \delta_{ac}\delta_C(t - t'),\end{aligned}\quad (5.9)$$

and the product of Green's functions in the second equation above is understood in the



$$-i\frac{U}{2}(i)^2 \times 2 \int d^4x G_{11}(x,x) G_{22}(x,x) \quad -i\frac{U}{2}(i)^2 \times \int d^4x G_{12}(x,x) G_{21}(x,x)$$

Figure 5.2: All two-particle irreducible diagrams which enter Γ_2 to first order in U , with their proper combinatorial factors. The diagrams can be turned into equations using the following Feynman rules: (i) a factor of $-iU/2$ for each vertex, and (ii) a factor of i for each closed loop. By symmetry $G_{11} = G_{22}$ and $G_{12} = (G_{21})^*$.

matrix-multiplication sense: $(AB)(x, z) = \int_y A(x, y)B(y, z)$. We remark that these equations of motion are equivalent to the Bogoliubov-Hartree-Fock EOM derived in Ref. [315] when starting from the lab frame Hamiltonian, by making the ansatz $b_{k=0} = \varphi + \tilde{b}_{k=0}$, $b_{k \neq 0} = \tilde{b}_{k \neq 0}$, and then linearising any cubic terms in \tilde{b}_k .

Next, we open the closed time contour [318] by decomposing the Green's function into a spectral part $\rho(x, y)$ and a statistical part $F(x, y)$ according to

$$\begin{aligned} iG(x, x') &= F(x, x') - \frac{i}{2}\rho(x, x')\text{sgn}_C(t - t'), \\ F_{ab}(x, x') &= \frac{1}{2}\langle\{b_a(x), b_b^\dagger(x')\}\rangle_c = \frac{1}{2} \begin{pmatrix} \langle\{\tilde{b}(x), \tilde{b}^\dagger(x')\}\rangle & \langle\{\tilde{b}(x), \tilde{b}(x')\}\rangle \\ \langle\{\tilde{b}^\dagger(x), \tilde{b}^\dagger(x')\}\rangle & \langle\{\tilde{b}^\dagger(x), \tilde{b}(x')\}\rangle \end{pmatrix}_{ab} \\ \rho_{ab}(x, x') &= i\langle[b_a(x), b_b^\dagger(x')]\rangle_c = i \begin{pmatrix} \langle[\tilde{b}(x), \tilde{b}^\dagger(x')]\rangle & \langle[\tilde{b}(x), \tilde{b}(x')]\rangle \\ \langle[\tilde{b}^\dagger(x), \tilde{b}^\dagger(x')]\rangle & \langle[\tilde{b}^\dagger(x), \tilde{b}(x')]\rangle \end{pmatrix}_{ab}. \end{aligned} \quad (5.10)$$

The following relations follow immediately from the above definitions:

$$F_{12}(x, x') = F_{12}(x', x), \quad \rho_{12}(x, x') = -\rho_{12}(x', x),$$

$$F_{21}(x, x') = F_{21}(x', x), \quad \rho_{21}(x, x') = -\rho_{21}(x', x),$$

$$\begin{aligned}
F_{12}(x, x') &= F_{21}^*(x, x'), \quad \rho_{12}(x, x') = \rho_{21}^*(x, x'), \\
F_{11}(x, x') &= F_{11}^*(x', x), \quad \rho_{11}(x, x') = -\rho_{11}^*(x', x), \\
F_{22}(x, x') &= F_{11}^*(x, x'), \quad \rho_{22}(x, x') = \rho_{11}^*(x, x'). \tag{5.11}
\end{aligned}$$

We now assume that the system is translationally invariant, with periodic boundary conditions. This leads us to find the following system of coupled nonlinear EOM in momentum space for the condensate

$$\begin{aligned}
i\partial_t \varphi(t) &= (zJ_0 - \mu)\varphi(t) + \varepsilon_{k=0}(t)\varphi(t) \\
&\quad + \frac{U}{N_s} \left[\varphi^*(t)\varphi^2(t) + 2\varphi(t) \int_q F_{11}(t, t; q) + \varphi^*(t) \int_q F_{12}(t, t; q) \right], \tag{5.12}
\end{aligned}$$

and the statistical correlator F

$$\begin{aligned}
i\partial_t F_{11}(t, t'; k) &= (zJ_0 - \mu)F_{11}(t, t'; k) + \varepsilon_k(t)F_{11}(t, t'; k) \\
&\quad + \frac{U}{N_s} \left[2 \left(|\varphi(t)|^2 + \int_q F_{11}(t, t; q) \right) F_{11}(t, t'; k) \right. \\
&\quad \left. + \left(\varphi^2(t) + \int_q F_{12}(t, t; q) \right) [F_{12}(t, t'; k)]^* \right], \\
i\partial_t F_{12}(t, t'; k) &= (zJ_0 - \mu)F_{12}(t, t'; k) + \varepsilon_k(t)F_{12}(t, t'; k) \\
&\quad + \frac{U}{N_s} \left[2 \left(|\varphi(t)|^2 + \int_q F_{11}(t, t; q) \right) F_{12}(t, t'; k) \right. \\
&\quad \left. + \left(\varphi^2(t) + \int_q F_{12}(t, t; q) \right) F_{11}(t, t'; k) \right]. \tag{5.13}
\end{aligned}$$

For completeness, we also give the equations of motion for the spectral correlators ρ which, on the other hand, obey

$$\begin{aligned}
i\partial_t \rho_{11}(t, t'; k) &= (zJ_0 - \mu)\rho_{11}(t, t'; k) + \varepsilon_k(t)\rho_{11}(t, t'; k) \\
&\quad + \frac{U}{N_s} \left[2 \left(|\varphi(t)|^2 + \int_q F_{11}(t, t; q) \right) \rho_{11}(t, t'; k) \right]
\end{aligned}$$

$$\begin{aligned}
i\partial_t \rho_{12}(t, t'; k) = & (zJ_0 - \mu)\rho_{12}(t, t'; k) + \varepsilon_k(t)\rho_{12}(t, t'; k) \\
& + \frac{U}{N_s} \left[2 \left(|\varphi(t)|^2 + \int_q F_{11}(t, t; q) \right) \rho_{12}(t, t'; k) \right. \\
& \quad \left. + \left(\varphi^2(t) + \int_q F_{12}(t, t; q) \right) [\rho_{11}(t, t'; k)]^* \right]. \quad (5.14)
\end{aligned}$$

In the above equations, z is the lattice coordination number, $\varepsilon_k(t)$ is the time-periodic free lattice dispersion in the rotating frame, and the integrals are all taken over the first Brillouin zone.

Furthermore, if one is interested in the equal-time statistical correlator F , using the symmetry relations in Eq. (5.11) one arrives at the somewhat simplified equations

$$\begin{aligned}
\partial_t F_{11}(t, t; k) = & 2\text{Im} \left\{ \frac{U}{N_s} \left(\varphi^2(t) + \int_q F_{12}(t, t; q) \right) [F_{12}(t, t; k)]^* \right\}, \\
i\partial_t F_{12}(t, t; k) = & \left\{ [\varepsilon_k(t) + \varepsilon_{-k}(t) + 2(zJ_0 - \mu)]F_{12}(t, t; k) \right. \\
& + 2\frac{U}{N_s} \left[2 \left(|\varphi(t)|^2 + \int_q F_{11}(t, t; q) \right) F_{12}(t, t; k) \right. \\
& \quad \left. \left. + \left(\varphi^2(t) + \int_q F_{12}(t, t; q) \right) F_{11}(t, t; k) \right] \right\}. \quad (5.15)
\end{aligned}$$

5.2.3 Stability diagram

Coming back to the study of instabilities, the stability phase diagram for our model is shown in Fig. 5.1. Previous work has investigated the driven Bose-Hubbard model [185–188, 319–322] and related models [165, 166, 169, 323–328] using various approximation schemes; we go beyond these works by treating both the condensate and quasiparticle sectors, including the feedback between them. Thus, we are able to explore instabilities originating in either sector on equal footing.

We first discuss two analytically tractable limits, corresponding to high-frequency driv-

ing (i.e., going along the x axis of Fig. 5.1) and to low-amplitude driving (i.e., going along the y axis). In the first case, the dynamics is approximately governed by an effective *time-average* Hamiltonian [32, 33]:

$$H_{\text{ave}} = -J_{\text{ave}}(\zeta) \sum_{\langle ij \rangle} b_i^\dagger b_j + \frac{U}{2} \sum_j n_j(n_j - 1). \quad (5.16)$$

The periodic modulation renormalises the hopping to $J_{\text{ave}}(\zeta) = J_0 \mathcal{J}_0(\zeta)$, where $\mathcal{J}_0(\zeta)$ is the zeroth-order Bessel function of the first kind, which is a damped oscillatory function with the first zero at $\zeta \approx 2.4$, the second at $\zeta \approx 5.5$, etc. As ζ is increased, the time-averaged hopping decreases, until the dispersion flattens at $\zeta \approx 2.4$. For $\zeta > 2.4$ the dispersion flips sign, and acquires a stable minimum at $\boldsymbol{\pi} = (\pi, \pi)$. Thus, in the high-frequency limit the condensate at $\mathbf{0} = (0, 0)$ is stable when $\zeta < 2.4$, whereas the condensate at $\boldsymbol{\pi}$ is stable when $2.4 \lesssim \zeta \lesssim 5.5$. Moreover, for commensurate filling, the superfluid phase should transition into a Mott insulating state around $\zeta \approx 2.4$ determined by the phase boundary $J_{\text{ave}}(\zeta)/U \lesssim 0.06$. [329, 330] This transition regime, marked by the thin vertical strip in Fig. 5.1, is beyond the validity of the WCCA; our WCCA simulations in this regime give oscillatory behaviour, see 5.2.4.1.1.

A second analytically tractable limit is that of weak driving, at arbitrary Ω . The dominant effects can be inferred from linear stability analysis around the non-driven state. In terms of Bogoliubov quasiparticle operators $\gamma_{\mathbf{k}}$, the system-drive coupling includes terms of the form $e^{i\Omega t} \gamma_{\mathbf{k}}^\dagger \gamma_{-\mathbf{k}}^\dagger$, involving the emission of pairs of quasiparticles from the condensate. The emission rate is related to the density of states of two-quasiparticle excitations at Ω . Specifically, if the non-driven system has quasiparticle excitations at energy $E_{\mathbf{k}}, E_{-\mathbf{k}}$ such that $\Omega = E_{\mathbf{k}} + E_{-\mathbf{k}}$, absorption will occur and the system will be unstable. On the other hand, if $\Omega \geq 2W$, where $W \approx 2zJ_0$ is the approximate bandwidth of Bogoliubov excitations, then absorption does not occur and the system is stable.

Combining the insights from these two limits allows us to understand the entire stability phase diagram. The drive creates pairs of *renormalised* Bogoliubov quasiparticles,

which have an effective bandwidth $W_{\text{ave}} \approx 2zJ_{\text{ave}}(\zeta)$. We define $W_{\text{ave}} \equiv \max_k[E_{\text{ave}}(\mathbf{k})] - \min_k[E_{\text{ave}}(\mathbf{k})]$ as the time-averaged Floquet-Bogoliubov bandwidth; in terms of this, the stability condition reads

$$\Omega_c > 2W_{\text{ave}} \Leftrightarrow \text{stable.} \quad (5.17)$$

Equation (5.17) is consistent with our numerical results (Fig. 5.1), but see Ref. [331] for a detailed analysis of parametric instabilities and their rates in this and related band problems. This result is unexpected—since the time-averaged Hamiltonian is valid at infinite frequency whereas parametric resonance is a low-frequency phenomenon—but can be understood as follows. The hopping matrix element in the driven system can be expanded as $J(t) \sim J_0 \sum_\ell \mathcal{J}_\ell(\zeta) \exp(i\ell\Omega t)$. We absorb the time-independent $n = 0$ component in the unperturbed Hamiltonian, and treat the $\ell = 1$ term, which oscillates at Ω , perturbatively. The perturbation is small for $U \ll \Omega$, because the matrix element for creating two quasiparticles is proportional to both $\mathcal{J}_1(\zeta)$ [which need not be small] and U [which is assumed to be small]. We then use parametric instability analysis, see Sec. 3.3.2, with the renormalised dispersion, and conclude that an instability occurs when $\Omega = 2W_{\text{ave}}$. When $\Omega/J_0 \gg 1$, the critical driving frequency is given by

$$\Omega_c(\zeta) = 4\sqrt{zJ_{\text{ave}}(\zeta)(zJ_{\text{ave}}(\zeta) + n_0U)}. \quad (5.18)$$

Note that in the present case, resonant absorption occurs for drive strengths up to *twice* the single-particle bandwidth; by contrast, in noninteracting systems, no absorption occurs for $\Omega > W_{\text{ave}}$. The presence of absorption at frequencies exceeding the single-particle bandwidth is generic in interacting systems.

5.2.4 Stroboscopic Prethermalisation

In the following section, we discuss the time evolution of the condensate fraction, the momentum distribution and the energy density. We argue that at high drive frequencies and for weak interactions there exists a large prethermal window in the stable regime which is beyond the WCCA.

5.2.4.1 Condensate evolution

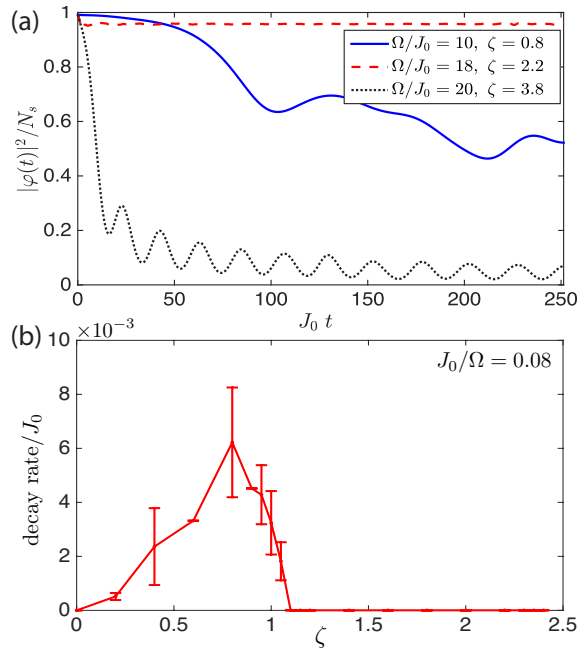


Figure 5.3: (a) Time evolution of the condensate fraction for 801 driving cycles, starting from a Bogoliubov initial state localised at $\mathbf{k} = \mathbf{0}$ for $U/J_0 = 0.2$. (b) Decay rate to 75% of the condensate curves for $\Omega/J_0 = 12$ (boldface points in Fig. 5.1). Error bars are set by the difference of the inverse times, determined by the first and last time the curve passes through $3/4$ taking into account the oscillatory behaviour.

Figure 5.3a shows the evolution of the condensate fraction in various regimes: in the parametrically unstable regime (solid blue line), the condensate slowly decays; in the stable regime (dashed red line), it saturates to a prethermalised value, which is generally lower than the Bogoliubov value (since $|J_{\text{ave}}(\zeta)| < |J_0|$). The system enters a steady-state with

constant in time evolution when measured stroboscopically. When the initial condensate is at the band maximum (dash-dotted black line), the condensate decays rapidly. Panel b shows the decay rate as a function of drive amplitude in the parametrically unstable regime: note that the decay rate depends not only on drive strength ζ , but also on U and Ω . Very close to the region $\zeta \sim 2.405$ (grey strip in Fig. 5.1), the WCCA gives strong oscillations of the particle density between the condensates at $\mathbf{0}$ and $\boldsymbol{\pi}$; however, as previously noted, the WCCA is not reliable here.

5.2.4.1.1 Phase Transition Region around $\zeta = 2.405$

Let us briefly mention the dynamics governed by the WCCA close to the first zero of the Bessel function, $\zeta = 2.405$, where the dispersion of the $\Omega \rightarrow \infty$ Hamiltonian becomes flat (central grey region in Fig. 5.1). For $\zeta < 2.405$ the dispersion of the free theory $U = 0$ supports a stable minimum for $\mathbf{k} = \mathbf{0}$, while for $\zeta > 2.405$ the stable minimum appears at $\mathbf{k} = \boldsymbol{\pi}$. Since the two stable regions support different momentum modes, a phase transition occurs for $\zeta = 2.405$. Therefore, it is required that one allows for a macroscopic population of both the modes in the immediate vicinity of $\zeta = 2.405$.

This can be achieved by reducing the translational symmetry of the problem. Intuitively, a condensate at $\mathbf{k} = \boldsymbol{\pi}$ with amplitude $\varphi_{k=\pi}$ flips a sign on every other site. Hence, one can choose to work in the original (momentum-resolved) basis $(\varphi_{k=0}, \varphi_{k=\pi})$, or in the site-resolved basis (φ^A, φ^B) . The two are related by a rotation. In order to allow for a dynamical population of the $\varphi_{k=\pi}$ condensate, the initial condition for $\varphi_\pi(0) = 1/\sqrt{2}(\varphi^A(0) - \varphi^B(0))$ must be nonzero. In the AB -basis, this is equivalent to saying that there is a slight difference in the condensate occupation on the two sublattices. Physically, this imbalance is caused by spontaneous symmetry breaking. However, in the WCCA one has to put in a small imbalance by hand. In the following we refer to the small imbalance value $s = |\varphi_\pi(0)|^2$ as *seed*.

When the effective dispersion becomes flat $\zeta \approx 2.405$ [Fig 5.4], the condensate undergoes oscillations between the $\mathbf{0}$ and $\boldsymbol{\pi}$ modes, with a period $\sim 1/U$ for small U . This behaviour

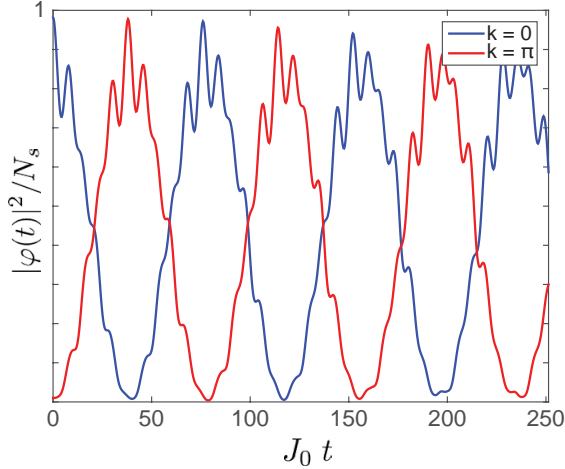


Figure 5.4: Time evolution of the condensate fractions for $\zeta = 2.405$ and $\Omega/J_0 = 20$ starting from a Bogoliubov initial state localised at $\mathbf{k} = \mathbf{0}$. The seed size is $s = 1\%$ and $U/J_0 = 0.2$. The initial condition for the condensate fractions is chosen to be $|\varphi^A(0)|^2/N_s = n_0/2$ for $\zeta < 2.405$ and $|\varphi^B(0)|^2/N_s = n_0/2$ for $\zeta > 2.405$, where n_0 is the total condensate fraction for the non-driven model in Bogoliubov theory.

is reminiscent of the collapse-and-revival effects seen for a BEC that is suddenly quenched into the Mott insulating phase [332], although the dynamics governed by WCCA is classical. The period of transfer oscillations is also seed-dependent and increases with $s \rightarrow 0$. Even though our approximation does not capture a true Mott insulating phase, the nonlinearities included in the WCCA are sufficient to give rise to these oscillations. Physically speaking, a quasiparticle-mediated channel is opened, through which particles flow from the condensate at $\mathbf{k} = \mathbf{0}$ to $\mathbf{k} = \pi$. Although it is present at any ζ , this channel is only effective when the dispersion is sufficiently flat since the amplitude for the phonon-mediated transition $\varphi_{k=0} \rightarrow b_k^\dagger \rightarrow \varphi_{k=\pi}$ scales as $(U/J_0)^2$.

5.2.4.2 (Quasi-)momentum distribution

Figure 5.5 plots snapshots of the quasimomentum (i.e., lattice momentum) distribution; the time evolution of this quantity is shown in Ref. [167]. Specifically, the quantity plotted is $n_{\mathbf{k}} = \langle b_{\mathbf{k}}^\dagger b_{\mathbf{k}} \rangle - n_0 \delta_{\mathbf{k},0}$, i.e., the condensate peak is subtracted. The quasimomentum distri-

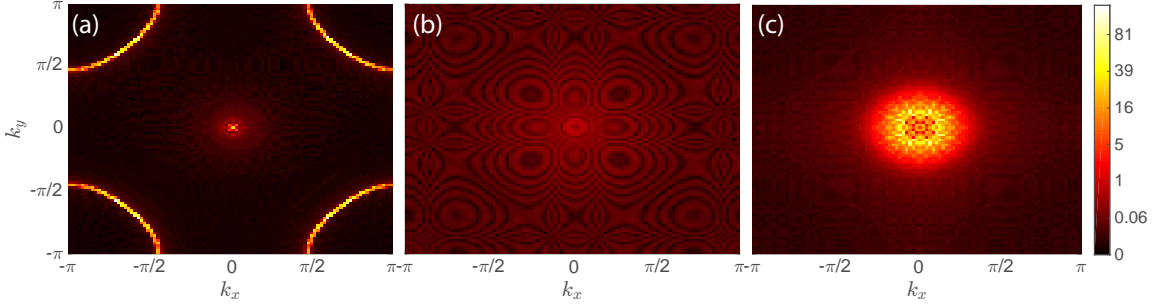


Figure 5.5: Snapshot of the momentum distribution $n_{\mathbf{k}} = \langle b_{\mathbf{k}}^\dagger b_{\mathbf{k}} \rangle - n_0 \delta_{\mathbf{k},0}$ after 801 driving cycles starting from a Bogoliubov initial state localised at $\mathbf{k} = \mathbf{0}$ for $U/J_0 = 0.2$. Panel (a) is in the unstable regime where the condensate is depleted due to parametric resonance. The bosons are excited by the drive to the quasienergy surface $\Omega = 2E_{\text{ave}}(\mathbf{k})$ (bright yellow-white circle around $\mathbf{k} = \pi$) where they occupy sharp peaks (white pixels). Panel (b) is in the regime where the condensate is stable on the pre-thermal time scales. In panel (c), the system is dynamically unstable due to the dispersion being inverted. The bright disc of excitations around $\mathbf{k} = \mathbf{0}$ corresponds to dynamically unstable modes. The parameters are (a) $\Omega/J_0 = 10$, $\zeta = 0.8$, (b) $\Omega/J_0 = 18$, $\zeta = 2.2$, and (c) $\Omega/J_0 = 20$, $\zeta = 3.8$.

bution can be directly accessed through band mapping followed by time-of-flight imaging. Moreover, as we are concerned with a single-band model, one can extract this distribution directly from time-of-flight imaging, by focusing on momenta within the first Brillouin zone.

Figure 5.5a shows the parametrically unstable case, where quasiparticles are strongly excited around the quasimomentum surface $\{\mathbf{k} : \Omega = 2E_{\text{ave}}(\mathbf{k})\}$ matching the resonance condition. Within Bogoliubov theory, the (time-averaged) excitation intensity should be uniform along this surface. However, as the points along this surface are not symmetry-related, the nonlinearities included in the WCCA favor some points on the excitation surface, as seen in the intensity pattern in Fig. 5.5a.

Figure 5.5b shows the *stable* case. Here, by contrast with panel a, the quasiparticle population remains low throughout the Brillouin zone. As expected from Bogoliubov theory, bosonic modes satisfying $J_{\text{ave}}(\mathbf{k}) \lesssim U$ should have appreciable occupation in the steady state; this region expands as the dispersion flattens. The intricate patterns in momentum space are due to the abrupt turn-on of the drive – which initialises the Floquet-Bogoliubov

quasiparticle states out of equilibrium – and are absent when the drive is instead gradually ramped up. These patterns evolve nontrivially with time [167].

Finally, Fig. 5.5c illustrates the case in which the initial state is a condensate at $\mathbf{k} = \mathbf{0}$, but the dispersion is inverted ($\zeta > 2.4$) so that the only *stable* condensate is supported at $\mathbf{k} = \pi$. Thus the initial state is unstable regardless of Ω . Let us consider the infinite-frequency limit; which amounts to a sudden quench of the single-particle dispersion. Computing the Bogoliubov spectrum around a condensate at $\mathbf{k} = \mathbf{0}$ in an inverted dispersion, we find that modes with momenta near $\mathbf{k} = \mathbf{0}$ acquire imaginary frequencies (and thus grow exponentially), whereas modes with large momenta are *stable*³. The unstable modes are determined by the condition $\varepsilon_{\text{ave}}(\mathbf{k}) + zJ_0 < 2n_0U$, where $\varepsilon_{\text{ave}}(\mathbf{k})$ is the single-particle Floquet dispersion (5.16). These modes are dynamically stabilised due to the nonlinear feedback of the self-consistent treatment [313]. Our numerical results with the WCCA confirm this picture: the unstable modes at small quasimomenta acquire large populations, whereas the large-quasimomentum modes do not. This behaviour is *specific* to the WCCA; in a real system it will correspond to intermediate-time dynamics $t \lesssim J_0/U^2$. On longer times, collisions between quasiparticles should cause large occupation numbers across the Brillouin zone.

5.2.4.3 Time-Dependence of the Energy

Last, we briefly address the issue of heating. Figure 5.6 shows the excess total (i.e., condensate plus quasiparticle) energy density in the system, relative to the non-driven state. Due to the abrupt turn-on of the periodic circularly polarised modulation, the energy changes discontinuously at $t = 0$. As expected, the energy density increases due to heating in the parametrically unstable region, saturates in the stable region, and exhibits a small growth for $\zeta \approx 3.8$. Notice the different behaviour in the parametrically unstable region compared to the dynamically unstable one: while in the former the energy grows due to the popu-

³This might seem counterintuitive, as the larger-momentum modes have “more negative” energies; note, however, that in the $U \rightarrow 0$ limit, *all* modes are stable as there are no decay processes.

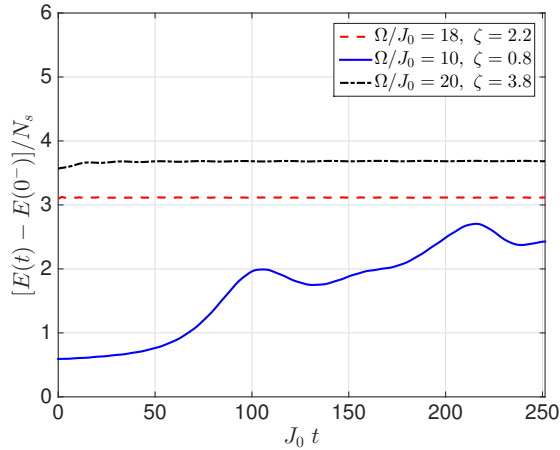


Figure 5.6: Total energy density of condensate and quasiparticles as a function of time for $U/J_0 = 0.2$ following the quench with frequency and amplitude as stated in the legend.

lation of modes lying on the high-energy surface, in the latter the dynamically unstable modes appear close enough to the origin [cf. Fig. 5.5c] so that the growth in energy density past the quench value is not substantial. Note that the system does not heat up even at fairly long times whenever the parameters are chosen to be in the stable region of the stability diagram. Although ergodic periodically-driven systems are expected to eventually heat up to infinite temperature [77, 78, 100, 309], in the weak-coupling limit this heating timescale (which is due to collisions between quasiparticles) is parametrically slower in the “stable” regimes of our phase diagram than in the “unstable” regimes. Thus, for a range of present-day experiments, we expect that in the stable high-frequency regime there is no significant heating on experimentally relevant timescales.

5.2.5 Validity of the Weak Coupling Conserving Approximation and Thermalisation Time Scales

Last we estimate the timescales on which the WCCA gives a reliable description of the physics, and discuss the dominant processes that (in the weak coupling regime) destabilise the various pre-thermal steady states discussed above. We discuss each of the three regimes

separately.

Parametrically unstable region. In this regime, the prethermalised phase is the one in which the momentum distribution is sharply peaked along momentum-space arcs as in Fig. 5.5a. Once again, we treat the time-averaged dispersion as the unperturbed Hamiltonian and look at the parametric instability growth rate due to a perturbation of the form $J_0\mathcal{J}_1(\zeta)b_{\mathbf{k}}^\dagger b_{\mathbf{k}} e^{i\Omega t}$. The matrix element for pair creation is then $\sim Un_0J_0\mathcal{J}_1(\zeta)/W_{\text{ave}}$ (the Fourier coefficient $c^l(\zeta)$ from the parametric instability analysis above is essentially given by the Bessel function), and for reasonably large drives this is linear in U . Parametric instability predicts that these features will grow at the rate $\Gamma \sim Un_0$, where n_0 is the condensate amplitude. The decay rate (i.e., inverse lifetime) of the quasiparticles along these arcs, once they are formed, is limited by collisions, and Fermi's Golden Rule implies that this decay rate is of order U^2 ; this is the rate at which these features spread out in momentum space. Thus there is a parametric separation in U between the formation and decay rate of these peaks. The leading collisional process comes from cubic terms of the form $U\varphi^*b_{\mathbf{k}_1}^\dagger b_{\mathbf{k}_2} b_{\mathbf{k}_1 - \mathbf{k}_2}$ (plus appropriate conjugates) in the Hamiltonian. The Golden Rule rate for this particular process is

$$\Gamma_c(\mathbf{k}) \sim U^2 n_0 n_{\mathbf{k}} \mathcal{N}_{2p}(E_{\text{ave}}(\mathbf{k})) \quad (5.19)$$

where $\mathcal{N}_{2p}(E_{\text{ave}}(\mathbf{k})) \sim \int dE' d^2q \delta(E' - E_{\text{ave}}(\mathbf{q})) \delta(E_{\text{ave}}(\mathbf{k}) - E' - E_{\text{ave}}(\mathbf{q} - \mathbf{k}))$ is the accessible two-particle density of states. Here, $E_{\text{ave}}(\mathbf{q})$ is the energy of an excitation with quasimomentum \mathbf{q} . On dimensional grounds this two-particle density of states must be inversely proportional to W_{ave} ; thus, the overall Golden Rule lifetime of a particular quasiparticle state will go as

$$\Gamma_c(\mathbf{k}) \sim U^2 n_0 n_{\mathbf{k}} / W_{\text{ave}} \quad (5.20)$$

up to a multiplicative constant. The ratio between the decay rate and the creation rate scales as $Un_{\mathbf{k}}/(J_0\mathcal{J}_1(\zeta))$. Thus the decay rate of a mode is slower than the creation

rate whenever the condensate amplitude is large compared with the population of the mode (essentially because the matrix element is not Bose-enhanced to the same degree). However, the decay rate is also suppressed with decreasing the interactions (expected) or increasing the drive amplitude. At short times, when the condensate is not appreciably depleted, the WCCA is therefore reliable; however, when the depletion becomes large the WCCA also fails. Thus the regimes of validity of the WCCA and Bogoliubov theory in the parametrically unstable regime are essentially the same, although the WCCA has the advantage of respecting particle number conservation *exactly* at all times.

Stable region. In the stable region there are two types of physical processes beyond the WCCA. (1) The excitations created by the original quench into the phase have finite collisional lifetimes, as discussed above. The momentum-space patterns in the stable region will dephase on this Golden-Rule timescale Γ_c ; however, the condensate fraction will remain large and stable even after dephasing. (2) Eventually, the system will absorb energy from the drive. If the drive frequency is Ω and the bandwidth of single-particle excitations is W_{ave} , then resonant absorption must involve at least $m \equiv \Omega/W_{\text{ave}}$ quasiparticles. It is straightforward to check that the associated Golden Rule rate, at weak coupling, is of the form U^m/W_{ave}^{m-1} . When U is sufficiently small, this heating timescale is much longer than the timescale on which the momentum-space patterns dephase; thus the system should remain *stable* for extremely long times at high frequencies.

Dynamically unstable region. In this regime, the growth rates of unstable modes are of order $\sqrt{J_{\text{ave}}(\zeta)U}$, whereas the collision rates are of order U^2/W_{ave} at best, so at weak coupling we have a parametric window in U where the WCCA remains valid.

5.2.6 Discussion

The main experimental prediction of this section – a parametric change in heating rates as a function of drive amplitude and frequency – can be measured in present-day experiments, which are naturally in the weak-coupling regime. For the experiment in Ref. [57] the parameters were chosen as $U/J_0 \approx 0.1$, $\Omega/J_0 \approx 20$, and $\zeta \approx 0.6$, which is within the

regime we considered. For realistic experiments in optical lattices, the presence of higher bands can lead to instability even at high drive frequencies Ω . In this case there are three regimes: (i) if Ω is less than twice the renormalised bandwidth W_{ave} of the lower band, the system is parametrically unstable as discussed above; (ii) if Ω is larger than $2W_{\text{ave}}$, smaller than the band gap to the upper band, and furthermore chosen such that any n -photon resonances to higher bands [333] are suppressed, then the system is stable within WCCA. (iii) if Ω exceeds the band gap, the drive can mediate interband transitions, leading to instability again. For a square optical lattice with typical lattice potential $V_{\text{latt}} = 10E_{\text{recoil}}$, $E_{\text{recoil}} = h \times 4$ kHz, the bandwidth of the lowest band is $W_0 = 4J_0 = h \times 0.3$ kHz [the time-averaged bandwidth W_{ave} is reduced by a factor of $\mathcal{J}_0(\zeta)$], and the gap to the second Bloch band is $\Delta = 4.57E_{\text{recoil}} = h \times 18.28$ kHz.

Although we focused on a square lattice, the arguments generalise to other lattices, such as the honeycomb lattice, in which topologically non-trivial states exist. Note that topological gaps in *mechanically shaken* optical lattices scale as Ω^{-1} [38, 39, 56]. Hence, in order to engineer topological insulators with large gaps (and a large region of non-zero Berry curvature around them), it is desirable to go to lower frequencies. Our results impose a fundamental limit for *weakly-interacting bosonic* systems on how small the frequency can be, since for $\Omega < 2W_{\text{ave}}$ the system becomes unstable. More generally, our results suggest that conserving approximations, whether controlled by weak coupling or some other parameter as in large- N models [284, 313, 334–336], are ways of exploring dynamical phase transitions in models that are both *interacting* (unlike free-particle models) and *finite-dimensional* (unlike the Kapitza pendulum). The critical properties of such transitions are a fruitful theme for future work. Although in practice such phase transitions will be smeared out by higher-order effects, the associated crossovers should still be experimentally observable.

5.3 Infinite Time Behaviour: Thermalisation through Many-Body Resonances

In this section, we study the dynamics and stability in a strongly-interacting resonantly-driven two-band model. Using exact numerical simulations, we find a stable regime at large driving frequencies where the time evolution is governed by a local Floquet Hamiltonian that is approximately conserved out to very long times. For slow driving, on the other hand, the system becomes unstable and heats up to infinite temperature. While thermalisation is relatively fast in these two regimes (but to different “temperatures”), in the crossover between them we find slow non-thermalising time evolution: temporal fluctuations become strong and temporal correlations long-lived. Microscopically, we trace back the origin of this non-thermalising time evolution to the properties of rare Floquet many-body resonances, whose proliferation at lower driving frequency removes the approximate energy conservation, and thus produces thermalisation to infinite temperature.

In particular, we demonstrate that there are regimes where a resonant coupling of two bands does not produce strong heating on the experimentally accessible time scales even in the presence of strong interactions. For sufficiently large driving frequencies, we find evidence, based on exact numerical simulations, that heating is perturbatively weak and, therefore, controllable. On the other hand, decreasing the driving frequency below a crossover scale Ω^* of order the single-particle bandwidth of the noninteracting system, our model exhibits strong heating. In the crossover regime, we find a range of driving frequencies where the system displays slow non-thermalising time-evolution: we observe long-lived temporal fluctuations and correlations which do not decay on the experimentally relevant time scales. We argue that this non-thermalising behaviour arises due to rare Floquet many-body resonances.

Besides the study of thermalisation in periodically-driven systems from a theory point of view, the second purpose of this section is to study the onset of heating at the experimentally-observable times. Present-day experiments with cold atoms performed in the high-frequency

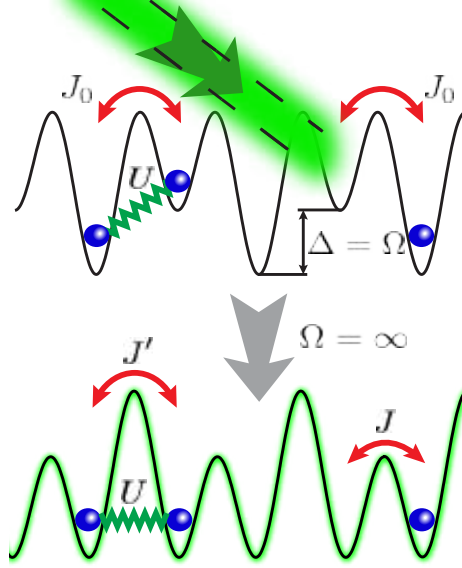


Figure 5.7: Floquet realisation of the interacting SSH model: the non-driven system represents a two-band model, coupled resonantly by a strong periodic drive. As a result, the ground state of the infinite-frequency Floquet Hamiltonian features an interesting topological phase.

regime report heating after a few hundred driving cycles [57]. Interestingly, heating seems to be more pronounced in bosonic rather than fermionic [56, 60] systems, presumably due to the unbounded character of the on-site Hilbert space dimension. A Density Matrix Renormalisation Group (DMRG) study in the weakly-interacting, periodically-driven Bose-Hubbard chain [257] found that heating is indeed suppressed at the large frequencies necessary to create novel Floquet Hamiltonians [43, 44, 46, 139]. Moreover, the existence of long-lived prethermal Floquet steady states has been predicted [101, 102] (see previous section) and confirmed numerically [167, 304]. In this chapter we study a minimal model of two resonantly-coupled bands, and find that heating is suppressed at large frequencies allowing for controlled Floquet engineering.

5.3.1 A Resonantly Driven Two-Band Model

Consider a system of interacting hardcore bosons satisfying three main properties, as illustrated in Fig. 5.7: (i) the non-driven system represents a two-band model, (ii) the periodic drive couples resonantly the two bands, and (iii) the ground state of the infinite-frequency Floquet Hamiltonian exhibits an interesting topological phase. The model can be equivalently mapped with a Jordan-Wigner transformation to spinless fermions, but we choose to present it here as hardcore bosons.

Concretely, the full dynamics is encoded in the Hamiltonian $H(t) = H_0 + H_{\text{drive}}(t)$ with H_0 the non-driven two-band model:

$$H_0 = -J_0 \sum_{j=1}^{L-1} (a_{j+1}^\dagger a_j + \text{h.c.}) - \frac{\Delta}{2} \sum_{j=1}^L (-1)^j n_j + U \sum_{j=1}^{L-1} \left(n_j - \frac{1}{2} \right) \left(n_{j+1} - \frac{1}{2} \right). \quad (5.21)$$

Here the operator a_j^\dagger creates a hardcore boson at $j = 1, \dots, L$ with L the total number of lattice sites, $n_j = a_j^\dagger a_j$ the number operator, J_0 denotes the bare hopping amplitude, Δ – the strength of a staggered potential, and U – the interaction strength. We limit the discussion to half filling with L even. When J_0 , Δ and U are all nonzero this model is non-integrable [337]. The non-interacting model has two bands, separated by the gap Δ . The periodic drive is step-like, and couples through

$$H_{\text{drive}}(t) = \text{sign}[\cos(\Omega t)] \sum_{j=1}^L \left[\frac{A}{2} (-1)^j - \delta A j \right] n_j, \quad (5.22)$$

with A – the amplitude of the modulated superlattice, δA – the amplitude of the shaken external field, and $T = 2\pi/\Omega$ – the driving period. Compared to a monochromatic driving, the step drive contains higher harmonics of Ω which, however, we checked does not change the phenomena discussed below. Therefore, in what follows, using the relation $\Omega = 2\pi/T$, we shall refer to Ω as the frequency of the drive.

In the following, we always set $\Delta = \Omega$, which resonantly couples and mixes the two

bands of the non-driven Hamiltonian H_0 [86, 105]. In the high-frequency regime, the effective Floquet Hamiltonian H_F governing the stroboscopic time-evolution of the system,

$$U_F = \mathcal{T}_t \exp \left(-i \int_0^T H(t) dt \right) = e^{-i H_F T}, \quad (5.23)$$

can be found with the help of an inverse-frequency expansion [9, 10, 32, 33, 59, 86, 87]. We refer to U_F as the Floquet operator. Since we choose the driving amplitude A as well as the superlattice potential Δ to be on the order of the driving frequency Ω , the time-average to obtain the leading-order Floquet Hamiltonian has to be performed in the rotating frame [33], see Sec. 2.2.5. In the infinite-frequency limit the Floquet Hamiltonian reads:

$$H_F^{(0)} = \sum_{j=1}^{L-1} -J_j (a_{j+1}^\dagger a_j + \text{h.c.}) + U \left(n_{j+1} - \frac{1}{2} \right) \left(n_j - \frac{1}{2} \right), \quad (5.24)$$

where the drive-renormalised hopping elements are $J_j = J = J_0 \chi(\zeta - \delta\zeta)$ for j odd, and $J_j = J' = J_0 \chi(\zeta + \delta\zeta)$ for j even. Here $\chi(x) = 2x\pi^{-1} \cos(\pi x/2)/(1 - x^2)$, $\zeta = A/\Omega$, and $\delta\zeta = \delta A/\Omega$. Thus, $H_F^{(0)}$ realises the Su-Schrieffer-Heeger (SSH) model including additionally nearest-neighbour interactions. When $J \neq J'$ and $U \neq 0$, this model is quantum chaotic with GOE level statistics, see Sec. 5.3.5.2. For $U = 0$, the system features two topological bands whenever $J \neq J'$, separated by a gap of energy width $2|J - J'|$. Notice how the topological gap is opened solely due to the drive, in close analogy with the experimental realisations of the Harper-Hofstadter model and the Haldane model in two-dimensions [52, 53, 55–57].

In analogy to recent experiments we study the following general protocol. We initialise the system in the ground state $|\psi\rangle$ of the topological infinite-frequency Floquet Hamiltonian $H_F^{(0)}$ which, to a good accuracy, can be also generated experimentally via adiabatic state preparation [52, 53, 55–57, 240]. Heating effects due to the adiabatic state preparation in the presence of the drive [240] are discussed in Chapter 4, where we demonstrated that at high driving frequencies one can generally prepare ground states of Floquet Hamiltonians with a high, though not perfect, fidelity. The subsequent dynamics, which we are interested

in, is generated by the full time-dependent Hamiltonian, see Eqs. 5.21, 5.22 and 5.23. To study the dynamics numerically, (i) we calculate the exact evolution w.r.t. the Hamiltonian $H(t)$ using a Lanczos algorithm with full reorthogonalisation based on Krylov’s method, which allows us to study the first several thousand driving periods for system sizes up to $L = 20$. Since we are interested in stroboscopic evolution, (ii) we also compute the exact Floquet operator U_F and apply exact diagonalisation (ED): projecting the initial state onto the Floquet basis allows us to directly reach the infinite-time limit for system sizes up to $L = 16$, by means of a quench to the diagonal ensemble of U_F . A detailed comparison between the two methods, as well as the system-size dependence of the results discussed below is presented in Sec. 5.3.3.5.

5.3.2 Definitions for the Microscopic Observables and Entropies Pertinent to Heating.

Let us begin by defining all key observables and entropies analysed throughout this sequence. We denote by $\{|n\rangle\}$ the eigenstates of the exact many-body Floquet operator $U_F = \mathcal{T}_t \exp \left(-i \int_0^T H(t) dt \right)$, and by $\{|\nu\rangle\}$ – the eigenstates of the approximate Floquet Hamiltonian $H_F^{(0)}$ obtained in the leading order in the inverse-frequency expansion. Note that $H_F^{(0)}$ is a local Hamiltonian with unfolded spectrum so we can choose the initial state to be the ground state of $H_F^{(0)}$, which we denote by $|\psi\rangle$ such that $H_F^{(0)}|\psi\rangle = E_F^{(0)}|\psi\rangle$. We shall discuss how observables, defined below, can be extended to initial mixed states. The “transition” probability between an approximate and an exact Floquet eigenstate is given by $|\langle \nu | n \rangle|^2$. The transition matrix containing all these probabilities is denoted by $C_{\nu n} = C_{n \nu} = |\langle \nu | n \rangle|^2$.

Assuming that there are no degeneracies in the exact Floquet spectrum, the stroboscopic diagonal expectation value of any observable \mathcal{O} and its fluctuations are given by

$$\langle \mathcal{O} \rangle_d = \lim_{N_T \rightarrow \infty} \frac{1}{N_T} \sum_{l=1}^{N_T} \langle \psi(lT) | \mathcal{O} | \psi(lT) \rangle = \sum_n \langle n | \mathcal{O} | n \rangle C_{n \psi}, \quad (5.25)$$

$$\langle \delta \mathcal{O} \rangle_d = \sqrt{\lim_{N_T \rightarrow \infty} \frac{1}{N_T} \sum_{l=1}^{N_T} \left(\langle \psi(lT) | \mathcal{O} | \psi(lT) \rangle - \langle \mathcal{O} \rangle_d \right)^2} = \sqrt{\sum_{n \neq m} |\langle n | \mathcal{O} | m \rangle|^2 C_{n\psi} C_{m\psi}}.$$

In order to define how much energy is pumped into the system by the drive, we measure the energy associated with the approximate Floquet Hamiltonian, i.e we choose $\mathcal{O} = H_F^{(0)}$. The diagonal expectation value then becomes

$$\langle \psi | H_F^{(0)} | \psi \rangle_d = \sum_n \langle n | H_F^{(0)} | n \rangle C_{n\psi} = \sum_{\nu} E_{F,\nu}^{(0)} p_{\nu\psi}, \quad (5.26)$$

where $p_{\nu\psi} = \sum_n C_{\nu n} C_{n\psi}$ is the probability to occupy the ν -th eigenstate of $H_F^{(0)}$ in the diagonal ensemble (i.e. for $t \rightarrow \infty$), starting from its GS $|\psi\rangle$. The transition probability matrix p can be also understood as a result of a double quench, where the system is prepared in the ground state of $H_F^{(0)}$. Then it is evolved periodically according to the Hamiltonian $H(t)$ and after many periods $N_T \rightarrow \infty$, it is projected back to the basis of $H_F^{(0)}$. It is easy to see that under these conditions the transition probability becomes a Markov matrix and satisfies the factorisation property (see also Ref. [308] for more details).

We can now define the following infinite-time quantities, which are used to analyse heating in the system:

- Normalised energy (or equivalently normalised work) \bar{Q}_ψ pumped into the system during the drive:

$$\bar{Q}_\psi = \frac{\langle \psi | H_F^{(0)} | \psi \rangle_d - E_{F,\psi}^{(0)}}{E_{F,\beta=0}^{(0)} - E_{F,\psi}^{(0)}}, \quad (5.27)$$

where $E_F^{(0)} = \langle \psi | H_F^{(0)} | \psi \rangle$ is the ground state energy of $H_F^{(0)}$, $E_{F,\beta=0}^{(0)} = 1/\mathcal{D} \sum_{\nu} E_{F,\nu}^{(0)}$ is the energy at infinite temperature and \mathcal{D} is the dimensionality of the Hilbert space. For the system considered in this section, in the thermodynamic limit $L \rightarrow \infty$, $E_{F,\beta=0}^{(0)}/L \rightarrow 0$ [$E_{F,\beta=0}^{(0)}/L = -U/(4L)$ for half-filling].

- Normalised diagonal (double-quench) entropy \mathcal{S}_ψ :

$$\mathcal{S}_\psi = \frac{S_{\psi,d} - S_\psi^{(0)}}{S_{\beta=0} - S_\psi^{(0)}} = \frac{S_{\psi,d}}{S_{\beta=0}}, \quad (5.28)$$

where $S_{\psi,d} = -\sum_\nu p_{\nu\psi} \log p_{\nu\psi}$ is the entropy in the diagonal ensemble in the basis of $H_F^{(0)}$, i.e. with $p_{\nu\psi} = \sum_n C_{\nu n} C_{n\psi}$. The initial state is the ground state of $H_F^{(0)}$ and therefore $S_\psi^{(0)} = 0$, while the maximum possible entropy (at infinite-temperature) is $S_{\beta=0} = L \log 2$. This entropy characterizes the spreading of the initial state $|\psi\rangle$ over other eigenstates of $H_F^{(0)}$ after the system is driven for infinitely many periods. Note that there is a universal non-extensive correction to the entropy $S_{\psi,d}$ given by $\gamma - 1$, where γ is the Euler constant [338]. This correction originates from the fact that the entropy is a non-linear function of the density matrix.

- Floquet diagonal entropy:

$$S_{\psi,d}^F = -\sum_n C_{\psi n} \log C_{n\psi}. \quad (5.29)$$

This entropy measures spreading of the initial state $|\psi\rangle$ over the eigenstates of the Floquet Hamiltonian. It is equivalent to the von-Neumann's entropy of the (stroboscopically) time averaged density matrix of a driven system.

- Normalised entanglement entropy of the half chain $\overline{\mathcal{S}_\psi^{\text{ent}}}$ produced by the drive:

$$\begin{aligned} \overline{\mathcal{S}_\psi^{\text{ent}}} &= \frac{\overline{s_\psi^{\text{ent}}} - s_\psi^{\text{ent}}(t=0)}{\log(2) - s_\psi^{\text{ent}}(t=0)}, \\ \overline{s_\psi^{\text{ent}}} &= \lim_{N_T \rightarrow \infty} \frac{1}{N_T} \sum_{l=1}^{N_T} \frac{1}{L/2} \text{Tr}_B [-\rho_B(lT) \log \rho_B(lT)] \end{aligned} \quad (5.30)$$

Here, B denotes the set of the first $L/2$ lattice sites, $\rho_B(lT)$ – the reduced density matrix of B at time $t = lT$, and $s_\psi^{\text{ent}}(t=0)$ is the entanglement entropy of the initial state.

- Energy density fluctuations $\overline{\delta\mathcal{E}}_\psi$:

$$\overline{\delta\mathcal{E}}_\psi = \frac{1}{L} \sqrt{\lim_{N_T \rightarrow \infty} \frac{1}{N_T} \sum_{l=1}^{N_T} \left(\langle \psi(lT) | H_F^{(0)} | \psi(lT) \rangle - \langle \psi | H_F^{(0)} | \psi \rangle_d \right)^2}. \quad (5.31)$$

5.3.3 Heating

After having specified the details of the model system, the protocol of the drive and the observables of interest, it is the purpose of the following section to study the heating dynamics as a function of the driving frequency Ω . Specifically, we characterize heating based on the energy absorbed by the system from the drive in Sec. 5.3.3.1, as well as the half-chain entanglement entropy in Sec. 5.3.3.2. Last but not least, in Sec. 5.3.3.3, we briefly discuss the dependence of heating on the interaction strength.

5.3.3.1 Energy Absorption

Let us begin the study of the heating dynamics by looking at the energy of the system. In analogy to experiments, where it is the Floquet-engineered infinite-frequency Hamiltonian $H_F^{(0)}$ that is the prime object of interest, we characterize heating by measuring the energy $H_F^{(0)}$ in the time-evolved state. Specifically, we calculate the stroboscopic evolution [160] of the energy density \mathcal{E}_ψ of $H_F^{(0)}$:

$$\mathcal{E}_\psi(lT) = \frac{1}{L} \langle \psi | H_F^{(0)}(lT) | \psi \rangle, \quad (5.32)$$

with $l \in \mathbb{N}$, and the time-dependence of $H_F^{(0)}(T) = U_F^\dagger H_F^{(0)} U_F$ is understood in the Heisenberg picture. While in the infinite-frequency limit $\mathcal{E}_\psi(lT) = \mathcal{E}_\psi(0) = \text{const.}$ and heating is absent, at finite Ω the system will be driven out of the initial ground-state manifold and will increase its energy.

Depending on the magnitude of the driving frequency, we identify two different regimes, separated by a crossover scale Ω^* , see Figs. 5.8, 5.9. A quantitative analysis of Ω^* for small

interactions can be found in Sec. 5.3.3.3 and specifically in Eq. 5.35. For $\Omega \ll \Omega^*$ the system heats up quickly close to an infinite-temperature state where all states of $H_F^{(0)}$ are occupied with equal probability. For $\Omega \gg \Omega^*$, on the other hand, heating is weak and the evolution is well-approximated by the local Floquet Hamiltonian $H_F^{(0)}$. It is interesting, from the point of view of both theory and experiment, to study the full crossover from the stable to the unstable regime as a function of the driving frequency. For that purpose, we introduce a normalised heating \bar{Q}_ψ , which measures the amount of energy absorbed by the system from the drive:

$$\bar{Q}_\psi = \frac{\bar{\mathcal{E}}_\psi - \mathcal{E}_\psi(0)}{\mathcal{E}_{\beta=0} - \mathcal{E}_\psi(0)}. \quad (5.33)$$

\bar{Q}_ψ interpolates continuously between absence of heating, where $\bar{Q}_\psi = 0$, and heating to infinite temperature, where $\bar{Q}_\psi = 1$, see also Fig. 5.9. Here, $\bar{\mathcal{E}}_\psi = \lim_{N_T \rightarrow \infty} N_T^{-1} \sum_{l=1}^{N_T} \mathcal{E}_\psi(lT)$ is the stroboscopic time average of $\mathcal{E}_\psi(lT)$, while $\mathcal{E}_{\beta=0}$ is the infinite-temperature average, which is close to the centre of the many-body band, up to L^{-1} -corrections [$\mathcal{E}_{\beta=0} = -U/(4L)$ for half-filling]. We calculated the long-time limit from a time average of the stroboscopic evolution over the last 4×10^3 of 5×10^3 total driving periods obtained via the aforementioned Lanczos algorithm. We checked that nonzero initial temperatures do not change the physical picture, see Sec. 5.3.3.4. A more detailed analysis of finite-size effects is given in Sec. 5.3.3.5. While we find that the results appear to be only weakly sensitive to increasing L , finite-size effects become most pronounced in the vicinity of the crossover scale Ω^* .

To understand the origin of this behaviour, we show both the short-term evolution, Fig. 5.8d, relevant for present-day experiments with cold atoms, as well as the longer-term behaviour, Fig. 5.8b, which allows us to make a statement about energy absorption in the longer run. For $\Omega \gg \Omega^*$, the energy density stays at a value near the ground state of $H_F^{(0)}$, which is perturbatively controlled by the inverse frequency Ω^{-1} and becomes vanishingly small upon including higher-order Ω^{-1} -corrections to the approximate Floquet Hamiltonian cf. Sec. 5.3.5.1. Therefore, in this regime the dynamics is completely stable on the experimentally relevant time scales for the numerically simulated system sizes.

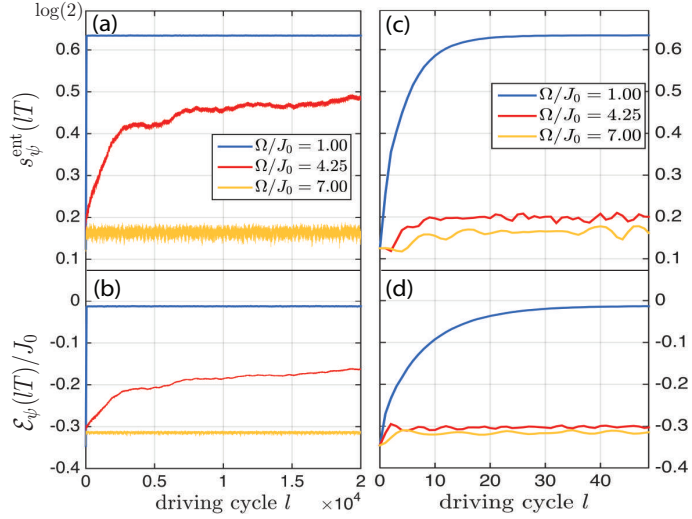


Figure 5.8: Short and long-time stroboscopic dynamics of the entropy density (a) and (c), and the energy density (b) and (d). The linewidths in (a) and (b) show the size of temporal fluctuations. The parameters are $U/J_0 = 1$, $\zeta = 0.6$, $\delta\zeta = 0.12$, and $L = 20$, which in the high-frequency limit gives $J'/J_0 = 0.41$ and $J/J_0 = 0.29$.

It follows that heating can be well-controlled making this parameter regime particularly suitable for Floquet engineering.

Conversely, for $\Omega \ll \Omega^*$, the energy absorption becomes strong which leads to fast heating with the energy quickly approaching its infinite-temperature value. Hence, the system is unstable and experiments in this regime are rendered uncontrollable. It is, thus, crucial to acquire a better understanding of the frequency-dependence of the onset of heating. Interestingly, in the vicinity of the crossover scale $\Omega \approx \Omega^*$, the dynamics changes its character completely. Although the system still heats up, [but not to infinite temperature for finite system size L], the time scales become so extended that the final relaxation cannot be resolved within the studied 2×10^4 driving cycles, see Fig. 5.8. The origin of this substantially slowed down dynamics we analyse in more detail in Sec. 5.3.4 and Sec. 5.3.4 where we also give explanations for the microscopic mechanism behind this unexpected behaviour.

5.3.3.2 Entanglement Entropy Production

The two heating regimes separated by the crossover scale Ω^* are also clearly identifiable from the analysis of the entanglement entropy density of half the chain:

$$s_\psi^{\text{ent}}(lT) = -\frac{1}{L/2} \text{Tr}_B [\rho_B(lT) \log \rho_B(lT)], \quad (5.34)$$

where B denotes the set of the first $L/2$ lattice sites and $\rho_B(lT)$ – the reduced density matrix of B after l periods. The behaviour of $s_\psi^{\text{ent}}(lT)$ as a function of time is plotted in Fig. 5.8a,c, and clearly shows the same three qualitatively different behaviours already revealed by \mathcal{E}_ψ . (i) At high frequencies [compared to the bare model parameters], the production of entanglement entropy remains low. The non-zero tail most likely has a two-fold origin: part of it comes from the non-zero entanglement entropy of the Floquet ground state [cf. value at $l = 0$], while the dynamically produced entanglement is due to the small temperature resulting from the energy density injected in the system by abruptly turning on the periodic drive. (ii), in the crossover, $\Omega \approx \Omega^*$, the dynamics is again found to be slow. Notice that extremely long observation times are required to fully resolve the crossover regime. (iii), for $\Omega \ll \Omega^*$ the entanglement entropy grows quickly to its infinite-temperature value of $\log(2)$ per lattice site, signalling that an infinite-temperature state is reached. From a fundamental point of view, however, s_ψ^{ent} is an even stronger indicator of the described phenomenology, since it contains information about the entire reduced density matrix. We note that the generation of entanglement entropy in integrable periodically-driven systems was studied in Refs. [298, 339], while its thermalisation in a non-integrable spin chain was discussed in Ref. [340].

5.3.3.3 Heating Dependence on the Interaction Strength

It is interesting to briefly mention the heating dependence on the interaction strength U . Intuitively, one would expect that a strongly interacting nonintegrable system subject to a non-energy-conserving driving protocol can easily redistribute the absorbed energy among

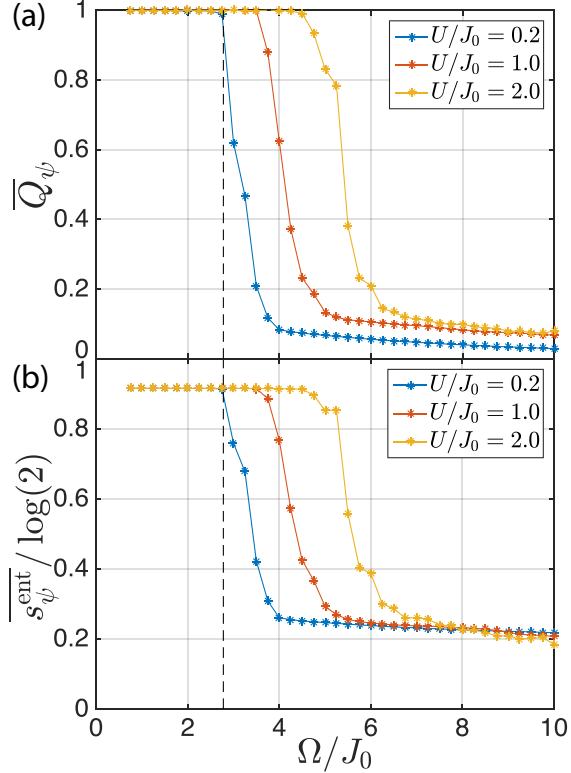


Figure 5.9: Dependence of the crossover regime on the interaction strength: excess heat (a) and excess entanglement entropy density (b). Unity on the vertical axis corresponds to an infinite-temperature state, while zero – to no heating. The parameters are $\zeta = 0.6$, $\delta\zeta = 0.12$, and $L = 20$, which in the high-frequency limit gives $J'/J_0 = 0.41$ and $J/J_0 = 0.29$.

many states due to the presence of enhanced collisions. Contrary to this naive expectation, for the system sizes up to $L = 20$, we find that this does not happen for large driving frequencies, cf. Fig. 5.9. Instead, we find that the crossover scale $\Omega^* = \Omega^*(J_0, U, A)$ slowly shifts to higher frequencies with increasing the interaction strength U . Notice that in the high-frequency regime $\Omega \gg \Omega^*$, for $U/J_0 = 2$ the system is already strongly interacting due to the dynamically suppressed effective hopping matrix elements of the relevant infinite-frequency Floquet Hamiltonian: $U/J, U/J' \approx 10$.

For small U , the energy absorption appears once the full bandwidth of the single-particle Floquet Hamiltonian exceeds $\Omega/2$. This enables heating via the basic two-particle-two-hole

interaction process where two particles from the very bottom of the lower single-particle band get scattered to the very top of the upper band. As a consequence, asymptotically for weak interactions, heating starts to occur whenever such a single-particle resonance is available. This implies the following dependence of the crossover scale for weak interactions up to corrections vanishing asymptotically for $U/J_0 \rightarrow 0$:

$$\Omega^* = 4(J + J') + \mathcal{O}(U). \quad (5.35)$$

Beyond the weakly interacting limit, we observe that the onset of heating Ω^* is shifted to larger values for increasing U , see Fig. 5.9, presumably because higher-order processes become the effective sources of heating. Here we do not consider the limiting case of $J_0 \ll \Omega \sim U$, which can be treated using the generalised Schrieffer-Wolff transformation for periodically-driven systems [105], see Sec. 3.2.

5.3.3.4 Finite-Temperature Effects

Until now we focused on the system initially prepared in the ground state of $H_F^{(0)}$. In this section we check the sensitivity of the results to the presence of a finite temperature. Specifically, we assume that the system is initially prepared in a state according to the equilibrium Boltzmann distribution with respect to the Hamiltonian $H_F^{(0)}$. Technically, we initialise the system in one of the eigenstates of $H_F^{(0)}$, $|\nu\rangle$, with the probability given by the Gibbs distribution $\rho_\nu \propto \exp[-\beta E_{F,\nu}^{(0)}]$. Then we calculate all observables such as $\mathcal{E}_\psi = \langle \psi | H_F^{(0)} | \psi \rangle$, $S_{\psi,d}$ and $\delta\mathcal{E}_\psi$ for this eigenstate. Finally, we take the average of the result over all available eigenstates. The observables computed in this way characterize the delocalisation of individual eigenstates exclusively due to the driving, and disentangles it from the initial thermal broadening. For instance, in the infinite-frequency limit, where the eigenstates of the Floquet Hamiltonian coincide with the eigenstates of $H_F^{(0)}$ the (eigenstate) diagonal entropy computed in this way, will be zero at any temperature as each initial eigenstate remains fully localised in energy space. In particular, we extend the definitions

of the observables and entropies in the following way:

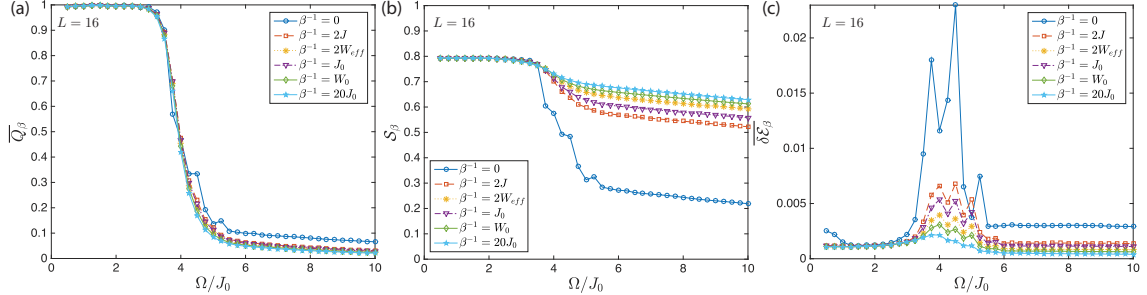


Figure 5.10: Dependence of the infinite-time normalised energy \bar{Q}_β (a), (eigenstate) diagonal entropy S_β (b), and energy-density fluctuations $\bar{\delta E}_\beta$ (c) on the temperature β^{-1} of the initial state for $L = 16$. The parameters are $U/J_0 = 1$, $\zeta = 0.6$, $\delta\zeta = 0.12$, which amounts to $J'/J_0 = 0.41$, $J/J_0 = 0.29$.

- Dimensionless normalised energy \bar{Q}_β starting from a finite-temperature state:

$$\bar{Q}_\beta = \frac{\sum_\nu \langle \nu | H_F^{(0)} | \nu \rangle_d \rho_\nu(\beta) - \sum_\nu E_{F,\nu}^{(0)} \rho_\nu(\beta)}{E_{F,\beta=0}^{(0)} - \sum_\nu E_{F,\nu}^{(0)} \rho_\nu(\beta)}, \quad (5.36)$$

- Normalised (eigenstate) diagonal entropy S_β at finite-temperature:

$$S_\beta = \frac{\sum_\nu S_{\nu,d} \rho_\nu(\beta)}{S_{\beta=0}}, \quad (5.37)$$

where $S_{\nu,d}$ is defined exactly as for the ground state, see Eq. (5.28), if we replace $|\psi\rangle$ by $|\nu\rangle$. Note that S_β is *not* the normalised (eigenstate) diagonal entropy corresponding to the density matrix $\rho(lT) = \sum_\nu \rho_\nu |\nu(lT)\rangle \langle \nu(lT)|$. It is rather a measure of the average delocalisation of the individual eigenstates of $H_F^{(0)}$ in the basis of the exact Floquet operator.

- (Eigenstate) energy density fluctuations $\bar{\delta E}_\beta$ at finite-temperature:

$$\bar{\delta E}_\beta = \sum_\nu \delta E_\nu \rho_\nu(\beta)$$

$$= \sum_{\nu} \rho_{\nu}(\beta) \frac{1}{L} \sqrt{\lim_{N_T \rightarrow \infty} \frac{1}{N_T} \sum_{l=0}^{N_T} \left(\langle \nu(lT) | H_F^{(0)} | \nu(lT) \rangle - \langle \nu | H_F^{(0)} | \nu \rangle_d \right)^2} \quad (5.38)$$

As with the entropy, $\overline{\delta\mathcal{E}}_{\beta}$ is not measuring density fluctuations in the system. Rather it measures the long-time fluctuations of the energy starting from a specific eigenstate and then averages over all eigenstates.

Let us now analyse the behaviour of these observables in different driving regimes. Figure 5.10a-c shows the frequency dependence of the normalised energy \overline{Q}_{β} , the normalised (eigenstate) diagonal entropy \mathcal{S}_{β} and the energy-density fluctuations $\overline{\delta\mathcal{E}}_{\beta}$ for various initial temperatures (see legend for details). Here, $2J$ sets the bandwidth of the lowest band of $H_F^{(0)}$, while $W_{\text{eff}} = 2(J + J')$ – the total bandwidth of the two effective SSH bands. The bare hopping and bandwidth are denoted by J_0 and W_0 , respectively. Fig. 5.10a shows the normalised energy of the system absorbed from the drive. Figure 5.10b illustrates the temperature dependence of the normalised (eigenstate) diagonal entropy. While at low frequencies all states heat up uniformly to infinite temperature, at large frequencies the states are only spread around the mean energy. Due to the high density of states in the middle of the spectrum, this spreading results in a higher (eigenstate) diagonal entropy than for the initial ground state. Finally, Fig. 5.10c shows the energy-density fluctuations as a function of temperature. Quite generally, it becomes visible that the size of the fluctuations decreases with increasing temperature. This effect is likely due to the additional statistical average involved. More interestingly, however, one sees that the high-frequency tail goes down significantly. Hence, the exponential decay of fluctuations as a function of the system size [see Fig. 5.15] is more pronounced for high-energy-density initial states in the high-frequency thermalising phase, which is expected from typicality.

Last, in Fig. 5.11 we also show the energy pumped into the system after the experimentally-relevant time scales of 200 driving cycles of evolution, starting from a finite-temperature Gibbs state. We limit the discussion to high frequencies where the system does not heat

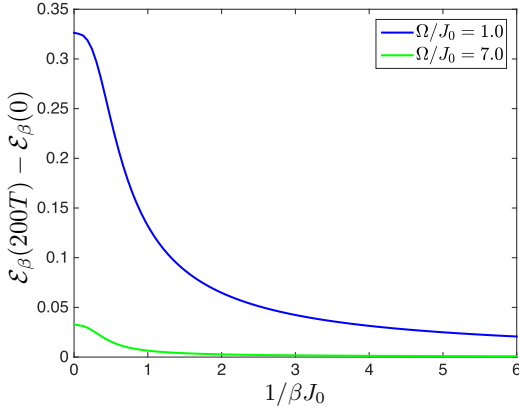


Figure 5.11: Energy density $\mathcal{E}_\beta(200T) - \mathcal{E}_\beta(0)$ pumped into the system as a function of the temperature of the Gibbs initial state localised around the GS. The parameters are $L = 16$, $U/J_0 = 1$, $\zeta = 0.6$, $\delta\zeta = 0.12$, which amounts to $J'/J_0 = 0.41$, $J/J_0 = 0.29$.

up. For $\beta^{-1} = J$ the temperature is set within the lowest *effective* band of $H_F^{(0)}$, but we can also consider other interesting cases where the temperature lies in the *effective* band gap $\beta^{-1} = 2J$, or within the non-driven band $\beta = J_0$. Interestingly, one sees that higher-temperature initial states absorb less energy. Note also that, at low temperatures, the energy density absorbed from the drive decreases with increasing the drive frequency.

5.3.3.5 System Size Dependence. Comparison between Exact Diagonalisation and Lanczos Time Evolution

The discussion in this section carries a two-fold purpose: (i) to study the system size dependence of the observables considered here, i.e. the normalised energy, its fluctuations, the entanglement and diagonal entropy, and (ii) to compare the long-time Lanczos dynamics of these quantities with the infinite-time ED expectation values defined in the previous section. For all the data presented in this section, we initiate the evolution from the ground state of the infinite-frequency Floquet Hamiltonian $H_F^{(0)}$, while we evolve with the exact time-dependent Hamiltonian $H(t)$. All measurements are taken stroboscopically.

Exact Diagonalisation (ED) allows us to discuss system sizes of up to $L = 16$ sites,

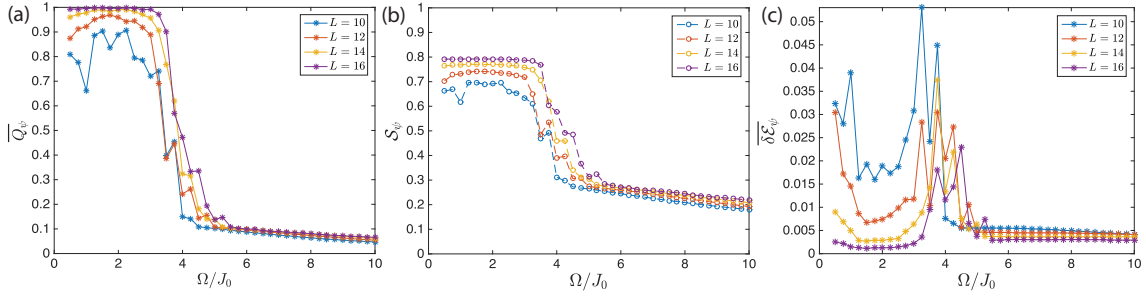


Figure 5.12: System size dependence of the exact diagonalisation results. (a) normalised energy, (b) diagonal entropy and (c) energy density fluctuations. The parameters are $U/J_0 = 1$, $\zeta = 0.6$, $\delta\zeta = 0.12$, which amounts to $J'/J_0 = 0.41$, $J/J_0 = 0.29$.

taking into account all symmetries present in the problem. Although these system sizes are admittedly far away from the realistic thermodynamic limit, ED is still a very useful tool, since it allows us to make statements about the infinite-time limit. Figure 5.12a and b shows the infinite-time system-size dependence of the normalised energy and the relative diagonal entropy curves, respectively. The data suggests a small drift of the transition region in the direction of increasing driving frequency. However, given that the drift is small and that the crossover frequency is close to the single-particle bandwidth, based on this data, we cannot draw conclusions about the thermodynamic limit. Due to the presence of resonances in the crossover regime, we were unable to scale-collapse the data. Fig. 5.12c shows the system size dependence of the energy density fluctuations. Clearly, the region of large fluctuations coincides nicely with the crossover between the infinite-heating and no-heating regimes.

Lanczos Time Evolution. For comparison, we also show the system-size dependence of the long-time averaged curves, obtained using Lanczos evolution. Figure 5.13a, b and c show the system-size dependence of the normalised energy, the entanglement entropy and the energy density fluctuations. Here we can go to larger system sizes, while the evolution is limited to finite, but long times. We evolve the initial state for 5000 periods and average the data between periods $T_1 = 1000$ and $T_2 = 5000$, to make sure we avoid any initial transients. From this figure we see that the drift of the crossover frequency with

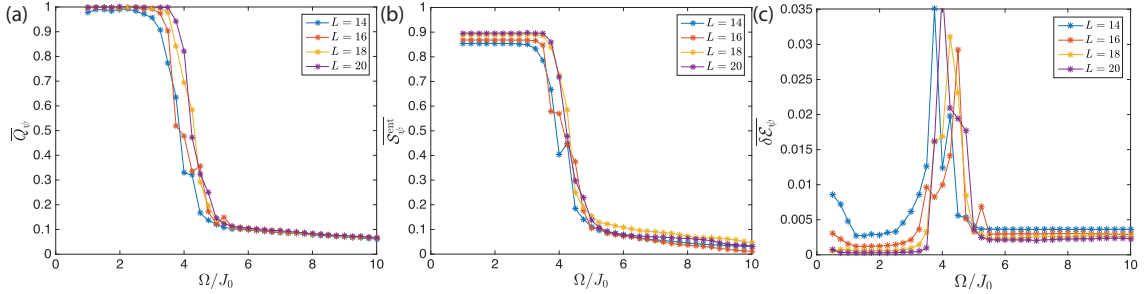


Figure 5.13: System size dependence of the Lanczos evolution curves. (a) normalised energy, (b) entanglement entropy and (c) energy density fluctuations. The parameters are $U/J_0 = 1$, $\zeta = 0.6$, $\delta\zeta = 0.12$, which amounts to $J'/J_0 = 0.41$, $J/J_0 = 0.29$.

the system size becomes almost negligible as we reach $L = 20$. In Fig. 5.14 we show the comparison between the data obtained by the Lanczos and ED methods. We see that in the two thermalised phases of low and high frequencies the two methods agree to excellent precision. In the glassy crossover region, however, the disagreement is significant due to extremely slow dynamics, which does not saturate after 5000 periods.

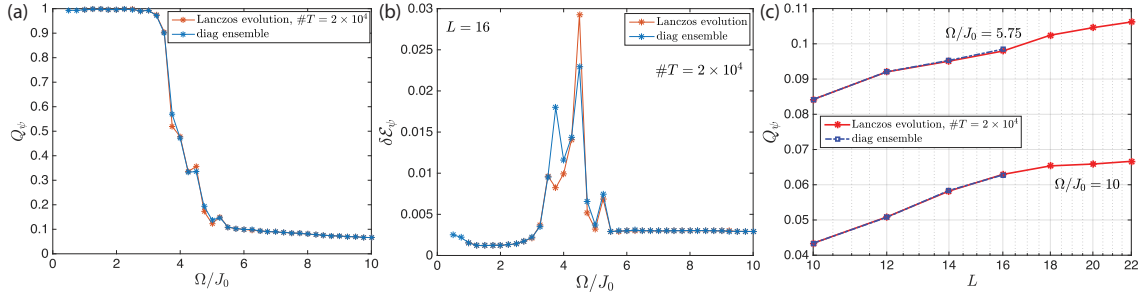


Figure 5.14: Comparison between infinite-time ED and long-time average of the exact Lanczos time evolution. Panels (a) and (c) show the normalised energy and energy-density fluctuations for $L = 16$. In panel (a) we have assumed $E_{F,\beta=0}^{(0)} = 0$. Panel (b) shows the system-size dependence of the normalised energy on a logarithmic scale. The parameters are $U/J_0 = 1$, $\zeta = 0.6$, $\delta\zeta = 0.12$, which amounts to $J'/J_0 = 0.41$, $J/J_0 = 0.29$.

To shed more light on the localisation-delocalisation dilemma, we choose two points from the $Q_\psi(\Omega/J_0)$ curve in Fig. 5.14a, both in the high-frequency localised region, and monitor the behaviour of the normalised energy as a function of the system size L , see Fig. 5.14c. In this regime, we observe a nice agreement between the infinite-time ED curves and the time-averaged Lanczos evolution data taken over 2×10^4 driving periods.

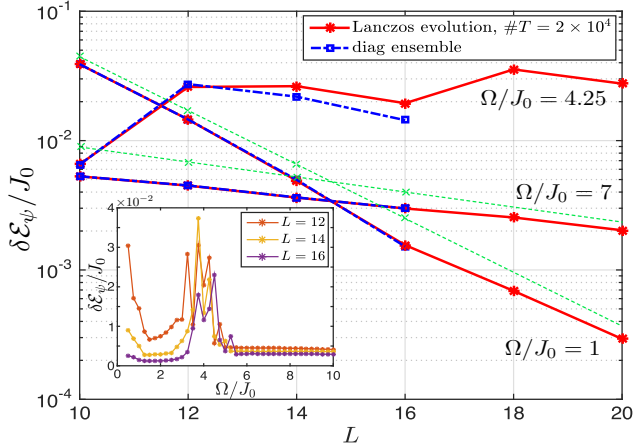


Figure 5.15: Energy density fluctuations as a function of the system size. The dashed green lines show the numerical data for $\exp(-S_{\psi,d}^F/2)$ at $\Omega/J_0 = 1$ and $\Omega/J_0 = 7$ up to $L = 16$, and are extrapolated for $L > 16$. Here $S_{\psi,d}^F$ is the Floquet diagonal entropy, cf. Sec. 5.3.2. Inset: frequency dependence of the fluctuations at infinite time obtained using ED. The parameters are $U/J_0 = 1$, $\zeta = 0.6$, $\delta\zeta = 0.12$.

An interesting feature is observed if we plot the system-size dependence logarithmically: both the frequency closer to the transition region and the one deep into the thermalising phase feature apparently sublogarithmic growth. Moreover, the $\Omega/J_0 = 10$ curve seems to even saturate at large system sizes. If this trend remains to infinite L , that would mean that there is a true finite-frequency transition between a localised and a delocalised phase in the thermodynamic limit.

5.3.4 Thermalisation – Temporal Fluctuations and Correlations

In the previous Section we studied the heating dynamics as a function of driving frequency. As a main observation, we identified an extended crossover region with extremely slow dynamics that separates the regimes of unstable heating from the stable region where the dynamics is approximately governed by the desired infinite-frequency Floquet Hamiltonian. In the following, we aim to provide additional insights into the dynamics in these three regimes by analyzing their respective ergodicity and thermalisation properties. In particular, it will be the goal to further characterize the slow crossover regime by studying

temporal fluctuations and correlations.

One of the key properties of systems obeying the Eigenstate Thermalisation Hypothesis (ETH) is that long-time temporal fluctuations of expectation values of observables after a quench are exponentially small in the system size [307, 308, 341]. Equivalently, in the long-time limit the density matrix, from the point of view of local observables, is exponentially close to its time average at almost all times. Moreover, this exponential scaling can serve as a defining criterion to check whether the observables are equilibrated, especially when the exact Hamiltonian is not accessible and one cannot analyse the level statistics. Hence, this represents a well-suited criterion that can be utilised to investigate thermalisation both experimentally and numerically.

Let us define the stroboscopic temporal fluctuations $\delta\mathcal{O}$ of an expectation value of an operator \mathcal{O} : $\mathcal{O}_\psi = \langle \psi | \mathcal{O} | \psi \rangle$, as measured over N_T periods:

$$\overline{\delta\mathcal{O}}_\psi = \sqrt{\frac{1}{N_T} \sum_{l=1}^{N_T} [\mathcal{O}_\psi(lT) - \overline{\mathcal{O}_\psi}]^2}. \quad (5.39)$$

In isolated ergodic systems, according to ETH, thermalisation implies that for any physical observable $\overline{\delta\mathcal{O}}_\psi \approx e^{-S/2}$, where $S \propto L$ is the thermodynamic entropy of the system. This ETH prediction implies that from the point of view of observables the state $|\psi(t)\rangle$ at almost all times is equivalent to the time-averaged density matrix, up to terms exponentially suppressed in the system size. In Floquet systems it is hard to define a thermodynamic entropy as all the Floquet energies are defined modulo Ω and thus the density of Floquet energy states is uniform. This is in agreement with expectations from thermodynamics that any thermal state of a Floquet system corresponds to infinite temperature, and is thus characterised by a flat density of states. On the other hand, in the high-frequency driving regime for the finite systems we consider here the system does not heat up, and one can intuitively expect that one should use the entropy of an approximate extensive Floquet Hamiltonian, which can be computed perturbatively within a high-frequency expansion [9, 32, 33, 59, 87]. Alternatively, one can use the fact that in ergodic systems

$S \approx S_{\psi,d}^F$, where $S_{\psi,d}^F$ is the diagonal entropy [von Neumann entropy of the time-averaged density matrix] [308]. The diagonal entropy is readily computable from projecting the wave function of the system onto the exact Floquet eigenstates and does not depend on folding the spectrum. Then one can use this value of $S_{\psi,d}^F$ to estimate the expected scaling of $\overline{\delta\mathcal{O}}_\psi$ and compare with the numerical results.

The main plot in Fig. 5.15 shows how the fluctuations of $\mathcal{O} = H_F^{(0)}$ decay with the system size. We compare the long-time average obtained with the Lanczos algorithm (red) to the infinite-time limit from the diagonal ensemble (blue). In both the high and the low-frequency regimes this decay is consistent with exponential, with the exponent close to the one expected from ETH (green dashed lines), and hence the system thermalises. Clearly, slight deviations are visible which, however, might result from finite-size effects as we are not able to extrapolate to the thermodynamic limit. To fully clarify this, it would be necessary to study larger system sizes which, however, is not possible within the used methodology. This thermalisation corresponds to a finite temperature in the high-frequency regime, set by the energy density $\overline{\mathcal{E}}_\psi$, and to infinite temperature in the low-frequency regime. Note that in an extended region near the crossover scale Ω^* the situation is fundamentally different, similarly to the slow evolution discussed above. Specifically, the fluctuations $\overline{\delta\mathcal{E}}_\psi$ are strong and irregular such that ETH is not fulfilled and the evolution is non-thermalising (non-ergodic) in this regime. The inset of Fig. 5.15 shows the infinite-time energy fluctuations, calculated with ED, versus the driving frequency for three different system sizes, indicating the frequency domain of strong temporal fluctuations. Because of the very slow dynamics, it has not been possible to determine the infinite-time properties on the basis of the Lanczos algorithm. Instead, we have used full ED here, which limits the system sizes up to $L = 16$. In the inset of Fig. 5.15 one can see that the regime of strong temporal fluctuations of the energy with nonvanishing support over an extended frequency range features relatively sharp boundaries to the thermalising regions. Upon increasing the system size, we observe a slight drift of this extended region to larger driving frequencies. However, on the basis of the system sizes accessible within our numerical simulation, see

Fig. 5.13, it is unclear whether this region remains extended in the thermodynamic limit. Still, the extent over a few hopping amplitudes J_0 is substantial even for $L = 16$ without a very strong finite-size dependence.

From the preceding analysis we have seen that temporal fluctuations can become strong in the crossover region. In the following, we provide further evidence for nonergodic dynamics by studying temporal correlations. Specifically, an important indicator of non-thermalising evolution – the long memory of fluctuations – becomes manifest in the anomalously slow decay of nonequal-time correlation functions. To study this we now focus on the energy autocorrelation function:

$$\mathcal{G}(lT) = \frac{1}{\delta H_F^2} \sum_n \langle n | H_F^{(0)}(lT) H_F^{(0)}(0) | n \rangle_c = \frac{1}{\delta H_F^2} \sum_{m \neq n} |\langle n | H_F^{(0)} | m \rangle|^2 e^{-i(E_F^m - E_F^n)lT}, \quad (5.40)$$

where $|n\rangle$ is an eigenstate of the exact Floquet operator U_F corresponding to the eigenvalue $\exp[-iE_F^n T]$. In the definition of $\mathcal{G}(lT)$ we have included the average variance $\delta H_F^2 = \sum_n |\langle n | [H_F^{(0)} - \langle H_F^{(0)} \rangle]^2 | n \rangle|$ for normalisation such that $\mathcal{G}(0) = 1$. We sum over all eigenstates of U_F to obtain better statistics. Consequently, $\mathcal{G}(lT)$ measures temporal correlations over the full many-body spectrum which goes beyond what we have studied before, where we have determined the dynamics starting from the ground-state manifold. The dynamics of $\mathcal{G}(lT)$, obtained from ED, we show in Fig. 5.16a. Although, in the absence of exact degeneracies, for any finite system $\mathcal{G}(lT) \rightarrow 0$ as $l \rightarrow \infty$, the time scales which govern this decay differ tremendously between the thermalising and the nonergodic regimes. Similar to the strong temporal fluctuations in the crossover region, we thus also find a very slow decay of temporal correlations which further supports the evidence for a strongly nonergodic regime separating the stable from the unstable phase.

5.3.5 Floquet Many-Body Resonances

As we discussed in the previous sections, the crossover regime exhibits nonergodic properties in terms of strong temporal fluctuations and correlations. In the following, we argue

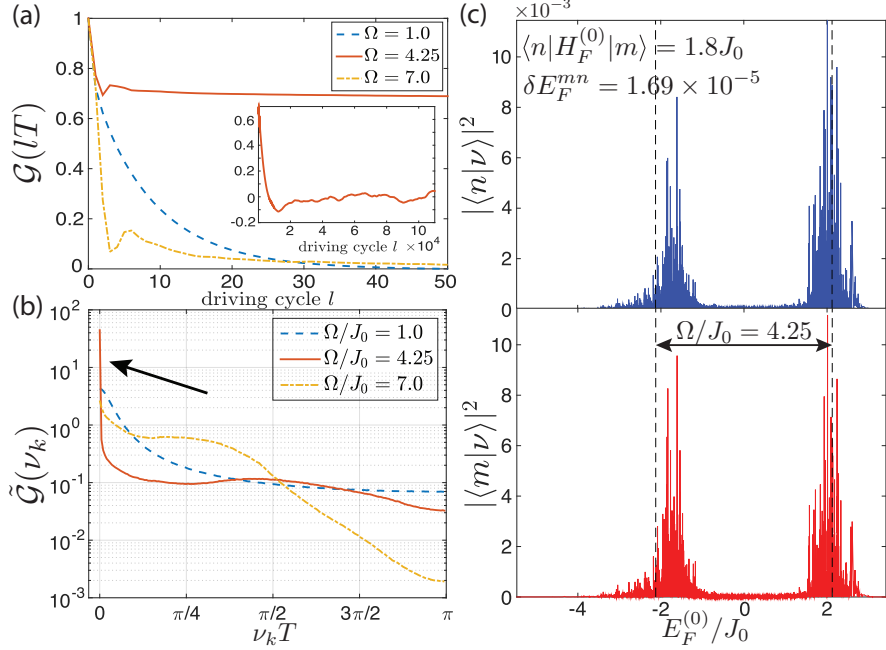


Figure 5.16: The energy autocorrelator \mathcal{G} as a function of time (a), and its Fourier transform $\tilde{\mathcal{G}}$ (b) for $\delta\nu T = \pi/200$. The arrow shows the many-body resonances peak. (c) A pair of many-body resonant Floquet eigenstates, $|m\rangle$ and $|n\rangle$, in the crossover regime. Here $|\nu\rangle$ are the eigenstates of the approximate Floquet Hamiltonian $H_F^{(0)}$ with energy $E_{F,\nu}^{(0)}$. The vertical dashed lines mark the boundaries of the Floquet zones, while the x -axis range corresponds to the many-body bandwidth. A similar procedure is used in time-of-flight images of superfluid Bose gases in optical lattices where quasimomentum states are projected onto momentum states to visualise the momentum (Bragg) peaks in nearby Brillouin zones. The parameters are $U/J_0 = 1$, $\zeta = 0.6$, $\delta\zeta = 0.12$, and $L = 16$.

that this numerical observation can be related microscopically to the appearance of rare Floquet many-body resonances. To demonstrate this, we introduce the discretised Fourier transform of the energy autocorrelation function

$$\tilde{\mathcal{G}}(\nu_k) = \frac{1}{\delta H_F^2} \sum_{m \neq n} |\langle n | H_F^{(0)} | m \rangle|^2 \delta(\nu_k \leq |E_F^n - E_F^m| \leq \nu_{k+1})$$

with $\nu_k = k\delta\nu$, $k \in \mathbb{N}$, and $\delta\nu$ a small quasienergy shell, see Fig. 5.16b. Interestingly, in the crossover regime, it features a well-pronounced peak near zero frequency, implying that near-resonant pairs of states of very small quasienergy difference dominate the long-

time physics. In terms of their physical energy, these pairs of states differ by integer multiples of the driving frequency and, therefore, represent resonances in the many-body spectrum. In Sec. 4.5, we argued that these resonances lead to the breakdown of adiabatic perturbation theory in periodically-driven systems [240, 288]. We note in passing that their manifestation in the form of non-analytic behaviour in expectation values of observables has been studied for integrable systems [103].

By looking closer at the spectral properties, we can finally give an explanation for the observed heating–no-heating crossover. While we find many-body resonances over the full range of driving frequencies, their influence onto the dynamics differs substantially in the three observed regimes. In the high-frequency limit $J_0, U \ll \Omega$, the resonances are so weak and rare that they do not affect the dynamics of the system. The absorption of one quantum of Ω at these elevated energies requires the excitation of a complex many-body state due to the locality of H_F in this regime – a process which is at least exponentially suppressed in frequency. Entering the crossover regime $\Omega \approx \Omega^*$, a small amount of the resonant pairs begin to exhibit a very strong coupling, such that there is always some small number of eigenstates of the Floquet operator which carry significant weights in nearby Floquet zones, see Fig. 5.16c. This results in large matrix elements on the order of a few J_0 , which represent a small but significant fraction of the total off-diagonal matrix elements of $H_F^{(0)}$ and which, according to Eq. (5.40), determine the slow dynamics of the system. These rare resonances cannot be neglected any more but rather dominate the long-time dynamics leading to a very slow non-thermalising time evolution. This observation, that rare resonances dominate the low-energy spectral properties, is reminiscent of Griffith phases in disordered systems, but here for a system without disorder. Once the driving frequency is lowered further, $\Omega \ll \Omega^*$, the many-body resonances proliferate and the eigenstates of the Floquet operator become quite delocalised over the Floquet zones in the eigenbasis of $H_F^{(0)}$, see Sec. 5.3.5.3. At the same time, the distribution of the off-diagonal matrix elements of $H_F^{(0)}$ becomes more uniform [see blue curve in Fig. 5.16b]. This delocalisation of the Floquet eigenstates in energy signifies rapid transfer of energy between the system and the drive, and the system

quickly heats up to infinite temperature.

5.3.5.1 Leading-Order Finite-Frequency Corrections

In this section, we calculate the leading Ω^{-1} -corrections to the effective (drive-phase independent) Floquet Hamiltonian and the kick operator within van Vleck perturbation theory, see Sec. 2.2.2. The general form of the van Vleck Floquet Hamiltonian can be calculated to 4th order for step-like periodic in the lab frame, see App. F. Instead, here we choose to work in the rotating frame which, as we explained in Sec. 2.2.5, leads to a resummation of an infinite subseries.

We begin by casting the exact time-dependent rotating frame Hamiltonian in spin language via $S_m^- = a_m$ and $T_m^- = b_m$. The spin operators obey the spin-1/2 algebra $[S_m^-, S_n^+] = -2\delta_{mn}S_m^z$, $[T_m^-, T_n^+] = -2\delta_{mn}T_m^z$. Then the Hamiltonian in the rotating frame can be written as

$$\begin{aligned} H^{\text{rot}}(t) = & -J_0 g(t) \sum_{m=1}^{L/2} (T_m^+ S_m^- + \text{h.c.}) - J_0 h(t) \sum_{m=1}^{L/2-1} (S_{m+1}^+ T_m^- + \text{h.c.}) \\ & + U \sum_{m=1}^{L/2} S_m^z T_m^z + U \sum_{m=1}^{L/2-1} S_{m+1}^z T_m^z, \end{aligned} \quad (5.41)$$

where the functions $g(\tau)$ and $h(\tau)$ with $\tau = \Omega t$ are given by

$$\begin{aligned} g(\tau) &= e^{-i[\tau - (\zeta - \delta\zeta)F(\tau)]}, \\ h(\tau) &= e^{+i[\tau - (\zeta + \delta\zeta)F(\tau)]}, \end{aligned}$$

$$F(\tau) = \int \text{sign}[\cos(\tau)] d\tau = \begin{cases} \tau & \text{for } -\pi/2 \leq \tau \leq \pi/2 \\ -\tau + \pi & \text{for } \pi/2 \leq \tau \leq 3\pi/2 \end{cases}$$

Using Eqs. (2.45) and (2.46) for the effective (non-stroboscopic) Hamiltonian H_{eff} and the time-periodic kick operator $K_{\text{eff}}(t)$, the leading Ω^{-1} -corrections are calculated with

the help of the van Vleck inverse-frequency expansion [9, 10, 32, 33, 59, 86, 87]. We find

$$\begin{aligned}
H_{\text{eff}}^{(1)} &= \frac{1}{\Omega} \left\{ J_0^2 \sum_m c_{hh} (S_m^z - T_m^z) + c_{gg} (T_m^z - S_{m+1}^z) \right. \\
&\quad \left. - J_0^2 c_{gh} \sum_m (S_{m+1}^+ T_m^- S_m^- - T_{m+1}^+ S_{m+1}^z T_m^- + \text{h.c.}) \right\}, \\
K_{\text{eff}}^{(1)}(t=0) &= \frac{1}{\Omega} \left\{ - J_0 \sum_m (\kappa_- T_m^+ S_m^- + \kappa_+ S_{m+1}^+ T_m^- + \text{h.c.}) \right\}. \tag{5.42}
\end{aligned}$$

The first-order correction contains a staggered potential term, and a correlated (interaction-dependent) hopping. The on-site staggered potential breaks the topological properties of the Floquet Hamiltonian, similarly to other one-dimensional Floquet topological insulators [342]. Stroboscopic symmetry-protected topological phases have been studied extensively in Ref. [342]. If we set $\zeta_{\pm} = \zeta \pm \delta\zeta$, the affective coefficients governing the dynamics in the localised phase can be evaluated in a closed form for the periodic step drive:

$$\begin{aligned}
c_{gg}(\zeta_-) &= \frac{1}{4\pi i} \int_0^{2\pi} d\tau_1 \int_0^{\tau_1} d\tau_2 \left[\left(1 - \frac{\tau_1 - \tau_2}{\pi} \right) \bmod 2\pi \right] \left[g(\tau_1)[g(\tau_2)]^* - (\tau_1 \leftrightarrow \tau_2) \right] \\
&= \frac{1}{(\zeta_- - 1)} - 8\zeta_-^2 \frac{\cos(\pi\zeta_-) + 1}{\pi^2(\zeta_-^2 - 1)^3}, \\
c_{hh}(\zeta_+) &= \frac{1}{4\pi i} \int_0^{2\pi} d\tau_1 \int_0^{\tau_1} d\tau_2 \left[\left(1 - \frac{\tau_1 - \tau_2}{\pi} \right) \bmod 2\pi \right] \left[h(\tau_1)[h(\tau_2)]^* - (\tau_1 \leftrightarrow \tau_2) \right] \\
&= -c_{gg}(\zeta_+), \\
c_{gh}(\zeta_-, \zeta_+) &= \frac{1}{4\pi i} \int_0^{2\pi} d\tau_1 \int_0^{\tau_1} d\tau_2 \left[\left(1 - \frac{\tau_1 - \tau_2}{\pi} \right) \bmod 2\pi \right] \left[g(\tau_1)h(\tau_2) - (\tau_1 \leftrightarrow \tau_2) \right] \\
&= -\frac{4}{\pi^2(\zeta_-^2 - 1)^2(\zeta_+^2 - 1)^2} \left(4\zeta_- \zeta_+ (\zeta_+^2 + \zeta_-^2 - 2) \cos \frac{\pi\zeta_-}{2} \cos \frac{\pi\zeta_+}{2} \right. \\
&\quad \left. - \pi(\zeta_-^2 - 1)(\zeta_+^2 - 1)(\zeta_-^2 + \zeta_+^2 - \zeta_- \zeta_+ - 1) \frac{\sin \frac{\pi(\zeta_- - \zeta_+)}{2}}{\zeta_- - \zeta_+} \right), \\
\kappa_-(\zeta_-) &= -\frac{1}{2} \int_0^{2\pi} d\tau \left[\left(1 - \frac{\tau}{\pi} \right) \bmod 2\pi \right] g(\tau) \\
&= -i \frac{4\zeta_- \cos \frac{\pi\zeta_-}{2} + \pi(\zeta_-^2 - 1) \left(1 + \zeta_- \left(1 - \sin \frac{\pi\zeta_-}{2} \right) \right)}{\pi(\zeta_-^2 - 1)^2}, \\
\kappa_+(\zeta_+) &= -\frac{1}{2} \int_0^{2\pi} d\tau \left[\left(1 - \frac{\tau}{\pi} \right) \bmod 2\pi \right] h(\tau) = -\kappa_-(\zeta_+). \tag{5.43}
\end{aligned}$$

The effective Hamiltonian and the effective kick operator are related to the stroboscopic Floquet Hamiltonian, which governs the dynamics at times integer multiples of the driving period, by $H_F[0] = e^{-iK_{\text{eff}}(0)} H_{\text{eff}} e^{iK_{\text{eff}}(0)}$, where the square bracket $[\cdot]$ denotes the Floquet gauge [33] (or equivalently the initial phase of the drive), see Chapter 2.

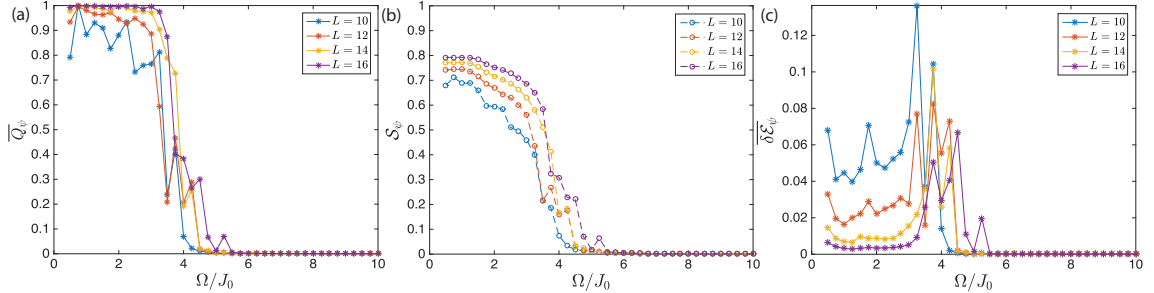


Figure 5.17: Frequency dependence of the normalised energy pumped into the system at infinite times \tilde{Q}_ψ (a), the diagonal entropy \tilde{S}_ψ (b), and the energy-density fluctuations $\tilde{\delta E}_\psi$ (b), starting from the ground state of the corrected Floquet Hamiltonian $H_{\text{eff}}^{(0)} + H_{\text{eff}}^{(1)}$, properly brought back to the lab frame by the leading-order kick operator $K_{\text{eff}}^{(1)}(0)$. The parameters are $U/J_0 = 1$, $\zeta = 0.6$, $\delta\zeta = 0.12$, which leads to $J/J_0 = 0.41$ and $J'/J_0 = 0.29$.

When included, the leading correction term is expected to reduce the energy injected into the system in the high-frequency tail by suddenly starting the drive. To test this, we start from the ground state of the Hamiltonian $H_{\text{eff}}^{(0)} + H_{\text{eff}}^{(1)}$, appropriately rotated back to the lab frame by the kick operator $K_{\text{eff}}^{(1)}(0)$, and simulate the normalised energy at infinite times, and the diagonal entropy as shown in Fig. 5.17. When compared to the curves in Fig. 5.9, we see that, while the small-frequency behaviour leading to heating to infinite temperature remains qualitatively the same, the energy injected into the system due to suddenly starting the drive at time $t_0 = 0$ becomes negligible, as expected. This check is important, as experiments are always performed at finite frequencies.

5.3.5.2 Level Spacing Statistics

One of the standard measures of ergodicity in quantum systems is the level spacing statistics. According to Random Matrix Theory, ergodic Hamiltonians are well-described by the Gaussian Orthogonal Ensemble (GOE) with their level spacing statistics following the

Wigner-Dyson distribution. For non-ergodic Hamiltonians, on the other hand, one expects a Poisson distribution. In general, it is believed that there exists a one-to-one correspondence between Wigner-Dyson distributed level spacings of a quantum model and chaotic dynamics in the classical limit [343]. Periodically-driven systems feature the additional subtlety that quasienergies are defined only modulo multiples of the driving frequency. In this respect, it has been shown that the level statistics of the approximate Hamiltonian obtained via the inverse-frequency expansion is not a good measure of ergodicity, since the folding of the many-body spectrum can introduce artificial correlations in the level spacings. This is intimately related to the fact that the inverse-frequency expansions do not capture any photon-absorption resonances [240], and the hybridisation of the corresponding levels. Nevertheless, the folded spectrum of the exact Floquet Hamiltonian can still be used to extract useful information about ergodicity of the underlying dynamics [78]. The classification of the symmetry classes allowed for the Floquet Hamiltonian in the presence of disorder has been studied in Ref. [344].

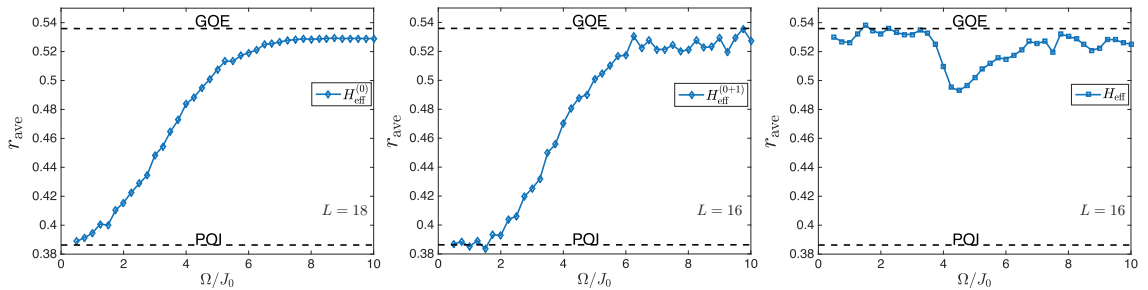


Figure 5.18: Frequency-dependence of the mean level spacing $r_{\text{ave}} = \min(\delta_{i+1}, \delta_i)/\max(\delta_{i+1}, \delta_i)$ in the spectra of the infinite-frequency Hamiltonian $H_{\text{eff}}^{(0)}$ describing the interacting SSH model (a), the corrected Floquet Hamiltonian to leading order $H_{\text{eff}}^{(0+1)} = H_{\text{eff}}^{(0)} + H_{\text{eff}}^{(1)}$ (b), and the exact Floquet Hamiltonian H_{eff} (c). The dashed horizontal $U/J_0 = 1$, $\zeta = 0.6$, $\delta\zeta = 0.12$, which amounts to $J'/J_0 = 0.41$, $J/J_0 = 0.29$.

Studying the level statistics of a Hamiltonian requires a careful binning of the data. Fortunately, the mean level spacing $r_{\text{ave}} = \min(\delta_{i+1}, \delta_i)/\max(\delta_{i+1}, \delta_i)$ where the phases $\delta_i = (E_F^{i+1} - E_F^i)T$ already contain the necessary information to reveal the statistics of the level spacings: if $r_{\text{ave}} = 0.5358$, the level statistics is Wigner-Dyson, whereas if $r_{\text{ave}} =$

0.3862 – it is Poisson distributed. Figure 5.18a shows r_{ave} as a function of frequency for the infinite-frequency Floquet Hamiltonian $H_{\text{eff}}^{(0)}$, the leading correction $H_{\text{eff}}^{(0)} + H_{\text{eff}}^{(1)}$, Fig. 5.18b, and the exact Floquet Hamiltonian H_{eff} , 5.18c. We would like to make a few remarks: (i) it becomes clear that ergodicity at infinite-frequencies is indeed fully attained, due to the drive-engineered small level of dimerisation of the chain, which renders the model non-integrable. This is correlated with the presence of Wigner-Dyson statistics of the spectrum at high-frequencies. Including the leading-order finite-frequency correction, which features interaction-dependent hopping terms, does not change the level spacing. (ii) at intermediate-to-low frequencies, the level statistics of the inverse-frequency expansion is messed up due to the folding of the spectrum which influences the level spacings in an artificial way. Our results are in full agreement with those in Ref. [78]. (iii) the level statistics of the exact Floquet Hamiltonian features Wigner-Dyson statistics both at high and low frequencies [as expected for a system featuring thermalising dynamics], while a clear dip is visible in the crossover regime, signalling non-thermal statistics. This is yet another evidence for the glassy dynamics observed at intermediate frequencies.

5.3.5.3 Resolving the Resonances with the Inverse-Frequency Expansion

The Floquet many-body resonances defined in the previous section were identified by projecting the exact Floquet eigenstates to the eigenstates of the infinite-frequency Floquet Hamiltonian $H_F^{(0)}$, which represents the leading order of the high-frequency expansion for the Floquet Hamiltonian. One can anticipate that these resonances can be made narrower and better defined if instead of $H_F^{(0)}$ one uses a better approximate local Floquet Hamiltonian \tilde{H}_F , which can be e.g. obtained by including higher-order terms in the inverse-frequency expansion. Indeed, physically the Floquet resonances occur when the rate of absorption and emission of photons from and to the drive is much smaller than the drive frequency. Without such resonances the system is described by \tilde{H}_F , whose exponential is a close approximation to the exact Floquet operator, i.e. $U_F \approx \exp(-i\tilde{H}_F T)$, but whose spectrum is extensive.

At high frequencies, the exact eigenstates $|n\rangle$ of U_F can all be assigned energies and each have high overlap with corresponding eigenstates of \tilde{H}_F . The Floquet many-body resonances occur at frequencies where this assignment is beginning to break down: they represent eigenstates of U_F that appear as linear combinations of two (or more) eigenstates of \tilde{H}_F that differ in energy by almost exactly one (or more) photon. In the regime we are considering, the eigenstates of \tilde{H}_F that are involved in the resonances are typical thermalising states [in the sense of the Eigenstate Thermalisation Hypothesis] with nonzero entropy density, so each resonant state involves many “bare” configurations of the system; this is why we call them “many-body” resonances. In contrast, in noninteracting tight-binding systems, drive-assisted resonances can occur only when the frequency is smaller than the single-particle bandwidth of the Floquet Hamiltonian, which remains bounded in the thermodynamic limit.

Floquet many-body resonances are beyond the van Vleck inverse-frequency expansion [240], as we demonstrated several times in this thesis, see Secs. 2.2.5, 3.1.3.1, and 4.5. We shall now show that these resonances can be nicely resolved using the approximate Floquet Hamiltonian, including the leading order correction. To this end, we proceed as follows:

- (i) We first calculate an approximation to the Floquet Hamiltonian using the van Vleck high-frequency expansion $H_F^{(0+1)}$. In the present discussion we stop after we take into account the leading Ω^{-1} -correction, see Sec. 5.3.5.1. It is interesting to note how much resolution one gains by including only the first Ω^{-1} -correction [compare Fig. 5.16(c) and Fig. 5.19c below which show the same resonant pair resolved with the zeroth and first correction, respectively].
- (ii) Diagonalise $H_F^{(0+1)}$; denote its eigenenergies by $E_F^{(0+1)}$ and its eigenstates by $|\nu\rangle$.

In principle, to visualise a Floquet many-body resonance it suffices to project a candidate eigenstate $|n\rangle$ of U_F onto the eigenstates $|\nu\rangle$ of \tilde{H}_F , and map out a probability distribution as a function of the energy \tilde{E}_F . This reveals the Floquet zones in which the resonant states

have most of their weight. It works because the inverse-frequency expansion necessarily produces an unfolded Floquet spectrum, as it becomes exact at infinite-frequencies. This procedure is analogous to time-of-flight imaging in cold atom systems, where one projects a Bose-Einstein condensate formed in an optical lattice onto free space, and reads off the quasimomentum peaks and their weights from the interference image. Figure 5.16c above is obtained after applying points (i) and (ii) to the Hamiltonian $H_F^{(0)}$.

The above two points are indeed enough to show the existence of many-body resonances, localised in neighbouring Floquet zones. However, by looking at the distance between the resonance peaks, we find that the approximation [e.g. $H_F^{(0+1)}$] to \tilde{H}_F obtained from the inverse-frequency expansion does not “know” the correct value of Ω . Thus, the resonant peaks after applying (i) and (ii) differ in energy by more than Ω . Therefore, we choose to correct the eigenenergies $E_F^{(0+1)}$ as follows:

- (iii) We calculate the expectation value of the exact Floquet operator in the approximate eigenstates, $\langle \nu | U_F | \nu \rangle$. In the regime of resonances, this gives complex numbers of magnitude close to unity. Hence, we obtain quasienergies for each state as $\mathcal{K}_{F,\nu}^{(0+1)} = i/T \log [\langle \nu | U_F | \nu \rangle / |\langle \nu | U_F | \nu \rangle|]$.
- (iv) Last, one has to unfold the spectrum to get the “revised” energies $\tilde{E}_{F,\nu}^{(0+1)}$. For this purpose, one can plot $\mathcal{K}_{F,\nu}^{(0+1)}$ vs. $E_{F,\nu}^{(0+1)}$ for each state. At high enough frequency these points are all near smooth curves with slope near one in each Floquet zone, thus providing a natural unfolding of the spectrum. But with this unfolding the energies do not properly match the quasi-energies. To get the proper revised energies $\tilde{E}_{F,\nu}^{(0+1)}$ we do two more steps: First, we shift all energies $E_{F,\nu}^{(0+1)}$ by some smooth function (in practice a linear function suffices) of the energy, to make the spectrum all close to $E_{F,\nu}^{(0+1)} \approx \mathcal{K}_{F,\nu}^{(0+1)} \bmod \Omega$. Thus in the linear approximation we define a revised approximate Hamiltonian as $\tilde{H} = b + mH_F^{(0+1)}$, with m near one and a shift b of the zero of energy. Then, finally, we add a small amount to each energy to make the revised energies $\tilde{E}_{F,\nu}^{(0+1)}$ precisely match the quasi-energies $\mathcal{K}_{F,\nu}^{(0+1)}$, modulo Ω . Thus

we have produced a revised approximate Floquet Hamiltonian \tilde{H}_F whose eigenstates are identical to those of $H_F^{(0+1)}$, but whose spectrum has been shifted to agree with the $\mathcal{K}_{F,\nu}^{(0+1)}$.

Step (iv) of this procedure fails at low frequency, where many states have $|\langle \nu | U_F | \nu \rangle| \ll 1$ and thus do not have well-defined quasi-energies. This results in ambiguities in the unfolding procedure (iv). For the model under consideration, we have found that for $L \leq 16$ we obtain meaningful and reliable revised energies for $\Omega/J_0 \gtrsim 1.5$. Interestingly, this frequency is significantly less than the crossover scale Ω^* suggesting that the heating transition occurs through proliferation of these resonances in the regime where they are still narrow and well defined.

Figure 5.19 shows four nearly-degenerate pairs of exact Floquet eigenstates at different values of Ω/J_0 . To take into account the effect of the density of states, we sum the projections $|\langle n | \nu \rangle|^2$ over a small shell of revised approximate energies, see caption. At high-frequencies, Fig. 5.19d, we do not find resonances. Here the matrix elements $\langle \nu | U_F | \mu \rangle$ between states in different Floquet zones are all small compared to the quasi-energy level spacing in the spectrum of U_F , so even almost-degenerate eigenstates of U_F map almost purely on to a single Floquet zone. Thus in this regime the spectrum of U_F can be unambiguously unfolded, and an excellent local approximation to the exact H_F exists. Whether or not this regime inevitably “retreats” to infinite Ω as $L \rightarrow \infty$ is an interesting question for future investigation. As the frequency is decreased, Fig. 5.19c and Fig. 5.19b, Floquet many-body resonances do appear. We find that the matrix element between resonant states $\langle m | H_F^{(0+1)} | n \rangle$ is enhanced up to a few times the bare hopping amplitude J_0 . As a result, for intermediate frequencies, these Floquet many-body resonances constitute the dominant fraction of off-diagonal matrix elements of the energy operator $H_F^{(0+1)}$. Moreover, they connect different Floquet zones, and the system thus starts absorbing (or emitting) energy. Consequently, due to the small number of resonant pairs with large off-diagonal matrix elements, the dynamics of the energy is, to a large extent, dominated by these drive-induced

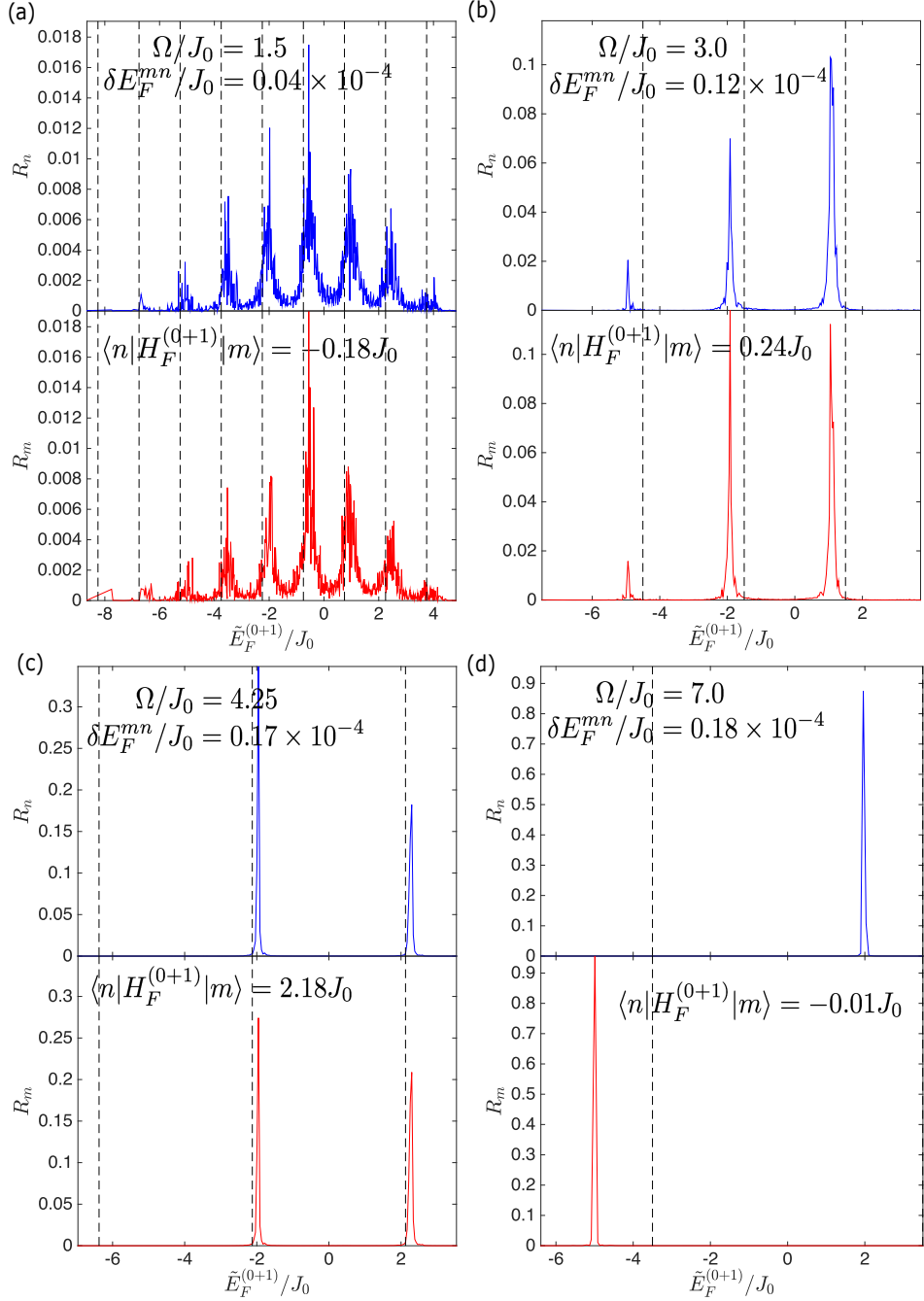


Figure 5.19: Examples of nearly-degenerate pairs of exact Floquet eigenstates, including Floquet many-body resonances, in the dynamical regimes of interest. The resonant state $|n\rangle$ is quantified by the quantity $R_n = \sum_{\mu} |\langle n | \mu \rangle|^2 \delta(\nu_k \leq \tilde{E}_F^{(0+1),\mu} \leq \nu_{k+1})$, with $\nu_k = k\delta\nu$, $k \in \mathbb{N}$, and the small energy shell $\delta\nu = \Omega/100$. Here $|\mu\rangle$ denotes an eigenstate of $H_F^{(0+1)}$. The range of the x -axis coincides with the many-body bandwidth, while the vertical dashed lines mark the boundaries of the Floquet zones. The parameters are $U/J_0 = 1$, $\zeta = 0.6$, $\delta\zeta = 0.12$, which amounts to $J'/J_0 = 0.41$, $J/J_0 = 0.29$, and $L = 16$.

transitions, which leads to the observed non-thermalising glassy behaviour. It follows that a description based on statistical mechanics w.r.t. the approximate Hamiltonian $H_F^{(0+1)}$ fails to capture the stroboscopic physics at any sensible time scale in this crossover regime. In this same crossover regime, we also find that the eigenstates of $H_F^{(0+1)}$ can be cleanly assigned quasi-energies, so there is a well-defined “folding” procedure, see steps (iii) and (iv) above, to define the energies $\tilde{E}_{F,\nu}^{(0+1)}$, but the unfolding of the *exact* quasispectrum of U_F is no longer well-defined, due to the presence of the Floquet many-body resonances. Finally, Fig. 5.19a, when the driving frequency is reduced even further, the Floquet many-body resonances proliferate. At the same time, however, the matrix elements $\langle m | H_F^{(0+1)} | n \rangle$ between the resonant states decrease again and become closer to the average off-diagonal matrix element [which is small since these states are well-thermalised to infinite temperature]. Hence, the system continuously absorbs energy and heats up to infinite temperature, thereby delocalising along the energy ladder. This heating is rapid, as indicated by the broad line widths in Fig. 5.19a. The dynamics of the system is completely chaotic and, therefore, thermalising again. Decreasing the frequency even further to $\Omega/J_0 = 1$, \tilde{H}_F is no longer well-defined, as we explained above, while $H_F^{(0+1)}$ is becoming a very poor approximation to the correct, now highly-nonlocal H_F . Hence, the eigenstates of U_F are completely delocalised over the $E_F^{(0+1)}$ -axis.

Applying the van Vleck inverse-frequency expansion to a given order n_{HFE} yields a truncated (approximate) Floquet Hamiltonian $H_F^{(0+\dots+n_{\text{HFE}})}$ and the corresponding truncated (approximate) time-periodic Kick operator $K_F^{(0+\dots+n_{\text{HFE}})}(t)$. The Hamiltonian $H_F^{(0+\dots+n_{\text{HFE}})}$ is a sum of local many-body operators with an unfolded spectrum, the bandwidth of which necessarily goes to infinity in the thermodynamic limit. If we now use this truncated kick operator to transform the original lab-frame Hamiltonian $H(t)$ to a rotating frame, the corresponding rot-frame Hamiltonian has the form $\tilde{H}^{\text{rot}}(t) = H_F^{(0+\dots+n_{\text{HFE}})} + W(t)$, where $W(t) = W(t + T) \sim \Omega^{-(n_{\text{HFE}}+1)}$ by construction [9, 32, 102]. In this rotating frame, we can interpret the heating problem as follows: the inverse-frequency expansion takes care only of the virtual photon-absorption processes, pretty much like any ordinary Schrieffer-

Wolff transformation does [105]. As a result, this shifts the energy levels of the non-driven Hamiltonian H_0 by a small amount. This is why the width of the resonances is reduced tremendously by taking into account the leading-order correction, compare Fig. 5.16c and Fig. 5.19c. Although these virtual transitions do have an effect on the underlying physics, they can only result in heating to a small finite temperature [e.g. due to the abruptly switching on the drive or a possible adiabatic preparation of the initial state]. At this level, if one insists that the spectrum of the Hamiltonian $H_F^{(0+\dots+n_{\text{HFE}})}$ is only defined modulo Ω and folds it artificially, the original Wigner-Dyson level spacing statistics of the non-integrable $H_F^{(0+\dots+n_{\text{HFE}})}$ will suddenly change to Poisson statistics, due to the lack of photon-assisted level repulsion, see Sec. 5.3.5.2. On the other hand, taking back into consideration the time-dependent piece $W(t)$, we find that it is responsible for driving real photon-absorption transitions between the approximate Floquet levels of $H_F^{(0+\dots+n_{\text{HFE}})}$, which are not captured by the inverse-frequency expansion to any order. Note that these pairs of states with energy difference $E_{F,m}^{(0+\dots+n_{\text{HFE}})} - E_{F,n}^{(0+\dots+n_{\text{HFE}})} \approx l\Omega$ with $l \in \mathbb{N}$ are guaranteed to exist in the TD limit where the spectrum becomes dense and unbounded. It is these direct transitions between the Floquet many-body states of $H_F^{(0+\dots+n_{\text{HFE}})}$ which can potentially lead to heating to infinite temperature in the longer run, irrespective of the driving frequency. Ultimately whether this heating happens or not in the thermodynamic limit will be determined by the ratio of the width of the many-body resonances in the basis of $H_F^{(0+\dots+n_{\text{HFE}})}$ and the splitting between these resonances due to $W(t)$. We leave this interesting and important question for future work.

5.3.6 Discussion

In summary, we presented numerical evidence that strongly interacting two-band systems which are resonantly coupled via a periodic drive feature a large window of stable controllable time-evolution at high frequencies. The studied two-band system only weakly absorbs energy from the drive at the experimentally-relevant time scales and is, therefore, amenable to Floquet engineering. This opens up the possibility of studying also other

interesting strongly interacting systems including, for example, fractional Floquet topological insulators [69] or Heisenberg models with artificial gauge fields [105]. By studying the heating-to-no-heating crossover, we laid the foundations to understand the microscopic origin of heating in non-integrable periodically-driven systems.

It is important to emphasise, that our two-band model might not be fully sufficient to describe some undergoing experiments, due to the presence of even higher bands. However, their influence on heating, can be estimated from our results. Although the typical driving frequencies may not necessarily be large enough to induce direct transitions to these bands, higher-order photon absorption processes with reduced matrix elements can occur [333]. Since higher bands have much larger bandwidths, it becomes much more likely to hit a single-particle resonance which defines the crossover scale Ω^* , cf. Sec. 5.3.3.3. If such a single-particle resonance is present, we expect that we will again see heating. Last, while we did not consider this, it also bears mentioning that the presence of perpendicular to the lattice plane dimensions, comprising continuous degrees of freedom (tubes/pancakes), plays a crucial role for heating. In such cases, heating effects are enhanced by photon-stimulated scattering into these additional dimensions, which can act as reservoirs and facilitate thermalisation at a higher temperature [165, 166, 168, 169].

The existence of nonthermalising time-evolution, featuring strong temporal fluctuations and correlations, at the crossover between a stable and an unstable regime is reminiscent of a dynamical phase transition between many-body localised and delocalised phases in energy space [77]. We have identified many-body resonances as the microscopic origin of this behaviour. Nevertheless, our results do not allow for a direct extrapolation to the thermodynamic limit. Whether or not infinite isolated ergodic Floquet systems at high-frequencies eventually heat up to infinite temperature at infinite times or remain localised in energy space forever, remains yet to be revealed. While this is still an open problem with examples existing indicative of either outcome [74, 75, 77, 78, 80, 104, 106, 113, 183, 297, 303, 309, 345–347], recently developed rigorous proofs suggest that heating in fermionic and spin systems, if at all present, happens at most exponentially slowly in the driving

frequency [98, 100–102].

A natural way to prevent infinite heating is to couple the driven system to a thermal bath. In this case it is expected that the system will eventually approach a non-equilibrium steady state in which the energy absorbed from the driving is balanced by the energy dissipated into the environment [348–351]. The value of measurable quantities (such as transport coefficients and correlation functions) will depend crucially on the nature of the (putative) non-equilibrium steady state [38–40] which, for this reason, has been the focus of intense research [352, 353]. Despite this intense effort, a general understanding of the non-equilibrium steady state is still missing but it seems clear that the steady state will, in general, be non-thermal [351, 354, 355]. Therefore the thermodynamic behaviour of periodically driven systems is expected to be qualitatively different from those of non-driven systems [356, 357].

Chapter 6

Concluding Remarks

6.1 Outlook and Future Perspectives

Periodically driven systems in the high-frequency limit can be used to engineer interesting effective Hamiltonians, which are very difficult or impossible to realise in equilibrium systems. They provide an important step towards the simulation of quantum condensed matter systems, and can be used to test predictions of physical theories in new regimes.

In this thesis, we have presented a systematic and self-contained analysis of periodically driven systems, identifying three mainstreams: (i) *Floquet engineering*, which deals with ascribing desired properties to the Floquet Hamiltonian with the help of a suitably chosen periodic modulation. (ii) *Floquet adiabatic perturbation theory*, which addresses the problem how to load a physical system into a desired Floquet eigenstate in order to access the corresponding physics. And (iii), *pre-thermalisation and thermalisation* in driven systems which are ultimately related to the energy absorption rates, and the stability of Floquet systems exposed to a continuous periodic modulation in the absence of energy conservation.

In particular, we have started by precisely defining the Floquet stroboscopic (FS) and Floquet non-stroboscopic (FNS) dynamics and computed the dressed operators and the dressed density matrices required to correctly describe both these measurement techniques. The Floquet non-stroboscopic dynamics (FNS), which suits very well the current experimental techniques, often opens up the possibility of measuring Floquet gauge-invariant physical observables like the proper current associated with the Floquet Hamiltonian. Special emphasis was put on the Floquet gauge structure associated with the choice of

the stroboscopic frame, and how one can translate between the stroboscopic and the non-stroboscopic picture.

As the main tools to study Floquet engineering in the high-frequency limit, we employed the Floquet-Magnus and the van Vleck inverse-frequency expansions. We showed that they can be used to calculate the leading corrections, to the infinite-frequency Floquet Hamiltonian. When applied to time-independent Hamiltonians in the rotating frame, one can use them to eliminate a high-energy scale from the problem and derive an effective dressed low-energy Hamiltonian with renormalised parameters similarly to the celebrated Schrieffer-Wolff transformation. Moreover, we discussed how one can naturally extend this transformation to periodically-driven setups and identified new terms in the dressed Hamiltonian, which appear due to the driving, and which lead to heating and other non-equilibrium effects. We elaborated on the systematic calculation of higher-order corrections to the Rotating-Wave approximation, as well as its relation to the mathematical modelling of Floquet resonances.

A prerequisite for finding non-trivial high-frequency limits is a strong coupling of the driving protocol to the system, in the form of a driving amplitude which scales with a power of the driving frequency. Often times, a systematic way of studying the inverse-frequency expansion of the Floquet Hamiltonian is to first go to the rotating frame w.r.t. the driving Hamiltonian. We proved that this amounts to the resummation of an infinite lab-frame subseries and demonstrated this on several examples. Moreover, we identified three classes of universal high-frequency driving protocols leading to well-defined local Floquet Hamiltonians (c.f. Fig. 6.1), but there may be more. For each class, we have calculated the form of the effective Floquet Hamiltonian which differs significantly from the time-averaged one.

The Kapitza class is characterised by a kinetic energy term which is quadratic in momentum, and a driving amplitude which scales linearly in Ω . We gave examples of both a single- and many-body systems which realise this limit. The Dirac class is benchmarked by a linear kinetic energy term which requires adding a spin structure via the Pauli matrices.

$$V^\dagger H_0 V \stackrel{?}{=} \text{local} \quad \text{as} \quad A \sim \Omega \rightarrow \infty$$

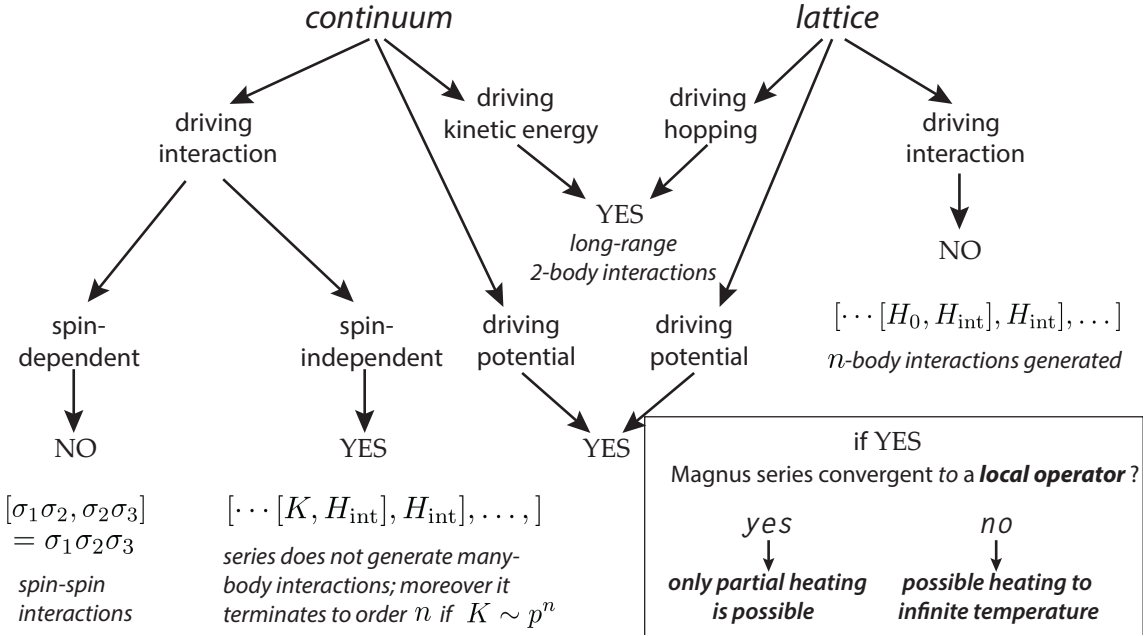


Figure 6.1: This figure summarises the scenarios discussed in this thesis: globally periodically driven continuum and lattice models. Depending on whether one drives the interaction or the external potential the Floquet Hamiltonian can be local (YES) or a non-local one (NO). A local Floquet Hamiltonian is a sum of spatially local terms and can include only few-body interactions. Different scenarios might appear in locally driven systems. For example, driving any local in space term like the local hopping strength or the local interaction coupling does not produce any long-range terms in the infinite-frequency Floquet Hamiltonian.

One can periodically drive either an external magnetic field, in which case the amplitude should scale as Ω or, alternatively, the drive can couple to an external potential but then the driving amplitude is required to scale as Ω^2 . The Dunlap-Kenkre (DK) class applies to lattice systems with an arbitrary dispersion relation, where, one drives an external single-particle scalar potential, whose amplitude scales linearly with Ω . We illustrated all three classes with various examples and discussed recent experimental progress made with ultracold atoms.

Chapter 4 was devoted to the extensive study of adiabatic perturbation theory in the presence of the drive. The notion of Floquet adiabaticity is intriguing and can naturally

be extended and applied to a variety of novel physical situations. Our conclusions tell us about possible issues with any low-frequency linear response theory applied to isolated Floquet systems, which is very relevant as a method for measuring these systems and has been discussed extensively in the recent literature [290, 291, 355, 358, 359]. We have derived FAPT by looking into properties of the Floquet gauge potential \mathcal{A}_F , which is an operator whose diagonal components give generalisations of the Berry connections. However, as an operator, this actually gives us access to many more properties such as off-diagonal connections. Furthermore, it readily gives access to non-Abelian Floquet Berry connections in the presence of degeneracies, as has recently been explored in non-driven systems [359–362]. This is particularly important as experiments involving Floquet systems are quite active in the creation of topologically non-trivial states, the most interesting of which have non-trivial non-Abelian Berry phases. The generalisation of these techniques to cases with degeneracies will, therefore, lead to a proposal for a measurement protocol for these non-Abelian effects, and will provide valuable insight on differences in topological physics between driven and non-driven systems. Moreover, the methods we discussed are expected to naturally extend to mixed states, and an important open question is how they are modified by weak interactions with the environment [92, 363–365]. At the same time, the absence of a well-defined adiabatic limit in open periodically-driven systems poses interesting fundamental questions regarding the stability of Floquet phases which, in equilibrium systems, is based on the maximum entropy principle and the resulting equivalence of adiabatic generalised forces. In the absence of adiabaticity, one must re-examine fundamental questions, such as the existence of the equations of state, and many other statements which we take for granted in equilibrium thermodynamics.

In Chapter 5, we studied thermalisation in periodically-driven systems. At high frequencies, it is known to happen exponentially slowly, thus opening large pre-thermal windows where the time evolution of the system is well-captured by the inverse-frequency expansion. Fermionic and spin systems absorb energy less efficiently compared to bosonic systems whose short-time dynamics can easily be dominated by parametric resonance effects which

then set the relevant heating time scale. In general, we have shown that many-body Floquet systems thermalise through a proliferation of Floquet resonances in the quasienergy spectrum as a function of the drive frequency, which appear as a result of a strong hybridisation of resonant states in the spectrum of the approximate Floquet Hamiltonian obtained using the inverse-frequency expansion. We have further demonstrated that it is these Floquet resonances which lead to the ultimate breakdown of the inverse-frequency expansion and are, therefore, naturally not captured by it. While there exists solid numerical evidence that at small driving frequencies, many-body Floquet systems quickly heat up to an infinite temperature state, while at large frequencies energy absorption is at least exponentially suppressed, the ultimate fate of heating at infinite times remains a major open problem. These important issues are not yet fully settled. We hope that they will be resolved in future experiments and theoretical work.

While classical few body Floquet systems, such as the Kapitza pendulum and its variations, found a multitude of interesting and useful applications, the experimental realisation and systematic theoretical analysis of many-particle periodically driven systems is very recent. We discussed several realisations of Floquet systems both in cold atoms and in solid state materials, where new, hard to achieve otherwise, regimes have been accessed using a periodic modulation. This lead to the emergence of a new research direction, dubbed “Floquet engineering”, which has the potential to develop systems with unique properties in the near future. Floquet systems constitute a playground for studying many different phenomena such as information and entanglement propagation in the absence of conservation laws, finding non-equilibrium optimum quantum annealing protocols, designing materials with tunable properties, and many more. There are also many open conceptual problems in Floquet systems, which we mentioned only briefly in this thesis but which are obviously important for our overall understanding of driven systems. In particular, the nature of steady states in open Floquet systems, i.e. Floquet systems coupled to a thermal bath, robustness and universality of topological Floquet phases, nature and classification of phase transitions in driven open and isolated systems, and others. We hope that these and other

questions will be understood in the near future.

6.2 A Collection of Open Problems in Closed Floquet Systems

In the last section of this thesis, we provide a short list of potentially interesting open (at the time this thesis was written) problems, the solution of which, we believe, should bring our understanding of Floquet systems a good deal forward. While some of these problems are sufficiently complex and pose a considerable challenge, others are seemingly straightforward which makes them suitable for undergraduate and other research projects.

1. From the point of view of Floquet theory, parametric resonance results in a continuous quasienergy spectrum, see Sec. 3.3.2 and Ref. [238]. Is the spectrum near Floquet resonances in arbitrary (non-linear) driven systems also continuous in the limit of infinite system size? One way to approach this problem is to (i) numerically verify the results of Ref. [238] paying specific attention to the way the Floquet spectrum on resonance becomes continuous as a function of the system size (i.e. the number of states in the Hilbert space). (ii) once this mechanism has been established, one can study the Kapitza pendulum which is non-linear and thus, more generic since the exponential growth of observables due to parametric resonance will be cut off. (iii) is it possible to extrapolate the results to many-body Floquet systems with dense spectra.
2. What is the fate of classical chaos induced by periodic kicks in the quantum limit, and how is the latter related to the Floquet resonances? For example, one can consider the Kapitza Pendulum: while the quantum system is governed by a time-periodic Hamiltonian which constitutes a linear operator on a Hilbert space and, therefore, obeys Floquet's theorem, the classical EOM are nonlinear which violates a major condition for the applicability of Floquet's theorem. This suggests the existence of an interesting intrinsic difference between the classical and quantum dynamics. Nevertheless, the Floquet Hamiltonian obtained for the quantum problem has a well-

defined classical limit and, moreover, it appears to describe the essential features of the dynamics of the classical system accurately (e.g. dynamical stabilisation).

3. Can one construct a frame where the inverse-frequency expansion for a *globally*-driven system is guaranteed to converge (to a possibly *non-local* Floquet Hamiltonian) at least for small drive amplitudes (compared to the drive frequency)? Such a construction has been demonstrated for local drives in Sec. 2.3.2.2.1.
4. (mathematical physics) How does taking resonances into account improve the rigorous upper bounds found on energy absorption in Refs. [98, 100–102]? Can one prove a *non-negative* lower bound on energy absorption to extract its ultimate fate in the thermodynamic limit?
5. Study systematically the appearance and behaviour of resonances as a function of the drive frequency in strongly disordered many-body Floquet systems (which are believed to be in a many-body localised phase) and compare it to those in clean (i.e. disorder-free) systems. If one believes that generic clean isolated many-body Floquet systems always heat up to an infinite-temperature state, find a property of the resonances which clearly displays a different behaviour in the clean compared to a disordered Floquet system, as the system size is scaled up.
6. Study thermalisation and energy absorption in finite-size *bosonic* many-body Floquet systems. Are there any distinctive qualitative differences to fermionic and spin systems?
7. Extend the Weak-Coupling Conserving Approximation (WCCA) for the driven Bose-Hubbard model (See Sec. 5.2.2) to second order in U and simulate the resulting (nonlocal in time) EOM: do the intuitively predicted time scales for the validity of the WCCA hold true? [this has been done for fermions in Ref. [346]]
8. Find conclusive evidence whether closed many-body Floquet systems heat up to an infinite-temperature state at *infinite times* and in the *thermodynamic limit*. Formu-

late condition(s) for a driven system to remain localised (see e.g. the energy-space many-body localised system of Eq. (3.115) for $\zeta = 0$ where the Floquet Hamiltonian at any frequency is given by the Fermi-Hubbard model with interaction strength Ω).

9. Are there other alternatives, possibly better than FAPT, to load into a desired Floquet state, which are sufficiently flexible to be applicable to a wide class of systems? One can use as a motivation the loading protocol sequence of Sec. 4.6, where the drive amplitude is first quenched and then ramped to obtain optimal fidelity.
10. Extend Floquet theory to problems where the driving field itself is a dynamical degree of freedom. Find out which features of Floquet theory survive, and which undergo modifications. What if the driving field becomes quantum (e.g. the number of photons is small)? What is the manifestation of Floquet resonances in this quantised-drive problem?
11. Formulate a consistent Floquet theory for two-frequency drives. How important is the commensurability of the two driving frequencies? Can Floquet theory be extended to study aperiodic time-dependent systems?

Appendix A

Lattice vs. Continuum Models

In this appendix we discuss some subtle differences between the lattice and continuum models discussed in the Secs. 3.1.1, 3.1.2 and 3.1.3. In particular, we show how to combine the results of Sec. 3.1.2 and Sec. 3.1.3.4. We demonstrate the relation between the models for one-dimensional non-interacting systems, but the generalisation to higher dimensions including interactions is straightforward.

Systems with linear dispersion.—Consider first the following static, non-interacting Hamiltonian with linear dispersion

$$H_{\text{cont}} = \int dx \frac{J_0}{2} \left(-i\psi^\dagger(x)\partial_x\psi(x) + \text{h.c.} \right). \quad (\text{A.1})$$

To discretise the model, we put it on a lattice with lattice constant a . The corresponding lattice Hamiltonian is given by

$$H_{\text{latt}} = \sum_x \frac{J_0}{2a} (-i\psi^\dagger(x)\psi(x+a) + \text{h.c.}) \quad (\text{A.2})$$

If one goes to momentum space, the dispersion relation is $\varepsilon(k) = \frac{J_0}{a} \sin(ak)$, and in the long-wavelength limit, $ak \ll 1$, we conveniently recover the continuum linear dispersion $\varepsilon_k \approx J_0 k$. In particular, it follows that in lattice theories with linear dispersion, the hopping matrix element should scale as $1/a$. If one, on the other hand, starts with a lattice theory, one can recover the Hamiltonian (A.1) from Eq. (A.2) in the limit $a \rightarrow 0$ by using the

identity $\psi(x + a) = \psi(x) + a\partial_x\psi(x) + \mathcal{O}(a^2)$, and collecting powers of a .

Let us now add to this Hamiltonian a time-dependent electric field with the amplitude V_0 and frequency Ω :

$$H(t) = \int dx \frac{J_0}{2} \left(-i\psi^\dagger(x)\partial_x\psi(x) + \text{h.c.} \right) + V_0 \cos(\Omega t) x \psi^\dagger(x)\psi(x). \quad (\text{A.3})$$

In Sec. 3.1.2.2, we showed that the zeroth-order Floquet Hamiltonian for this relativistic continuum theory is not affected by the drive if we keep $\zeta = V_0/\Omega$ independent of Ω , i.e. scale the electric field amplitude V_0 linearly with the frequency:

$$H_{F,\text{cont}}^{(0)} = \int dx \frac{J_0}{2} \left(-i\psi^\dagger(x)\partial_x\psi(x) + \text{h.c.} \right). \quad (\text{A.4})$$

On the contrary, in Sec. 3.1.3.4 we considered the same Hamiltonian on the lattice, and found the following non-trivial zeroth-order Floquet Hamiltonian:

$$H_{F,\text{latt}}^{(0)} = \sum_x \frac{J_0}{2a} \mathcal{J}_0(\zeta a) \left(-i\psi^\dagger(x)\psi(x+a) + \text{h.c.} \right). \quad (\text{A.5})$$

At first sight, the two results seem contradictory. To find the proper continuum theory, we expand Eq. (A.5) in powers of the inverse lattice constant. Using the identity $\mathcal{J}_0(\zeta a) = 1 + \mathcal{O}(a^2)$, we see that the low-energy effective Hamiltonian is independent of ζ . Consequently, all the non-trivial effects introduced by the driving vanish in the long-wavelength limit and, therefore, the lattice and continuum models are consistent and yield the same result. A similar derivation applies to higher order corrections in the Magnus expansion. From Eq. (A.5) we also see the condition under which the continuum approximation holds:

$$\zeta a \ll 1 \Leftrightarrow V_0 a \ll \Omega. \quad (\text{A.6})$$

where, the equivalence of these two conditions follows from the definition $\zeta = V_0/\Omega$. The product $V_0 a$ is the maximum energy difference generated by the driving potential between

two lattice sites. So the continuum approximation holds only in the limit when this difference is small compared to the driving frequency. Once this condition is violated, the full lattice dispersion has to be taken into account and the continuum approximation breaks down.

Systems with quadratic dispersion.—We now show the correspondence between the continuum and lattice theories for systems with quadratic dispersion. The non-driven continuum and lattice Hamiltonians read as

$$\begin{aligned} H_{\text{cont}} &= \int dx \phi^\dagger(x) (-\partial_x^2) \phi(x), \\ H_{\text{latt}} &= -\frac{J_0}{a^2} \sum_x \left(\phi(x)^\dagger \phi(x+a) - 2\phi(x)^\dagger \phi(x) + \phi(x+a)^\dagger \phi(x) \right). \end{aligned} \quad (\text{A.7})$$

Notice that in the case of a quadratic dispersion, the hopping matrix element scales as $1/a^2$. Now consider the driven model

$$H(t) = \int dx \phi^\dagger(x) (-\partial_x^2) \phi(x) + V_0 \cos \Omega t f(x) \phi^\dagger(x) \phi(x). \quad (\text{A.8})$$

Recall that the continuum model fits into the Kapitza class, c.f. Sec. 3.1.1, while the lattice model is part of the DK class, Sec. 3.1.3. A careful reader might be worried that in the former case, in the limit $\Omega \rightarrow \infty$, we found an emergent effective potential leading to dynamical stabilisation whereas, in the latter case, we obtained the following modification to the hopping matrix element:

$$H_{F,\text{latt}}^{(0)} = -\frac{J_0}{a^2} \sum_x \mathcal{J}_0 (\zeta f(x+a) - \zeta f(x)) \left(\phi^\dagger(x+a) \phi(x) + \text{h.c.} \right) + \frac{2J_0}{a^2} \sum_x \phi(x)^\dagger \phi(x). \quad (\text{A.9})$$

where, as usual, $\zeta = V_0/\Omega$. To reconcile the two approaches, again we take the limit $a \rightarrow 0$. In doing so, we write $f(x+a) - f(x) = af'(x) + \mathcal{O}(a^2)$, and use the expansion

$\mathcal{J}_0(z) = 1 - z^2/4 + \mathcal{O}(z^4)$. The results is

$$H_{F,\text{cont}}^{(0)} = \int dx \phi^\dagger(x) \left(-\partial_x^2 + \frac{\zeta^2}{4} [f'(x)]^2 \right) \phi(x). \quad (\text{A.10})$$

We therefore see that indeed the continuum theory features an emergent potential given by $\zeta^2/4[f'(x)]^2$ which establishes the relation between the Kapitza and the DK classes, c.f. Eq. (3.5).

Appendix B

Outline of the Derivation of the Floquet-Magnus and van Vleck Inverse-Frequency Expansions

In this appendix, we briefly summarise the most important steps in the derivation of the Floquet-Magnus Expansion (FM HFE) for the stroboscopic Floquet Hamiltonian and the van Vleck Expansion (vV HFE) for effective Hamiltonian.

B.1 The Floquet-Magnus Expansion

The evolution operator for a single period, starting at time t_0 , is given by

$$U(T + t_0, t_0) = \mathcal{T}_t \exp \left(-i \int_{t_0}^{t_0+T} dt H(t) \right) = \exp(-i H_F[t_0]T), \quad (\text{B.1})$$

where we used Floquet's theorem for the second equality. Inverting this equation,

$$H_F[t_0] = \frac{i}{T} \log \left[\mathcal{T}_t \exp \left(-i \int_{t_0}^{t_0+T} dt H(t) \right) \right], \quad (\text{B.2})$$

and we find the unique stroboscopic Floquet Hamiltonian¹. Now, we can expand the RHS in powers of the inverse frequency $\Omega = 2\pi/T$ using the Baker-Campbell-Hausdorff lemma. It can be verified that this immediately results in Eqs. (2.41) from the main text.

To obtain the stroboscopic kick operator $K_F[t_0](t) = i \log P(t, t_0)$, we invert Floquet's

¹The uniqueness of the evolution operator is provided by the uniqueness of the solution to Schrödinger's equation. The uniqueness of $H_F[t_0]$ is understood up to the quasi-energy spectrum folding ambiguity.

theorem $U(t + t_0, t_0) = P(t, t_0) \exp(-iH_F[t_0](t - t_0))$:

$$K_F[t_0](t) = i \log \left[\mathcal{T}_t \exp \left(-i \int_{t_0}^{t_0+t} dt' H(t') \right) \exp(iH_F[t_0](t - t_0)) \right]. \quad (\text{B.3})$$

Expanding the RHS in powers of Ω^{-1} yields Eqs. (2.43). Since $K_F[t_0](t)$ is constructed order by order in the inverse frequency, it is also a unique operator.

B.2 The van Vleck Expansion

To derive the High-Frequency Expansion, we make use of the results from Appendix B.1 above. Starting from the relation between the fast-motion operator $P(t, t_0) = \exp(-iK_F[t_0](t))$ and the effective kick operator $K_{\text{eff}}(t)$ in Eq. (2.15), we have

$$K_F[t_0](t) = i \log [\exp(-iK_{\text{eff}}(t)) \exp(iK_{\text{eff}}(t_0))]. \quad (\text{B.4})$$

Notice that the Ω^{-1} -expansion of the LHS is already known from Appendix B.1. Hence, postulating $K_{\text{eff}} = \sum_{n=1}^{\infty} K_{\text{eff}}^{(n)}$ with $K_{\text{eff}}^{(n)} \sim \Omega^{-n}$, we can again apply the Baker-Campbell-Hausdorff lemma. Note that the boundary condition for the vV HFE enters here, since K_{eff} does not have a zeroth harmonic by construction. By comparing equal powers of the inverse frequency, we arrive at Eq. (2.46). Notice again that K_{eff} is an operator, whose uniqueness is inherited by that of $K_F[t_0](t)$.

Once we have the effective kick operator, we can apply Floquet's theorem again to determine uniquely the effective Hamiltonian H_{eff} order by order in Ω^{-n} . Equivalently, one can use the transformation law $H_{\text{eff}} = \exp(iK_{\text{eff}}(t)) H_F[t_0] \exp(iK_{\text{eff}}(t))$ to find the perturbative expansion of the *unique* effective Hamiltonian from the Magnus expansion. For alternative derivations of the high-frequency expansion, see Refs. [9, 32, 87]. We mention in passing that expanding the LHS and the RHS in powers of the inverse frequency and matching the coefficients is essentially the same idea which also lies behind the derivation of the generator of the Schrieffer-Wolff transformation, c.f. the discussion in Sec. 3.2.

Appendix C

Corrections to the Inverse-Frequency Floquet Hamiltonian for the Harper-Hofstadter Model

C.1 Corrections to the Effective Hamiltonian $H_F[t_0]$

C.1.1 First-order Coefficients for the 1D Driven Boson Model

Here, we briefly list the expressions for the nnn hopping, and the staggered potential, found to first order in the Magnus expansion to the model discussed in Sec. 3.1.3.2. All the integrals are given in the Floquet gauge $t_0 = 0$. We recall that

$$g^{m,m+1}(\tau; \zeta) = \exp[-i\zeta \sin(\tau - \phi_{nm})],$$

where $\tau = \Omega t$. Then the coefficients to the Hamiltonian $H_F^{(1)}$ given in Eq. (3.60) are given by the following time-ordered integrals

$$\begin{aligned} \mathcal{C}^{m,m+2}(\zeta) &= \frac{1}{4\pi i} \int_0^{2\pi} d\tau_1 \int_0^{\tau_1} d\tau_2 [g^{m,m+1}(\tau_1) g^{m+1,m+2}(\tau_2) - (1 \leftrightarrow 2)], \\ \mathcal{G}^{m,m+1}(\zeta) &= \frac{1}{2\pi} \int_0^{2\pi} d\tau_1 \int_0^{\tau_1} d\tau_2 \text{Im} \left\{ (g^{m,m+1}(\tau_1))^* g^{m,m+1}(\tau_2) \right\}. \end{aligned} \quad (\text{C.1})$$

We mention that these expressions are the same as the corresponding one for nnn hopping along the y -direction $\uparrow C_0^{m,m+2}(\zeta)$, and a staggered potential along the y -direction and $\uparrow E_0^{m,m+1}(\zeta)$ found in the 2D extension of the model from Sec. 3.1.3.3 (see below).

C.1.2 First-order Coefficients for the Harper-Hofstadter Model

In this appendix we discuss the parameters of the leading correction, Eq. (3.73). Let us define two auxiliary functions f and g by

$$\begin{aligned} f_{m,m+1}^n(\tau; \zeta) &= \exp[-i\zeta \sin(\tau - \phi_{nm}) + i\tau] \\ g_m^{n,n+1}(\tau; \zeta) &= \exp[-i\zeta \sin(\tau - \phi_{nm})]. \end{aligned} \quad (\text{C.2})$$

The coefficients B , C , D , and E in Eq. (3.73) are given by the following time-ordered integrals:

$$\begin{aligned} \rightarrow B_{m,m+1}^n(\zeta) &= \frac{1}{4\pi i} \int_0^{2\pi} d\tau_1 \int_0^{\tau_1} d\tau_2 [f_{m,m+1}^n(\tau_1) - f_{m,m+1}^n(\tau_2)], \\ \uparrow B_m^{n,n+1}(\zeta) &= \frac{1}{4\pi i} \int_0^{2\pi} d\tau_1 \int_0^{\tau_1} d\tau_2 [g_m^{n,n+1}(\tau_1) - g_m^{n,n+1}(\tau_2)]. \end{aligned} \quad (\text{C.3})$$

$$\begin{aligned} \rightarrow C_{m,m+2}^n(\zeta) &= \frac{1}{4\pi i} \int_0^{2\pi} d\tau_1 \int_0^{\tau_1} d\tau_2 [f_{m,m+1}^n(\tau_1) f_{m+1,m+2}^n(\tau_2) - (1 \leftrightarrow 2)], \\ \uparrow C_m^{n,n+2}(\zeta) &= \frac{1}{4\pi i} \int_0^{2\pi} d\tau_1 \int_0^{\tau_1} d\tau_2 [g_m^{n,n+1}(\tau_1) g_m^{n+1,n+2}(\tau_2) - (1 \leftrightarrow 2)], \end{aligned}$$

$$\begin{aligned} \nearrow D_{m,m+1}^{n,n+1}(\zeta) &= \frac{1}{4\pi i} \int_0^{2\pi} d\tau_1 \int_0^{\tau_1} d\tau_2 \left[f_{m,m+1}^n(\tau_1) g_{m+1}^{n,n+1}(\tau_2) \right. \\ &\quad \left. + f_{m,m+1}^{n+1}(\tau_2) g_m^{n,n+1}(\tau_1) - (1 \leftrightarrow 2) \right], \\ \nwarrow D_{m,m-1}^{n,n+1}(\zeta) &= \frac{1}{4\pi i} \int_0^{2\pi} d\tau_1 \int_0^{\tau_1} d\tau_2 \left[(f_{m-1,m}^n(\tau_1))^* g_{m-1}^{n,n+1}(\tau_2) \right. \\ &\quad \left. + (f_{m-1,m}^{n+1}(\tau_2))^* g_m^{n,n+1}(\tau_1) - (1 \leftrightarrow 2) \right], \end{aligned}$$

$$\rightarrow E_{m,m+1}^n(\zeta) = \frac{1}{2\pi} \int_0^{2\pi} d\tau_1 \int_0^{\tau_1} d\tau_2 \text{Im} \left\{ (f_{m,m+1}^n(\tau_1))^* f_{m,m+1}^n(\tau_2) \right\},$$

$$\uparrow E_m^{n,n+1}(\zeta) = \frac{1}{2\pi} \int_0^{2\pi} d\tau_1 \int_0^{\tau_1} d\tau_2 \text{Im} \left\{ (g_m^{n,n+1}(\tau_1))^* g_m^{n,n+1}(\tau_2) \right\},$$

All the coefficients are defined on the bonds between sites, labelled by (m, n) . Apart from E , the coefficients B , C , and D are complex numbers, and hence modify the properties of the artificial magnetic field. Furthermore, the diagonal hoppings $\nearrow D$ and $\nwarrow D$ are different, due to broken rotational symmetry.

C.2 Corrections to the Effective Hamiltonian H_{eff}

C.2.1 First-order Coefficients for the 1D Driven Boson Model

In this appendix, we list the expressions for the nnn hopping, and the staggered potential, found to first order in the High-Frequency expansion to the model discussed in Sec. 3.1.3.2. In order to distinguish them from those in the Magnus expansion, we use an extra tilde in the notation. Formally, the difference is the factor $(1 - \frac{\tau_1 - \tau_2}{\pi})$ in the integrands, which ensures that the expressions are Floquet-gauge independent. We recall that

$$g^{m,m+1}(\tau; \zeta) = \exp [-i\zeta \sin(\tau - \phi_{nm})],$$

where $\tau = \Omega t$. Then the coefficients to the Hamiltonian $H_{\text{eff}}^{(1)}$ given in Eq. (3.60) are given by the following time-ordered integrals

$$\begin{aligned} \tilde{C}^{m,m+2}(\zeta) &= \frac{1}{4\pi i} \int_0^{2\pi} d\tau_1 \int_0^{\tau_1} d\tau_2 \left(1 - \frac{\tau_1 - \tau_2}{\pi} \right) [g^{m,m+1}(\tau_1) g^{m+1,m+2}(\tau_2) - (1 \leftrightarrow 2)], \\ \tilde{G}^{m,m+1}(\zeta) &= \frac{1}{2\pi} \int_0^{2\pi} d\tau_1 \int_0^{\tau_1} d\tau_2 \left(1 - \frac{\tau_1 - \tau_2}{\pi} \right) \text{Im} \left\{ (g^{m,m+1}(\tau_1))^* g^{m,m+1}(\tau_2) \right\}. \end{aligned} \quad (\text{C.4})$$

We mention that these expressions are the same as the corresponding one for nnn hopping along the y -direction $\uparrow \tilde{C}_0^{m,m+2}(\zeta)$, and a staggered potential along the y -direction and $\uparrow \tilde{E}_0^{m,m+1}(\zeta)$ found in the 2D extension of the model from Sec. 3.1.3.3 (see below).

C.2.2 First-order Coefficients for the Harper-Hofstadter Model

In this appendix we discuss the parameters of the leading correction, Eq. (3.73). Let us define two auxiliary functions f and g by

$$\begin{aligned} f_{m,m+1}^n(\tau; \zeta) &= \exp[-i\zeta \sin(\tau - \phi_{nm}) + i\tau] \\ g_m^{n,n+1}(\tau; \zeta) &= \exp[-i\zeta \sin(\tau - \phi_{nm})]. \end{aligned} \quad (\text{C.5})$$

The coefficients \tilde{C} , \tilde{D} , and \tilde{E} in Eq. (3.73) are given by the following time-ordered integrals:

$$\begin{aligned} \rightarrow \tilde{C}_{m,m+2}^n(\zeta) &= \frac{1}{4\pi i} \int_0^{2\pi} d\tau_1 \int_0^{\tau_1} d\tau_2 \left(1 - \frac{\tau_1 - \tau_2}{\pi}\right) [f_{m,m+1}^n(\tau_1) f_{m+1,m+2}^n(\tau_2) - (1 \leftrightarrow 2)], \\ \uparrow \tilde{C}_m^{n,n+2}(\zeta) &= \frac{1}{4\pi i} \int_0^{2\pi} d\tau_1 \int_0^{\tau_1} d\tau_2 \left(1 - \frac{\tau_1 - \tau_2}{\pi}\right) [g_m^{n,n+1}(\tau_1) g_m^{n+1,n+2}(\tau_2) - (1 \leftrightarrow 2)], \\ \nearrow \tilde{D}_{m,m+1}^{n,n+1}(\zeta) &= \frac{1}{4\pi i} \int_0^{2\pi} d\tau_1 \int_0^{\tau_1} d\tau_2 \left(1 - \frac{\tau_1 - \tau_2}{\pi}\right) \left[f_{m,m+1}^n(\tau_1) g_{m+1}^{n,n+1}(\tau_2) \right. \\ &\quad \left. + f_{m,m+1}^{n+1}(\tau_2) g_m^{n,n+1}(\tau_1) - (1 \leftrightarrow 2) \right], \\ \nwarrow \tilde{D}_{m,m-1}^{n,n+1}(\zeta) &= \frac{1}{4\pi i} \int_0^{2\pi} d\tau_1 \int_0^{\tau_1} d\tau_2 \left(1 - \frac{\tau_1 - \tau_2}{\pi}\right) \left[(f_{m-1,m}^n(\tau_1))^* g_{m-1}^{n,n+1}(\tau_2) \right. \\ &\quad \left. + (f_{m-1,m}^{n+1}(\tau_2))^* g_m^{n,n+1}(\tau_1) - (1 \leftrightarrow 2) \right], \\ \rightarrow \tilde{E}_{m,m+1}^n(\zeta) &= \frac{1}{2\pi} \int_0^{2\pi} d\tau_1 \int_0^{\tau_1} d\tau_2 \left(1 - \frac{\tau_1 - \tau_2}{\pi}\right) \text{Im} \left\{ (f_{m,m+1}^n(\tau_1))^* f_{m,m+1}^n(\tau_2) \right\}, \\ \uparrow \tilde{E}_m^{n,n+1}(\zeta) &= \frac{1}{2\pi} \int_0^{2\pi} d\tau_1 \int_0^{\tau_1} d\tau_2 \left(1 - \frac{\tau_1 - \tau_2}{\pi}\right) \text{Im} \left\{ (g_m^{n,n+1}(\tau_1))^* g_m^{n,n+1}(\tau_2) \right\}. \end{aligned}$$

All the coefficients are defined on the bonds between sites, labelled by (m, n) . Apart from \tilde{E} , the coefficients \tilde{C} , and \tilde{D} are complex numbers, and hence modify the properties of the artificial magnetic field.

Appendix D

Details in the Derivation of Floquet Adiabatic Perturbation Theory

In this Appendix, we give the details of the derivation of Eq. (4.16) from the main text.

To this end, let us write down again Eq. (4.14):

$$i\dot{c}'_n = -\dot{\lambda} \sum_{m \neq n} \langle n_F(\lambda) | \mathcal{A}_\lambda^F(\lambda, t) | m_F(\lambda) \rangle e^{i(\Phi_n^F(t) - \Phi_m^F(t))} c'_m, \quad (\text{D.1})$$

which is an exact Schrödinger equation describing Floquet systems. If $\lambda(t)$ is a slowly-varying, monotonic function of time, and the ramp is adiabatic: $\dot{\lambda} \rightarrow 0$, the RHS vanishes identically and the system remains in the instantaneous adiabatically-connected state. However, any finite ramp speed results in excitations, the magnitude of which is governed by the instantaneous velocity $\dot{\lambda}(t)$. In order to understand these excitations, our strategy is to formally integrate Eq. (D.1) perturbatively, using the ramp speed as a small parameter.

Let us assume that at time t_i we start the evolution in the ground state of the non-driven Hamiltonian, i.e. $c_n(t_i) = \delta_{n0}$. Straightforward integration then leads us to the first correction to the amplitude for making a transition to the n -th excited state ($n \neq 0$):

$$c'_n(\lambda(t), t) = i \int_{t_i}^t dt' \dot{\lambda}(t') e^{i(\Phi_n^F(t') - \Phi_0^F(t'))} A_{n0}^F(\lambda(t'), t') + \mathcal{O}(\dot{\lambda}^2), \quad (\text{D.2})$$

where we define $A_{n0}^F(\lambda, t) = \langle n_F(\lambda) | \mathcal{A}_\lambda^F(\lambda, t) | 0_F(\lambda) \rangle$ to simplify notation. Next we need to evaluate the rapidly oscillating integral in Eq. (D.2). To do this, we cast the Floquet gauge

potential at fixed λ in Fourier space

$$\mathcal{A}^F(\lambda, t) = \sum_{\ell=-\infty}^{\infty} \mathcal{A}^{F,\ell}(\lambda) e^{i\Omega\ell t}. \quad (\text{D.3})$$

Thus, Eq. (D.2) assumes the form:

$$c'_n(\lambda(t), t) = i \sum_{\ell} \int_t^t dt' \dot{\lambda}(t') e^{i(\Phi_n^F(t') - \Phi_0^F(t') + \Omega\ell t')} A_{n0}^{F,\ell}(\lambda(t')) + \mathcal{O}(\dot{\lambda}^2). \quad (\text{D.4})$$

We are faced with a rapidly oscillating phase, multiplied by a slow function in the integral so we can use standard techniques for evaluating it approximately. For finite values of $\lambda(t_i)$ and $\lambda(t_f)$, this can be done by integration by parts, assuming $\dot{\lambda}(t_i) = 0$ and staying to linear order in $\dot{\lambda}(t)$:

$$\begin{aligned} & i \sum_l \int_t^t dt' \dot{\lambda}(t') e^{i(\Phi_n^F(t') - \Phi_0^F(t') + \Omega\ell t)} A_{n0}^{F,\ell}(\lambda(t)) \\ &= \int_t^t dt' \frac{\dot{\lambda}(t') A_{n0}^{F,\ell}(\lambda(t'))}{\epsilon_n(\lambda(t')) - \epsilon_0(\lambda(t')) + \ell\Omega} \frac{d}{dt'} e^{i(\Phi_n^F(t') - \Phi_0^F(t') + \Omega\ell t')} \\ &= \frac{\dot{\lambda}(t) A_{n0}^{F,\ell}(\lambda(t)) e^{i(\Phi_n^F(t) - \Phi_0^F(t) + \Omega\ell t)}}{\epsilon_n(\lambda(t)) - \epsilon_0(\lambda(t)) + \ell\Omega} + \mathcal{O}(\dot{\lambda}^2, \ddot{\lambda}). \end{aligned} \quad (\text{D.5})$$

To simplify the notation, it is useful to suppress some of the t -dependence. Going back to the original $c_n(t)$ frame we obtain:

$$c_n(t) = e^{-i\Phi_0^F(t)} \dot{\lambda}(t) \sum_{\ell=-\infty}^{\infty} e^{i\ell\Omega t} \frac{\langle n_F(\lambda) | \mathcal{A}_{\lambda}^{F,\ell} | 0_F(\lambda) \rangle}{\epsilon_n^F - \epsilon_0^F + \ell\Omega} + \mathcal{O}(\ddot{\lambda}, \dot{\lambda}^2). \quad (\text{D.6})$$

Appendix E

Exact Solution to the Harmonic Oscillator with Periodically Displaced Potential

In this appendix we outline the exact solution to the driven Harmonic oscillator from Sec. 4.3.2, as well as derivations of various formulas from the main text. Once again, throughout the derivations below we set $\hbar = 1$. The general solution is outlined in a set of notes by Peter Hänggi on periodically driven systems and can be found online [91]. As we follow the derivation of Ref. [91], we use the notion of rotating frames to be consistent with the discussion in the main text.

The Hamiltonian we would like to solve reads as:

$$H(t) = \frac{p^2}{2m} + \frac{1}{2}m\omega_0^2x^2 - f(t)x = H_{\text{HO}} - f(t)x \quad (\text{E.1})$$

By going to a rotating frame using the *consecutive* transformations

$$V_1(t) = e^{-i\eta(t)p}; \quad V_2(t) = e^{im\dot{\eta}(t)x}, \quad (\text{E.2})$$

one finds that transformed Hamiltonian:

$$H^{\text{rot}}(t) = H_{\text{HO}} + x [m\ddot{\eta}(t) + m\omega_0^2\eta(t) - f(t)] - L(\eta, \dot{\eta}, t), \quad (\text{E.3})$$

where L is the classical Lagrangian for the lab frame $H(t)$:

$$L(\eta, \dot{\eta}, t) = \frac{1}{2}m\dot{\eta}^2(t) - \frac{1}{2}m\omega_0^2\eta^2(t) + \eta(t)f(t). \quad (\text{E.4})$$

Throughout, we adopt the notation $(\dot{\cdot}) = d/dt = \partial_t + \dot{\lambda}\partial_\lambda$.

We see that we can remove the linear term in x from the Hamiltonian (E.3), if $\eta(t)$ satisfies the classical equation of motion:

$$m\ddot{\eta} + m\omega_0^2\eta = f(t) \quad (\text{E.5})$$

Finally, by doing another unitary transformation one can also remove the Lagrangian for the classical variable $L(\eta, \dot{\eta}, t)$, leaving just H_{HO} . In this frame the exact solution to the time-dependent Schrödinger equation is simply given in terms of the eigenstates and eigenenergies of H_{HO} , $|n\rangle$ and $E_n = \omega_0(n + 1/2)$:

$$|\psi^{\text{rot}}(t)\rangle = \sum_n c_n e^{-iE_n t} |n\rangle \quad (\text{E.6})$$

where c_n are *time independent*. Transforming back to the original lab frame, the exact solution can be written as:

$$|\psi(t)\rangle = \sum_n c_n |\chi_n(t)\rangle \quad (\text{E.7})$$

$$|\chi_n(t)\rangle = e^{i\varphi_n(\eta(t), \dot{\eta}(t), t)} e^{-i\eta(t)\hat{p}} e^{im\dot{\eta}(t)\hat{x}} |n\rangle \quad (\text{E.8})$$

where $\varphi_n(\eta, \dot{\eta}, t) = -E_n t + \int_{t_i}^t dt' L(\eta, \dot{\eta}, t')$. Here we explicitly put hats on \hat{x} and \hat{p} to emphasize that they act as operators on the state $|n\rangle$.

In the following, it will prove useful to distinguish between two classical solutions: (i) $\eta(t) = \xi(t)$ is defined as the exact solution to the ramped classical problem (E.5), i.e. for $f(t) = \lambda(t)A_f\Omega^2 \cos(\Omega t + \varphi_0)$. We shall see below that in this case we need not require that $\lambda(t)$ changes slowly. (ii) we denote by $\eta(t) = \zeta(t)$ the classical trajectory for the Floquet

solution at a fixed λ , i.e. for $f(t) = \lambda A_f \Omega^2 \cos(\Omega t + \varphi_0)$ at a fixed λ .

E.0.1 Exact Floquet Solution

Floquet Solution.—In this subsection we discuss the application of the solution outlined above to the Harmonic oscillator in the presence of a periodically displaced potential. We then use that solution to calculate various quantities in FAPT. In this subsection, we consider $\lambda = \text{const}(t)$.

From the previous discussion, it is clear that no assumptions are made about the initial conditions for the classical trajectory in the definition of the solution. Even though the initial conditions do not matter for the solution itself, the initial conditions effect the basis $|\chi_n(t)\rangle$. Therefore, in order to make use of the general solution to find the Floquet Hamiltonian and micromotion operator, the initial conditions of $\zeta(t)$ must be chosen such that $|\chi_n(t)\rangle$ manifestly satisfy Floquet's theorem. This can be accomplished if $\zeta(t)$ is the *periodic* solution of:

$$m\ddot{\zeta} + m\omega_0^2\zeta = \lambda A_f \Omega^2 \cos(\Omega t + \varphi_0),$$

which given by [91]:

$$\zeta(t) = \frac{A_f \Omega^2 \lambda \cos(\Omega t + \varphi_0)}{m(\omega_0^2 - \Omega^2)}. \quad (\text{E.9})$$

Note that the notation V_1 and V_2 for the rotators in Eq. (E.2) was not an accident. Indeed, if we take the $\Omega \rightarrow \infty$ limit of ζ , we see that V_1 and V_2 become the same transformations mentioned in the main text, see Eqs. (4.34). To get the Floquet quasi-energies one must separate the periodic and non-periodic parts of $\varphi_n(t)$ [91]:

$$\epsilon_n^F(\lambda) = \omega_0 \left(n + \frac{1}{2} \right) - \frac{A_f^2 \Omega^4 \lambda^2}{4m(\omega_0^2 - \Omega^2)} \quad (\text{E.10})$$

$$|n^F(\lambda, t)\rangle = e^{i\varphi(\zeta, \partial_t \zeta, t)} e^{-i\zeta \hat{p}} e^{im\partial_t \zeta \hat{x}} |n\rangle \quad (\text{E.11})$$

where the λ dependent constant part of ϵ_n^F comes from the period average of L , and $\varphi(\zeta, \partial_t \zeta, t) = \varphi_n(\zeta, \partial_t \zeta, t) - \epsilon_n^F t$ is a periodic function with frequency Ω .

For the rest of the calculation it will be convenient to use the instantaneous Floquet basis $|n^F(\lambda, t)\rangle = P(\lambda, t)|n_F(\lambda)\rangle$ because of its simple form. It should be noted, that the form above suggests that the non-stroboscopic Floquet Hamiltonian H_{eff} and kick operator $K_{\text{eff}}(t)$, cf. Ref. [33], are given by:

$$H_{\text{eff}} = H_{\text{HO}} - \frac{A_f^2 \Omega^4 \lambda^2}{4m(\omega_0^2 - \Omega^2)} \quad (\text{E.12})$$

$$e^{-iK_{\text{eff}}(t)} = e^{i\varphi(\zeta, \partial_t \zeta, t)} e^{-i\zeta \hat{p}} e^{im\partial_t \zeta \hat{x}} \quad (\text{E.13})$$

By doing simple manipulations on the moving frame basis, one can find the stroboscopic micromotion operator $P(t)$, and the Floquet eigenstates which can be used to determine the stroboscopic $H_F[t_i]$ ¹:

$$H_F[t_i] = \frac{1}{2m} (p - m\partial_t \zeta(t_i))^2 + \frac{1}{2} m\omega_0^2 (x - \zeta(t_i))^2 - \frac{A_f^2 \Omega^4 \lambda^2}{4m(\omega_0^2 - \Omega^2)} \quad (\text{E.14})$$

$$P(t) = e^{i\varphi(\zeta, \partial_t \zeta, t)} e^{-i(\zeta(t) - \zeta(t_i))p} e^{im(\partial_t \zeta(t) - \partial_t \zeta(t_i))(x + \zeta(t_i))} \quad (\text{E.15})$$

where t_i defines the Floquet gauge [33]. Note that we don't show the explicit λ -dependence in $P(t)$, but it indeed comes in through the classical solution ζ which depends on the driving amplitude. Just as we mentioned in the main text, the Floquet spectrum only depends on λ via a constant shift. Also, note that even at finite Ω , all of the Floquet eigenstates are smooth functions of λ and, therefore, satisfy the assumptions of FAPT.

FAPT calculations.—Now that we know the Floquet solution we can use it to calculate physical quantities to test FAPT. In order to do this, we first need the Floquet gauge potential $\mathcal{A}_{\lambda, m, n}^F = \langle m^F(\lambda, t) | i\partial_\lambda | n^F(\lambda, t) \rangle$, see Sec. 4.2.2. This calculation is very simple if one uses Eq. (E.11), which leads to:

$$\mathcal{A}_{\lambda, m, n}^F = \mathcal{A}_{\lambda, 0}^F \delta_{m, n} + \mathcal{A}_{\lambda, n, n+1}^F \delta_{m, n+1} + \mathcal{A}_{\lambda, n, n-1}^F \delta_{m, n-1} \quad (\text{E.16})$$

¹Note that while the stroboscopic Floquet Hamiltonian $H_F[t_i]$ depends explicitly on the initial time, the non-stroboscopic H_{eff} is manifestly t_i -independent.

$$\mathcal{A}_{\lambda,0}^F = (m\partial_t\zeta\partial_\lambda\zeta - \partial_\lambda\varphi) \quad (\text{E.17})$$

$$\mathcal{A}_{\lambda,n,n+1}^F = \sqrt{\frac{n+1}{2m\omega_0}} \frac{A_f\lambda\Omega^2}{(\omega_0^2 - \Omega^2)} [\Omega \sin(\Omega t + \varphi_0) + i\omega_0 \cos(\Omega t + \varphi_0)] \quad (\text{E.18})$$

$$\mathcal{A}_{\lambda,n,n-1}^F = \sqrt{\frac{n}{2m\omega_0}} \frac{A_f\lambda\Omega^2}{(\omega_0^2 - \Omega^2)} [\Omega \sin(\Omega t + \varphi_0) - i\omega_0 \cos(\Omega t + \varphi_0)] \quad (\text{E.19})$$

An important observation here is that the off-diagonal elements of \mathcal{A}^F only have two harmonics: $\ell = \pm 1$. From this, we conclude that only the micromotion operator $P(t)$ plays a role for the non-adiabatic corrections, because the Floquet Hamiltonian only appears in the FAPT expression via the $\ell = 0$ harmonic, cf. Eq. (4.16). Another important observation is that we can always find a driving phase φ_0 which makes $\mathcal{A}_{\lambda,10}^F$ imaginary. As a result, observables which have real matrix elements in the moving Floquet basis have no $\dot{\lambda}$ corrections in FAPT. This implies that if one has precise control of the driving phase and ramp time, it should be possible to systematically reduce excitations at the measurement time.

Now that we have the Floquet gauge potential we can calculate the leading non-adiabatic corrections to the probability amplitudes of our wave function (see Eq. (4.16)):

$$|\psi(t)\rangle = \sum_n c_n(t) |n^F(\lambda(t), t)\rangle \quad (\text{E.20})$$

with initial conditions: $c_n(t_i) = \delta_{n,0}$. Using Eq. (E.19) and the Floquet quasi-energies we find that $c_n(t)$ is given by:

$$c_n(t) \approx i\dot{\lambda}(t) e^{-i\Phi_0^F(t)} \sqrt{\frac{1}{2m\omega_0}} \frac{A_f\lambda\Omega^2}{2} \left(\frac{e^{i(\Omega t + \varphi_0)}}{(\omega_0 + \Omega)^2} + \frac{e^{-i(\Omega t + \varphi_0)}}{(\omega_0 - \Omega)^2} \right) \delta_{n,1} + \mathcal{O}(\ddot{\lambda}, \dot{\lambda}^2). \quad (\text{E.21})$$

As a result, the general expression for the expectation values for observables reads:

$$\begin{aligned} \langle O(\lambda(t), t) \rangle &= \langle 0^F(\lambda(t), t) | O | 0^F(\lambda(t), t) \rangle + \sum_{n>0} \left(e^{i\Phi_0^F(t)} c_n(t) \langle 0^F(\lambda(t), t) | O | n^F(\lambda(t), t) \rangle + c.c. \right) \\ &\quad + \mathcal{O}(\ddot{\lambda}, \dot{\lambda}^2) \end{aligned} \quad (\text{E.22})$$

Calculating matrix elements of the form: $\langle 0^F(\lambda(t), t) | O | n^F(\lambda(t), t) \rangle$ is straightforward using Eq. (E.11). We show here the final results for $\langle p^2 \rangle$ and $\langle x \rangle$:

$$\langle p^2(t) \rangle \approx m^2[\partial_t \zeta(t)]^2 + \frac{m\omega_0}{2} + \dot{\lambda}(t)m\partial_t \zeta(t) \frac{4A_f \Omega^2(\Omega^2 + \omega_0^2)}{(\omega_0^2 - \Omega^2)^2} \cos(\Omega t + \varphi_0) + \mathcal{O}(\ddot{\lambda}, \dot{\lambda}^2) \quad (\text{E.23})$$

$$\langle x(t) \rangle \approx \zeta(t) + \dot{\lambda}(t) \frac{2A_f \Omega^3}{m(\omega_0^2 - \Omega^2)^2} \sin(\Omega t + \varphi_0) + \mathcal{O}(\ddot{\lambda}, \dot{\lambda}^2), \quad (\text{E.24})$$

which are plotted in Fig. 4.3 and discussed in Sec. 4.3.2. One can also calculate a closed expression for the probabilities of occupying a given Floquet state $|n^F(\lambda(t), t)\rangle$, which is given by $|c_n(t)|^2$:

$$p_n^F(t) \approx \frac{A_f^2 \Omega^4 \dot{\lambda}(t)^2}{2m\omega_0} \frac{(4\omega_0^2 \Omega^2 \sin^2(\Omega t + \varphi_0) + (\omega_0^2 + \Omega^2)^2 \cos^2(\Omega t + \varphi_0))}{(\omega_0^2 - \Omega^2)^4} \delta_{n,1} + \mathcal{O}(\ddot{\lambda}, \dot{\lambda}^3) \quad (\text{E.25})$$

which can be used to calculate the log-fidelity f_d and the Floquet diagonal entropy S_d^F , cf. Sec. 4.2.2.

E.0.2 Exact Solution to the Ramped Problem

In this subsection, we discuss the exact solution of the ramped problem. As mentioned above, the solution entails solving the classical equations of motion:

$$m\ddot{\xi}(t) + m\omega_0^2\xi(t) = f(t); \quad f(t) = \lambda(t)A_f \Omega^2 \cos(\Omega t + \varphi_0)$$

Note that in this subsection we have a time-dependent ramp function $\lambda = \lambda(t)$, and thus $\dot{\xi} = \partial_t \xi + \dot{\lambda} \partial_\lambda \xi$ is the full time derivative.

Any initial conditions for $\xi(t)$ gives a valid solution, but one can simplify the solution greatly by picking the proper initial condition: as we start in the ground state of H_{HO} initially, a natural choice for the initial condition on $\xi(t)$ is: $\xi(t_i) = \dot{\xi}(t_i) = 0$. With this

choice the basis $|\chi_n(t)\rangle$ (see Eq. (E.8)) at $t = t_i$ is simply the eigenbasis of H_{HO} , $\{|n\rangle\}$, and so we find that the solution has a very simple form:

$$|\psi(t)\rangle = e^{i\varphi_0(\xi, \dot{\xi}, t)} e^{-i\xi\hat{p}} e^{im\xi\hat{x}} |0\rangle \quad (\text{E.26})$$

This has a simple physical interpretation: the wave function is simply a Gaussian wave packet following the classical trajectory. Using the initial conditions given above, $\xi(t)$ can be calculated for any $f(t)$ as:

$$\xi(t) = \sin(\omega_0 t) \int_{t_i}^t dt' \cos(\omega_0 t') \frac{f(t')}{m} + \cos(\omega_0 t) \int_{t_i}^t ds \sin(\omega_0 t') \frac{f(t')}{m} \quad (\text{E.27})$$

If we pick $\lambda(t)$ to have a simple enough form (e.g. a power law in t), these integrals can be evaluated exactly in terms of simple functions, although the expressions are too long to give here. Using the quadratic form in Eq. (E.26), it is a simple to evaluate the expectation value of any analytic function of \hat{x} and \hat{p} :

$$\langle \psi(t) | g(\hat{x}, \hat{p}) | \psi(t) \rangle = \langle 0 | g(\hat{x} + \xi(t), \hat{p} + m\dot{\xi}(t)) | 0 \rangle \quad (\text{E.28})$$

Finally, we also calculate is the overlap with the instantaneous Floquet basis which define the exact $c_n(t)$:

$$c_n(t) = \langle n^F(\lambda(t), t) | \psi(t) \rangle. \quad (\text{E.29})$$

This can also be evaluated exactly by rewriting this overlap as an integral and then using the generating function of the Hermite Polynomials. Nevertheless, the result is quite long and not very useful. Fortunately, the exact probabilities p_n^F can be defined in terms of a function of the difference between the classical trajectories ζ and ξ . To this end, we define

$$\Theta(t) = \frac{m}{2\omega_0} \left[\left[\partial_t \zeta(t, \lambda(t)) - \dot{\xi}(t) \right]^2 + \omega_0^2 [\zeta(t, \lambda(t)) - \xi(t)]^2 \right]. \quad (\text{E.30})$$

In terms of this function the probabilities, log-fidelity and Floquet diagonal entropy are

given as:

$$p_n^F(t) = e^{-\Theta(t)} \frac{\Theta(t)^n}{n!} \quad (\text{E.31})$$

$$f_d(t) = \Theta(t) \quad (\text{E.32})$$

$$S_d^F(t) = \Theta(t)(1 - \log(\Theta(t))) + e^{-\Theta(t)} \sum_{k=0}^{\infty} \frac{\Theta(t)^n \log(n!)}{n!} \quad (\text{E.33})$$

One can also check that if one expands the exact solutions above to leading order in $\dot{\lambda}$, one recovers all the expressions from FAPT, as expected.

Appendix F

Floquet Theory for Periodic Step Driving Protocols

Consider a system, periodically-driven by switching on and off two Hamiltonians V and W , each of them acting for the same time $T/2$. The Hamiltonian of the system reads

$$H(t) = \begin{cases} V, & t \in [t_0, t_0 + T/2] \\ W, & t \in [t_0 + T/2, t_0 + T] \end{cases} \mod T \quad (\text{F.1})$$

In the following, we are interested in deriving the approximate Floquet Hamiltonian and kick operators within the van Vleck inverse-frequency expansion for this model. While not necessarily the most general case, we shall assume that the driving sequence is time-reversal symmetric, i.e. $H(-t) = H(t)$ which is ensured by choosing $t_0 = -T/4$. This will have the advantage that the Floquet Hamiltonian is time-reversal symmetric and, consequently, real-valued. However, it will become clear from the discussion below how to generalise the analysis to drives of arbitrary time symmetry. Notice also, that by rescaling the relative strength of V and W , it is possible to use the formalism below to study problems with possibly non-equal duration between the Hamiltonian switches.

We begin by casting the Hamiltonian $H(t)$ in the form

$$\begin{aligned} H(t) &= H_0 + \text{sgn}(\cos \Omega t) \tilde{H}_0, \\ H_0 &= \frac{1}{2} (V + W), \end{aligned}$$

$$\tilde{H}_0 = \frac{1}{2}(V - W), \quad (\text{F.2})$$

where $\Omega = 2\pi/T$ is the period of the driving sequence. According to Floquet's theorem the evolution operator for this system factorises as follows:

$$U(t, 0) = \mathcal{T} \exp \left(-i \int_0^t dt H(t) \right) = e^{-iK_{\text{eff}}(t)} e^{-iH_{\text{eff}}t} e^{iK_{\text{eff}}(0)}, \quad (\text{F.3})$$

with the non-stroboscopic Floquet Hamiltonian H_{eff} and the corresponding micromotion K_{eff} . Fourier expanding the Hamiltonian $H(t) = \sum_{\ell \in \mathbb{Z}} H_{\ell} e^{i\ell\Omega t}$ with the operator-valued coefficients H_{ℓ} the approximate van Vleck Floquet Hamiltonian was derived to third order in Ref. [59]. The expansion formulas simplify tremendously in the present problem by noticing that $H_{\ell} = c_{\ell} \tilde{H}_0$, where the Fourier coefficients c_{ℓ} of the driving protocol $f(t)$ are given by

$$f(t) = \sum_{\ell \in \mathbb{Z}} c_{\ell} e^{i\ell\Omega t}. \quad (\text{F.4})$$

For the time-reversal symmetric step-like drive $f(t) = \text{sgn}(\cos \Omega t)$ we find $c_{\ell} = -[-1 + (-1)^{\ell}] \sin(\frac{\ell\pi}{2})/(\pi\ell)$. Due to the property $H_{\ell} = c_{\ell} \tilde{H}_0$, the expansion reduces to

$$\begin{aligned} H_{\text{eff}}^{(0)} &= H_0, \\ H_{\text{eff}}^{(1)} &= \mathbf{0}, \\ H_{\text{eff}}^{(2)} &= \frac{1}{\Omega^2} \sum_{\ell \neq 0} \frac{c_{-\ell} c_{\ell}}{2\ell^2} [[\tilde{H}_0, H_0], \tilde{H}_0], \\ H_{\text{eff}}^{(3)} &= -\frac{1}{\Omega^3} \left(\sum_{\ell \neq 0} \frac{c_{-\ell} c_{\ell}}{2\ell^3} [[[\tilde{H}_0, H_0], H_0], \tilde{H}_0] + \sum_{\ell \neq 0} \sum_{n \neq 0, \ell} \frac{c_{-\ell} c_{\ell-n} c_n}{3\ell^2 n} [[[[\tilde{H}_0, H_0], \tilde{H}_0], H_0], \tilde{H}_0] \right). \end{aligned} \quad (\text{F.5})$$

and the corresponding Kick operators read:

$$K_{\text{eff}}^{(0)}(t) = \mathbf{0}, \quad (\text{F.6})$$

$$\begin{aligned}
K_{\text{eff}}^{(1)}(t) &= \frac{1}{i\Omega} \sum_{\ell \neq 0} \frac{c_\ell}{\ell} e^{i\ell\Omega t} \tilde{H}_0, \\
K_{\text{eff}}^{(2)}(t) &= \frac{1}{i\Omega^2} \sum_{\ell \neq 0} \frac{c_\ell}{\ell^2} e^{i\ell\Omega t} [\tilde{H}_0, H_0], \\
K_{\text{eff}}^{(3)}(t) &= \frac{1}{i\Omega^3} \left(\sum_{\ell \neq 0} \frac{c_\ell}{\ell^3} e^{i\ell\Omega t} [[\tilde{H}_0, H_0], H_0] + \sum_{\ell \neq 0} \sum_{n \neq 0, \ell} \frac{c_n c_{\ell-n}}{2\ell n^2} e^{i\ell\Omega t} [[\tilde{H}_0, H_0], \tilde{H}_0] \right).
\end{aligned}$$

One readily observes the nice property that the commutators decouple from the infinite sums over the drive harmonics. Moreover, a close inspection reveals that by calculating the orders of the effective Hamiltonian, one obtains also the Kick operator for free.

One can also resum all infinite series for the particular driving protocol of interest. To this end, we use the identities

$$\begin{aligned}
\sum_{\ell \neq 0} \frac{c_{-\ell} c_\ell}{2\ell^2} &= \sum_{n \in \mathbb{Z}} \frac{c_{-(2n+1)} c_{2n+1}}{2(2n+1)^2} = \frac{\pi^2}{24}, \\
\sum_{\ell \neq 0} \frac{c_{-\ell} c_\ell}{2\ell^3} &= \sum_{n \in \mathbb{Z}} \frac{c_{-(2n+1)} c_{2n+1}}{2(2n+1)^3} = 0, \\
\sum_{\ell \neq 0} \sum_{n \neq 0, \ell} \frac{c_{-\ell} c_{\ell-n} c_n}{3\ell^2 n} &= \sum_{l \in \mathbb{Z}} \sum_{n \in \mathbb{Z}, n \neq l} \frac{c_{-(2l+1)} c_{2(l-n)} c_{2n+1}}{3(2l+1)^2 (2n+1)} = 0
\end{aligned} \tag{F.7}$$

Note that the last coefficient above vanishes identically because $2(l-n)$ is necessarily even, while $c_{2(l-n)} = 0$. Further, the periodic functions in the expansion for the Kick operator read

$$\kappa_1(t) = \frac{1}{i\Omega} \sum_{\ell \neq 0} \frac{c_\ell}{\ell} e^{-i\ell\Omega t} = - \int^t dt' \sum_\ell c_\ell e^{-i\ell\Omega t'} = - \int^t dt' f(t') = \frac{1}{\Omega} \left[-\frac{\pi}{2} + \arccos(\sin \Omega t) \right]$$

where we can safely include the missing $\ell = 0$ component back into the sum, provided that we impose that $\kappa_1(t)$ has zero mean, which is nothing but the boundary condition on the effective Kick operator $K_{\text{eff}}(t)$. Similarly, upon successive integration one finds

$$\kappa_2(t) = -\frac{1}{\Omega^2} \sum_{\ell \neq 0} \frac{c_\ell}{\ell^2} e^{-i\ell\Omega t} = \frac{1}{\Omega^2} \left(\left\{ \begin{array}{ll} -\frac{\pi^2}{8} + \frac{(\Omega t)^2}{2}, & t \in [-T/4, T/4] \\ \frac{\pi^2}{8} - \frac{(\Omega(t-T/2))^2}{2}, & t \in [T/4, 3T/4] \end{array} \right\} \bmod T \right)$$

$$\kappa_3(t) = \frac{1}{i\Omega^3} \sum_{\ell \neq 0} \frac{c_\ell}{\ell^3} e^{-i\ell\Omega t} = \frac{1}{\Omega^3} \left(\left\{ \begin{array}{ll} -\frac{\pi^2\Omega t}{8} + \frac{(\Omega t)^3}{6}, & t \in [-T/4, T/4] \\ \frac{\pi^2(\Omega t - T/2)}{8} - \frac{(\Omega t - T/2)^3}{6}, & t \in [T/4, 3T/4] \end{array} \right\} \bmod T \right)$$

$$\begin{aligned} \tilde{\kappa}_3(t) &= \frac{1}{i\Omega^3} \sum_{\ell \neq 0} \sum_{n \neq 0, \ell} \frac{c_n c_{\ell-n}}{2\ell n^2} e^{-i\ell\Omega t} = \frac{1}{i\Omega^3} \sum_{l \neq 0} \sum_{n'} \frac{c_{2n'+1} c_{2(l-n')-1}}{2(2l)(2n'+1)^2} e^{-i2l\Omega t} \\ &= -\frac{1}{2\Omega^2} \int^t dt' \sum_{l \neq 0} \sum_{n'} \frac{c_{2n'+1} c_{2(l-n')-1}}{(2n'+1)^2} e^{-i2l\Omega t'} \\ &= -\frac{1}{2\Omega^2} \int^t dt' \sum_{n'} \sum_{l' \neq -n'} \frac{c_{2n'+1} c_{2l'-1}}{(2n'+1)^2} e^{-i(2l'-1)\Omega t'} e^{-i(2n'+1)\Omega t'} \\ &= -\frac{1}{2\Omega^2} \int^t dt' f(t') \sum_{n'} \frac{c_{2n'+1}}{(2n'+1)^2} e^{-i(2n'+1)\Omega t'} - \sum_{n'} \frac{c_{2n'+1} c_{-2n'-1}}{(2n'+1)^2} \\ &= \frac{1}{2\Omega^2} \int^t dt' f(t') \kappa_2(t') + \frac{\pi^2}{12} = \frac{1}{\Omega^3} \left(\frac{1}{2} \left\{ -\frac{\pi^2\Omega t}{24} + \frac{(\Omega t)^3}{6} \right\} \bmod T \right), \quad t \in [-T/4, T/4]. \end{aligned}$$

In the second equality in $\tilde{\kappa}_3(t)$ we used that $n = 2n' + 1$ has to be odd which means that $\ell = 2l$ needs to be even, since $c_{2\ell} = 0$.

At the end of the day, the van Vleck inverse-frequency expansion for the time-reversal symmetric step-like drive $f(t) = \text{sgn}(\cos \Omega t)$ reduces to

$$\begin{aligned} H_{\text{eff}}^{(0)} &= H_0, & K_{\text{eff}}^{(0)}(t) &= \mathbf{0}, \\ H_{\text{eff}}^{(1)} &= \mathbf{0}, & K_{\text{eff}}^{(1)}(t) &= \kappa_1(t) \tilde{H}_0, \\ H_{\text{eff}}^{(2)} &= \pi^2/(24\Omega^2) [[\tilde{H}_0, H_0], \tilde{H}_0], & K_{\text{eff}}^{(2)}(t) &= \kappa_2(t) i[[\tilde{H}_0, H_0], H_0], \\ H_{\text{eff}}^{(3)} &= \mathbf{0}, & K_{\text{eff}}^{(3)}(t) &= \kappa_3(t) [[\tilde{H}_0, H_0], H_0] + \tilde{\kappa}_3(t) [[\tilde{H}_0, H_0], \tilde{H}_0]. \end{aligned} \tag{F.8}$$

Of particular importance is the property $K_{\text{eff}}^{(2n+1)}(0) = \mathbf{0}$ which shows that if one is interested in stroboscopic evolution only, one can proceed without calculating these odd-order terms. Notice also that the periodic functions $\kappa_j(t)$ are universal, in the sense that they do not depend on the Hamiltonian, and thus, Eqs. (F.8) apply to a fairly large class of systems. This is a consequence of Floquet's theorem, according to which the kinematics,

as defined by the Floquet Hamiltonian, is in general independent of the dynamics which in turn is governed by the kick operator. Last but not least, one should keep in mind that the inverse-frequency expansion in the lab frame, as carried out above, does not capture the Floquet resonances in the many-body spectrum.

Bibliography

- [1] J. H. Shirley, *Phys. Rev.* **138**, B979 (1965).
- [2] H. Sambe, *Phys. Rev. A* **7**, 2203 (1973).
- [3] H. P. Breuer, K. Dietz, and M. Holthaus, *Physica (Amsterdam)* **46D**, 317 (1990).
- [4] H. P. Breuer and M. Holthaus, *Ann. Phys. (N.Y.)* **211**, 249 (1991).
- [5] P. L. Kapitza, *Soviet Phys. JETP* **21**, 588 (1951).
- [6] H. W. Broer, I. Hoveijn, M. van Noort, C. Simó, and G. Vegter, *Journal of Dynamics and Differential Equations* **16**, 897 (2004).
- [7] L. D. Landau and E. M. Lifshitz, *Mechanics* (Elsevier, Amsterdam, 2008).
- [8] B. V. Chirikov, F. M. Izrailev, and D. L. Shepelyansky, *Soviet Scientific Reviews. Section C* **2**, 209 (1981).
- [9] S. Rahav, I. Gilary, and S. Fishman, *Phys. Rev. A* **68**, 013820 (2003).
- [10] S. Rahav, I. Gilary, and S. Fishman, *Phys. Rev. Lett.* **91**, 110404 (2003).
- [11] L. E. Reichl, *The transition to Chaos: Conservative Classical Systems and Quantum Manifestations* (Springer, New York, 2004).
- [12] F. Grossmann, T. Dittrich, P. Jung, and P. Hänggi, *Phys. Rev. Lett.* **67**, 516 (1991).
- [13] F. Grossmann and P. Hänggi, *Europhys. Lett.* **18**, 571 (1992).
- [14] M. Gavrila, *J. Phys. B: At. Mol. Opt. Phys.* **35**, R147R193 (2002).
- [15] M. Grifoni and P. Hänggi, *Physics Reports* **304**, 229 (1998).
- [16] R. Bavli and H. Metiu, *Phys. Rev. Lett.* **69**, 1986 (1992).
- [17] P. Neu and R. J. Silbey, *Phys. Rev. A* **54**, 5323 (1996).
- [18] Q. Su and J. H. Eberly, *Phys. Rev. A* **43**, 2474 (1991).
- [19] I. Bialynicki-Birula, M. Kaliński, and J. H. Eberly, *Phys. Rev. Lett.* **73**, 1777 (1994).
- [20] J. H. Eberly and K. C. Kulander, *Science* **262**, 1229 (1993).
- [21] B. Piraux and R. M. Potvliege, *Phys. Rev. A* **57**, 5009 (1998).

- [22] M. Pont and M. Gavrila, *Phys. Rev. Lett.* **65**, 2362 (1990).
- [23] J. Zakrzewski and D. Delande, *J. Phys. B: At. Mol. Opt. Phys.* **28**, L667 (1995).
- [24] M. Holthaus, *Chaos, Solitons & Fractals No 5* **7**, 1143 (1995).
- [25] A. Buchleitner, D. Delande, and J. Zakrzewski, *Physics Reports* **368**, 409547 (2002).
- [26] S. Denisov, L. Morales-Molina, S. Flach, and P. Hänggi, *Phys. Rev. A* **75**, 063424 (2007).
- [27] A. Auerbach and G. V. Pai, *Phys. Rev. B* **76**, 205318 (2007).
- [28] D. Poletti, G. Benenti, G. Casati, P. Hänggi, and B. Li, *Phys. Rev. Lett.* **102**, 130604 (2009).
- [29] T. Salger, S. Kling, S. Denisov, A. V. Ponomarev, P. Hänggi, and M. Weitz, *Phys. Rev. Lett.* **110**, 135302 (2013).
- [30] S. Denisov, S. Flach, and P. Hänggi, *Physics Reports* **538**, 77120 (2014).
- [31] C. Grossert, M. Leder, S. Denisov, P. Hänggi, and M. Weitz, *Nature Comm.* **7**, 10440 (2016).
- [32] N. Goldman and J. Dalibard, *Phys. Rev. X* **4**, 031027 (2014).
- [33] M. Bukov, L. D'Alessio, and A. Polkovnikov, *Advances in Physics* **64**, 139 (2015).
- [34] V. M. Bastidas, C. Emery, B. Regler, and T. Brandes, *Phys. Rev. Lett.* **108**, 043003 (2012).
- [35] V. M. Bastidas, C. Emery, G. Schaller, and T. Brandes, *Phys. Rev. A* **86**, 063627 (2012).
- [36] G. Engelhardt, V. M. Bastidas, C. Emery, and T. Brandes, *Phys. Rev. E* **87**, 052110 (2013).
- [37] V. M. Bastidas, P. Pérez-Fernández, M. Vogl, and T. Brandes, *Phys. Rev. Lett.* **112**, 140408 (2014).
- [38] T. Kitagawa, T. Oka, A. Brataas, L. Fu, and E. Demler, *Phys. Rev. B* **84**, 235108 (2011).
- [39] T. Oka and H. Aoki, *Phys. Rev. B* **79**, 081406 (2009).
- [40] B. M. Fregoso, J. P. Dahlhaus, and J. E. Moore, *Phys. Rev. B* **90**, 155127 (2014).
- [41] D. H. Dunlap and V. M. Kenkre, *Phys. Rev. B* **34**, 3625 (1986).
- [42] D. H. Dunlap and V. M. Kenkre, *Phys. Rev. B* **37**, 6622 (1988).

- [43] H. Lignier, C. Sias, D. Ciampini, Y. Singh, A. Zenesini, O. Morsch, and E. Arimondo, *Phys. Rev. Lett.* **99**, 220403 (2007).
- [44] C. Sias, H. Lignier, Y. P. Singh, A. Zenesini, D. Ciampini, O. Morsch, and E. Arimondo, *Phys. Rev. Lett.* **100**, 040404 (2008).
- [45] A. Eckardt, M. Holthaus, H. Lignier, A. Zenesini, D. Ciampini, O. Morsch, and E. Arimondo, *Phys. Rev. A* **79**, 013611 (2009).
- [46] A. Zenesini, H. Lignier, D. Ciampini, O. Morsch, and E. Arimondo, *Phys. Rev. Lett.* **102**, 100403 (2009).
- [47] C. E. Creffield, F. Sols, D. Ciampini, O. Morsch, and E. Arimondo, *Phys. Rev. A* **82**, 035601 (2010).
- [48] J. Struck, C. Ölschläger, R. Le Targatn, P. Soltan- Panahi, A. Eckardt, M. Lewenstein, P. Windpassinger, and K. Sengstock, *Science* **333** (6045), 996 (2011).
- [49] J. Struck, C. Ölschläger, M. Weinberg, P. Hauke, J. Simonet, A. Eckardt, M. Lewenstein, K. Sengstock, and P. Windpassinger, *Phys. Rev. Lett.* **108**, 225304 (2012).
- [50] P. Hauke, O. Tielemann, A. Celi, C. Ölschläger, J. Simonet, J. Struck, M. Weinberg, P. Windpassinger, K. Sengstock, M. Lewenstein, and A. Eckardt, *Phys. Rev. Lett.* **109**, 145301 (2012).
- [51] J. Struck, M. Weinberg, C. Ölschläger, P. Windpassinger, J. Simonet, K. Sengstock, R. Höppner, P. Hauke, A. Eckardt, M. Lewenstein, and L. Mathey, *Nature Physics* **9**, 738 (2013).
- [52] M. Aidelsburger, M. Atala, M. Lohse, J. T. Barreiro, B. Paredes, and I. Bloch, *Phys. Rev. Lett.* **111**, 185301 (2013).
- [53] H. Miyake, G. A. Siviloglou, C. J. Kennedy, W. C. Burton, and W. Ketterle, *Phys. Rev. Lett.* **111**, 185302 (2013).
- [54] M. Atala, M. Aidelsburger, M. Lohse, J. T. Barreiro, B. Paredes, and I. Bloch, *Nature Physics* **10**, 588 (2014).
- [55] C. J. Kennedy, W. C. Burton, W. C. Chung, and W. Ketterle, *Nature Physics* **11**, 859 (2015).
- [56] G. Jotzu, M. Messer, R. Desbuquois, M. Lebrat, T. Uehlinger, D. Greif, and T. Esslinger, *Nature* **515**, 237 (2014).
- [57] M. Aidelsburger, M. Lohse, C. Schweizer, M. Atala, J. T. Barreiro, S. Nascimbène, N. R. Cooper, I. Bloch, and N. Goldman, *Nature Physics* **11**, 162 (2015).
- [58] N. Fläschner, B. S. Rem, M. Tarnowski, D. Vogel, D.-S. Lühmann, K. Sengstock, and C. Weitenberg, *Science* **352**, 1091 (2016).

- [59] T. Mikami, S. Kitamura, K. Yasuda, N. Tsuji, T. Oka, and H. Aoki, *Phys. Rev. B* **93**, 144307 (2016).
- [60] G. Jotzu, M. Messer, F. Görg, D. Greif, R. Desbuquois, and T. Esslinger, *Phys. Rev. Lett.* **115**, 073002 (2015).
- [61] M. S. Rudner, N. H. Lindner, E. Berg, and M. Levin, *Phys. Rev. X* **3**, 031005 (2013).
- [62] N. H. Lindner, E. Berg, and M. S. Rudner, *arXiv* , 1603.03053 (2016).
- [63] K. Jiménez-García, L. J. LeBlanc, R. A. Williams, M. C. Beeler, C. Qu, M. Gong, C. Zhang, and I. B. Spielman, *Phys. Rev. Lett.* **114**, 125301 (2015).
- [64] V. Galitski and I. B. Spielman, *Nature* **494**, 49 (2013).
- [65] Y. H. Wang, H. Steinberg, P. Jarillo-Herrero, and N. Gedik, *Science* **342**, 453 (2013).
- [66] M. C. Rechtsman, J. M. Zeuner, Y. Plotnik, Y. Lumer, D. Podolsky, F. Dreisow, S. Nolte, M. Segev, and A. Szameit, *Nature* **496**, 196 (2013).
- [67] M. Hafezi, *Phys. Rev. Lett.* **112**, 210405 (2014).
- [68] S. Mittal, J. Fan, S. Faez, A. Migdall, J. M. Taylor, and M. Hafezi, *Phys. Rev. Lett.* **113**, 087403 (2014).
- [69] A. G. Grushin, Á. Gómez-León, and T. Neupert, *Phys. Rev. Lett.* **112**, 156801 (2014).
- [70] T. Dubček, C. J. Kennedy, L. Lu, W. Ketterle, M. Soljačić, and H. Buljan, *Phys. Rev. Lett.* **114**, 225301 (2015).
- [71] A. V. Ponomarev, S. Denisov, and P. Hänggi, *Journal of Computational and Theoretical Nanoscience* **7**, 2441 (2010).
- [72] A. V. Ponomarev, S. Denisov, and P. Hänggi, *Phys. Rev. Lett.* **102**, 230601 (2009).
- [73] R. Blatt and C. F. Roos, *Nature Physics* **8**, 277 (2012).
- [74] T. Prosen, *Phys. Rev. Lett.* **80**, 1808 (1998).
- [75] T. Prosen, *Phys. Rev. E* **60**, 3949 (1999).
- [76] M. Bukov and M. Heyl, *Phys. Rev. B* **86**, 054304 (2012).
- [77] L. D’Alessio and A. Polkovnikov, *Annals of Physics* **333**, 19 (2013).
- [78] L. D’Alessio and M. Rigol, *Phys. Rev. X* **4**, 041048 (2014).
- [79] P. Ponte, A. Chandran, Z. Papić, and D. A. Abanin, *Annals of Physics* **353**, 196 (2015).
- [80] A. Lazarides, A. Das, and R. Moessner, *Phys. Rev. E* **90**, 012110 (2014).

- [81] G. Floquet, *Annales de l'École Normale Supérieure* **12**, 4788 (1883).
- [82] M. M. Maricq, *Phys. Rev. B* **25**, 6622 (1982).
- [83] M. M. Maricq, *Phys. Rev. B* **37**, 7215 (1988).
- [84] W. Magnus, *Commun. Pure Appl. Math.* **VII**, 649 (1954).
- [85] A. Verdeny, A. Mielke, and F. Mintert, *Phys. Rev. Lett.* **111**, 175301 (2013).
- [86] N. Goldman, J. Dalibard, M. Aidelsburger, and N. R. Cooper, *Phys. Rev. A* **91**, 033632 (2015).
- [87] A. Eckardt and E. Anisimovas, *New. J. Phys.* **17**, 093039 (2015).
- [88] D. Jaksch and P. Zoller, *Ann. Phys.* **315**, 52 (2005).
- [89] S. Blanes, F. Casas, J. A. Oteo, and J. Ros, *Physics Reports* **470**, 151 (2009).
- [90] T. P. Grozdanov and M. J. Raković, *Phys. Rev. A* **38**, 1739 (1988).
- [91] P. Hänggi, *Driven Quantum Systems* (2016).
- [92] C. Xu, A. Poudel, and M. G. Vavilov, *Phys. Rev. A* **89**, 052102 (2014).
- [93] J. P. Dahlhaus, B. M. Fregoso, and J. E. Moore, *Phys. Rev. Lett.* **114**, 246802 (2015).
- [94] G. Casati, B. V. Chirikov, F. M. Izrailev, and J. Ford, *Lecture Notes in Physics*, Springer N.Y. **93**, 334 (1979).
- [95] B. V. Chirikov, *Research concerning the theory of nonlinear resonance and stochasticity*, Institute of Nuclear Physics, Novosibirsk **267** (1969).
- [96] M. Bandyopadhyay and S. Dattagupta, *Pramana – J. of Phys.* **70**, No 3, 381398 (2008).
- [97] T. Mori, *Phys. Rev. A* **91**, 020101 (2015).
- [98] T. Mori, T. Kuwahara, and K. Saito, *Phys. Rev. Lett.* **116**, 120401 (2016).
- [99] A. Alvermann and H. Fehske, *J. Comp. Phys.* **230**, 59305956 (2011).
- [100] D. A. Abanin, W. De Roeck, and F. Huveneers, *Phys. Rev. Lett.* **115**, 256803 (2015).
- [101] T. Kuwahara, T. Mori, and K. Saito, *Annals of Physics* **367**, 96 (2016).
- [102] D. Abanin, W. De Roeck, and W. W. Ho, *arXiv* , 1510.03405 (2015).
- [103] A. Russomanno, A. Silva, and G. E. Santoro, *Phys. Rev. Lett.* **109**, 257201 (2012).
- [104] A. Lazarides, A. Das, and R. Moessner, *Phys. Rev. Lett.* **112**, 150401 (2014).

- [105] M. Bukov, M. Kolodrubetz, and A. Polkovnikov, *Phys. Rev. Lett.* **116**, 125301 (2016).
- [106] R. Citro, E. G. Dalla Torre, L. D’Alessio, A. Polkovnikov, M. Babadi, T. Oka, and E. Demler, *Annals of Physics* **360**, 694 (2015).
- [107] B. L. Altshuler, Y. Gefen, A. Kamenev, and L. S. Levitov, *Phys. Rev. Lett.* **78**, 2803 (1997).
- [108] I. V. Gornyi, A. D. Mirlin, and D. G. Polyakov, *Phys. Rev. Lett.* **95**, 206603 (2005).
- [109] D. M. Basko, I. L. Aleiner, and B. L. Altshuler, *Annals of Physics* **321**, 1126 (2006).
- [110] V. Oganesyan and D. A. Huse, *Phys. Rev. B* **75**, 155111 (2007).
- [111] A. Pal and D. A. Huse, *Phys. Rev. B* **82**, 174411 (2010).
- [112] J. Z. Imbrie, *arXiv* , 1403.7837 (2014).
- [113] T. Prosen, *J. Phys. A: Math. Gen.* **31**, L645 (1998).
- [114] M. Heyl and S. Kehrein, *Phys. Rev. B* **81**, 144301 (2010).
- [115] I. Towers and B. A. Malomed, *J. Opt. Soc. Am. B* **19**, 537 (2002).
- [116] F. K. Abdullaev, J. G. Caputo, R. A. Kraenkel, and B. A. Malomed, *Phys. Rev. A* **67**, 013605 (2003).
- [117] H. Saito and M. Ueda, *Phys. Rev. Lett.* **90**, 040403 (2003).
- [118] M. Matuszewski, E. Infeld, B. A. Malomed, and M. Trippenbach, *Phys. Rev. Lett.* **95**, 050403 (2005).
- [119] B. A. Malomed, *Soliton management in periodic systems* (Springer: New York, 2006).
- [120] G. Casati, I. Guarneri, and G. Mantica, *Phys. Rev. A* **50**, 5018 (1994).
- [121] H. Wiedemann, J. Mostowski, and F. Haake, *Phys. Rev. A* **49**, 1171 (1994).
- [122] M. Gavrila, *Atoms in Intense Laser Fields* (Academic Press, New York, 1992).
- [123] C. O. Reinhold, J. Burgdörfer, M. T. Frey, and F. B. Dunning, *Phys. Rev. Lett.* **79**, 5226 (1997).
- [124] O. M. Braun and Y. S. Kivshar, *Physics Reports* **306**, 1 (1998).
- [125] J. J. Sakurai, *Modern Quantum Mechanics* (Addison–Wesley, New York, 1993).
- [126] A. H. Castro Neto, F. Guinea, N. M. R. Peres, K. S. Novoselov, and A. K. Geim, *Rev. Mod. Phys.* **81**, 109 (2009).
- [127] A. A. Burkov and L. Balents, *Phys. Rev. Lett.* **107**, 127205 (2011).

- [128] T. Uehlinger, G. Jotzu, M. Messer, D. Greif, W. Hofstetter, U. Bissbort, and T. Esslinger, *Phys. Rev. Lett.* **111**, 185307 (2013).
- [129] L. Tarruell, D. Greif, T. Uehlinger, G. Jotzu, and T. Esslinger, *Nature* **483**, 302 (2013).
- [130] B. M. Anderson, I. B. Spielman, and G. Juzeliūnas, *Phys. Rev. Lett.* **111**, 125301 (2013).
- [131] Z.-F. Xu, L. You, and M. Ueda, *Phys. Rev. A* **87**, 063634 (2013).
- [132] J. Struck, J. Simonet, and K. Sengstock, *Phys. Rev. A* **90**, 031601 (2014).
- [133] S. Zhang, W. S. Cole, A. Paramekanti, and N. Trivedi, *arXiv:1411.2297* (2014).
- [134] A. López, Z. Z. Sun, and J. Schliemann, *Phys. Rev. B* **85**, 205428 (2012).
- [135] P. Plötz, P. Schlagheck, and S. Wimberger, *Euro Phys. J D* **63**, 47 (2011).
- [136] P. Plötz and S. Wimberger, *Euro Phys. J D* **63**, pp 199205 (2011).
- [137] R. Diener and Q. Niu, *J. Opt. B: Quantum Semiclass. Opt.* **2**, 618627 (2000).
- [138] N. Gemelke, E. Sarajlic, Y. Bidel, S. Hong, and S. Chu, *Phys. Rev. Lett.* **95**, 170404 (2005).
- [139] A. Eckardt, C. Weiss, and M. Holthaus, *Phys. Rev. Lett.* **95**, 260404 (2005).
- [140] D. Ciampini, O. Morsch, and E. Arimondo, *Int. J. Quantum Inform.* **09**, 139 (2011).
- [141] C. E. Creffield and F. Sols, *Phys. Rev. A* **84**, 023630 (2011).
- [142] C. E. Creffield and F. Sols, *Phys. Rev. A* **90**, 023636 (2014).
- [143] N. Goldman, G. Juzeliunas, P. Ohberg, and I. B. Spielman, *Rep. Prog. Phys.* **77**, 126401 (2014).
- [144] C. V. Parker, L.-C. Ha, and C. Chin, *Nature Physics* **9**, 769774 (2013).
- [145] A. Eckardt, P. Hauke, P. Soltan-Panahi, C. Becker, K. Sengstock, and M. Lewenstein, *EPL* **89**, 10010 (2010).
- [146] M. Hafezi, A. S. Sørensen, E. Demler, and M. D. Lukin, *Phys. Rev. A* **76**, 023613 (2007).
- [147] T. Iadecola, D. Campbell, C. Chamon, C.-Y. Hou, R. Jackiw, S.-Y. Pi, and S. V. Kusminskiy, *Phys. Rev. Lett.* **110**, 176603 (2013).
- [148] V. M. Bastidas, C. Emery, G. Schaller, A. Gómez-León, G. Platero, and T. Brandes, *arXiv* , 1302.0781 (2013).
- [149] N. H. Lindner, G. Refael, and V. Galitski, *Nat. Phys.* **7**, 490 (2011).

- [150] A. Verdeny and F. Mintert, *Phys. Rev. A* **92**, 063615 (2015).
- [151] M. Di Liberto, C. E. Creffield, G. I. Japaridze, and C. M. Smith, *Phys. Rev. A* **89**, 013624 (2014).
- [152] S. Greschner, G. Sun, D. Poletti, and L. Santos, *Phys. Rev. Lett.* **113**, 215303 (2014).
- [153] J. Gong, L. Morales-Molina, and P. Hänggi, *Phys. Rev. Lett.* **103**, 133002 (2009).
- [154] T. Wang, X.-F. Zhang, F. E. A. d. Santos, S. Eggert, and A. Pelster, *Phys. Rev. A* **90**, 013633 (2014).
- [155] E. Arimondo, D. Ciampini, A. Eckardt, M. Holthaus, and O. Morsch, *Adv. At. Mol. Opt. Phys.* **61**, 515 (2012).
- [156] C. Sias, H. Lignier, Y. P. Singh, A. Zenesini, D. Ciampini, O. Morsch, and E. Arimondo, *Phys. Rev. Lett.* **100**, 040404 (2008).
- [157] A. Eckardt and M. Holthaus, *Phys. Rev. Lett.* **101**, 245302 (2008).
- [158] A. Zenesini, H. Lignier, O. Morsch, D. Ciampini, and E. Arimondo, *Laser Physics* **20**, 1182 (2010).
- [159] E. J. Mueller, *Phys. Rev. A* **70**, 041603 (2004).
- [160] M. Bukov and A. Polkovnikov, *Phys. Rev. A* **90**, 043613 (2014).
- [161] P. G. Harper, *Proc. Phys. Soc. London Sect. A* **68**, 874 (1955).
- [162] D. R. Hofstadter, *Phys. Rev. B* **14**, 2239 (1976).
- [163] A. R. Kolovsky, *EPL* **93**, 20003 (2011).
- [164] C. E. Creffield and F. Sols, *EPL* **101**, 40001 (2013).
- [165] S. Choudhury and E. J. Mueller, *Phys. Rev. A* **91**, 023624 (2015).
- [166] S. Choudhury and E. J. Mueller, *Phys. Rev. A* **92**, 063639 (2015).
- [167] M. Bukov, S. Gopalakrishnan, M. Knap, and E. Demler, *Phys. Rev. Lett.* **115**, 205301 (2015).
- [168] T. Bilitewski and N. R. Cooper, *Phys. Rev. A* **91**, 033601 (2015).
- [169] T. Bilitewski and N. R. Cooper, *Phys. Rev. A* **91**, 063611 (2015).
- [170] H. M. Price and N. R. Cooper, *Phys. Rev. A* **85**, 033620 (2012).
- [171] Z. Yan, B. Li, X. Yang, and S. Wan, *Scientific Reports* **5**, 16197 (2015).
- [172] P. M. Perez-Piskunow, G. Usaj, C. A. Balseiro, and L. E. F. F. Torres, *Phys. Rev. B* **89**, 121401 (2014).

- [173] G. Usaj, P. M. Perez-Piskunow, L. E. F. Foa Torres, and C. A. Balseiro, *Phys. Rev. B* **90**, 115423 (2014).
- [174] E. Suárez Morell and L. E. F. Foa Torres, *Phys. Rev. B* **86**, 125449 (2012).
- [175] H. L. Calvo, H. M. Pastawski, S. Roche, and L. E. F. Foa Torres, *Applied Physics Letters* **98**, 232103 (2011).
- [176] M. A. Sentef, M. Claassen, A. F. Kemper, B. Moritz, T. Oka, J. K. Freericks, and T. P. Devereaux, *Nature Communications* **6**, 7047 (2015).
- [177] L. D'Alessio and M. Rigol, *Nature Communications* **6**, 8336 (2015).
- [178] P. M. Perez-Piskunow, L. E. F. Foa Torres, and G. Usaj, *Phys. Rev. A* **91**, 043625 (2015).
- [179] E. Anisimovas, G. Žlabys, B. M. Anderson, G. Juzeliūnas, and A. Eckardt, *Phys. Rev. B* **91**, 245135 (2015).
- [180] F. D. M. Haldane, *Phys. Rev. Lett.* **61**, 2015 (1988).
- [181] D. V. Khomitsky, L. V. Gulyaev, and E. Y. Sherman, *Phys. Rev. B* **85**, 125312 (2012).
- [182] T. Iadecola, L. H. Santos, and C. Chamon, *Phys. Rev. B* **92**, 125107 (2015).
- [183] A. Das, *Phys. Rev. B* **82**, 172402 (2010).
- [184] S. S. Hegde, H. Katiyar, T. S. Mahesh, and A. Das, *Phys. Rev. B* **90**, 174407 (2014).
- [185] A. R. Kolovsky and A. Buchleitner, *Phys. Rev. E* **68**, 056213 (2003).
- [186] A. R. Kolovsky, H. J. Korsch, and E.-M. Graefe, *Phys. Rev. A* **80**, 023617 (2009).
- [187] C. A. Parra-Murillo, J. Madroñero, and S. Wimberger, *Phys. Rev. A* **88**, 032119 (2013).
- [188] C. A. Parra-Murillo, J. Madroñero, and S. Wimberger, *Comput. Phys. Comm.* **186**, 19 (2015).
- [189] J. R. Schrieffer and P. A. Wolff, *Phys. Rev.* **149**, 491 (1966).
- [190] F. C. Zhang and T. M. Rice, *Phys. Rev. B* **37**, 3759 (1988).
- [191] S. Bravyi, D. Di Vincenzo, and D. Loss, *Ann. Phys.* **326**, 2793 (2011).
- [192] T. Barthel, C. Kasztelan, I. P. McCulloch, and U. Schollwöck, *Phys. Rev. A* **79**, 053627 (2009).
- [193] J. Keeling, *Quantum Magnetism, online lecture notes* (2015).

- [194] S. Trotzky, P. Cheinet, S. Fölling, M. Feld, U. Schnorrberger, A. M. Rey, A. Polkovnikov, E. A. Demler, M. D. Lukin, and I. Bloch, *Science* **319**, 295 (2008).
- [195] M. Nakagawa and N. Kawakami, *Phys. Rev. A* **89**, 013627 (2014).
- [196] J. H. Mentink, K. Balzer, and M. Eckstein, *Nature Comm.* **6**, 6708 (2015).
- [197] A. Bermudez and D. Porras, *New J. Phys.* **17**, 103021 (2015).
- [198] S. Teitel and C. Jayaprakash, *Phys. Rev. Lett.* **51**, 1999 (1983).
- [199] S. Ryu and D. Stroud, *Phys. Rev. Lett.* **78**, 4629 (1997).
- [200] N. H. Lindner, A. Auerbach, and D. P. Arovas, *Phys. Rev. Lett.* **102**, 070403 (2009).
- [201] N. Lindner, A. Auerbach, and D. P. Arovas, *Phys. Rev. B* **82**, 134510 (2010).
- [202] C. Wu, H.-d. Chen, J.-p. Hu, and S.-C. Zhang, *Phys. Rev. A* **69**, 043609 (2004).
- [203] Z. Cai, X. Zhou, and C. Wu, *Phys. Rev. A* **85**, 061605 (2012).
- [204] J. Radić, A. Di Ciolo, K. Sun, and V. Galitski, *Phys. Rev. Lett.* **109**, 085303 (2012).
- [205] W. S. Cole, S. Zhang, A. Paramekanti, and N. Trivedi, *Phys. Rev. Lett.* **109**, 085302 (2012).
- [206] M. Piraud, Z. Cai, I. P. McCulloch, and U. Schollwöck, *Phys. Rev. A* **89**, 063618 (2014).
- [207] Y.-F. Wang, Z.-C. Gu, C.-D. Gong, and D. N. Sheng, *Phys. Rev. Lett.* **107**, 146803 (2011).
- [208] N. Regnault and B. A. Bernevig, *Phys. Rev. X* **1**, 021014 (2011).
- [209] S. Kourtis and C. Castelnovo, *Phys. Rev. B* **91**, 155134 (2015).
- [210] C. Kollath, A. Iucci, I. P. McCulloch, and T. Giamarchi, *Phys. Rev. A* **74**, 041604 (2006).
- [211] S. D. Huber and A. Rüegg, *Phys. Rev. Lett.* **102**, 065301 (2009).
- [212] A. Tokuno and T. Giamarchi, *Phys. Rev. Lett.* **106**, 205301 (2011).
- [213] A. Tokuno and T. Giamarchi, *Phys. Rev. A* **85**, 061603 (2012).
- [214] D. Greif, L. Tarruell, T. Uehlinger, R. Jördens, and T. Esslinger, *Phys. Rev. Lett.* **106**, 145302 (2011).
- [215] R. Sensarma, D. Pekker, M. D. Lukin, and E. Demler, *Phys. Rev. Lett.* **103**, 035303 (2009).
- [216] N. Strohmaier, D. Greif, R. Jördens, L. Tarruell, H. Moritz, T. Esslinger, R. Sensarma, D. Pekker, E. Altman, and E. Demler, *Phys. Rev. Lett.* **104**, 080401 (2010).

- [217] F. Hassler and S. D. Huber, *Phys. Rev. A* **79**, 021607 (2009).
- [218] K. Balzer and M. Eckstein, *EPL* **107**, 57012 (2014).
- [219] P. Werner and M. Eckstein, *Struct. Dyn.* **3**, 023603 (2016).
- [220] M. Bello, C. E. Creffield, and G. Platero, *arXiv* , 1510.01379 (2015).
- [221] N. Tsuji, T. Oka, P. Werner, and H. Aoki, *Phys. Rev. Lett.* **106**, 236401 (2011).
- [222] L. Arrachea and A. A. Aligia, *Phys. Rev. Lett.* **73**, 2240 (1994).
- [223] A. A. Aligia, K. Hallberg, C. D. Batista, and G. Ortiz, *Phys. Rev. B* **61**, 7883 (2000).
- [224] A. A. Aligia and L. Arrachea, *Phys. Rev. B* **60**, 15332 (1999).
- [225] B. Bauer et al., *J. Stat. Mech.* **05**, P05001 (2011).
- [226] M. Dolfi, B. Bauer, S. Keller, A. Kosenkov, T. Ewart, A. Kantian, T. Giamarchi, and M. Troyer, *Comput. Phys. Commun.* **185**, 3430 (2014).
- [227] G. I. Japaridze and A. P. Kampf, *Phys. Rev. B* **59**, 12822 (1999).
- [228] S. Greschner, L. Santos, and D. Poletti, *Phys. Rev. Lett.* **113**, 183002 (2014).
- [229] K. Friedrichs, *Commun. Pure Appl. Math.* **1**, 361 (1948).
- [230] N. Yamada, K.-i. Noba, S. Tanaka, and T. Petrosky, *Phys. Rev. B* **86**, 014302 (2012).
- [231] K. Noba, N. Yamada, Y. Uesaka, S. Tanaka, and T. Petrosky, *J. Phys. A: Math. Theor.* **47**, 385302 (2010).
- [232] I. Bloch, *Nature Physics* **1**, 23 (2005).
- [233] I. Bloch, J. Dalibard, and W. Zwerger, *Rev. Mod. Phys.* **80**, 885 (2008).
- [234] D. Braak, *Phys. Rev. Lett.* **107**, 100401 (2011).
- [235] M. Tomka, O. El Araby, M. Pletyukhov, and V. Gritsev, *Phys. Rev. A* **90**, 063839 (2014).
- [236] M. Schiró, M. Bordyuh, B. Öztop, and H. E. Türeci, *Phys. Rev. Lett.* **109**, 053601 (2012).
- [237] H. Pichler, A. J. Daley, and P. Zoller, *Phys. Rev. A* **82**, 063605 (2010).
- [238] S. Weigert, *J. Phys. A: Math. Gen.* **35**, 41694181 (2002).
- [239] V. S. Popov and A. M. Perelomov, *Soviet Physics JETP* **30**, 1684 (1970).
- [240] P. Weinberg, M. Bukov, L. D'Alessio, A. Polkovnikov, S. Vajna, and M. Kolodrubetz, *arXiv* , 1606.02229 (2016).

- [241] L. D. Landau and E. M. Lifshitz, *Statistical Physics* (Elsevier, 2013).
- [242] R. Balian, *From Microphysics to Macrophysics* (Springer Verlag, 1992).
- [243] E. Farhi, J. Goldstone, S. Gutmann, and M. Sipser, *arXiv* , 0001106 (2000).
- [244] G. E. Santoro and E. Tosatti, *Journal of Physics A* **39**, R393 (2006).
- [245] A. Das and B. K. Chakrabarti, *Rev. Mod. Phys.* **80**, 1061 (2008).
- [246] A. Tannús, M. Garwood, *et al.*, *NMR in Biomedicine* **10**, 423 (1997).
- [247] M. Garwood and L. DelaBarre, *Journal of Magnetic Resonance* **153**, 155 (2001).
- [248] M. Silver, R. Joseph, C.-N. Chen, V. Sank, and D. Hoult, *Nature* , 681 (1984).
- [249] R. S. Staewen, A. J. Johnson, B. D. Ross, T. Parrish, H. Merkle, and M. Garwood, *Investigative radiology* **25**, 559 (1990).
- [250] M. Garwood and Y. Ke, *Journal of Magnetic Resonance* **94**, 511 (1991).
- [251] D. G. Norris and A. Haase, *Magnetic resonance in medicine* **9**, 435 (1989).
- [252] S. Hediger, B. Meier, and R. Ernst, *Chemical Physics Letters* **240**, 449 (1995).
- [253] M. R. Bendall, *Journal of Magnetic Resonance, Series A* **112**, 126 (1995).
- [254] T.-L. Hwang, P. C. van Zijl, and M. Garwood, *Journal of Magnetic Resonance* **124**, 250 (1997).
- [255] N. V. Vitanov, T. Halfmann, B. W. Shore, and K. Bergmann, *Annual review of physical chemistry* **52**, 763 (2001).
- [256] M. Bukov, M. Heyl, D. A. Huse, and A. Polkovnikov, *Phys. Rev. B* **93**, 155132 (2016).
- [257] D. Poletti and C. Kollath, *Phys. Rev. A* **84**, 013615 (2011).
- [258] G. Rigolin, G. Ortiz, and V. H. Ponce, *Phys. Rev. A* **78**, 052508 (2008).
- [259] C. De Grandi and A. Polkovnikov, *Quantum Quenching, Annealing and Computation* **802**, 75 (2010).
- [260] M. Kolodrubetz, P. Mehta, and A. Polkovnikov, *arXiv:1602.01062* (2016).
- [261] J. G. Kirkwood, *J. Chem. Phys.* **14**, 180 (1946).
- [262] R. Zwanzig, *J. Chem. Phys.* **40**, 2527 (1964).
- [263] M. V. Berry and J. M. Robbins, *Proceedings of the Royal Society of London A: Mathematical, Physical and Engineering Sciences* **442**, 659 (1993).
- [264] D. A. Sivak and G. E. Crooks, *Phys. Rev. Lett.* **108**, 190602 (2012).

- [265] L. D'Alessio and A. Polkovnikov, *Annals of Physics* **345**, 141 (2014).
- [266] R. H. Young and W. J. Deal, *Journal of Mathematical Physics* **11**, 3298 (1970).
- [267] H. P. Breuer and M. Holthaus, *Zeitschrift für Physik D Atoms, Molecules and Clusters* **11**, 1 (1989).
- [268] D. Viennot, G. Jolicard, J. P. Killingbeck, and M.-Y. Perrin, *Phys. Rev. A* **71**, 052706 (2005).
- [269] K. Dietz, M. Pröbsting, and L. Jaeger, *The Journal of Chemical Physics* **104**, 8943 (1996).
- [270] H. P. Breuer and M. Holthaus, *The Journal of Physical Chemistry* **97**, 12634 (1993).
- [271] H. P. Breuer, K. Dietz, and M. Holthaus, *Journal of Physics B: Atomic, Molecular and Optical Physics* **24**, 1343 (1991).
- [272] W. Gabriel and P. Rosmus, *The Journal of Physical Chemistry* **97**, 12644 (1993).
- [273] W. Jakubetz, B. Just, J. Manz, and H. J. Schreier, *The Journal of Physical Chemistry* **94**, 2294 (1990).
- [274] D. W. Hone, R. Ketzmerick, and W. Kohn, *Phys. Rev. A* **56**, 4045 (1997).
- [275] K. Drese and M. Holthaus, *The European Physical Journal D* **5**, 119 (1999).
- [276] L. D'Alessio, Y. Kafri, and A. Polkovnikov, *arXiv* , 1405.2077 (2015).
- [277] M. Kardar, *Statistical Physics of Particles* (Cambridge University Press, 2007).
- [278] S. Yang, S.-J. Gu, C.-P. Sun, and H.-Q. Lin, *Phys. Rev. A* **78**, 012304 (2008).
- [279] B. Damski, *Phys. Rev. E* **87**, 052131 (2013).
- [280] J. P. Provost and G. Vallee, *Commun. in Math. Phys.* **76**, 289 (1980).
- [281] P. Zanardi, P. Giorda, and M. Cozzini, *Phys. Rev. Lett.* **99**, 100603 (2007).
- [282] M. Kolodrubetz, V. Gritsev, and A. Polkovnikov, *Phys. Rev. B* **88**, 064304 (2013).
- [283] Y. Liao and M. S. Foster, *Phys. Rev. A* **92**, 053620 (2015).
- [284] A. Chandran and S. L. Sondhi, *Phys. Rev. B* **93**, 174305 (2016).
- [285] V. Gritsev and A. Polkovnikov, *PNAS* **109**, 6457 (2012).
- [286] L. D'Alessio and M. Rigol, *Nat. Commun.* **6**, 8336 (2015).
- [287] C. De Grandi, A. Polkovnikov, and A. W. Sandvik, *J. Phys.: Condens. Matter* **25**, 404216 (2013).
- [288] A. Russomanno and E. G. Dalla Torre, *arXiv* , 1510.08866 (2015).

- [289] V. Khemani, R. Nandkishore, and S. L. Sondhi, *Nature Physics* **11**, 560 (2015).
- [290] H. Dehghani, T. Oka, and A. Mitra, *Phys. Rev. B* **91**, 155422 (2015).
- [291] H. Dehghani and A. Mitra, *Phys. Rev. B* **92**, 165111 (2015).
- [292] M. D. Schroer, M. H. Kolodrubetz, W. F. Kindel, M. Sandberg, J. Gao, M. R. Vissers, D. P. Pappas, A. Polkovnikov, and K. W. Lehnert, *Phys. Rev. Lett.* **113**, 050402 (2014).
- [293] P. Roushan, C. Neill, Y. Chen, M. Kolodrubetz, C. Quintana, N. Leung, M. Fang, R. Barends, B. Campbell, Z. Chen, B. Chiaro, A. Dunsworth, E. Jeffrey, J. Kelly, A. Megrant, J. Mutus, P. J. J. O’Malley, D. Sank, A. Vainsencher, J. Wenner, T. White, A. Polkovnikov, A. N. Cleland, and J. M. Martinis, *Nature* **515**, 7526 (2014).
- [294] D. J. Thouless, *Phys. Rev. B* **27**, 6083 (1983).
- [295] S. Sachdev, *Quantum Phase Transitions* (Cambridge University Press, New York, 1997).
- [296] V. M. Bastidas, C. Emary, G. Schaller, and T. Brandes, *Phys. Rev. A* **86**, 063627 (2012).
- [297] A. Russomanno, R. Fazio, and G. E. Santoro, *EPL* **110**, 37005 (2015).
- [298] A. Russomanno, G. E. Santoro, and R. Fazio, *arXiv* , 1603.03663 (2016).
- [299] A. Russomanno, S. Sharma, A. Dutta, and G. E. Santoro, *Jour. Stat. Mech.* **P08030** (2015).
- [300] A. Russomanno, A. Silva, and G. E. Santoro, *Jour. Stat. Mech.* **P09012** (2013).
- [301] H. Kim and D. A. Huse, *Phys. Rev. Lett.* **111**, 127205 (2013).
- [302] V. Novicenko, E. Anisimovas, and G. Juzeliūnas, *arXiv* , 1608.08420 (2015).
- [303] T. Prosen, *Phys. Rev. E* **65**, 036208 (2002).
- [304] E. Canovi, M. Kollar, and M. Eckstein, *Phys. Rev. E* **93**, 012130 (2016).
- [305] J. M. Deutsch, *Phys. Rev. A* **43**, 2046 (1991).
- [306] M. Srednicki, *Phys. Rev. E* **50**, 888 (1994).
- [307] M. Rigol, V. Dunjko, and M. Olshanii, *Nature* **452**, 854 (2008).
- [308] L. D’Alessio, Y. Kafri, A. Polkovnikov, and M. Rigol, *arXiv* , 1509.06411 (2015).
- [309] P. Ponte, Z. Papić, F. Huveneers, and D. A. Abanin, *Phys. Rev. Lett.* **114**, 140401 (2015).

- [310] J. Berges, S. Borsányi, and C. Wetterich, *Phys. Rev. Lett.* **93**, 142002 (2004).
- [311] J. M. Cornwall, R. Jackiw, and E. Tomboulis, *Phys. Rev. D* **10**, 2428 (1974).
- [312] J. Bauer, M. Babadi, and E. Demler, *Phys. Rev. B* **92**, 024305 (2015).
- [313] M. Babadi, E. Demler, and M. Knap, *Phys. Rev. X* **5**, 041005 (2015).
- [314] P. C. Hohenberg and P. C. Martin, *Ann. Phys. (N.Y.)* **34**, 291 (1965).
- [315] A. Griffin, *Phys. Rev. B* **53**, 9341 (1996).
- [316] A. M. Rey, B. L. Hu, E. Calzetta, A. Roura, and C. W. Clark, *Phys. Rev. A* **69**, 033610 (2004).
- [317] A. Kamenev, *Field Theory of Non-Equilibrium Systems* (Cambridge University Press, Cambridge, England, 2011).
- [318] J. Berges, *AIP Conf. Proc.* **3-62**, 739 (2005).
- [319] A. Buchleitner and A. R. Kolovsky, *Phys. Rev. Lett.* **91**, 253002 (2003).
- [320] A. Tomadin, R. Mannella, and S. Wimberger, *Phys. Rev. Lett.* **98**, 130402 (2007).
- [321] C. E. Creffield, *Phys. Rev. A* **79**, 063612 (2009).
- [322] A. Kolovsky, *EPL* **93**, 20003 (2011).
- [323] C. Zhang, J. Liu, M. G. Raizen, and Q. Niu, *Phys. Rev. Lett.* **92**, 054101 (2004).
- [324] T. Stöferle, H. Moritz, C. Schori, M. Köhl, and T. Esslinger, *Phys. Rev. Lett.* **92**, 130403 (2004).
- [325] C. Schori, T. Stöferle, H. Moritz, M. Köhl, and T. Esslinger, *Phys. Rev. Lett.* **93**, 240402 (2004).
- [326] M. Krämer, C. Tozzo, and F. Dalfovo, *Phys. Rev. A* **71**, 061602 (2005).
- [327] C. Tozzo, M. Krämer, and F. Dalfovo, *Phys. Rev. A* **72**, 023613 (2005).
- [328] I. Carusotto, R. Balbinot, A. Fabbri, and A. Recati, *Eur. Phys. J. D* **56**, 391 (2009).
- [329] B. Capogrosso-Sansone, i. m. c. G. m. c. Söyler, N. Prokof'ev, and B. Svistunov, *Phys. Rev. A* **77**, 015602 (2008).
- [330] M. Knap, E. Arrigoni, and W. von der Linden, *Phys. Rev. B* **81**, 024301 (2010).
- [331] S. Lellouch, M. Bükov, E. Demler, and N. Goldman, *arXiv* , 1610.02972 (2016).
- [332] M. Greiner, O. Mandel, T. W. Hänsch, and I. Bloch, *Nature (London)* **419**, 51 (2002).

- [333] M. Weinberg, C. Ölschläger, C. Sträter, S. Prelle, A. Eckardt, K. Sengstock, and J. Simonet, *Phys. Rev. A* **92**, 043621 (2015).
- [334] M. Moshe and J. Zinn-Justin, *Phys. Rep.* **385**, 69 (2003).
- [335] B. Sciolla and G. Biroli, *Phys. Rev. B* **88**, 201110 (2013).
- [336] P. Smacchia, M. Knap, E. Demler, and A. Silva, *Phys. Rev. B* **91**, 205136 (2015).
- [337] G. Benenti, G. Casati, T. Prosen, D. Rossini, and M. Žnidarič, *Phys. Rev. B* **80**, 035110 (2009).
- [338] T. N. Ikeda, N. Sakumichi, A. Polkovnikov, and M. Ueda, *Annals of Physics* **354**, 338 (2015).
- [339] A. Sen and K. Sengupta, *arXiv* , 1511.03668 (2015).
- [340] L. Zhang, H. Kim, and D. A. Huse, *Phys. Rev. E* **91**, 062128 (2015).
- [341] M. Srednicki, *J. Phys. A* **32**, 1163 (1999).
- [342] T. Iadecola, L. H. Santos, and C. Chamon, *Phys. Rev. B* **92**, 125107 (2015).
- [343] O. Bohigas, M. J. Giannoni, and C. Schmit, *Phys. Rev. Lett.* **52**, 1 (1984).
- [344] N. Regnault and R. Nandkishore, *Phys. Rev. B* **93**, 104209 (2016).
- [345] A. Roy and A. Das, *Phys. Rev. B* **91**, 121106 (2015).
- [346] M. Genske and A. Rosch, *Phys. Rev. A* **92**, 062108 (2015).
- [347] C. Sträter and A. Eckardt, *arXiv* , 1604.00850 (2016).
- [348] H.-P. Breuer, W. Huber, and F. Petruccione, *Phys. Rev. E* **61**, 4883 (2000).
- [349] R. Ketzmerick and W. Wustmann, *Phys. Rev. E* **82**, 021114 (2010).
- [350] D. Vorberg, W. Wustmann, R. Ketzmerick, and A. Eckardt, *Phys. Rev. Lett.* **111**, 240405 (2013).
- [351] T. Iadecola and C. Chamon, *Phys. Rev. B* **91**, 184301 (2015).
- [352] M. Langemeyer and M. Holthaus, *Phys. Rev. E* **89**, 012101 (2014).
- [353] H. Dehghani, T. Oka, and A. Mitra, *Phys. Rev. B* **90**, 195429 (2014).
- [354] T. Iadecola, T. Neupert, and C. Chamon, *Phys. Rev. B* **91**, 235133 (2015).
- [355] K. I. Seetharam, C.-E. Bardyn, N. H. Lindner, M. S. Rudner, and G. Refael, *arXiv* , 1502.02664 (2015).
- [356] W. Kohn, *J. of Stat. Phys.* **103**, 417 (2001).

- [357] D. W. Hone, R. Ketzmerick, and W. Kohn, *Phys. Rev. E* **79**, 051129 (2009).
- [358] T. Iadecola and C. Chamon, *Phys. Rev. B* **91**, 184301 (2015).
- [359] G. Rigolin and G. Ortiz, *Phys. Rev. A* **90**, 022104 (2014).
- [360] G. Rigolin and G. Ortiz, *Phys. Rev. Lett.* **104**, 170406 (2010).
- [361] G. Rigolin and G. Ortiz, *Phys. Rev. A* **85**, 062111 (2012).
- [362] M. Kolodrubetz, *Phys. Rev. Lett.* **117**, 015301 (2016).
- [363] J. E. Avron, M. Fraas, G. M. Graf, and P. Grec, *Commun. in Math. Phys.* **314**, 163 (1980).
- [364] J. E. Avron, *J Stat. Phys.* **148**(5), 800 (1980).
- [365] V. V. Albert, B. Bradlyn, M. Fraas, and L. Jiang, *arXiv:1512.08079* (2015).

Curriculum Vitae

<i>Contact</i>	Marin Georgiev Bukov Department of Physics, Boston University, 590 Commonwealth Ave, Boston, MA 02215, USA
<i>Education</i>	Ludwig-Maximilians-Universität München , B.Sc., Physics, October 2008 – July 2011. Thesis advisor: Stefan Kehrein. Ludwig-Maximilians-Universität München , B.Sc., Mathematics, October 2008 – July 2011. Thesis advisor: Laszlo Erdős. Ludwig-Maximilians-Universität and Technische Universität München , M.Sc. (<i>with high distinction</i>), Theoretical and Mathematical Physics, October 2011 – June 2013. Thesis advisor: Lode Pollet Boston University , PhD candidate, September 2013 – 2017. Thesis advisor: Anatoli Polkovnikov.
<i>Publications</i>	<ol style="list-style-type: none">1. M. Bukov and M. Heyl, <i>Parametric instability in periodically driven Luttinger liquids</i>, <i>Physical Review B</i> 86, 054304 (2012).2. M. Bukov and L. Pollet, <i>Mean-Field phase diagram of the Bose-Fermi-Hubbard model</i>, <i>Physical Review B</i> 89, 094502 (2014).3. M. Bukov and A. Polkovnikov, <i>Stroboscopic versus non-stroboscopic dynamics in the Floquet realization of the Harper-Hofstadter model</i>, <i>Physical Review A</i> 90, 043613 (2014).4. M. Bukov, L. D’Alessio and A. Polkovnikov, <i>Universal high-frequency behaviour of periodically driven systems: from dynamical stabilization to Floquet engineering</i>, <i>Advances in Physics</i>, 2015, Vol. 64, No. 2, 139-226.5. M. Bukov, S. Gopalakrishnan, M. Knap and E. Demler, <i>Prethermal Floquet Steady States and Instabilities in the Periodically Driven, Weakly Interacting Bose-Hubbard Model</i>, <i>Physical Review Letters</i> 115, 205301 (2015).6. M. Bukov, M. Kolodrubetz and A. Polkovnikov, <i>The Schrieffer-Wolff Transformation for Periodically-Driven Systems: Strongly-Correlated Systems with Artificial Gauge Fields</i>, <i>Physical Review Letters</i> 116, 125301 (2016).7. M. Bukov, M. Heyl, D. A. Huse and A. Polkovnikov, <i>Heating and many-body resonances in a periodically-driven two-band system</i>, <i>Physical Review B</i> 93, 155132 (2016).

8. P. Weinberg, M. Bukov, L. D'Alessio, A. Polkovnikov, S. Vajna and M. Kolodrubetz, *Adiabatic Perturbation Theory and Geometry of Periodically Driven Systems*, [arXiv:1606.02229](https://arxiv.org/abs/1606.02229) (2016).
9. P. Weinberg and M. Bukov, *QuSpin: a Python Package for Dynamics and Exact Diagonalisation of Quantum Many Body Systems. part I: Spin Chains*, *SciPost Phys.* **2**, 003 (2017).
10. S. Lellouch, M. Bukov, E. Demler and N. Goldman, *Parametric Instability Rates in Periodically-Driven Band Systems*, *Physical Review X*